



Final Report
ONR Grant – N00014-02-1-0623

Office of Naval Research

Attn: Terry Ericson
Office of Naval Research
Arlington, VA 22203

Submitted By:

**Florida State University, Center for Advanced Power Systems,
2000 Levy Avenue, Tallahassee, FL 32310**

On Behalf of:

The Electric Ship Research and Development Consortium

Florida State University

Massachusetts Institute of Technology

Mississippi State University

University of South Carolina

University of Texas at Austin

Purdue University

United States Naval Academy

DECEMBER 19 2008

Technical POC

Dr. Steinar J. Dale, Director
Center for Advanced Power Systems
Florida State University
2000 Levy Ave
Tallahassee, FL 32310
Telephone: (850) 645-1183
Email: dale@caps.fsu.edu

1.	Contract Information	4
2.	Technical Section	4
3.	Power Systems	5
4.	Simulations and Early Design Tools	53
5.	Power train technology	168
6.	Thermal Management	215
7.	Controls	231
8.	ESRDC DESCRIPTION OF FACILITIES	270
	The Florida State University Center for Advanced Power Systems (CAPS) Research Facilities	270
	Purdue University Laboratory Facilities and Research Centers	271
	University of Texas Laboratory Facilities	273
	University of South Carolina Facilities and Laboratories	275
	Mississippi State University Research Capabilities	275
	Massachusetts Institute of Technology Research and Facilities Capabilities	276
9.	Publications (Oct 2002 – March 2008)	278
	Journals	278
	Theses/Dissertations	288
	Proceedings / Technical Reports	291
9.1.	Inventions	319
9.2.	Honors	320
9.3.	Book or Chapters	321
10.	Personnel Statistics (Oct 2002 – March 2008)	323

1. CONTRACT INFORMATION

Contract Number	N00014-02-1-0623
Title of Research	Electric Ship Research and Development Consortium
Principal Investigator	Steinar J. Dale
Organization	Florida State University, Center for Advanced Power Systems

C0- PI

- Chrys Chrysostomidis - Massachusetts Institute of Technology
- Roger Dougal University of South Carolina
- Robert Hebner University of Texas at Austin
- Noel Schulz Mississippi State University
- Scott sudhoff Purdue University
- Ed Zivi United States Naval Academy

2. TECHNICAL SECTION

Objectives

The Electric Ship Research and Development Consortium (ESRDC) objectives have been to develop and apply methodologies for the design and operation of the all-electric ship (AES), taking into account the multi-scale, multi-domain, and multi-disciplinary aspects of the problem. This project will provide methods, algorithms and corresponding software tools for design, especially early design. It is a fundamental tenet of complex system design that early decisions have very serious consequences, both in the later stages of design and development, and in the operation of the ship. ESRDC is accelerating the development and demonstration of technologies, modeling, and simulation tools to provide critical design and operational capabilities of AES program. The consortium continues to address the national shortage of electrical power engineers.

The work under this program addressed a broad spectrum of issues, related to the development of electric ship systems including methods and models for design and simulation of highly-integrated multidisciplinary ship systems, methods for power routing and control, methods for characterizing and understanding the performance of the electric plant, and methods for controlling the plant. It is impossible to capture the full breadth and depth of the research in this one report, so instead the report content has been developed to provide a detailed insight into some of the achievements in illustrative areas. The reader is then encouraged to review the list of publications at the end of this report to comprehend the full breadth of the achievements and to refer to the appropriate publications where this report provides insufficient information. Broadly speaking, the topics of this team's investigations can be classified into the categories of Simulation Tools, Power Systems, and Control Systems. Highlights in each of these areas are mentioned next.

3. POWER SYSTEMS

The focus for the power systems group centered on several areas. A notional base-line shipboard power system is developed. This notional next generation integrated power system (NGIPS) is modeled on Real-Time Digital Simulator (RTDS) at CAPS. High fidelity simulations on RTDS provided the base for various studies of dynamic scenarios in shipboard power systems, such as stability analysis, wide area protection, DC fault location, electrical-thermal system co-simulation, power quality study, and probabilistic study. The concept of the hardware in the loop is developed to include controller hardware in the loop (CHIL) and power hardware in the loop (PHIL). Hardware in the loop simulations were carried out for testing new equipment of interest by Navy, such as the 5MW high temperature superconducting prototype propulsion motor developed by AMSC for ONR. The test results provided important validation of the design tools and design methodologies for the design and manufacturing of a 36.5 MW full scale HTS propulsion motor by AMSC. During 2007, the ESRDC conducted a study an energy storage challenge problem for the all-electric ship. The final report included several important contributions, such as transient performance metrics for comparative studies of dispersed and centralized energy storage schemes, models of energy storage components and pulse load, and converter control dynamics. To improve the power hardware in the loop (PHIL) simulation capability, a 5MW ABB converter was installed at CAPS at the end of 2007. The installation of this converter will enable PHIL testing of equipment at voltage levels of 4.16kV AC and 1.15kV DC. Controller hardware in the loop (CHIL) simulations have been made to improve the controller performance of this 5MW voltage amplifier.

During the five-year period from 2003 to 2007, significant contributions were made to the notional integrated power system (IPS) for the next generation war ship. This included the development and validation of high fidelity models of the majority of the components in the notional IPS system and the zonal IFTP on the RTDS. Together, the 5MW PHIL facility and the RTDS constitute a core research and validation facility for further research work and hardware testing for the Navy shipboard power systems.

More extensive use of electric energy onboard ships is accompanied by a need to move a large amount of thermal energy that is dissipated in electrically driven loads, in power conversion devices, and in power generating devices. Our work on power systems thus encompasses not just the architecture of the electric power delivery network, but also the architecture of the thermal energy network, and the interactions between these two.

Thermal systems include not only the usual heat exchangers that cool power electronic equipment, but also the heat engines that utilize either primary heat or waste heat to drive production of electric energy. Our work in this area has focused on assessing the performance of integrated thermal systems such as combined cycle solid-oxide fuel cells that use heat engines to enhance energy recovery. This has led to development of transient thermal models for heat exchangers, heat engines such as turbo compressors and expanders, fluid piping systems, chillers or refrigeration units, and the development of component-wise models of gas turbine engines.

Power routing is as much a control issue and an information issue as it is a power system issue, and has been approached from that wholistic standpoint. Methods of power routing and load power management based on "agent" technologies have been explored in great detail, and tools to test those technologies in simulation and on hardware have been developed. A combined hardware/software testbed incorporates low-power (few kW) machinery, simulation environment, and Java agent technologies to develop these new methods for power routing. A combination of simulation agents, monitoring and diagnostic agents, and load agents have been defined and successfully tested to deal with local power shortages, graceful degradation of power, and load shedding.

Methods for assessing power quality based on time-frequency methods have been defined and applied to basic ship power system architectures. Metrics such as "harmonic distance" and "harmonic similarity" for power quality, and propagation of power quality disturbances, have been defined. These provide means for

characterizing the impact of specific loads on the performance of the power system, or for specifying the locations of active power filters to compensate for untoward load behaviors or interactions.

2.1.2 Key Accomplishments

- Developed a scheme for dynamic reconfiguration that respects stability, via a hybrid systems approach
- Broke new ground in optimization problems subject to power or communication constraints
- Developed a new set of power quality indices for transient events based on joint time-frequency signal analysis
- Utilized higher-order statistics to enhance the state-of-the-art of machine-condition monitoring
- Developed new methodologies for detection and analysis of interharmonics in shipboard power systems
- Developed a new matrix-based procedure for locating faults in power systems, using monitored voltage sag data at several nodes
- Characterized the interaction between voltage and current harmonics for the most common single-phase loads
- Developed a new technique to determine the penetration levels of power electronic loads on a power system from total load response to voltage sags
- Developed a load model for power electronic loads that is suitable for conventional power system stability studies.
 - Ship power system development
 - Modeling the notional base-line shipboard power system
 - Simulation aspects of the 5MW AMSC motor tests
 - Hardware in the loop simulations
 - Pulsed power management and energy storage
 - Stability analysis
 - Wide area differential protection for shipboard power systems
 - Fault location in ungrounded DC distribution systems
 - Impact of fault current limiters (FCL) for Navy shipboard power systems
 - Electrical-thermal system co-simulation
 - Advanced power quality management of the all-electric ship
 - Advanced signal processing tools for power quality analysis
 - Probabilistic aspects of all-electric ship system simulations and surrogate models
 - Analysis of Network Reconfiguration Potential

Ship Power System Development

Ship-system simulation activities continued with work to improve the baseline notional destroyer-class ship model, especially the nine-rack version that contains 5 distribution zones. The power electronics in those zones is a continuing area of study, with improved models for the choppers and rectifiers and their controls being implemented to provide better fidelity to a realistic system. Documentation took a major step forward with a comprehensive users guide that will make it easier for the increasing number of users who come to the existing system with a desire to test controls or power-systems concepts on an existing, sophisticated, simulation test bed. This documentation will continue to evolve and expand as CAPS' library of ship systems and subsystems improves in size and sophistication. A version of this manual was made available to the members of CAPS' industrial advisory board in order to provide them and their staffs with a fuller understanding of CAPS'

capabilities in ship-system simulation, as well as to provide them an opportunity to comment and advise on improvements.

Validation of this system is continuing in collaboration with the power systems group. The question of how to simulate power electronics as accurately as possible with CAPS' real-time simulator is being addressed through a systematic program of comparisons between simulations of standard power electronics configurations on the simulator and on other platforms. The new small-time-step capability for power electronics recently developed for the simulator, as well as the older long-time-step power-electronics models, provide opportunities for simulations of power electronics with various levels of speed and accuracy. The detailed comparisons of waveforms, spectra, etc., obtained with different simulation options will provide a guide on how to get the best results in different situations.

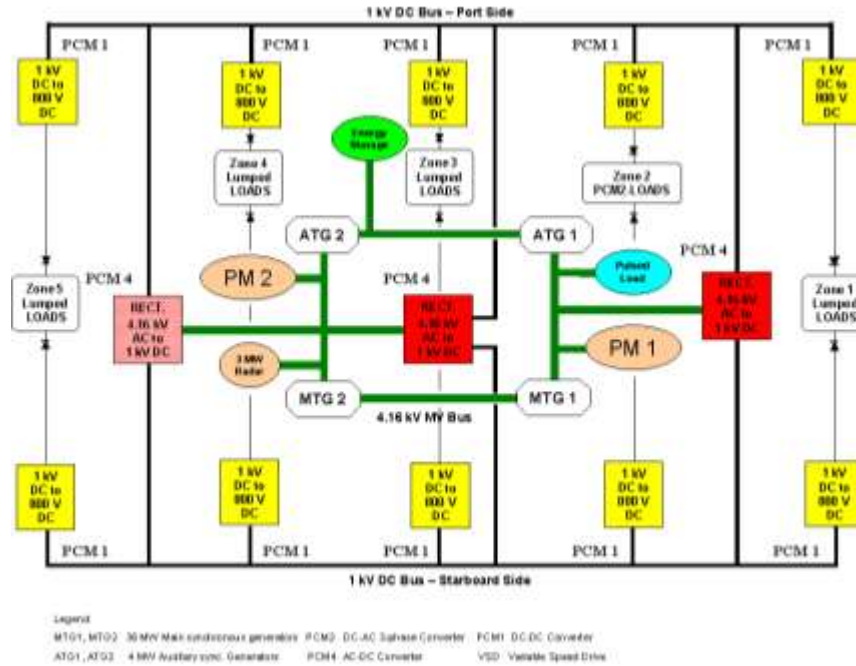


Figure 1 RTDS IPS Model Diagram

Modeling the notional base-line shipboard power system

In order to facilitate validation of the notional base-line shipboard power system model for RTDS, various uncertainty and sensitivity analysis techniques were investigated for applicability. Several techniques, including local, first order sensitivity methods, random sampling methods, the Morris factor screening method, and a fractional factorial experimental design were used to assess the relative influence of thirteen uncertain parameters for the ship system on six response variables for two different transient scenarios. While the results from each of the methods were similar, the experimental design approach provides a number of advantages in terms of flexibility and extensibility, as well as in the incorporation of system knowledge into the experimental process. Using geometric considerations, this provides a sequential approach to methodically gain more information about the system and refine the model with the addition of new simulation runs. At each stage in the process, the experimenter augments and extends the design based on available data and intuitive knowledge of the system. Thus, the experimenter is able to incorporate hypotheses about the system model into the design, but is able to validate or invalidate these hypotheses as the process proceeds. This allows a methodical sampling of the parameter space, as opposed to the random sampling employed by the other global techniques. This method is being used to construct response surfaces for each of the response variables for each scenario, from which

tolerance intervals can be constructed for each response based on probability distributions for the uncertain parameters.

Two types of problems in developing applications of large-scale ship-system simulations to design are discussed. The first is optimization of the component values for the filter between the test-bed controllable AC bus and a motor drive. A comparison of the spectra of the desired and actual voltage waveforms at the motor drive input is given. The second design problem is that of ship-wide control of the DDX-type ship system simulation being developed at CAPS. Design exercise shows the improvement possible with the current ship-wide control system and demonstrates the performance possibilities inherent in design optimization involving system-wide simulations, in this case of a controller that might be used to mitigate the effects of the loss of auxiliary generators.

Simulation aspects of the 5MW AMSC motor tests

AC loss determination experiments were performed, using sinusoidal torque variations. Additional variable load torque tests were conducted, including full ship propulsion modeling on the RTDS. Through RTDS control of the dynamometer, variable load torques that corresponded to a range of sea states were imposed on the AMSC motor shaft over a range of speeds. Testing focused on variable power tests, with the introduction of RTDS control to minimize AMSC power variation in a variable load torque environment. A series of tests designed to monitor the sensitivity of the motor to AC losses were conducted in hardware-in-the-loop tests with ship loading and sea state computed according to dynamic models, in real time, and the dynamometer controlled to supply this loading to the test motor. The simulator (RTDS) was responsible for computing the behavior of the ship's propeller under the influence of hydrodynamic forces, which includes modeling the motion of the ship and the sea state in order to account for the effect of these conditions on the load torque developed by the propeller.

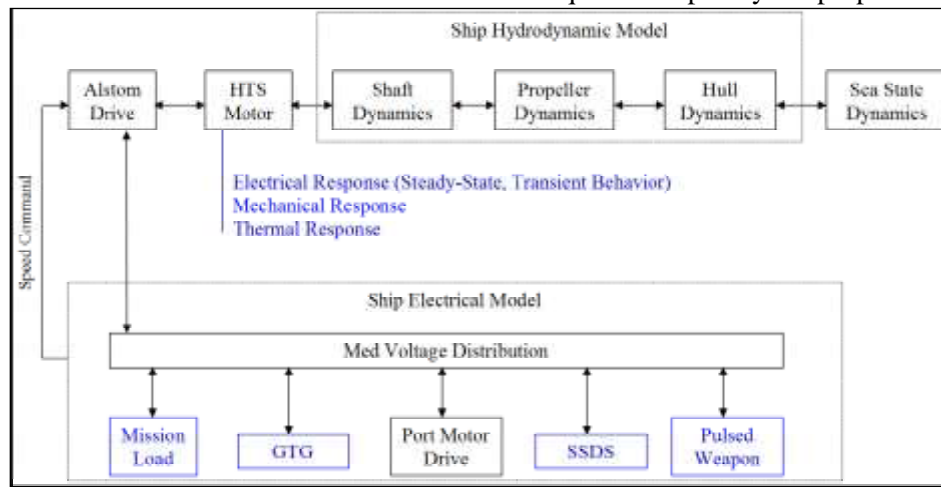


Figure 2 Torque Load Reference Provided by RTDS/ dynamometer based on Ship,

Hardware in the loop simulations

Interfacing algorithms and stability

A practical methodology was developed to evaluate the simulation accuracy effectively even for highly complex systems. Also, in 2007, the CHIL setup of the ABB-AC800PEC with RTDS was completed. A demo case for PHIL using the 16 kW Alstom MG set was developed. Several miscellaneous improvements and upgrades were made on the RTDS software and hardware. These improvements include upgrade of RSCAD

software & RTDS Interface firmware, new Component Builder software tested -- enables GPC and RPC custom model development, evaluation of GPC breakpoint method and scripting for case debugging and new co-simulation methods, and consideration of CAPS upgrade to an all-GPC system. Although support remains for the 110 3PC cards that CAPS owns, future enhancements to the RTDS will emphasize the GPC hardware shows the transfer function diagram for the interfaces of the PHIL simulations.

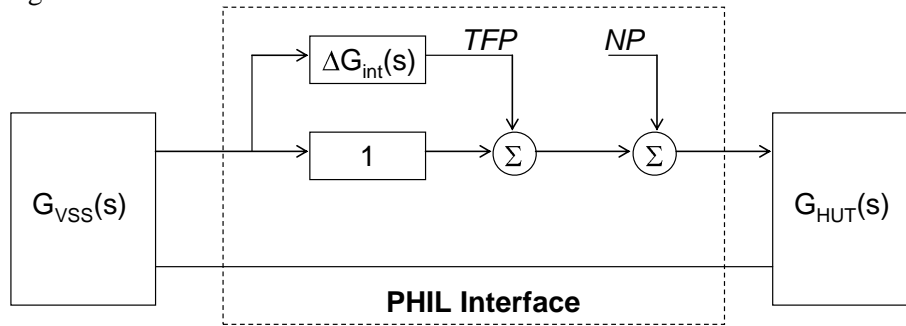


Figure 3 PHIL transfer function diagram

b) 50kW Power Electronic Building Blocks (PEBBs)

Before CAPS installed a 5 MW variable frequency, variable voltage converter (or power voltage amplifier) to enhance the experimental facility for ship propulsion motor testing, it is desired to first build a small-scale prototype to become familiar with the design, and gain necessary knowledge about the system. CAPS therefore carried out the 50 kW PEBB converter project. The 50kW converter was set up in CAPS's laboratory and utilizes a similar PEBB unit and controller to the 5MW converter. This setup can provide valuable insights into the technology and experiences for the future high-power testing.

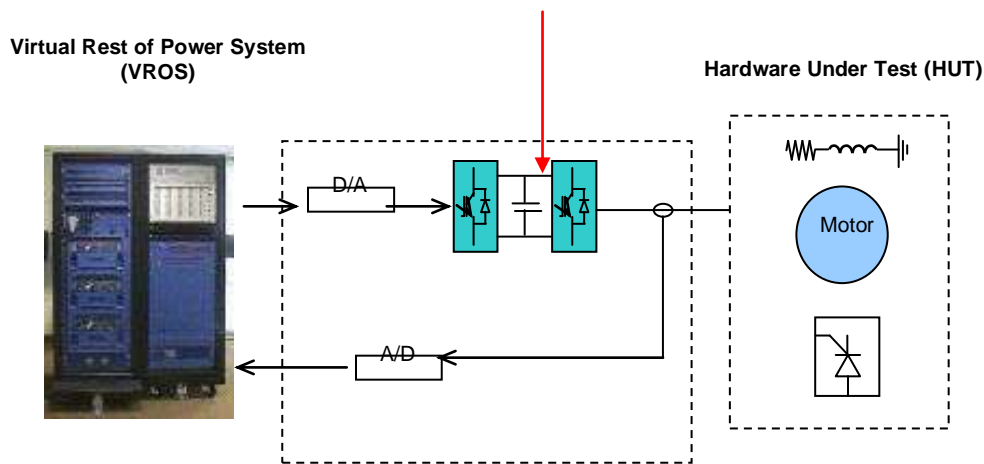


Figure 4 50kW PHIL set up

c) Controller improvement for the 5MW PEBB converter

The control algorithm for the inverter side of the PEBB converter was progressively improved during the first quarter of 2006. The improvements on RMS regulation and phase shift compensation in control were achieved on 50kW PEBB converter.

Controller parameter tuning was conducted on 5MW PEBB converter. Using simulation for evaluating and designing new controllers has been proven to be an efficient approach in a variety of power system and power electronics applications. In this research, we pushed this front even further to utilizing hardware-in-the-loop

with uncertainty considerations were considered. The detailed description of these issues can be found in the E-storage report submitted to ONR.

Table I List of metrics for comparison of energy storage options

Metric	Parameters of interest
Maximum voltage deviation	$sign(\pm) \times \max(V_{RMSn}(t) - 1) \times 100\%$, $n = 1, 2, \dots, N_{BUS}$,
Voltage stability	$\frac{V_n(t) - V_n(t-1)}{Q_n(t) - Q_n(t-1)}$ $n = 1, 2, \dots, N_{BUS}$
Sag energy	SE = $\Sigma[Ei] \times event\ duration$ where $Ei = \left[1 - \int_{event_start}^{event_end} \frac{Vi_event^2}{Vi_nom^2} dt \right] \times 100$, where V_{i_event} and V_{i_nom} are the magnitude of the voltage during the sag event and magnitude of nominal voltage respectively.
Asymmetry factor	$\left \frac{V_{peak}^+ - V_{peak}^-}{V_1} \right $, where V_{peak}^+ and V_{peak}^- are the positive and negative peaks respectively and V_1 is the peak of the fundamental of the voltage waveform
THD	$\max(THD_n(t))$, $n = 1, 2, \dots, N_{BUS}$. $THD_n = \sqrt{\frac{\sum_{k=2}^K V_k^2}{V_1^2}}$, where V_k is the magnitude of the k^{th} harmonic component and V_1 is the magnitude of the fundamental of the voltage waveform
Voltage RMS	$\sqrt{\frac{1}{T} \int_0^T v(t)^2 dt}$, where T is the period of the voltage waveform $v(t)$
Maximum frequency deviation	$sign(\pm) \times \max(f_n(t) - 1) \times 100\%$ $n = 1, 2, \dots, N_G$
Coherency	$\max(\theta_n(t)) - \min(\theta_n(t))$ $n = 1, 2, \dots, N_G$
Transient energy conversion	$\max(E_{kn} - E_{pn})$, $n = 1, 2, \dots, N_G$, where E_k and E_p (kinetic energy and potential energy) are defined
Transient recovery voltage	V_C , reference voltage a peak (crest) value in kV,

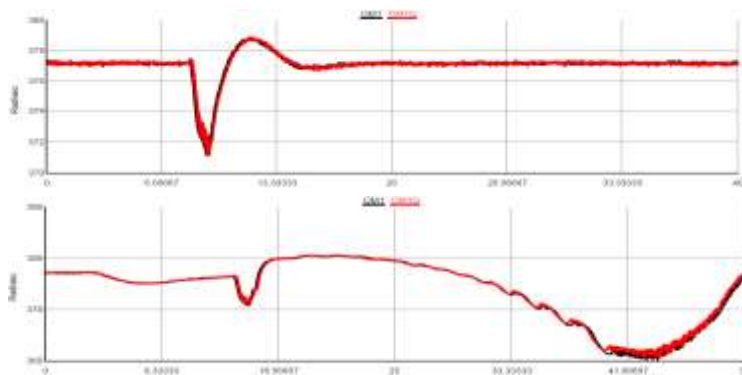
	t_3 , time to reach V_C in microseconds, R , rate of rise of TRV V' , reference voltage in kV, t' , time to reach V' in microseconds Peak, duration
--	---

Note – all quantities (except energy) are per unitized.

Stability Studies

Stability work has proceeded with continued efforts to develop fast and accurate means for identifying incipient instabilities in a system. The Prony method is being investigated, modified with various types of linear estimation techniques to find a means to get accurate damping factors in the presence of noise without excessive computation. This work has been applied to adaptive filtering work being conducted by the controls group; the Prony method provides information on the amplitude, phase and frequency of the part of the waveform to be eliminated by the filter.

Other stability related work continues in the effort to find out how best to use large-scale simulations to understand the dynamical properties of a power system. Investigations in applying oscillating and impulsive current injections to a power system at various points and monitoring other points in the system are being performed in order to arrive at means for understanding the dynamical nature of a system through simulations. These procedures are expected to provide means for evaluating the dynamical size of a system (that is, how large does the simulation have to be, how much opportunity is there for reduced-order models, etc.), for quantitatively determining how closely coupled one part of the system is to another, and for precisely describing how the system behaves under stresses. An example of the application of one of these techniques is shown, where an impulsive current injection is applied to the main generator bus of CAPS' notional destroyer-class ship-system simulation. This disturbance is similar to that seen if a fault were applied to the system, but permits more precise control of the numerical experiment. In the figure, the speed of one of the main generators is shown for two entirely separate simulations of the same system. Estimation techniques applied to the deviation between these simulations will provide an important quantitative assessment of the behavior of the disturbed system. This type of analysis (based on the standard numerical method for determining the Lyapunov exponent of a dynamical system) provides a means for assessing the stability and controllability of a ship system under a wide variety of conditions, from



steady-state operation, to ordinary operational stresses, to extreme stresses.

Figure 7 Top: Speed of one main generator in separate simulations with a current disturbance applied to the generator bus under steady-state conditions. The current disturbance in the simulation shown in red was delayed by 0.1 sec relative to the disturbance in the simulation shown in black. Bottom: Identical simulations, except now the motor speed is being ramped down.

Wide area differential protection for shipboard power systems

As part of the ongoing collaborative effort between MSU and FSU, Yanfeng Gong and colleagues spent 10 days in 2005 at CAPS conducting protection and reconfiguration studies on the RTDS. Based on initial RTDS modeling work by MSU, CAPS provided significant enhancements to that model. In particular, two PWM propulsion motor drive models were incorporated into the model. Furthermore, CAPS facilitated the RTDS-HIL experiment with two SEL relays which controlled a total of 24 circuit breakers in the simulated ship system model. A report on the activities is in preparation by MSU.

CAPS has now implemented both the primary protection and a wide area back up protection on the pair of SEL relays left by the MSU team. The relays have been configured and are being tested on the RTDS notional ship system. CAPS and MSU have now implemented both the primary protection and a wide area back up protection on part of an ac distribution scheme. The pair of SEL relays from MSU were configured to handle the primary protection and the CAPS Wide Area back up relay was implemented as a UDC on the RTDS. Signals for the protection system were taken from the power system running in real time on the RTDS. Various fault types and sensor failure scenarios were investigated and a joint paper was prepared for submission to the IEEE IAS.

Fault location in ungrounded DC distribution systems

The goal of this project is to derive methods for fast and robust ground fault location in ungrounded DCZEDS to avoid disruptive current caused by second ground fault. We contributed to IEEE P1709 “Recommended Practice for 1 to 35 KV Medium Voltage DC Power Systems on Ships” and filed provisional patent (9/28/07) on “Method for locating phase to ground faults in DC distribution systems”. The motivation of this project is to develop a fast fault location method to avoid secondary high-current faults. The disadvantages of the current fault location methods are employing large number of sensors or human activity, possible failures in systems with large power electronic penetration, and may provide no suitable backup protection. Our approach is to utilize inherent switching noise already present in the system in order for DC fault location. In 2007, we analyzed system conditions, including no fault, positive bus fault, zonal positive fault and negative rail fault. Significant background noise caused by power electronics and cable stray LC are analyzed and distinguished from the noise with different fault locations. Therefore, by employing advanced signal processing on noise signals at faults, such as wavelets, we can identify different fault locations. The simulation results of a notional ship system at different faults indicate suitable performance of the proposed method.

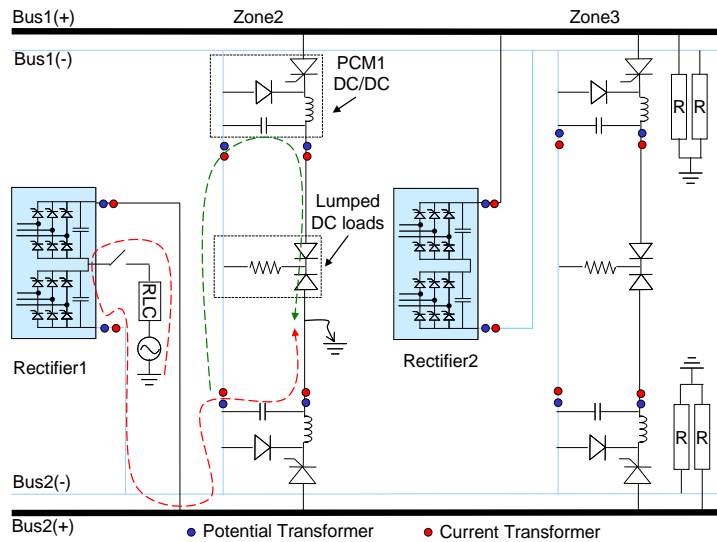


Figure 8 Zone2 positive rail (on bus2 side) ground fault

Impact of fault current limiters (FCL) for Navy shipboard power systems

The study has been finished and a final draft version of the report has been prepared. Since a total of five companies who are developing FCLs for utility applications have contributed technical information material the draft report has now been sent to those contributors for final comments before release of the report. The (preliminary) summary and conclusions of the study are as follows: In this study the application of fault current limiters on future all-electric navy ships was investigated. Therefore a notional power system design for a future all-electric navy ship first was introduced. As basis for the following considerations the rated currents and short-circuit currents in the power system were determined. The highest total subtransient short-circuit current of 30.6 kARMS occurs when the power system is operated in the common bus plant alignment configuration. Different locations for fault current limiters in the ship's power system were pointed out. The most promising locations for deployment of fault current limiters are at the connections of the main turbine generators to the switchboards. Through the insertion of the fault current limiters thermal and mechanical stresses in cases of faults can be reduced significantly depending on the actual design of the fault current limiters.

Despite the observed fault current limiting effects it is concluded that as long as the generator subtransient reactance is not significantly lower than 0.15 p.u. and the total generation power is not increased the resulting fault currents can be managed with conventional switchgear without the need to actively limit fault currents. However, it still might be advantageous to deploy fault current limiters in the system to lower mechanical and thermal stresses in the case of faults. Furthermore, all the bulk power devices such as generators, switchgear, bus work, cables, current sensors, and transformers could be designed for those lower stresses. This in turn is expected to result in overall weight, volume, and cost savings. Therefore, further studies should conduct a more detailed investigation to quantify possible benefits due to the lower stresses on the power devices. Benefits shall be compared to the additional effort of installing, maintaining, and operating fault current limiters on board a Navy ship.

Electrical-thermal system co-simulation

We established successful Co-simulation in RT and revealed strong system interactions leading to thermal run-away. •Benchmark co-simulations are executed. In these simulations, electrical system components

send power loss and adjust temperature dependent model parameters; thermal system is controlled to keep electrical system components at desired temperature; and thermal system sends required motor power. In the implementation V1, the step response of the system to sudden increase in DC zonal load on the 1 kV bus from 0.9 MW to 1.25 MW is shown. In the thermal system, it reacts by increasing coolant pump power in order to maintain the temperature set point of 70°C. In the implementation V2, we “accidentally” discovered an system instability due to the inherently “long” run of the real-time simulation model.. The remaining problems in this project are required strong support from USC to facilitate thermal system modeling needs in VTB-RT (VTB2003) and lack of run-time user interface in VTB-RT (needed to operate more sophisticated cases in VTB-RT). CAPS contributed to VTB model development in: valve – now controlled to open/close a specified percent per second; Pump – now can control pump pressure (motor models not required); water cooling models (heat sink & plate fin HEX) – now can easily measure temperature and heat load; analog signal I/O & Digital I/O – now compatible with multiple DAQ cards; PI controller – now can be reset; Reported that VTB-RT could falsely appear to run in real-time (simulation breakdown without giving notice to user); many models/components added to VTB-RT library (i.e. compiled for

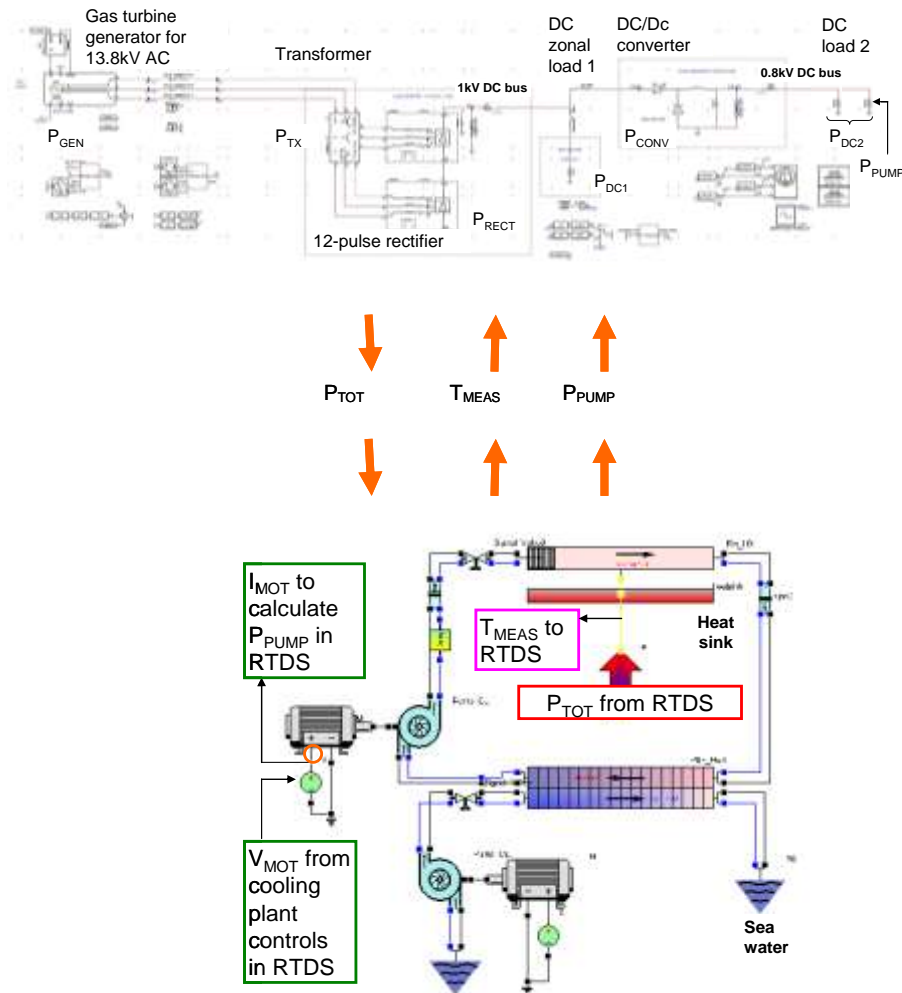


Figure 9 Co-simulation model diagram

Advanced Power Quality Management of the All-electric Ship

A simulation based rationale for introducing flexible thresholds of harmonic distortions on shipboard power systems was demonstrated. This study was performed in the perspective of equipment aging. The time-varying nature of harmonic distortions was taken into account to establish a proof-of-concept for introducing flexible/relaxed harmonic thresholds. Artificial time-varying current harmonics were injected into the system simulation model, while the load on the DC-ZEDS was varied randomly (within set limits). The associated harmonic distortion in voltage at the PCC was tabulated and the corresponding loss of life (or life expectancy) of an example load (three phase induction machine) was quantified. The same study was performed with no additional current harmonic injections in the system as well as a constant harmonic distortion corresponding to the relaxed threshold. By comparison of the results of the above simulation case studies, it was established that the time-varying nature of the harmonic distortion leads to a life expectancy that is better than the estimated loss of life of the equipment in the presence of steady harmonic injections. Future work relates to demonstration of the above concept through hardware in the loop studies.

Advanced signal processing tools for power quality analysis

The goal of this project is to assess the PQ requirements of the all-electric ship and to study the effect of time-varying waveform distortions and other PQ deviation parameters (unbalance, sags, etc). We filed a provisional patent application number 60939226, "System and methods for determining masking signals for empirical mode decomposition (EMD) and for demodulating intrinsic mode functions obtained from application of EMD," on May 21, 2007. An Empirical Mode Decomposition (EMD) is used. In this method, non-stationary nonlinear waveforms are decompose into intrinsic mode functions (IMF). Therefore, locally occurring oscillations are recognized. IMFs are extracted in decreasing order of frequency and can indicate local oscillations. The decomposed components are mutually orthogonal and mono-component and their residue is monotonic. The performance of EMD as a second order signal processing filter was analyzed. The enhancements to the original EMD accomplished were accomplished. In addition, application to online (adaptive) transfer function estimation of HTS motor model under sea-states was investigated successfully.

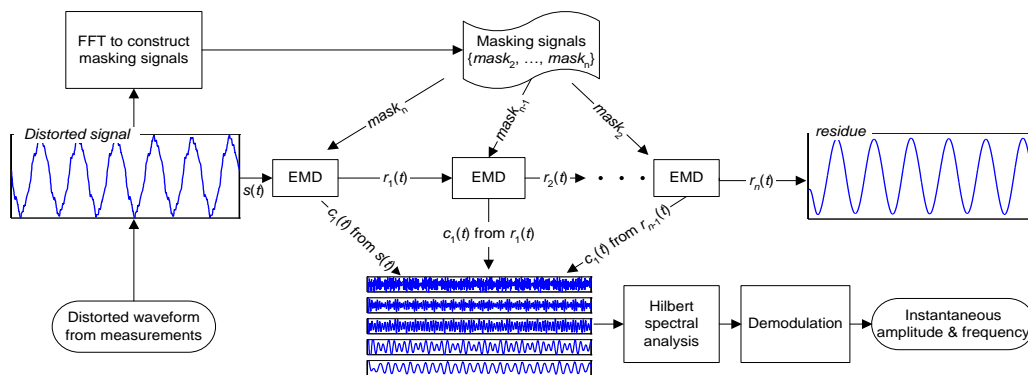


Figure 10 Illustration for advanced digital signal processing tool for power systems

Probabilistic aspects of all-electric ship system simulations and surrogate models

In order to facilitate validation of the notional base-line shipboard power system model for RTDS, various uncertainty and sensitivity analysis techniques were investigated for applicability. Several techniques, including local, first order sensitivity methods, random sampling methods, the Morris factor screening method, and a

fractional factorial experimental design were used to assess the relative influence of thirteen uncertain parameters for the ship system on six response variables for two different transient scenarios. While the results from each of the methods were similar, the experimental design approach provides a number of advantages in terms of flexibility and extensibility, as well as in the incorporation of system knowledge into the experimental process. Using geometric considerations, this provides a sequential approach to methodically gain more information about the system and refine the model with the addition of new simulation runs. At each stage in the process, the experimenter augments and extends the design based on available data and intuitive knowledge of the system. Thus, the experimenter is able to incorporate hypotheses about the system model into the design, but is able to validate or invalidate these hypotheses as the process proceeds. This allows a methodical sampling of the parameter space, as opposed to the random sampling employed by the other global techniques. This method is being used to construct response surfaces for each of the response variables for each scenario, from which tolerance intervals can be constructed for each response based on probability distributions for the uncertain parameters.

We completed characterization of AC/DC conversion system in terms of two scenarios involving 27 parameters and 30+ response variables. The remaining problems are difficulty obtaining sufficient surrogate model fits for some response variables and difficulty with augmentation of designs for nonparametric models in high dimensions. Uncertainty analysis was applied to 10-rack ship system with pulse load charging circuit connected to common bus with MTG1 and ATG1. MTG2 is islanded, supplying propulsion drive 2. ATG2 is islanded, but is connected to MTG1 and ATG1 through the DC distribution system. Parameters and ranges are Propulsion drive power (MW) [1...15], DC load power (MW) [0.5...4], MTG inertia constant (s) [2...4], ATG inertia constant (s) [2...4], Proportion of available power used for pulse (pu) [0.5...1], and DC bus capacitance (μF) [$5\text{e}3...50\text{e}3$]. Projections in two dimensions of sampling used by dimension adaptive collocation method were derived after 416 simulation runs.

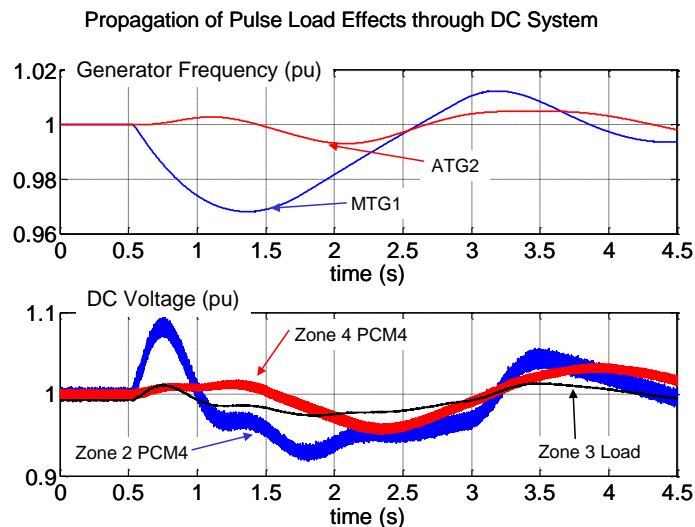


Figure 11 Pulse load effects through DC system

Analysis of Network Reconfiguration Potential

As part of our effort to develop a comprehensive basis for evaluating reconfiguration schemes, the investigation into the structural potential of a network for reconfiguration is continuing. In this work, tools are being developed to determine the intrinsic potential for reconfiguration of a particular network configuration. Focusing purely on the network structure, these tools provide a means for determining the upper limit of the reconfigurability of a network and thus will help to provide a meaningful assessment of

the effectiveness of proposed reconfiguration schemes. Network structures that maximize the reconfigurability according to this analysis are also being developed.

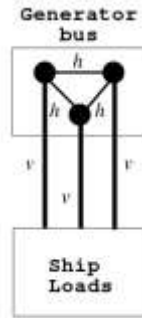


Figure 12. Stylized Version of Ship System Employed in Present Analysis

In the work conducted so far, the ship system has been viewed in the simplified form and the focus has been on the generator bus. (Extension to load distribution zones will be part of future work.) The question is then asked, how many simultaneous faults can the system sustain while still maintaining some or all of its generating capacity? Probabilities are assigned to the loss of a generator or a network link and overall probabilities of partial or total generator outage are computed for a given number of simultaneous faults. For four two-generator networks experiencing from one to eleven simultaneous faults. The graph below each network shows the probability of a loss sustained without the need for reconfiguration (gray), loss sustained but capability retained with load reconfiguration (white) and total capability lost (black). These probabilities may be used to construct composite figures of merit for the different network structures. The web-like structure on the right has a clear advantage over the others, at the cost of additional cabling. In fact, it compares favorably with three generators in a conventional network; cost and weight considerations will have to be included in order to determine whether the web configuration truly has an advantage. This work will continue with extensions of the analysis to detailed load zones and more realistic probabilities for component and link losses than the constant values used to date. It will ultimately be combined with the transient evaluation process for reconfiguration proposed earlier and currently being developed for the notional destroyer-class ship simulation (as described above) to provide a comprehensive means for evaluating network reconfiguration schemes.

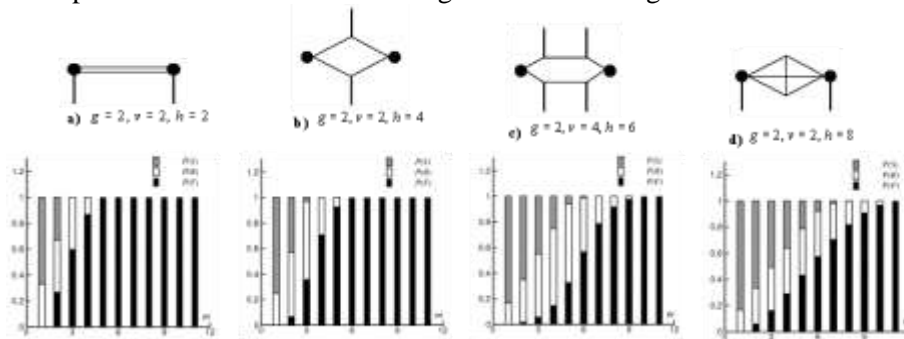


Figure 13. Susceptibility of Four Networks to Various Numbers of Simultaneous Faults

Power Quality Analysis Using Advanced Signal Processing Techniques

In shipboard electric power systems, transients will be generated by various switching events, while harmonics and interharmonics will be generated by various nonlinear devices. Copious amounts of interharmonics are likely to be generated by devices such as variable speed drives where nonlinear interactions between the source frequency (e.g., 60 Hz) and variable load frequencies result in the generation of many possible interharmonic frequencies. In this section we review progress made in developing a variety of new transient and interharmonic diagnostics. These new diagnostics rest upon the use of advanced signal processing techniques, namely joint time-frequency analysis for transients, and higher order spectral analysis techniques for interharmonics.

3.1.1.1. Power Quality Indices for Transient Disturbances

Power Quality (PQ) indices have been well developed for periodic non-sinusoidal waveforms. The approach rests upon Fourier series analysis of the periodic waveforms. However, Fourier series analysis is obviously not suitable for the analysis of transient events. For this reason, in [i, ii] we developed a new set of power quality indices for transient events based on the signal processing technique known as joint time-frequency analysis, or just T-F analysis for short. Such analysis indicates how the energy of a transient signal is distributed jointly in both time and frequency. In this work, we used the reduced interference distribution (RID) which is a member of a class of T-F distributions known as Cohen's class. The approach is to decompose a transient waveform into its fundamental 60 Hz component and a disturbance component. Then the T-F distribution for each component is computed. From these T-F distributions, the following transient PQ indices are calculated: (1) the instantaneous distortion energy ratio [$IDE(t)$], (2) the normalized instantaneous distortion energy ratio [$NIDE(t)$], (3) instantaneous frequency [$IF(t)$], and (4) instantaneous K-factor [$IK(t)$]. These PQ indices were defined in such a way as to be analogous to their steady-state harmonic counterparts. Both $IDE(t)$ and $NIDE(t)$ characterize the transient in terms of the disturbance energy associated with the transient, whereas $IF(t)$ and $IK(t)$ characterize the transient in terms of the deviation in instantaneous frequency from 60 Hz when the transient event occurs. Since we are dealing with transients, all of the transient PQ indices cited above are functions of time. In order to facilitate comparison of various transient events, we can also define each PQ index in terms of its "principal value," a single number, which is defined as the average of the appropriate instantaneous index over a fundamental period. The efficacy of the proposed transient PQ indices was demonstrated using real world transient data corresponding to fast and slow capacitor switching events, and voltage sag associated with motor starting. The method is quite flexible and adaptable in that once one has calculated the T-F distribution corresponding to the transient disturbance waveform, there are any number of other transient PQ indices that one might construct, depending on the features of the transient that one wishes to extract and quantify. The transient PQ indices software has been integrated into a MATLAB-based UT-TFTPQA (University of Texas, Time-Frequency Transient Power Quality Assessment) tool box. In collaboration with the University of South Carolina, this toolbox was integrated into their Virtual Test Bed (VTB) and was demonstrated by quantifying the transient effects of inserting a new capacitive load. The work on developing transient PQ indices and the associated tool box was principally carried out at UT Austin as part of Dr. YongJune Shin's PhD dissertation. Dr. Shin is now participating in the ESRDC program as a faculty member at the University of South Carolina.

3.1.1.2. Detection of Transient Disturbance Energy Flow

Transient events manifest themselves as a disturbance of the fundamental 60 Hz waveform. Of particular interest, from a diagnostic point of view, is the ability to determine the magnitude and direction of real and reactive energy flow associated with the disturbance. The so-called cross-power spectrum may be used to track the magnitude and direction of real and reactive power for steady-state harmonics and interharmonics. However, this approach is not suitable for transients, since transient disturbance energy flow depends not only on frequency but also on time. In [iii], we utilized the notion of a complex cross time-frequency distribution (XTFD), which is computed

from the voltage and current disturbance waveforms. The real and imaginary parts of the XTFD yield the magnitude and direction of the real and reactive disturbance energy flow, respectively, as a function of both time and frequency. In polar form, the phase difference between the disturbance current and voltage is provided as a function of both time and frequency. An EMTP simulation was carried out to illustrate how the XTFD may be used to quantify disturbance energy flow associated with capacitor switching and, thus, to lay the ground work for developing a methodology based on the XTFD to determine the location of a capacitor switching event in a network. Of course the XTFD signal analysis tool is not limited to capacitor switching events, but is applicable to any transient event.

We also mention that XTFD has been used to develop a new approach to determining load impedance and faults in coaxial cables based on joint time-frequency reflectometry [^{iv}, ^v, ^{vi}]. This work is being continued by UT Austin PhD graduate, YongJune Shin, in his position as a faculty member and ESRDC researcher at the University of South Carolina.

3.1.1.3. Real and Reactive Power Flow Analysis for Interharmonics

Because of their non-harmonic features, interharmonic properties and effects cannot be readily quantified using classical harmonic analysis tools such as Fourier series analysis. Therefore, we developed another digital signal processing-based technique [^{vii}] for the analysis of interharmonic events. The first step in the interharmonic analysis study is to investigate the magnitude and direction of real and reactive power flow associated with each frequency in the interharmonic spectrum.

The approach is to compute the so-called cross-power spectrum from the discrete Fourier transform (DFT) of the voltage and current waveforms. Since the cross power spectrum between voltage and current preserves the magnitude and phase difference information at every frequency, the magnitude and direction of real and reactive power at every frequency of interest can be easily determined.

To verify the proposed method, we simulated a current source type inverter drive system utilizing the ATP-EMTP simulation program. From the resulting waveforms, we demonstrated the ability to determine the magnitude and direction of real and reactive power flow at every frequency, including harmonics and interharmonics, at different measuring points in the simulated current source type inverter drive circuit. We believe that the detailed analysis of interharmonic power flow utilizing the cross power spectrum technique will provide an important tool with which to understand and address interharmonic-related problems in shipboard electric power systems.

3.1.1.4. Robust Interharmonic Detection in Adjustable Speed Drives using the Cross Bicoherence

Interharmonics from ASD (Adjustable Speed Drives) can cause potentially serious problems (e.g., excitation of undesirable electrical or mechanical resonances) to the entire power system even though their amplitudes are usually small compared to the fundamental frequency and its harmonics. According to a study of an offshore platform power system, a low frequency interharmonic was resonant with the mechanical natural frequency of a turbine-generator. This resonance caused severe vibration problems resulting in the shut-down of the entire power system.

Therefore, the detection and measurement of interharmonics have become important issues recently. However, the detection of the existence of interharmonics is often not an easy task, since interharmonic detection is sensitive to many factors, such as spectral leakage and measurement error. Hence, there may be a question as to whether the measured component at the suspected interharmonic frequency is a real interharmonic component or just an artifact of signal processing.

In an effort to evaluate interharmonics in a quantitative manner, several approaches have been proposed, but they have their own limitations since they mainly rely on detecting the small amplitude of the interharmonics.

Therefore, we proposed a new approach in [^{viii}] with a different point of view for the detection of interharmonics, particularly in ASD systems. Interharmonics mainly result from nonlinear frequency interactions between the source-side frequency and its harmonics with the load-side frequency and its harmonics which take place in the nonlinear rectifier and inverter in the ASD. Furthermore, the interharmonics exhibit a phase coupling or phase

coherence between various frequencies which satisfy appropriate frequency selection rules. These phase couplings provide a sensitive nonlinear signature, and it is for this reason that we utilize a high-order spectral quantity, the cross bicoherence, to detect the phase coupling and, hence, the presence of interharmonics. The principal advantage of this approach is that, unlike previous interharmonic detection approaches, it does not rely on detecting the low amplitude of the interharmonics.

For our specific application of cross bicoherence to interharmonic detection, we use a modified definition of cross bicoherence to investigate the degree of quadratic coupling between the source side current and the DC side current. Our experimental results for a simulated ASD system based on MATLAB Simulink[®] show that our cross-bicoherence-based interharmonic detector provides a more robust detection than conventional methods which rely on the amplitude of the interharmonics.

3.1.1.5. Interharmonic Detection with Noisy Measurements

We continue to further develop robust interharmonic detection methods using higher-order statistics of measured signals. Higher-order signal processing techniques are crucial parts of interharmonic analysis, since interharmonics are products of nonlinear interactions between fundamentals/harmonics of different operating frequencies such as are present in various frequency converter devices. Therefore, we developed a constant-false-alarm-rate (CFAR) interharmonic detector based on the cross bispectrum.

As we mentioned previously, interharmonics are responsible for various potentially serious problems including destructive sideband torques on motor/generator shafts and possible misoperation of control devices due to altered zero crossings. Therefore, the IEC recommended an interharmonic limit of 0.2% of the fundamental amplitude from 0-2 KHz. Since this limit is very small compared to the magnitude of the fundamental term, any undesirable side effects (e.g., spectral leakage and/or noise) can lead to inaccurate interharmonic detection results. This is mainly because the current interharmonic measurement standards only utilize the FFT magnitude of the measured signals.

In previous quarterly reports, we demonstrated that the FFT-based interharmonic detector can lead to a completely wrong decision when it deals with small magnitude interharmonics, particularly in the presence of noise (e.g., measurement error). To address this issue, we proposed the use of higher-order signal processing-based methods, particularly the cross bispectrum. Since interharmonics are the results of nonlinear interactions, any interharmonic appears as a peak in the cross bispectrum domain. The cross bispectrum values in other points in the bi-frequency domain are insignificantly small compared to the peak value. One advantage of using the cross bispectrum instead of the classical frequency spectrum is that the cross bispectrum rejects Gaussian noise in the bi-frequency domain, while the noise still remains in the frequency spectrum. In other words, the error in interharmonic measurement will be ideally removed if we use the cross bispectrum-based interharmonic detector. Therefore, we designed a new test statistic, which is the sum of the cross bispectrum magnitude squares, which is calculated from the source side measurements and the dc side measurements, along a diagonal line (in the bi-frequency plane) corresponding to a certain frequency. According to the statistical analysis of our specific definition of the cross bispectrum, we could derive the threshold which gives us the constant false-alarm (false-positive) rate (CFAR), and the corresponding CFAR detector. More detailed discussion and derivations about the statistical characteristics of the definition and the threshold decision process will be elaborated on in a journal article which is currently being prepared.

Figure 3-1 presents the interharmonic detection results using the proposed test statistics. Figure 3-1 (a) shows the test statistics for interharmonic-containing current signals with 3% measurement error. The test statistics in Figure 3-1 (a) clearly indicate that interharmonics are present at 30 and 150 Hz. Figure 3-1 (b) shows the test statistic values for non-interharmonics terms in Figure 3-1 (a) (Please note the change in the scale of vertical axis.). It shows that the test statistic values for non-interharmonics are consistently below the pre-determined threshold line. Figure 3-1 (c) shows the probability of false positive comparison result between the FFT-based detector (indicated as P_{fa-FFT}) and the cross bispectrum-based detector (indicated as $P_{fa-XBISP}$). While the probability of false positive of the FFT-based detector sharply increases as measurement error (i.e., noise)

increases, that of the cross bispectrum-based detector remains at almost zero. This result clearly indicates that our cross bispectrum-based interharmonic detector is robust to measurement error.

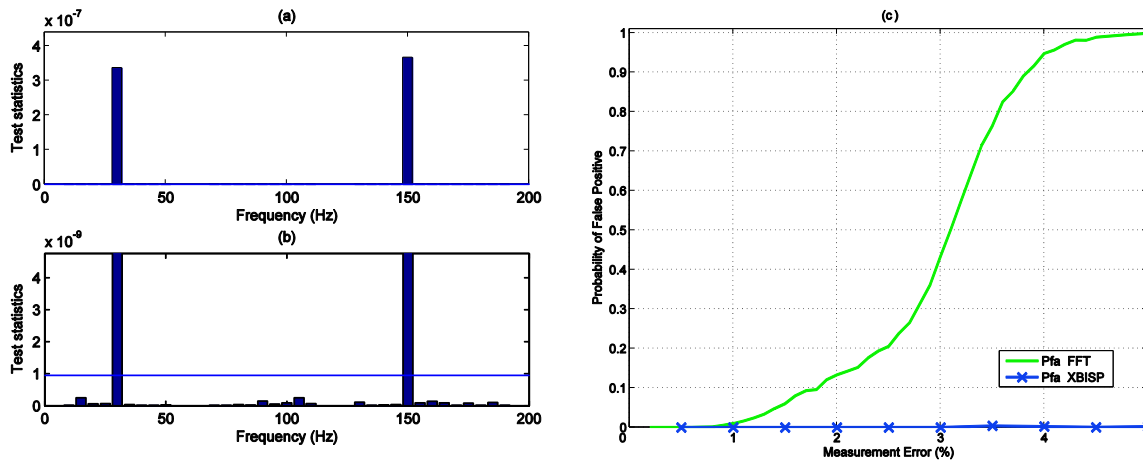


Figure 3-1: The cross bispectrum-based interharmonic detection with measurement error: (a) Test statistics with 3% measurement error, (b) Test statistics for non-interharmonic terms, (c) The probability of false positive comparison.

3.1.1.6. Light Flicker Assessment in the Presence of Interharmonics

In our continuing effort to study the effect of interharmonics on shipboard power systems, we investigated light flicker problems associated with high-frequency interharmonics from ASD systems. Light flicker is defined as noticeable illumination changes due to voltage fluctuations imposed on the fundamental power frequency component, and a flickermeter is an instrument capable of measuring the severity of it. The detailed specification for the flickermeter is presented in IEC standard 61000-4-15, and the current IEEE standard 1453-2004 recommends the adoption of the IEC standard.

However, according to recent studies, the current IEC standard-based flickermeter can not detect flicker caused by interharmonics whose frequencies are higher than 102 Hz. A real field case for the deficiency of the current standard was also reported. Utility customers complained about light flicker, but standard-compliant flickermeters could not detect it. We also found that the IEC flickermeter also has a limitation in representing flicker caused by low frequency interharmonics in terms of beat frequency. Therefore we proposed an approach based on peak detection by down-up sampling [x_i^x , $x_i^{x_i}$]. The basic idea is to examine the fluctuation imposed on the half cycle of the fundamental frequency. Since the input ac voltage is squared (e.g., incandescent lamps) or rectified (e.g., fluorescent lamps) in order to produce the light output, the fluctuations of the half-cycle should be considered.

In Figure 3-2, the sensitivity curve of the proposed method to detect interharmonics is presented along with that of the IEC flickermeter. These curves represent the minimum interharmonic magnitude to produce one PU (Perceptibility Unit) in the flickermeter output. The sensitivity curves for both methods appear identical in the frequency range from around 30 Hz to 90 Hz in Figure 3-2, where the IEC flickermeter works properly with interharmonics. However, the sensitivity curves for both methods exhibit different behavior in the lower frequency range below 30 Hz and higher frequency range above 90 Hz. Contrary to the inaccurate response of the IEC flickermeter in the low-frequency range (0~18 Hz) as discussed in previous quarterly reports, the curve corresponding to the newly proposed method shows that the proposed method sensitively reacts to the low-frequency interharmonics in that a smaller interharmonic magnitude is required to produce one PU. In the high-frequency range (90~120 Hz), according to the curve corresponding to the standard method, large magnitudes of interharmonic are required to produce one PU in the flickermeter output, which is contrary to the field case reported in recent papers. On the other hand, the curve corresponding to the proposed method is well extended into the high-frequency range, and shows that relatively small magnitudes of the interharmonic can produce one PU.

The numerical experimental results presented in Figure 3-2 indicate that our proposed flicker processing methods are able to properly detect flickers caused by interharmonics regardless of their frequencies. Furthermore, our proposed methods can be immediately combined with the current flicker standard, since we just replaced a few blocks in the standard with our proposed signal processing blocks.

We also investigated the flicker responses of various lamps including LED (light emitting diode) lamps using a laboratory interharmonic flicker station and a photo detector. The experimental results demonstrate that LED lamps exhibit a flicker response similar to compact fluorescent lamps, which are sensitive to those high-frequency interharmonics which are close to odd-order harmonics of the fundamental.

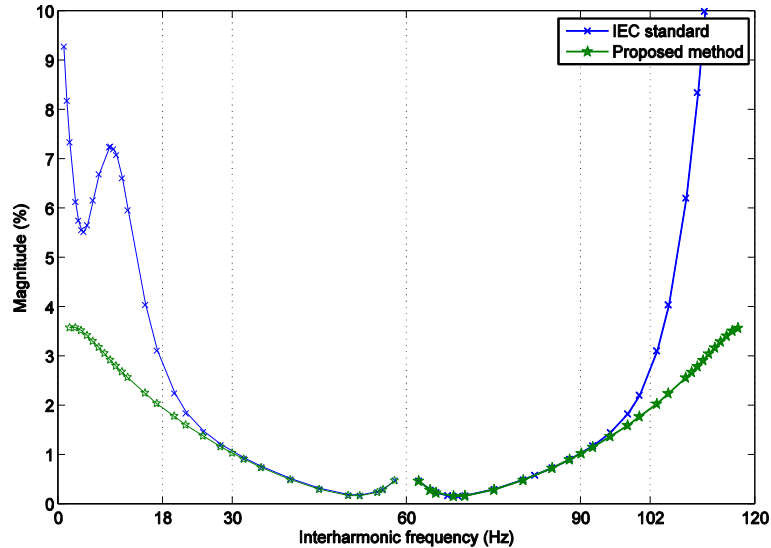


Figure 3-2: The minimum interharmonic magnitude necessary to produce 1 PU for the IEC flickermeter response and the proposed method vs. interharmonic frequencies.

3.1.2. Machine Condition Monitoring Using Higher-order Spectra

In this section we review progress made in developing new machine condition diagnostics. The key idea is that as machines degrade they tend to become progressively more nonlinear. Higher order spectral (HOS) analysis is a key signal processing tool with which to quantify the associated nonlinear signatures. The previous state-of-the-art involved the use of the so-called bispectrum to quantify the nonlinear signature. In this section we point out that, for many applications, the bicoherence and cross-bicoherence spectra are much more suitable. We also eliminate some of the ambiguities of the bicoherence approach to further improve the reliability of this new machine condition diagnostic.

3.1.2.1. Machine Fault Detection using Bicoherence Spectra

The purpose of machine condition monitoring in rotating machines, such as induction motors in shipboard power systems, is to provide appropriate signature or feature information that is a direct indicator of the health of either the complex overall system or a particular component of interest.

As machines degrade, they often tend to become more nonlinear rather than more linear. A characteristic of all nonlinear phenomena is the generation of “new” frequencies corresponding to various sum and difference combinations of the “original” nonlinear interacting frequencies. Both the original and new frequencies must satisfy a particular frequency selection rule which depends on the order of the nonlinearity. Of particular importance is the fact that the phase of each new frequency is related to the phase of the original primary interacting frequencies. Thus, a certain degree of phase coupling, or phase coherence, exists between the primary and new frequencies. This phase coupling is a true and significant signature or feature of the nonlinear interactions. The fact that higher-order spectra (HOS) are able to detect this phase coupling between the various

interacting frequency components is one of the principal reasons why HOS are such a powerful diagnostic in detecting and quantifying nonlinear features in signals for machine condition monitoring. Many condition monitoring techniques using HOS have focused mainly on bispectral analysis as a signature of a faulted or degraded machine. Thus, one of the dominant detection schemes is the bispectrum. However, a drawback of using the bispectrum method arises from the fact that its value not only depends on the degree of quadratic phase coupling, but also on the (complex) amplitude of the interacting frequency components. To overcome this challenge, we proposed in [xii] that the bicoherence to be used to remove the amplitude dependency of the bispectrum and, thus, to solely quantify the degree of quadratic phase coupling between the various nonlinearly interacting frequencies satisfying the appropriate frequency selection rule. The values of the bicoherence are bounded between 0 and 1. Therefore, the bicoherence is a useful measure of quadratic phase coupling.

To verify the performance of our proposed method, we utilized measured experimental data associated with degradation of an induction motor. Figure 3-3 represents the experimental setup. The induction motor was powered by a three-phase 60 Hz power source. Two phases were directly connected to the motor and the third phase was connected through a variable resistor in order to generate an unbalanced current in the stator of the induction motor. Therefore, the fault detection of the induction motor in this experiment is based on the analysis of vibration signals provided by an accelerometer attached to the stator core. The experiments were performed for three different resistances, 0, 10 and 20 Ω , respectively. The balanced phase case, 0 Ω resistor, was measured in order to be used as a reference for a healthy, no-fault case, and the asymmetrical unbalanced cases, 10 or 20 Ω resistors, were utilized to simulate faulty, degraded cases. In order to avoid any transient effects, the measurements were carried out while the motor showed steady-state behavior.

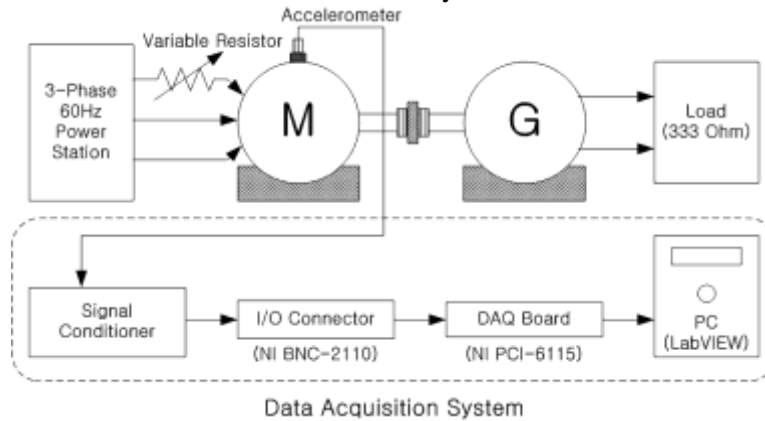


Figure 3-3: Schematic diagram of the experimental setup for measuring the unbalanced vibration signal.

The bicoherence spectra, $b^2(f_1, f_2)$, for the balanced 0 Ω case and for the asymmetrical fault 20 Ω case are presented in Figure 3-4 (a) and (b), respectively. In Figure 3-4 (a), two dominant peaks are apparent, indicating strong quadratic phase coupling, at the low and high frequencies. The peak at low frequencies is associated with the shaft rotation frequency and the peak at high frequencies is associated with the bearing frequencies. As the machine degrades with the 20 Ω asymmetric fault, many additional peaks begin to appear in Figure 3-4 (b). This is caused by the fact that the asymmetric unbalanced faults manifest themselves as a change in the vibration characteristics of the rotating machine, and this change in the vibration characteristics is associated with more quadratic phase coupling as shown in Figure 3-4 (b). These new peaks can be interpreted as quadratically nonlinear interactions between the shaft frequency and the bearing frequencies of the induction motor. These results demonstrate that the bicoherence is a powerful diagnostic in providing a nonlinear signature of a faulted or degraded machine for condition monitoring.

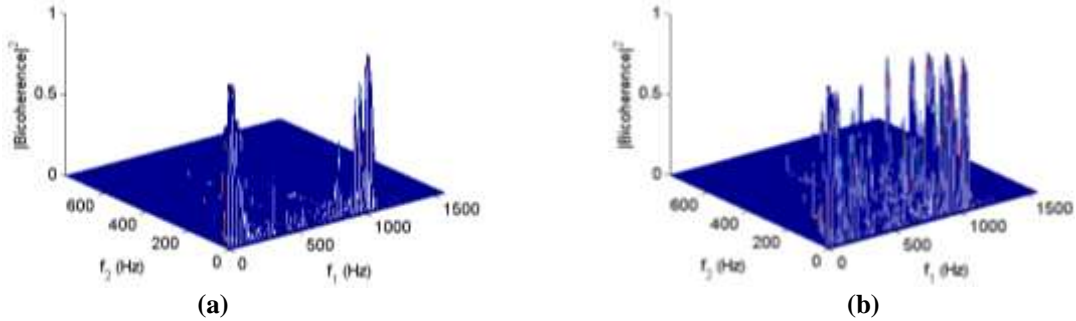


Figure 3-4: The bicoherence, $b^2(f_1, f_2)$, for (a) 0Ω , no-fault case and (b) 20Ω , asymmetrical faulty case.

3.1.2.2. Machine Condition Monitoring Utilizing Bispectral Change Detection

Since a damaged or abnormal-state machine often generates highly nonlinear signals, it is desirable to use a tool that can effectively detect and analyze nonlinear signatures. In the previous section, we reported on the advantages of using the bicoherence since it is a quantitative measure of the degree of phase coupling, or phase coherence, between nonlinearly interacting frequencies.

However, even though the bicoherence is a useful and powerful scheme in the detection of phase coupling, it has some limitations in a machine condition monitoring application due to the challenge of distinguishing between intrinsic nonlinear signatures associated with healthy machines and nonlinear signatures associated with a faulted machine. This can lead to ambiguous indications in machine condition monitoring. Therefore, the ability to discriminate the fault-induced nonlinearities from the intrinsic nonlinearities is a very important factor in determining the health of machine.

To address and resolve this issue, we proposed in [xiii] a novel method exploiting a bispectral change detection (BCD) to detect and analyze the health-state of a machine. The principal advantages of the proposed BCD method are that it can suppress the bicoherence associated with intrinsic nonlinearities of a healthy machine by nulling them out and emphasize the bicoherence associated with fault-induced nonlinearities. With these advantages, our proposed BCD method can discriminate the fault-only nonlinearities from the intrinsic nonlinearities, and, thus, is a strong and sensitive indicator for machine fault monitoring.

Based on the analysis of the vibration data from Figure 3-3, the usefulness and statistical robustness of our proposed BCD method are demonstrated, as shown in Figure 3-4 of the previous section, it is very challenging using just the bicoherence to (1) distinguish between the intrinsic nonlinearities associated with healthy machines and fault nonlinearities and (2) to determine the (f_1, f_2) coordinates of the dominant nonlinear frequency interactions associated with a fault.

Meanwhile, Figures 3-5 (a) and (b) show the results of our BCD method for the 0 and 20 Ω cases, respectively. The Z-axis in Figure 3-5 represents the relative nonlinearity increase over the balanced 0 Ω case. Note that the scale of the Z-axis in each case is adjusted for plotting purposes. Observe that in the 0 Ω case, the BCD result in Figure 3-5 (a) is essentially zero, indicating a normal healthy machine state. On the other hand, the BCD result is non-zero for the unbalanced 20 Ω cases in Figure 3-5 (b). Furthermore, note that due to the scale change, the value for the 20 Ω case is extremely high. Thus, our proposed BCD method is a sensitive indicator of fault-induced nonlinearities.

As we can see in Figure 3-5, our proposed BCD method successfully suppresses the intrinsic nonlinearity of a healthy machine and emphasizes the fault-only nonlinearities, compared to Figure 3-4. In addition, the plot in Figure 3-5 (b) clearly indicates the (f_1, f_2) coordinates of the dominant frequency interactions. From these results, we confirmed that our BCD method can remove the ambiguous indications in conventional bicoherence plots.

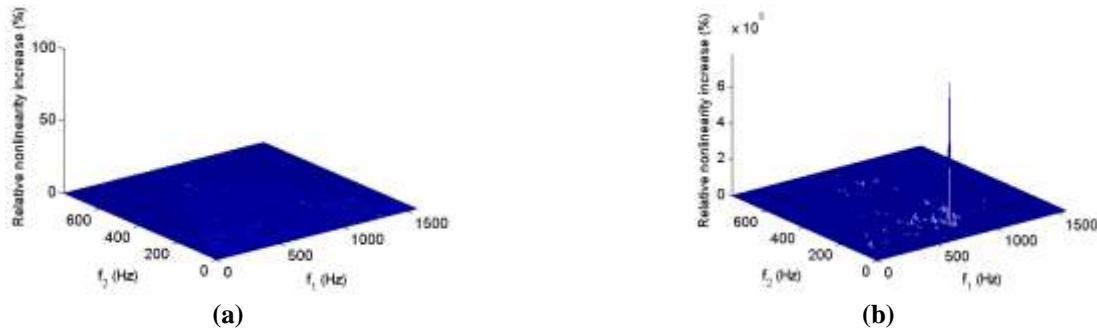


Figure 3-5: The BCD for (a) 0Ω , no-fault case and (b) 20Ω , asymmetrical faulty case.

3.1.2.3. Condition Monitoring Based on Estimating the Complex Coupling Coefficients

Our most recent work [xiv] has focused on providing a novel state-of-the-art diagnostic for condition monitoring of rotating machines. The key idea is to estimate, from measured single time series data, the complex coupling coefficients which characterize the strength of the dominant nonlinear interactions of interest. The approach is based on key concepts from the field of HOS analysis and least mean-square-error analysis. The proposed approach has the ability to estimate an optimal kernel $A(i, j)$, which is a complex quadratic coupling coefficient, characterizing the “strength” of quadratically nonlinear interactions associated with possible degradation of rotating machines in shipboard power system. The discrete interacting frequencies are denoted by i and j . Since the physics of the nonlinear interaction is embedded in the complex quadratic coupling coefficient, knowledge of $A(i, j)$ offers the possibility of providing new physical insight into the degradation process and enhancing the state-of-the-art for condition monitoring diagnostics. In addition, we verify that the goodness of our model can be quantitatively measured based on the well-known higher-order spectrum called the bicoherence. Future work entails tracking the direction of power flow associated with various nonlinear interactions connected to degraded machines, thereby providing possible insight into cause and effect. Such insight is not currently available. We have taken an important step in addressing this goal by being able to estimate the complex quadratic coupling coefficients. Since this step is successful, the next goal will be to investigate the feasibility of determining higher-order complex coupling coefficients (i.e., higher than quadratic) to analyze the nonlinear interactions. This is motivated by the fact that higher-order model analysis requires that we include, as a minimum, the lowest even-order and odd-order nonlinearities, i.e., quadratic and cubic, respectively.

3.1.2.4. ASD System Condition Monitoring using the Cross Bicoherence

Adjustable speed drives (ASD) for propulsion motors are among the most crucial components in the electric ship power system. Therefore, utmost attention should be paid to ASD system condition monitoring to prevent possible failures, since any anomalies of ASDs can effect the health of motors immediately. Furthermore, ASDs are also copious sources of harmonics/interharmonics which can create disturbances throughout the entire shipboard power system. Although many condition monitoring techniques have been proposed, they mainly focus on stand-alone motor status monitoring. Therefore, we propose condition monitoring methods specific to ASD and ASD-driven motors.

Our fundamental idea is to diagnose both the status of an ASD and the load side of the ASD (usually a propulsion motor in shipboard power systems) from information observable at the source side. This is a challenging problem because the load and source side operate at different frequencies, and from the source side one must “view” the load-side through nonlinear rectifiers and inverters. It is for this reason that higher-order-spectral (HOS) analysis forms the heart of our diagnostic technique.

Any anomalies in ASDs cause changes of voltage and/or current at the source side of the ASD. The changes are often too small to be detected by simple time-domain or frequency domain analysis. However, those changes can be sensitively detected by HOS techniques (e.g., the auto/cross bicoherence), since they are the result of nonlinear interactions occurring in the rectifier/inverter parts of the ASD. Due to the sensitivity of HOS techniques, we can

detect anomalies of the ASD and the load of the ASD at their incipient stage. This early detection is crucial for the pre-diagnosis of potential system problems.

Therefore, we developed in [xv] a modified HOS metric (the cross bicoherence) and the required theoretical background for ASD system anomaly detection. The proposed method is verified using a simulated ASD system using MATLAB. Asymmetric resistance or inductance is introduced at single phase of the load side feeding lines in order to simulate load side imbalance, and the corresponding cross bicoherence results are analyzed. Figures 6 (a), (b), and (c) illustrate the cross bicoherence results on the bi-frequency plane for the balanced case, unbalanced cases with asymmetric resistance and asymmetric inductance, respectively. In Figure 3-6, one axis corresponds to the source side frequency I_a and the other axis corresponds to the dc link side frequency I_{dc} .

In Figure 3-6, there are four dominant peaks aligned vertically at I_{dc} frequency 72 Hz. Among the four peaks, two peaks located at (60,72) and (-60,72) represent the normal interharmonics resulting from the nonlinear frequency interaction between 60 Hz source side ac power and the 6th harmonic of 12 Hz load side power. The two other peaks are symmetric “images” of the previous two peaks by the symmetry property of the cross bicoherence. Meanwhile, we can observe additional peaks in Figures 6 (b) and (c). Figure 3-6 (b) presents the cross bicoherence for unbalanced case with 40 Ω asymmetric resistance. Additional peaks are aligned vertically at I_{dc} frequency 24 Hz, which is the second harmonic of the load side operating frequency 12 Hz. Therefore, the peaks aligned at 24 Hz represent newly generated interharmonics due to phase imbalance at the load side of the ASD. In Figure 3-6 (c), the cross bicoherence result associated with 160 mH asymmetric inductance shows a similar pattern with the result in Figure 3-6 (b). However, other dominant peaks at 48 Hz are also observed in Figure 3-6 (c). This is because the phase imbalance due to asymmetric inductance has different harmonic characteristics compared with phase imbalance due to asymmetric resistance. For both types of asymmetric impedance, the dominant peaks on the bi-frequency plane provide valuable information about the nature of the phase imbalance at the load side.

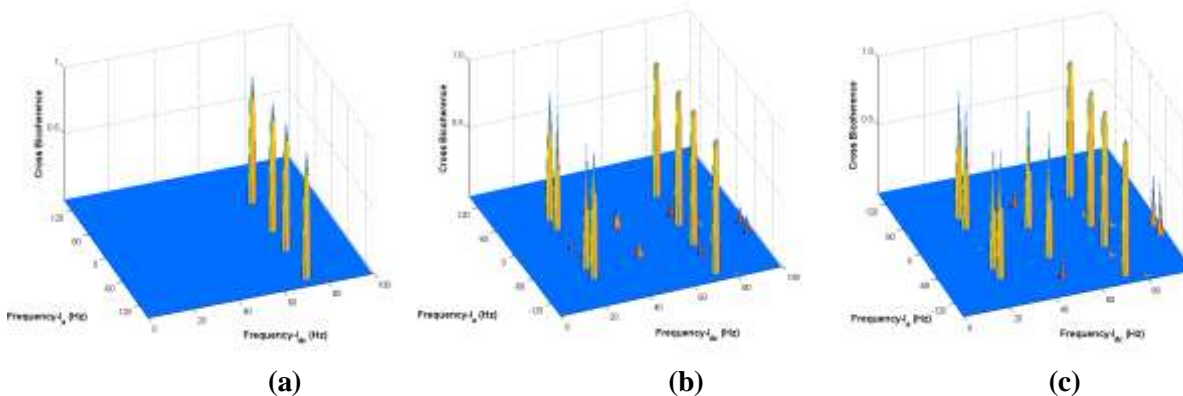


Figure 3-6: Cross bicoherence result comparison: (a) balanced, (b) unbalanced with 40 ohm asymmetric resistance, (c) unbalanced with 160 mH asymmetric inductance.

The characteristics of the dominant peaks in the cross bicoherence domain also suggest the possibility of classifying the imbalance by the type of asymmetric impedance. In addition, since we need information only at the source side for the anomaly detection, we do not need any extra information from the load side. This is helpful to reduce the number of required sensors, or to provide a redundant monitoring method when load-side sensors are not functional in an emergency situation.

3.1.2.5. A Novel QPC Detector for the Health Monitoring of Rotating Machines

The conventional non-parametric bispectrum/bicoherence approach is based on ensemble averaging over sample bispectra computed from independent time series segments. However, the conventional bicoherence estimation process can lead to misleading QPC (Quadratic Phase Coupling) detection results under certain circumstances. In the conventional non-parametric bicoherence estimation methods, *independent* data segments or realizations should be collected, and then sample bispectra are calculated from the DFT of each segment. Next, the sample

bispectra are ensemble-averaged to obtain an estimate of the bispectrum. The bicoherence is then computed from knowledge of the bispectrum. If the segments are not independent so that the phases of interacting frequencies are consistent over the segments rather than randomized over each segment, the corresponding bicoherence always results in spuriously high values regardless of the true existence of QPC relationship. Therefore, the so-called “phase randomization” assumption is required in order to achieve the proper bispectrum/bicoherence result. For health monitoring applications, a continuous time series with long data record length is often used, and the long time series is divided into segments for the estimation of the bicoherence. However, application of conventional bicoherence estimation methods to rotating machine time series data can cause problems, since the measurements from rotating machines usually have very long correlation times. In other words, each segment from the single long data record is correlated, and thus the phase randomization assumption is not satisfied. Therefore, the corresponding bicoherence analysis of rotating machine monitoring data can yield false QPC detection results. The exhibition of QPC indicates the presence of nonlinearity, which is often associated with system degradation. Therefore, false QPC detection results can trigger unnecessary tasks, such as additional maintenance or system reconfiguration.

If the so-called phase randomization assumption is violated, which requires the phase components of two primary frequencies to be independent and randomized over each individual data segment used to calculate the bicoherence, the bicoherence-magnitude-based QPC detectors always indicate a high value of bicoherence, regardless of whether there is true phase coupling or not. This false QPC detection is illustrated with the following test signal

$$x(t) = \cos(2\pi 40t + \theta_{40}) + \cos(2\pi 60t + \theta_{60}) + \cos(2\pi 100t + \theta_{100}) + v(t),$$

where $v(t)$ is additive white Gaussian noise with $\sigma_v^2 = 0.15$, equivalent to 10 dB signal-to-noise-ratio (SNR), and θ_i ($i = 40, 60$) is randomly chosen between $-\pi$ and π . θ_{100} is $\theta_{40} + \theta_{60}$ for the QPC case and is randomly chosen between $-\pi$ and π for no QPC case. The corresponding bicoherence values are computed using only a single data record (phases of frequency components are consistent over the record), and the results are illustrated in Figure 3-7. Even though Figures 3-7 (a) and (b) represent QPC and no-QPC cases, respectively, the two figures appear almost identical. Two peaks in Figure 3-7 (a) are generated from QPC relationship between 40 Hz and 60 Hz components, but peaks in Figure 3-7 (b) are the artifact of the bicoherence estimation process due to the failure of the phase randomization assumption.

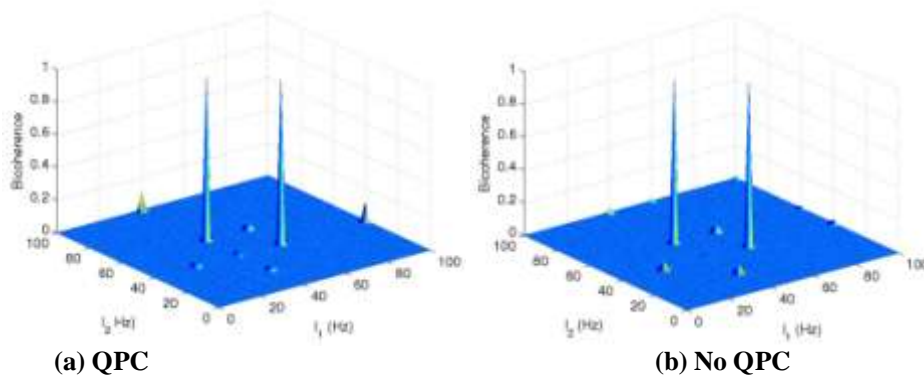


Figure 3-7: Example of false QPC detection: (a) QPC, (b) No QPC.

From this example, one can see that if the phase randomization assumption is violated, the traditional bicoherence-magnitude-based method yields a false detection result even when there is no QPC. More detailed mathematical analysis of the limitation of the conventional bicoherence is provided in [xvi, xvii].

To address the false detection problem, we propose a novel method, “phase randomized (PR) bicoherence.” The main idea is to introduce “artificial” phase randomization to each segment of a data record used to estimate the bicoherence. This can be done simply by multiplying the phase components of the sample bispectrum of each segment by a random variable \mathbf{R} during the calculation.

To illustrate the efficacy of the proposed PR bicoherence technique, we consider the same QPC detection example presented earlier, where the conventional method fails. PR bicoherence is computed using the same test signal, and the results are presented in Figure 3-8. Figure 3-8 (a) and (b) illustrate QPC and no-QPC cases, respectively. While peaks generated by QPC relationship between 40 Hz and 60 Hz components are clear in Figure 3-8 (a), no peak is observable in Figure 3-8 (b). Compared to the indistinguishable results from the conventional bicoherence in Figure 3-7, the QPC detection results via PR bicoherence are clearly distinguishable between the QPC and no-QPC cases in Figure 3-8. The mathematical justification of the proposed method for general signals is presented in a submitted journal paper.

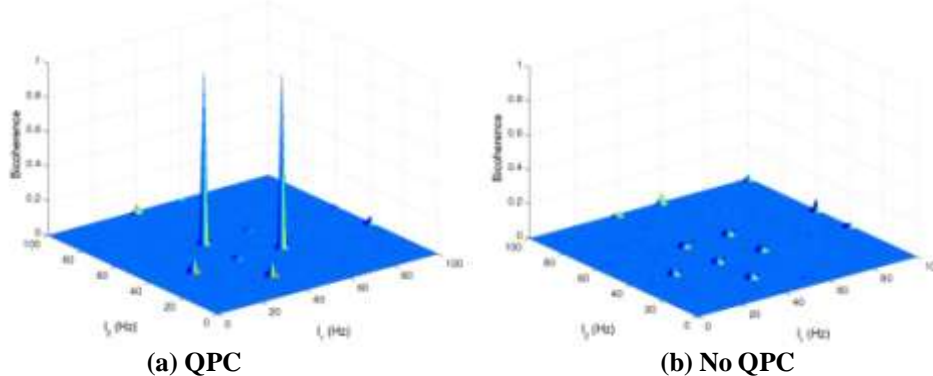


Figure 3-8: QPC detection example by PR bicoherence: (a) QPC, (b) No QPC.

We evaluated the detection error performance of the proposed method with respect to that of the previously proposed biphas-based approaches. The theoretical and numerical comparison results demonstrate that our proposed method has better detection error performance in terms of the probability of error at high SNRs. Furthermore, the conventional biphas-based methods fail to detect the practical partial QPC cases when coupled and uncoupled components are present at the same frequency. On the other hand, our proposed method is capable of addressing the partial QPC cases as well.

3.1.3. Using Voltage Sag Data to Decompose Utility Load and Determine Linear Load Characteristics

The two objectives of this section are to use voltage sag data to determine the fraction of load due to single-phase power electronics, and to determine the active and reactive linear load modeling coefficients needed for stability studies.

We begin by observing actual feeder load response data that was recorded during a transmission sag on a typical residential feeder in Austin, Texas. In Figure 3-9, the normalized voltage (dashed line) and current (solid line) are shown for a five cycle, 15% voltage sag. The majority of the load current is 60 Hz sinusoidal, but a fraction of the load is power electronic which causes the triangular peaked current distortion due to capacitor filtered diode bridge rectifiers.

The transient response of the power electronic load is quite different than that of traditional linear load. Using a decomposition technique, the power electronic load current component from Figure 3-9 is determined, and the estimated response of that load to the sag is shown in Figure 3-10. As can be seen, the composite power electronic load momentarily disconnects from the system while load power is provided by the dc capacitors of the bridge rectifiers. During the sag, the dc capacitors discharge to new steady state voltages. As the capacitor voltages decay, individual loads slowly begin to reconnect to the system. At voltage sag recovery, there is a substantial power inrush to recharge the capacitors back to their original steady state voltages.

As we will show later, the percentage of power electronic load on this feeder can reach as high as 15% of the total MW demand in the winter, and can be as low as 5% in the summer. The overall MW demand of the power electronic load, however, is relatively constant throughout the year.

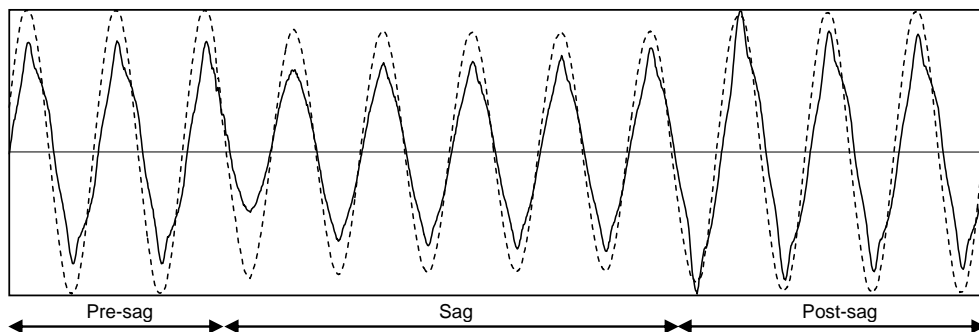


Figure 3-9: Actual utility voltage sag (dashed line) and current (solid line) response on a distribution feeder.

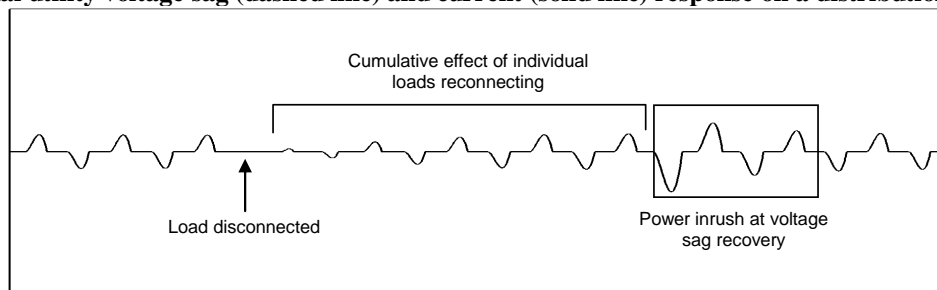


Figure 3-10: Estimated power electronic load current response for the event in Figure 3-9 (same scale).

Concerning stability load models, previous measurement-based procedures for calculating modeling coefficients do not distinguish between linear and power electronic load. And yet, the responses of these two types of loads to voltage sags are considerably different. This section determines the linear load coefficients by decomposing the composite load into linear and nonlinear components and then observing the variation of linear load with sag voltage.

We determined the total amount of nonlinear power electronic load for each of the 122 events captured over a two-year period on the distribution feeder. Each studied event is for the most affected phase. The monthly average single-phase power electronic MW demand per phase is shown in Figure 3-11. As expected, it is rather constant throughout the year.

Because the linear load varies by season, the percent of power electronic load changes by season. Due to air conditioning load, the percentage greatly decreases in the summer. Figure 3-12 shows the monthly average power electronic load in percent of total feeder MW. The average is greatest (12%) in December where there is little air conditioning load. In the summer, the linear load approximately doubles due to air conditioning, which causes the power electronic percentage to decrease by approximately half. For example, the average is 6% in August. For individual events, the seasonal range is 5-15%.

Coefficients dP/dV and dQ/dV are determined for the 84 events (of the total 122) that occurred strictly in the summer or winter months. Linear load coefficients for the summer months of June, July, and August are plotted in Figure 3-13. Recall that $dP/dV = 1.0$ is constant current and $dP/dV = 2.0$ is constant impedance. During these summer months, dP/dV averages 1.15 and dQ/dV averages 6.12. The linear active power load is primarily constant current, and the reactive load is much more voltage dependent than constant impedance.

Figure 3-14 shows the results for the winter months of December, January, and February. Coefficient dP/dV averages 1.62 and dQ/dV averages 5.45. The winter active power linear load is therefore slightly closer to constant impedance than constant current. Coefficient dQ/dV is still very large.

These average residential active power coefficients compare favorably to those suggested in commonly cited references (i.e., 1.2 in summer and 1.5 in winter).

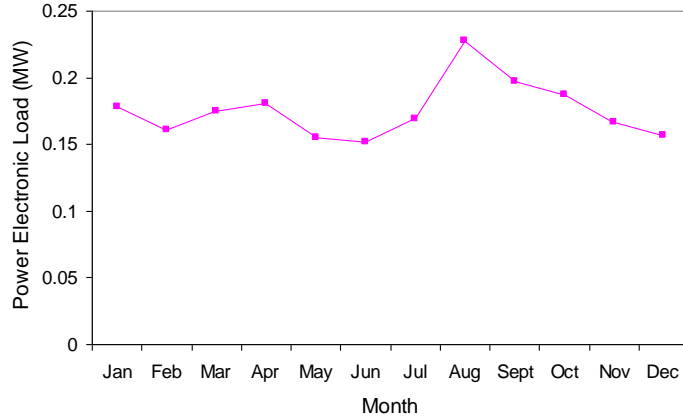


Figure 3-11: Monthly average power electronic load on the feeder, per phase.

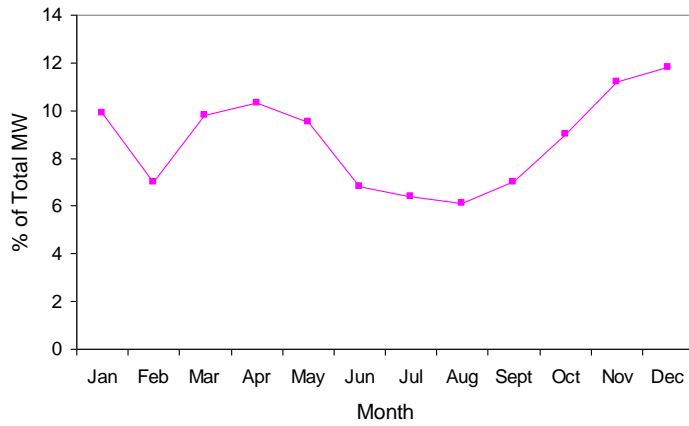


Figure 3-12: Monthly average power electronic load in percent of total feeder MW.

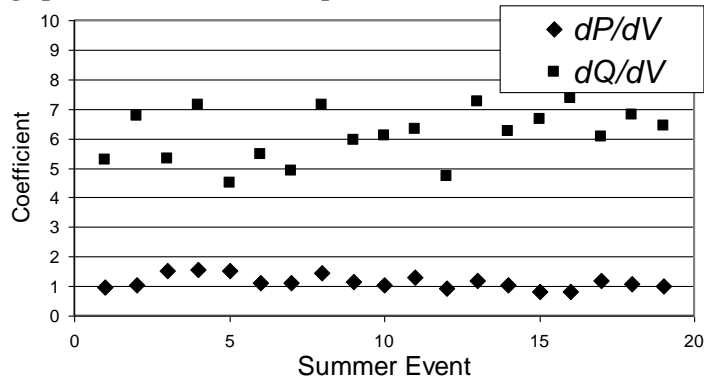


Figure 3-13: Summer linear load coefficients (Jun, Jul, Aug), dP/dV average = 1.15, dQ/dV average = 6.12.

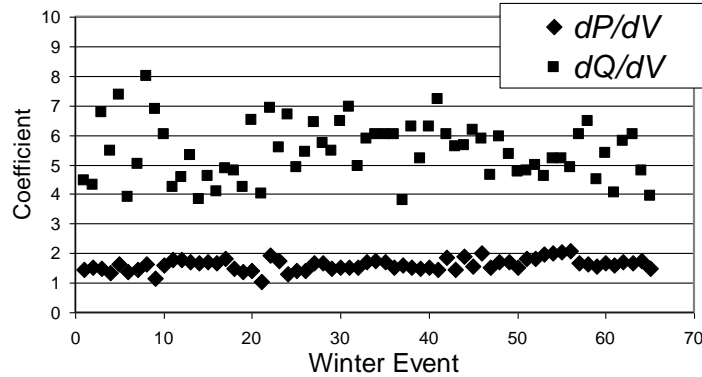


Figure 3-14: Winter linear load coefficients (Dec, Jan, Feb), dP/dV average = 1.62, dQ/dV average = 5.45.

The composite utility feeder load can successfully be decomposed into linear and single-phase power electronic components using data captured by power quality monitors and protection relays during transmission voltage sags.

For our 122 tests, the power electronic load (in MW) on the residential feeder is shown to be relatively constant throughout the year. Expressed as a percent of total MW, it ranges from about 5% in the summer to 15% in the winter.

The voltage response of the linear load during the sag is used to calculate the exponential load modeling coefficients dP/dV and dQ/dV required by most stability programs. The active power coefficients are strongly influenced by season. For the 19 summer events shown in Figure 3-13, the average load modeling coefficients are $dP/dV = 1.15$ and $dQ/dV = 6.12$.

For the 65 winter events shown in Figure 3-14, the average load modeling coefficients are $dP/dV = 1.62$ and $dQ/dV = 5.45$.

Summarizing, the techniques described in this section allow electric utilities to use actual data to estimate the percentage of single-phase power electronic load and to automate the process of determining the appropriate stability models for linear loads.

3.1.4. Experimental Apparatus, Testing Results, and Interpretation of the Impact of Voltage Distortion on the Current Distortion of Typical Single-Phase Loads

Current distortion (THDi) tests for individual appliances are supposed to be made using a low-distortion voltage (i.e., near-perfect sinewave). In practice, it is difficult to obtain a near-perfect sinusoidal voltage in any commercial building because of harmonic pollution in the building. Even if an amplifier is used, load currents interacting with the amplifier impedance corrupt the voltage waveform. As a result, actual test voltage waveforms can have 2-4% total harmonic voltage distortion (THDv), and the individual harmonics are uncontrollable and can vary considerably.

Technical literature is rich with publications that document the effect that THDi has on THDv. However, there are very few references available about the reverse effect – i.e., what impact does THDv have on THDi?

This section illustrates the effect of THDv on THDi through carefully controlled tests, where a harmonics testing station with corrective feedback on the load voltage energizes 120 V, single-phase loads with precision voltage waveforms. The results illustrate the sensitivity of common single-phase loads to voltage harmonics. Sensitivity varies considerably with load type.

The harmonics testing station, developed for CenterPoint Energy, uses an inverter together with software written in LabVIEW to create a single-phase 120 Vrms, 50/60 Hz ac voltage with a desired harmonic spectral content (through the 25th harmonic) for loads up to 1.5 kW. The two unique features of the station are the following:

- The testing station compensates for the distorting impact that harmonic currents in the test load have on the applied voltage by employing a specially-developed feedback method to adjust the

load voltage spectrum to the desired target. The station minimizes the total individual harmonic voltage error, normalized to the fundamental, within 1%.

- The testing station has the ability to operate in either a “stand alone” mode where it provides all the load power, or in a “summing junction” mode where it synchronizes with the grid and adds to the building voltage. Thus, the testing station need only provide the harmonic portion of the desired load voltage plus a few percent of the harmonic load power.

All amplifiers and inverters have output impedances. Thus, when powering a nonlinear load, harmonics in the load current create undesired harmonics in the amplifier/inverter output voltage. Feedback is necessary to adjust the amplifier/inverter input voltage in such a way that the output voltage waveform is driven to the desired target. Consider the feedback loop in the stand alone mode. Inverter input signal $V_{inverter}$ is comprised of two components – the user specified target value V_{target} , plus the computed correction needed (i.e., $V_{feedback}$) to drive the load voltage to the target value. Thus,

$$V_{inverter} = V_{target} + V_{feedback}$$

so that

$$V_{error} = V_{target} - V_{load} = 0.$$

For the summing junction mode, $V_{inverter}$ does not contain the portion of V_{target} that is supplied by the 120 Vac building voltage. Thus,

$$V_{inverter} = V_{target} - V_{buildingvoltage} + V_{feedback}$$

There are two methods for adjusting $V_{feedback}$ in the harmonics testing station, and each applies to both stand alone and summing junction operating modes. First, the user can make manual adjustments to the individual harmonic components of $V_{feedback}$ (i.e., the “Manual Method”). The manual method is useful for making simple corrections and for illustrating the interaction between load current harmonics and inverter output voltage. However, it is usually impossible to manually reduce V_{error} to the 1% range, especially when testing nonlinear loads.

The second feedback adjustment procedure is automatic and iterative. This iterative procedure employs the method of finite differences, where small changes are made to the individual harmonic components of $V_{feedback}$ and the corresponding changes in like harmonics of V_{error} are observed. This does mean that the interaction between harmonics is ignored, however, for any iteration only the most offending harmonic is controlled. Each iteration begins by identifying the harmonic k that has the highest V_{error} magnitude. Then, partial derivatives are approximated from finite differences, and $V_{feedback}$ is adjusted accordingly to reduce V_{error} .

Expressing harmonic k components of $V_{feedback}$ and V_{error} as phasors in rectangular form, we have

$$\tilde{V}_{feedback}^k = V_{f,real}^k + jV_{f,imag}^k$$

and

$$\tilde{V}_{error}^k = V_{e,real}^k + jV_{e,imag}^k$$

The objective is to adjust $V_{f,real}^k$ and $V_{f,imag}^k$ so that $V_{e,real}^k$ and $V_{e,imag}^k$ approach zero. For small changes,

$$\begin{bmatrix} \Delta V_{e,real}^k \\ \Delta V_{e,imag}^k \end{bmatrix} = \begin{bmatrix} \frac{\partial V_{e,real}^k}{\partial V_{f,real}^k} & \frac{\partial V_{e,real}^k}{\partial V_{f,imag}^k} \\ \frac{\partial V_{e,imag}^k}{\partial V_{f,real}^k} & \frac{\partial V_{e,imag}^k}{\partial V_{f,imag}^k} \end{bmatrix} \begin{bmatrix} \Delta V_{f,real}^k \\ \Delta V_{f,imag}^k \end{bmatrix}$$

At any iteration m , one must compute the changes in feedback voltage that will reduce the error to zero at iteration $m+1$. Writing the previous equation as

$$\Delta V_e = J \left[\Delta V_f \right],$$

then expanding to

$$V_{e_{m+1}} - V_{e_m} = J_m \left[V_f \right]_{m+1} - \left[V_f \right]_m,$$

and setting the $V_{e_{m+1}}$ term to the desired value (i.e., 0), yields

$$\left[V_f \right]_{m+1} = \left[V_f \right]_m - J_m^{-1} V_{e_m}$$

Summarizing, the partial derivatives given in the above Jacobian matrix are evaluated using the method of finite differences, and then new values of feedback are computed for harmonic k .

The test voltage waveforms have an underlying 120 Vrms, 60 Hz fundamental component. Harmonics through the 25th multiple can be added individually, or together, to add distortion. Even-ordered harmonics are zero in the test voltage because they are usually negligible in building supply voltages. With the use of feedback, the load voltage waveforms are controlled to within 1% of the desired target waveform. The waveforms are

- Sinusoidal voltage
- Simulated building voltage having THDv = 5% and a typical building voltage waveshape and harmonic content.
- Sinusoidal voltage plus 5% or 10% single odd-harmonic voltage 3rd, 5th, ..., 25th, and with harmonic phase angles either 0°, 90°, 180°, or 270°.

The 5% THDv simulated building voltage is fairly typical in commercial buildings. The building voltage is flattened due to large numbers of computers and other single-phase power electronic loads that draw current for a short interval near the voltage peak. The waveform shown has a somewhat higher THDv than normally seen, but it is still within the limit of what is considered acceptable (i.e., 5%).

Comparisons of load THDi for the sinusoidal and 5% THDv simulated building voltage are shown in Figure 3-15.

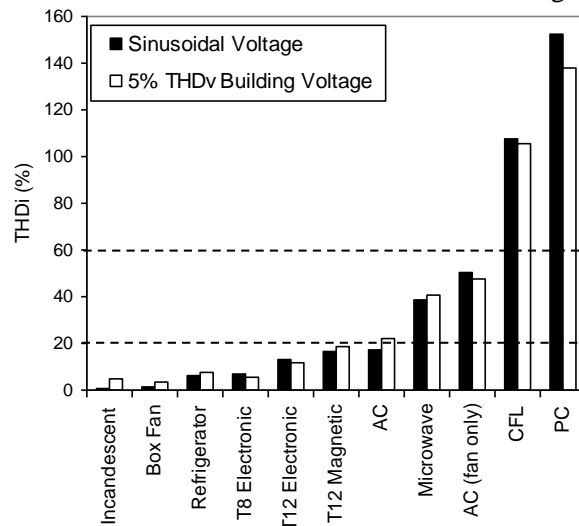


Figure 3-15: THDi for test loads excited by sinusoidal and 5% THDv building voltage.

The simulated 5% THDv building voltage can produce either higher or lower THDi than sinusoidal voltage. Specifically, the electronic ballasts and the fan of the window air conditioner have lower THDi when energized by the simulated building voltage. Also, the simulated building voltage has the flattened shape that causes the high distorting loads to conduct for longer periods of time each half cycle, thus reducing their THDi.

The sensitivity of load THDi to fundamental plus one voltage harmonic was investigated for all odd harmonics through the 25th multiple with cosine phase angle reference 0° (peaky), 90° (skewed left), 180° (flattened), and

270° (skewed right) for each of the test loads. The tests were made using single harmonic voltage magnitudes of 10.

Each of the following four graphs contain 49 individual measurements (four points for each of the 12 odd harmonics 3, 5, ..., 25), plus a dashed line that indicates THDi for the sinusoidal voltage case. To simplify the interpretation of the findings, the upper and lower envelopes of the measured THDi are plotted with solid lines, the reference sinusoidal voltage THDi is represented by the dashed line, and comments are added where needed. The refrigerator is most affected by low-order voltage harmonics which cause greater distortion than the reference case for all phase angles, as seen in Figure 3-16. Harmonic exciting voltages induce mostly 3rd harmonic current. The peaky 3rd harmonic voltage causes the THDi to be five times greater than the reference case, while the flattened 3rd harmonic voltage causes the THDi to be three times greater than the reference. The induced THDi exponentially decreases back to the reference case as the voltage harmonic order increases.

Harmonic excitation voltage induces mostly the 3rd and 5th harmonic currents. However, as the voltage harmonic order increases, the 3rd and 5th harmonic currents decrease. This causes the THDi to exponentially decay to the reference case for high-order voltage harmonics as seen in Figure 3-17. The THDi is especially impacted by the low-order voltage harmonics. The 5th harmonic voltage causes a resonance in the compressor increasing the THDi by approximately a factor of two for all phase angles of harmonic voltage. In all cases, a peaky voltage causes the THDi to be at the upper bound of the envelope while a flattened voltage results in the lower bound. In the PC, low-order exciting voltage harmonics induce low-order harmonic currents, while the high-order exciting voltage harmonics induce a broad range of harmonic currents. When the load is excited by low-order harmonics, the resulting THDi is significantly different for different phase angles, as seen in Figure 3-18. For the 3rd and 5th harmonic voltages, peaky harmonics increase the THDi, while flattened harmonics decrease the THDi from the reference case. Peaky harmonic voltages up to the 13th cause the load current to be one single narrow pulse each power frequency half cycle. After the 13th harmonic, the peaky voltage causes the current pulse to break into multiple conductions, therefore decreasing the THDi. Once that occurs, the phase angle of the voltage harmonic becomes less significant resulting in a convergence of the peaky and flattened THDi envelope. The THDi is greater than the reference case for high-order harmonic voltages.

Summarizing, this section gives the results of extensive harmonic testing on several common 120 Vac, 60 Hz, single-phase loads. THDi results obtained by using the 5% simulated building voltage are very similar to those obtained with sinusoidal excitation. Contrary to what might be expected, the THDi of electronic loads such as a personal computer actually decreases when the simulated building voltage is used because of the characteristic flattened waveshape of that voltage. This is also seen in the individual test for flattened 3rd harmonic voltage. The variation of THDi with harmonic voltage magnitude and phase angle depends greatly on load type. For all except the high-distorting loads, the 3rd harmonic voltage has the greatest impact on THDi. Load response depends largely on the phase angle of the harmonic voltage. This is especially true for the 3rd and 5th harmonic voltages, whose phase shift has a significant impact on the peaky or flattened nature of the composite voltage. The THDi of some loads is considerably worse with peaky voltage excitation. Other loads have an alternating peaky/flattened pattern of THDi sensitivity.

Two loads experienced serious resonance – the refrigerator near the 3rd harmonic, and the window air conditioner near the 3rd and 5th harmonics. There is a significant increase in THDi near those harmonics. The power consumed by these loads increases by 7% and 3%, respectively. This increase manifests itself as additional motor losses.

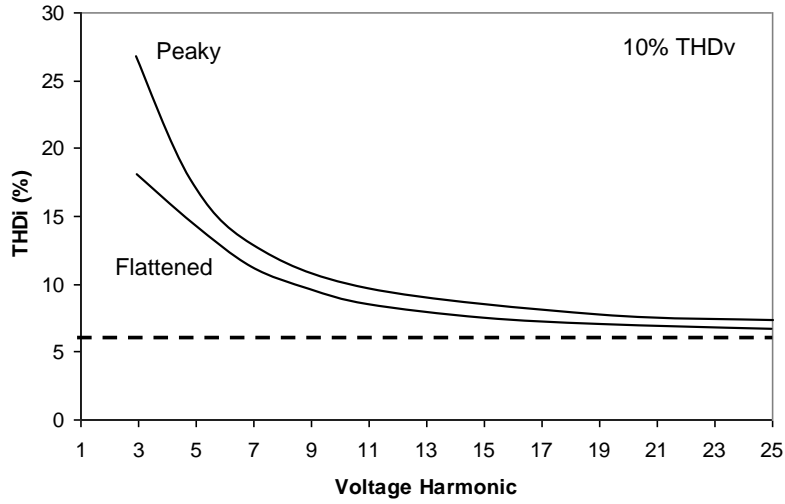


Figure 3-16: Refrigerator.

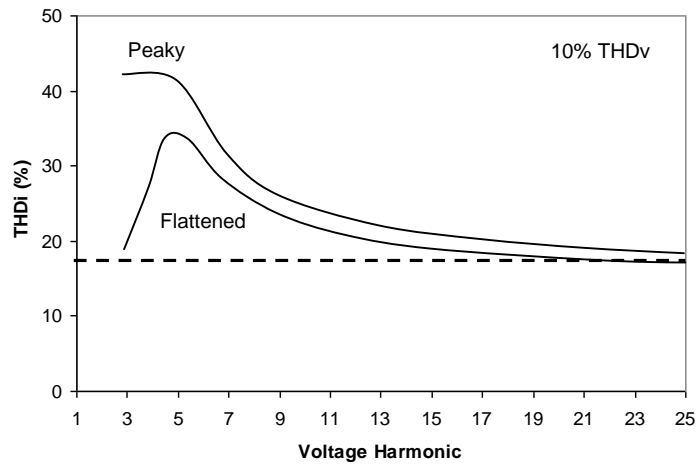


Figure 3-17: Window air conditioner.

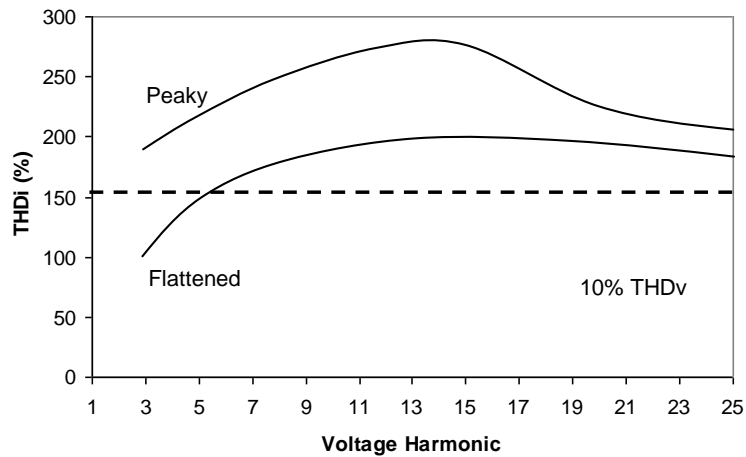


Figure 3-18: Personal computer.

3.1.5. Problems in the Use of Norton Equivalent Models for Single-Phase Nonlinear Loads

The use of Norton equivalent models for composite customer loads has been widely discussed. However, as explained in most circuit analysis textbooks, Norton equivalents are intended to be used only with linear circuits and loads. For a Norton equivalent to be valid, its complex impedance and phasor current, $Z_{n,k}$ and $I_{n,k}$, for any harmonic k should be constant and independent of the applied voltage waveshape. Our measurements show that neither $Z_{n,k}$ or $I_{n,k}$ are constant enough to justify the use of Norton equivalents for nonlinear loads.

The Norton equivalent model is shown in Figure 3-19. Its parameters for a harmonic k can be experimentally determined using two sets of voltage and current measurements.

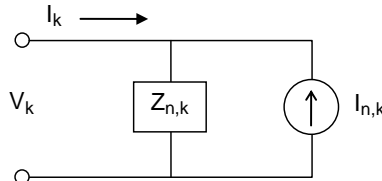


Figure 3-19: Norton equivalent load model.

The two sets of measurements, together with

$$Z_{n,k} = \frac{V_k^{(2)} - V_k^{(1)}}{I_k^{(2)} - I_k^{(1)}} \quad \text{and} \quad I_{n,k} = \frac{V_k^{(1)}}{Z_{n,k}} - I_k^{(1)}$$

are used to solve for $Z_{n,k}$ and $I_{n,k}$. The fundamental voltage phase angle must be the same in both experiments.

In our tests, we obtained the sets of V_k , I_k using the Harmonics Testing Station.

The four test loads used to evaluate the Norton equivalent load models include a personal computer, compact fluorescent lamp, window air conditioner, and incandescent lamp. The personal computer and compact fluorescent lamp are highly nonlinear loads. They have severe current distortion whose harmonics change significantly with voltage waveshape. The window air conditioner is representative of a significant portion of summer peak load and has a slight nonlinearity that causes noticeable interaction between voltage and current harmonics. The incandescent lamp, which obviously is a linear load, is used as a benchmark to confirm our testing and calculation procedures.

We performed two different types of harmonic tests. In single harmonic tests, we excited the load with 120 Vrms, 60 Hz plus 5% of 3rd, 5th, or 7th peaky or flattened voltage. In the mixed harmonic tests, we used the 5% THDv building voltage waveform.

At this point, it is helpful to explain the purpose of testing the incandescent lamp. The incandescent lamp has a known resistance and zero Norton current. Knowing this, we were able to ascertain that accuracy in Norton model calculations requires harmonic voltage changes of approximately 1% or greater. Therefore, we have limited our analysis and conclusions to tests where the complex difference between the two sets of voltage is 1% or greater.

The 3rd harmonic Norton parameters for the personal computer are given in Table 3-1. The eight voltage test waveforms are paired into 10 sets of data. In the “Waveform 1” and “Waveform 2” columns, the notation “P” means peaky single harmonic voltage, “F” means flattened single harmonic voltage, and “BV” means simulated building voltage. “Sgl” indicates the results are determined with single harmonic waveforms, while “Mixed” indicates the results are determined when one waveform is the simulated building voltage.

Table 3-1: Personal Computer 3rd Harmonic Norton Load Model (sine angles).

Waveform 1	Waveform 2		Z3_mag	Z3_ang	I3_mag	I3_ang
Sinusoidal	5% V3, P	Sgl	431	-151	0.393	-1
Sinusoidal	5% V3, F		5700	69	0.393	-1
5% V3, P	5% V3, F		897	-153	0.384	0
5% BV	Sinusoidal	Mixed	30	-55	0.396	-1
5% BV	5% V3, P		66	-69	0.349	-20
5% BV	5% V3, F		11	60	1.040	-41
5% BV	5% V5, P		31	-57	0.387	0
5% BV	5% V5, F		27	-69	0.344	7
5% BV	5% V7, P		32	-54	0.396	-2
5% BV	5% V7, F		29	-84	0.275	4

For any given row in Table 3-1, the values Z3_mag, Z3_ang, I3_mag, and I3_ang satisfy $Z_{n,k}$ and $I_{n,k}$ exactly for the circuit in Figure 3-19 using the two voltage waveforms indicated as “Waveform 1” and “Waveform 2.” If Norton modeling is valid for the personal computer, then every row of Norton impedance and current in the above table would be nearly identical. However, there is considerable variation, especially in the impedance of the top six rows.

Based upon the results in Table 3-1, our conclusions for the personal computer are as follows:

- Norton models for “Mixed” harmonic tests vary too much to be useful.
- “Sgl” harmonic tests produce mostly steady Norton currents, but the Norton impedance magnitudes and angles vary greatly.
- Two tests yield negative Norton resistances (i.e., Z3_ang of -151 and -153 degrees).

The Norton inaccuracies described above are not unique to the 3rd harmonic. The same inaccuracies are also evident in the results for the 5th and 7th harmonics.

The 3rd harmonic Norton load models for the compact fluorescent lamp are given in Table 3-2. Overall, for the compact fluorescent lamp, we conclude that

- Norton models for “Mixed” harmonic tests vary too much to be useful.
- “Sgl” harmonic tests produce steady Norton models.
- One test (i.e., fifth row of “Mixed” results) has a negative resistance.

Results for the 5th and 7th harmonic tests yield the same conclusions.

Table 3-2: Compact Fluorescent Lamp 3rd Harmonic Norton Load Model (sine angles).

Waveform 1	Waveform 2		Z3_mag	Z3_ang	I3_mag	I3_ang
Sinusoidal	5% V3, P	Sgl	59	2	0.614	83
Sinusoidal	5% V3, F		57	-25	0.613	83
5% V3, P	5% V3, F		59	-12	0.580	82
5% BV	Sinusoidal	Mixed	33	-68	0.612	83
5% BV	5% V3, P		57	-44	0.514	78
5% BV	5% V3, F		15	8	0.674	42
5% BV	5% V5, P		24	-24	0.642	65
5% BV	5% V5, F		59	-113	0.493	93
5% BV	5% V7, P		24	-11	0.607	60
5% BV	5% V7, F		54	-78	0.529	86

The window air conditioner is more linear than the computer and compact fluorescent lamp; however, the Norton model is not consistent. The 3rd harmonic Norton models are shown in Table 3-3.

Overall, for the window air conditioner, our conclusions are that

- Norton models for ‘Mixed’ harmonic tests vary too much to be useful.
- ‘Sgl’ harmonic tests indicate steady Norton models.

The conclusions for the 5th and 7th harmonic tests are the same.

Table 3-3: Window Air Conditioner 3rd Harmonic Norton Load Model (sine angles).

Waveform 1	Waveform 2		Z3_mag	Z3_ang	I3_mag	I3_ang
Sinusoidal	5% V3, P	S _{q1}	15	24	0.940	-72
Sinusoidal	5% V3, F		11	12	0.943	-72
5% V3, P	5% V3, F		13	17	0.946	-79
5% BV	Sinusoidal	Mixed	10	21	0.940	-72
5% BV	5% V3, P		12	21	0.895	-80
5% BV	5% V3, F		21	29	0.919	-98
5% BV	5% V5, P		9	36	1.160	-73
5% BV	5% V5, F		19	16	0.834	-95
5% BV	5% V7, P		13	40	1.070	-87
5% BV	5% V7, F		10	33	1.070	-77

Norton models for the personal computer, compact fluorescent lamp, and window air conditioner depend greatly on voltage waveshape. There is a wide range of Norton parameters for any one of these loads depending on the voltage waveforms used in the calculations. In some cases, the Norton impedance even has a negative resistance. Norton equivalents are intended to be used with linear circuits. Our tests show they are inappropriate for even mildly-nonlinear loads such as a window air conditioner.

If Norton equivalents are inappropriate for building block single-phase nonlinear loads, they are most likely inappropriate for composite nonlinear loads and three-phase nonlinear loads. If so, one should then ask the following two questions:

- Which two sets of voltage and current measurements are to be used in computing the Norton model?
- In practice, how does one create a significant ($\geq 1\%$) change in harmonic voltage so that the measurements can be made?

In our opinion, the above two questions must be addressed before a serious attempt is made to use Norton equivalent models to determine a customer's impact on the power system.

3.1.6. Dynamic Power System Reconfiguration

Much of the following section is detailed with an extensive bibliography in: K.C. Nagaraj, J. Carroll, T. Rosenwinkel, A. Arapostathis, M. Grady, and E.J. Powers, "Perspectives on power system reconfiguration for shipboard applications," IEEE Electric Ship Technologies Symposium, Arlington, Virginia, May 21-23, 2007. The power system network is modeled as a number of generators converting mechanical power input to electrical power which is supplied to different loads via a network of transmission and distribution lines. The generators are normally modeled as a set of nonlinear differential equations. The generators supply to loads that can be modeled as constant power demands, current injections, or impedances. The nodes of the network are called buses which are connected by mainly inductive transmission lines. The transfer of power between any two nodes is governed by algebraic equations that correspond to basic Kirchoff's laws.

For easier modeling and control of networks, it is common convention to model the network as being radial. That means that every load has a unique supplying substation. From a substation, the switches that divide the radiating lines into sections are known as sectionalizing switches. The switches which can connect two radiating lines to form a loop are called tie switches. An illustrative power network is shown in Figure 3-20.

The system state is retained close to a designed operating point under normal conditions. During sudden load changes, faults, or network expansion/maintenance activities, the network may not function efficiently. Over time, due to development, load distribution across network changes. This can cause undesirable power imbalance. It may become necessary to alter the topology of the network to minimize the ill effects of such phenomena or to improve the efficiency of the network. Reconfiguration of power systems is the process of altering the topological structure of the network by changing the status of open/closed switches in the network. Therefore reconfiguration is best framed as a combinatorial optimization of the switching status. It can be used as a tool in planning and maintenance as well as for real time control.

Optimal reconfiguration is a nonlinear combinatorial optimization problem. It involves choosing positions of the switches in the network to meet some optimization criteria without violating certain constraints. One may need to perform a load flow analysis of the network to observe the flow of power, voltage levels, and current flows in the network under the chosen configuration. If there are n switches in the network, there are 2^n possible switch position combinations. For even small number of switches, it becomes computationally formidable to attempt an exhaustive search. Hence, research effort has been directed towards minimizing the search space of candidate configurations, reducing the number of calculations per iteration, arriving at a global minimum without cycling, etc. The solution configuration may serve to meet the following objectives:

- Restore service to all/most of the loads under fault conditions
- Minimize resistive losses in transmission/distribution lines
- Balance loads across the network
- Minimize reactive power flow
- Enhance voltage stability
- Improve reliability and redundancy in the network
- Minimize operational cost, etc.

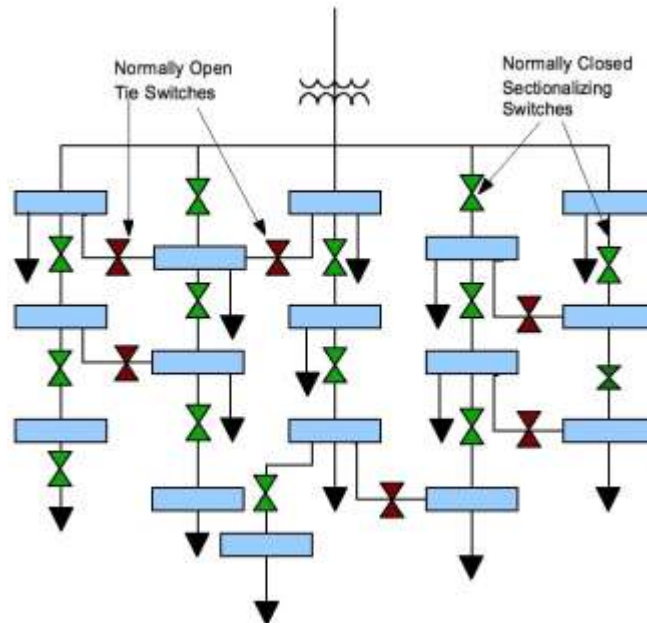


Figure 3-20: Illustrative radial network.

Depending on the time requirements of the purpose of reconfiguration, several methodologies have been proposed in the literature. We survey the different purposes for which reconfiguration has been used, the broad spectrum of optimization techniques that are employed to find an optimal reconfiguration.

If the loads are assumed constant PQ , the line model is as shown in Figure 3-21.

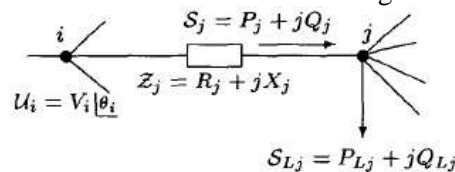


Figure 3-21: Line Model and Parameters

The resistive loss incurred in each branch is calculated as:

$$P_j^{loss} = R_j I_j^2 = R_j \frac{P_j^2 + Q_j^2}{V_j^2}.$$

The injected power at each node is the summation of the power generated minus power consumed at that node. From this model, several of the optimization objectives can be simply formulated. Service restoration is nothing but maximizing the total power delivered across the network. The function to be minimized for minimal resistive loss is:

$$\sum_{j=1}^b R_j \left[\frac{P_j^2 + Q_j^2}{V_j^2} \right],$$

where b is the number of branches. A popular estimate of the balance of load is given by the ratio of the complex power at the sending end of the branch to its rated KVA capacity. The objective function to improve load balance is given by:

$$LB_{index} = \sum_{i=1}^b \frac{S_i}{S_i^{max}} = \sum_{i=1}^b \frac{P_i^2 + Q_i^2}{S_i^{max}}$$

In a similar manner, objective functions have been formulated to achieve the objectives listed above, as well as other network specific objectives.

Clearly, the set of feasible configurations may not be the same as the set of possible switch states. Some switching combinations might produce an unsafe scenario. In order to guarantee an appropriate reconfiguration solution, the optimization problem is constrained to exclude bad switch states. Some of the typical constraints associated with the optimization problem are:

- Radiality of the network should be maintained
- All (or a specific set of) loads should be served
- Maximum limit on the number of switch operations should not be exceeded
- Stability must be maintained
- Frequency must remain within standard tolerances
- The voltage magnitudes must be within operational constraints
- Current capacity limits must not be exceeded
- Generation limits must be satisfied

Depending on the reconfiguration strategy, all of these constraints are legitimate concerns. The last five, however, must be taken into account for predictable behavior. Many studies take certain constraints for granted, assuming that most values will fall within tolerances. For large systems, such assumptions are usually valid. However, some constraints cannot be ignored in a smaller system.

The search for an optimal reconfiguration for the above goals is a nonlinear combinatorial optimization, which is NP-complete. For the power system reconfiguration, the size of the problem makes an exhaustive search computationally intractable. Practical reconfiguration techniques often incorporate algebraic simplifications to reduce the required number of calculations. In this direction, several simplified load flow formulas have been developed:

The node voltages are approximately one. This is nearly true under normal operating conditions. This makes the power loss term $P_j^{loss} \approx R_j (P_j^2 + Q_j^2)$.

The active power flow at a particular node is comprised of the active load downstream from that node, plus the active losses of the respective branches. The latter part is negligible in comparison to the total load, so the line losses can be ignored for some objectives. Similar approximations can be applied to the reactive power. Many reconfiguration methods avoid the complexity of the combinatorial optimization problem by adopting heuristic rules. Some of the earliest reconfiguration studies used “branch exchange” methods. Branch exchange

algorithms start with a radial configuration. Alternative configurations are found by closing a tie switch and opening a sectionalizing switch in order to maintain radiality. The switch pairs (one tie and one sectionalizing switch) are chosen based on heuristic rules and by calculating the change in loss obtained by the switching. The branch exchange stops when no further reduction in loss can be achieved. This method has the advantage of being fast and simple in implementation, but does not guarantee a global minimum. Another method trying to achieve the optimal flow pattern is the sequential switch opening algorithm. Since a completely meshed network provides the minimal loss solution, the algorithm starts with all switches closed. It aims at achieving a radial configuration that least disturbs the optimal power flow. From the completely meshed network, switches carrying the least current are opened successively. The algorithm stops when the system is radial. The advantage of this method is that it is independent of initial load flow. A similar formulation of reconfiguration for minimal resistive loss based on transshipment treats current flow as cost associated with transporting power from the generators to the loads.

Other heuristic rules are included in the optimization problem to reduce the search space directly. Examples include:

- Shifting loads from heavily loaded transformers to lightly loaded transformers. This will minimize losses and also improve load balance in the network.
- Avoiding shifting loads to branches which have recently violated constraints.
- Considering voltage drops from the substation to both ends of an open section. If load is transferred lower voltage drop side to higher voltage drop side, the losses will increase.
- A first level substation connected to second level substations with excess capacity is a good candidate to accept load transfers.
- If the voltage drop across an open tie switch is negligible, then that switch option is neglected.

Using these heuristic rules, the switching options are reduced and the calculation time decreases. Some studies have automated the reconfiguration process into an expert system that algorithmically applies heuristic rules to find a near optimal solution. Others have used petri nets to solve reconfiguration for loss minimization, to solve service restoration, and to enhance reliability. However, enforcing the heuristic rules might direct the solver away from the globally optimal solution.

To solve the reconfiguration problem in a globally optimal manner, a plethora of methodologies involving mixed integer programming, evolutionary algorithms, artificial intelligence, and fuzzy logic have been applied. Most use a randomized search to avoid dependency on the initial candidate solution. A popular modern method is simulated annealing. The simulated annealing algorithm relies on convergence parameters that must be adjusted to find reasonable solutions. That is, a “one-shot” simulation with fixed parameters of the algorithm does not yield a global optimum solution. Although techniques employing simulated annealing are time consuming, they have the advantage of being capable of handling ill-structured constraints. Genetic and evolutionary algorithms have invoked tremendous interest as a technique for optimal reconfiguration. The natural analogy between genetics and the growth of infrastructure over the decades have inspired engineers to use evolutionary algorithms to make power distribution more efficient. Since the algorithm searches from many initial points, the authors expect the near-optimal solution to be reached fast. The main drawback in using the traditional genetic algorithm formulation is that it converges to local minima. In order to circumvent this situation, gene crossover and mutation operators have been developed using network constraints to eliminate the initial infeasible gene pool. In conjunction with simulated annealing and genetic algorithms, tabu search is a mechanism that has been used to systematically eliminate some solutions and to avoid cycling and entrapment in local minima.

The techniques that have been surveyed above for terrestrial power systems are useful when considering shipboard power systems, but there are many important distinctions between large scale networks and the self-contained systems found on ships. Several characteristics of the shipboard system are directly relevant to the reconfiguration problem. The space and weight constraints of the electric ship can severely limit the amount of redundancy that can be incorporated. The shipboard distribution network is tightly coupled and spread over a small area; hence resistive losses are nearly negligible. Large dynamic loads and limited generator inertia can

lead to large voltage and frequency deviations. Large nonlinear loads make common assumptions about constant or linear power consumption inaccurate. Tight coupling may result in unexpected behavior if the system is not modeled accurately. For this reason, many of the constraints on reconfiguration that are less relevant in large scale systems require attention in the shipboard case. Also, specific models of the shipboard power system can often be used to simplify reconfiguration analysis.

The first shipboard reconfiguration studies applied the same principles as their land-based counterparts. The model was formulated so as to satisfy radiality constraints without stating them explicitly, and aimed at maximizing the power delivered to the load. The optimization was further improved to satisfy more constraints, include heuristic methods, and incorporate geographic fault information. Others extended these methodologies to account for non-radial topologies and mixed ac/dc systems, as well as islanding scenarios. Because the shipboard system is smaller than a typical power system, computational complexity is not a limiting factor in these methods. One of the most desirable characteristics of an integrated shipboard power system is the ability to survive catastrophic failure. For naval applications, component failure could be caused by a physical attack. Based on this scenario, some researchers have formulated a probabilistic reconfiguration algorithm that predicts component failure based on physical distance from a detected attack point. Because the shipboard system is limited in size, nearby components are more likely to fail or continue operation together. The optimization tries to reroute power around components that are likely to fail during an imminent attack, thereby maintaining service as much as possible throughout the attack. Another popular area of shipboard reconfiguration research is distributed control. Distributed controllers, called agents, exchange information to collectively achieve goals. Agent-based control has the benefit of continued control operation even when communication pathways break down, as in an attack scenario. Most of the research into agent-based reconfiguration is concerned with the practicalities of agent interaction rather than optimal reconfiguration. Some studies have yielded promising results when the network is restricted to a specific topology or a specific task suited to localized control. These methods are only interesting with regards to the specified network structure or task, though they may prove very useful within their respective paradigms. Even more general agent-based control schemes are currently lacking in rigorous proof of optimality, especially in severe failure scenarios.

One of the key considerations rarely accounted for in reconfiguration studies is the transient system response to reconfiguration actions. In the large-scale scenario, the system is often large and redundant enough that a mild reconfiguration will not produce a significant transient. For the shipboard system, the small system size and the relatively drastic reconfiguration actions may produce significant transient stability responses. The smaller system is well-coupled, so angle instability usually will be negligible, but voltage transients are of utmost concern.

To analyze and prevent dramatic voltage swings, we proposed an energy-function-based method for finding safe reconfiguration transitions. Our method involves approximating a region of safe convergence in the state space. A system trajectory starting within this region will remain within the region, and therefore within the user-determined voltage constraints. The safe region is numerically difficult to find exactly, but by using an approximate energy function, we can approximate the region to conservatively investigate the safety of a particular transition.

A great deal of work has been done over the years on developing energy functions for various power system models. However, most of the past work on energy functions for power system stability has focused on fault-based switching actions (i.e., breakers). However, in the reconfiguration problem, we are interested in every possible switching configuration, not just “normal” and “faulted” scenarios. Rather than work with the highly nonlinear dynamics of the system, we can linearize the singularly perturbed system model of each configuration around its respective equilibrium. Though the linearized version of the system is a rather extreme approximation, the area near the equilibrium is reasonable and the analysis involved is greatly simplified. Each switching configuration is represented generally by a differential-algebraic system which is then approximated as follows:

$$\text{Original System: } \begin{cases} \dot{x} = f_z(x, y) \\ 0 = g_z(x, y) \end{cases}, \text{ Singularly Perturbed System: } \begin{cases} \dot{x} = f_z(x, y) \\ \varepsilon \dot{y} = g_z(x, y) \end{cases},$$

Linearized System:

$$\begin{bmatrix} \dot{x} \\ \dot{y} \end{bmatrix} = J_z \left(\begin{bmatrix} x \\ y \end{bmatrix} - \begin{bmatrix} x_z^{eq} \\ y_z^{eq} \end{bmatrix} \right),$$

Energy Function:

$$V \left(\begin{bmatrix} \dot{x} \\ \varepsilon \dot{y} \end{bmatrix} \right) = \left(\begin{bmatrix} x \\ y \end{bmatrix} - \begin{bmatrix} x_z^{eq} \\ y_z^{eq} \end{bmatrix} \right)^T P_z \left(\begin{bmatrix} x \\ y \end{bmatrix} - \begin{bmatrix} x_z^{eq} \\ y_z^{eq} \end{bmatrix} \right),$$

where P solves the Lyapunov equation for J .

The safety of a transition is determined by comparing the energy level of the origin state (with respect to the target state's energy function) to the critical energy level of the target state. For hard constraints on the state space, such as voltage limits, the quadratic energy function shown above allows the calculation of the critical energy level via quadratic optimization along each of the bounds on the state space.

$$\text{Critical Energy Level} = \min_{\text{all bounds}} \min_{x \text{ on boundary}} (x - x_{eq})^T P (x - x_{eq})$$

For constant loads and reference voltages, each of the optimizations may be performed off-line; if the loads and references will change, the linearized system can be maintained as a function of the continuous variables. The quadratic energy functions produce hyper-elliptical level sets, and the critical energy levels define the boundaries of the region of safe convergence for each switch configuration. Once the critical energy levels have been calculated, all of the transitions between states can be classified as safe or unsafe. One can use energy functions to estimate the region of the state space that will converge safely to the desired equilibrium. System theory results dictate that the energy of a dynamic system must decrease along trajectories. If a valid energy function exists, the safe region of convergence can be estimated by finding the largest energy value with a level set entirely contained within the safety bounds. To illustrate the concept, Figure 3-22 shows the critical energy level sets for 15 arbitrary, 2-dimensional, linear systems bounded as indicated. Figure 3-22 also shows how a multi-step switching path, chosen based on those level sets, remains within bounds while a direct transition does not.

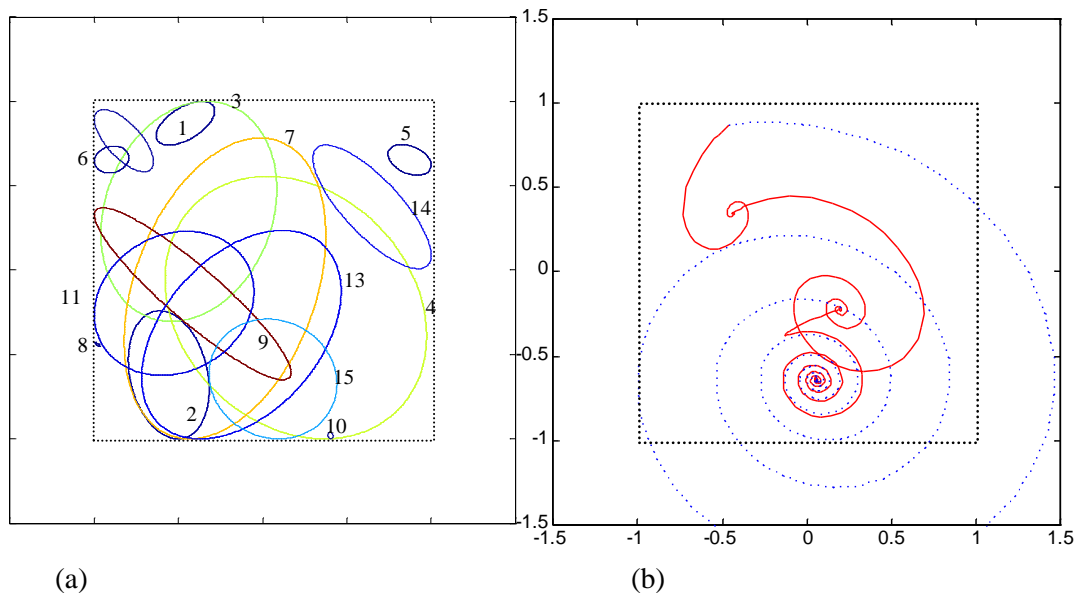


Figure 3-22: (a) Bounded energy level sets for 15 arbitrary 2-dimensional linear systems and (b) an unsafe direct transition (blue) and a safe switching path (red). State space bounds are shown in grey.

After the above analysis has been performed exhaustively on valid switching configurations, the resulting transition information can be formed into a reachability graph. Each configuration is represented by a node, and each safe transition is indicated by a directed edge between nodes. As an illustrative example, Figure 3-23 shows a partial reachability graph based on the 2-dimensional linear systems shown in Figure 3-22. Because the graphical representation quickly becomes crowded, the reachability graph is also conveniently shown in matrix form. A “1” in the $(i, j)^{\text{th}}$ position indicates a safe transition from configuration i to configuration j .

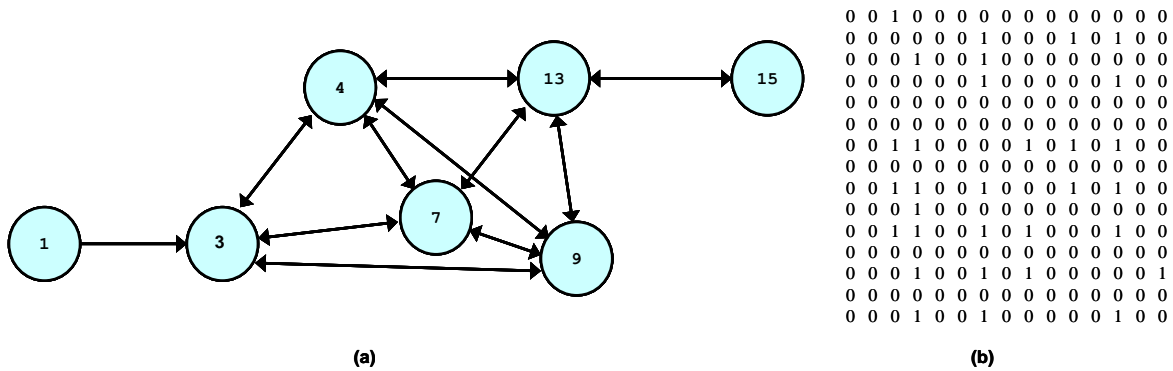


Figure 3-23: (a) Partial reachability graph and (b) complete reachability matrix for the systems in Figure 3-22.

We also adopt a different approach by considering soft constraints: instead of restricting the voltages/currents to stay within a certain safe region, we optimize the hybrid trajectory so that the deviation from the reference voltages/currents is minimized. Furthermore, by adding a penalty on switching, within this framework, Figure 3-24, we reach a tradeoff of the optimality of the voltage deviation and the number of switches required. This model fits well into the framework of optimal control and stabilization of switching systems: the objective is to minimize the total accumulated cost of the deviation of the system state, using analog controls and discrete controls which correspond to continuous feedback control and switching, respectively.

$$\sum_{n=1}^N \left(\underbrace{x_n^T P x_n}_{\text{Deviation from the reference}} + \underbrace{u_n^T Q u_n}_{\text{Cost on analog control signal}} + \underbrace{c(z_n)}_{\text{Switching cost}} \right)$$

Figure 3-24: A general cost function for switching optimization under soft constraints.

We have applied the above methodology to a simple nine-bus system, shown in Figure 3-25. We implemented switches by simply breaking or reconnecting various lines, and also adding lines with comparable impedance properties between various busses. Our constraints were based on reasonable voltage limits on all feeders. Though an exhaustive search of possible configurations was not executed, we were able to note several unusual pathologies of even such a simple system.

We considered a nine-bus system in the initial configuration shown in Figure 3-25 and in about 30 additional configurations. We found that the configuration eliminating the connection between nodes 4 and 5 is not easily achieved from the initial configuration. None of the configurations tested with busses 4 and 5 connected were able to safely transition to a new configuration with busses 4 and 5 disconnected. Additionally, out of all combinations of directly connecting generator external buses (busses 4, 7, and 9) that we considered, the only safe transition was to the state where busses 7 and 9 were connected. A graphical representation of the partial reachability graph described is shown in Figure 3-26.

The results for this simple system demonstrate the complexity of the reconfiguration problem. Non-intuitive switching issues can arise for even a small system under constraints. As more demanding constraints are implemented, a safe reconfiguration algorithm will prove valuable.

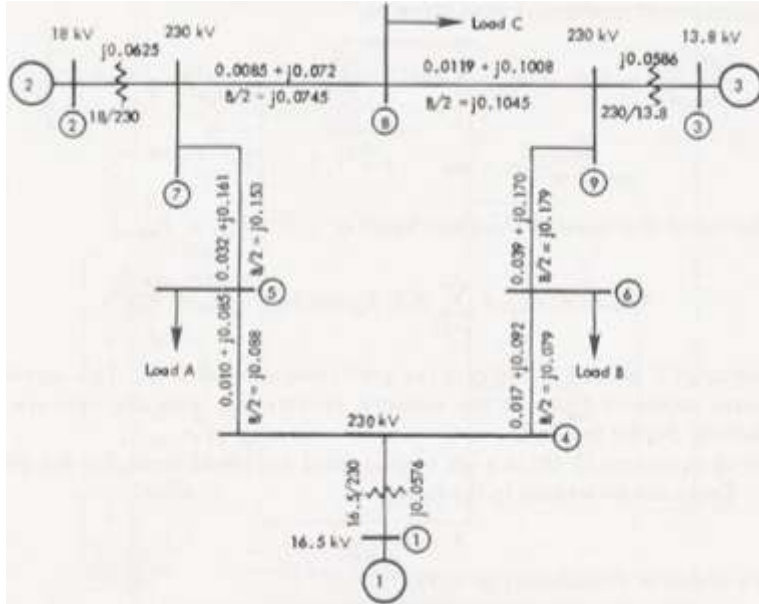


Figure 3-25: A sample nine-bus system used as the basis for our control implementation.

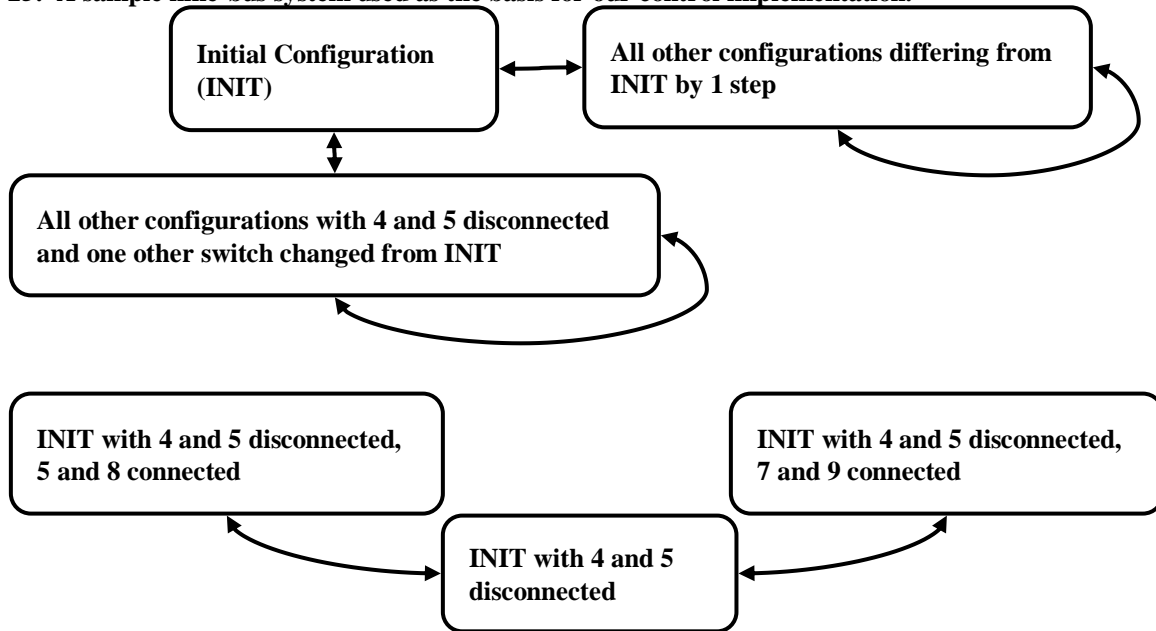


Figure 3-26: A partial reachability graph summary for the nine-bus system.

3.1.7. Optimal Generator Scheduling and Energy Storage

An area of particular interest for electric ships is efficient design and scheduling of the generators and energy storage systems. Figure 3-27 shows the specific fuel consumption for six commercial turbines. All turbines work most efficiently at peak load ratings, but lose considerable efficiency at partial power settings. Thus, intuitively, one should distribute the maximum load for some of the turbines and keep others idle. On the other hand, switching turbines from OFF to ON requires additional fuel for the start-up process. We formulate the dynamic generation scheduling of shipboard power systems as a controlled Markov process and consider an electric ship with a number of N turbine-generators. The total power required for the ship at speed v_k is \bar{P}_k . Let $P_{n,k}$ denote the power assigned to generator n at speed v_k . The specific fuel consumption of generator n indicates how much

fuel is required to generate unit power, and is typically an exponential function in $P_{n,k}$ (see Figure 3-27). Specifically,

$$\xi = \xi_0 + \frac{(\xi_2 - \xi_0)}{1 - e^{-m}} \cdot \left(1 - e^{-m \left(\frac{P - P_{\min}}{P_{\max} - P_{\min}} \right)} \right).$$

Given a mission profile, with η_k denoting the sojourn time fraction at speed v_k of a mission, generation scheduling can be formulated as the following optimization problem:

$$\text{Minimize } \sum_k \eta_k \sum_{n=1}^N P_{n,k} \xi_n(P_{n,k}) \text{ subject to } \sum_{n=1}^N P_{n,k} \geq \bar{P}_k.$$

However, the objective function is non-convex, thus the optimal solution is computationally hard to obtain. We use a reasonable convex approximation of the constraints and obtain the approximate optimal solution using convex optimization. However, the above formulation neglects the additional fuel consumption when generators switch from OFF to ON. We consider this effect by modeling the system as a Markov decision process (MDP), with state (k_t, n_{t-1}) and action $(n_t, P_{*,t})$, where n_t denotes the number of generators ON at time t , k_t denotes the state of the ship speed, and P_{*,k_t} denotes the power vector $P_{i,t}, 1 \leq i \leq n_t$ at time $t, 1 \leq k_t \leq K, 1 \leq n_t \leq N$.

Under the assumption that the speed of the ship changes according to an autonomous Markov chain, and c_{start} denoting the startup fuel consumption for each generator, the problem can be formulated as a MDP with state constraints:

$$\text{Minimize } \overline{\lim}_{T \rightarrow \infty} \frac{1}{T} \sum_{t=1}^T \left[\sum_{i=1}^{n_t} P_{i,t} \xi_n P_{i,t} + n_t - n_{t-1} c_{start} \right] \text{ subject to } \sum_{i=1}^{n_t} P_{i,t} \geq \bar{P}_{k_t}.$$

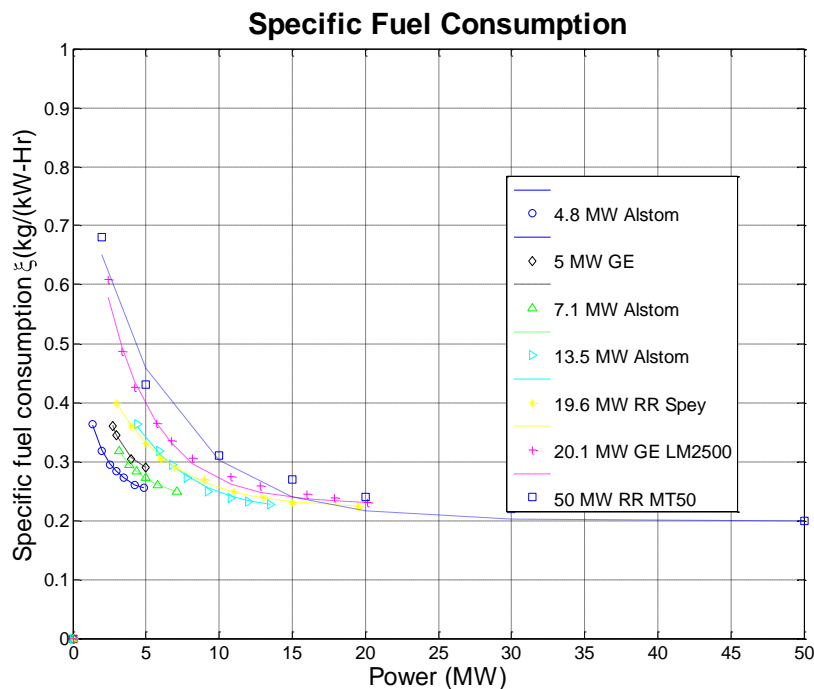


Figure 3-27: Predicted and measured specific fuel consumptions of various generators as a function of power.

Here we consider the infinite horizon long-term average cost and the optimal policy can be obtained by the value iteration algorithm. Details are omitted due to space limitations.

In Figure 3-28, we compare the total fuel consumption under the optimal power generation scheduling policy between the case without startup fuel consumption (i.e., $c_{start} = 0$) and the case with startup fuel consumption. In Figure 3-28, six 13.5 MW Alston turbine-generators are used and we consider a family of Markov chains characterizing the speed changes of the ship, which have the same stationary distribution (or mission profile) but different transition rates (acceleration factor of the ship). As we can see, with the transition rates increasing, the additional fuel consumption due to the startup fuel penalty also increases and can possibly be as much as 100 cubic meters, which is nearly 10% more than the expected fuel consumption obtained by the static optimization. By adding energy storage into the system, it opens up a new dimension for design and brings at least two advantages: first, it can reduce the frequency of turbines switching from OFF to ON, thus reducing their overhead; second, it can allow turbines to work mostly at peak load, the most efficient working point. The MDP model above can be amended to include a queue-like energy storage. The amount of energy in the storage system at time $k + 1$ is given by:

$$E_{k+1} = E_k + N_k P_k - D_k,$$

where E_k is the amount of stored energy, P_k is the power generated by each generator, N_k is the number of working generators, and D_k is the total power demand. The stored energy is constrained in that it cannot be negative, nor exceed the size of the storage. The model behaves as a MDP with the following transition probability:

$$\begin{aligned} P(X_{k+1} | X_k, U_k) &= P(D_{k+1}, E_{k+1} | N_k, P_k, E_k, D_k) \\ &= P(D_{k+1} | D_k) \end{aligned}$$

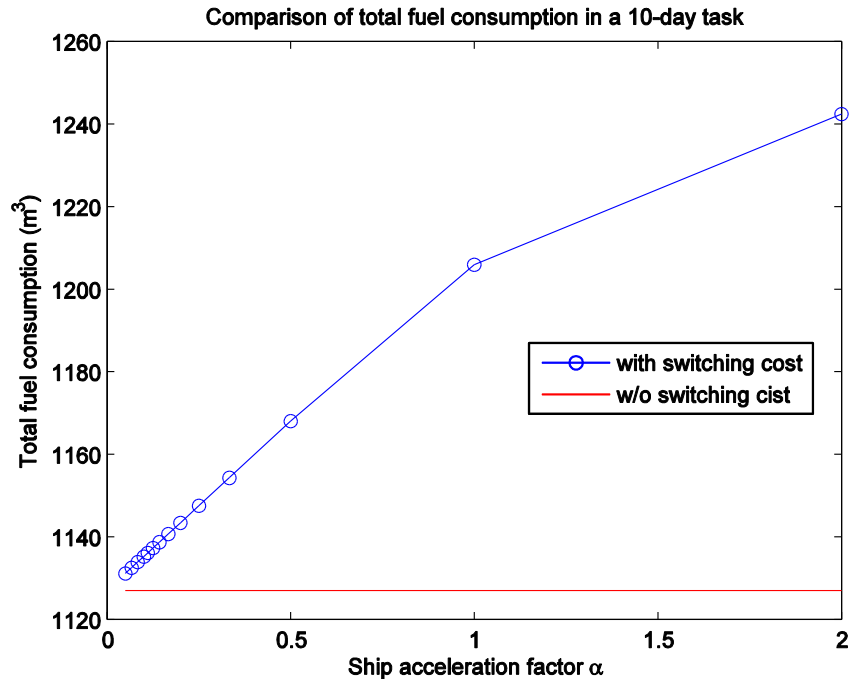


Figure 3-28: Comparison of total fuel consumption between static optimization and dynamic optimization for six Alston turbine-generators.

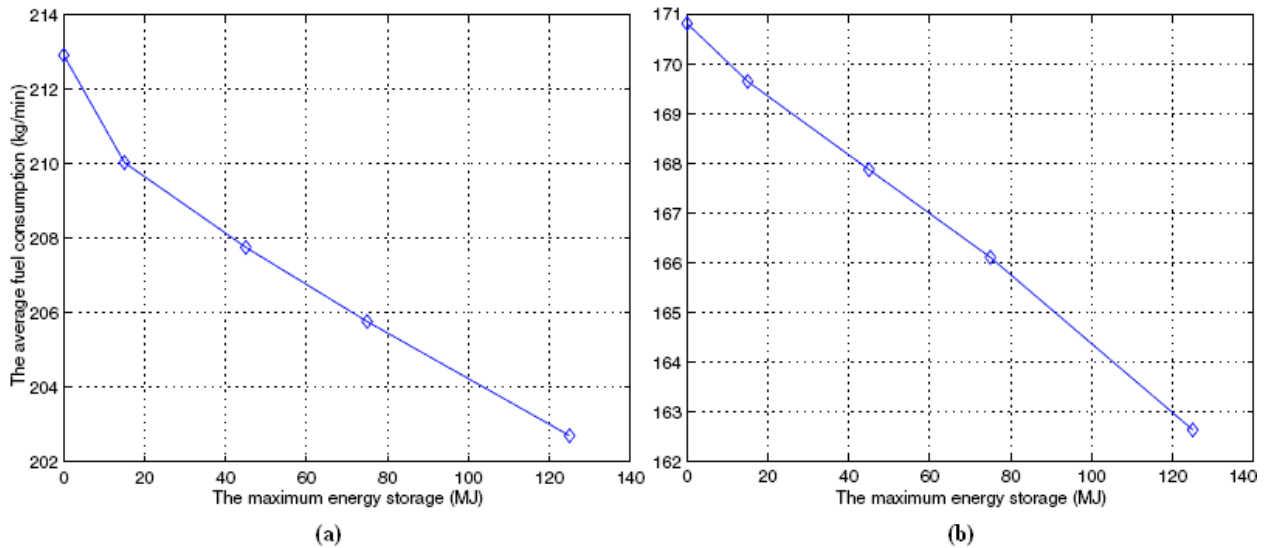


Figure 3-29: The relationship between energy storage and average rate of fuel consumption for (a) four 20.142 MW GE LM2500 generators and (b) two 5 MW GE and two 50 MW RR MT50 generators.

Lacking more comprehensive data, the ship's power consumption can be modeled as a random walk on the set $\{8 \text{ MW}, 8.25 \text{ MW}, \dots, 80 \text{ MW}\}$, with transition probabilities,

$$P(D_{k+1} = j | D_k = i) = \begin{cases} p_{ij} & \text{if } |j - i| \leq 1 \\ 0 & \text{else} \end{cases}.$$

We simulated the system for a typical four-day mission profile with two different generator configurations. These results demonstrate the importance of generator scheduling and energy storage in the design and operation of shipboard power systems. However, in order to be able to predict and accurately optimize the fuel consumption of generators, we need to have control data of the ship acceleration distribution, and not only the mission profile. With accurate data, adaptive scheduling schemes can be combined to enhance the performance of the generator system.

Research Work Related to Reconfiguration

As reported previously in various quarterly reports, the MSU research team has been active in looking at issues related to reconfiguration including optimization, islanding and distributed generation. In order to do analysis related to the ship systems, a three phase unbalanced distribution power flow was developed that would allow for the inclusion of distributed generation as a source instead of a negative load. Optimization techniques were employed on the shipboard power system to understand the impact of islanding and distributed generation on the survivability and fight through capabilities. Multi-agent systems have been developed to provide fault detection, fault removal and reconfiguration after a fault to minimize the impact of the fault. Additionally genetic algorithm and graph theory have been used in applications to provide reconfiguration in a centralized manner.

Besides the reconfiguration of the power system, research activities have been accomplished that look at the possibility of an adaptive protection scheme where the protection system reconfigures to match the new conditions of a reconfigured power system. Research activities demonstrated the possibility of using group settings or a look up table to allow reconfiguration. While these techniques provide some adaptability they do not provide coverage for all possible power system reconfigurations. As an extension to modeling activities described below, MSU researchers are working to develop an integrated power system and protection system for analysis and optimization.

The other area of analysis and reconfiguration has related to medium voltage DC systems. Simulation activities have modeled the various types of faults and grounding to understand how that impacts signals within the MVDC system. These studies have provided the foundation for MVDC work that will be continued in the renewal.

This next section provides additional details on a recent research project related to reconfiguration.

Summary

Graph theory has been applied to represent the shipboard power system and all possible islands formed due to the fault are found with their load and generation capacities along that path. Then binary particle swarm optimization is applied to optimally reconfigure the set of loads satisfying the operational requirements and priorities of load. The proposed method is applied to 8-bus shipboard power system model and extending it to a bigger systems with more constraints in ongoing research work.

Highlights:

- Developed new algorithm and methodology to apply particle swarm optimization for shipboard power system
- Tested algorithm for 8-bus shipboard power system

Summary of Technical Activities:

Particle Swarm Optimization (PSO) approach has been applied for restoration of shipboard power system having buses, breakers, generators and loads. When a severe bus fault affecting the generator occurs, it causes a power deficiency for the rest of the power system. Fast reconfiguration function can identify the outcome of the fault isolation, reduce the fault's impact to the minimum, and thus prevent power system collapse. Using the fast reconfiguration algorithm, any unfaulted zone that imports power from the faulted zone, can merge with other unfaulted zones to avoid loss of power if it does not have enough power surplus to compensate for the imported power from the faulted zone. Particle swarm algorithm enables to find the optimal combination of loads that can be supplied after the occurrence of the fault, considering the priorities of the loads and the constraint of balance between the total load and total generation. Figure 1 shows a generic shipboard power system model. The shipboard power system has been divided into eight protection zones containing the connectivity of the breakers.

The power system topology is modeled in the form of matrices. Depending on the type of fault, corresponding changes are made in the matrix and the revised matrices are processed.

Mathematically the problem can be formulated as the combined objective function subject to the weighted values of load priorities and load magnitudes depending on the requirement of the situation. The objective of this optimization problem can be expressed by the maximization of the total loads in the formed island after the occurrence of fault with fitness as:

$$\text{Fitness} = w_1 (L_1 + L_2 \dots L_n) + w_2 (p_1 L_1 + p_2 L_2 \dots p_n L_n) \quad \dots \text{eq. (6)}$$

Subject to

$$P_{\text{gen}} \geq P_{\text{load}} \text{ (Load should not be more than generation)}$$

Where:

n shows the total number of loads

$L_1, L_2 \dots L_n$ shows load magnitude values

$p_1, p_2 \dots p_n$ shows load priority values

w1 shows the weighing factor for load selection based on magnitude

w2 shows the weighing factor for load selection based on priority.

Parameters w1 and w2 determine the mode of load selection. If w1 is taken as 1 and w2 as zero, the reconfiguration will be done, based on the maximum load magnitude only. If w1 is zero and w2 is 1, prioritization of load is implemented and high priority loads are selected until the generation capacity is less than the total load without the consideration of load magnitudes. The status of the loads is coded as a binary variable. All the possible load states are then stored in a vector x_{id} with '0' and '1'. The value '0 (Zero)' denotes that the load is disconnected, and '1 (One)' denotes that it is connected.

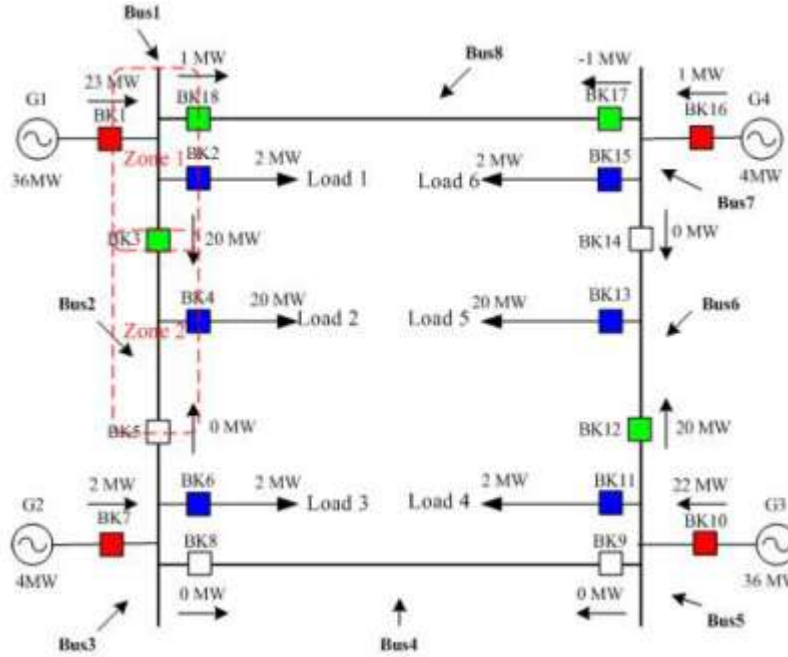


Fig. 1. 8-bus shipboard power system

Step-wise algorithm is as follows:

1. Set population size, maximum number of iterations and stopping criterion.
2. Randomly select feasible solutions x_{id} , compute p_{id} from each x_{id} , p_g is the maximum in all p_{id} and the initial values of v_{id} are taken to be zero.
3. Use (1) in section IV to calculate v_{id} for particle 'i' in dimension d.
4. Use (2) in section IV to update x_{id} .
5. Calculate fitness function using (6).
6. If the fitness value of particle 'i' is better than the previous particle, the value is set to 'i' otherwise it remains same as the previous.
7. If the best p_{id} is better than p_g , the value is set to p_g .
8. If stop criterion is satisfied, p_g is the best optimal solution, otherwise, go to Step 3.

When either the stopping criterion is satisfied or the maximal iteration number is reached, the algorithm ends and the results are obtained.

TABLE 2: SIMULATION RESULTS

The developed formulation was applied to 8-bus shipboard power system. Test results containing different possible conditions with negative power bus, power supply bus sequence, possible load shedding and breaker reconfiguration are shown in Table 1. Faulted bus shows bus faults comprising of all combinations of single and double generator faults. Negative buses are those buses where power balance is negative after the fault occurrence. Possible supply bus sequence is the sequence of buses through which the negative power bus can be supplied. If even after the path search, the resulting power balance comes out to be negative, some load has to be

Faulted bus number	-ve power bus	Power supply bus sequence	Load shed	Breaker reconfiguration (open/close)
B1(G1)	B2	B2-B3-B4-B5-B6-B7-B8	L2	BK4(O) BK5,8,9,14,17 (C)
B3(G2)	-	-	-	-
B5(G3)	B6	B6-B7-B8- B1-B2-B3- B4	L7	BK13(O) BK5, 8,14,17,18(C)
B7(G4)	-	-	-	-
B1(G1) B3(G2)	B2	No generation	L2	-
B1(G1) B5(G3)	B6 B2	B6-B7 B2-B3-B4	L2 L5	BK4,13(O) BK5,14(C)
B3(G2) B7(G4)	-	-	-	-
B5(G3) B7(G4)	B6	No generation	L5	-

shed which is represented as possible load shedding. In the results below, w1 is taken to be one and w2 as zero i.e. load magnitude has been taken in consideration. At last, the system is restored after fault occurrence by reconfiguring the breaker status.

Results are satisfactory when compared with Genetic Algorithm and other mathematical approaches and found to be little faster. There is flexibility of options to adapt the system for load prioritization or load magnitude by just changing the weight values. The proposed method can be easily extended for application to bigger shipboard power systems with more system constraints as future work.

4. SIMULATIONS AND EARLY DESIGN TOOLS

Work under this program addressed a broad spectrum of issues related to the development of electric ship systems including methods and models for design and simulation of highly-integrated multidisciplinary ship systems, methods for power routing and control, methods for characterizing and understanding the performance of the electric plant, and methods for controlling the plant. It is impossible to capture the full breadth and depth of the research in this one report, so instead the report content has been developed to provide a detailed insight into a few achievements in illustrative areas. The reader is then encouraged to review the list of publications at the end of this report to comprehend the full breadth of the achievements and to refer to the appropriate publications where this report provides insufficient information. Broadly speaking, the topics of this team's investigations can be classified into the categories of Simulation Tools, Power Systems, and Control Systems. Highlights in each of these areas are mentioned next.

The early days of this project saw the maturation of the Virtual Test Bed software version known as VTB2003 and the final days saw the maturation of version VTB Pro. The transition from VTB 2003 to VTB Pro was dramatic, as the latter incorporated many improvements and new capabilities (such as version control, user management, etc.) related to enterprise use of the software as a design tool. More significant to individual users was the development of tools such as Entity Builder and Component Builder for creating new models. Also, means for bi-lateral interaction with other software using COM, ActiveX, HLA and other protocols which enabled solutions to challenging problems using federated software packages such as Matlab, Simulink, ESL, ACSL, LabView, and others. This work also addressed issues of software speed for simulation of large systems, including the use of methods such as multi-rate and distributed simulation. A significant focus on real time and hardware-in-the loop methods produced new approaches for ensuring the stability and accuracy of combined hardware/software systems and for interfacing simulation software with power electronic systems. An ability to export executable system models in ANSI C format permits compilation of simulation models so that those models can be executed in arbitrary environments (such as on Digital Signal Processor chips, or on computer systems running non-Windows environments such as Linux or realtime versions of Windows or Linux, which then permit simulation with hardware in the loop.) High speed FPGA-based interfaces were developed to support interaction between the realtime simulation engine and power hardware.

Incorporation of methods based on Polynomial Chaos Theory allowed VTB to be the first simulation engine to support prediction and propagation of uncertainty (in the form of probability distribution functions) throughout an energy-conserving network model.

New methods for representing the performance of power semiconductor devices, using a Fourier series approach, allow more accurate assessment of losses and dynamic response of the power converters that will direct the flow of electric energy from origin to point of use in the ship systems. Procedures have been defined for automatic extraction of model parameters from experimental data.

At the component level, the research effort addresses design issues of electromagnetic and electromechanical design. In particular, the concept of a high-fidelity magnetic equivalent circuit was introduced. For some geometries, this technique is as accurate as a 3-D FEA analysis at a fraction of the computational cost. Another new analytical technique developed was the FEA waveform reconstruction that has been applied to permanent magnet synchronous and induction machines. Using this technique, a small number of static FEA solutions are used to obtain basis functions for the air-gap flux density. These basis functions are then used to predict the flux densities and forces within the machine under arbitrary excitation and rotational velocity. This technique greatly reduces the computational effort (from many hours to seconds) of fields-based modeling of the machine and has near the accuracy of time-stepping FEA. In working through the field reconstruction technique, it was found that analytical expressions for the radial forces acting inside machines could be derived, which helps to establish expressions for the forces that potentially act on the bearing system of machines. Evolutionary

optimization based design codes for EI core inductors and permanent magnet synchronous machines were also developed under this effort. These codes drastically reduce the engineering time required to develop new machine designs.

At the system level, two efforts were undertaken. One of these is focused on the stability analysis of power electronics based systems. In particular, a new method was developed to determine how strongly a power electronics based power distribution system could be perturbed without leaving the safe operating area. The other system level effort focused on energy storage. In particular, the beginnings of a method to best allocate energy storage on a ship in order to improve the robustness of the integrated engineering plant was developed.

In addition to early design tools, there has been some research on the powertrain design. This has focused mainly on developing methods to improve the fault-tolerance of electric-drive based powertrains. For permanent magnet synchronous machines a new position observer was developed that uses sensed vibration in tandem with a single hall-effect sensor to predict rotor position with accuracy approaching that of a high precision position encoder. Thus, in navy applications, a vibration sensor that is used to monitor drive system health could be readily used in a dual role to improve drive fault tolerance. Related, a new sensor was derived that uses torque-ripple-induced vibration to establish the speed/position of induction machines. The sensor is relatively easy to implement, and can serve a dual use role as part of a vibration-based health monitoring system.

Survivability, or the ability to provide uninterrupted power flow to loads in spite of multiple simultaneous faults caused by natural or hostile disruptions, is a desirable feature of any power system. In all-electric naval platforms, the ability to withstand multiple simultaneous unrecoverable faults in a battle field is a vital requirement for the integrated power system (IPS), since power interruption or its total loss during a battle would most certainly lead to mission failure, personnel loss, and possibly complete destruction of a ship. The goal of this study is to enhance survivability of power systems subject to multiple simultaneous faults caused by natural and/or hostile events.

The project objectives are to develop mathematical framework to analyse power system survivability, develop computational algorithms for evaluating power system survivability, and design power systems of enhanced survivability.

Key factor determining survivability of the power system is its topology or design – the number of generators, their connections with one another and loads. Indeed, reliability of equipment alone is no protection against destruction caused by direct hits. How much reconfiguration is possible in a given IPS is also limited by its topology. Therefore, structural (topological) survivability is the current focus of the Project. In our study, we develop mathematical and numerical tools to analyze structural (topological) survivability of IPS under multiple simultaneous unrecoverable faults. In particular, we developed probabilistic approach to evaluate structural survivability of different power system topologies; evaluated and compared structural survivability of various generator bus topologies of two, three, and four generators; suggested a new web topology of enhanced structural survivability; and developed and validated a computational algorithm based on the graph approach to evaluate structural survivability of power systems.

Possibility of detecting and isolating faults in a given power system topology also influences the total system survivability. Current protection standards do not meet the challenges associated with increased complexity of modern power systems. We are working on adapting the model-based fault detection and isolation approach based on structural analysis to evaluate the monitoring potential of the power system in a systematic and automated manner. Such an approach is particularly promising for successful wide-area protection of the complex IPS.

The focus of the Purdue / USNA ESRDC research has primarily been in the area of early design tools. At the materials level, one of the key contributions Purdue has made has been correcting an error in the IEEE

standard for the characterization of magnetic materials. As this procedure is in widespread use, the fact that the standard was in error has far reaching implications – including the fact that the error undoubtedly propagated into thousands of analysis by engineers and researchers in the power engineering area. In addition, a new method of characterizing losses of magnetic materials was invented. This method is advantageous for automated design in that it allows losses to be found from knowledge of only the minimum and maximum field values – the entire waveform was not required. This results in a considerable computational advantage in design activities.

At the component level, the research effort addresses design issues in electromagnetic and electromechanical design. In particular, the concept of a high-fidelity magnetic equivalent circuit was introduced. For some geometries, this technique is as accurate as 3-D FEA analysis at a fraction of the computational cost. Another new analytical technique developed was FEA waveform reconstruction that has been applied to permanent magnet synchronous and induction machines. Using this technique, a small number of static FEA solutions are used to obtain basis functions for the air-gap flux density. These basis functions are then used to predict the flux densities and forces within the machine under arbitrary excitation and rotational velocity. This technique greatly reduces the computational effort (from many hours to seconds) of fields-based modeling of the machine and has near the accuracy of time-stepping FEA. In working through the field reconstruction technique, it was found that analytical expressions for the radial forces acting inside machines could be derived, which helps to establish expressions for the forces that potentially act on the bearing system of machines. Evolutionary optimization based design codes for EI core inductors and permanent magnet synchronous machines were also developed under this effort. These codes drastically reduce the engineering time required to develop new machine designs.

At the system level, two efforts were undertaken. One of these is focused on the stability analysis of power electronics based systems. In particular, a new method was developed to determine how strongly a power electronics based power distribution system could be perturbed without leaving the safe operating area. The other system level effort focused on energy storage. In particular, the beginnings of a method to best allocate energy storage on a ship in order to improve the robustness of the integrated engineering plant was developed.

The Virtual Test Bed software

The VTB 2003 software was used as the basis for creating the third generation simulation environment named VTB Pro. The concepts of simulation based design and simulation as specification require support from appropriate computing tools. The Virtual Test Bed software has continued to evolve to provide this support. Requirements that were deemed essential in order to support the Navy in these efforts included support for early-stage top-down collaborative design, system and subsystem decomposition for detailed design, management and security of the ship design process, as well as various simulation features such as the execution of subsystems at independent time steps, variable resolution of models, and multi-core and distributed simulation. In addition incorporation of several features into the core software was essential in order to provide a simulation platform which could easily evolve over time.

Large systems are generally designed using a top-down philosophy that decomposes a large system into smaller subsystems. These subsystems may be further decomposed (often even successively decomposed) along both disciplinary and functional lines, until work tasks ultimately become manageably small. In order to better suit the needs of this type of large system development the concept of systems and subsystems were introduced into the VTB Pro framework. This permitted VTB to move from a single document tool to a multi-document simulation tool. Complicated ship design problems can now be decomposed into smaller more manageable pieces. After the system is decomposed, the resulting subsystems are generally designed in isolation, but then reviewed together at predetermined times set by the design review schedule. After the initial design work for the individual

subsystems has been completed the engineers will likely need to simulate the system at a higher level incorporating the design work from many teams across multiple disciplines. VTB Pro provides subsystem connectors as a means to allow the user to connect subsystems together for simulation purposes. The capability to quickly decompose a system into multiple subsystems permits the engineer to better focus on a particular design problem and at the same time the ability to quickly reassemble the subsystems via subsystem connectors allows engineers the ability to understand the capabilities and limitations of each individual subsystem and the impact of design features of one subsystem on another subsystem. In addition subsystem connectors can also be used to connect components within the same subsystem without visually representing physical connections. This helps produce schematics which are clearer and easier to comprehend.

There are many artifacts created during the design process, and it is imperative that management have a complete picture of the design, know where all design documents reside, control access to such documents, and track changes to them. Without such a controlled process it is impossible to know the precise state of the system's design or to effectively manage the design process. VTB Pro has added database support to help manage this process. Systems are persisted to a central repository and designs can be shared between teams without having to move files between computers. This helps to eliminate the problem of where the design resides and which design is the latest version. In order to share designs with others that are not in the same team or organization the systems can be exported to an XML (Extensible Markup Language) format. In order to ensure that the design documents are secure, permissions and security have been added to VTB Pro. After a user logs onto the windows environment the user's credentials are captured. The credentials are then used to help identify them within the VTB Pro environment. Permissions have been added to the system, subsystem, and simulation objects and can be assigned as needed by the owner or administrator of the document. The owner can add permissions to any of the various documents that constitute the design at the individual user or group level as they see fit. The set of permissions that can be assigned to each document is read, write, or execute. As modifications are made to the design documents, VTB records the user making the change and the date and time that the change was initiated. In order to ensure that the document remains in a consistent state document locks have been added to VTB Pro. Users check out the document or subsystem they wish to make changes to and then, once the change is completed, they check the document back into the central repository. Once the document is checked in, all other users who have permission and who care to be alerted of such changes are informed that their version of the document is out of date and the document is automatically updated. While a document is locked and checked out, no other users may make modifications to it. This ensures that the design document remains in a consistent state and that change modifications are not lost. The administrator has the ability to remove such a lock on the design document if deemed necessary.

Users of VTB Pro are categorized into three roles, administrators, component developers, and standard users. Administrators are responsible for assigning users to roles and can revoke or grant access to all documents. Users in the administrator role have the ability to perform all tasks within the VTB Pro environment. In particular they have permission to open, create, delete, and modify any system or subsystem and to execute any simulation. Component developers are allowed to create new or modify existing components or modules for use by the system engineers in their designs. A component developer typically creates a new component and after it has been adequately tested makes it publicly available to system engineers for general use in their system studies. A user in the component development role is also allowed to manage the component database by adding or removing components. Standard users have the ability to create, delete, and open systems for which they are the owner or for which they have been given explicit permissions.

In order to keep all designers of a system informed of changes made to the various subsystems a notification mechanism was implemented in VTB Pro. A publish and subscribe service was added to the framework in order to send notifications to interested users. A user that is currently logged onto VTB Pro and that has a particular subsystem opened for viewing will be notified if any changes are made to that subsystem while it is opened for viewing. In addition any newly created or modified components also cause a notification to be sent to permit users to refresh their component databases.

Solver efficiency and precision are of critical importance and will likely become all the more important as systems become increasingly larger and more complex. Over the last few years analysis of and modification to the underlying implementation has led to improvements in these areas. A new approach for inverting and solving matrices involving large systems that contain complex components was implemented. This has led to better convergence of these systems. New solver settings now permit the use of an absolute error and relative error setting. The user can use either or both of these settings simultaneously during the execution of a simulation. When an error condition occurs the user is given a visual cue as to where the problem might lie by way of highlighting the node with the greatest amount of error. This feedback gives the user some idea of which components are most problematic in the simulation and the user can then attempt to make the necessary modifications in order to get the solution to converge. The amount of error in a simulation can be plotted alongside any other values the user may be interested in.

Distributed computing has performance advantages over single-processor computing, and is conceptually consistent with a simulation-based-design philosophy in the sense that independent subsystems are “owned” by those who are responsible for them, and should be independently computable, either with highly-abstracted boundary conditions when the subsystem is tested outside of the larger system context, or with boundary conditions that result from direct interaction with the larger system. Distributed computing faces challenges due to the strongly-coupled nature of electrical networks but several methods support decomposition of large systems into smaller subsystems. These subsystems may have different dynamics but where the system as a whole would have its time step determined by the subsystem with the fastest dynamics, for both performance and strategic reasons, these independent subsystems should be computable with independent time steps. Research and development has continued in this area resulting in the development of a set of components which permit the user to manually break a large system at predefined points into two smaller systems. These systems can then be simulated on different cores of the same processor, different processors on the same computer, or even on different computers. It is anticipated that this approach will lead to an increase in the size and complexity of systems that can be simulated in the VTB Pro environment.

Early-stage conceptual designs often make use of idealized representations of system components; great complexity is not needed in the model, since much is unknown at this point in the design. As the design is explored further, the level of detail in the design increases and the complexity of the model likewise increases. VTB Pro provides the capability for the engineer to use models of varying levels of fidelity based upon the current maturity of the system design. In VTB Pro, under certain conditions, the simulation engine for a model may be swapped out at run time with another simulation engine. This is a complex operation that requires that the simulation engines being swapped have intimate knowledge of each other. In addition it is required that each engine know how to handle the current and past values for all state equations. It is often the case, when moving from a lesser to a more complex model, that the system engineer will be required to supply more data either in the form of model parameters or possibly via coupling the component to existing or new components. This feature permits the user to determine the level of detail he or she is interested in achieving during a simulation and can manage this with respect to time constraints.

In order to adequately test the robustness of a system design a user needs the capability to introduce events or changes into a simulation at specific points in time. A tool for creating scripts was created which allows a user to create events such as the closing or opening of switches, adding or removing of components, connecting and disconnecting components, creating faults etc... which occur at specific points in time during a simulation. This tool can be used to test various scenarios and determine the systems ability to degrade gracefully. Once the script is created it can be executed from the command line or through the traditional schematic editor tool.

The architecture of VTB Pro permits the dynamic addition of new solvers and components to the application. The VTB Pro framework was extended to permit the use of complex numbers and a phasor solver was implemented as well as a basic assortment of components such as sources and impedances. Test systems were created including a three bus transmission network with constant impedance loads, notch filters, and a

system frequency controller. A test system was created and the results were compared with an analytical solution to the system and were found to be in agreement. The successful development of the phasor solver demonstrated that the VTB Pro environment is capable of integrating third party solvers and components and can now be extended in multiple ways.

In order to permit VTB Pro to be used in a hardware in the loop simulation it is necessary to move the application into a real time environment. Methods for developing a real time version of VTB Pro were researched. Possible approaches ranged from using a real time version of Windows to code generation in the “C” language as well as parallelizing the solver to reduce the required simulation time. This initial research has led to exploring both approaches as well as proceeding with optimizations to the solver in order to reduce the required run time through parallelizing the simulation.

In support of user requests, enhancements to VTB Pro’s interpreted language were made. These extensions were made to support functions typically found in other modeling languages primarily mathematical functions such as trigonometry, as well as basic functions such as ceiling, floor, truncate, etc... These additions were made in order to increase the probability of a user or another tool being able to translate models from one language such as Verilog or VHDL-AMS into the native modeling language of VTB Pro. In addition we are extending the language to support user defined functions. The capabilities of the interpreted language are being extended to fully support the compiled “C” family of languages.

A major thrust of the development effort was made in the area of component development. The signal control library was augmented with additional models such as a state space model and zero pole gain model to complement the transfer function model. A suite of various timers were also created as a means of introducing regular triggers at certain times or with a certain frequency of time step intervals. Several encoder and decoders were added including a priority encoder. A feedback component was created which allows a user to break a cyclical control circuit at a point determined by the user in order to permit the system to be solved. A PID controller, integrator and differentiator were also added to the library. Additions signal sources were added as well. The mathematical library was also augmented and now includes a full set of trigonometry functions, the gamma function, Airy, Bessel, Dirichlet, etc...

Certain components were created in order to permit integration of VTB Pro with other applications such as the Excel wrapper components that permit data to be both extracted from and inserted into Excel spreadsheets. In addition a set of socket based components were created which allows data to be either sent or received from VTB Pro to other external applications. In addition a suite of file readers and writers were also created that can dump data generated during a simulation to a comma separated file for later processing by other applications.

Certain components were created for the express purpose of allowing users to easily interact with a system while a simulation is executing. A HID (human interface device) wrapper component was incorporated into the component library for VTB Pro. This component acts as a wrapper to an actual hardware device connected to the computer via a USB port. This hardware device can then be used within a simulation as a means of control. In this case the HID device used was a steering wheel. In addition a component which permits the user to use an Xbox controller was also created. These HID devices can be used to permit a user to interact in a realistic manner with a simulator such as occurs when training military or civilian personnel. In order to add more realism to the simulation a terrain model was developed which can be used to read in the topology of an actual location and permit the components to make use of such information in the simulation. This model has been used to create a realistic terrain model for simulating vehicle operations.

Several models were developed which permit the user to quickly create a model without having to use the Entity Builder or Module Builder tools. The UDD (user defined device) has both signal and natural versions which permit the user to directly enter the governing equations when placed on the schematic. In addition a parameter event and a parameter sink model were created in order to permit the user to turn a parameter on a component into a signal input port. Thus, allowing the component to be controlled via some control logic.

Another component was created that permits the user to combine information from multiple sources on the schematic into a single mathematical expression which can then be used or displayed to the user.

In the electrical component library components were added such as a single line fault which introduces faulting conditions between multiple phases. There were also several components created which provide variations on three phase loads that have resistance, inductance, and capacitance. A set of SPICE compliant components was created that cover some of the basic models present in a SPICE simulator although this set is not yet complete.

Power sources were added to the component library in the area of electro-chemical sources such as a set of standard batteries, PEM fuel cell, Lithium Ion battery, and a generic battery that lets the user specify the voltage vs. amp / hour curve.

In the hydraulic and thermal libraries components were created such as a gas tank, air compressor, fluid mixer, vertical pipe, five different types of fluid pumps, throttle valve, check valve, signal controlled valve, gate valve, sea water inlet and outlet, counter flow heat exchanger, plate fin heat exchanger, heat sink, plate frame heat exchanger, and six versions of heat exchangers.

In order to provide better support for the users of VTB Pro a web site has been created to field general questions and to allow for the download of evaluation versions of VTB Pro. Professional bug tracking tools have been used to help manage and improve the quality of the software as well as to help plan the release of new requirements and features. An academic version of VTB Pro has been created in order to support the ongoing research work of universities within the ESRDC. Although this version does not support all the functionality of the enterprise environment it does support all of the major elements. The academic version in general does not support features of the cooperative team environment that is found in the enterprise version.

Several workshops were held to educate users on the general use of VTB Pro as well as on the creation of models. Workshops have been hosted for personnel at NGSS, students and faculty at Mississippi State University, University of Arkansas, and Florida State University, as well as several at the University of South Carolina for both academic and industrial users.

Model development tools – Component Builder

When designing and modeling systems and especially during the conceptual phase of design, the capability to quickly create simulation models is essential. Models developed early in the conceptual phase will likely be minimally complex in order to simply convey the general idea, to reduce the time required to configure or reconfigure the conceptual system, and to rapidly execute many simulation experiments. Rapid exploration of the design space with minimal time investment is crucial. As the various conceptual designs are examined, the engineer can quickly focus on the set of most-promising designs; those that will require additional elaboration and examination. In order to facilitate such rapid prototyping and model development VTB Pro ships with two tools, Entity Builder and Module Builder. These tools permit the engineer to create the specification for the component, to define configuration parameters, terminals or points of connectivity with other components, to define its symbolic or iconic representation, and to define the behavior of the component during simulation. VTB Pro allows components to define their behavior at simulation time in one of two ways - either by the use of an interpreted language that is automatically compiled at run time, or by supplying an assembly that provides the necessary information for simulation. The modeling language provides a convenient and rapid way to prototype a model. After the component has been created in this tool it can be deployed with the single push of a button and then used in the drag and drop environment of VTB Pro. In some situations a new component can be defined by merely repackaging existing components in some pre-arranged configuration with an established set of parameters. VTB Pro ships with a tool called Module Builder that allows engineers to quickly define new components by assembling and configuring existing components into reusable objects. These components (modules) can then be used in the drag and drop environment.

These tools bring improvements to the original model development process by seeking to simplify and reduce the coding requirements of the developer, incorporate all activities in a single tool, and simplify the deployment process. All aspects of the creation of a component such as the creation of the icon, the definition of the component, and the behavior at simulation time, can now be completed within a single tool. This helps to expedite the development of new components and at the same time reduces the complexities of deployment. Modifications to the interpreted language have also permitted simplification and rapid development of new components. The new language closely resembles the “C” family languages.

VTB Pro has implemented a different approach to defining and processing a component’s specification. In VTB Pro a component is described by its metadata. The metadata in its natural form is expressed in XML (eXtensible Markup Language) and validated by a schema file “vtbpro.objects.xsd” found in the install directory for the application. This metadata is processed by the VTB Pro framework and used to create an instance of the component. This permits the separation of the metadata from the implementation of the engine responsible for simulation thus simplifying the implementation. A component developer does not have to understand how to write, read or format the XML since Entity Builder and Module Builder automatically provide the ability to produce a fully documented and valid component. An additional benefit of providing the metadata in XML format is that other third party tools can extract and use this information as well.

An entity consists of one or more icons which represent the component visually on a schematic, an interface which determines how a user and how other components may interact with the component as well as an engine which performs the mathematical calculations necessary and which govern how the component behaves during simulation. When all three pieces have been fully defined the entity is ready to be used within the VTB Pro environment.

A module is a fixed configuration of components (entities and other modules) grouped as a black box represented by an icon that can be reused across disparate subsystems where a particular piece of functionality or behavior could be used repeatedly. A module exposes some of the interaction points of the components it contains to allow it to connect to other components, be configured using parameters, and plot data from viewables.

The capability to version components (both in terms of complexity and release history) is imperative in order to permit both the concept of variable resolution models as well as allowing for patches or bug fixes to be applied to the components. The versioning process is managed using the Entity Builder tool. Model development progresses along three axes. One axis represents the type or family of the model, the other axis represents the complexity of the model, and the third axis represents the revision number of a particular model type and complexity. Resistors, capacitors, and inductors are different types of devices and lie at different points along the first axis. Each device can have multiple complexity levels and lies on the second axis. Once a specific type and complexity level of a component has been identified the version or lineage through time of that particular component is represented along the third axis.

From Entity Builder the modeler can choose to increase the complexity of an existing entity. As component complexity increases the modeler is indicating that the device, although of the same type, exhibits a behavior at simulation time that is closer in fidelity to the actual physical device. For instance, the modeler may want to add thermal characteristics to a resistor. The user could select the resistor type and choose to increase its complexity, add a thermal port, modify its equations and save this new version. Complexity of a component can then be used by the designer of a system as an indicator in determining the level of sophistication or accuracy needed in their simulation. In addition because the version history of an entity is now included in the metadata for the component the user can now determine whether they have the latest version of a component and if not update their environment with a single click.

In order to expedite component development a user can create a new entity type from an existing entity type. This can significantly reduce the development time required in cases where the user deems that an existing

type is a close enough starting point to for a new type of device. A component that has been cloned becomes an entirely new component and is not really related in any way to the original component from which it was cloned.

An entity is comprised of interaction points which define how it interacts with the simulation environment, users, and other components. Extensions have been added to interaction points to provide support for a wider range of data types. In addition to the integer and real number data types originally provided the framework now supports datetime, xml, enumerations, strings, booleans, and complex numbers. The component developer simply selects the underlying data type of an interaction point within the Entity Builder tool.

VTB Pro now supports and honors the use of units associated with interaction points. Units such as ohms, volts, radians, meter / second are now supported. This is useful when displaying information to the user in plots as well as when attempting to connect components together.

Support for read only parameters now exists in Entity Builder. From the tool the developer can indicate that a parameter is read only. A parameter that is read only can not be modified from the schematic. This can be useful when the component developer would like to expose the value of a parameter that is for informational purposes only such as a derived attribute.

Constraints can now be added directly to a parameter to ensure that the value of the parameter falls into a valid range. In Entity Builder a constraint can be added to a parameter and if it has been added then all values entered by the user are first checked against the constraint before being applied to the actual parameter. Multiple constraints can be applied and must be separated by a semicolon and are considered to be logically "ANDed". That is to say all constraints must be satisfied in order for the new value to be accepted by the parameter. If the user attempts to enter a value which violates the constraint then the request is ignored and the previous value is still in effect. Constraints only apply to parameters that have a numeric data type.

VTB Pro permits callbacks into the engine when a connection is established between any ports that belong to the component. In Entity Builder, the user simply indicates that they would like to receive these callbacks and can then respond to the event. Typical reasons for responding to such an event include the need to modify a port's attributes. For example a signal port that has a dynamic matrix may want to adjust its dimensions based on the dimensions of the connecting port. Other possibilities include modifying the underlying units of one port so that it can work with another port.

An interaction point's value by default is scalar but can be designated to be a matrix value in Entity Builder. In addition an interaction point can change its dimensions at any point in time if configured to do so in Entity Builder.

Support for single line diagrams is achieved through the use of a multi-port. A multi-port is a single icon that actually represents multiple physical ports on the component. In this situation all of the ports represented by the single icon must be of the same type, that is to say all ports must be natural ports or all ports must be signal input ports or all ports must be signal output ports. These ports do not have to have the same underlying data type, units, dimensions, etc... but must be of the same type.

By allowing the developer to specify all of the metadata for the model in the Entity Builder GUI, they are no longer required to programmatically specify this in the source code for their entity. In VTB Pro the iconic information and interaction point information for the entity is no longer placed in the source code file greatly speeding up and simplifying the model development process. In added benefit is the reduction of the size of the source code making it easier to navigate and maintain.

Using Entity Builder, users can graphically construct the icon for the entity using a standard set of shapes. The color and style of each shape in the icon can be adjusted and by combing an array of shape types the user can build very sophisticated looking icons without altering the source code for the model. Entities can be represented by more than one icon. The locations of the ports must remain consistent between icons. This requirement is enforced automatically by Entity Builder.

VTB Pro has been extended and now permits the component developer the ability to write code for the model in several languages. The list of supported languages in Entity Builder now includes C++, C#, VB, Java, FORTRAN, and any .NET compliant language. A wider range of supported languages increases the user's acceptance of and reduces the learning curve required when developing VTB Pro compliant components.

In VTB Pro, the component developer now has the option to use a native interpreted language instead of learning the base classes necessary to code a component and the complexities of the C++ language. The mathematical equations for an entity can be entered directly into the Entity Builder GUI using this language. Typically the domain expert for a model is an electrical or mechanical engineer and does not usually possess an advanced background in computer languages, compilers, etc... and so the interpreted language helps to reduce this barrier by removing the requirement to be familiar with these concepts. Another feature now permitted in the Entity Builder tool is to allow the developer to generate the source code from the equations already entered via a process called code generation. The developer may choose to perform code generation to produce a compiled model for a variety of reasons such as to better protect their intellectual property rights or as a tool for learning how to write compiled models.

In addition to expanding the language options for the developer, Entity Builder reduces the amount of code required by reducing the number of functions that must be coded from four to two. A typical natural entity is now only required to implement two functions "OnRuntimeChange" and "Step" in order to simulate successfully.

Modules are created from an existing subsystem using the Module Builder tool. During the creation process the user specifies the subsystem from which to create the module. In the tool, the user is shown an interactive view of the subsystem they have chosen. This view of the subsystem is then used during the module creation process allowing the developer to select the interaction points that are to be exposed in the module. There is no longer a requirement to perform port mapping as the user directly selects the ports to expose in the GUI. The current process greatly reduces the time required for creating a module. An additional feature allows the developer the capability to rename the interaction point being exposed to something more intuitive.

Specifying the icon for the module in the Module Builder is specified in exactly the same way as the Entity Builder tool. The only difference is that a module can only ever have a single icon to whereas an entity may have multiple icons.

Help documentation can be associated with the entity directly while using the Entity Builder tool. This documentation can be in any format such as a Word document, PDF File, or html page. Entity Builder can also automatically generate an outline for the help documentation for an entity. The user contributes content to just a few of the sections of the document, greatly reducing the burden of writing help documents.

Cosimulation methods: Stepping API

In order to permit the greatest possible integration with other tools, VTB Pro has incorporated the use of COM (Component Object Model) as well as Microsoft's .NET technology in its underlying architecture. Support of both a COM and .NET interface now permits VTB Pro to be driven programmatically just as it can be from the native user interface. In particular systems and subsystems can be built, components connected and disconnected, parameters changed, simulation results accessed, and the solver controlled at a granular level all through the interfaces provided. In addition events can be raised either by conditions at the solver level or by the hosting application programmatically adding arbitrary events of interest. In order to reduce the complexity of controlling the VTB Pro software a façade was created which simplifies the object hierarchy and lets third party developers perform most actions by utilizing the services of a single object. Alternatively if the developer would like to use the more sophisticated features of the framework this is permitted through the individual objects directly via the COM or .NET interface.

In order for VTB Pro to be controlled as a simulation service it was necessary to implement a stepping API which permitted a client to dictate how much VTB Pro stepped in time and when it stepped. VTB Pro can be

controlled in an asynchronous mode by calling the “Start” and “Stop” functions in order to execute a simulation. In this mode the caller dictates only the time to start and stop but not the rate at which VTB Pro steps. The caller can request that VTB Pro run a simulation and return only when it has completed by calling the “Execute” function. This mode is most useful when the caller does not need to control the simulation but is only interested in the result and would like a synchronous call to obtain the result. This call does not return until the simulation has completed. The third and final way of controlling the simulation is to use the “Step” function. In this mode the caller passes in the amount of time for the solver to run forward before returning to the caller. In this mode the caller controls how the solver moves forward in time and can use this mode to co-simulate with other simulation tools.

In order to exercise the interfaces to VTB Pro an application was developed that involved the optimization of a hybrid fuel cell power system. In this case VTB Pro was used as a service to perform various simulations of the power system while another application processed the results of the simulations and made changes to the design in order to determine some minimal weight and volume for the fuel cell used as a power source for a specific load. In this case Matlab was chosen as the primary tool to drive the simulation within VTB Pro, analyze the results, and to make modifications of the design parameters. Using the COM interface to VTB Pro we successfully demonstrated the potential to drive, analyze, and modify a system design in VTB Pro from an external tool.

Another project made use of VTB Pro to simulate and provide analysis of a system consisting of various batteries and a set of configurable loads in various operating conditions. This application demonstrated several powerful capabilities of the VTB Pro software, primarily the ability to dynamically build and configure a subsystem as well as to cause VTB Pro to dynamically create and raise events to the calling application when certain conditions occurred. The user selected a power source and load from a list of sources and loads available in the VTB Pro component library. Once the user chooses the type of source and load the application made the appropriate calls to dynamically connect the components in some predetermined configuration. At the same time the application wanted to be informed whenever the battery supply being used was depleted to a certain level. In this case every time the battery’s state of charge fell to 5% the application was notified. The application could then remove the used battery and re-insert a fully charged battery and resume the simulation. Examples of the types of events that can be raised include the passing of a particular amount of time, the violation of some constraint such as an excessive current or voltage level, or when a particular condition has been satisfied such as a satisfactory level of power being delivered to a motor. Upon firing of the event the application can perform whatever action is required such as modifying the system parameters, adding or removing components, or disconnecting or making new connections.

VTB Pro is also capable of driving the simulation and using another tool as its server. Several components exist within VTB Pro to co-simulate with Matlab. These components use COM to connect to Matlab and open a model file for co-simulation purposes. Data is passed into and out of Matlab at the appropriate times in the simulation. In addition VTB Pro has integrated with Simsmart’s fluid simulation tool in a similar manner. A custom component was developed in VTB Pro that permits a system in VTB Pro to communicate with the Simsmart solver and send and receive data during a simulation. Testing of this mechanism was performed with VTB Pro simulating an electrical system which drove a fresh water pump responsible for cooling a system simulated in Simsmart. Collaboration with ISIM has resulted in the capability to import components directly from the ESL simulation environment into VTB Pro. A tool called ESL importer was built to perform this importing procedure and has been tested and validated against several ESL components. Further development of the feature set is expected to occur to more fully implement all features.

Co-simulation Techniques using ActiveX

Many complex systems are an integration of various subsystems. The complexity of a system may bridge various technical expertises. As results of that, the classical approach is to simulate each subsystem into the most

appropriate environment. The concept of co-simulation equips the user with an environment where different languages can be used to perform the simulations and a set of solvers interact. This means that any part can be solved using the most appropriate tool without affecting the solution of the rest of the system. This possibility not only increases the set of problems that can be analyzed but also provides the user with a more exhaustive, user friendly approach to solve the problem.

The Virtual Test Bed (VTB) [1], [2], [4] has previously used DLL-based methods to set up interfaces with external solvers. This approach is certainly effective and provides the desired results but it also calls for redundant effort in compiling the code to generate the DLLs. The users are required to go over the procedure of generating the DLLs and then copying them into the destination folder each time. This procedure prevents the users from changing the code on the fly and increases development time. For example distributing the DLLs to all VTB users who need to use the Matlab Engine interface for using Matlab as an external solver is inconvenient.

The use of Matlab Engine to call Matlab from a C++ code is well described in [6]. This report discusses about the Matlab Engine class and the method to link an application with Matlab. We can see that the appropriate DLLs have to be imported to the required destination folders.

Approaches to co-simulation can also be viewed in [5] where an engine cycle simulation code (WAVE) with Simulink provides a complete modeling of a vehicle system. The link makes use of the Matlab S-function protocol. This again requires the need to import certain DLLs.

Many institutions have built custom tool sets to enable co-simulation. PyMat [11], e.g., is an interface between the Python software and Matlab. This interface also makes use of the Matlab engine. The TC-toolbox is another tool used to interface Thermo-Calc software with Matlab.

In this report, the authors define an ActiveX based “Application Program Interface” (API) to perform co-simulation between VTB and other software and compare it with the already existing techniques. As result of that the way in which VTB interacts with external environments is generalized and simplified at the same time. In particular the authors analyze the case of VTB-Matlab and VTB-LabVIEW, but the framework is a guideline for other cases.

Past co-simulation experience in VTB

The approach of distribution of DLLs was previously adopted as a means of realizing the interface between VTB and other simulation softwares. This report focuses mainly on the interfaces between VTB & Matlab and VTB & LAB View.

Review of existing methods: VTB-Matlab/Simulink

The previous version of the API for Matlab/Simulink was developed using the Matlab engine. It allows the data exchange between Matlab and C++ custom software. The Matlab engine is a communication protocol that allows the user to benefit from the Matlab computation engine.

The interface is realized by a dedicated class inside the VTB architecture. This class invokes the following procedure [2].

- The VTB calls the Matlab engine at the start of the simulation.
- The VTB calls a Null-time execution of the target Simulink model.
- At every simulation step the VTB calls a step execution of the Simulink model. The required data is provided at the input.
- The output is then used by VTB for further computations.

One of the main advantages of using the Matlab engine is that instead of requiring the linking of the complete Matlab code, only a small engine communication library is needed [8].

Review of existing methods: VTB-LabVIEW

The process of interaction between VTB and LabVIEW was based on the Dynamic Link Library (DLL). The LabVIEW software is equipped with a tool called the Application Builder that generates DLLs for LabVIEW VIs. These DLLs can then be exported to be used in other environments. The DLL is also the basis for library management in the VTB software. A model class in the VTB software is able to load and execute LabVIEW DLLs. A case study to verify the effectiveness of this approach has been presented in [2].

Disadvantages of using DLLs

The existing API have been developed by distributing the component either as DLLs or executables. A DLL can be linked in two ways, Statically and Dynamically. We can summarize the disadvantages of their use as follows.

In static linking the object code of our program is linked with the object code of the library function during the stage of compilation and building of the application. This increases the size of the code as there is no way of sharing the library if many applications intend to use it.

Dynamic linking solves this problem of redundant code. All the applications using the DLL will share the DLL. The software follows a client-server based relationship between the application and server. The application is called the client as it calls for the services of the component (server). Although the problem of redundant code is solved using dynamically linked DLLs, the problem of having to compile the foreign code each time to generate the DLLs and then the need to copy them in the destination folder is not solved. The use of DLLs thus increases the development and simulation time significantly. The DLLs cannot be heavily relied on as there are chances of the application crashing due to some error in the DLLs. Version Management is another area causing problems while using the DLLs. As there are no standard rules for developing new versions, there is often a chance of a problem being created.

Introduction to ActiveX

ActiveX is the general name for a set of Microsoft technologies that allows users to reuse code and link individual programs together to suit their computing needs. Based on Component Object Model (COM) technologies, ActiveX was originally developed as an extension of a previous technology called Object Linking and Embedding (OLE) in order to facilitate the development requirements of internet-based applications. OLE applications now fall under the umbrella of ActiveX.

The concept of API relies on the theory of Component Object Model (COM). COM is a specification for solving problems of software integration and defines certain rules for writing software components. Applications can then be built using these components. These components can be built using any language. COM basically uses the concept of client-server relationship. COM also has the advantage of being object oriented and is build using the theory of encapsulation and polymorphism [9].

A COM component can be defined as a set of functions and methods that provide services to external applications. A COM component makes its services available through one or more COM interfaces. The COM interface establishes the communication between the client and server through a group of related functions. The DLLs on the other hand uses the exported functions.

The transparency of a COM interface as opposed to using a DLL is seen as the component does not have to change if the client changes keeping the interface the same and vice versa.

The COM interface essentially follows a certain set of rules that make it unique [9].

- Every interface has a unique 128-bit identifier called Interface Identifier (IID)
- An interface cannot be changed once it's been created. A new interface with a new IID is created if such an attempt is made. This solves the problem of Version management.

- The interface is derived from a standard interface called IUnknown interface.
- As the component can be built in any language it must follow a standard memory layout defined by COM.

However, there is no uniform way of developing such an interface between applications using COM. OLE automation simplifies the task of automating applications. On one hand it enables an application to manipulate objects implemented in another application and on the other hand, it helps an application to expose objects that can be manipulated by other applications. OLE Automation is very similar to COM and also follows the concept of client-server interaction. In this case the server is called the Automation server and the interface is called the dispatch interface. However, this is not the final interface that makes the properties of an automation server available to automation client or automation controller. Another interface called the IDispatch interface establishes the connection. The Dispatch Interface in this case can be defined as a group of functions and methods that provide their services to external applications. The Dispatch Interface is accessed through the IDispatch by automation controllers. The following figure gives an overview of COM applications.

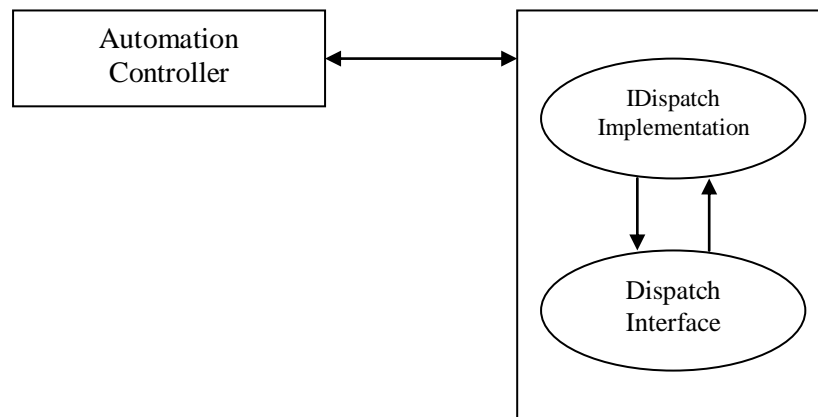


Figure 14: COM Interface

ActiveX in VTB to implement co-simulation

The Resistive Companion Method is the basis of the VTB solver. The RCM requires that device model equations be expressed in a specific form which allows for handling of device interconnections. A recent version of the VTB solver [10] has been enriched with a new backplane for supporting different type of coupling according to the IEEE standard VHDL-AMS. According to this standard, the VTB entities can be coupled with each other in two ways, Signal Coupling and Natural Coupling.

In the following a brief description of the interaction between the VTB solver and an external solver is reported both for Natural and Signal coupling:

- In Signal coupling the challenge of the VTB solver is to determine the sequence of execution of the VTB schematic. Thus at every time step the VTB solver communicates with each VTB entities and solves them. While sequentially solving all the models, when the VTB solver reaches the model with the interface, the control is then passed to the external solver. The modeler is supposed to code the required initial conditions to set up the interface in the Init function. The appropriate data is transferred to the other solver through the interface and the solution is then taken back during the SignalStep function. The VTB solver just waits for the solution form the external solver before moving on to the next time step. The output from the interface model is then forced at the input of the next model in the sequence of execution. The models then update the equations in the post step function so as to provide the appropriate inputs during the next time step. Thus in signal coupling of the models, the VTB solver never provides a solution for the entire system as a whole.

- In Natural coupling, the solver communicates with all the entities in the VTB schematic. It then represents the system in the form of the resistive companion equation. In general it generates the conductance matrix for the entire system. The initial conditions for setting up the interface are coded in the Init step of the VTB program. The solver then obtains the output from the external solver (this is the point where the ActiveX interface exchanges data) and forces it as a known input in the appropriate branch of the equation. This is done in the Step function of the code. The system is then solved by the solver and the solution is then given back to the models. The models can then update the equations in the post step function so as to provide the appropriate inputs during the next time step. Thus the solver provides a solution for the entire system as a whole.

More generally the natural coupling is applied to represent multi-physics systems. Every model, representing any system for example, thermal, mechanical or electrical can be represented in its equivalent electrical format. This equivalent electrical circuit is then represented in the form of the resistive companion equation.

A simple diagrammatic representation of the resistive companion simulation flow can be seen in Figure 15.

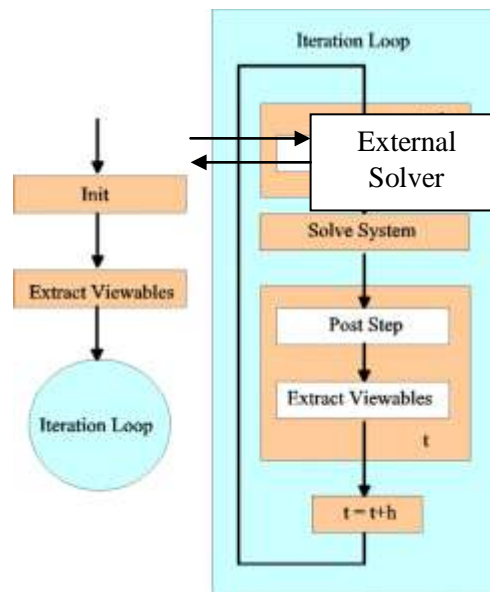


Figure 15: Resistive Companion simulation flow

Let us now focus on the possibility of embedding in a VTB model the communication through ActiveX with an external software/solver.

Applying the above theory, VTB is the automation client and Simulink and LabVIEW become the automation servers. The interaction between the VTB and the external solver can be summarized in the following manner.

- In the Initialization step the VTB initializes the COM interface with the external simulation environment.
- Depending on the requirements of the specific experiment, it then sets up the appropriate input values.
- With every signal step, the VTB then calls for an execution of the external code passing the right values as inputs and receives the outputs.
- These outputs are then passed to the next connecting block in the VTB schematic.
- This eliminates the need to follow different routines to generate the DLLs for different solvers. We can see a formalized way of interfacing the external solvers.

Summarizing the methods describe in what above an interface class requires the following methods:

- *Init*: the init method is used to initialize the communication with the external solver. If the external solver allows for initial condition definition the init should force the value of the variable according to the user input. The method returns a false or a true depending on the effectiveness of the communication
- *Step*: the step is the real kernel of the simulation. The main solver (VTB in this case) should enforce the initial condition for the step, provide value for external inputs of the interface software and collect the outputs. In the case of natural coupling the input/output must be applied to enforce conservation of energy. In order to do that two options are given: the main solver provides the value for the across variable at the interface point and receives back the value for the through variable or vice versa the main solver provides the value for the through variable and receives back the value of the across. This protocol is not necessary for signal input being the external solver simply embedded in the signal chain.
- *PostStep*: the post step phase is adopted to adjourn the current value of the state. It is important that the main solver keeps a copy of the state of the external solver in order to be able to repeat a step with a different value of integration step when needed (a classical case is given by the definition of crossing point event)

Coming to the coding details of the implementation, the COM object is defined in a C++ class. Instances of this class can be created using special COM functions. The ordinary C++ new and delete operators do not work. The following steps describe the process of building the COM component using C++ language.

- We first initialize the COM library on the current thread using the command `CoInitialize(NULL)`.
- Every application has a program ID called the ProgID, for example the ProgID for Matlab is `Matlab.Application` and the ProgID for LabVIEW is `Labview.Application`. Given this ProgID we obtain the class ID from the system registry of the corresponding application using the command `CLSIDFromProgID`
- The next step would logically lead us to the extraction of an Interface Identifier for the IDispatch interface. This identifier is called DIID (dispatch iid). Please note that the dispatch interface is not the COM interface.
- The dispatch interface has a number of methods and properties. These members can be accessed only through the IDispatch interface. The DIID for the IDispatch interface is then obtained using the command `CoCreateInstance()`.
- Once this interface is set up, it is easy to obtain the IDs of each of the methods and properties of the dispatch interface. This is done using the function `GetIDsOfNames()`. The parameters passed in the parenthesis define the name of the method to be used.
- Once the dispid of the members is obtained, the methods or properties are invoked and data is manipulated in the required sense.

We will now see the application of this technology in the case studies described in sections 6 and 7.

LabVIEW case study

LabVIEW on MS Windows supports ActiveX Automation Server capabilities. This can be done by interfacing with the LabVIEW type library that is located in the `..\LabVIEW\resource` directory. The idea is to open an Instance of LabVIEW using which we then open an Instance of a VI. This VI is then made to run asynchronously so as to enable the extraction of data during run time. Appropriate Flags are then exchanged between C++ and LabVIEW using ActiveX commands to achieve proper synchronization in their execution.

The Simulink software has a timing model with which the VTB interacts. If the time step of the VTB schematic is smaller than that of the Simulink schematic, the VTB forces its time step on the Simulink solver. If the Simulink time step is smaller then it solves multiple time until it reaches the end of the time step of the VTB solver. However, LabVIEW does not have its own timing model. So the control over the LabVIEW code can be obtained only by exchanging certain flags to determine the status of the VI execution as mentioned above. This however demands from the user, an effort to customize the models to suit the requirements of their LabView VI.

Common commands such as CreateInstance and GetVIReference are used to open instances of LabVIEW and its VIs. Commands such as SetControlValue and GetConrolValue are used to set the control values in the VI and to extract readings from it respectively. The key is in running the VI asynchronously using the command Run (1). With the parameter “1” passed in the Run command the user is able to extract data during real time, i.e. during the execution of the VI [3].

We will now use an example that makes use of the VTB-LabVIEW interface. The model implementing this interface in the VTB environment acts as a simulation agent on a network based monitoring system. A DC electrical drive with an AC interface was chosen as the monitored system.

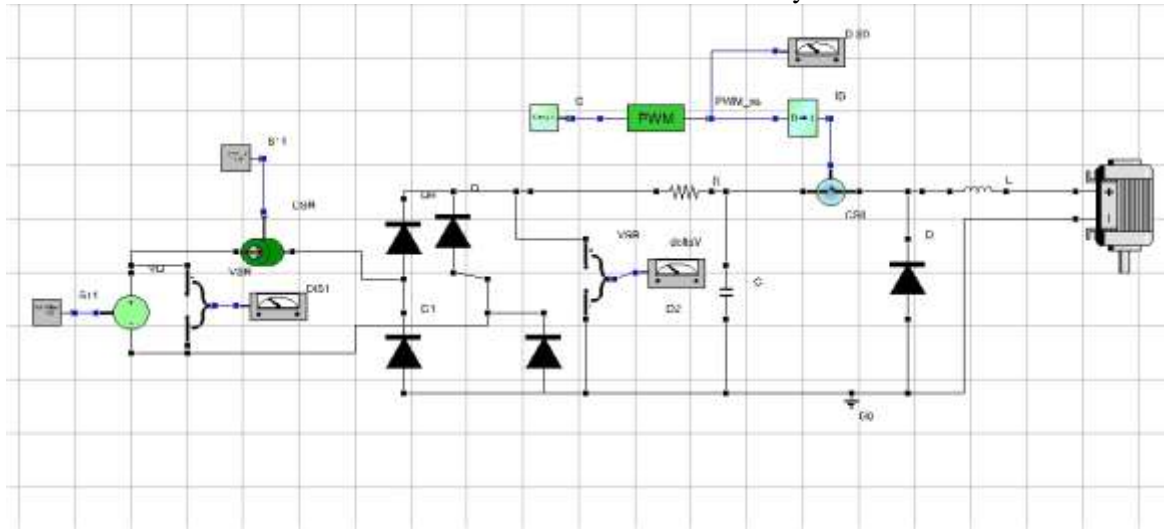


Figure 16: VTB Schematic of the System using the VTB-LabVIEW Interface

The drive system is simulated within the VTB environment. The idea is to compare the simulated results with the actual results using the same inputs for the simulated as well as the real system. The schematic adopted for the simulation is shown in Figure 16 [3]. The AC side input current is the variable of interest in this simulation. The input voltage in simulation is the AC side input voltage.

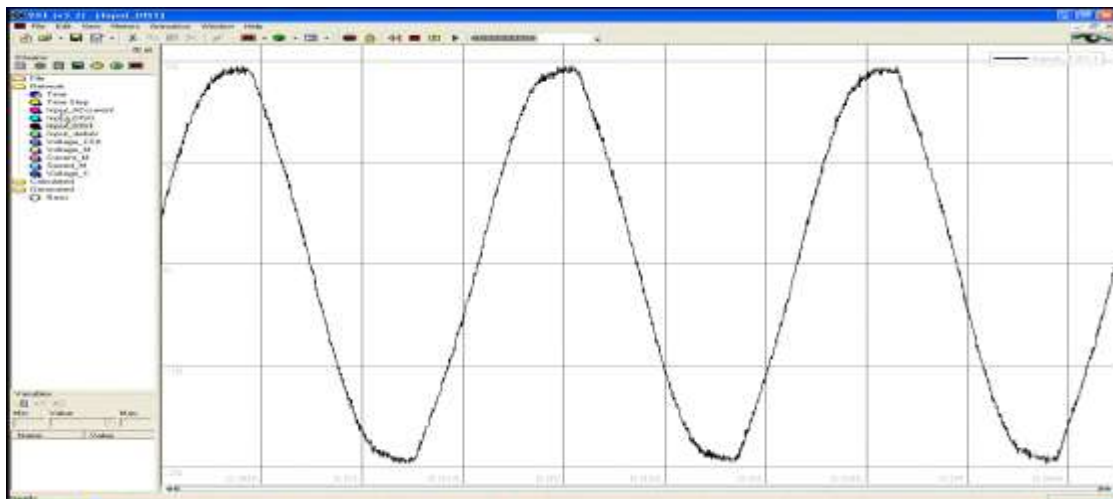


Figure 17: Input Voltage as it appears on the VTB scope display

This measured voltage is shown in Figure 17. Thus, instead of using an ideal sinusoid voltage we have now used in the simulation, the actual voltage input given to the real system. The simulation generates the current

which is then collected by another model supporting the VTB-LabVIEW interface. The values are again stored in a buffer in the LabVIEW schematic. These are collected by other simulation agents over the internet using LabVIEW programs implementing the TCP/IP protocol. In Figure 18 we can see the simulated current and in Figure 19 we see the actual measured current.

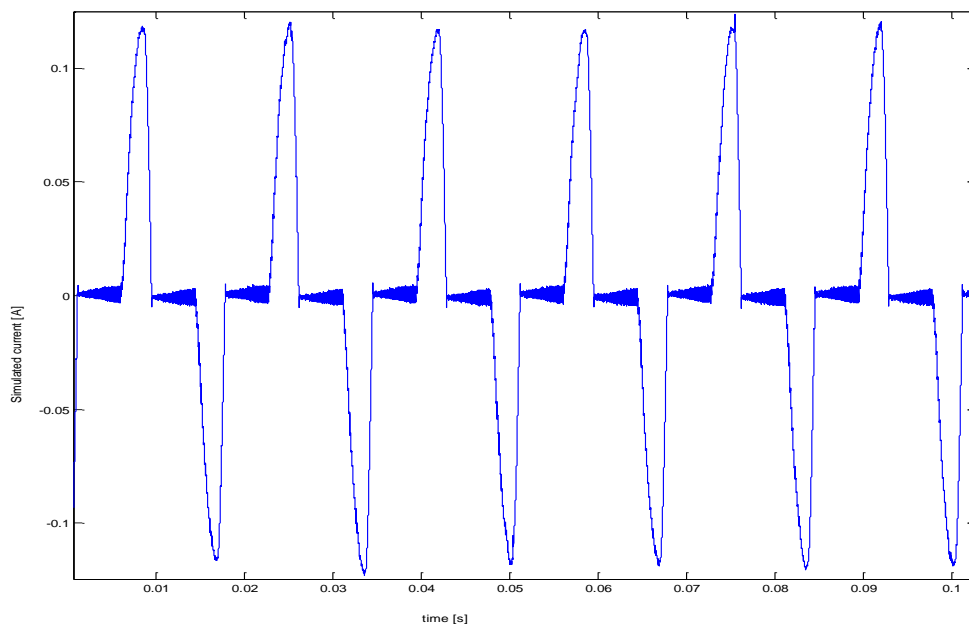


Figure 18: simulated current when the system is supplied with real voltage

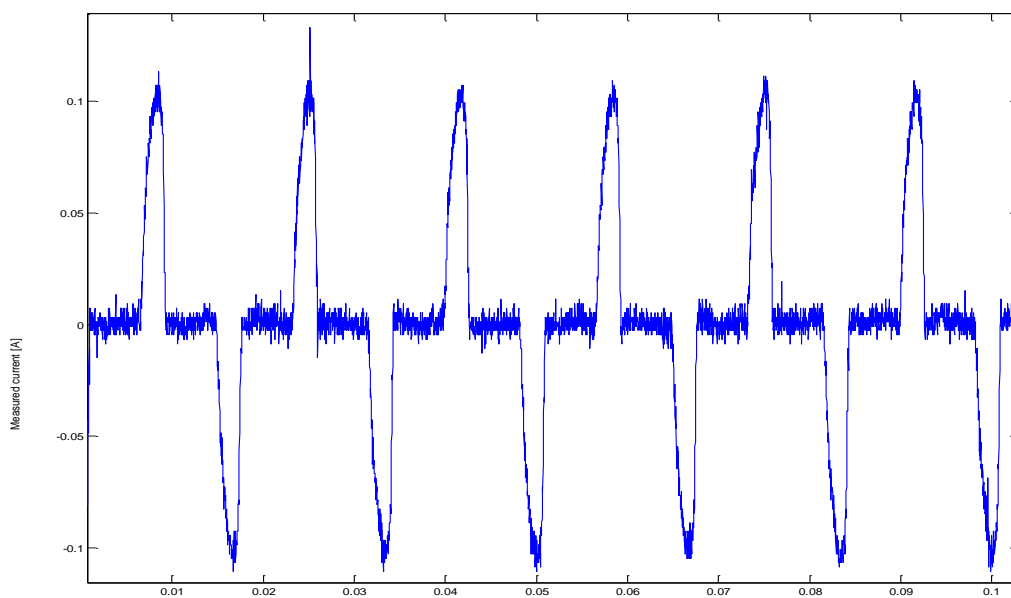


Figure 19: Measured Current

The LabVIEW interface with VTB performs the following functions.

A LabVIEW code is used to extract data from a GPIB port on a Tektronix oscilloscope. This data is temporarily stored in a buffer.

This data is then transferred to the VTB simulation on its approval over the internet. This is done using TCP/IP routines in the LabVIEW code.

The model in the VTB schematic that receives this data is the model implementing the VTB-LabVIEW interface. This LabVIEW code collects the data and delivers each data point as and when the VTB schematic sets a flag. This exchange of data and the flags uses the ActiveX interface between the two environments.

Another block implementing the VTB-LabVIEW interface collects each data point of the simulated result and sends it over the internet to another agent in the network.

Simulink case study

Interfacing Matlab with VTB follows the same pattern as stated above. Having replaced the Matlab engine with ActiveX commands gets rid of the problem of distributing certain DLLs that support the Matlab engine and also the problems with version management.

The Schematic used for this case is a simple system that takes a square wave input from a VTB signal source model, uses an integrator in the Simulink environment to integrate it and then returns the integrated waveform back to VTB. The data is exchanged between the two environments using the methods of the component model.

A Simulink .mdl with the correct number of inputs and output is required to be in a working directory of Matlab. The validity range of the VTB-Simulink models depends on the meeting of requirements and the validity of the Simulink file being interfaced into. The following figures show the schematics and the result of this simulation.

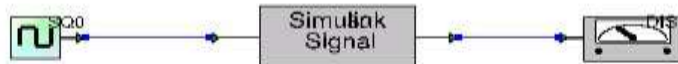
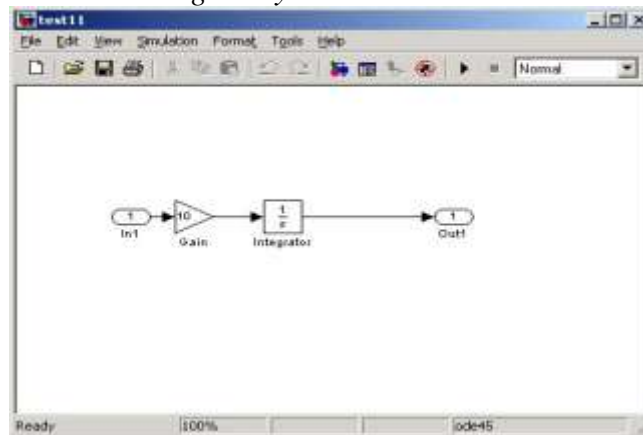


Figure 20: VTB schematic showing the system



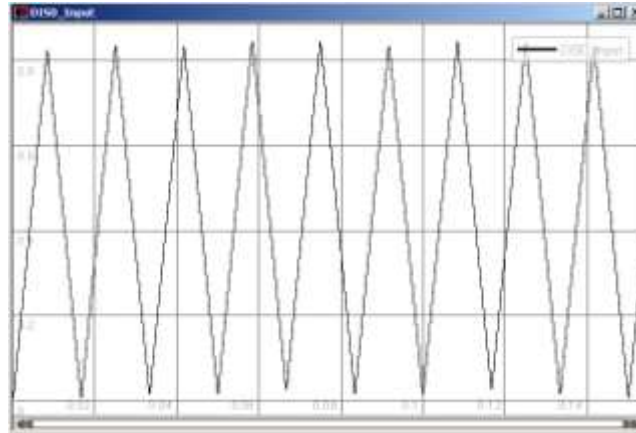


Figure 21: a) Simulink file implementing the Integrator and b) Integrated output seen on VTB scope

Conclusion.

The ActiveX technology clearly poses an advantage over the previous method of distributing DLLs. The need for compiling the external code to generate the DLLs each time and copying them in the destination folder has been eliminated. With ActiveX the external code can be modified on the fly which reduces the simulation and development time. Problematic issues such as that of version management have been disposed off. Co-simulation has enabled each part of the system to be solved in its native environment assuring optimum output.

The VTB has now become a more powerful and a user friendly environment. Thus we have now defined a better approach towards the development of Application program interfaces.

VTB Realtime

Traditional software-based simulation has the disadvantage of being unable to exactly replicate real operational conditions. One way to bridge the gap between simulation and real conditions is the Hardware-in-the-loop (HIL) simulation. Real-time HIL simulation replaces the emulated hardware under test or control logic in the simulation model with real hardware that interacts with the computer models. This increases the realism of the simulation and provides access to the hardware features currently not available in software-only simulation models, hence reduces the risks of discovering an error in the very last stage of the on-the-field testing.

Over the years, many HIL simulation experiments have been proposed in literature; however, these systems are soft real-time or even non-real-time, hardware dependent or based on costly proprietary solutions, or supported only by a single platform or solver. In order to extend the application of this technology, a very low-cost hard real-time simulation environment for HIL experiments is developed at the University of South Carolina, completely built on open-source software and off-the-shelf hardware. This system is referred as VTB-RT, VTB-RT has unique properties such as multi-platform, multi-solver, and hard real-time. Instead of competing with commercial systems, it is designed to provide a very low-cost alternative for real-time HIL applications while maintaining acceptable resolutions.

Real-time HIL simulation has a wide application, such as power quality disturbances investigation, and modern automotive electronic control unit development. This paper focuses on the power electronics applications. The application of Real Time Simulation (RTS) to Power Electronics system is in particular a very active field of research. In effect Power Electronics can be considered a significant challenge for RTS considering the requirement in terms of time accuracy.

In the following, we will focus on the description of the main features and on the use of VTB-RT, an efficient real-time HIL testing approach for power electronics control system design. To meet with the hard real-time constraint, fast dynamics, and the ever-increasing complexity of the power electronics systems, distributed simulation using VTB-RT is also adopted in this testing approach.

The full procedure including both software simulation and hardware implementations of the proposed approach is then applied to two classical power electronics application examples: a boost converter control system and an H-bridge inverter control system, representing a very low cost and a relatively advanced hardware setup, respectively. Since the results of these examples are well-known in textbooks, they are adopted here intentionally to validate the applicability of the proposed testing approach.

In the case that real hardware is involved in the simulation process, the software must deal with additional challenges. These challenges motivate towards the VTB-RT, the real-time extension of the VTB. Hardware-oriented simulation has to deal with more problems than software-based simulation, especially the inexorable forward progression of time. This requires the simulation environment to operate in hard real-time mode. However, operating systems like Windows and Linux are unable to provide hard real-time capabilities. To address this issue, an open source Linux kernel modification package, the Real-Time Application Interface (RTAI), has been developed by the Department of Aerospace Engineering of Politecnico di Milano. RTAI completely changes the way Linux receives and handles hardware interrupts and enables the hard real-time capability of Linux. In VTB-RT, Linux and RTAI were adopted as the underlying real-time operating system. The VTB-RT shares the major parts of its architecture with the VTB. It reads the same file format created by the VTB schematic editor under Windows, thus makes it convenient to export simulations from the non-real-time platform, the VTB, into the real-time platform, the VTB-RT.

VTB-RT Components

Many systems for HIL simulation have already been developed, such as RT-Lab, RTDS, and HyperSim. However, all of them are based on proprietary solutions. The objective of the VTB-RT is not to compete with these commercial systems, but instead, to provide a very low-cost solution for real-time HIL applications, while maintaining acceptable speed and resolutions. The VTB-RT is completely implemented with open-source software and low-cost off-the-shelf hardware. From the software point of view, the VTB-RT consists of four free software packages:

Linux

Linux is selected as the operating system of the VTB-RT because of its low cost, high performance, and open source. It provides the user interface, basic functions, and development tools. In the development process of the VTB-RT, various Linux distributions including Mandrake, Redhat, Caldera, and Suse have been demonstrated to be suitable as the operating system. The open source feature of Linux makes it possible to modify its kernel code to become real-time capable.

RTAI

Hard real-time requires the operating system to be preemptive and deterministic. In the VTB-RT, RTAI is used to achieve this requirement. The RTAI is a kernel modification package of Linux that permits the handling of hardware interrupts and therefore enables the hard real-time capability of Linux.

Comedi

An HIL simulation system requires I/O interfaces to the hardware. In the VTB-RT, this is achieved by Comedi, freeware that develops open-source device drivers for many different data acquisition (DAQ) devices. It consists of two complementary packages: “comedi,” which implements the kernel space functionality; and “comedilib,” which implements the user space access to the device driver functionality. Comedi works with a standard Linux kernel as well as the RTAI.

VTB Solvers and Simulation Models

The SAC solver and the SRC solver are used by both the VTB and the VTB-RT. The solvers and simulation models are developed using C++ language and the same source codes are shared in these environments. In the VTB-RT, the source codes of the solvers and models need to be recompiled and made compatible with the real-time Linux environment. An important consideration to use the SRC solver is that it manipulates the real hardware interface, and as a result, it enables the natural coupling between the simulation environment and the hardware plant, and thus makes possible the virtual power exchange between the simulation software and the hardware under test. At this point, the SRC solver is the main solver for both VTB and VTB-RT. The application examples in section 0 and 0 use the SRC solver.

A complete description of the VTB-RT and its components is available in **Error! Reference source not found.**

VTB-RT Configuration

Minimum and suggested hardware configurations for the VTB-RT host computer are listed in TABLE III. The minimum configuration represents the first version VTB-RT. The suggested configuration is the one used in the application example in section 0. The speed and resolution of VTB-RT can be improved easily by choosing higher level hardware, as in the application example in section 0.

TABLE III
Minimum and Suggested Hardware Configurations for VTB-RT

	Minimum configuration	Suggested configuration
CPU	Intel P200MHz	Intel P800MHz
Hard drive	2 Gigabytes	10 Gigabytes
RAM	64M	128M
Free PCI Slots	1	At least 1
I/O DAQ Cards	Yes (†)	Yes (†)

†: DAQ card should be listed in the Comedi supported hardware list as Appendix B of **Error! Reference source not found.** Otherwise, Comedi does not support the device and the driver has to be developed individually.

The software configuration for the VTB-RT includes the components listed in section **Error! eference source not found.**: a clean Linux kernel with an RTAI patch, Comedi drivers, and VTB solvers. Details VTB-RT implementation procedure is presented in the Appendix.

Real Time Implementation

There are three major components in the VTB-RT real-time implementation: a real-time task, a Linux process, and a real-time FIFO (first in first out buffer).

Real-time Task

The RTAI preempts the standard Linux kernel and handles hardware interrupts. In the VTB-RT, a real-time task is generated by the RTAI to manage the 8254 chip (clock generator) to generate a real time clock, which is used as the basis for defining the simulation step. This real-time task is a loadable module in Linux; it stays in the kernel-space upon being loaded. Fig. 1 shows the pseudo code of a typical real-time task.

In a typical real-time task as Fig. 1, the following code sections are included:

- Application interface between the real-time task and the real-time FIFO:

The interface between the real-time task and the real-time FIFO is defined in this section.

- Real-time task initialization function:

<pre>#include Header Files <Linux module, i/o, math, rtai, rtai_sched, rtai_fifos> #define RT_Step_Size #define RT_Task_Priority RTAI_API() { Send_RT_Clock_Message_to_RT_FIFO(); }</pre>	<pre>init_module() { Set_RT_Step_Size(); Initialize_RT_Task(); Create_RT_FIFO(); Run_RT_Task_Periodicly(); } cleanup_module() { Stop_RT_Clock(); Destroy_RT_FIFO(); Destroy_RT_Task(); }</pre>
---	---

Fig. 1 Pseudo code of a typical real-time task.

A kernel module must always contain an *init_module()* function. It is invoked by the “*insmod*” command when the module is loaded. It prepares for later invocation of the module’s functions. The step size and real-time application task are defined in this section. The application task sends a real-time clock message into the FIFO at the beginning of each time step. This message indicates a new simulation time interval for the user-space, where the VTB-RT solver is located.

- Real-time task cleanup function:

A cleanup function *cleanup_module()* is also required for any kernel module. It is invoked by the “*rmmmod*” command when the module is unloaded. It informs the kernel that the module has been

removed and none of its functions are called anymore.

Linux Process

VTB-RT solvers are realized by a set of standard Linux processes. They are similar to other Linux programs, such as a text editor. In each step interval, the solver takes in the system input from the input channel of the DAQ device, solves the system state, and sends the system output through the output channel of the DAQ device. The Linux process is a user-space application program and hence has no direct communication with the real-time task. Fig. 2 shows the pseudo code of a typical VTB-RT solver.

In a typical VTB-RT solver as Fig. 2, the following code sections are included:

- DAQ input function:

This function reads the input data of the under test system from the input channels of the DAQ device.

- DAQ output function:

This function sends the output data of the under test system to the output channels of the DAQ device.

- VTB-RT solver function:

This function transplants the VTB solver from Windows environment to Linux environment. It is the “heart” of the VTB-RT platform. It solves the state of the under test system using the input data and generates the system outputs during each simulation interval.

- Main program:

The main program incorporates the previous three functions. It polls the real-time FIFO for the real-time clock update. If an updated real-time clock is detected, it will call the DAQ input function, VTB-RT solver function, and DAQ output function in sequence.

<pre> #include Header Files <Standard Linux header files> <Header files for a specific VTB-RT solver> #define Input_Channels #define Output_Channels DAQ_Input (Input_Channels) { Open_DAQ_Device(); Set_Mode&Range_of_DAQ(); Read_Data_From_DAQ(); Data_Scaling(); Close_DAQ_Device(); Return_Input_Data; } DAQ_Output (Output_Data, Output_Channels) { Open_DAQ_Device(); Set_Mode&Range_of_DAQ(); Data_Rescaling(); Send_Data_to_DAQ(); Close_DAQ_Device(); Return; } </pre>	<pre> VTB-RT_Solver (System_Inputs) { System_Outputs = Solve_State(System_Inputs); Return_System_Outputs; } main() { Initialize_RT_FIFO(); Initialize_VTB-RT_Solver(); While(!end) { Read_RT_Clock_From_RT_FIFO(); If (RT_Clock_Updated) Then { System_Inputs = DAQ_Input(Input_Channels); System_Outputs = Solve_State(System_Inputs); DAQ_Output(System_Outputs, Output_Channels); } } } </pre>
--	---

Fig. 2 Pseudo code of a typical VTB-RT solver.

Real-time FIFO

Because in the VTB-RT the real-time clock information has to be passed to the solver, a real-time FIFO is applied as the “bridge” between the real-time task and the Linux process. The real-time FIFO is a uni-directional read/write buffer created by the RTAI. After simulation starts, it continuously records the real-time clock generated by the real-time task. Simultaneously, the Linux process polls the real-time FIFO, detects the real-time clock, and performs the simulation. From the programming point of view, the real-time FIFO can be divided into two parts: one part embedded in the real-time task, and the other in the Linux process, as shown in Fig. 1 and Fig. 2.

Fig. 3 graphically illustrates how real time is achieved in the VTB-RT platform using the previously discussed three major components. More detailed explanations and example codes of these components are available in vtb.ee.sc.edu

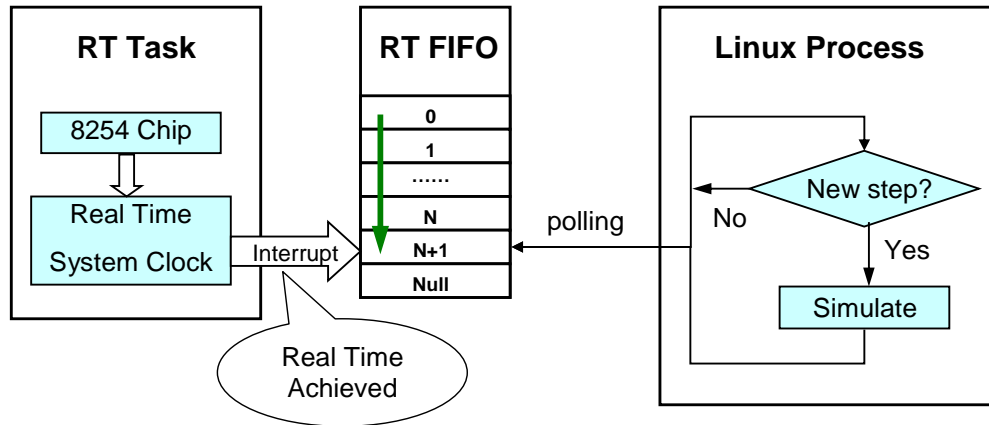


Fig. 3 Real time implementation of VTB-RT.

VTB-RT Architecture

Fig. 4 shows the architecture of the VTB-RT. This architecture allows the user to perform a real-time HIL testing of a system that includes real hardware. This testing phase can be considered as the very last step before the real on-line testing of power electronics controls. Through this process the user can verify not only the algorithmic correctness of the system (e.g., a controller) in the simulator, but also its capability to meet the real-time constraints.

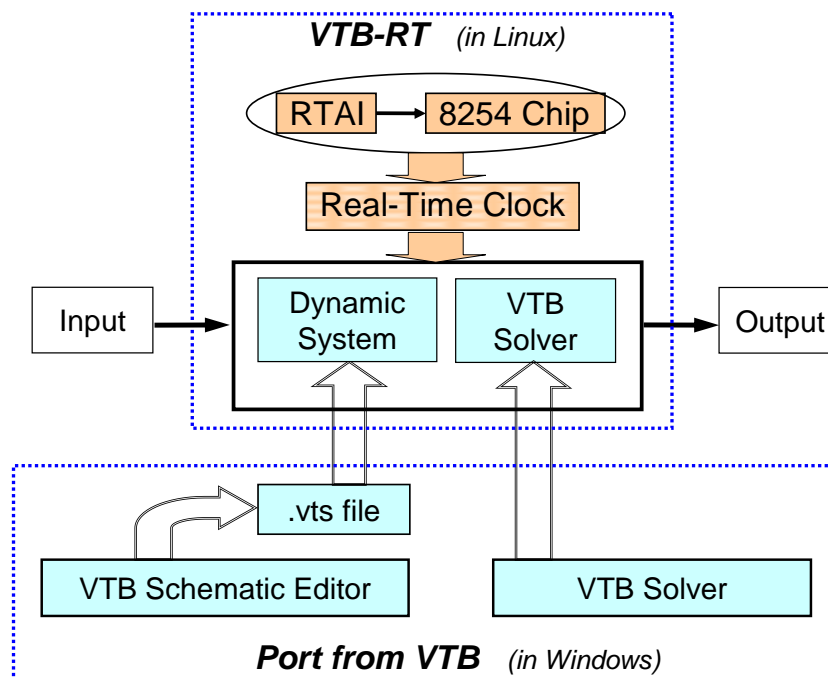


Fig. 4 The architecture of VTB-RT.

The simulation schematics can be created using the VTB Schematic Editor under a Windows platform. The schematic file format, .vts, is compatible with the VTB-RT under Linux. This enables

the user to directly export a simulation from non-real-time platform to hard real-time platform. It is important to underline that this step does not require any compilation process. The .vts file is shared among different platforms and is an ASCII file describing the system by using an XML-based notation.

Real-Time Control for Power Electronics using VTB-RT

Power electronics control designers often use simplified models of the plant in the early stages of the system design. By doing this, they can focus on the control algorithm itself rather than the complexity of the plant. However, many factors may affect the viability of the derived controller, such as over-simplification of the model and data communication time delays. Therefore, in order to be confident of the design, the control system must be tested under more strict conditions. For instance, in the case of the switching power converter, different levels of models could be considered subsequently.

- Averaged model.
- Switching model.
- Real hardware real-time HIL testing.

Reference **Error! Reference source not found.** gives a detailed example of using both the averaged model and the switching model of a boost converter. This paper focuses on the real-time HIL testing with real hardware. Using the VTB-RT, a very low-cost real-time HIL testing approach for control designs in power electronics applications is proposed. This approach is summarized in four steps, as shown in Fig. 5.

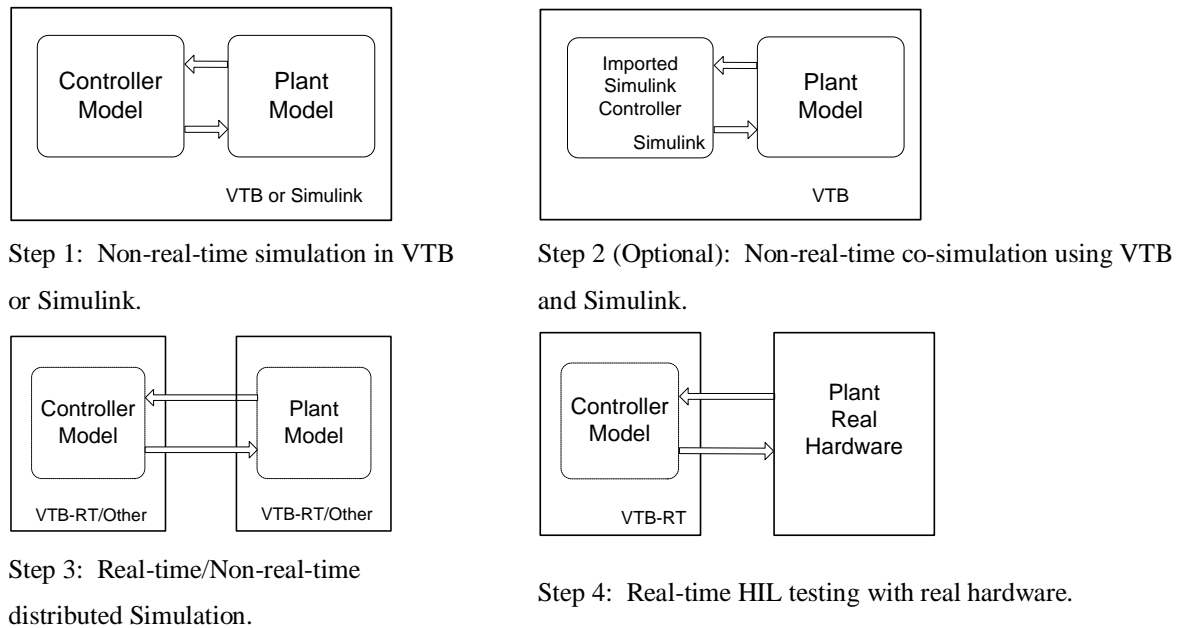


Fig. 5. Design approach of real-time control for power electronics.

Step 1:

Design a high-fidelity system model for both the controller and the plant in the VTB or other non-real-time simulation environment, such as Simulink. Tune the control parameters if necessary. The result of this step will be the ideal result.

Step 2:

Link the controller model in Simulink developed in step 1 into the VTB and perform the VTB-Simulink co-simulation (refer to example I). This result can be used as a comparison to analyze the HIL results in step 3 and step 4. This step can be skipped for an even lower cost VTB/VTB-RT only design, where Simulink is not involved (refer to example II).

Step 3:

This is the distributed simulation stage. The whole system is partitioned into two subsystems: one contains the model of the controller; and the other contains the model of the plant. Different simulation environments can be used to host these subsystems. This step can be either real-time or not, depending on the host environments. Application example I shows the non-real-time distributed simulation using dSpace and VTB. Application example II shows the hard real-time distributed simulation using two separate VTB-RT computers.

Step 4:

Keep the controller model in the VTB-RT and replace the plant model with real power electronics hardware. Perform the hard real-time HIL testing.

Following these steps, the VTB-RT provides an efficient design and testing approach for power electronics controls. The real-time HIL testing eliminates the costly hardware and greatly reduces the design cost. It should be pointed out that the limitation of VTB-RT and the proposed design approach primarily lies in the fact that for a given hardware platform, the minimum real-time step is limited. It means only a limited bandwidth of the system under test can be used. Therefore, in the actual design stage, special attention must be paid to compromise between the VTB-RT platform cost and the bandwidth of the system under test. At this time, a minimum real-time step of 250 μ s has been achieved using low level hardware and 50 μ s has been achieved using medium level hardware. This time resolution satisfies most of the power electronics controls.

Application Example I: RT State Space Feedback Control for Boost Converter

This application example illustrates the process during the implementation of a state space feedback control for a boost converter, showing all of the steps described in section 0. Particularly, it focuses on the real-time HIL testing with very low-cost hardware **Error! Reference source not found.**

First, the analytical control design uses pole placement on the linearized system. Poles are selected so that the closed-loop system has satisfactory dynamic behavior. The designed system is then built in the VTB to obtain the ideal results. Then, the VTB-Simulink co-simulation is performed by importing the Simulink controller into the VTB. After that, the non-real-time distributed simulation is performed on this system using dSpace and the VTB. This step is not hard real-time, since the plant model is still hosted in Windows. However, it gives a general approach for the HIL testing where a hard

real-time system is not available. Finally, the real-time HIL testing is performed using the VTB-RT and a real boost converter.

The hardware and software configurations of the VTB-RT computer used in this example are listed in TABLE IV. The boost converter has the parameters given in TABLE V.

TABLE IV
VTB-RT Configurations in Boost Converter Control Example

Hardware configuration		Software configuration	
CPU	Intel PIII 800MHz	Linux release	Mandrake 9.0
Hard drive	10 Gigabytes	Linux kernel	2.4.20
RAM	128M SDRAM	RTAI	24.1.10
Network	10 Mbps ether net	Comedi	0.7.66
I/O DAQ	Advantech PCI1710	Comedilib	0.7.19
Devices	Advantech PCI1720	gcc version	3.2

TABLE V
Parameters of Prototype Boost Converter

Rated input voltage	12V
Rated output voltage	40V
Maximum output power	100W
Input inductance	46 μ H
Output filter capacitance	1.360mF
Main switch	IRF540N
Switching frequency	50kHz
Load resistance	35 Ω

Designing and Testing Procedures

Step 1: Non-real-time simulation in VTB

The plant and the feedback controller are designed in the VTB as Fig. 6. The desired closed-loop poles are chosen as -2000, -5000, and the desired output voltage 20V, which result in the parameters of the controller: $k_1 = -0.0161$ and $k_2 = -0.0206$. Fig. 7 shows that when the reference output voltage steps up from 12 volts to 20 volts, the actual output voltage follows the reference.

Step 2: Non-real-time VTB-Simulink co-simulation

The controller is then implemented in Simulink and imported into the VTB by using the interactive interface between the VTB and Simulink. The schematic of the co-simulation system is shown in Fig. 8.

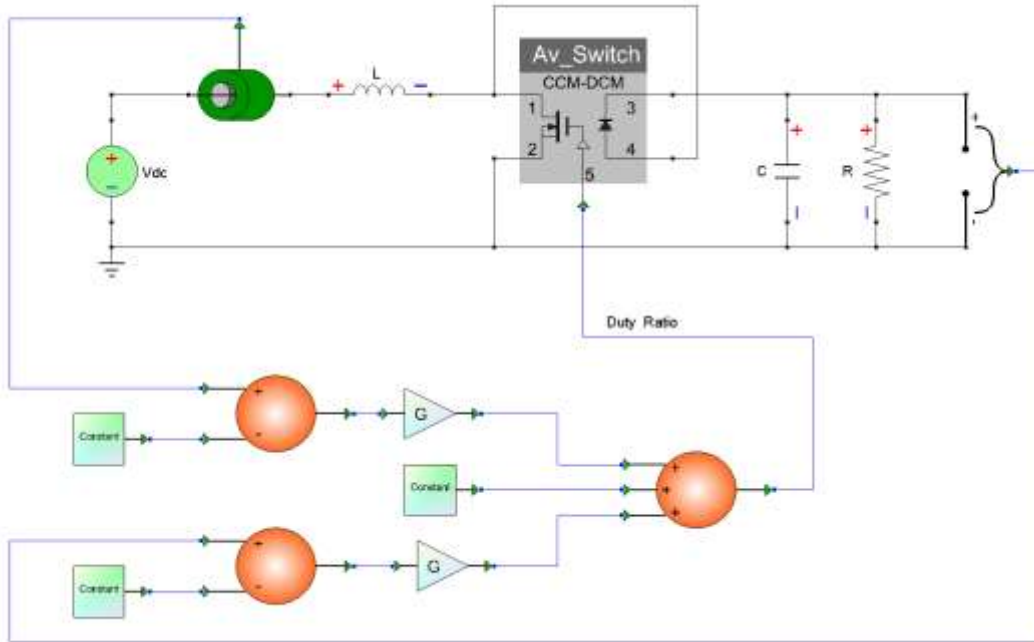


Fig. 6. Schematic of the boost converter control system in the VTB.

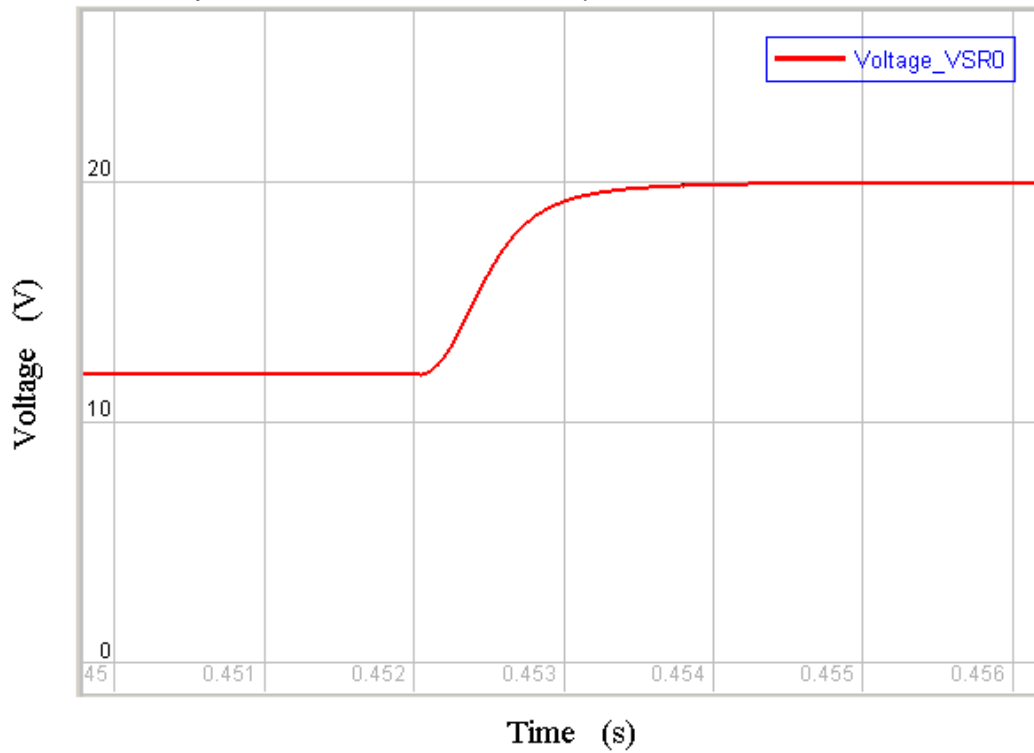


Fig. 7. Output voltage of the closed-loop system in the VTB, when reference voltage steps from 12 V to 20 V (software-only simulation case).

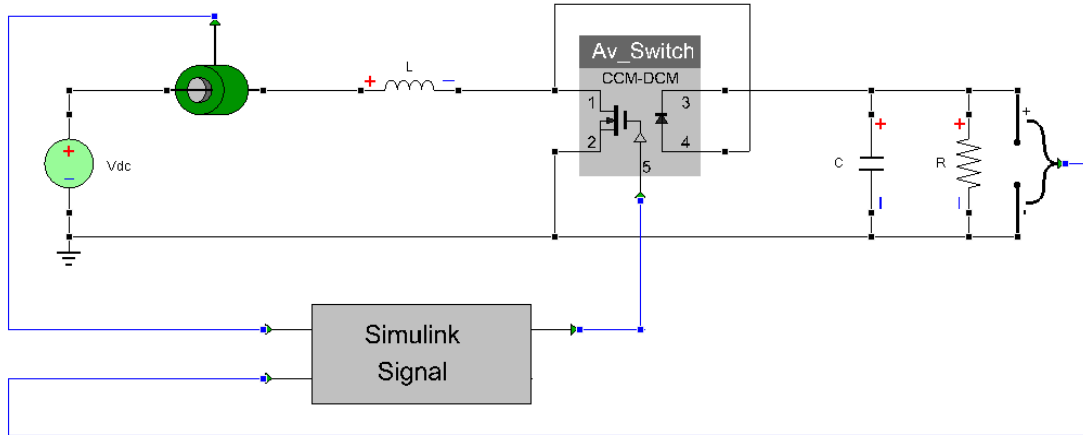


Fig. 8. VTB schematic for VTB-Simulink co-simulation.

Step 3: Non-real-time distributed simulation

The dSpace system supports direct compilation of the Simulink control definition, and the compiled code can be downloaded into the dSpace platform without any change. Benefiting from this, the Simulink controller model is compiled and downloaded into the dSpace platform, and non-real-time distributed simulation is performed between the VTB and dSpace. Since step 2 and step 3 do not deal with hard real-time, for simplicity, the simulation results are omitted here. Detailed results are available in **Error! Reference source not found.**

Step 4: VTB-RT HIL testing with a real boost converter

The state space feedback controller is implemented in the VTB and then exported into the VTB-RT, as shown in Fig. 9. The “RT clock” model represents the real-time clock in the VTB-RT. Three “VTB-RT ADV PCI-1710 I/O Card” interface models are used for signal exchange between the VTB-RT and the boost converter hardware.

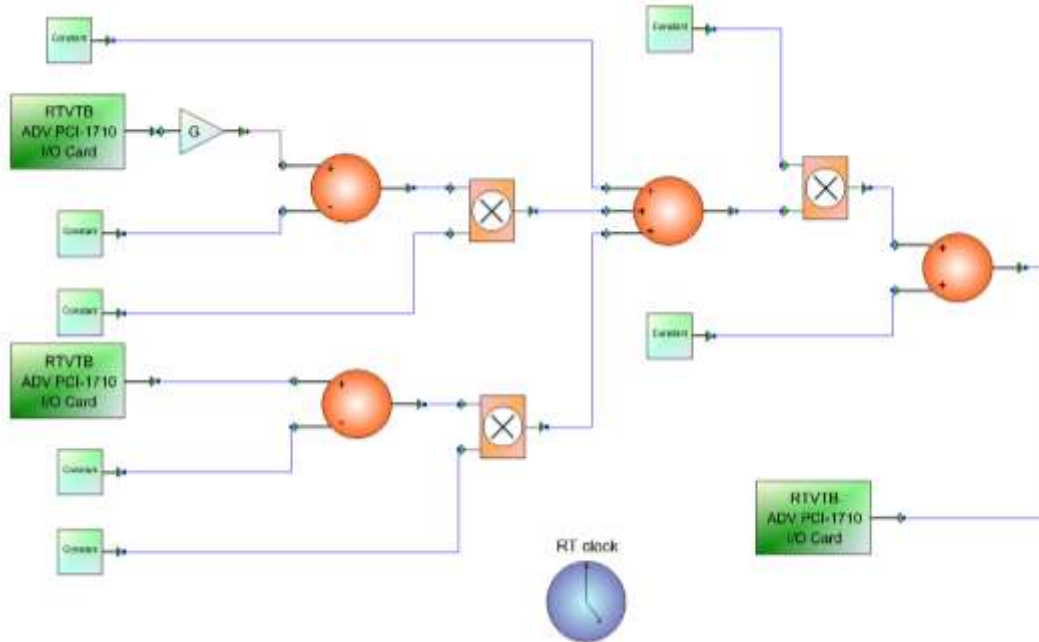


Fig. 9. State space feedback controller model in the VTB (exported into the VTB-RT).

Finally, the hard real-time HIL testing is performed with the controller in the VTB-RT and a real boost converter. Fig. 10 shows the response of the boost converter when the reference voltage steps up from 12 volts to 20 volts. It is in good agreement with Fig. 7, the ideal result predicted in step 1.

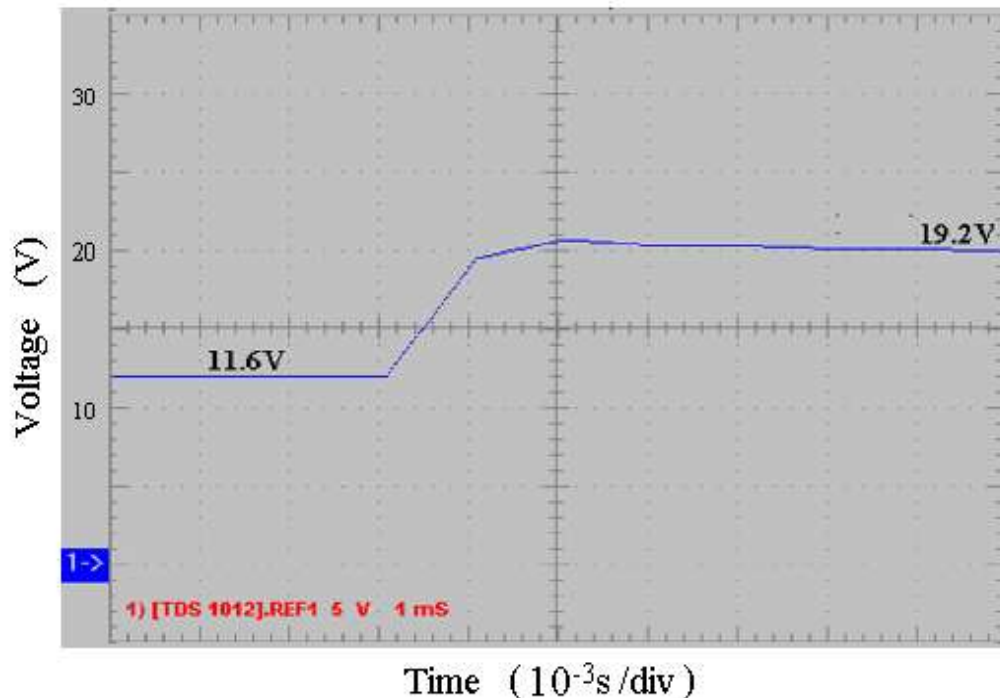


Fig. 10. Output voltage of the real boost converter, when reference voltage steps from 12V to 20V (hard real-time HIL simulation case).

Notice that the steady state output voltages in Fig. 10, 11.6 volts and 19.2 volts, are less than the ideal case in Fig. 7, 12 volts and 20 volts. This is because the simplified models in the ideal case do not take into account the losses

in the actual hardware. Also it is observed that the experimental result has piecewise-like behavior caused by the real-time simulation step size. In this case, the step size is 300 μ s.

If a faster host computer is used for the VTB-RT, the simulation step size can be easily reduced, and the result will be smoother. For instance, a time step of 50 μ s has been achieved for a similar example using a more advanced VTB-RT platform, whose configurations are listed in Table IV **Error! Reference source not found.**

TABLE VI
Configurations of a More Advanced VTB-RT Platform

Hardware configuration		Software configuration	
CPU	Intel P4 2.66GHz	Linux release	RedHat 8.0
Hard drive	60 Gigabytes	Linux kernel	2.4.20
RAM	512M SDRAM	RTAI	24.1.11
Network	10 Mbps ether net	Comedi	0.7.69
I/O DAQ	Advantech PCI1710	Comedilib	0.7.20
Devices	Advantech PCI1720	gcc version	3.2

The agreement between Fig. 7 and Fig. 10 confirms that the real-time state space feedback control of a boost converter is achieved through the proposed VTB-RT hard real-time HIL testing approach.

Application Example II: Real-Time Feedback Control for An H-Bridge Inverter

The second example demonstrates the design of a digital controller for an H-bridge inverter using only the VTB and the VTB-RT, eliminating any other third party design software. This example focuses on the real-time distributed simulation step **Error! Reference source not found.**

First, a proportional-integral (PI) controller is designed analytically at desired bandwidth and phase margin. The system stability is analyzed in discrete-time domain and stable integration time step limit is obtained. The designed closed-loop system is then built in the VTB to obtain the ideal results. The VTB-Simulink co-simulation step is skipped, since in this example the design capability of VTB/VTB-RT without help of third party software is concerned. After that, the whole system is partitioned into an inverter subsystem model and a controller subsystem model, hosted by two identical NI VXI-872Bpc computers. As the focus of this example, hard real-time distributed simulation is performed.

The configurations of the VTB-RT computer used in this example are listed in TABLE VII.

TABLE VII
VTB-RT Configurations in H-Bridge Inverter Control Example

Hardware configuration		Software configuration	
CPU	Intel PIII 1.26 GHz	Linux release	Mandrake 9.0
Hard drive	15 Gigabytes	Linux kernel	2.4.19
RAM	128M SDRAM	RTAI	24.1.10
Network	100 Mbps ether net	Comedi	0.7.66
I/O DAQ	NI PCI-6070E	Comedilib	0.7.19
Device		gcc version	3.2

The whole system is described in Fig. 11. A sinusoidal voltage source is rectified and supplies the dc voltage level for the inverter. The output current of the inverter is fed into a PI controller. This current is compared with the reference, and the output of the controller determines the duty ratio of the switching of the inverter. The load is a 1 mH inductor with an internal resistance of 0.01 ohm

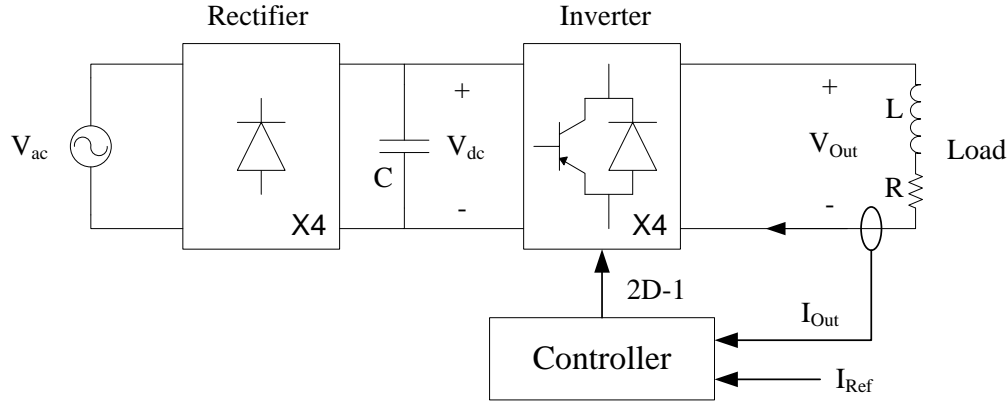


Fig. 11. Description of the H-bridge inverter system.

Analytical Design of the PI Controller

Choose the bandwidth and the phase margin of the open-loop transfer function as

$$\omega_{BW} = 2\pi \times 100 \text{ Hz} = 628 \text{ rad/s} \quad \text{and} \quad \phi_{PM} = 550^\circ .$$

To compensate for the delay effect caused by the D/A and A/D conversion and by the signal transition between the plant and the controller, the phase margin is modified as

$$\phi_{PM}^* = 50^\circ + \Delta\phi = 50^\circ + \frac{\omega_{BW} \times T_s}{2} = 54.5^\circ .$$

Choosing the sampling period of the controller T_s to be 250 μs , the parameters of the PI controller can be calculated as

$$K_p = 0.0169 \quad \text{and} \quad K_i = 7.8213 .$$

The open-loop transfer function of the whole system is then obtained as (2).

$$G_o(s) = \frac{0.506s + 234.4}{0.001s^2 + 0.01s} \quad (2)$$

Stability Analysis

The SRC solver uses the trapezoidal integration method. Therefore, the open-loop transfer function of the whole system can be transformed from s-domain to Z-domain as (3).

$$G_o(z) = \frac{0.506 \frac{2}{T_s} \frac{z-1}{z+1} + 234.4}{0.001 \left(\frac{2}{T_s} \frac{z-1}{z+1} \right)^2 + 0.01 \frac{2}{T_s} \frac{z-1}{z+1}} \quad (3)$$

The main stability issue of this system is related to the delay introduced by the signal processing, A/D and D/A conversion and model integration. With a proper sampling frequency, the system can be approximated as a hybrid system with an internal one-step delay. Based on this estimation, the system characteristic function can be derived as (4).

$$1 + \frac{G_o(Z)}{Z} = 0 \quad (4)$$

The stability analysis gives the root locus of the system with different sampling periods, as shown in Fig. 12. When the time step is greater than 2.1 ms, the system becomes unstable. Because of the system complexity and the hardware limit, the minimum time step that can be achieved while satisfying the real-time constraints is 250 μ s with system configuration shown in TABLE VII. Therefore, the time step is chosen to be 250 μ s in this example.

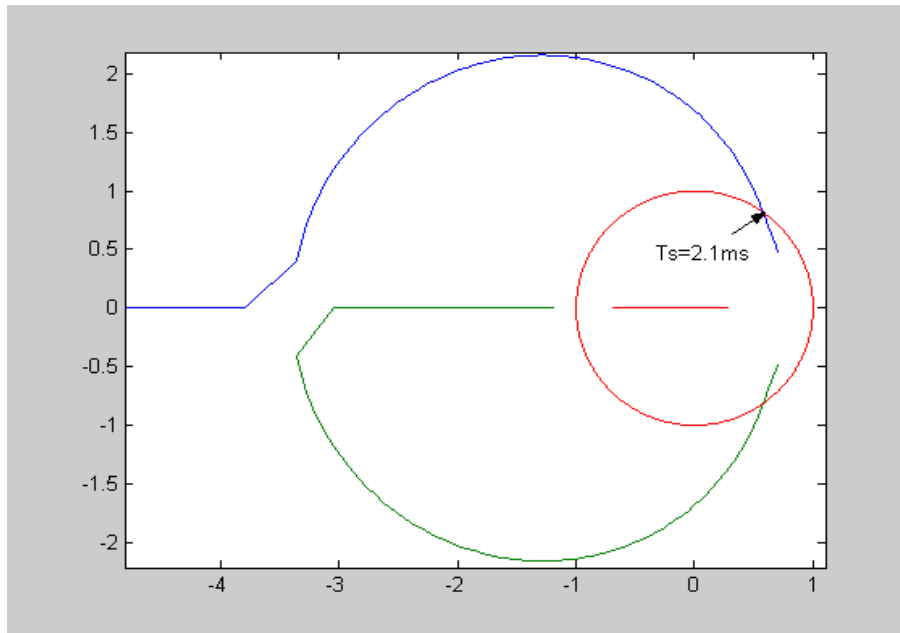


Fig. 12. Root locus of the discrete system with one-time-step delay.

Testing Procedures

Non-real-time simulation in VTB

The entire system is simulated using the VTB as shown in Fig. 13. A delay in the feedback loop is inserted into the close loop simulation, to emulate the effect of the connection between the two separated machines at the distributed simulation stage. Two output current reference signals at frequency of 10 Hz are applied separately, a square wave and a sinusoidal, with amplitudes 1.5 amps and 2.5 amps respectively. Fig. 14 shows that the output currents track the current references at a typical second order behavior.

Real-Time distributed simulation

The entire system is then partitioned into two subsystems, a plant model and a controller model, as shown in Fig. 15.

The two subsystems are exported into two separate VTB-RT computers. These computers are two identical National Instruments VXI-872Bpc controllers (system configurations in TABLE VII). The two simulation processes communicate through a direct analog connection between the DAQ devices embedded in each VXI controller, as shown in

Fig. 16.

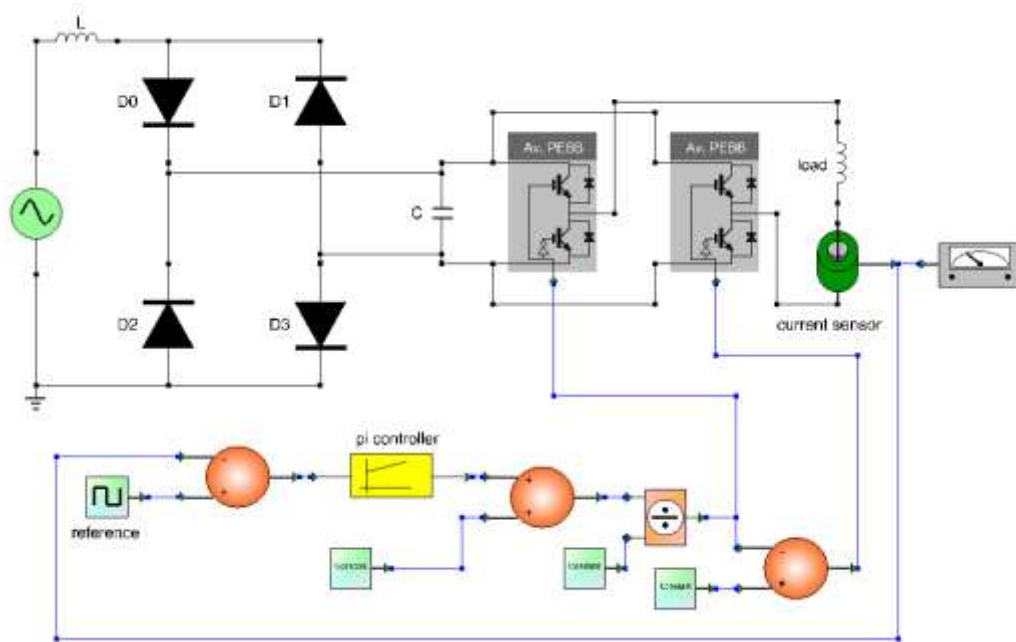


Fig. 13. Schematic of the H-Bridge inverter control system in VTB.

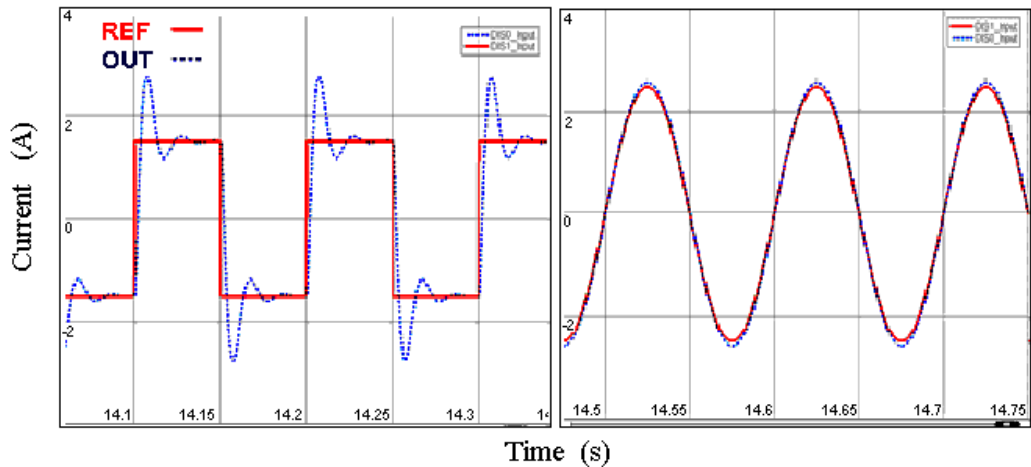


Fig. 14. Output currents and current references of the closed-loop system in VTB (non-real-time simulation case).

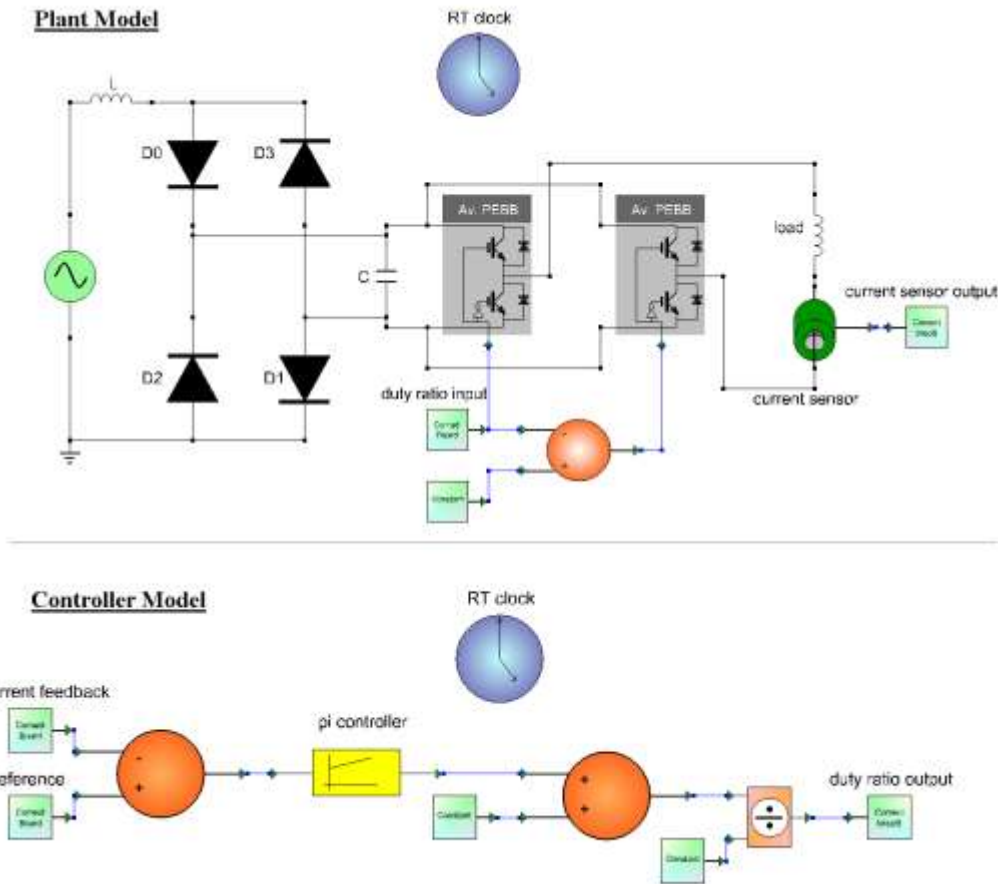


Fig. 15. The subsystem models of plant and controller in VTB (exported into two separate VTB-RT host computers).

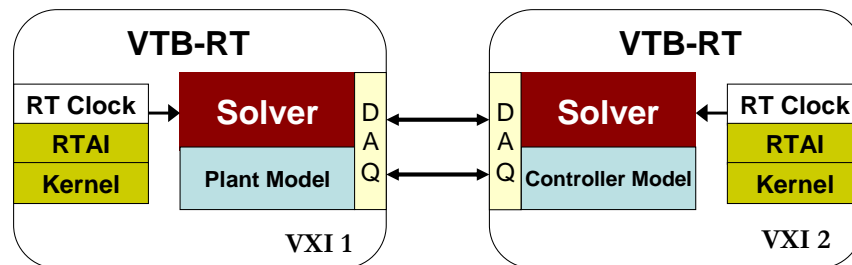


Fig. 16. The architecture of VTB-RT real-time distributed simulation.

The results of the real-time distributed simulation are shown in Fig. 17. The agreement between Fig. 14 and Fig. 17 validates that a PI controller of an H-bridge inverter is successfully designed by using the VTB-RT real-time distributed simulation. The design of the controller has already been achieved at this stage. Following this, the hard real-time HIL testing can be easily performed by substituting the plant host VTB-RT computer with real inverter hardware.

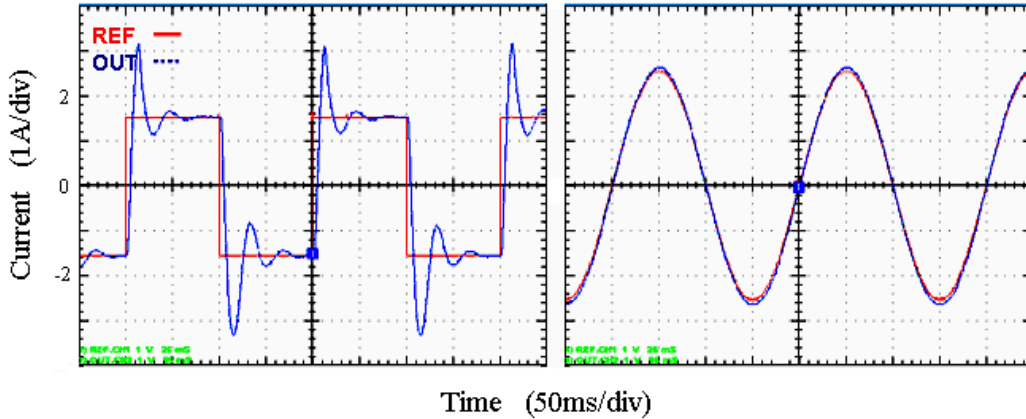


Fig. 17. Output currents and current references of the real-time distributed simulation in VTB-RT (real-time distributed simulation case).

The simulation time step cannot be lower than 250 μs because of the speed limitations of the VTB-RT platform. TABLE VIII shows the distribution of time consumed by the VTB-RT in this example within each simulation time step. In this example, there are components (voltage source, diodes, switches, resistor, and inductor) that are solved using resistive companion modeling (RCM) method and other components (sensors, math functions, and DAQ interface models) using signal extension resistive companion (SRC) method. As shown in TABLE VIII, most of the simulation time is spent in solving and interfacing the SRC models. At this stage, the VTB-RT presents undesirable overhead that counts at least for 30 μs . In addition, 33 μs are used for outputting and logging the simulation results; this time can vary depending on how many variables the user prints in a log file at every time step. Minimizing data logging processes and using the advanced VTB-RT platform listed in TABLE VI, a time step of 100 μs has been achieved for this experiment **Error! Reference source not found.**

TABLE VIII
VTB-RT TIME ANALYSIS IN H-BRIDGE INVERTER CONTROL EXAMPLE

	Time Consumption
Solving system equation	
- RCM	71 μs
- SRC	116 μs
Output and logging	33 μs
Additional overhead	30 μs
Minimum time step	250 μs

Conclusions and Recent Progresses

A multi-solver, hard real-time HIL simulation environment, the VTB-RT, is introduced. Using this platform, a complete design and testing procedure for power electronics controls is proposed. The applicability of the VTB-RT and the proposed testing approach is validated through two application examples.

The proposed real-time HIL testing approach eliminates the need of using costly hardware in the design process, and therefore greatly reduces the overall design cost. However, for a given hardware platform, the minimum time resolution is limited and only a limited bandwidth of the system under test can be used. Consequently, in the actually design stage, special attention must be paid to compromise between the VTB-RT platform cost and the bandwidth of the system under test.

The most attractive feature of the VTB-RT is that it is very low cost, yet is capable of yielding comparable performance as the expensive commercial real-time simulation software. As shown in the first example, hard real-time could be realized without advanced hardware. But certainly, the minimum real-time step that can be achieved depends on the hardware configuration of the VTB-RT platform (i.e., the speed of the processor, the sampling frequency of the DAQ devices, etc.), as well as the complexity of the system under test.

In the first example, the VTB-RT platform is based on a standard PC with an Intel PIII 800 MHz CPU and 128M SDRAM, and the minimum step that can be achieved to simulate the boost converter control system in hard real-time is 300 μ s. In the second example, the VTB-RT platform is based on a National Instruments VXI-872Bpc controller with an Intel PIII 1.266 GHz CPU and 128M SDRAM, and the minimum time step is reduced to 250 μ s for an even more complex H-bridge inverter control system. The time resolution of the VTB-RT can be improved by using faster processors and DAQ devices. If more advanced hardware is used, the minimum step can be further reduced to 50 μ s and 100 μ s respectively for the same experiments. These resolutions are good enough to simulate the dynamic behavior of most power electronics control systems and are comparable with the commercial real-time systems. Additionally, a high-speed device, such a field programmable gate array (FPGA), connected to the VTB-RT platform can improve the performance of the overall simulation process, providing means to accurately acquire and generate high frequency signals **Error! Reference source not found.**

Signal extension resistive companion (SRC) solver used by the VTB-RT enables the natural coupling between the simulation environment and the hardware under test, and thus enables the power-hardware-in-the-loop (PHIL) testing, where virtual power exchange between the simulation environment and the hardware under test is possible. The theoretical framework and experimental results of the PHIL testing using VTB-RT are reported in **Error! Reference source not found.** The most recent research advances in the VTB-RT has accessfully extended VTB-RT and the proposed HIL testing approach to more complex systems, such as three phase systems and motor drive systems **Error! Reference source not found.** These applications usually include witched circuit that requires high and variable frequency switching gating signals, for example, fast switching PWM signals and encoder signals. This poses a major challenge to the simulation platform due to the high time resolution required. A FPGA-based signal conditioning hardware interface has been recently adopted in VTB-RT as the I/O interface to the hardware under test **Error! Reference source not found.** It greatly reduces the computational burden of the simulation in the acquisition and generation of fast switching signals. These recent advances have greatly extended the design and testing capability of the VTB-RT from mere control system to almost any hardware system.

Automatic Synthesis of Uncertain Models

Representaiton of uncertainty, when applied to circuit simulation, can be a powerful tool for producing and designing robust systems. Various methods have been proposed which can be used to quantify and propagate uncertainty. There are interesting examples of research in which Artificial Intelligence techniques are applied to provide a simplified or qualitative definition of the physics of systems when uncertainty is involved. Reviews of this topic can be found in [^{xxviii}, ^{xix}, ^{xx}, ^{xxi}, ^{xxii}, ^{xxiii}]. Similar issues have been considered in the electrical engineering field to overcome specific design problems caused by uncertainty [^{xxiv}, ^{xxv}]. The numerical evaluation of the effects of uncertainty is traditionally achieved by using the Monte Carlo method, which is widely accepted as an “exact method” for determining uncertainty [^{xxvi}]. The Monte Carlo method can give the entire probability density function (PDF) of any system variable through reiterations of the system simulation. Another method used for the evaluation of uncertainty is “true worst-case circuit tolerance” analysis, which gives only the results concerning the upper and lower statistical bounds of the circuit response to uncertainty ([^{xxvii}]). The polynomial chaos approach to the evaluation of uncertainty also yields the full PDF of the system’s variables using only one execution of the simulation. A method to automate the process of generating a circuit’s polynomial chaos representation for use in simulation is presented in the paper.

It has been common practice in engineering to analyze systems based on deterministic mathematical models with precisely defined input data. However, since such ideal situations are rarely encountered in practice, the need to address uncertainties is now clearly recognized and there has been a

growing interest in the application of probabilistic and other methods. Among the existing methods for uncertainty analysis, Ghanem & Spanos pioneered a polynomial chaos expansion method ([^{xxviii}, ^{xxix}]). This method is based on the homogeneous chaos theory of Wiener [^{xxx}], which uses a spectral expansion of random variables. The use of the term chaos in this context represents uncertainty and should not be confused with the chaos theory used frequently in theoretical physics. The homogeneous chaos expansion employs Hermite orthogonal polynomials in terms of Gaussian random variables. Cameron & Martin have proved that this expansion converges to any L_2 functional in random space in the L_2 sense [^{xxx}]. Combined with Karhunen-Loeve decomposition [^{xxxii}] of the inputs, polynomial chaos results in computationally tractable algorithms for large engineering systems. Recently, a more general framework, called generalized polynomial chaos or Askey chaos, has been proposed [^{xxxiii}]. This expansion technique utilizes more orthogonal polynomials from the Askey scheme than the original homogeneous chaos theory [^{xxxiv}] and is can represent general non-Gaussian processes. Applications to ODE, PDE, Navier-Stokes equations and flow-structure interactions have been reported and convergence has been demonstrated for model problems [^{xxxv}, ^{xxxvi}]. In recent years, polynomial chaos has been applied to measurement uncertainty [^{xxxvii}][^{xxxviii}], entropy multivariate analysis [^{xxxix}], control design [^{xl}][^{xli}][^{xlii}], design of a Two-Planar Manipulator [^{xliii}] and polynomial chaos based observers for use in control theory [^{xliv}]. Reference [^{xlvi}] presents an overview of applications of Polynomial Chaos Theory to Electrical Engineering. Among other possible applications, circuit simulation by means of Polynomial Chaos Expansion is introduced. In that paper though the problem is solved for a specific topology without providing a generalized algorithm for the solution starting from a SPICE-like netlist and information about the uncertainty of some parameters The major contribution of this present work is in effect the formalization of the automatic solution process while using resistive companion method ([^{xlvi}]). In particular, a systematic algorithm to automatically define the conductance matrix of an uncertain system is presented. This theory yields the definition of a new approach to Nodal Analysis where the topology of a network is mapped to a multilayer topology where each layer represents one level of polynomial expansion. This approach helps to pave the way for a new generation of uncertainty based CAD tools.

Table IX
Variable Definitions

ξ	Independent random variable
Θ	Individual random event
n_v	Total number of random variables
n_p	Single variable polynomial order
P	Multi variable polynomial order
Ψ	Denotes a single polynomial term (single or multivariable polynomials)
X	General second order random process
A	Single variable polynomial coefficient
β, y	Multi variable polynomial coefficient
H_n	Hermite polynomial
He_n	Rescaled Hermite polynomial
$w(\cdot)$	Weighting function
Ω	Region of space (polynomial basis dependent)
I	Electrical current
G	Electrical conductance
V, v	Electrical voltage
B	History source (same units as current)

H	Time step
T	Current simulation time
C	Capacitance
R	Resistance

Polynomial Chaos

N. Wiener first introduced polynomial chaos theory in the form of Homogeneous Chaos Expansion in 1938 [13]. This expansion uses a rescaled version of the Hermite polynomials, which correspond to a Gaussian or Normal distribution when used in combination with Gaussian random variables. This expansion technique is based on independent random variables ξ_i , which are associated with an individual random event θ . Every uncertain parameter or variable in the examined system is represented by a random variable ξ_i . The total number of random variables is denoted by the symbol n_v . Each random variable is represented by a single variable polynomial expression in terms of ξ_i . While in principle each decomposition comprises an infinite number of terms, for practical purposes the polynomial order for each single variable polynomial is limited to a finite number of terms denoted by the symbol n_p . When the examined system contains multiple uncertain parameters, a single variable polynomial basis is no longer sufficient to represent the uncertainty of the system. The single variable polynomial contributions from each uncertain variable in the system, are combined into a multivariable polynomial that comprises all of the uncertainty in the system. Equation (2.1) represents the order of the resulting multi-variable polynomial as a function of n_v and n_p .

$$P = \binom{n_v + n_p}{n_v! n_p!} - 1 \quad (2.1)$$

The variables n_p and P are both indexed starting at zero, representing the first polynomial order.

Every variable in the examined system must be expanded along the entire multi-variable polynomial basis. The individual polynomial terms of the basis will be denoted by the symbol Ψ . Equation (2.2) represents a variable $Y(t)$ that is being expanded along the multi-variable polynomial basis.

$$Y(t) = \sum_{i=0}^P y_i(t) \Psi_i \quad (2.2)$$

The multi-variable polynomial basis mathematically describes a general second-order random process $X(\theta)$ by (2.3) ([xxxiii]).

$$X(\theta) = a_0 \Psi_0 + \sum_{i_1=1}^{\infty} a_{i_1} \Psi_1(\xi_{i_1}(\theta)) + \sum_{i_1=1}^{\infty} \sum_{i_2=1}^{i_1} a_{i_1 i_2} \Psi_2(\xi_{i_1}(\theta), \xi_{i_2}(\theta)) + \sum_{i_1=1}^{\infty} \sum_{i_2=1}^{i_1} \sum_{i_3=1}^{i_2} a_{i_1 i_2 i_3} \Psi_3(\xi_{i_1}(\theta), \xi_{i_2}(\theta), \xi_{i_3}(\theta)) \dots \quad (2.3)$$

Notice that there is no limit on the number of terms in (2.3). This equations represents the case in which $P \rightarrow \infty$. The number of terms resulting from the summations in (2.3) ultimately equals P . For simplification purposes (2.3) can be rewritten as in (2.4).

$$X(\theta) = \sum_{i=0}^P \beta_i \Psi_i(\xi(\theta)) \quad (2.4)$$

The indexing of the variable Ψ in (2.4) and (2.2) is different than in (2.3) on one hand place because (2.4) represents a truncated decomposition, and in second place because in (2.4) each index i refers to a set of polynomial terms of the decomposition. Once the values of n_v and n_p have been chosen, the summations from (2.3) are expanded and Ψ variables are re-indexed according to their new positions. The re-indexing is a result of the process of transforming single variable polynomials to multi-variable polynomials. The expansion performed on (2.2) is the act of projecting $Y(t)$ onto this multi-variable polynomial basis.

Wiener's original Homogeneous Chaos used a rescaled version of the Hermite polynomials. The Rodriguez formula for the Hermite polynomials is (2.5).

$$H_n(x) = (-1)^n e^{x^2} \frac{d^n}{dx^n} (e^{-x^2}) \quad (2.5)$$

Rescaling of these polynomials with a factor of the square root of two is required to achieve the popular polynomials He_n associated with probability theory and the Gaussian distribution. The rescaling and resulting Rodriguez formulae are (2.6) and (2.7).

$$He_n(x) = H_n\left(\frac{x}{\sqrt{2}}\right) \quad (2.6)$$

$$He_n(x) = (-1)^n e^{\frac{1}{2}x^2} \frac{d^n}{dx^n} (e^{-\frac{1}{2}x^2}) \quad (2.7)$$

The first three single variable polynomials are shown in Table X.

Table X
Rescaled Hermite Polynomials

$He_n(x)$	
$He_0(x)$	1
$He_1(x)$	x
$He_2(x)$	$x^2 - 1$

The multi-variable representation of these polynomials is shown in (2.8).

$$X(\theta) = a_0 He_0 + \sum_{i_1=1}^{\infty} a_{i_1} He_1(\xi_{i_1}(\theta)) + \sum_{i_1=1}^{\infty} \sum_{i_2=1}^{i_1} a_{i_1 i_2} He_2(\xi_{i_1}(\theta), \xi_{i_2}(\theta)) + \sum_{i_1=1}^{\infty} \sum_{i_2=1}^{i_1} \sum_{i_3=1}^{i_2} a_{i_1 i_2 i_3} He_3(\xi_{i_1}(\theta), \xi_{i_2}(\theta), \xi_{i_3}(\theta)) \dots \quad (2.8)$$

The following table demonstrates the meaning behind the multivariable polynomial notation.

Table XI
Multivariable Polynomial Notation

Multivariable Notation	Polynomial Realization
$He_2(x, y)$	$He_1(x)He_1(y)$
$He_2(x, x)$	$He_2(x)$
$He_3(x, x, y)$	$He_2(x)He_1(y)$

An example using the expansion in (2.2) with two random variables and a polynomial order of 2 results in the following equation.

$$\begin{aligned}
 Y(t, \theta) = & y_0(t) + y_1(t)\xi_1(\theta) + y_2(t)\xi_2(\theta) + y_3(t)(\xi_1^2(\theta) - 1) \\
 & + y_4(t)\xi_1(\theta)\xi_2(\theta) + y_5(t)(\xi_2^2(\theta) - 1)
 \end{aligned} \tag{2.9}$$

Polynomial chaos theory is not limited to the Hermite polynomials. Generalized polynomial chaos (otherwise known as Wiener-Askey Polynomial Chaos) expanded the theory to use all the polynomials from the Askey scheme of orthogonal polynomials. The polynomials of interest in this paper are the Hermite, Legendre, and Laguerre polynomials. These specific polynomials are chosen because they represent the most common physically realizable distributions of uncertainty. Hermite polynomials are associated with the Gaussian distribution, Legendre polynomials are associated with the uniform distribution, and Laguerre polynomials are associated with the exponential distribution ([xxxiii]). The use of Hermite, Legendre, and Laguerre polynomials will from now on be referred to as Hermite-Chaos, Legendre-Chaos, and Laguerre-Chaos respectively.

When all of the variables in the examined system have been expanded onto the basis of choice, a Galerkin projection onto the basis is applied. The Galerkin projection is realized by the integration of each component of the examined system with the polynomial basis. The projection takes the form of an integral because the chosen polynomial bases are all continuous. The limits of the integral correspond to the region where the chosen polynomials are valid. The limits for Hermite-Chaos, Legendre-Chaos, and Laguerre-Chaos are $-\infty$ to ∞ , -1 to 1 , and 0 to ∞ respectively. This region is represented by the symbol Ω . An example of this process appears in section III part B and many examples in [xxxiii,xxxv,xxxvi]. The Galerkin projection results in inner products of the polynomials. Equation (2.10) is an example of an inner product for a polynomial basis.

$$\langle \Psi_i \Psi_j \Psi_k \rangle = \int_{\Omega} \Psi_i \Psi_j \Psi_k w(\xi) d\xi \tag{2.10}$$

A polynomial basis dependent weighting function which is a function of the number of uncertain variables is included in each inner product. The weighting function for the rescaled Hermite polynomials is given by (2.11).

$$w(\xi) = \left(\frac{1}{\sqrt{2\pi}^{\bar{n}_v}} \right) e^{-\frac{1}{2}\xi^T \xi} \tag{2.11}$$

An example of an inner product of three Hermite polynomials and this weighting function is located in (2.12).

$$\langle He_1(\xi_1) He_1(\xi_2) He_2(\xi_2, \xi_1) \rangle = \int_{-\infty}^{\infty} \int_{-\infty}^{\infty} \xi_1 \xi_2 \xi_2 \xi_1 \left(\frac{1}{\sqrt{2\pi}^2} e^{-\frac{1}{2}(\xi_1^2 + \xi_2^2)} \right) d\xi_1 d\xi_2 \tag{2.12}$$

The inner products must be separately calculated for each polynomial basis. Since the polynomial bases are orthogonal, the majority of the inner products result in zero. The number of inner products required increases according to (2.13).

$$\#inner_products = (\#polynomials_in_inner_product)^P \quad (2.13)$$

Calculating (2.13) with three polynomial inner products with two uncertain variables expanded by second order polynomial chaos results in the needed calculation of 1000 inner products. The inner products are dependent solely on the multi-variable polynomial basis. This dependency allows for the inner products to be calculated only once during a simulation. The calculation of the inner products of the polynomial terms can be automated for simulation purposes when the fundamental polynomial basis and its weighting function are known. The polynomial basis itself can be automatically generated with the knowledge of variables n_p , n_v and the Rodriguez formulae for the fundamental polynomial basis.

It should be clarified though that when the number of uncertainties grows significantly the Galerkin method here proposed may not be the most efficient approach. When the number of uncertainties grows significantly the Galerkin projection is usually substituted by the collocation approach [xlvi][xlviii]. A comprehensive comparison between Galerkin approach and collocation method can be found in [xlix].

In this paper, polynomial chaos is used to expand a commonly used circuit analysis modeling method called resistive companion. Section III introduces the resistive companion modeling method and its polynomial chaos expansion. The expansion of the resistive companion modeling method allows for a general and automated approach to the simulation of circuits and systems containing uncertainty.

Extended Resistive Companion Method

Resistive Companion Modeling Method

The resistive companion modeling method is based on equations resulting from nodal analysis. This method is commonly used in the computer simulation of dynamic systems. This modeling method is a general format for models that can easily automate the model creation process to achieve a system solution. Individual model equations are represented in a specific form called the resistive companion equation. All models must be represented in this format in order to combine them into a system representation. The resistive companion equation is shown in (3.1).

$$I(t) = G(h) * V(t) - B(t-h) \quad (3.1)$$

Equation (3.1) relates the current ($I(t)$) of a model (or more in general its *through variables*) to its voltage ($V(t)$) (or more in general its *across variables*) using the model's conductance ($G(h)$) and equivalent current source representation ($B(t-h)$). The time step of the simulation is denoted by the variable h . Equation (3.1) can be realized through the use of an equivalent circuit. The equivalent circuit representation is shown in Fig. 18.

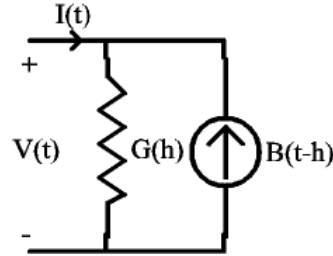


Fig. 18. Equivalent circuit representation of the resistive companion equation.

All resistive companion models are represented in this fashion. The equivalent circuit parameters are modified at each time step of the simulation according to the time relation defined by (3.1).

To exemplify this technique the defining equations of a capacitor will be manipulated into the form of (3.1). The defining voltage to current relationship for a simple linear capacitor is shown in (3.2) and rearranged in (3.3).

$$I = C \frac{dv}{dt} \quad (3.2)$$

$$\frac{dv}{dt} = \frac{I}{C} \quad (3.3)$$

Applying the trapezoidal rule to (3.3) results in (3.4).

$$v(t) = v(t-h) + \frac{h}{2} \left(\frac{I(t)}{C} + \frac{I(t-h)}{C} \right) \quad (3.4)$$

Rearranging (3.4) into the form of (3.1) results in (3.5).

$$I(t) = \frac{2C}{h} v(t) - \frac{2C}{h} v(t-h) - I(t-h) \quad (3.5)$$

Equating (3.1) to (3.5) results in the equivalent terms $G(h)$ and $B(t-h)$ for the capacitor that is represented by (3.6) and (3.7).

$$G(h) = \frac{2C}{h} \quad (3.6)$$

$$B(t-h) = \frac{2C}{h} v(t-h) + I(t-h) \quad (3.7)$$

The capacitor is now in a form where it can be combined with other models represented in the same format. The system representation is created using the node numbers from nodal analysis to combine the individual resistive companion representations of the models ([xlvi, **Error! Bookmark not defined.**]). Once all the models are combined into the system matrix form of the resistive companion equation, the Kirchhoff Current Law is applied. The resulting solvable equation is located in (3.8).

$$V(t) = G(h)^{-1} B(t-h) \quad (3.8)$$

Equation (3.8) is solved for $V(t)$ and then the corresponding voltages are placed into the model and a new resistive companion representation is retrieved. The cycle continues until the simulation is complete ([xlvi]).

Polynomial Chaos Expanded Resistive Companion Equation

The introduction of uncertainty into circuit analysis is achieved through the application of the polynomial chaos expansion to the resistive companion equation. Each variable in (3.1) is expanded onto the polynomial basis as in (2.2). Equations (3.9)-(3.12) show the expansion onto the basis.

$$I(t) = \sum_{i=0}^P I_i(t) \Psi_i \quad (3.9)$$

$$V(t) = \sum_{i=0}^P V_i(t) \Psi_i \quad (3.10)$$

$$G(h) = \sum_{i=0}^P G_i(h) \Psi_i \quad (3.11)$$

$$B(t-h) = \sum_{i=0}^P B_i(t-h) \Psi_i \quad (3.12)$$

Replacing these variables into (3.1) yields the expanded resistive companion equation shown in (3.13).

$$\sum_{i=0}^P I_i(t) \Psi_i = \sum_{i=0}^P \sum_{j=0}^P G_i(h) V_j(t) \Psi_i \Psi_j - \sum_{i=0}^P B_i(t-h) \Psi_i \quad (3.13)$$

The process of applying the Galerkin projection onto the polynomial chaos basis results in (3.14).

$$\begin{aligned} \sum_{i=0}^P \int_{\Omega} I_i(t) \Psi_i \Psi_l w(\xi) d\xi = \\ \sum_{i=0}^P \sum_{j=0}^P \int_{\Omega} G_i(h) V_j(t) \Psi_i \Psi_j \Psi_l w(\xi) d\xi - \sum_{i=0}^P \int_{\Omega} B_i(t-h) \Psi_i \Psi_l w(\xi) d\xi \end{aligned} \quad (3.14)$$

The following identities from (3.15) and (3.16) are used to replace the integrals in (3.14) with inner products.

$$\int_{\Omega} \Psi_i \Psi_l w(\xi) d\xi = \langle \Psi_i \Psi_l \rangle \quad (3.15)$$

$$\int_{\Omega} \Psi_i \Psi_j \Psi_l w(\xi) d\xi = \langle \Psi_i \Psi_j \Psi_l \rangle \quad (3.16)$$

These relationships are then applied to the individual terms of (3.14) resulting in (3.17a-c).

$$\int_{\Omega} I_i(t) \Psi_i \Psi_l w(\xi) d\xi = I_i(t) \int_{\Omega} \Psi_i \Psi_l w(\xi) d\xi = I_i(t) \langle \Psi_i \Psi_l \rangle \quad (3.17a)$$

$$\begin{aligned} \int_{\Omega} G_i(h) V_j(t) \Psi_i \Psi_j \Psi_l w(\xi) d\xi = G_i(h) V_j(t) \int_{\Omega} \Psi_i \Psi_j \Psi_l w(\xi) d\xi \\ = G_i(h) V_j(t) \langle \Psi_i \Psi_j \Psi_l \rangle \end{aligned} \quad (3.17b)$$

$$\int_{\Omega} B_i(t-h) \Psi_i \Psi_l w(\xi) d\xi = B_i(t-h) \int_{\Omega} \Psi_i \Psi_l w(\xi) d\xi = B_i(t-h) \langle \Psi_i \Psi_l \rangle \quad (3.17c)$$

The result of replacing the terms from (3.17) back into (3.14) yields (3.18).

$$\sum_{i=0}^P I_i(t) \langle \Psi_i \Psi_l \rangle = \sum_{i=0}^P \sum_{j=0}^P G_i(h) V_j(t) \langle \Psi_i \Psi_j \Psi_l \rangle - \sum_{i=0}^P B_i(t-h) \langle \Psi_i \Psi_l \rangle \quad (3.18)$$

The inner product of two orthogonal polynomials can be replaced by the identity in (3.19).

$$\langle \Psi_i \Psi_l \rangle = \langle \Psi_l^2 \rangle \delta_{il} \quad (3.19)$$

The nature of orthogonal polynomials enforces the relationship in (3.19). Placing (3.19) into (3.18) yields (3.20).

$$\sum_{i=0}^P I_i(t) \langle \Psi_l^2 \rangle \delta_{il} = \sum_{i=0}^P \sum_{j=0}^P G_i(h) V_j(t) \langle \Psi_i \Psi_j \Psi_l \rangle - \sum_{i=0}^P B_i(t-h) \langle \Psi_l^2 \rangle \delta_{il} \quad (3.20)$$

The Kronecker delta eliminates the summations of the I(t) and B(t-h) terms, resulting in (3.21).

$$I_l(t) \langle \Psi_l^2 \rangle = \sum_{i=0}^P \sum_{j=0}^P G_i(h) V_j(t) \langle \Psi_i \Psi_j \Psi_l \rangle - B_l(t-h) \langle \Psi_l^2 \rangle \quad (3.21)$$

Dividing both sides of the equation by $\langle \Psi_l^2 \rangle$ yields (3.22).

$$I_l(t) = \frac{1}{\langle \Psi_l^2 \rangle} \sum_{i=0}^P \sum_{j=0}^P G_i(h) V_j(t) \langle \Psi_i \Psi_j \Psi_l \rangle - B_l(t-h) \frac{\langle \Psi_l^2 \rangle}{\langle \Psi_l^2 \rangle} \quad (3.22)$$

The complete polynomial chaos expansion of the resistive companion equation is shown in (3.23).

$$I_l(t) = \frac{1}{\langle \Psi_l^2 \rangle} \sum_{i=0}^P \sum_{j=0}^P G_i(h) V_j(t) \langle \Psi_i \Psi_j \Psi_l \rangle - B_l(t-h) \quad (3.23)$$

The symbolic derivation can be taken no further due to the necessity of calculating the inner products. In order to calculate the inner products, a polynomial basis must be chosen and the uncertain variables of the system must be determined. The model representation stage in part C addresses these problems.

Model Representation

The capacitor example from section III part A will now be expanded according to the polynomial chaos theory. The capacitance parameter of the capacitor model will be the uncertain element. Every coefficient of the expanded input variables is known for the each term of the polynomial basis. Equation (3.24) is the expanded version of the capacitance.

$$C(\xi) = C_0 \Psi_0 + C_1 \Psi_1 + C_2 \Psi_2 \dots \quad (3.24)$$

All of the values for C are therefore known. Since C will only be associated with one random variable (ξ), thanks to an appropriate choice of the base, the majority of the C terms will be zero.

Consider (3.24) with the Hermite polynomial basis, two uncertain variables, and using, for example second order polynomials. Equation (3.25) represents (3.24) with the parameters described.

$$C(t, \theta) = C_0(t) + C_1(t)\xi_1(\theta) + C_2(t)\xi_2(\theta) + C_3(t)(\xi_1^2(\theta) - 1) + C_4(t)\xi_1(\theta)\xi_2(\theta) + C_5(t)(\xi_2^2(\theta) - 1) \quad (3.25)$$

If the capacitance is associated with only one of the uncertain variables (let us say ξ_1) then the values of C2, C4, and C5 are all zero. In general, it is convenient to associate each uncertain parameter with one random variable. If the probability density of the capacitance is perfectly Gaussian, then there is no need for C3 term, and the corresponding polynomial term is zero. In this case, only the first two terms of the Hermite polynomial basis are needed for a perfect Gaussian distribution representation. If the uncertain parameter has a perfect Gaussian distribution, then all of the C_i terms other than C0 and C1 are equal to zero.

The same decomposition process described for the capacitance, can be applied to the conductance of the resistive companion model and thus to calculate $G(\xi, h)$ from $G(h)$ in (3.6). In fact because the terms 2 and h in (3.6) are constant and their only non-zero Ψ variable is Ψ_0 , which is equal to 1, the resulting $G(\xi, h)$ is (3.26).

$$G(\xi, h) = \frac{2 * C_0}{h} \Psi_0 + \frac{2 * C_1}{h} \Psi_1 + \frac{2 * C_2}{h} \Psi_2 \dots \quad (3.26)$$

The only non-zero C coefficients are C_0 and C_1 , which result in the only non-zero G terms being G_0 and G_1 . The summation of the expanded resistive companion equation in (3.23) can now be reduced to only the non-zero G terms thus yielding (3.27).

$$I_l(t) = \frac{1}{\langle \Psi_l^2 \rangle} \sum_{j=0}^P G_0(h) V_j(t) \langle \Psi_0 \Psi_j \Psi_l \rangle + \frac{1}{\langle \Psi_l^2 \rangle} \sum_{j=0}^P G_1(h) V_j(t) \langle \Psi_1 \Psi_j \Psi_l \rangle - B_l(t - h) \quad (3.27)$$

The polynomial basis must be chosen so that the inner products can be calculated. The Hermite polynomials will be chosen in this example. The non-zero inner product results from using third order polynomial chaos with one uncertain variable are shown in Table IV.

Table XII

Non-zero inner products using Hermite polynomials with G term restriction

$\langle \Psi_0 \Psi_0 \Psi_0 \rangle = 1$	$\langle \Psi_0 \Psi_2 \Psi_2 \rangle = 2$
$\langle \Psi_1 \Psi_1 \Psi_0 \rangle = 1$	$\langle \Psi_1 \Psi_1 \Psi_2 \rangle = 2$
$\langle \Psi_0 \Psi_1 \Psi_1 \rangle = 1$	$\langle \Psi_1 \Psi_2 \Psi_1 \rangle = 2$
$\langle \Psi_1 \Psi_0 \Psi_1 \rangle = 1$	$\langle \Psi_0 \Psi_0 \rangle = 1$
$\langle \Psi_1 \Psi_1 \rangle = 1$	$\langle \Psi_2 \Psi_2 \rangle = 2$

The series of resistive companion equations, through the substitution of the inner products from Table IV into (3.27) results in equations (3.28a-c).

$$I_0(t) = G_0 V_0 + G_1 V_1 - B_0(t - h) \quad (3.28a)$$

$$I_1(t) = \mathbf{G}_1 V_0 + G_0 V_1 + 2G_1 V_2 - B_1(t-h) \quad (3.28b)$$

$$I_2(t) = \mathbf{G}_1 V_1(t) + G_0 V_2(t) - B_2(t-h) \quad (3.28c)$$

Equation (3.28a-c) can be represented by the equivalent circuit representation located in Fig. 19.

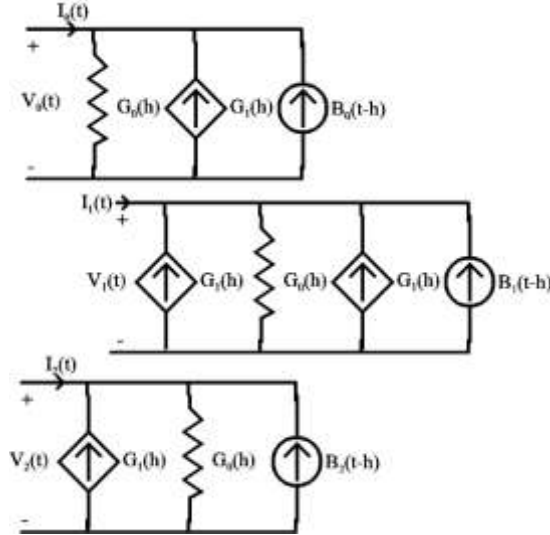


Fig. 19. Equivalent circuit representation of the extended resistive companion equation.

The values of G and B can now be replaced with C and h yielding equation (3.29a-c).

$$I_0(t) = \left(\frac{2C_0}{h} V_0(t) + \frac{2C_1}{h} V_1(t) \right) - \left(\frac{2C_0}{h} V_0(t-h) + \frac{2C_1}{h} V_1(t-h) \right) - I_0(t-h) \quad (3.29a)$$

$$I_1(t) = \left(\frac{2C_1}{h} V_0(t) + \frac{2C_0}{h} V_1(t) + \frac{4C_1}{h} V_2(t) \right) - \left(\frac{2C_1}{h} V_0(t-h) + \frac{2C_0}{h} V_1(t-h) + \frac{4C_1}{h} V_2(t-h) \right) - I_1(t-h) \quad (3.29b)$$

$$I_2(t) = \left(\frac{2C_1}{h} V_1(t) + \frac{2C_0}{h} V_2(t) \right) - \left(\frac{2C_1}{h} V_1(t-h) + \frac{2C_0}{h} V_2(t-h) \right) - I_2(t-h) \quad (3.29c)$$

Equation (3.30) shows the matrix form of equation (3.29a-c).

$$\begin{bmatrix} I_0(t) \\ I_1(t) \\ I_2(t) \end{bmatrix} = \begin{bmatrix} \frac{2C_0}{h} & \frac{2C_1}{h} & 0 \\ \frac{2C_1}{h} & \frac{2C_0}{h} & \frac{4C_1}{h} \\ 0 & \frac{2C_1}{h} & \frac{2C_0}{h} \end{bmatrix} * \begin{bmatrix} V_0(t) \\ V_1(t) \\ V_2(t) \end{bmatrix} - \begin{bmatrix} \frac{2C_0}{h} & \frac{2C_1}{h} & 0 \\ \frac{2C_1}{h} & \frac{2C_0}{h} & \frac{4C_1}{h} \\ 0 & \frac{2C_1}{h} & \frac{2C_0}{h} \end{bmatrix} * \begin{bmatrix} V_0(t-h) \\ V_1(t-h) \\ V_2(t-h) \end{bmatrix} - \begin{bmatrix} I_0(t-h) \\ I_1(t-h) \\ I_2(t-h) \end{bmatrix} \quad (3.30)$$

The extended resistive companion equation representation of each model is then combined into a system representation through the use of nodal analysis. The resulting system equations can then be solved using (3.8). Equation (3.8) is identical to the solution of a network where all of the components are replaced by their equivalent circuit representations from Fig. 19. The number of equations to be solved at each time step is the product of P by the size of original resistive companion representation.

Even with this increased number of equations, there is a considerable computational speed improvement over the Monte Carlo method for this system. The improvement in simulation speed is dependent on the length of the simulation, the number of components used, and the size of P.

An interesting symmetry appears in every model using this technique. The zero index of the uncertain parameter always falls on the diagonal of the G matrix. If there were no uncertainties in this model, its conductance matrix would be purely diagonal. The models, whether they are certain or uncertain, have a diagonal entry associated with each term of the polynomial basis. If the system being expanded has only one uncertain model, with only one uncertain parameter (the capacitance of a capacitor), then (3.30) is valid representation of the model of the capacitor. All models within this system, would have conductance matrices of this same size, and this is true in general, that is in any system model matrices will have the same size as the uncertain model. With reference to the example of the system with the uncertain capacitor, since all the other models in the system are certain, then their G matrices will be strictly diagonal. Models can automatically generate their matrix representation based on P and on which is their uncertain parameter. Each model have access to the non-zero inner product coefficients, so that it can build up the matrix representation corresponding to its uncertainty. The capacitor example is very basic. When deriving the equations for a resistor or inductor, the G matrix must first be inverted before the equations can be placed into resistive companion form. This is due to the fact that the Galerkin projection is conveniently performed if Ψ is at the numerator. This restriction enables the projection integrals to be pre-calculated, which greatly simplifies the process of automating the model generation and the network solution. This restriction, for example, requires that the Galerkin projection is applied to the equations of a linear resistor in the form in (3.32).

$$\sum_{j=0}^P \sum_{i=0}^P R_j(h) I_i(t) \langle \Psi_i \Psi_j \Psi_l \rangle = \sum_{j=0}^P V_j(t) \langle \Psi_i \Psi_l \rangle \quad (3.32)$$

Equation (3.32), represents the expansion post the Galerkin projection and the inner products are in one of the pre-calculated forms. Limiting the inner product calculations to the polynomials in their standard forms, is much easier than having to calculate additional integrals containing inverses of the polynomial terms. It is much easier to automate the expansion of the equation in the form of (3.32) because it contains only the inner products of the original polynomials. Once the equations are in matrix form the R matrix can be inverted and brought to the right side of the equation placing it in resistive companion form. Models that are certain are not as difficult to treat, because their conductance matrix is diagonal and the inverse is much easier to calculate requiring minimal additional effort.

The analysis of the output data is achieved by the reconstruction of (2.3). The coefficients of each term are the result of the solution of the extended resistive companion equation. The resulting voltage coefficients from the system representation can be used to construct the PDF using equation (3.32).

$$\begin{aligned} V(t, \theta) = & V_0(t) + V_1(t) \xi_1(\theta) + V_2(t) \xi_2(\theta) + V_3(t) (\xi_1^2(\theta) - 1) \\ & + V_4(t) \xi_1(\theta) \xi_2(\theta) + V_5(t) (\xi_2^2(\theta) - 1) \end{aligned} \quad (3.32)$$

Equation (3.33) represents a system with two uncertain variables and a Hermite polynomial order of two. Placing the corresponding voltage values into (3.33), along with random variables from the distribution corresponding to the polynomial basis used, results in an individual voltage value. This process is then repeated with numerous random values to recreate the PDF. The resulting voltage values are then plotted using a histogram. The histogram is the PDF of the voltage. The more random points

that are replaced into equation (3.33), the higher the resolution of the output PDF becomes. All of the ξ variables must be uncorrelated random variables. The PDF can be reconstructed at any time instant and the only values to be stored in memory are the coefficients of the voltage polynomial. This is a highly desirable side effect of the proposed method that allows the storage of the full PDF through a minimal number of terms and therefore minimal memory occupancy.

The Automation of Network Theory with Polynomial Chaos

The mathematical relationships in the previous sections can be automated for use in CAD simulators using the modeling method derived in (3.23). This resistive companion equation expanded via polynomial chaos is used in section III part C to synthesize an uncertain representation of a linear capacitor. Models derived using this method can be combined together into a system representation of the polynomial chaos expanded resistive companion equation. The resulting system equations can then be solved in time domain yielding the full probability density function of all of the system variables at each time step. This automation process is made possible definition and implementation of utilities and processes to make the uncertainty equations manageable. This section will cover in detail the processes and methods required to make this automation possible.

The first step in the automation process requires input from the application user. The user must first build a network out of the predefined components. This process corresponds to the creation of a graphical schematic in PSPICE or SABER or to the creation of a net list without graphical means. It is in fact only the models that compose the system and their interconnectivity that matters. The user's next responsibility is to set the parameters of each model, knowing that some of these models may represent uncertain components. For example some of the parameters of the system be resistances or capacitances with related tolerances. The coefficients of (3.25) are an example of possible parameters that can be made available for an uncertain model. The user must then select the standard simulation parameters such as time step and simulation length. Polynomial Chaos simulation also requires specific parameters such as the single variable polynomial order, the number of random variables used to create PDFs and the chosen polynomial basis (Hermite, Laguerre, or Legendre). The process of simulating an uncertain network begins with the stages shown in Fig. 20.

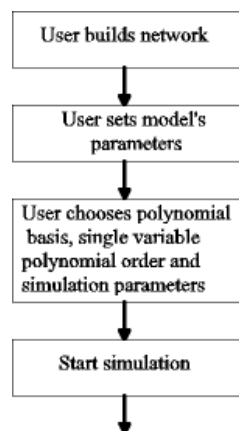


Fig. 20. Pre-simulation operations

Another required parameter for the simulation is the number of uncertainties present within the network. This number corresponds to the number of uncertain models present in the network. The

number of uncertainties together with the order of the single variable polynomial allow the calculation of the multivariable polynomial order using (2.1). The single variable polynomial basis can be constructed automatically by utilizing the Rodriguez formula for the chosen basis. The single variable polynomial terms can then be combined together to form the multivariable polynomial using (2.3). The requested number of random variables for the chosen basis can also be predetermined at this stage so as not to slow down the simulation during the main execution loop. The random variables are used to reconstruct the PDFs of the system variables such as in (3.32). The process of simulating the uncertain network is shown in Fig. 21.

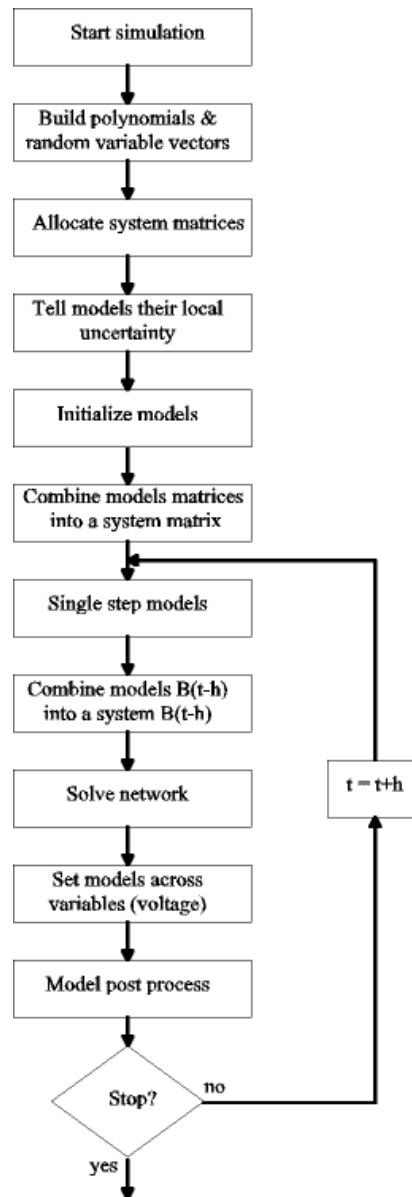


Fig. 21. Uncertain model simulation process

The system and individual model matrices can now be allocated. The size of the system matrix is the size of the equivalent system without uncertainty multiplied by the multivariable polynomial order. The size of each individual model matrix is dependent on the number of nodes attached to and

within the model multiplied by the multivariable polynomial order. All of the model matrices are combined together using the system interconnectivity to form the system matrix. This process will be described in further detail further on.

The next step is to communicate to each model which terms of the multivariable polynomial basis correspond to its own uncertain variables. This information is needed to facilitate the calculation of the matrix equations. The models can then enter the initialization stage where they can calculate their own conductance matrices. This process is shown in detail within Fig. 22.

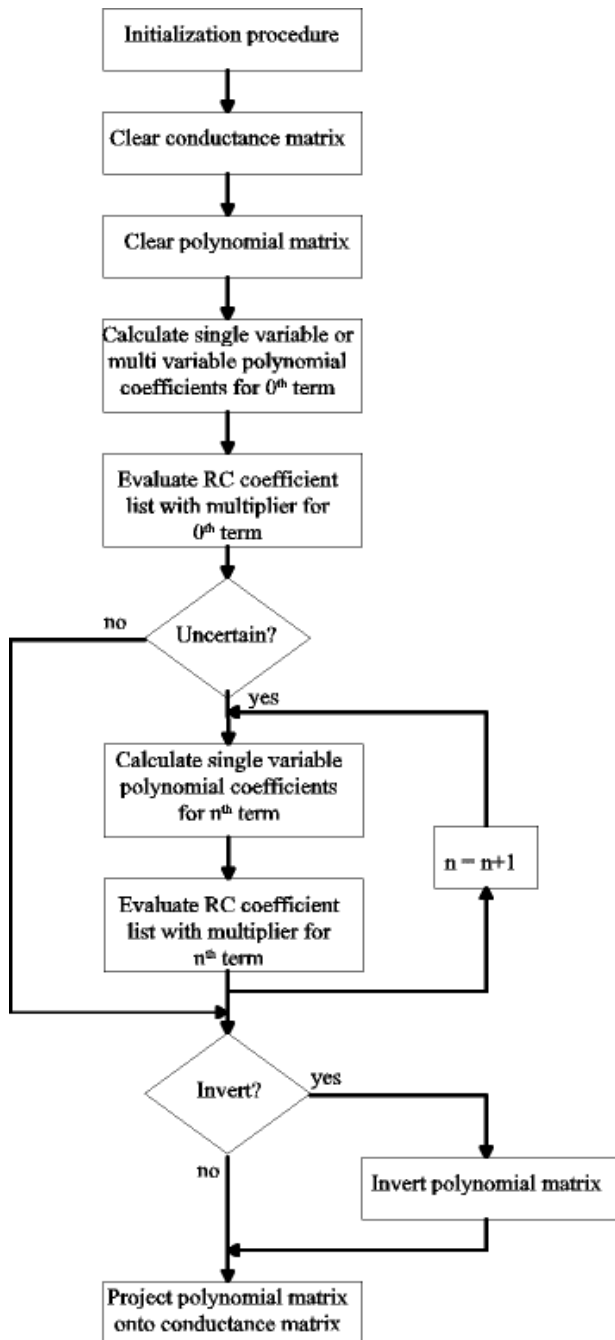


Fig. 22. Uncertain model initialization procedures

Linear, time invariant models are only required to calculate their conductance matrices once during a simulation run. This simplification only applies if the matrix elements are constant during the simulation run. For example, the capacitor example from section III part C meets these requirements. The first step in this process is the clearing of the conductance and polynomial matrices. The polynomial matrix is an intermediate step used to simplify the process of creating the model specific conductance matrix. The polynomial matrix is allocated to the size of the multivariable polynomial order. Clearing out these matrices allows for the building of the polynomial and conductance matrices incrementally for each conductance value.

The model specific polynomial matrix is represented by (4.1) which is an excerpt from (3.23). The index l represents a term from the multivariable polynomial basis and corresponds to the current of the model. This index forms the row indexing of the polynomial matrix. The column index is denoted by j and represents the voltage term that the polynomial matrix is multiplied by. The i index from (4.1) represents the conductance term G such as in (3.26).

$$\frac{1}{\langle \Psi_l^2 \rangle} \sum_{i=0}^P \sum_{j=0}^P G_i(h) \quad (4.1)$$

Each G term's contribution to the polynomial matrix can be calculated using a two step process. This process begins by calculating the non-zero coefficients corresponding to a given i, j and l index combination with a fixed i index. This process entails the calculation of the inner products for these index combinations such as in (2.12). The next step is multiplying the resulting coefficients by the G variable and adding the result to the correct cells in the polynomial matrix. The l and j indices determine the location within the polynomial matrix while the i term represents the conductance value used to multiply with the inner product's resulting coefficient. This process can be repeated for all of the non-zero G terms of the model. Models that contain no tolerances only need to go through this process one time for the G_0 term. This process for both certain and uncertain models is shown in Fig. 22.

Once the polynomial matrix has been created, it may have to be inverted depending on the mathematics of the model involved. Resistors and inductors are examples of models whose characteristic equations require an inversion of the polynomial matrix. Depending on which variables of the model are user inputs, the Galerkin projection may be conveniently applied before the equations of the model are put in resistive companion form. An example of this condition is found in (3.32). Matrix inversion is required to put these models into the expanded resistive companion form. The polynomial matrix can then be projected onto the model's conductance matrix.

The polynomial matrix does not contain any port or node relationships as opposed to the model's conductance matrix and the system matrix. Each component of the polynomial matrix must now be mapped to the conductance matrix depending on the port connections within the model. A graphical representation of the mapping process from a polynomial matrix to a model conductance matrix is shown in Fig. 23.

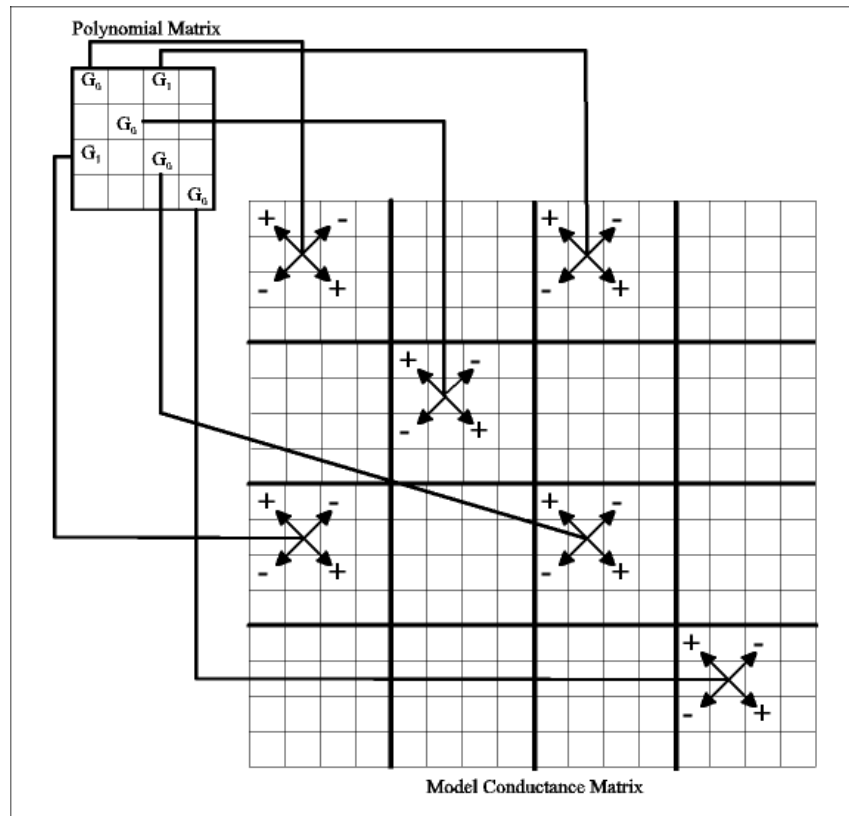


Fig. 23. Polynomial matrix to conductance matrix mapping

Every conductance located within a model should follow this process to incrementally create the conductance matrix from each conductance's polynomial matrix. The process depicted in Fig. 22 only represents a model with a single conductance value. If a model has more than one conductance then the polynomial matrix should be cleared, created and then mapped for each conductance value. This technique is used to formalize the creation process of uncertain models that can be solved using the uncertain resistive companion equation modeling method.

The creation of the conductance matrix completes the initialization stage of the model and the simulation can now enter the main execution loop from Fig. 21. This process consists of single stepping the model, solving the system matrix and advancing time. The model's responsibility during the step phase is to calculate the past history term $B(t-h)$. In most cases, the $B(t-h)$ term is a function of the current conductance matrix, the voltage and the current. The derivation of the $B(t-h)$ term results from the reordering of the model's equations as in section III part C.

The system conductance matrix is built from the contributions of all the models in the system. Each model's conductance matrix is mapped to the system conductance matrix depending upon the model's connectivity to the rest of the network. This mapping process is different from the mapping of the polynomial matrix onto the model's conductance matrix. This mapping process is shown in Fig. 24.

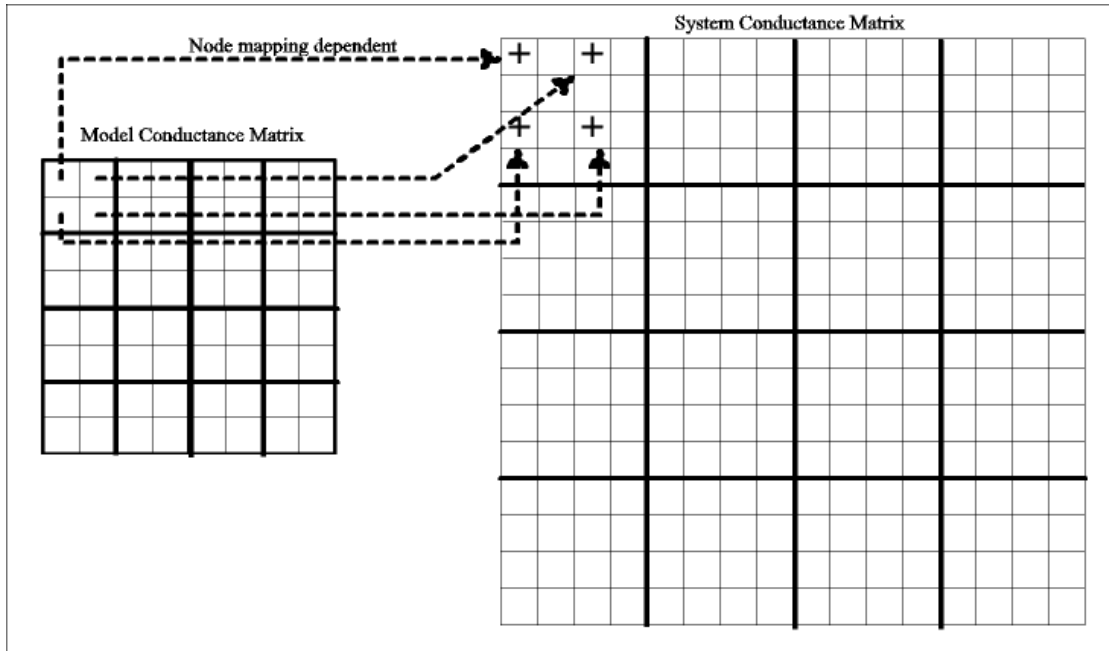


Fig. 24. Model conductance matrix to system conductance matrix mapping

The model matrix is broken into components that represent specific terms in the multivariable polynomial basis. This partitioning is shown in Fig. 24. The contributions of the model are mapped to the corresponding multivariable polynomial term section of the system conductance matrix. A similar mapping is also used to map the model's $B(t-h)$ vector to the corresponding system vector.

The system representation can now be solved using (3.8). The resulting voltages are then given to the models so that they can calculate their next $B(t-h)$ values. The voltages can also be used in the models post processing stage to evaluate the models polynomial chaos expanded resistive companion equation. All of the variables on the right side of (3.3) are known in this post processing stage so the model can calculate its own current. The simulation time is then advanced by the time step and the execution loop starts over again.

This automation scheme is meant to help standardize the process of creating uncertain models and the methods used to solve networks of these models. The dependence of the model's equations on the number of uncertain variables and the single variable polynomial order complicates the model creation process. This section introduced techniques that help simplify the process of creating these uncertain models.

Simulation Results and Discussion (RLC Circuit Example)

Circuits containing multiple uncertain variables greatly increase the number of terms located in the multi-variable polynomial basis. The increase in the number of terms is clear when considering the calculation of P in (2.1). The RLC circuit example explores multiple uncertain variables and extreme levels of uncertainty. This example uses Legendre-Chaos exclusively. The circuit consists of a 10 v DC voltage source, a 1 m Ω resistor (RSRC), two 0.5 Ω resistors (RL & RC), one 20 Ω resistor (RO), an inductor at 1 mH and a 10 μ F capacitor. The simulations are run with a time step of 5 μ s until a time of 2 ms. The results from hand-coded Monte Carlo analysis, polynomial chaos theory, and PSPICE are compared. The RLC circuit schematic is shown in Fig. 25.

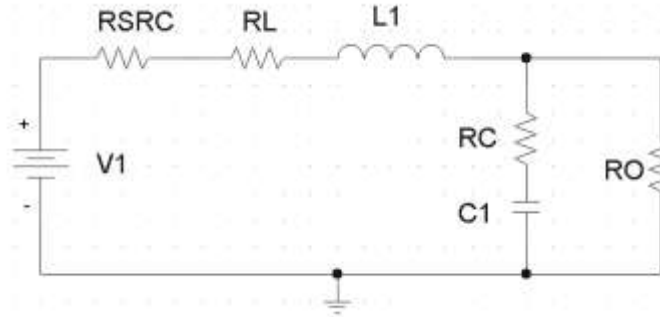


Fig. 25. RLC circuit example

The first scenario uses the schematic from Fig. 25 with the predefined parameter values. The system has five uncertain variables including a 10% tolerance on resistances R_L , R_C , and R_O along with a 10% tolerance on the capacitance of C_1 and the inductance of L_1 . This tolerance is represented by the uniform distribution. Legendre-Chaos will be used with third order polynomials. The hand-coded Monte Carlo analysis and PSPICE will use random variables from the uniform distribution. The number of random points used by Legendre-Chaos is 5000 and the number of hand-coded Monte Carlo iterations is 5000. PSPICE uses 400 Monte Carlo iterations. Fig. 26a shows the time domain results of the current through the inductor using the statistical curves of the mean, maximum and minimum. The hand-coded Monte Carlo analysis and Legendre-Chaos results are both shown in Fig. 26a. The PSPICE results of the inductor current are shown in Fig. 26b. There is no visible difference between any of the waveforms.

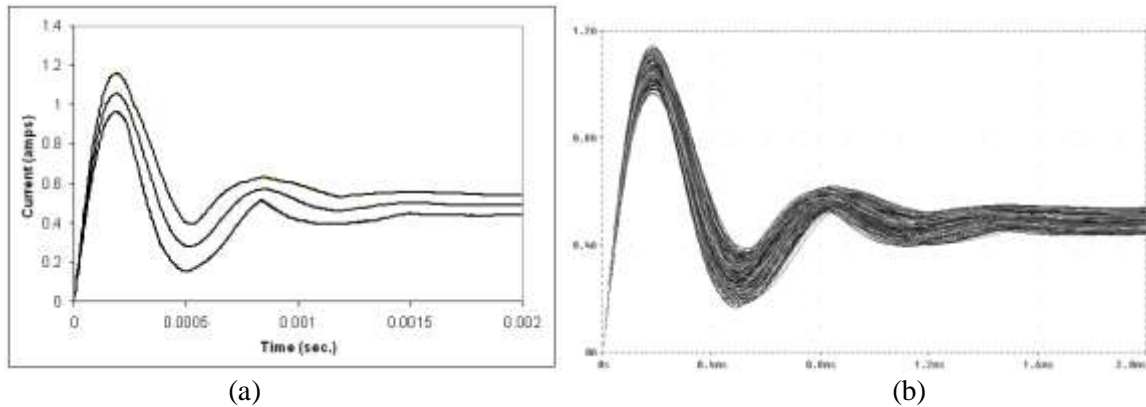


Fig. 26. 10% tolerance RLC example. (a) Legendre-Chaos and Monte Carlo analysis inductor current results. (b) PSPICE Monte Carlo inductor current results

The PDFs of the inductor current at 0.4 milliseconds from Legendre-Chaos and PSPICE are shown in Fig. 27.

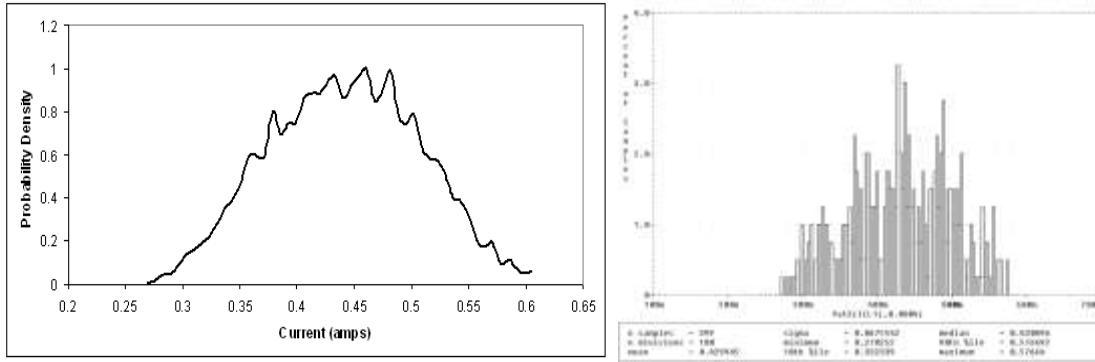
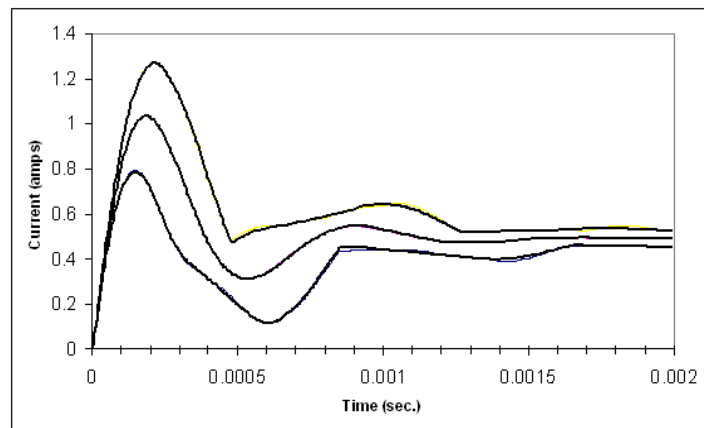
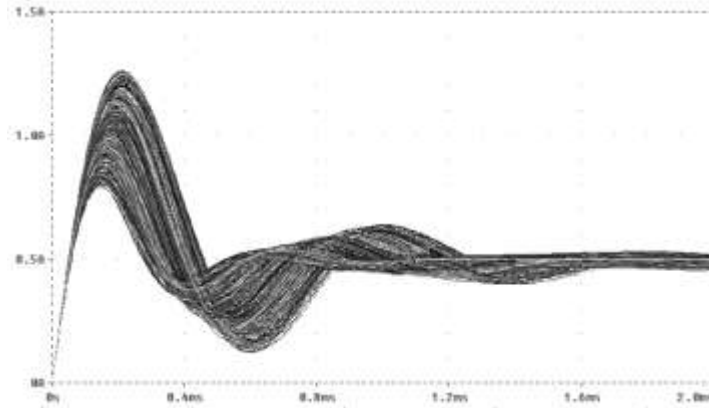


Fig. 27. PDF of inductor current at time = 0.4 ms from 10% tolerance simulation. (a) Legendre-Chaos. (b) PSPICE

The second scenario uses the schematic from Fig. 25 with five uncertain variables where not all of the uncertainties are of equal magnitude. This situation places a 5% tolerance on the resistance of RL, RC, and RO, along with a 5% tolerance on the inductance of L1. The largest uncertainty is a 50% tolerance on the capacitance of C1. Third order Legendre-Chaos is used along with the same simulation parameters from the previous scenarios. Fig. 28 shows the time domain statistics of the current through the inductor. The range of uncertainty for this scenario is much higher due to the 50% tolerance on the capacitor. Even with this high range of uncertainty the third order Legendre-Chaos and the hand-coded Monte Carlo analysis match up extremely well. The resultant waveforms can be seen in Fig. 28.



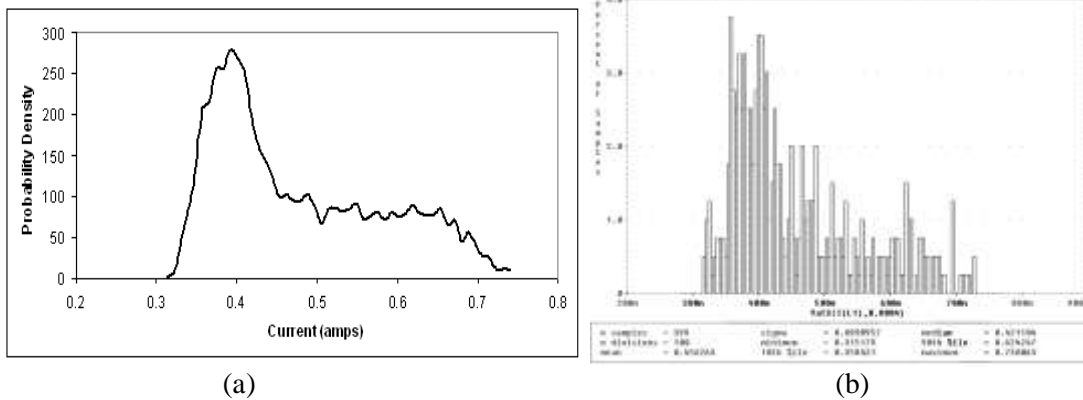
(a)



(b)

Fig. 28. 50% tolerance RLC example. (a) Legendre-Chaos and Monte Carlo analysis inductor current results. (b) PSPICE Monte Carlo inductor current results.

The normalized PDFs of the inductor current at time 0.4 milliseconds from the Legendre-Chaos and PSPICE simulations are shown in Fig. 29. The shapes of the PDFs are consistent with one another. Since the shapes of these waveforms are more distinctive it is easier to recognize the similarities between them.



(a)

(b)

Fig. 29. PDF of inductor current at time = 0.4 ms from 50% tolerance simulation. (a) Legendre-Chaos. (b) PSPICE

DC – DC Open Loop Power Converter Example

Let us now consider the application of the PCT to a more complex situation and in particular to the analysis of the behavior of a closed-loop power converter. We start first with the operation of the open loop topology and then we consider the impact of the closed loop on the operations of the uncertain system. The converter is supplied with a DC voltage source of 20V with an internal resistance of 1mΩ. The ideal switch has on and off resistances of 1μΩ and 10MΩ respectively. The switch is controlled and switched by a square signal source and a frequency of 10kHz with a duty cycle of 50%. The inductor and capacitor are 3mH and 100μF. The inductor and capacitor both contain a series resistance of 1mΩ. The output resistance is 10Ω and is considered to have a 30% tolerance that is uniformly distributed.

Fourth order Legendre-chaos will be used to simulate this system and the results will be compared to an equivalent Monte Carlo simulation. The schematic for the buck converter is shown in Fig. 13.

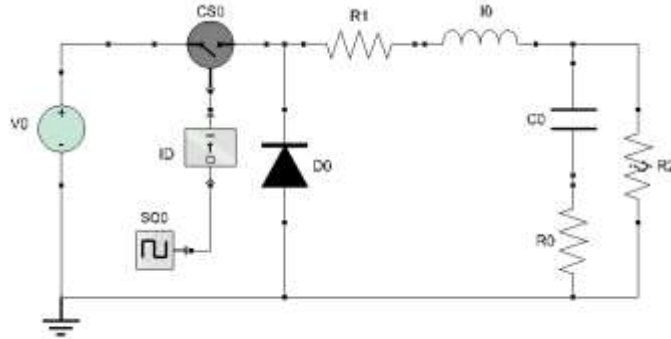


Fig. 30: Buck converter schematic

The schematic from Fig. 13 has been simulated with a time-step of $1\mu\text{s}$ until a time of 10ms. The simulation results are displayed in the time-domain with five statistical curves. Three of these curves are the minimum, maximum and mean of the output variable. The remaining two curves are the average of all the values located above the mean and conversely the average of all the values below the mean. The statistical representation is designed to show the general shape of the variables PDF as it evolves in time. The Legendre-Chaos simulation uses 5000 random points from the uniform distribution to reconstruct the PDF. The Monte Carlo simulation will use only 500 Monte Carlo iterations. The voltage and current statistical waveforms are displayed in Fig. 14(a,b).

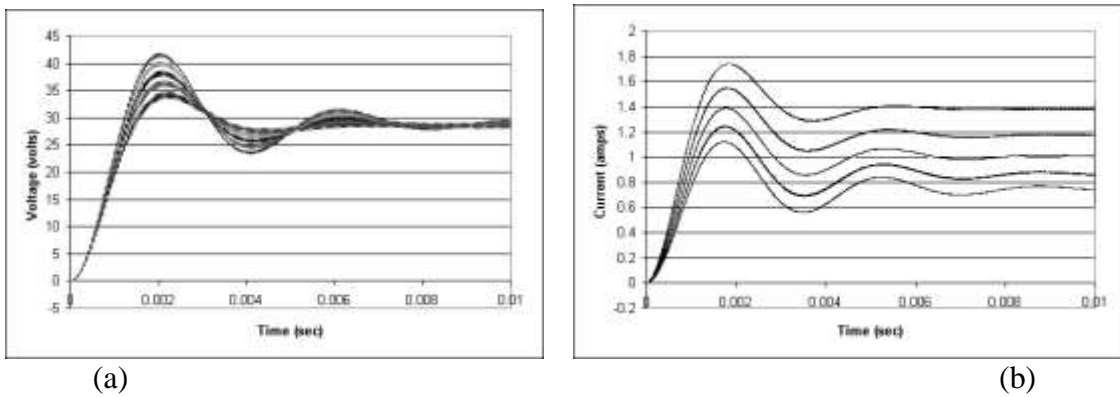


Fig. 31: Buck converter output waveforms (a) output voltage (b) output current

The five statistical curves from both the Legendre-chaos and Monte Carlo simulations are displayed in Fig. 14(a,b). The waveforms are nearly indistinguishable from one another. Zooming in on the peaks from the voltage graph gives better resolution to compare the two simulation methods. The zoomed in graph of the output voltage is located in Fig 15. There is still no visible difference between the statistical waveforms from the two methods even at this resolution.

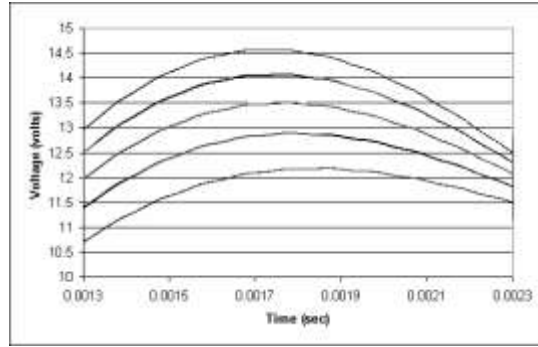


Fig. 32: Buck converter output voltage peaks

Closed Loop Power Converter Example

The buck converter from Fig. 13 is now supposed to be controlled using a feedback loop. The control technique used will be the state-feedback control using optimal control theory.. The state feedback control law used is located in (7.1).

$$u = k_r V_{ref} - k_i I - k_v V \tag{7.1}$$

The variables V and I represent the state variables of the converter and Vref represents the desired output voltage. The k coefficients are determined using optimal control theory. The averaged buck converter model must also be expanded using the polynomial chaos method. The duty cycle for each term of the polynomial basis is the new signal input into this expanded buck converter model. The schematic of the polynomial chaos expanded buck converter with state feedback is located in Fig. 33:

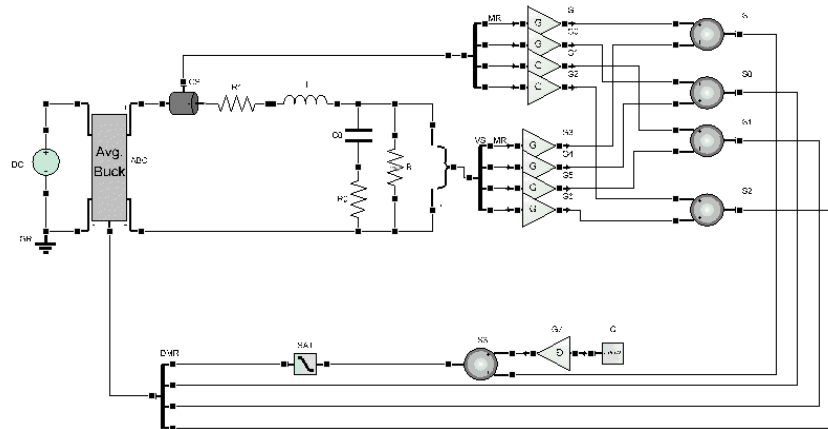


Fig. 33: Buck converter with polynomial chaos state feedback

The schematic from Fig. 16 is simulated using fourth order Legendre-Chaos. The voltage and current sensors must be designed to output the voltage and current from each term of the polynomial basis. The resulting signals must be applied as inputs into the polynomial chaos expanded control logic and fed into an averaged buck converter model. The polynomial chaos expanded control logic is located in (7.2).

$$\begin{bmatrix} u_0 \\ u_1 \\ \vdots \\ u_p \end{bmatrix} = \begin{bmatrix} k_r V_{ref} \\ 0 \\ 0 \\ 0 \end{bmatrix} - \begin{bmatrix} k_i & 0 & \cdots & 0 \\ 0 & k_i & \cdots & 0 \\ \vdots & \vdots & \ddots & \vdots \\ 0 & 0 & \cdots & k_i \end{bmatrix} \cdot \begin{bmatrix} I_0 \\ I_1 \\ \vdots \\ I_p \end{bmatrix} - \begin{bmatrix} k_v & 0 & \cdots & 0 \\ 0 & k_v & \cdots & 0 \\ \vdots & \vdots & \ddots & \vdots \\ 0 & 0 & \cdots & k_v \end{bmatrix} \cdot \begin{bmatrix} V_0 \\ V_1 \\ \vdots \\ V_p \end{bmatrix} \quad (7.2)$$

This expansion is performed under the hypothesis that the control is digital and then there is no uncertainty on the control parameters.

The averaged buck converter model must also be expanded using the polynomial chaos method. The duty cycle for each term of the polynomial basis is the new signal input into this expanded buck converter model. The simulations represent the performance of the closed loop system when the output resistance is 10Ω with a 30% tolerance uniformly distributed. The time-domain statistics of output voltage and current resulting from both the simulations are located in Fig 17(a,b).

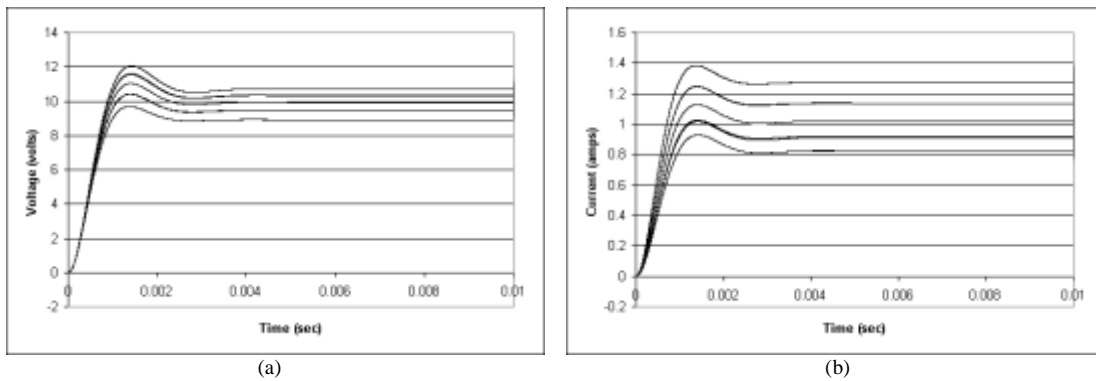


Fig. 34: Feedback controlled buck converter output results (a) output voltage (b) output current

The resulting waveforms of Legendre-chaos and Monte Carlo analysis are nearly identical. The effect of the output resistance uncertainty is extremely noticeable because it results in different steady-state output voltage values. The voltage peaks from Fig. 17 are zoomed in on in Fig. 18 so that a more direct comparison of the two resulting waveforms can be made.

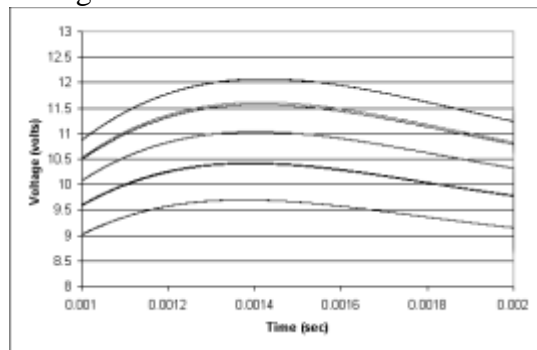


Fig. 35: Feedback controlled buck converter output voltage peaks

Conclusion

The examples demonstrate that polynomial chaos theory can be used to generate accurate simulation results for uncertain systems. The primary technical innovation within this paper is the derivation of a formal modeling theory based on polynomial chaos theory. This new modeling theory is an enabler for new CAD simulators focused on the evaluation and propagation of uncertainty. This paper demonstrates multiple advantages that this new modeling theory has over other uncertainty evaluation methods. The first advantage is that the polynomial chaos theory can calculate the entire PDF of each variable during only one execution of the simulation. This allows statistical information about the circuit to be available after each time step of the simulation. Monte Carlo analysis requires all of the simulations to be performed in parallel in order to have the full statistics after each time step. If the Monte Carlo iterations are not executed in parallel then it must wait for each entire simulation to be completed before the statistics are available. Secondly, the information required for the reconstruction of the PDF can be compactly stored by polynomial chaos in the form of the coefficients of the multi-variable polynomial basis. Monte Carlo analysis, on the other hand, requires the storage of all of the data resulting from each Monte Carlo iteration. A third advantage is that polynomial chaos automatically allows for irregular shapes of PDFs to be used for inputs, making it easier to represent complicated uncertainties.

Power Semiconductor Device Models

Advances in power semiconductor devices are one of the main enabling technologies that make the All Electric Ship concept possible. The overall goal of this activity is to develop models of power semiconductor devices at different levels of detail from behavioral to physics-based and implement them in VTB and other simulation platforms. Particular emphasis is placed on detailed physics-based models for these devices that can be used in circuit-oriented simulators. High-voltage shipboard power converters typically use Insulated Gate Bipolar Transistors (IGBT's), Integrated Gate Commutated Thyristors (IGCTs) and p-i-n diodes as switching semiconductor devices.

Besides the development of mathematical models describing these devices, it is critical that these models be implemented, debugged and tested in simulation environments used in shipboard power converter design. Parameter extraction procedures based on a small number of measurements must be defined in order to obtain the model parameters needed. The models should then be validated against experimental results under realistic operating conditions.

ESRDC research activities focus on helping the design process and providing simulation tools to support this process. This requires the ability to simulate the entire electrical system aboard the ship and parts of it at different levels of detail. This means very high-level simulations and more detailed simulations that capture more of the system physics. At the more detailed level, physics-based models are extremely important, especially to accurately predict converter losses, which represent a large percentage of the thermal load on a ship. An accurate prediction of the thermal load is critical for an appropriate dimensioning of the ship cooling system, which in turn is critical to long-term reliability. Physical models are also needed for trade-off studies on new devices (e.g., devices realized using wide bandgap materials such as Silicon Carbide), for the sizing of snubbers and clamps, for EMI estimation and also to provide a solid basis for the development of behavioral models.

As part of this power semiconductor modeling effort, accurate physics-based circuit-oriented models have been developed for various power semiconductor devices: IGBTs, IGCTs and p-i-n diodes.

The dynamic behavior of these conductivity-modulated devices is determined mostly by the low-doped drift region that supports the voltage across the device when it is not conducting. The ambipolar diffusion equation (ADE) describes the carrier dynamics in this region. A Fourier-series solution of the ADE is implemented in the physics-based models, so that at each instant in time the model calculates the instantaneous carrier distribution in the drift region. This model captures a significant amount of the relevant physics inside the device and as a result accurately predicts the device dynamic behavior.

Prior research efforts have led to the development of Fourier-series models for non-punch-through IGBTs and p-i-n diodes described in [1]. These models have then been extended to other types of IGBTs, such as punch-through and field-stop IGBTs [2], [3]. The Fourier-series modeling approach has then been applied to IGCTs as described in [4]. All these models have been extensively validated against experiments over a wide temperature range under various voltage and current conditions under resistive and inductive switching conditions.

The current work consists of several developments and extensions of the Fourier-series model [5] – [10]. The following contributions will be described in detail:

1. A practical and accurate parameter extraction method has been developed for the Fourier-based-solution physics-based IGBT and power diode models. The goal is to obtain a model accurate enough to allow switching loss prediction under a variety of operating conditions. In the first step of the extraction procedure, only one simple clamped inductive load test is needed for the extraction of all the parameters required for the diode model and for the IGBT model. The second part of the extraction procedure is an automated formal optimization step that refines the parameter estimation. Validation with experimental results from various structures of IGBT demonstrates the accuracy of the proposed IGBT and diode models and the robustness of the parameter extraction method. [5]
2. In order to optimize device characteristics, diode manufacturers frequently utilize lifetime control by proton irradiation. Using this procedure, the diode lifetime can be varied within the device, improving the trade-off between switching speed and forward drop. The Fourier-series diode model is extended to account for variable lifetime and a parameter extraction procedure is developed [7-8].
3. Modeling of IGBTs has traditionally focused on turn-off, where the stored charge inside the device causes the well-known current tail effect, with associated switching losses. However, significant losses also occur at IGBT turn-on, especially in the case of inductive turn-on, where the diode reverse recovery causes an overcurrent in the IGBT. A detailed study of IGBT turn-on has been performed, showing that the proposed model is capable of accurately predicting switching waveforms for resistive and inductive turn-on. For completeness, turn-off results are also included, showing that a single model is capable of accurately predicting device behavior under all of these conditions [9].
4. An extension of the IGBT model has been proposed to accurately represent MOS-side carrier injection. This effect is particularly important for device turn-on [10].

Only the first of these contributions is described in detail in this report.

Parameter Extraction for Physics-Based IGBT and PIN Diode Models

In recent years, the characteristics of IGBTs have been greatly improved. For example, with the application of advanced lifetime killing technology and structure development [Powerex], the 4th generation IGBTs (trench-gate punch-through), which have been available in the market for some time, exhibit fast turn-off speed and low saturation voltage. Buffer-layer IGBTs also exhibit tail-free turn-off current under high voltage conditions [Hefner]. The application of light punch through [Yamada] and field-stop technology now offers the new 5th generation IGBT with superior characteristics. These external characteristics, brought about by internal device design changes, can only be accurately modeled by a physics-based (analytical) IGBT model. However, in spite of the accuracy of physics-based IGBT models, either overly complex or inaccurate parameterization procedures often discourage electronic engineers from attempting to use IGBT models in their system designs.

Reviewing the IGBT circuit model parameter extraction methods described in the literature shows that further work must be done in the field. The parameter extraction provided for the accurate and comprehensive Hefner model [Hefner], [Hefner2] is so complex that it is not practical for electrical engineers. The extraction method proposed in [Lauritzen] is only for the lumped-charge IGBT model. In [Claudio], the parameter extraction for the Hefner model was further developed with seven very precise but complex experiments. The parameters extracted in [Musumeci] are used for IGBT behavioral models. In [Sigg], the parameter extraction lacks detail.

One of the primary reasons for device and circuit simulation in power electronic system design is estimation of power losses. The significant source of such losses is generally the switching devices. Hence an accurate and physically-based model is required, as the simulations must be valid over a wide range of conditions. This is also the case in determining other characteristics such as electromagnetic compatibility.

Crucially, the parameters must be found for a good fit with the devices and circuit. In most power electronics circuits the IGBTs operate under clamped inductive switching with a free-wheeling diode. In order to obtain good switching loss estimates, an accurate physics-based model for the power diode is also needed.

In conclusion, accurate physics based models for the IGBT and diode are needed. On the other hand, the parameter extraction procedure has to be simple enough to be practical. In order to meet these conflicting requirements in this work we propose a two-step parameter extraction, consisting of a simple parameter estimation based on datasheet data and a single clamped inductive measurement, followed by an automated optimization procedure to refine the extracted parameters.

Previous attempts at an automated parameterization procedure have concentrated on either fitting DC characteristics [OrtizConde1999] or key performance indicators, for example reverse recovery currents and times in the case of the power diode [Chante1993], [Strollo1997]. None allow a model to be fitted sufficiently to produce accurate switching power loss estimates.

This paper describes parameter extraction and refinement using a formal optimization procedure. One of the goals is to provide a complete extraction procedure for IGBT and power diode that describes in sufficient details both the initial parameter estimation and the optimization procedure. The extraction procedure is valid for different families of IGBTs such as punch-through, non-punch-through, field-stop and trench gate. The physics-based model has been proven accurate for all of these devices [Palmer], [Kang1]-[Kang5]. The procedure is based on accurate device and circuit models coupled with an

optimization algorithm and hardware data acquisition. All of these run from or within MATLAB. However, once the parameter extraction is complete, the parameters may be used for the models implemented on any platform, including circuit simulators such as PSpice.

Physics-Based Circuit Simulator IGBT and Diode Models

Being a conductivity-modulated power device, the behavior of an IGBT or a PIN diode depends heavily on the carrier distribution in its wide drift region. For diodes, the carrier distribution across the wide drift region is approximately one-dimensional. For IGBTs, it is one-dimensional across 90% of the drift region [Palmer], and so may be reasonably assumed as such for the whole region provided some modifications are made.

Under these conditions, assuming high-level injection, the Ambipolar carrier Diffusion Equation (ADE) describes the carrier dynamics,

$$D \frac{\partial^2 p(x,t)}{\partial x^2} = \frac{p(x,t)}{\tau_{HL}} + \frac{\partial p(x,t)}{\partial t}$$

where D is the ambipolar diffusion coefficient, τ_{HL} is the high-level carrier lifetime within the drift region and $p(x,t)$ is the excess carrier concentration.

Most physics-based circuit simulator modeling approaches focus on the simulation of the drift region, and consequently implement the modeling of the ADE. The Fourier-based-solution (FBS) model is adopted in this research [Leturcq],[Palmer]. For a more comprehensive description of the IGBT and diode models used in this work, refer to [Palmer], [Kang2]. This approach preserves the essentials of the distributed nature of charge dynamics within the drift region and offers reasonable simulation speed while preserving satisfactory accuracy. It effectively reduces the PDE into a set of coupled first-order ODEs which may be solved in circuit simulators (e.g. PSpice [Palmer], Saber) or general-purpose simulators (e.g. MATLAB/Simulink [Bryant2002]). The representation used for the whole region is shown in fig. 1, and the ADE requires boundary conditions of the carrier density gradients $\partial p/\partial x|_{x_1}$, $\partial p/\partial x|_{x_2}$ (dependent on the device current) and boundary positions x_1 , x_2 . The carrier density $p(x)$ is solved using the FBS model, and the carrier densities p_{x_1} , p_{x_2} at the boundaries are used to generate the boundary conditions and device terminal voltage. The formulation of the boundary conditions depends on the device modeled, giving the device its characteristic behaviour. Table 1 gives the relationships between the boundary carrier densities and currents for the diode and IGBT.

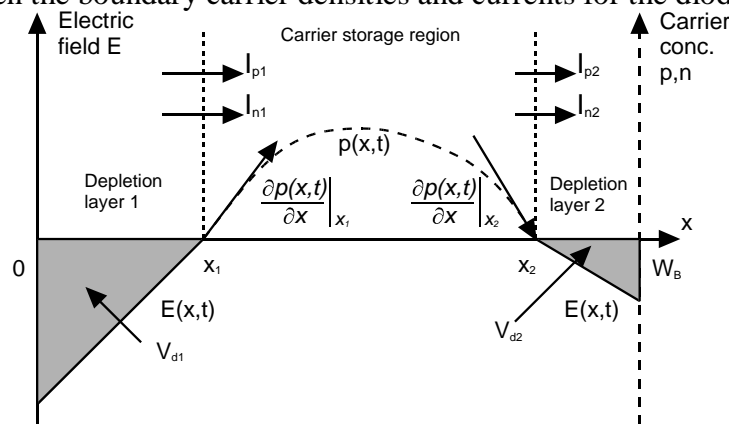


Fig. 1: General arrangement of carrier storage region and depletion layers in the FBS model, shown for the diode and the N-base region of the IGBT; the doping is N_B . The

anode (IGBT collector terminal) is on the left, and the cathode (IGBT emitter terminal) is on the right. The carrier density $p(x,t)$ is solved for the boundary carrier density gradients $\partial p/\partial x|_{x_1}$, $\partial p/\partial x|_{x_2}$ and boundary positions x_1 , x_2 .

TABLE I: BOUNDARY CURRENT FORMULATION FOR THE DIODE AND IGBT

	I_{n1}	I_{p1}	I_{n2}	I_{p2}
Diode	$qAh_p p_{x1}^2$	$I_A - I_{n1}$	$I_A - I_{p2}$	$qAh_n p_{x2}^2$
NPT IGBT	$qAh_p p_{x1}^2$	$I_C - I_{n1}$	I_{mos} (channel current)	$I_C - I_{n2}$
PT IGBT	$I_C - I_{p1}$	$I_{p1} = \frac{qAD_{pH}}{L_{pH} \sinh\left(\frac{W_H}{L_{pH}}\right)} \left[p_{H0} - p_{HW} \cosh\left(\frac{W_H}{L_{pH}}\right) \right] + I_{QH}$	I_{mos} (channel current)	$I_C - I_{n2}$

For PIN diodes, the P+ and N+ layers act as emitter regions when the diode is on. The electron and hole boundary currents I_{n1} , I_{p2} are given in terms of the boundary carrier densities p_{x1} , p_{x2} by the classic recombination equation [Schlangenotto]. For the IGBT, the MOS channel current I_{mos} can be found as a function of the gate-source voltage using the well-known MOSFET equation. At the left (anode) side of the drift region, different equations are used for the NPT and PT IGBT due to the structural differences. For the NPT IGBT, the emitter recombination equation is used to calculate the electron current element at the junction between the P+ emitter and the N- drift region. For the PT IGBT, the buffer layer formulation in [Kang2] is used to obtain the hole current component I_{p1} at the junction between the N buffer layer and the N- drift region. Some modifications required to take into account capacitive currents are described in detail in [Palmer] and [Kang2].

Two-Step Parameter Extraction Procedure

The proposed parameter extraction procedure consists of two separate steps:

2. INITIAL PARAMETER EXTRACTION. This is based on device datasheets and at most one clamped inductive switching experiment.
3. OPTIMIZATION PROCEDURE. Refinement of parameters through a formal optimization procedure.

Generally, there are three kinds of parameter extraction methodologies, which include: 1) simple estimation based on the empirical value range, 2) extrapolation according to the manufacturer's datasheet, and 3) extraction with simple experiments. To make the extraction procedure practical, the three methods are employed jointly.

Some of the diode and IGBT parameters listed in Tables II and III can be obtained from the datasheet or calculated based on textbook equations, so there is no need to use measurement for their extraction. Extra measurement can be used to verify the mathematical results. But some parameters, like IGBT carrier lifetime, have to be determined by experiment, which also needs to be simple. Accordingly, the clamped inductive load test experiment is used. The second step in the procedure is a formal optimization which may be completely automated. An advantage of this procedure is that inaccuracies in the initial parameter estimation may be corrected by the optimization procedure.

The parameter extraction process can be summarized in the following list and in Fig. 2:

1. Initial estimates of parameters made from device datasheets and basic measurements,

2. Measurement of device switching behavior, i.e. acquisition of switching waveforms,
3. Simulation of circuit behavior using parameters estimated,
4. Comparison of simulated and measured waveforms to produce an error value,
5. Variation of the parameter values to minimize the error value.

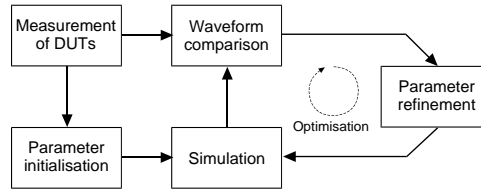


Fig. 2: Diagram showing the procedure of parameter extraction

Step e) is the optimization procedure. Once the error value has been determined, the parameters are varied and the simulation in step c) re-executed to produce a waveform valid for that set of parameters. This is again compared to the measured waveform in step 4), and the optimization continues accordingly. Once the parameters have converged to give a minimum error, the optimization procedure stops.

Step 1: Initial Parameter Estimation

Initial Parameter Estimation for Power Diodes

One of the major advantages of the physically-based diode model is that only six parameters from manufacturers are needed and can be easily estimated from the datasheets or from a single diode turn-off measurement.

Table II. Diode model parameter list.

Symbol	Description	Step
A (cm ²)	Active die area	1
τ_{HL} (μ s)	High-level lifetime	2
W_B (μ m)	Drift region width	3
N_B (cm ⁻³)	Drift region doping	4
h_n, h_p (cm ⁴ s ⁻¹)	Emitter recombination parameters	5

Five important ratings given in the diode manufacturer datasheets are: *i*) repetitive maximum voltage, V_{RRM} , *ii*) DC forward current, I_F , *iii*) reverse recovery charge, Q_{RR} , *iv*) reverse recovery peak current, I_{RM} , and *v*) reverse recovery time. The following steps describe the parameter estimation:

1) *Diode Area A*: Since the maximum current density J is for most power diodes from 100Acm⁻² to 150Acm⁻², the active die area A can be roughly estimated from the average forward DC current in the datasheet using (1).

$$A = \frac{I_F}{J} \quad (1)$$

A more precise estimate can be obtained by opening the device and measuring the actual die area.

2) *Diode lifetime* τ_{HL} : Neglecting the recombination effect in the reverse charge, equation (2) is used to make an initial estimate τ_0 for the high-level lifetime:

$$\tau_{HL} \approx \tau_0 = \frac{Q_{RR}}{I_F} \quad (2)$$

In the case that the reverse recovery charge Q_{RR} in the datasheet is given for a temperature other than room temperature, the parameter τ_0 can be scaled accordingly [Palmer]. A more accurate estimate for the lifetime may be made using an inductive turn-off measurement [Lauritzen2],[Tien]. This will only be necessary if the automated parameter optimization in section V is not carried out.

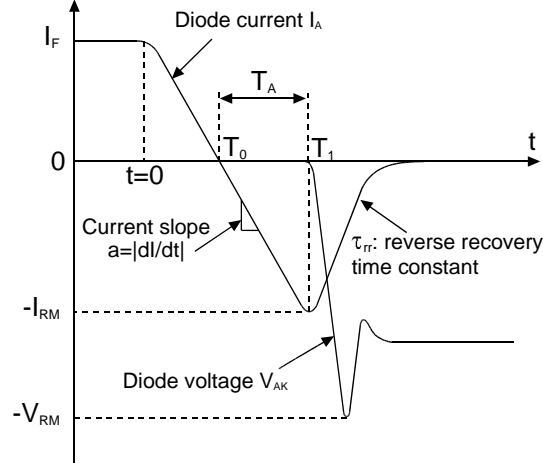


Fig. 3. Diode reverse recovery.

The extraction of the lifetime using the inductive measurement refers to fig. 3. After time T_1 the current waveform has the form:

$$i(t) = -I_{RM} \exp\left(-\frac{t-T_1}{\tau_{rr}}\right) \quad \text{for } t \geq T_1 \quad (3)$$

where τ_{rr} is the reverse recovery time constant and can be extracted from the experimental reverse recovery current waveform. In [Lauritzen2] it is shown that the following relationship holds:

$$I_{RM} = a(\tau_{HL} - \tau_{rr}) \left[1 - \exp\left(-\frac{T_1}{\tau_{HL}}\right) \right] \quad (4)$$

All parameters can be determined from the experimental waveform: current fall slope a , peak reverse current I_{RM} and time T_1 at which it occurs, reverse recovery time constant τ_{rr} . The lifetime τ_{HL} can be obtained by solving the implicit equation (5). Alternatively, following the approach of [Tien] the lifetime can be read from a graph. Substituting $I_{RM} = aT_A$ and $T_1 = T_0 + T_A$ equation (4) can be rewritten as:

$$\frac{T_A}{\tau_{rr}} = \left[\frac{\tau_{HL}}{\tau_{rr}} - 1 \right] \left\{ 1 - \exp\left[-\frac{\tau_{rr}}{\tau_{HL}} \left(\frac{T_0}{\tau_{rr}} + \frac{T_A}{\tau_{rr}} \right) \right] \right\} \quad (5)$$

In this expression there are three dimensionless quantities: T_0/τ_{rr} , τ_{rr}/T_A and τ_{rr}/τ_{HL} . The first two are known and the third can be read from the graph in fig. 4. Notice that parameter $S = \tau_{rr}/T_A$ gives an indication of the snappiness of a diode and is related to the classical snappiness factor (also called softness factor).

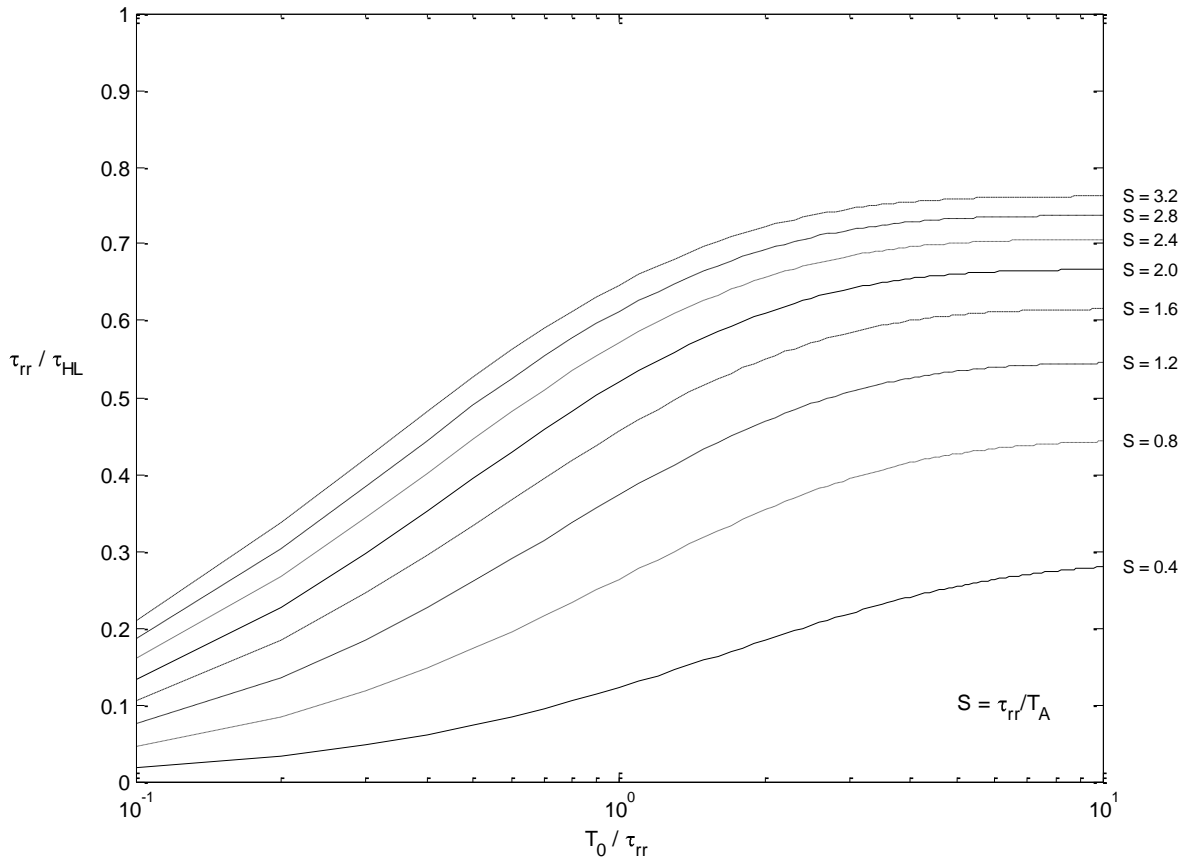


Fig. 4. Diode reverse recovery lifetime extraction.

c) *Diode drift region width W_B* : The electric field (E) dependence of the ionization coefficients for electrons and holes in Si, α , has been shown to fit experimental data fairly well in the form as given in (7), [Overstraeten] [Kokosa] [Sze],

$$\alpha_{n,p} = a \exp(-b/E) \quad (6)$$

where a varies between 7×10^5 and $3.8 \times 10^6 \text{ cm}^{-1}$ with a corresponding variation in b from 1.47×10^6 to $1.75 \times 10^6 \text{ Vcm}^{-1}$. Assuming breakdown in the bulk, an abrupt junction, equal ionization coefficients for holes and electrons, and a P^+NN^+ structure, an expression for the breakdown voltage in terms of the parameters a , b , and the N-drift region (base) width, W_B , can be obtained (8).

$$V_{BD} = \frac{bW_B}{\ln(aW_B)} \quad (7)$$

The N-drift region width, W_B , used in the model is derived based on (8) using $a = 1.07 \times 10^6 \text{ cm}^{-1}$, $b = 1.65 \times 10^6 \text{ Vcm}^{-1}$, and the value of the breakdown voltage from the manufacturer's data sheet plus some margin.

d) *Diode drift region doping N_B* : For purposes of the modeling and based on the empirical effective impurity doping concentration range ($6 \times 10^{13} - 2 \times 10^{14} \text{ cm}^{-3}$) in the N-drift region, the doping concentration is assumed to be 10^{14} cm^{-3} .

e) *Diode recombination parameters h_n , h_p* : The recombination parameters h_n and h_p control the amount of charge present in the diode during the on-state; their increase results in a reduction in stored charge and therefore a reduction in reverse recovery charge. An initial estimate of $1 \times 10^{-14} \text{ cm}^4 \text{ s}^{-1}$ may be made for both.

Fig. 3 shows typical reverse recovery current and voltage waveforms obtained from an inductive turn-off measurement. In the model, the lifetime is the dominant parameter affecting the recovery waveforms. With the correct high-level lifetime τ_{HL} , not only good matching of the reverse current can be obtained, but also a good match of the diode voltage waveform during turn-off, including overshoot and ringing, can be made. The first estimate of high-level lifetime, τ_{HL} , is given by the initial recovery time τ_0 . A better estimate can be obtained by trying to match the reverse recovery current. After this, the N-base width estimate can be improved by trying to improve the matching of the diode voltage waveform. It has been found empirically that, compared with lifetime τ_{HL} , the width and doping of the N-drift region do not have significant effects on the reverse recovery current, but have an obvious effect on the diode voltage waveform in the simulation. The recombination parameters h_n and h_p affect the reverse recovery current – in particular the peak reverse recovery current I_{RM} – and should be used to improve the matching further.

Initial Parameter Estimation for IGBTs

The Fourier-based-solution IGBT model requires 12 and 15 non-silicon parameters for the NPT and PT structure IGBTs respectively. Table III lists the parameters, which are classified into three categories based on the related device part: MOS-gate, geometry, and collector body parameters.

TABLE III. IGBT MODEL PARAMETER LIST

Part	Symbol	Description	St e p
MO S Gate	V_{TH} (V)	MOS threshold voltage	1
	K_{pl} (AV ⁻¹)	MOS transconductance coefficient	1
	λ (V ⁻¹)	Short-channel parameter	1
	C_{GE} (nF)	Gate-emitter capacitance	2
	C_{OX} (nFcm ⁻²)	Oxide capacitance	2
	l_m (μm)	Inter-cell half-width	2
Geo metr y	A (cm ²)	Effective die area	2
	a_i	Ratio of inter-cell to total die area	2
Coll ector Bod y	N_B (cm ⁻³)	Doping concentration of N-drift region	3
	W_B (cm)	Width of N-drift region	3
	τ_{HL} (μs)	Carrier high-level lifetime in N-drift region	4
	τ_{BF} (μs)	Carrier lifetime in N buffer-layer (PT)	4
	h_p (cm ⁴ s ⁻¹)	Hole recombination coefficient in emitter (NPT)	5
	W_H (cm)	Width of N-buffer layer (PT)	5

	N_H (cm ⁻³)	Doping concentration of N-buffer Layer (PT)	5
	I_{sne} (A)	Minority carrier saturation current (PT)	5

Because a behavioral MOSFET model is used for the IGBT MOS gate, the relevant parameters can be extracted following the extraction procedure for a MOSFET. The information given in the manufacturers' datasheets is enough to extract these five parameters.

1) *MOS parameters*: The first three MOSFET parameters, MOS threshold voltage V_{TH} , transconductance coefficient K_{pl} , and short channel parameter λ , can be obtained from the known I-V characteristic curve, shown in fig. 5. Note that this curve is only used for obtaining initial parameter estimates and is not used in further processing. The electron current I_{mos} that flows through the elemental MOSFET is a fraction of the total IGBT current I_C and can be calculated as:

$$I_{mos} = \frac{b}{b+1} I_C \quad \left(\begin{array}{l} 8 \\ 8 \end{array} \right)$$

where b is the ratio of electron and hole mobilities. The assumption of this fraction is necessary to obtain an initial estimate of the MOS parameters. The MOS channel voltage V_{DS} is approximately equal to the collector-emitter voltage V_{CE} during saturated operation of the channel ($V_{DS} \geq V_{GS} - V_{TH}$).

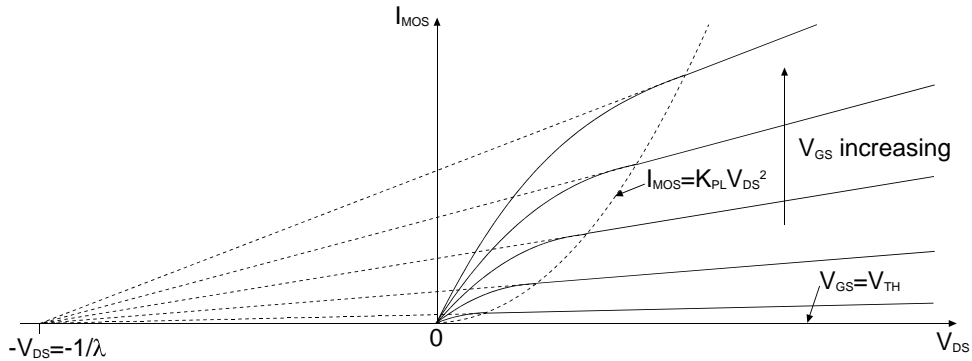


Fig. 5 Forward I-V characteristics of the IGBT MOS gate

2) *IGBT geometry and capacitances*: The active die area A can be measured directly by opening the device package. Another method is based on the empirical range of IGBT maximum current density J . Therefore, the active die area can be roughly estimated as:

$$A = \frac{I_{CM}}{J} \quad (9)$$

where I_{CM} is the peak collector current from the RBSOA curve given in the datasheet. Practically, the I_{CM} value is decided by many factors, not only the chip but also the package and heat extraction. Nevertheless, the range of current density J generally is 100Acm^{-2} - 250Acm^{-2} .

The ratio of inter-cell area to total die area a_i can be extracted based on the capacitances in the datasheet. Figs. 6 and 7 show the IGBT capacitance distribution. It can be seen that the displacement current I_{disp} , due to variation of the depletion region width, flows through two branches: the first branch is under the emitter terminal, which is represented by the collector-emitter capacitance C_{CE} , while the other is the Miller capacitance branch, which includes collector-gate capacitance, C_{GC} and gate-emitter

capacitance C_{GE} . When the gate is shorted to the emitter ($V_{GE}=0V$), the second branch only includes C_{GC} . Using analysis in [Kang4] and [Leturcq], the intercell ratio can be obtained as:

$$a_i \approx \frac{\min C_{res}}{\min C_{oes}} \quad (10)$$

Equation (11) is only valid under the condition that the collector-emitter voltage V_{CE} is sufficiently high to allow for an approximately uniform space-charge layer capacitance over the whole crystal area. Therefore, the minimum values of C_{oes} and C_{res} in the datasheet should be chosen, as a sufficiently high V_{CE} is reached at that point.

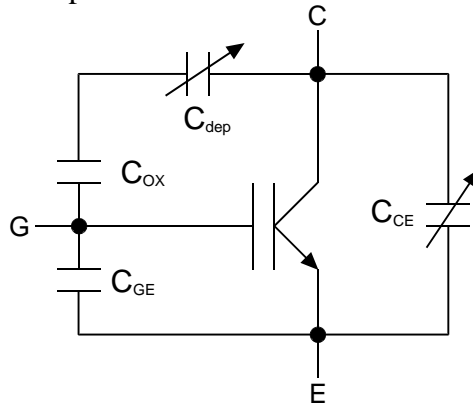


Fig. 6: IGBT capacitances.

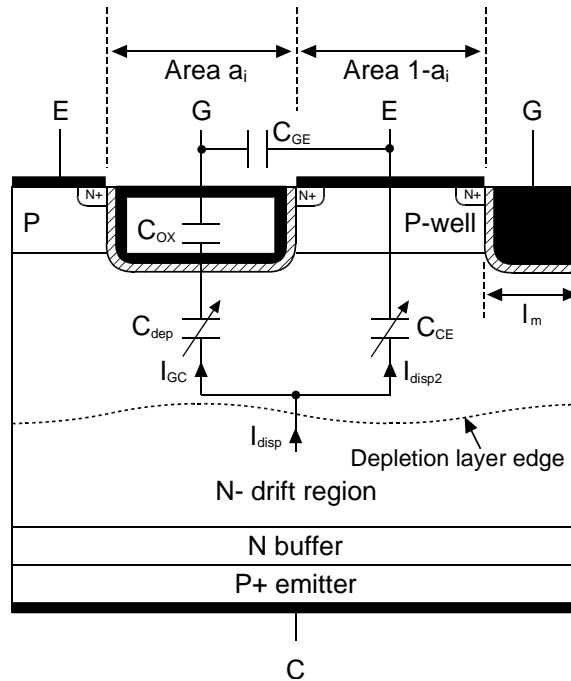


Fig. 7: Capacitance distribution diagram for a trench gate IGBT.

As shown in figs. 6 and 7, the MOS oxide capacitance C_{OX} , together with the series-connected depletion capacitance C_{dep} determines the gate-collector capacitance C_{GC} , which is also called the reverse transfer capacitance C_{res} in datasheets and is commonly referred to as the Miller capacitance between gate and collector. C_{OX} is the maximum value of the Miller capacitance when the depletion

region under the gate area has not formed ($C_{dep}=\infty$). That point corresponds to the maximum point of the C_{res} curve in the datasheet. C_{OX} is strictly the oxide capacitance per unit area, and therefore is written as:

$$C_{ox} = \frac{\max(C_{res})}{Aa_i} \quad (11)$$

The inter-cell half-width l_m is typically 5-15 μ m. Along with the Miller capacitance C_{GC} it controls the length of the gate voltage plateau during switching; larger values of l_m give longer plateau durations.

The gate-emitter capacitance C_{GE} can be directly obtained from the input capacitance C_{ies} (measured gate-emitter capacitance when collector is shorted to emitter) provided in the datasheet. Since the input capacitance C_{ies} is the sum of the C_{GE} and the Miller capacitance C_{GC} , and the former is much larger than the latter at higher voltages, C_{GE} can be chosen equal to C_{ies} at 100V.

3) *IGBT drift region parameters*: There are several different ways to extract the doping concentration of the drift region N_B . The first is the direct estimation based on the normal range of the drift region background doping, which is from 6×10^{13} to $2 \times 10^{14} \text{cm}^{-3}$ for the IGBT device. The typical value, $1 \times 10^{14} \text{cm}^{-3}$, is generally chosen as the doping concentration N_B during the simulation. The second way is based on the relation between the doping concentration and the breakdown voltage [Hudgins] using equation (13):

$$N_B = 2.88 \times 10^{17} V_{BR}^{-1} \quad (12)$$

where V_{BR} is the breakdown voltage value from the manufacturer's data sheet plus about 150V-200V typical margin for general IGBTs. The breakdown voltage could also be measured with a curve tracer.

Besides the above simple but rough extraction method, the extrapolation based on the C_{oes} and C_{res} versus collector-emitter voltage curves in the datasheet can also lead to a reasonable extraction value of N_B using the analysis in [Kang4] and [Leturcq]. This leads to a linear relationship between $1/(C_{oes}-C_{res})^2$ and V_{CE} , shown in equation (14). The slope of this relationship, which may be obtained using linear regression performed on the datasheet curves, can be used to find N_B since the area A and intercell area ratio a_i are already known.

$$\frac{1}{(C_{oes} - C_{res})^2} = \frac{2}{q\epsilon N_B (A(1 - a_i))^2} V_{CE} \quad (13)$$

The extraction of the drift region (base) width W_B is different for PT and NPT devices. The NPT has a triangular shape of electric field distribution, and it is designed to punch through at the same voltage as avalanche breakdown.

Under the triangular shape of the electrical field distribution in the NPT IGBT, the breakdown voltage due to punch-through is:

$$V_{PT} = \frac{qN_B(W_B)^2}{2\epsilon} \quad (14)$$

For PT devices, where the electric field is trapezoidal, the breakdown voltage due to avalanche is:

$$V_{BR} = E_C W_B - \frac{qN_B}{2\epsilon} W_B^2 \quad (15)$$

where E_C is the critical electrical field value for silicon ($E_C \approx 2 \times 10^5 - 3 \times 10^5 \text{Vcm}^{-1}$). Fig. 8 shows the curves of V_{BR} against drift region width W_B with a doping N_B of $1 \times 10^{14} \text{cm}^{-3}$ for both NPT and PT

structures. As can be seen from the figure this gives a maximum breakdown voltage of approximately 1330V. The intersection of the two curves gives the width for which avalanche and punch-through occur for the same voltage, i.e. the width for which a NPT device would be designed. A PT design would typically have a drift region width less than this. The breakdown voltage advantage of the PT structure for the same drift region width can clearly be seen in the figure.

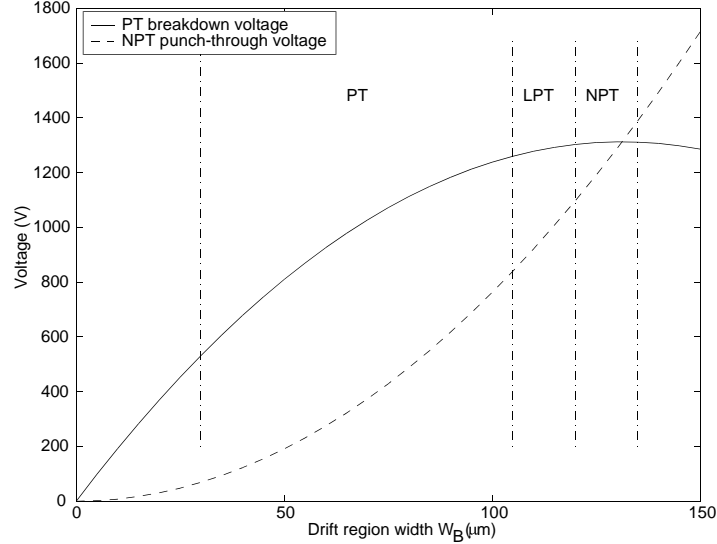


Fig. 8: Punch-through and breakdown voltages as a function of drift region width for NPT, LPT (light punch-through) and PT structures, with $N_B=1 \times 10^{14} \text{ cm}^{-3}$. The NPT, LPT and PT regions are indicated in the figure.

Hence this figure can be used to determine W_B and the likely structure. Solving the quadratic in equation (16) gives the following expressions for W_B :

$$W_B = \begin{cases} \frac{\varepsilon E_C}{qN_B} & \text{(NPT)} \\ \frac{\varepsilon}{qN_B} \left(E_C - \sqrt{E_C^2 - \frac{2qN_B V_{BR}}{\varepsilon}} \right) & \text{(PT)} \end{cases} \quad (16)$$

4) IGBT lifetime parameters: Extraction of the high-level lifetime τ_{HL} , and, in the case of the PT structure, the buffer layer lifetime τ_{BF} , must be obtained from inductive turn-off measurements, specifically the current tail. This is shown in fig. 9. The decay rate of the current tail is set by the lifetime.

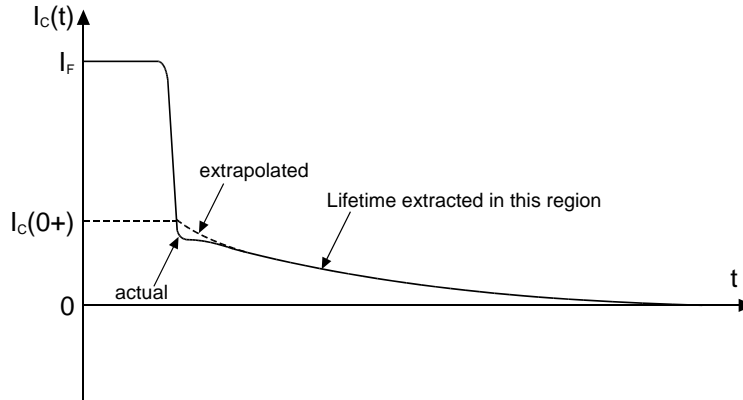


Fig. 9: IGBT current waveform under inductive turn off.

Based on the theory in [Hefner2], the IGBT current decay during the current tail for a constant collector voltage is given by:

$$I_C(t) = \frac{I_C(0^+)}{\left[\frac{I_C(0^+)}{I_k^\tau} + 1 \right] \exp\left(\frac{t}{\tau_{HL}}\right) - \frac{I_C(0^+)}{I_k^\tau}} \quad (17)$$

where $I_C(t)$ is the collector current, and I_k^τ is defined as:

$$I_k^\tau \equiv \frac{q^2 A^2 D_p n_i^2}{I_{sne} \tau_{HL}} \quad (18)$$

This expression can be approximated for $t > 2\tau_{HL}$ as:

$$I_C(t) \approx \frac{I_C(0^+)}{\left[\frac{I_C(0^+)}{I_k^\tau} + 1 \right]} \exp\left(-\frac{t}{\tau_{HL}}\right) \quad (19)$$

Therefore, the high-level lifetime can be extracted by extracting the time constant of the exponential current decay a couple of time constants after the initial current fall time as shown in fig. 9. It should be noted the accuracy of this method will not be assured for IGBTs with lifetimes greater than approximately 10 μ s due to the assumption of a linear charge profile made in [Hefner2]. However, this method will provide an initial estimate of the lifetime which can be refined either by hand or using the automated optimization described in section V.

Fig. 10 shows the measured results of a *Dynex* NPT IGBT with a 90A current rating. Notice that the effective lifetime is approximately independent of the collector current, therefore the collector current level used to extract the high-level lifetime is unimportant.

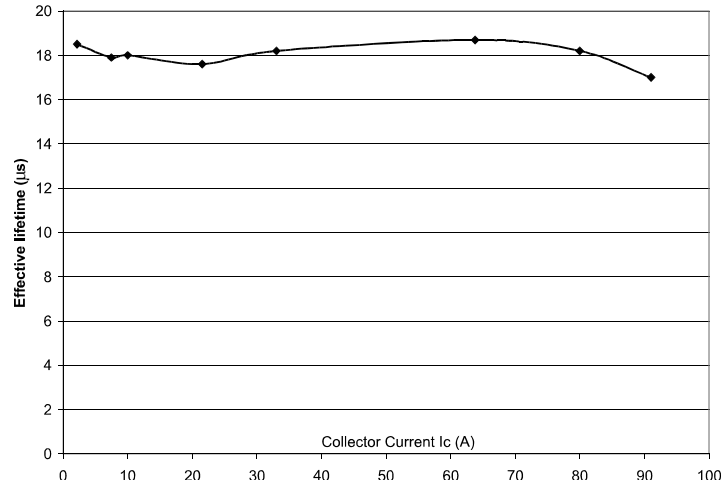


Fig. 10. High-level lifetime extraction for the Dynex NPT IGBT. (The x-axis is collector current, 10A/div, and the y-axis is time, 2 μ s/div)

For the lifetime extraction of the PT IGBT, a method similar to the NPT case can be used. The difference is that the effective lifetime τ_{eff} , instead of the high-level lifetime τ_{HL} in the NPT case, is used in (20) for the PT case. The effective lifetime is function of the high-level lifetime in the drift region and low-level lifetime in the buffer layer τ_{BF} (equal to the minority (hole) lifetime τ_{pH}). Moreover, τ_{eff} is dependent on the clamp voltage, unlike τ_{HL} in the NPT case, which is independent of the voltage. Therefore, lifetime extraction for the PT IGBT needs to be performed under several clamp voltages. The effective lifetime extraction under clamp voltage condition is the same as in the NPT case. Fig. 11 shows the curve of the effective lifetime τ_{eff} versus the clamp voltage based on the test results for a PT IGBT. Notice that fig. 10 and fig. 11 have different x-axes: in fig. 11 the x-axis is the collector-emitter voltage, whereas in fig. 10 the x-axis is the collector current. The high-level carrier lifetime τ_{HL} corresponds to the low-voltage τ_{eff} value, while the low-level carrier lifetime in the buffer layer τ_{BF} is equal to the τ_{eff} value at high clamp voltage since the drift region is depleted under that condition.

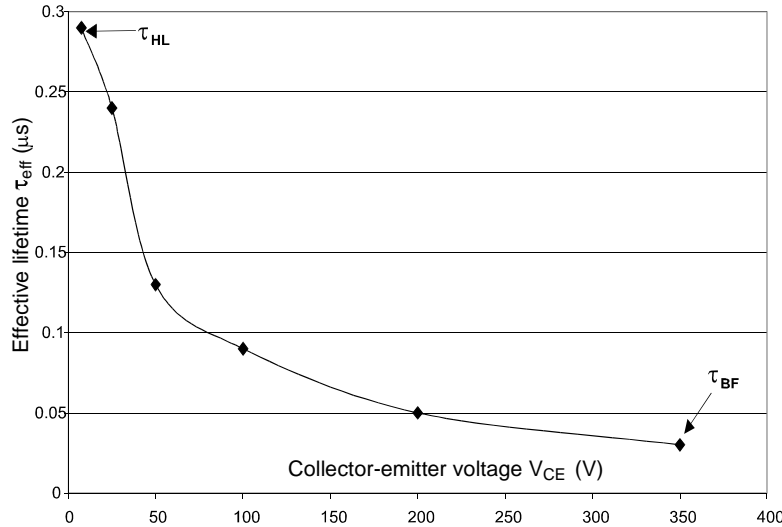


Fig. 11. Effective lifetime extraction under different clamped voltages for the PT IGBT (The x-axis is collector-emitter voltage, 50V/div, and the y-axis is time 0.05 μs /div)

5) IGBT recombination and buffer layer parameters: The recombination parameter h_p (in the NPT case) and the buffer layer parameters N_H , W_H and I_{sne} (in the PT case) set the level of injection from the P+ emitter into the N- drift region. The initial height of the current tail $I_C(0+)$ is set by the level of stored charge within the drift region, which is in turn set by the level of injection from the P+ emitter. Increasing h_p for the NPT IGBT, or increasing I_{sne} , W_H or N_H for the PT IGBT, reduces the level of stored charge and therefore reduces the initial height $I_C(0+)$. Generally, a value of $1 \times 10^{-12} \text{cm}^4 \text{s}^{-1}$ may be used for an initial estimate for h_p in the NPT case.

The remaining parameters of the buffer layer for PT IGBTs can be obtained based on their empirical value range. The typical PT IGBT buffer layer width W_H is about 4-10 μm . The normal range of the doping concentration N_H is 10^{16} - 10^{17}cm^{-3} . For a relatively low-doped buffer region used in structures such as the CSTBT or field-stop (FS) IGBT, smaller W_H and N_H values should be chosen. In the PT model, I_{sne} is used instead of h_p and an empirical value of 10^{-14} - 10^{-12}A may be chosen as an initial estimate. As for the NPT IGBT, the tail current height decreases with increasing values of I_{sne} . Note that the hole diffusivity D_{pH} used in the PT model is reduced from its intrinsic value due to the high doping of the buffer layer, and therefore depends on the buffer layer doping N_H [Leturcq2].

Initial Circuit parameter Estimation

Estimation of the stray inductance L_S in the switching loop of the circuit is critical for modeling the switching process. It controls the slope of the reverse recovery current waveform in the case of the diode, and the current and voltage waveforms in the case of IGBT switch-off. The diode reverse recovery waveforms are traditionally used to estimate the stray inductance:

$$L_S = \frac{V_{DC}}{|dI_A/dt|} \quad \left(\begin{array}{c} \\ 20 \\ \end{array} \right)$$

A disadvantage with this method is that it assumes that the IGBT voltage V_{CE} is negligible, which is not necessarily true. A more accurate method would be to use the voltage dropped across the stray inductance,

$V_{DC} - V_{CE}$. However, this suffers from non-constant V_{CE} during turn-on, making the choice of point at which to estimate the stray inductance more difficult.

Therefore a more robust method is recommended for estimating L_S using the IGBT turn-off waveforms, since the diode voltage is negligible during this phase of the switching cycle (it is undergoing forward recovery).

$$L_S = \frac{V_{CM} - V_{DC}}{|dI_C / dt|} \quad \left(\begin{array}{c} 21 \\) \end{array} \right)$$

V_{CM} is the peak collector voltage during IGBT turn-off and V_{DC} is the supply voltage. The current slope dI_C/dt is measured during the initial current fall. It is also essential to include the Kelvin emitter inductance L_E (between the emitter terminal and the return path to the IGBT gate drive) in the simulation of the switching circuit, since this affects the shape of the IGBT collector voltage waveform during IGBT turn-on. This is typically 5-20nH for a 1cm² IGBT.

Optimization Procedure

Experimental measurement of switching waveforms

The optimization procedure requires suitable experimental waveforms from inductive switching tests to compare with the simulation waveforms. Ideally these should be captured using a digital oscilloscope and transferred to the host computer, allowing a direct comparison with the simulation waveforms to produce an error figure which is then used to guide the optimization. The waveforms acquired for the tests described had the features shown in fig. 12. A frame of 50μs was captured at a sample rate of 200MHz, giving 10⁴ samples per frame. A switching “period” of $T_S=40\mu s$ was included within this, incorporating both switching events, with the turn-on occurring 5μs from the start of the frame. In addition to the extraction of IGBT parameters, these waveforms also allow the extraction of diode parameters from the diode reverse recovery current reflected in the IGBT turn-on waveform.

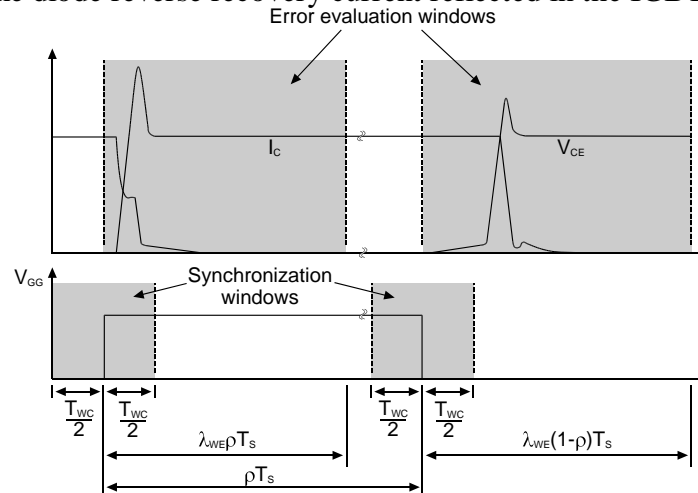


Fig. 12. Typical features of experimental waveforms. T_S : switching period, ρ : duty ratio, λ_{WE} : proportion of cycle used for waveform error evaluation, T_{WC} : length of window used for cross-correlation (synchronization).

Waveform Evaluation

One possible method of comparison of the measured and simulated waveforms is using the salient points of the waveforms, e.g. diode reverse recovery current, reverse recovery time or IGBT switching time. This gives a small number of points to match, but can suffer from low accuracy. Most importantly, the waveforms may differ quite substantially during the switching instants, especially in di/dt and dv/dt . This would give a large error in estimated power during simulation. A much more accurate method of comparison is to simply calculate the sum of the squared errors at each time point in the waveforms. This requires:

- A method to compare the different traces of each waveform, typically voltage and current.
- Normalization of the errors used, so that the conditions imposed such as supply voltage and load current do not affect the consistency of the parameter extraction.
- Accurate synchronization of the waveforms, otherwise the errors in di/dt and dv/dt will be significant and lead to inaccuracy of the power loss estimates during simulation.

Accurate power loss estimation is the goal of the parameter extraction. One possible basis for the error is the instantaneous power dissipation. This encompasses the most critical points in matching the voltage and current traces, since maximum instantaneous power dissipation is usually where di/dt and dv/dt are high. Therefore, a possible waveform comparison method is to compute the sum of the squared errors at each time point of the instantaneous power dissipation. However there is the significant disadvantage of the independence of the voltage and current traces being lost when optimization takes place. For example, the same power dissipation waveform can be maintained by the voltage increasing and the current decreasing; while the power dissipations match, the voltage and current waveforms do not. Therefore the voltage and current waveforms should be used separately, and given that these are matched the power dissipations will match too. Matching voltage and current waveforms will tend to ensure that any oscillations, the waveform slopes and the switching energies are all matched. Normalization to the supply voltage and load current may be performed before the power dissipation is calculated, allowing comparisons between different operating conditions. Finally, summing the squared errors, rather than the magnitudes of the errors, assigns more significance to any large errors between measured and simulated waveforms. It has the effect of emphasizing the switching losses. This is useful since it forces the optimization to reduce the large errors first and converges quickly. The error figure used is therefore the sum of the normalized squared errors for the current and voltage at both turn-on and turn-off:

$$f_e = SSE\left(\frac{V_{CE,on}}{V_{DC}}\right) + SSE\left(\frac{I_{C,on}}{I_F}\right) + SSE\left(\frac{V_{CE,off}}{V_{DC}}\right) + SSE\left(\frac{I_{C,off}}{I_F}\right) \quad (22)$$

$$SSE(x) = \sum_{n=1}^N (x_{sim} - x_{meas})^2 \quad (23)$$

where N = number of samples in window.

Typically, synchronization is carried out 'by eye', and matches both the time scales and the slopes (di/dt and dv/dt). A simple synchronization is to align the gate drive signals, which are available in both the hardware and the simulation used and are square waves [Palmer]. An alternative is to compare the instantaneous power dissipations and find the relative delay of the waveforms which produces the minimum error between them, thus removing the effect of the gate drive circuit. This method was found to be the most effective. To perform the synchronization automatically, the cross-

correlation between the experimental and simulated traces is calculated. The cross-correlation between two continuous signals $x(t)$ and $y(t)$ can be defined as:

$$r_{xy}(\tau) = \int_{-\infty}^{+\infty} x(t + \tau) y^*(t) dt \quad (24)$$

Here the waveforms are sampled, so the cross-correlation for discrete signals $x(n)$ and $y(n)$ is used:

$$c_{xy}[k] = \sum_{n=-\infty}^{+\infty} x(n+k) y^*(n) \quad (25)$$

If the waveforms are similar enough, which will be the case since the model is relatively accurate and the initial parameter set should give reasonable results, then the time delay τ or k at which the cross-correlation is at a maximum equals that which will produce the best matching. The appropriate function in MATLAB is `xcorr`, which in this case is set to produce the unbiased estimate of the correlation:

$$c_{xy,unbiased}[k] = \frac{1}{|N-k|} \sum_{n=0}^{N-k-1} x(n+k) y^*(n) \quad (26)$$

The correlation of the power dissipation waveforms uses a window of length $T_{WC}/2 = 4\mu\text{s}$ either side of the gate step, to ensure that the switching event is captured. Once the matching delay is determined, the error between the waveforms can be calculated at each point, squared and summed to produce a single error estimate. The windows used for the error estimation are set to 50% ($\lambda_{WE} = 0.5$) of the on- or off-state period. In this case the sum of these periods (T_S) is $40\mu\text{s}$. Refer to fig. 12 for details. A summary of the simulation and waveform evaluation process is:

1. Update the parameters to reflect the new point in the search space.
2. Simulate the switching cycle.
3. Obtain the waveforms from simulation and experiment. The simulation waveform may need to be interpolated to get a uniform sample rate. Also normalize the waveforms to the off-state voltage and on-state current (i.e. divide V_{CE} by V_{DC} , I_C by I_F).
4. Calculate the instantaneous power dissipation for each ($= V_{CE} \times I_C$).
5. Window two sections of each waveform: one around the turn-on event, one around turn-off.
6. Calculate the cross-correlation of the windowed waveforms (MATLAB function `xcorr`).
7. Search for the maximum cross-correlation (MATLAB function `max`).
8. Apply the shift (the number of samples to which the maximum cross-correlation applies) to synchronize the waveforms for both turn-on and turn-off.
9. Re-window the shifted waveforms.
10. Subtract the simulated waveforms (V_{CE} and I_C for both turn-on and turn-off) from their experimental counterparts. Square the differences and sum them to give the sums of square errors (SSEs).
11. The error figure f_e equals the sum of the four SSEs.

Parameter Optimization

Optimization techniques rely on finding the minimum of an objective function (also known as a cost function). This is specific to a particular problem, and must be a function of the system parameters. The optimum set of parameter values will give the minimum objective function, which is in this case the error figure f_e between the measured and simulated waveforms.

Common optimization techniques used in power engineering, including the design of circuits, components and machines, are optimization by steepest descent or stochastic searches. Steepest descent, a traditional method of optimization, suffers from only being able to find a local minimum, not necessarily the global minimum, and is dependent on the start position. This can be ameliorated using additional heuristics such as a variant of the Tabu Search [Connor1998]. Stochastic searches such as simulated annealing and genetic algorithms find the global minimum more effectively by introducing random parameter variation [Lindfield]. The advantage of using these is their complete and relatively quick search of the parameter space. However this is only of benefit where the objective function is likely to be multi-modal, i.e. contain many minima.

In the case of parameterization the starting point is likely to lead directly to the global minimum since the model is accurate and the initial parameter set should be a good estimate. Hence a simple direct search, without additional heuristics, may be used. In addition, the search time must be kept reasonably low, particularly since the number of parameters is high, giving a large parameter space. Using genetic algorithms or simulated annealing would increase the search time prohibitively.

In the direct search [Murray], locating a minimum relies on the method of steepest descent. For analytic objective functions, the gradient can be calculated at any point. Frequently though, the objective function is not an analytic function of the parameters, and as this is the case here, the use of the direct search is dictated. Therefore the objective function must be evaluated at points surrounding the current position in the parameter space.

The Hooke and Jeeves Search [HookeJeeves1961] is a variant on the direct search. After evaluating the objective function at points surrounding the current (base) point, a move in a particular direction is made, and then a test is made to see if further movement in the same direction would give another reduction in the objective function. This is known as a *pattern move*, and can increase the speed at which the minimum is reached. It is particularly useful with a large number of parameters, where the cost of re-evaluating the space surrounding a particular point is high. A feature from the Tabu Search is added, which ensures that points visited recently (i.e. the last M base points) are not re-visited. M is typically between 5 and 10 for small-scale problems (up to 12 parameters), and is set to 8 here. If the error figure does not improve on the global minimum within two base points, the search terminates. Finally, if the simulation suffers from convergence problems, including a time-out, where the number of time steps exceeds a specified limit, the waveform evaluation returns an objective value of infinity. This forces the optimization algorithm to ignore this point and continue searching in other directions. Fig. 13 shows a graphical example of the direct search with two variables.

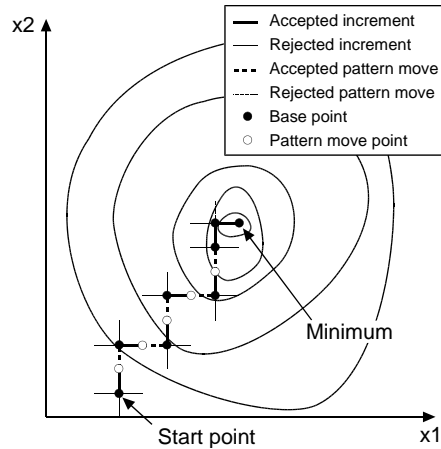


Fig. 13. Example of Hooke & Jeeves direct search with two variables.

A summary of the optimization process is:

1. Start at initial (base) set of parameters, perform the simulation and obtain the error f_e (i.e. the objective function).
2. Simulate and evaluate the error at each surrounding point, i.e. $\pm\Delta x_i$ for each parameter x_i . This requires twice the number of evaluations as there are parameters.
3. Find the lowest (i.e. best) out of these, and move there. If this is lower than the base point, this becomes the new minimum and the new base point. If none are lower than the base point, the minimum has been found so the search is terminated.
4. Move in the same direction as the move to the new base point and re-simulate and evaluate the error (this is the pattern move). If the error is lower still, then this becomes the new base point and minimum.
5. Return to step 2, ensuring that previously visited points are not re-visited (this feature from the Tabu search saves the execution time).

Results

A. Validation of the IGBT Model and Parameter Extraction

In order to validate the analytical IGBT model and the initial parameter extraction method (step 1), the IGBT model with extracted parameters was used to simulate the switching behavior of various structure IGBTs from different manufacturers. They are listed in Table IV.

TABLE IV. IGBTs TESTED

IGBT	Structure	Rating	Manufacturer
A	Trench PT	600V/600A	Powerex
B	DMOS PT	1200V/600A	Powerex
C	DMOS NPT	1200V/100A	Dynex
D	Trench Field Step	1200V/80A	Infineon
E	DMOS NPT (with diode)	1700V/400A	Semikron

In order to avoid the effects introduced by the external circuit, the validation experiments were performed under a simple hard switching environment, including resistive and clamped inductive load test circuits. The current generation of IGBTs generally has very fast switching speeds and becomes

sensitive to the circuit parameters; therefore these parameters, such as parasitic inductance, have to be precisely measured and accounted for in the simulation.

The comparison between the experimental and simulated results for various IGBTs at turn-off under clamped inductive load circuit is seen in Figs. 14(a), 14(b) and 14(d). Note that large snubbers across the diode and the IGBT were used in these tests as described in the figure captions. Resistive switching was used for the results shown in Fig. 14(c). The time scale is 200ns per division. The simulations were carried out in PSpice.

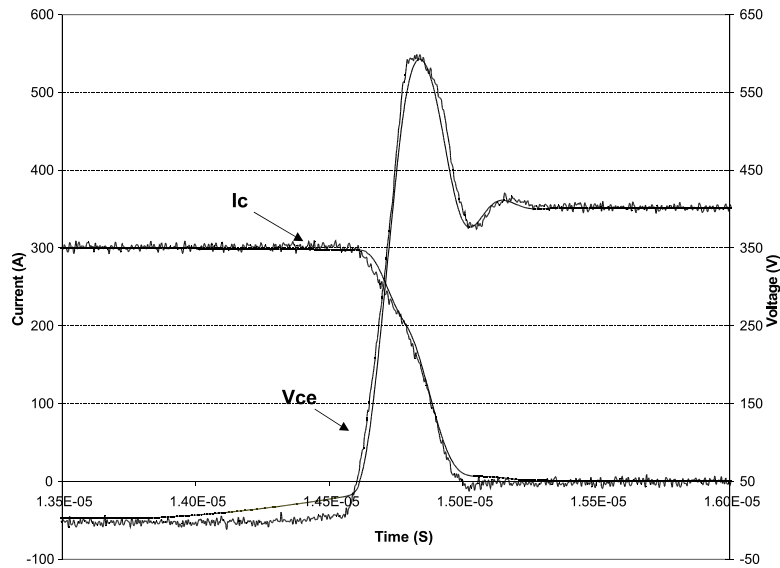


Fig. 14(a). Comparison of experiment and simulation for IGBT A at turn off at 400V/300A (inductive switching). The IGBT had an R-C snubber of 3.4Ω -9.4nF and the diode had an R-C snubber of 3.4Ω -20nF.

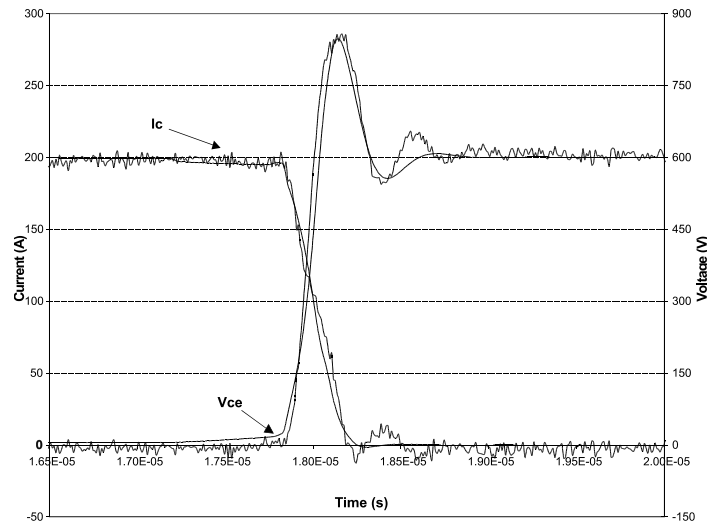


Fig. 14(b). Comparison of experiment and simulation for IGBT B at turn off at 600V/200A (inductive switching).

The IGBT had an R-C snubber of 3.4Ω -9.4nF and the diode had an R-C snubber of 3.4Ω -5nF.

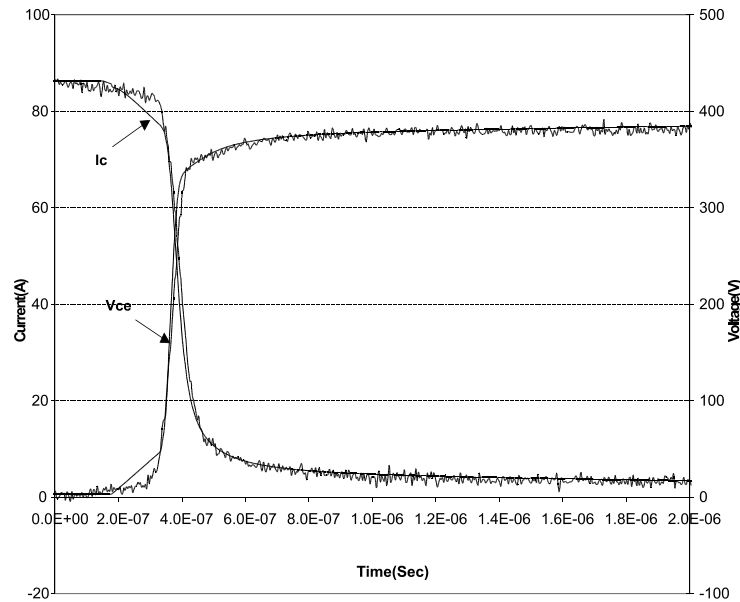


Fig. 14(c). Comparison of experiment and simulation for IGBT C at turn off at 400V/90A (resistive switching). No snubber was used.

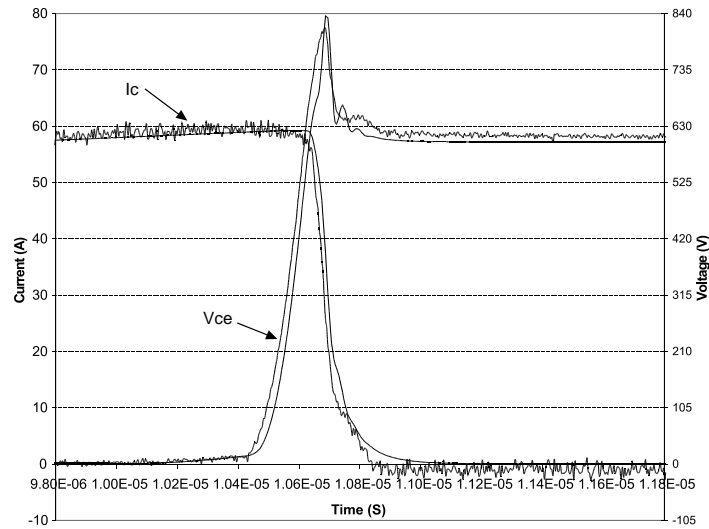


Fig. 14(d). Comparison of experiment and simulation for IGBT D at turn off at 600V/60A (inductive switching). The IGBT had no snubber and the diode had an R-C snubber of 3.4Ω -14nF.

Optimization of IGBT and diode parameters

IGBT E was tested in a clamped inductive load circuit. The initial parameter extraction (step 1) was used to obtain estimates of the parameters, a selection of which is shown in table V.

Experimental waveforms for both turn-on and turn-off were obtained for several sets of conditions. The conditions varied were the load current I_F , the supply voltage V_{DC} and the on-state period $t_{on} = \rho T_S$. Optimization of the parameters in table V was performed for each set of conditions. The simulations were carried out in Simulink. The conditions, the resulting parameter variation and the percentage error reduction in total switching energy E_{SW} (relative to the experimental waveforms) are given in table V. Each of the 12 parameter optimizations took an average of 21 minutes to run, using a Pentium IV machine with 512MB RAM running Windows 2000. Each simulation lasted between 3 and 4 seconds, therefore requiring approximately one minute for the search space around each base point to be evaluated with nine parameters.

TABLE V. PARAMETER VALUES BEFORE AND AFTER OPTIMIZATION.

Index	Conditions			IGBT					Diode		Circuit		E_{SW} error	
	V_{DC}	I_F	t_{on}	A	τ	W_B	N_B	h_p	A	τ	L_E	L_S	Before	After
Initial				4.0	6.7	200	6.7	5.0	4.0	0.30	1	400		
1	225	51	20	3.8	6.7	157	5.3	14.4	4.4	0.19	1	357	47	26
2	230	53	10	3.8	6.7	170	4.2	14.4	4.0	0.19	1	318	56	26
3	220	51	30	3.8	6.7	170	4.2	11.1	4.0	0.19	1	357	45	17
4	345	78	30	3.5	6.7	123	5.3	20.0	4.0	0.19	1	357	33	5
5	350	80	20	3.0	10.6	157	5.3	14.4	3.0	0.19	1.2	357	75	2
6	350	80	10	3.0	10.6	200	5.3	11.1	3.6	0.15	1	357	38	7
7	450	128	10	2.1	5.3	123	6.7	6.5	3.8	0.19	1	357	33	5
8	450	58	10	2.3	10.6	235	10.6	0.5	2.0	0.24	1	357	61	49
9	455	59	20	4.0	6.7	200	8.4	2.9	3.3	0.24	1	400	52	52
10	800	101	20	2.1	100.0	105	16.8	2.3	2.0	0.24	1	357	17	8
11	810	147	20	3.2	6.7	157	6.7	5.0	3.0	0.24	1	357	13	2
12	800	212	20	2.4	33.6	114	13.4	2.3	3.5	0.24	1	357	16	0
Units	V	A	μs	cm^2	μs	μm	$10^{13} cm^{-3}$	$10^{-12} cm^4 s^{-1}$	cm^2	μs	nH	nH	%	%
Mean				3.1	17.6	159	7.7	8.7	3.4	0.21	1.0	357		
Standard deviation				0.7	25.9	37.6	3.8	6.0	0.7	0.03	0.1	17		
Std dev as % of mean				22	147	24	50	69	22	14	5	5		

Figs. 15 and 16 show the normalized voltage and current waveforms before and after optimization for test 1, table V for turn-on and turn-off respectively. The power dissipation waveforms are obtained by multiplying the voltage (V_{CE}) and current (I_C) waveforms.

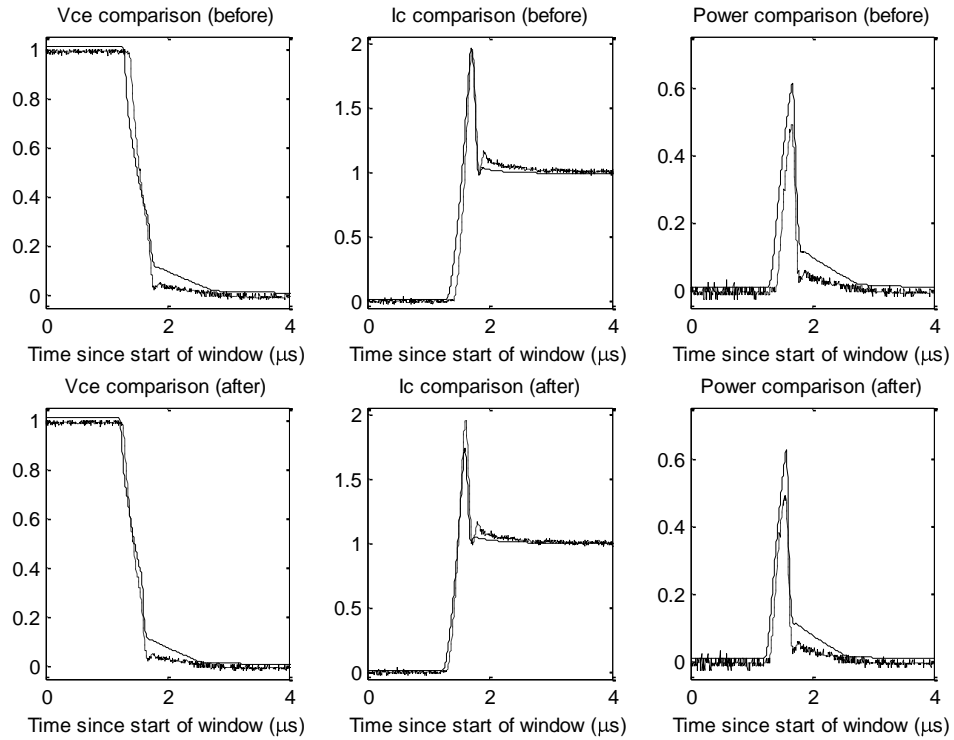


Fig. 15. Comparison of experimental waveforms (dashed) and simulated waveforms (solid) of IGBT turn-on before and after optimization for test 1 (IGBT E, 225V, 51A). Voltage and current traces are normalized relative to the supply voltage V_{DC} and load current I_F , and the power dissipation is normalized relative to $V_{DC}I_F$.

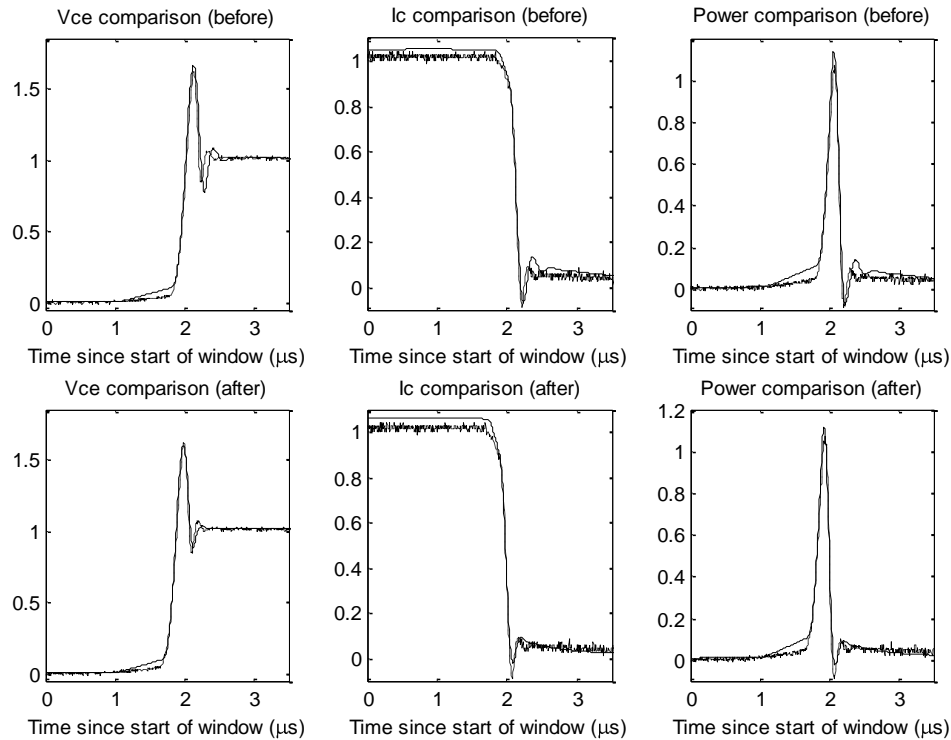


Fig. 16. Comparison of experimental waveforms (dashed) and simulated waveforms (solid) of IGBT turn-off before and after optimization for test 1 (IGBT E, 225V, 51A). Voltage and current traces are normalized relative to the supply voltage V_{DC} and load current I_F , and the power dissipation is normalized relative to $V_{DC}I_F$.

Discussion

The waveforms in figs. 15-16 show that the optimization procedure improves the matching of both the device waveforms and the power dissipation during switching. The waveforms are shown after synchronization, with the start of the window ($t=0\mu\text{s}$) coincident with the appropriate edge of the simulation gate drive signal V_{GG} . The synchronization using the power dissipation for cross-correlation produces well-aligned voltage and current waveforms.

The matching of experimental and simulated waveforms is particularly close during turn-off. The main source of error is in the voltage (V_{CE}) waveforms, where the voltage ramps during the gate plateau are too large. This is also visible in figs. 14(a)-14(c), and is being addressed in current work.

The results in table V show that most parameters vary by up to approximately 25%. The diode and IGBT areas A , the diode lifetime τ_{HL} and IGBT drift region width W_B only vary slightly from the initial set of parameters. This shows that both the initial parameter estimation is good and that the optimization is effective: indeed it recognizes that no significant refinement of these parameters is necessary. The switching energy errors decrease significantly in all optimizations, except for runs 8 and 9. This is because the devices have a long tail current, and the small error in current during the tail gives a large error in switching energy loss due to the integration end point timing. The choice of least squared errors between waveforms for the objective function results in a reduced sensitivity to this

period of the switching waveform. Thus the estimated values of the IGBT carrier lifetime τ_{HL} and the recombination parameter h_p can be expected to vary more widely than the other parameters. As no lifetime control is used in NPT IGBTs, a carrier lifetime of 100 μ s is not unusual, as found in run 10, and the behaviour of an IGBT under conventional switching is not greatly influenced unless very short lifetimes are used. A further issue arises associated with the absolute accuracy of the experimental current tail waveform, where an error will cause a poor estimate for h_p . Finally, in index 5 the simulated waveforms before optimization exhibit reduced convergence (while still completing simulation), giving a large turn-off energy loss. The waveforms after optimization do not show this, demonstrating the ability of the optimization to remove this discrepancy.

The diode reverse recovery clearly affects the IGBT current overshoot at turn-on. The current overshoot is an important contribution to the power dissipation of the IGBT, and as a result the diode parameters must be optimized in addition to those of the IGBT. This is an example of the coupled nature of IGBT and diode interaction in an inductive hard-switching environment, previously discussed in [Bryant2002].

The validity of the model across the range of conditions chosen is good, shown by the low variation (up to 25%) of the parameter values. This emphasizes the accuracy of the model. It may be observed that the on-state period t_{on} , associated with the duty ratio ρ , has no significant effect on the optimized parameter values. Therefore there is no need to vary this condition in practical parameter optimization. It is left to the user to choose representative operating conditions, having no practical impact on the optimization and resulting simulations, as would be expected for a robust and well-formed model. If several sets of conditions are used, taking the mean of the parameters across the conditions would be a suitable method of obtaining one set of parameter values.

A number of sets of conditions should be tested, over a wide range as illustrated in table V, to obtain a set of final parameter estimates which are robust across a wide range of conditions. Achieving this avoids the danger of creating a set of parameters unique to particular conditions. Adopting the mean parameter values offers a practical approach. A parameter validity map [AllardPESC2003] could be generated to indicate the matching of the experimental and simulated waveforms for different conditions, allowing designers to make informed decisions regarding the validity of the models. The conditions important in the application considered can be determined with the use of condition maps [BryantIAS2004], which give the most likely sets of conditions for a particular load cycle. The use of these would allow the suitability of the models and parameters to be justified and point towards the suitable conditions under which the optimization of parameters should take place.

Conclusions

A practical parameter extraction method is provided for the Fourier-based-solution analytical IGBT model. Since the extraction procedure is general in nature, some methods used in the research are also suitable for the extraction of some parameters needed for other kinds of IGBT models. Once the parameter optimization is complete, the parameters may be used in models on any platform, including circuit simulators such as PSpice.

By jointly using three general parameter extraction methods – empirical value-based extraction, datasheet-based extrapolation, and simple test-based extraction – the total extraction procedure only needs a simple clamped inductive load test for the extraction of 12 and 15 parameters needed for the NPT and PT IGBT models respectively.

The validation with the experimental results from various structure IGBTs demonstrates the accuracy of the proposed IGBT model and the parameter extraction method. The combination of an initial parameter extraction and a parameter optimization procedure provides a solid foundation for automated parameter extraction. The use of MATLAB as a common environment allows simple implementation of the extraction procedure. The optimization results show a clear improvement in simulation accuracy from the initial parameter estimates. However, depending on the intended use of the simulation models, in some cases the accuracy obtained from the initial parameter extraction may be deemed sufficient, making the optimization step unnecessary.

Designing Survivable Electric Power Systems

Survivability, or the ability to provide uninterrupted power flow to loads in spite of multiple simultaneous faults caused by natural or hostile disruptions, is a desirable feature of any power system. In all-electric naval platforms, the ability to withstand multiple simultaneous unrecoverable faults in a battle field is a vital requirement for the integrated power system (IPS), since power interruption or its total loss during a battle would most certainly lead to mission failure, personnel loss, and possibly complete destruction of a ship. The goal of this study is to enhance survivability of power systems subject to multiple simultaneous faults caused by natural and/or hostile events.

The Project has three objectives:

- develop mathematical framework to analyse power system survivability;
- develop computational algorithms for evaluating power system survivability;
- design power systems of enhanced survivability.

Key factor determining survivability of the power system is its topology or design – the number of generators, their connections with one another and loads. Indeed, reliability of equipment alone is no protection against destruction caused by direct hits. How much reconfiguration is possible in a given IPS is also limited by its topology. Therefore, structural (topological) survivability is the current focus of the Project.

In our study, we develop mathematical and numerical tools to analyze structural (topological) survivability of IPS under multiple simultaneous unrecoverable faults. In particular, we

- developed probabilistic approach to evaluate structural survivability of different power system topologies;
- evaluated and compared structural survivability of various generator bus topologies of two, three, and four generators;
- suggested a new web topology of enhanced structural survivability;
- developed and validated a computational algorithm based on the graph approach to evaluate structural survivability of power systems.

Possibility of detecting and isolating faults in a given power system topology also influences the total system survivability. Current protection standards do not meet the challenges associated with increased complexity of modern power systems. We are working on adapting the model-based fault detection and isolation approach based on structural analysis to evaluate the monitoring potential of the power system in a systematic and automated manner. Such an approach is particularly promising for successful wide-area protection of the complex IPS.

Technical Details by Task or Project:

- Key Accomplishments

Developed and validated a computational algorithm based on the graph approach to evaluate structural survivability of different power system topologies (designs) under multiple simultaneous unrecoverable faults.

- Technical Detail

Introduction

The ability to withstand multiple simultaneous faults caused by natural and hostile disruptions is a desirable feature of any power system. Such disruptions are sudden, massive in scale, often without the possibility of being repaired in the short term. For some complicated modern systems, such as the integrated power system of an all-electric ship, the requirement of survivability is vital. Power interruption on a battlefield can have drastic consequences for a ship, its crew, and the mission. Natural and hostile disruptions are less expected in utility power systems. However, the consequences of such an occurrence can be enormous in cost and scale. Therefore, survivability is a critical issue in designing any power system.

Total survivability of the power system is determined by various factors [1]. One of the key contributors to power system survivability is its topology (or design). The number of generators included in the system, how they are connected with each other and with loads, and how the loads are connected between themselves determine whether power will be available to the loads after disruption occurs. A highly reliable system with a poorly chosen topology might not survive a natural disaster or hostility.

To compare survivability of different topologies, the quantitative analysis of topological survivability – the capacity inherent in a system’s structure to maintain operations after receiving damage – is required. Due to specifics of damage resulting from natural and hostile disruptions, the traditional reliability/availability analysis is not applicable to the present problem. Notice that the analysis of structural (topological) survivability complements rather than replaces the reliability/availability analysis for a specific type of damage. It is a part of the comprehensive system analysis.

The analysis of structural survivability of existing power systems and the design of power systems with enhanced structural survivability is the goal of the current study.

The theoretical background for the analysis of structural survivability of power systems was developed in [2-5] and was employed for comparing structural survivability of existing topologies of the IPS generator bus containing up to four generators. However, evaluation of the structural survivability of complex IPS systems requires automated computer analysis. We developed a graph-based approach (described below) to compute and compare structural survivability of power systems.

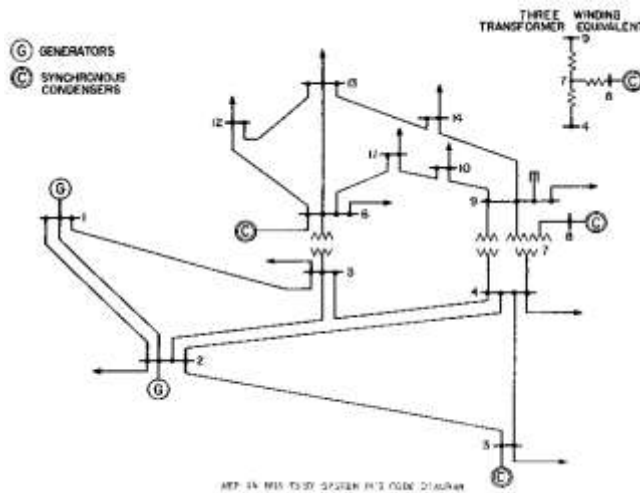
Analysis of Structural Survivability

For the purpose of the analysis of topological survivability, all elements of the power system may be divided into two groups. The first group contains generators and the transmission lines linking them. We call the links between generators horizontal links. The first group also includes the links connecting the generators with the system loads (vertical links). A vertical link can be attached to any element in the first group. Loads and the links between them form the second group. Faults in the first group can result in decreasing the power supply to loads up to complete service interruption. Faults in the loads and the links between them do not influence the ability of the first group to supply power. Clearly, survivability of the first group determines survivability of the whole system. Therefore, the main focus of the analysis of topological survivability of the power system is on the survival ability of the first group topology.

As an example of grouping elements of a power system for the analysis of its topological survivability, let us consider the IEEE 14 Bus Test Case (Fig. 1), representing a portion of the American Electric Power System (in the Midwestern United States) as of February 1962. Fig. 2 represents this test case, with the elements of the power system being grouped according to the scheme just described. In the dashed box representing the first group, two black circles marked by G represent the two generators. The six links, which start from nodes 2-5 and end with arrowheads, are the vertical links from the first group to the second group. All links inside the dashed box representing the first group are horizontal links. Nodes 1-5 in Fig. 2a correspond to nodes 1-5 in the IEEE 14 Bus Test Case. In the dashed box representing the second group, loads and links between them are not shown; nodes 6-14 from the IEEE 14 Bus Test Case are inside this box.

Fig. 1. IEEE 14 Bus Test Case

Since the topology of only the first group of the power system is under investigation, the second group can be



removed entirely from consideration. For the IEEE 14 Bus Test Case, this results in the transformation of Fig. 2a into Fig. 2b.

If one denotes the number of generators as g , the number of horizontal links as h , and the number of vertical links as v , then the total number of elements in the first group is $M = g + v + h$. In Fig. 1b, $M = 18$, $g = 2$, $v = 6$, and $h = 10$. In the present analysis it is assumed that all horizontal links in the first group are in operation prior to damage occurring. Potential reconfiguration schemes within the elements of the first group are not considered.

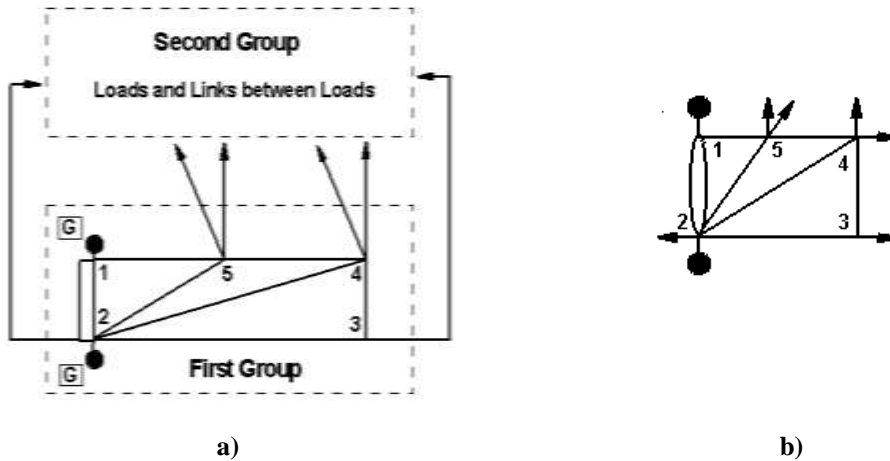


Fig. 2. Group representation of the IEEE 14 Bus Test Case [(a) and the topology of the first group for the same test case (b).

Faults considered here are those connected with the multiple losses of cables and generators due to combat damage. The nature and sequence of faults do not enter into this study; multiple faults are considered to be simultaneous and not repairable in the time frame in which survivability is being studied. (That is, system protection will be assumed to have isolated short circuits, but the short circuits themselves will not be repaired.)

Each possible combination of m damaged elements from the total number of elements M is defined as a fault scenario. There are three types of fault scenarios, based on the three types of responses from the second group of the power system:

- “no response” scenarios;
- reconfiguration scenarios;
- scenarios of complete failure.

In “no response” scenarios, no generator is damaged, and faults in horizontal and vertical links do not isolate any of the generators. That is, after the faults, the first group of the power system is still able to supply power produced by all generators to the second group and no response from the second group is required. In such cases, we say that the system survives without requiring reconfiguration in the second group. We denote the number of “no response” scenarios by S .

Scenarios in which power supplied from the first group to the second group is reduced, either due to damage of at least one generator or due to faults in vertical and horizontal links isolating at least one generator, require reconfiguration in the second group. Therefore, such scenarios are called reconfiguration scenarios. In this case, we say that the system survives but requires reconfiguration in the second group. The total number of reconfiguration scenarios is R .

Scenarios in which all generators, or all vertical links, are damaged, or in which generators, horizontal and vertical links are damaged so as to lead to a complete interruption in power supply, are called scenarios of complete failure. Their number is denoted by F .

At a number of faults m , the total number of fault scenarios leading to each response of the second group can be used to determine the response probability P , under the assumption that each scenario is equally likely. We thus define the probability P as the ratio of the number of fault scenarios resulting in a second group response to the total number of fault scenarios N at a given m :

$$P(S) = S(m) / N(m), P(R) = R(m) / N(m), P(F) = F(m) / N(m),$$

where $P(S)$ is the survival probability without reconfiguration in the second group, $P(R)$ is the survival probability with reconfiguration in the second group, and $P(F)$ is the probability of complete failure. The probabilities of the three responses sum to unity: $P(S) + P(R) + P(F) = 1$.

The total number of scenarios N at a given m is

$$N(m) = \frac{M!}{m!(M-m)!}, \quad m \leq M \tag{1}$$

where $k! = 1 \cdot 2 \cdot \dots \cdot k$ ($k = m, M$) is the factorial. If $m > M$, there is only one scenario and this is the scenario of complete failure, because all elements in the first group have already been damaged and no power is available for the second group. In this case, $N(m) = F(m) = 1$, $P(F) = 1$, and $P(S) = P(R) = 0$ at any m .

These three probabilities characterize survivability of the first group topology at a given number of faults and can be used to compare the performance of different topologies. To calculate these probabilities in a more realistic manner, one should also take into account the probability of occurrence of each scenario, which depends on the probability of damage for links and generators included in the scenario. Such an analysis is called a susceptibility analysis and, to the best of our knowledge, it has not yet been developed. It is clear, however, that realistic evaluation of the probability to be damaged for different elements in the first group requires knowledge of the sizes of the system elements, the scales of possible damage, the protection scheme in use, and other specifics. Without such information, it is reasonable to assume that all elements in the first group have equal probability of being damaged and all fault scenarios are equally likely. This is the approach currently used in our study. However, this is not a requirement of the analysis or of the numerical algorithm discussed below. If the probabilities of different scenarios are known, the analysis and the algorithm can easily incorporate this knowledge. We are going to combine the analysis of topological survivability with the susceptibility analysis in our future studies.

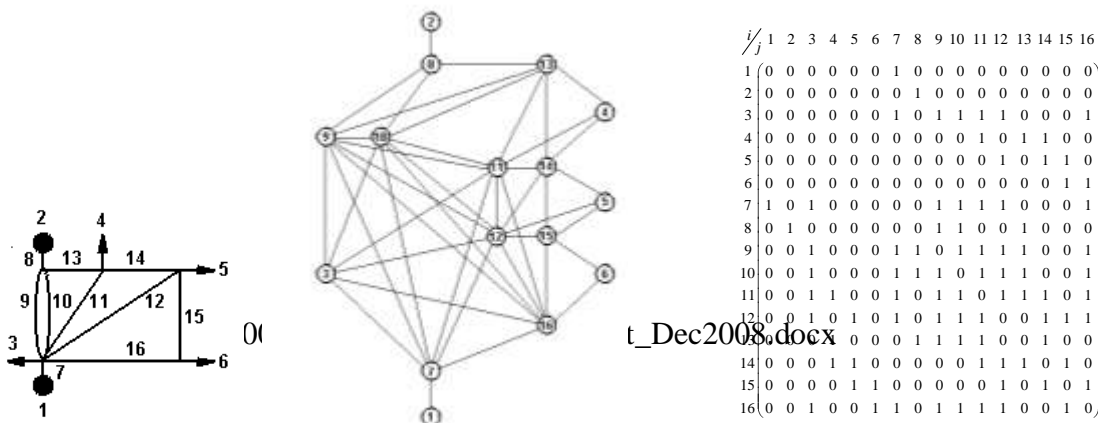
Numerical Algorithm

As the number of elements in the first group increases, the total number of scenarios N at a given m increases drastically (see (1)). Computational solutions become the only choice. Below we describe a numerical algorithm, which allows one to compute the numbers $S(m)$, $R(m)$, $F(m)$, $N(m)$, and the corresponding probabilities.

Graph Representation of the First Group Topology

The first step is to represent the first group of a power system as an undirected graph, with each group element being considered as a node. If between two elements there exists a physical connection, we say that the two nodes corresponding to these two elements are connected by the edge.

As an example, let us consider the topology shown in Fig. 3a. Comparing it with the topology in Fig. 3b, we see that there are only single vertical links adjacent to the nodes. The influence of multiple vertical links adjacent to the same node on system survivability was discussed in detail [3-4]. The topology in Fig. 3a contains 16 elements ($M = 16$), which are now considered as 16 graph nodes. Generator 2 and horizontal link 8 (nodes 2 and 8), for example, are physically connected. Therefore, there is an edge between



elements 12 and 14, elements 5 and 12, and so on. Elements 9 and 10 have two physical connections. However, when there is a fault in one of the elements, any connection between them becomes inactive. Therefore, connections between these two elements should be represented by a single edge. Graph representation of the topology in Fig. 3a is given in Fig. 3b.

a) b) c)

Fig. 3. Topology of the first group (a), its graph representations (b), and the corresponding adjacency matrix (c).

An undirected graph can be represented by the adjacency matrix, which is the $M \times M$ symmetric matrix \mathbf{X} . If there is an edge from node i to node j , then the matrix element $X_{i,j}$ is 1, otherwise it is 0. Matrix indices correspond to the graph nodes. In our study, indices from 1 to g are reserved for the generators, and indices from $g + 1$ to $g + v$ for the vertical links. The matrix corresponding to the graph in Fig. 3b is shown in Fig 3c. Diagonal matrix elements are equal to zero.

A graph like the one in Fig. 3b and a matrix like the one in Fig. 3c represent only the topological structure of the first group of a power system. To evaluate the structural survivability, a numerical algorithm should also “know” which nodes are generators, that is, power sources, and which are vertical links, that is, power sinks. It is achieved by assigning to the graph node i some quality E_i , which is equal to 1 if a node is a generator and to -1 if a node is a vertical link. For the horizontal links, that is, the nodes with i running from $g + v + 1$ to M , $E_i = 0$. For the graph in Fig. 3b, the corresponding vector $\mathbf{E} = E_i, i = 1, \dots, M$ is

$$\begin{array}{l}
 i: \quad 1 \ 2 \ 3 \ 4 \ 5 \ 6 \ 7 \ 8 \ 9 \ 10 \ 11 \ 12 \ 13 \ 14 \ 15 \ 16 \\
 \mathbf{E} = 1 \ 1 \ -1 \ -1 \ -1 \ -1 \ 0 \ 0 \ 0 \ 0 \ 0 \ 0 \ 0 \ 0 \ 0 \ 0
 \end{array}$$

Matrix \mathbf{X} and vector \mathbf{E} contain the complete information on how many elements the first group contains, how many of them are generators, how many links deliver power to the second group, and how the elements are connected with each other. For the sake of simplicity, we assume that all generators produce the same amount of power and all vertical links have equal loads. For specific applications, this assumption can easily be adjusted by changing the values of E_i from 1 and -1 to values between 1 and -1 .

Representation of Faults

The next step in the algorithm is to represent faults in elements of the first group. We assign to the graph node i some quality K_i such as $K_i = 0$ if there is a fault in node i and $K_i = 1$ otherwise. Remember that this study considers only unrecoverable faults. That is, nodes once damaged are considered being unavailable for power flow. Multiple faults in the same node do not influence the results of the analysis and therefore, are not considered. For the graph in Fig. 3b, the following vector $\mathbf{K} = K_i, i = 1, \dots, M$

$$\begin{array}{l}
 i: \quad 1 \ 2 \ 3 \ 4 \ 5 \ 6 \ 7 \ 8 \ 9 \ 10 \ 11 \ 12 \ 13 \ 14 \ 15 \ 16 \\
 \mathbf{K} = 0 \ 1 \ 1 \ 0 \ 1 \ 1 \ 1 \ 1 \ 0 \ 0 \ 0 \ 1 \ 1 \ 0 \ 1 \ 0
 \end{array}$$

reflects, for example, faults in one generator (node 1), one vertical link (node 4), and five horizontal links (nodes 9-11, 14, and 16). In this topology, such faults cause the complete interruption of the power supply from the first group to the second group. The total number of \mathbf{K} -vectors is $N = 2^M$. For the graph in Fig. 3b, $N = 65536$. The vector with all $K_i = 1$ corresponds to no damage in the first group.

Each \mathbf{K} -vector, except the one with no damage in the nodes, represents a fault scenario. The relation between the total number N of \mathbf{K} -vectors and the total number of fault scenarios $N(m)$ at $m \leq M$ is $N = \sum_{m=1, \dots, M} N(m) + 1$.

\mathbf{K} -vectors are generated in the following manner. Each vector is assigned its order number r running from 1 to 2^M . Then, for each vector with order number r , we convert the decimal number equal to $r-1$ to the corresponding binary number. As an example, let us consider again the graph in Fig. 3b. For this graph, the number r runs from 1 to 65536. The first vector with $r=1$ has the corresponding number $r-1=0$, which is (0 000 000 000 000 000) in binary form. That is, this is the vector with all nodes being damaged. The vector with $r=1001$ has the corresponding number $r-1=1000$, which is (0 000 001 111 101 000) in binary form. That is, nodes 1-6, 12, and 14-16 are damaged. The vector with order number r equal to 65536 corresponds to the graph with no damage in the nodes. Indeed, the number $65535 = 65536 - 1$ is (1 111 111 111 111 111) in binary form.

Information on the topological structure contained in matrix \mathbf{X} can be combined with information about faults contained in the \mathbf{K} -vector by forming matrix \mathbf{Y} such that its elements are determined as $Y_{i,j} = X_{i,j} \cdot K_i \cdot K_j$. That is, matrix \mathbf{Y} is, in fact, matrix \mathbf{X} where connections between a faulty node and neighboring no-fault nodes have been removed.

Analysis of Matrix \mathbf{Y}

After disruption, the initial topology of the first group changes, because some elements in the first group become unavailable for power flow. One has to analyze whether in a new topology there are generators to produce power, vertical links to deliver power to the second group, and connections between available generators and vertical links. For instance, if all generators have no damage and there is at least one vertical link with no damage, and each generator can be connected to this vertical link by any combination of other generators and horizontal links or only by horizontal links, then this fault scenario is a “no response” scenario, and the number $S(m)$ is increased by 1 at a given number of faults. Any combination of the first group elements, which connect a generator to a vertical link, is called the path. Let us emphasize that a single path between a generator and a vertical link is sufficient to state that power produced by this generator is available for the second group of the power system. The number of generators for which power is available after damage to the second group, indicates whether the power supply was preserved, reduced, or interrupted.

Graph representation of the first group topology allows one to employ mathematical tools for conducting such an analysis in an efficient manner. In matrix \mathbf{Y} corresponding to the topology, the elements $Y_{i,j} \neq 0$, $i, j = 1, \dots, g$, and $i, j = g + 1, \dots, g + v$ indicate the presence of generators and vertical links without faults after damage described by a vector \mathbf{K} . Then, the depth-first search algorithm for traversing a graph is used to check whether there is a path between an undamaged generator and a vertical link without fault. This algorithm is generally known (see, e.g., [6]) and will not be described here. The search for a connection between a generator and vertical links stops as soon as at least one path between the generator and any vertical link without fault is established. The search for connection between the next undamaged generator and available vertical links is initiated immediately afterwards.

The \mathbf{E} -vector after faults is called the \mathbf{E}' -vector with elements E'_i . If a generator is damaged or there is no path between a generator and the available vertical links, the element E'_i corresponding to this generator is set to zero. Then, the amount of power $E_{tot} = \sum_{i \leq g} E_i$ produced in a given topology before faults is compared with the amount of power available after faults $E_{avl} = \sum_{i \leq g} E'_i$. If $E_{avl} = E_{tot}$, the fault scenario given by vector \mathbf{K} is a “no

response” scenario; if $0 < E_{avl} < E_{tot}$, the scenario is a reconfiguration scenario; and if $E_{avl} = 0$, the scenario is the scenario of complete failure. Respectively, either the number $S(m)$, $R(m)$, or $F(m)$ is increased by 1 at a given number of faults.

When all matrices \mathbf{Y} corresponding to the entire set of \mathbf{K} -vectors have been analyzed, that is, the numbers $S(m)$, $R(m)$, and $F(m)$ are computed at $m \leq M$, the probabilities $P(S)$, $P(R)$, and $P(F)$ are calculated at each $m \leq M$.

For the topology in Fig. 3b, the probabilities $P(S)$, $P(R)$, and $P(F)$ at different m are shown in Table 1. Figure 4 shows how these probabilities change with increasing m .

TABLE I
 TOPOLOGY IN FIG. 3A
 ($g = 2, v = 4, h = 10$)

m	N	S	R	F	$P(S)$	$P(R)$	$P(F)$
1	16	12	4	0	0.75	0.25	0
2	120	66	50	4	0.55	0.42	0.03
3	560	219	289	52	0.39	0.52	0.09
4	1820	485	1019	316	0.27	0.56	0.17
5	4368	744	2434	1190	0.17	0.56	0.27
6	8008	782	4120	3106	0.1	0.51	0.39
7	11440	520	4982	5938	0.05	0.43	0.52
8	12870	177	4179	8514	0.01	0.33	0.66
9	11440	30	2260	9150	0	0.2	0.8
10	8008	2	767	7239	0	0.1	0.9
11	4368	0	160	4208	0	0.04	0.96
12	1820	0	19	1801	0	0.01	0.99
13	560	0	1	559	0	0	1
14	120	0	0	120	0	0	1
15	16	0	0	16	0	0	1
16	1	0	0	1	0	0	1

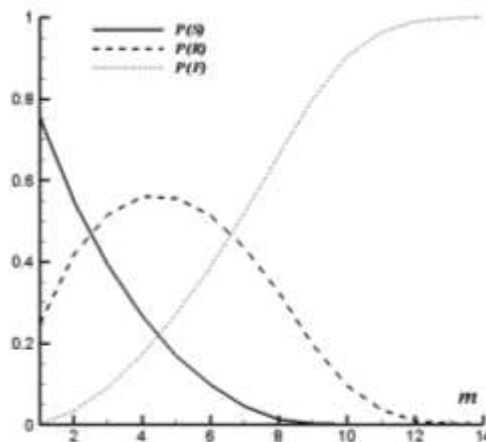


Fig. 4 Probabilities of different fault scenarios at different m for the topology in Fig. 3a.

Additional Considerations

A topology for the first group of a power system can be represented as a graph in multiple ways. Depending on the size of elements included in the first group and the scale of damage under consideration, separate elements of the first group topology can be treated as separate graph nodes or be combined into a single graph node. If the scale of disruption exceeds, for example, the length of a link, this link should be combined into a single node with other topological elements adjacent to it that would be influenced by a fault in this link.

The protection scheme should also be accounted for. For instance, if in the topology shown in Fig. 3a, link 7, generator 1, and the interconnection of links 3, 7, 9-12, and 16 are inside the same protected zone of a size smaller than damage under consideration, all of these elements should be combined into a single node-generator in the graph.

The current algorithm does not consider an interconnection of links as a separate node. An example of such an interconnection is, for instance, a point in Fig. 3a, where horizontal links 11, 13, and 14 are connected with vertical link 4. Interconnections are usually of smaller size than other topological elements and possibly have better protection due to their importance. That is, faults in interconnections are assumed to be a less probable event than faults in generators and links. Realistic evaluation of the probability of being damaged for an interconnection (or any topological element) is possible only if information on the specifics related to the real power system is available. In the general analysis as conducted in the current study, it is reasonable to assign zero probability of been damaged to an interconnection rather than an arbitrary number. Moreover, damage of an interconnection can be represented by faults in the links, which meet in the interconnection. If, however, it is of importance to consider interconnections as separate nodes, and all necessary information is available, the algorithm presented above can include (without any restriction) interconnections as separate graph nodes.

Web Topology

In the design of IPS, the redundancy of generators is a limited option for increasing survivability of the power system due to many factors including (but not limited to) the overall cost of the system's construction and weight. The link-redundancy (i.e., an increase in the number of cables connecting generators and the use of topologies where cables are interconnected in a more sophisticated manner) should also be considered. In fact, if one can show that additional links increase survivability with minimal expense, such links can be incorporated into the existing power system.

In [2], we introduced a new web topology based on the biological prototype: a web created by orb-weavers. Principal elements of the web are:

- 1 – key elements (points through which a web is connected to the remainder of the system);
- 2 – external links extending from the key elements to the remainder of the system;
- 3 – an external ring connecting key elements;
- 4 – a central point;
- 5 – links connecting a key element and the central point;
- 6 – links connecting the central point with ring segments;
- 7 – internal rings connecting the links from the central point to the key elements.

In a power system, a key element is a generator, an external link is a vertical link, and rings and links between the central point and the key elements and the ring segments are the horizontal links. For a system of k generators, the simplest algorithm to build a web is:

- link k generators in the external ring;
- place the central point;
- connect all generators with the central point;
- connect the external ring segments with the central point;

- if design and budget allow, connect the links from the central point to the key elements by additional rings.

A control center (and an additional generator) can be placed at the central point. Vertical links can be multiple and adjacent to any node including those that intersect horizontal links or at any place just for the sake of partitioning a long link. More on positioning vertical links and partitioning horizontal links can be found in [3,4]. Fig. 5 shows an example of simple two-generator and three-generator webs.

Fig. 5. Two-generator (a) and three-generator (b) webs

The superior ability of the web to withstand multiple simultaneous faults was demonstrated in [2-5] by comparing it with existing topologies containing the same number of generators or more. Among the topologies considered are radial, ring, star, meshes with different numbers of links connecting generators, and single and dual buses. Comparisons were made for topologies containing two, three, and four generators. In Fig. 7, the structural survivability of the three-generator web (Fig. 5b) is compared with the structural survivability of the four-generator ring (Fig. 6a) and the four-generator partitioned mesh (Fig. 6b). Note that crossing cables are interconnected in both the web and the partitioned mesh.

Fig. 6. Four-generator ring (a) and partitioned mesh (b)

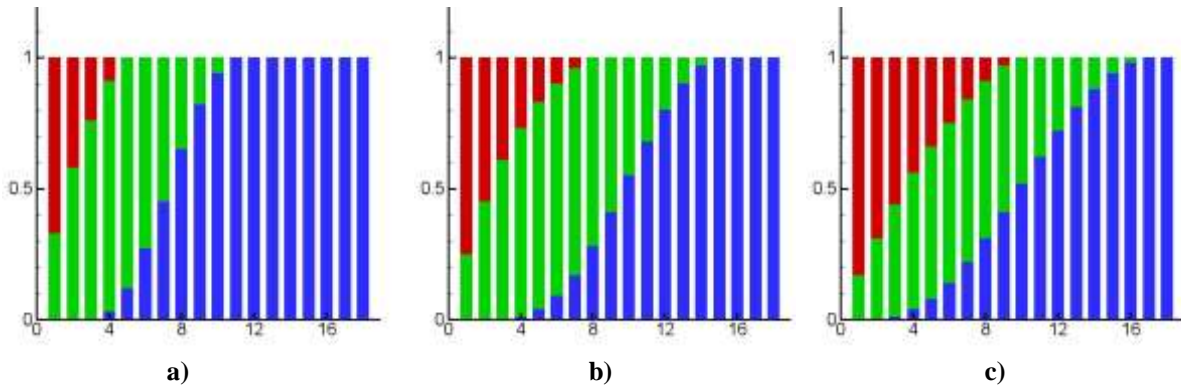
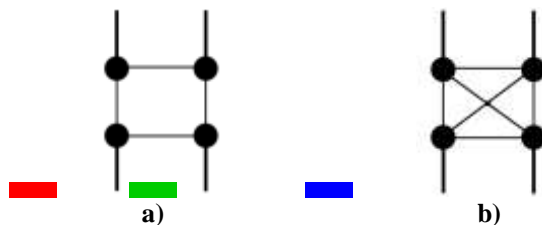


Fig. 7. Variation of structural survivability (y-coordinate) with the number m of simultaneous faults (x-coordinate) for the four-generator ring (a), the four-generator partitioned mesh (b), and the three-generator web (c). Notations: $P(S)$, $P(R)$, and $P(F)$ at a given m .

Figure 7 shows that even though the considered web-topology is applied to less number of generators than the four-generator ring, it has much better structural survivability than the ring, that is, it has higher $P(S)$ and higher the total survival probability ($P(S) + P(R)$) at a given number of simultaneous faults as well as higher number of



faults at which $P(S) + P(R) > 0$. Furthermore, it has much better ratio $P(S) / P(R)$ than the four-generator partitioned mesh, that is, it requires less reconfiguration in loads. This quality is highly valuable in a battlefield.

Research Work Related to Modeling and Simulation

Initial work activities revolved around developing models that could be integrated into the power system analysis and design tools. Many of these models were developed in VTB. More recent modeling activities have revolved around developing an integrated power system and control model that allows optimization of both systems within one algorithm.

Executive Summary

This work emphasizes modeling, simulation, rapid prototyping and hardware-in-the-loop (HIL) testing as the key stages in the design process to achieve advanced adaptive protection scheme for next generation Shipboard Power System (SPS). Developed protective controller can adapt to different protection schemes depending upon requirements. Real-time Hardware in the Loop (HIL) simulation is becoming an essential simulation tool for engineering design, especially in protection equipment. The first step for this research work is to develop relay models. Developed relay model can be validated against a commercial relay using hardware in the loop (HIL) simulation.

Researchers have developed relay model using LabVIEW. Developed relay model was tested with hardware in the loop with simulated power system in Real Time Digital Simulator (RTDS). HIL platform was developed for SEL 421, distance relay and SEL 351 over-current relay using RTDS, MATLAB/Simulink and also using National Instruments PXI controller.

Key Accomplishments:

- Development of hardware in the loop platform to test the SEL 351 (over-current) and SEL-421 (distance) relay using RTDS
- Development of hardware in the loop platform using MATLAB/Simulink and NI PXI controller
- Design and modeling of over-current relay using LabVIEW and NI PXI controller
- Organized and conducted workshop as well as hands-on experience on LabVIEW
- Presented more than 10 papers/posters based on this research work in national and international conferences

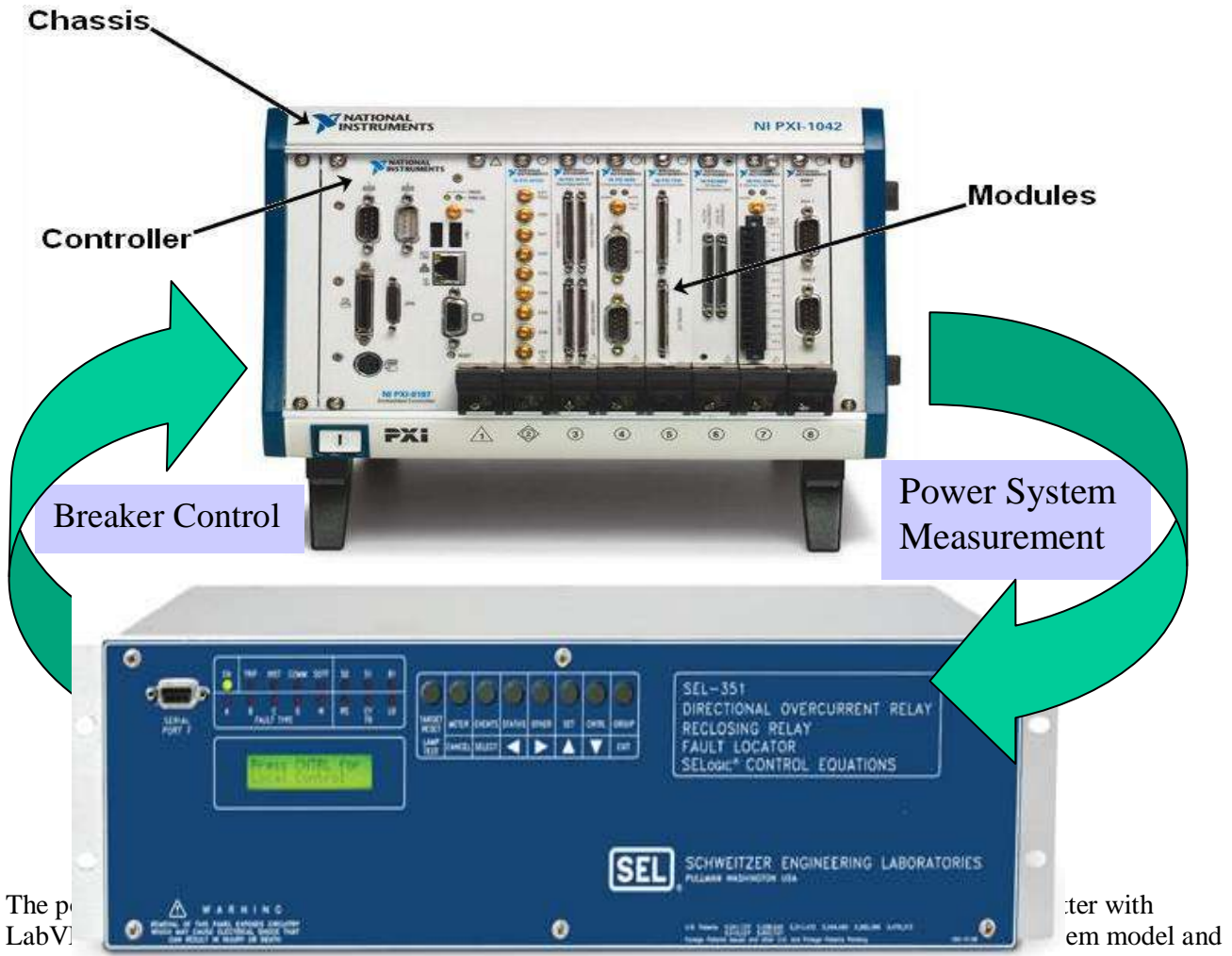
Summary of Research Activities:

1) Hardware in the loop test using National Instruments PXI controller and SEL 351

A HIL simulation refers to a system in which parts of a pure simulation have been replaced with actual physical components. HIL simulation is often used to understand the behavior of a new device, or to predict an outcome under different system conditions without knowing the detail of device design. Also, HIL could help to build model and validate a data model of a new power device. For better understanding the functionality and influence introduced by new hardware to the electric ship, either equipment or a controller, we should have it tested in a virtual environment.

LabVIEW is a software tool for designing, testing, measurement and control of a system. National Instruments provides different modules for particular applications as real time module as well as measurement and automation explorer (MAX) to configure hardware. Interfaces with other development and simulation software such as MATLAB/ Simulink are available through the simulation interface toolkit (SIT) module. LabVIEW suits well for HIL tests as it provides an effective platform for developing and testing real-time embedded systems. PXI controller and SEL relay are connected as shown in fig. 1. Hardware-in-the-loop test using LabVIEW for relays contains three stages:

- Software Simulation
- Hardware in the open loop
- Hardware-in-the-loop test



The power system model is implemented in LabVIEW. The SEL-351 relay is connected to the PXI-1042 chassis. The LabVIEW software establishes a relationship between the two devices. We can control simulation parameters through LabVIEW user interface by using SIT Server.

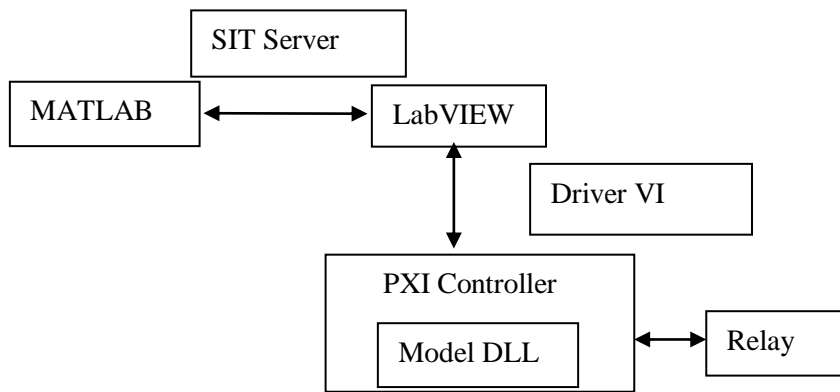


Figure 2: Block Diagram for HIL test using NI

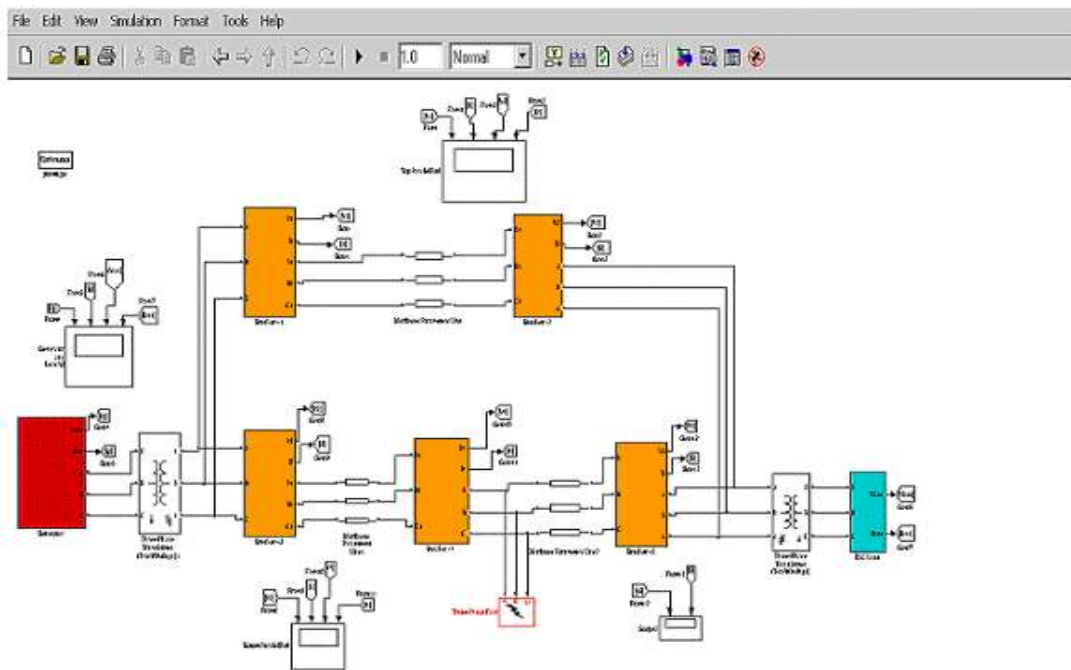


Figure 3: Power system model in Simulink

The SIT server generates a folder containing the model DLL file, driver base file and others necessary files. The model DLL file has to be downloaded into the PXI controller and by having an LAN connection, we can communicate with the power system model. A block diagram of HIL test has been shown in Fig. 2, which shows, how the HIL test is performed starting from designing a power system in Matlab/Simulink to getting back control signal from relay using Simulation Interface Toolkit (SIT), driver VI and NI PXI controller. Figure 3 shows the modeling of power system for software simulation. Before connecting SEL relay to PXI controller, hardware interface test was performed using function generator and switch. A switch was connected to input pin of the DAQ card in PXI controller and output pins of DAQ card were connected to a CRO to observe the O/P current waveforms. Voltage and current waveforms obtained through simulation have been shown in figure 4 to be used by relay to generate the trip and reclose signal in real time.



Figure 4: Voltage and current waveforms for power system model running in real time

Improving power system model and improving interface of NI controller hardware with Simulink are ongoing research related to this research work.

2) Hardware in the loop test using National Instruments PXI controller and RTDS

This research work relates to development of over-current relay model with some logical assumption using LabVIEW and PXI controller. Different modes of operation were designed to test the developed model. In internal mode, power system signal was depicted using sine wave signal and fault simulation logic to test the relay model. In external mode, power system signal from external hardware device is required. RTDS was used to create voltage and current signal and fault simulation. Over-current relay modeling is done in LabVIEW graphical programming language. The features of the model include fast detection of the fault in less than half a cycle, transient override capability, locking feature and user operated lock release. The model has analog filtering, ADC component, digital filter, threshold detector. The model's performance is rigorously tested with function generator in real time. After achieving satisfactory performance, closed loop testing is done with RTDS, with power system running in RTDS. When simulated power system signal goes above threshold value, fault indicator shown by green button demonstrates faults in different phases. Here three phase currents I_a , I_b , I_c from RTDS were fed into the relay model running in NI PXI controller. Filtering this current in and getting fundamental component was done to create correct trip and reclose signal. Figure 5 shows lock release for all the phases, to unlock relay, if the faults is sustained more than 60 cycles. Fig. 5, 6, 7, 8, 9 shows three-phase voltage, current, trip and reclose signal in real time as observed by LabVIEW using PXI controller, RTDS and DAQ devices. Voltage signal are sinusoidal and not as distorted as currents.

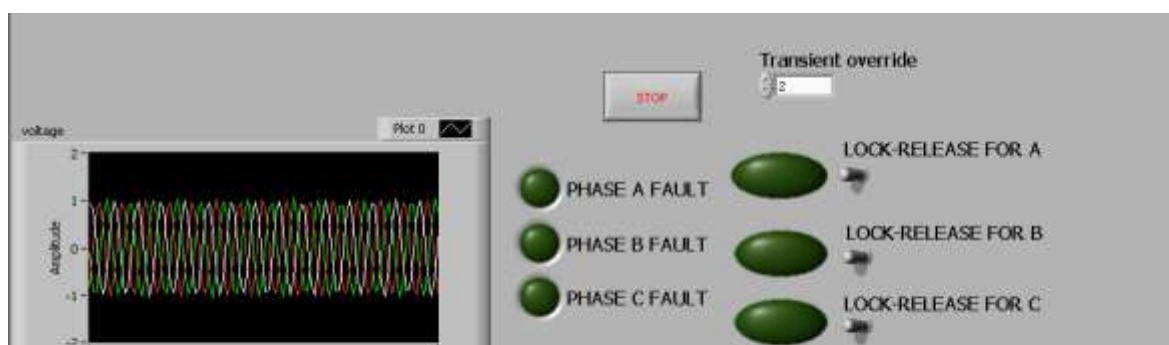




Figure 5: Three phase voltages in real time using RTDS and PXI controller

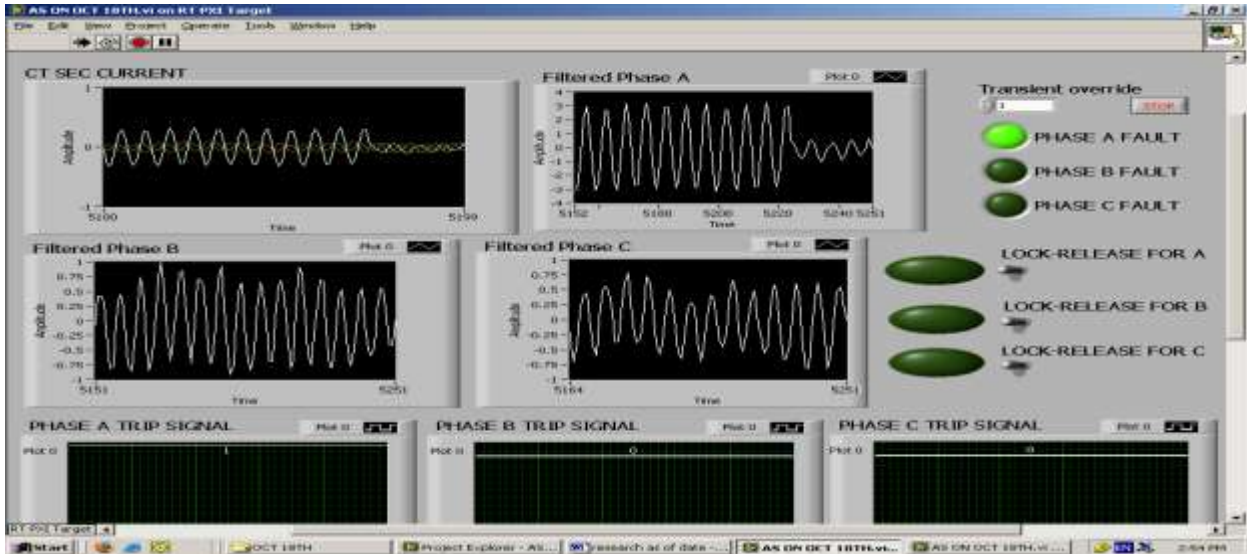


Fig.6. User interface for relay model

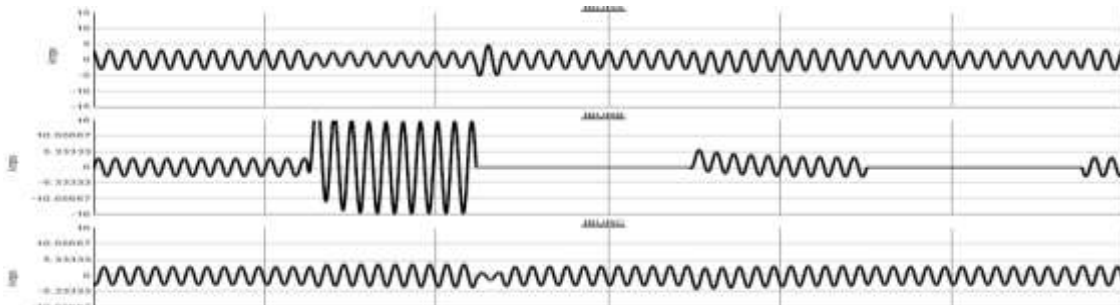


Fig. 7. Closed loop testing

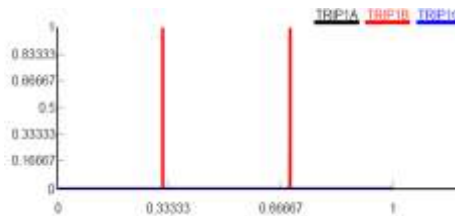


Fig. 8. Trip signals

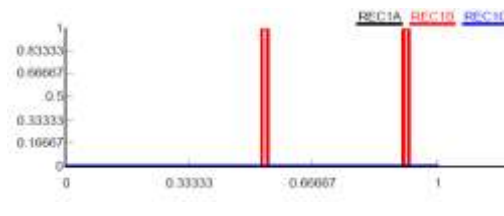


Fig. 9. Reclose signal

In future, we plan to improve the model by validation and verification using SEL 351 and RTDS.

3) Hardware in the loop test using RTDS and SEL 421

Hardware in the loop test for SEL-421 distance relay have been set up using RTDS with help of RTDS engineers. Power system used was 14 buses 3 generators system. Fault was simulated in middle of one of the transmission line and 3-phase currents and voltage was sent out to SEL relay and relay trip signal was given back to system. HIL test results obtained shows successful operation of developed setup. By using RSCAD components, protective relay modeling can be created. For the case of impedance relay, it is simple in RTDS to calculate the phase-to-phase and phase-to-ground impedances. Relay settings, like protection parameter, automatic re-closure can be loaded into relay using SEL software. In the case of over-current relay, which should operate for any direction of current, magnitude and phase angle is measured using two samples of a waveform taken at discrete time intervals. Expected operation time and reset time can also be calculated using certain equations.

Power system test case was developed as shown in figure 10. Actual setup for hardware platform for testing SEL 421 distance relay using RTDS is shown in figure 11. Lower level signal for 3 phase currents, voltage and ground was given as input to SEL relay through RTDS. Output of SEL relay to open and reclose the breaker for all 3 phase was given to RTDS to operate the breaker in simulated power system. Fault was simulated in one of the transmission line at 50% of the distance and operation of relay was observed. Relay was setup in a way that there will not be any re-close after faults happen on two phases. One end of the line breaker is directly controlled by the signal received from the physical relay for each phase. Other end of the line breaker is controlled by simulated logic in RTDS.

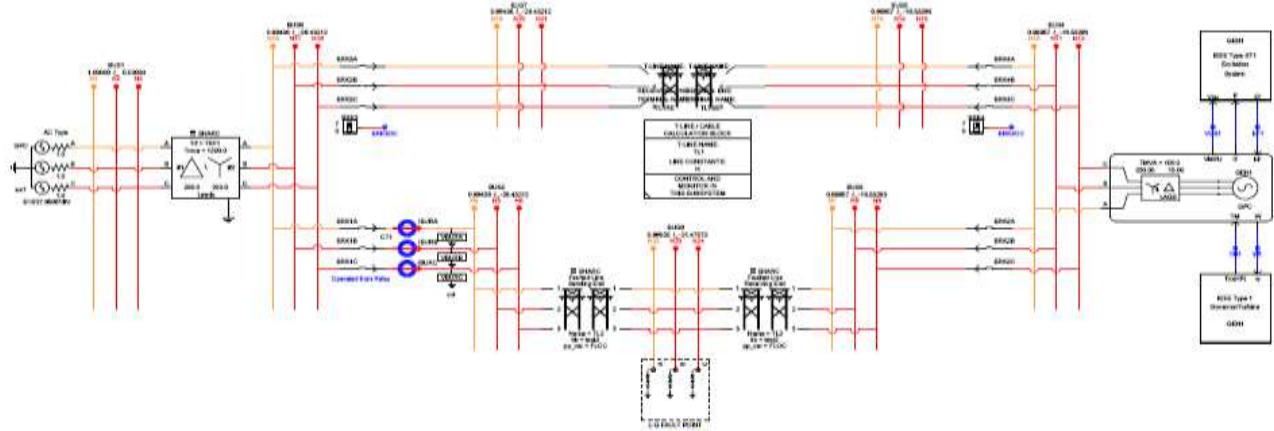


Figure 10. 8-bus power system test case.



Figure 11. Hardware setup for HIL test of SEL 421 relay using RTDS

Single phase line to ground and two-phase line to ground fault were simulated at 50% distance on the transmission line in the eight-bus test case. Simulation results for single-phase fault on ‘phase A’ are shown in fig. 12. Current on ‘phase A’ becomes high when the fault is initiated and becomes zero when the relay operates and the breaker open.

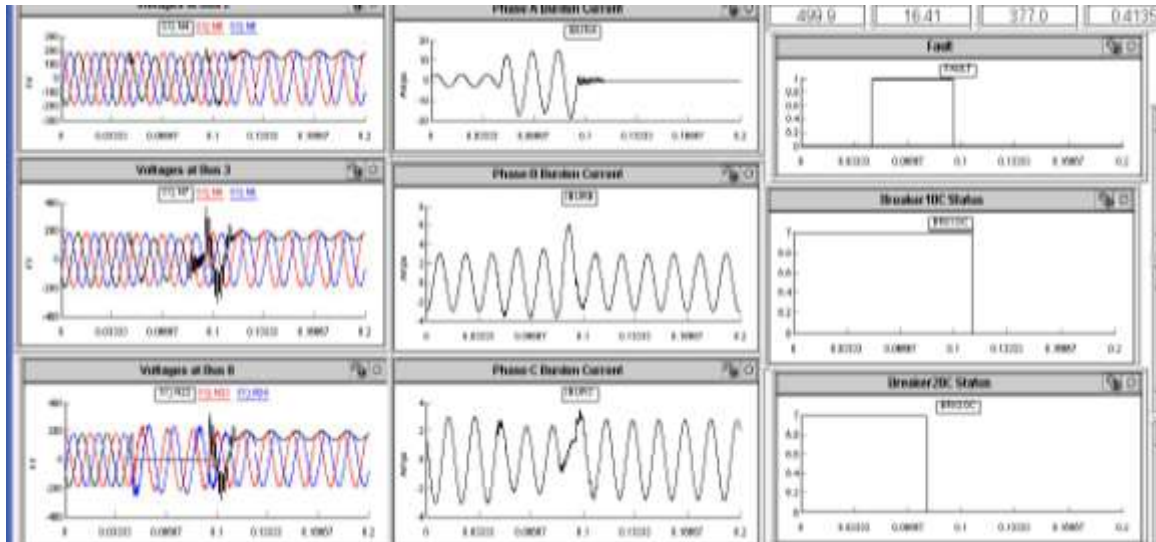


Figure 12. Single-phase fault on phase A

The transient response in case of two-phase line to ground fault is shown in fig. 13. Fault on ‘phase A and phase B’ to ground was simulated. Relay signals open the breakers and current become zero for all 3 phases. The breakers will not reclose until the manual reclose button is pressed. Simulation results for faults on ‘phase A and phase C’ to ground and also ‘phase B and phase C’ to ground were obtained in a similar manner, but have not been shown here due to space limitation.

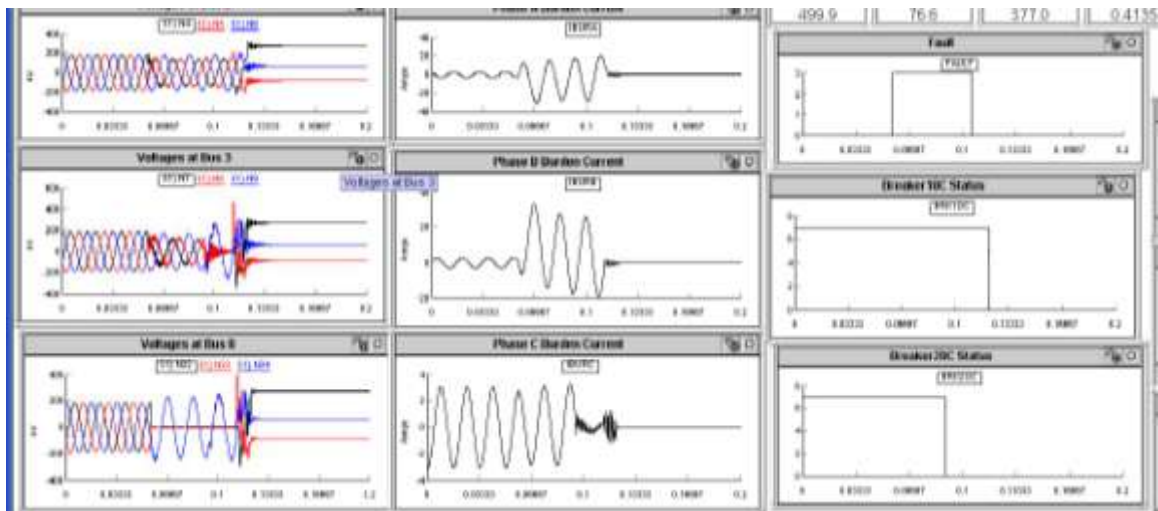


Figure 13. Two-phase fault on phase A and phase B

This experiment clearly explained the operation of relay and RTDS simulation really helped students to understand the protection concept.

4) Hardware in the loop test using RTDS and SEL 351

SEL 351 was connected to RTDS and HIL test was performed similar to 421 relay.

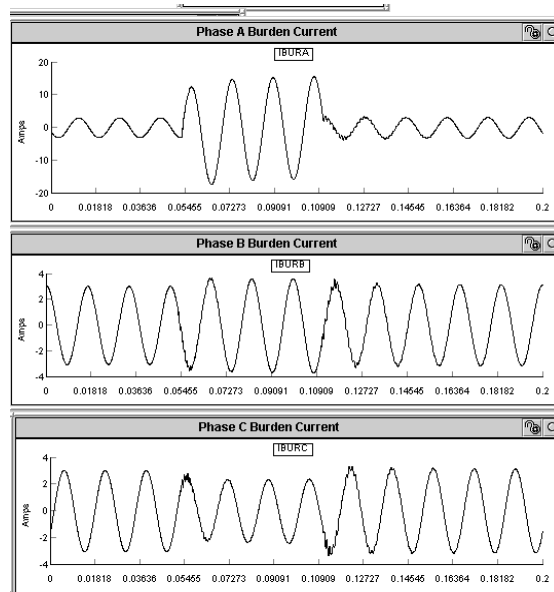


Figure 14: Three phase currents using RTDS and SEL 351 for fault on phase A

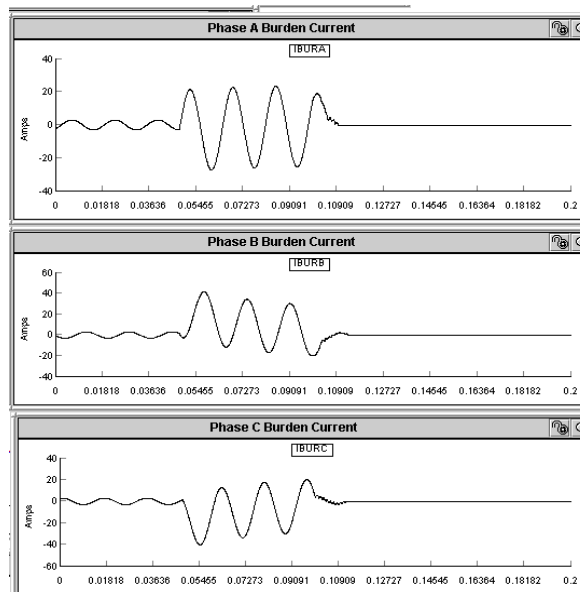


Figure 15: Three phase currents using RTDS and SEL 351 for fault on phase A, B and C

Efforts in HIL simulation of SEL 351 and RTDS have been completed and it was further improved by simulating test cases with different setting of SEL and several fault cases. An effort in developing

comprehensive test suites for model validation and verification is in progress. Figure 14, 15 shows part of the results obtained with HIL test of SEL 351 and RTDS.

Early Design Tools at Purdue University

Key accomplishments over the last two years include

- Finding and correcting a significant error in the IEEE standard for characterizing magnetic materials.
- Introduction of the concept of a high-fidelity magnetic equivalent circuit to support the design of electromagnetic and electromechanical components.
- Automated design methodologies for EI core inductors and permanent magnet synchronous machines.
- A new method to determine Lyapunov functions for the stability analysis of power electronics based power distribution systems.
- The start of a mathematical approach for optimal energy storage allocation.
- A new waveform reconstruction method that greatly reduces the computational effort (orders of magnitude reduction in simulation time) of field-based modeling of permanent magnet synchronous and induction machines.
- A new position observer for permanent magnet synchronous machines was developed that improves the fault tolerance of high-performance drives.
- A new speed/position sensor for induction machines was developed that uses torque-ripple-induced vibration to establish speed. It also serves a dual role for health monitoring of induction drives.

4.1. Technical Detail

There have been many accomplishments in this effort. One of the most fundamentally of these has been addressing a serious flaw in the IEEE Standard 1991-393 for the characterization of magnetic materials. This error resulted in the incorrect characterization of magnetic materials. This incorrect characterization leads to analysis errors in almost all magnetic analysis methods - from finite element analysis through analytical methods. This error in analysis method invariable leads to error in design. A detailed discussion of this error, and an means for avoiding it, is set forth in

J.L. Cale, S.D. Sudhoff, "An Improved Magnetic Characterization Method for Highly Permeable Materials," IEEE Transactions on Magnetics. Vol. 42, Issue 8, August 2006

The new method for characterizing magnetic materials is the subject US Patent Application 11/807,196, "Methods and Apparatus for Characterizing Magnetic Properties of Materials".

Another key accomplishment of this effort is the concept of a high-fidelity magnetic equivalent circuit. The point of this work is that if done correctly, a magnetic equivalent circuit can produce results of similar accuracy as 3-D finite element analysis, but in a fraction of the time. The reduction in computer time allows the magnetic equivalent circuit method to be incorporated into evolutionary optimization based design approaches. Details on the high fidelity magnetic equivalent circuit and its application to automated design are set forth in

J.L. Cale, S.D. Sudhoff, "Accurately Modeling EI Core Inductors Using a High Fidelity Magnetic Equivalent Circuit Approach," IEEE Transactions on Magnetics, Vol. 42, Issue 1, Jan 2006, pp. 40-46.

and

J. Cale, S.D. Sudhoff, "EI Core Inductor Designs using Population-Based Design Algorithms," 2007 Applied Power Electronics Conference, Anaheim, CA, February 25-March 1, 2007.

Another detailed account of all this work appears on the PhD dissertation:

J. Cale, "Computationally Efficient Magnetic Modeling and Material Characterization Methods for Automated Ferromagnetic Inductor Design", PhD Dissertation, Purdue University, July 2007

Additional journal publications are in progress.

Another area of contribution of this effort is in permanent magnet synchronous machine design. In particular, a methodology for the semi-automated design of permanent magnet synchronous machines was developed under this effort. Currently, two journal papers have been submitted under this effort. These include

B.N. Cassimere, S.D. Sudhoff, "Population Based Design of Permanent Magnet Synchronous Machines: Part I – Problem Formulation and Solution," submitted to IEEE Transactions on Energy Conversion.

B.N. Cassimere, S.D. Sudhoff, "Population Based Design of Permanent Magnet Synchronous Machines: Part II – Machine Analysis," submitted to IEEE Transactions on Energy Conversion.

A highly detailed account of the work appears in the PhD dissertation:

Brandon Cassimere, "Modeling and Evolutionary Design of Permanent Magnet Synchronous Machines," PhD Dissertation, Purdue University, May 2008

Note that this particular work has been transitioned to both the U.S. Army for its man-portable power program and to Rolls-Royce.

We have also focused on reducing the computational effort required to solve fields-based models of electric machines so that these can be used earlier in the design cycle and more effectively in the analysis of machines under various operating conditions. Our technique – which we refer to as a field reconstruction method- uses a minimal number of solutions of static finite element models to establish basis functions for the airgap flux density within the machines. These basis functions are then used to predict the fields and forces acting within the machine under arbitrary speed and stator excitation. Our earliest efforts on this were for the permanent magnet synchronous machine. The field reconstruction method applied to PM machines reduced the computational effort by several orders of magnitude compared to finite element modeling. Details are provided in the publications:

W. Zhu, B. Fahimi, and S. Pekarek, "A Field Reconstruction Method for Optimal Excitation of Surface Mounted Permanent Magnet Synchronous Machines," IEEE Transactions on Energy Conversion, Vol. 21, No. 2, June 2006, pp. 303-313.

B. Deken, S. Pekarek, B. Fahimi, "An Enhanced Field Reconstruction Technique for Design of PM Synchronous Machines," Proceedings of the 2007 Vehicular Power and Propulsion Conference (VPPC 2007), September 2007, TS6-3 (CD-ROM Proceeding).

Using the results of the field reconstruction model – the behavior of the basis functions of the radial and tangential component of flux density, it was found that analytical techniques could be used to determine a closed-form expression for radial force acting over a pole within permanent magnet synchronous machines. Ideally, when summing the radial forces over all poles, the net force acting on the rotor is zero. However, in practice with eccentricities that occur within the manufacturing effort, the pole forces are not equal and so the radial forces act to increase bearing wear. Interestingly, it was found that there is a quadratic relationship between q- and d-axis stator current and the radial force. It was also found that the d-axis current could be used to increase or decrease the radial force. In contrast, the q-axis current only acts to increase the radial force. Therefore, in high performance permanent magnet machines, the results point to the fact that it may be advantageous to use d-axis current to reduce radial force. These results were published in:

W. Zhu, S. Pekarek, B. Fahimi, B. Deken, "Investigation of Force Generation in a Permanent Magnet Synchronous Machine," IEEE Transactions on Energy Conversion, Vol. 22, No. 3, September 2007, pp. 557-565.

As a second step, we developed a field reconstruction technique for induction machines. This was more challenging than for the permanent magnet machine since the rotor has induced currents. Thus, the basis functions are functions of time. Nonetheless, a successful technique was developed and has been validated against transient finite element analysis. A particular focus was to compare the computational effort required for each. Using a desktop computer 4 Ghz computer, the finite element method required 9 hours to compute a start-up response for an induction motor drive. In contrast, the FR method required 4 minutes for the same study. The error between the two models is negligible. A conference and a journal paper were written on method that contains the respective details.

D. Wu, S. Pekarek, B. Fahimi, "A Field Reconstruction Technique for Efficient Modeling of the Fields and Forces within Induction Machines," Proceedings of the 2007 Industrial Electronics Society Conference (IECON 2007), November 2007, pp. 1274-1279.

D. Wu, S. Pekarek, B. Fahimi, "A Field Reconstruction Technique for Efficient Modeling of the Fields and Forces within Induction Machines," accepted for publication in IEEE Transactions on Energy Conversion – to appear in 2008.

The initial field reconstruction models for the induction and permanent magnet synchronous machine both used stator current as an input. In many instances it is convenient to use voltage as an input to the model. Therefore, we developed a voltage-input based field reconstruction model for the induction machine so that it can be conveniently coupled to external drive circuits. This is detailed in the paper.

D. Wu, S. Pekarek, B. Fahimi, "A Voltage-Input-Based Field Reconstruction Technique for Efficient Modeling of the Fields and Forces within Induction Machines," invited for publication in the IEEE Transactions on Industrial Electronics, 2008.

Another area of work in this effort relates to a new control strategy. In order to deal with modeling errors and uncertainties, a real-time method to approximate continuous-time dynamical systems using a novel self-organizing RBF network was developed together with an adaptive robust control scheme. This self-organizing RBF network has hierarchically layered structure. It can add or remove RBFs to meet the error constraints of the designer while keeping the network size from growing unnecessarily large. An adaptation strategy for the weight matrix of the RBF network is developed using the Lyapunov approach. Our proposed approximation approach guarantees uniform ultimate boundedness of the approximation error, which is proved using the second Lyapunov method. This approach is also capable of achieving uniform asymptotic stability of the approximation error if the self-organizing RBF network can capture the dynamics of uncertainties perfectly.

Different types of radial basis functions can be employed by the proposed self-organizing RBF network. The implementations using Gaussian RBF and raised-cosine RBF are discussed and compared. It is verified that the property of compact support of the raised-cosine RBF enables much faster network's training and output evaluation as the complexity of the network and the dimensionality of the input space increase. A detailed derivation and analysis of the employed controller and a comparison study with supervisory type adaptive robust controller was undertaken in this effort. A detailed of this work is set forth in

Y. Lee, S. Hui, E. Zivi and S. H. Žak , "Variable neural adaptive robust controllers for uncertain systems," International Journal of Adaptive Control and Signal processing, Vol. 22, 2008, in print

S. Hui, S. D. Sudhoff, and S. H. Žak, "On estimating regions of stability of the estimation error of sliding mode observers for uncertain systems," Proc. 2006 American Control Conference, Minneapolis, Minnesota, Session ThB15.6, pp. 3328--3333, June 14--16, 2006.

Jianming Lian, Yonggon Lee, Scott D. Sudhoff, and Stanislaw H. Žak, "Variable Structure Neural Network Based Direct Adaptive Robust Control of Uncertain Systems," to appear in Proceedings of 2008 American Control Conference, Seattle, WA, June 11--13, 2008

Jianming Lian, Scott D. Sudhoff, and Stanislaw H. Żak, "Control of Uncertain Systems with Guaranteed Performance," to appear in Proceedings of 2008 American Control Conference, Seattle, WA, June 11--13, 2008

The work described thus far has been at the component level. At the system level, considerable effort has gone into the fundamental stability analysis of power electronics based distribution systems. The key design consideration here is that power electronics based power distribution systems can exhibit negative-impedance instability which leads to power system failure. Small signal analysis methods can be used to determine in a proposed operating point is stable or not. However, even if the operating point is stable, a sufficiently large perturbation can cause the system to go unstable. The problem of computing the Estimated Restricted Region of Attraction (ERROA) is the problem of determining how far a stable operating point can be perturbed without the system going unstable or entering an undesirable operating regime (over voltage or over current). This problem can be addressed using Lyapunov's second method. In fact, recently researchers at Purdue developed a practical method of applying this theory to high order system of arbitrary mathematical description. Even so, the results were overly conservative. Over the last two years, under the support of the ESRD, methods to construct Lyapunov functions that yielded greatly improved estimates of the ERROA were developed. These methods have been documented in:

C. Sullivan, S. Sudhoff, E. Zivi, S. Żak, "Methods of Optimal Lyapunov Function Generation With Application to Power Electronic Converters and Systems," IEEE Electric Ship Technologies Symposium, Arlington, VA, May 21-23, 2007

C. Sullivan, "Optimization of Estimated Restricted Regions of Attraction with Application to Power Electronic Converters and Systems," PhD Dissertation, Purdue University, May 2008

A journal paper submission is also currently in progress.

Another area of work at the system level has been in energy storage. One reason to incorporate energy storage devices in the ship power system is to increase the quality of service in terms of the continuity of electric power availability during damage scenarios. In order to quantify this, ESRDC researchers have proposed the concept of operability as:

$$O(\theta) = \frac{\int_0^T \sum_{i=1}^I w_i \langle \theta \rangle_i^* \langle \theta \rangle_i dt}{\int_0^T \sum_{i=1}^I w_i \langle \theta \rangle_i^* \langle \theta \rangle_i dt}$$

In this expression, the operation status of load i at time t is denoted $o_i(t)$ and is 1 if fully operational and 0 if non-operational, $o_i^*(t)$ is the commanded operating status of load i , and $w_i(t, \theta)$ is the weighting factor relative to the importance of a given load. To be operational, a load needs be supplied with electric power and/or cooling and/or potentially other services, depending on the load. The vector θ includes information about the damage scenario – for example the location of a weapon detonation. If the operability is 1, it implies that all ship loads were adequately supplied with services. An operability of 0 implies the ship was dead and dark in the water throughout a given damage scenario.

The concept of operability can be used to quantify the benefits of energy storage on the ability of the system to fight through battle damage. Since operability is directly related to the percentage of the ship's operating capability retained after a damage event, comparing operability with and without energy

storage is a reasonable method of determining its effectiveness. Beyond this, operability can be used as a basis to determine both the amount and distribution of energy storage units within a ship.

Before describing this however, it is appropriate to consider how operability is calculated. The key consideration in the calculation of operability is that the operational status of each component is dynamic and depends on a dynamically interconnected system – the integrated engineering plant. Thus the determination of operability requires a simulation of not only the power distribution system, but of all other systems pertaining to the integrated engineering plant as well.

As alluded to earlier, and as will be demonstrated in Section 13h, the concept of operability can be used to quantify the benefits of energy storage on system performance. However, it can also be used to determine the best distribution of energy storage within the system. To this end, let us recall the basic definition of operability, i.e.

$$O(\theta) = \frac{\int_0^T \sum_{i=1}^I w_i \langle \theta | \mathcal{G}_i^* | \mathcal{G}_i \rangle dt}{\int_0^T \sum_{i=1}^I w_i \langle \theta | \mathcal{G}_i^* \rangle dt}$$

Recall θ is a vector which describes a disruptive event. For example, θ could denote the location of a missile detonation within the ship. The event vector θ falls within a set of disruptive events Ω .

Clearly, operability is a function of all of the parameters of the ship. Let \mathbf{e} denote the vector of parameters of the energy storage units. This vector could include the energy storage capacity and power capability of each energy storage unit. Pointing out this explicit dependence on operability, we have

$$O(\theta, \mathbf{e}) = \frac{\int_0^T \sum_{i=1}^I w_i \langle \theta | \mathcal{G}_i^* | \mathcal{G}_i | \mathbf{e} \rangle dt}{\int_0^T \sum_{i=1}^I w_i \langle \theta | \mathcal{G}_i^* \rangle dt}$$

We may then calculate the expected value of operability over a set of disruptions

$$\hat{O}(\mathbf{e}) = \frac{\int_{\theta \in \Omega} O(\theta, \mathbf{e}) d\Omega}{\int_{\theta \in \Omega} d\Omega}$$

Finally, let $E(\mathbf{e})$ denote the total cost of the energy storage units, in terms of capital, mass, or volume metrics. Then, the parameters of the energy storage units may be calculated by minimizing $E(\mathbf{e})$ subject to $\hat{O}(\mathbf{e}) > \hat{O}_{\min}$, where \hat{O}_{\min} is the desired minimum value of expected operability. In other words, the cost of the energy storage is minimized subject to achieving a minimum expected operability. Solving this problem is one way to allocate the energy storage units.

This optimization problem is computationally intense and will require potentially millions of evaluations of the objective functions, which calls for millions of time-domain simulations of the integrated engineering plant. However, there is precedence. In particular, the solution of similarly numerically intense optimization problems involving operability have been documented, in, for example

A. Cramer, “Metric Based Design of Integrated Engineering Plants for Robust Performance During Hostile Disruptions”, PhD Thesis, Purdue University, July 2007

The chief difficulty in performing this approach to energy storage allocation is the time required by the time domain simulation. The chief reason the time domain simulation is itself computationally

formidable is the numerical stiffness – the separation of time constants between the electrical and thermal time constants.

Future work in this area will be twofold. First, the component parameters and placement will be changed to realistic values appropriate for a warship. Next, the framework will be used to support optimization of the placement and amount of energy storage. Details of this work are contained in the ESRDC Final Report on the Energy Storage Challenge Problem. A highly detailed explanation of the work will be documented in future publications, including a PhD Dissertation by graduate student Ricky Chan

5. POWER TRAIN TECHNOLOGY

5.1. Key Accomplishments

- Completed the design study of a 20 MW propulsion power train
- Completed the study of 40 MW propulsion motors
- Studied integration of power electronics with a propulsion motor
- Performed modeling and analysis of ONR/AMSC 5 MW superconducting motor
- Studied modeling and simulation of the electric ship power system
- Completed modeling and simulation of a naval EM railgun system
- Studied active filtering of the electric ship power system using stored energy and power electronics equipment of a naval EM railgun
- Improved Simulink[®] power system model and investigated a new modeling environment
- Studied coordination of large pulse loads onboard electric ships
- Conducted a generator-set optimization study for electric ships
- Completed a design and analysis study of high-speed gas turbine-generator systems
- Studied prime power generation onboard electric ships using directly-coupled gas turbine permanent magnet gen-sets
- Analyzed propulsion cross connection concept that allows fuel savings in present-day navy ships
- Studied the effect of electric frequency on generator size
- Studied NAVSEA energy storage challenge problems

5.2. Technical Detail

5.2.1. Design Study of a 20 MW Propulsion Power Train

The initial task of the electric ship research program at the Center for Electromechanics was focused on enabling a major reduction in the size of the all-electric ship power train. An extensive literature search was conducted prior to a study of a complete drive train as a system, from fuel to propulsion motors. The goal of the study was to understand the technical challenges associated with a successful development of an all-electric Navy ship, identify critical, high pay-off technology development needs, and advance a few of the most promising technologies. The baseline design and analysis of a 20 MW ship power train consisting of a 25 MVA, 3600 rpm radial flux permanent magnet generator, a 20 MVA PWM converter, and a 20 MW, 150 rpm radial flux permanent magnet motor, along with the amount of fuel sized for an assumed mission profile, were completed. The widely used LM2500 gas turbine was chosen as the prime mover. The options considered in the selection of the power train components are shown in Figure 2-1. The main results of the study can be summarized as follows:

- Fuel is by far the dominant component.
- Overall efficiency of the power train is the most relevant parameter.
- The 3600 rpm generator is the smallest and improving its size wouldn't have a significant impact, but improving its efficiency would.
- The 150 rpm motor is the next heaviest component weighing ~97 tonnes.

Relative weights and volumes of the different components are shown in Figure 2-2.

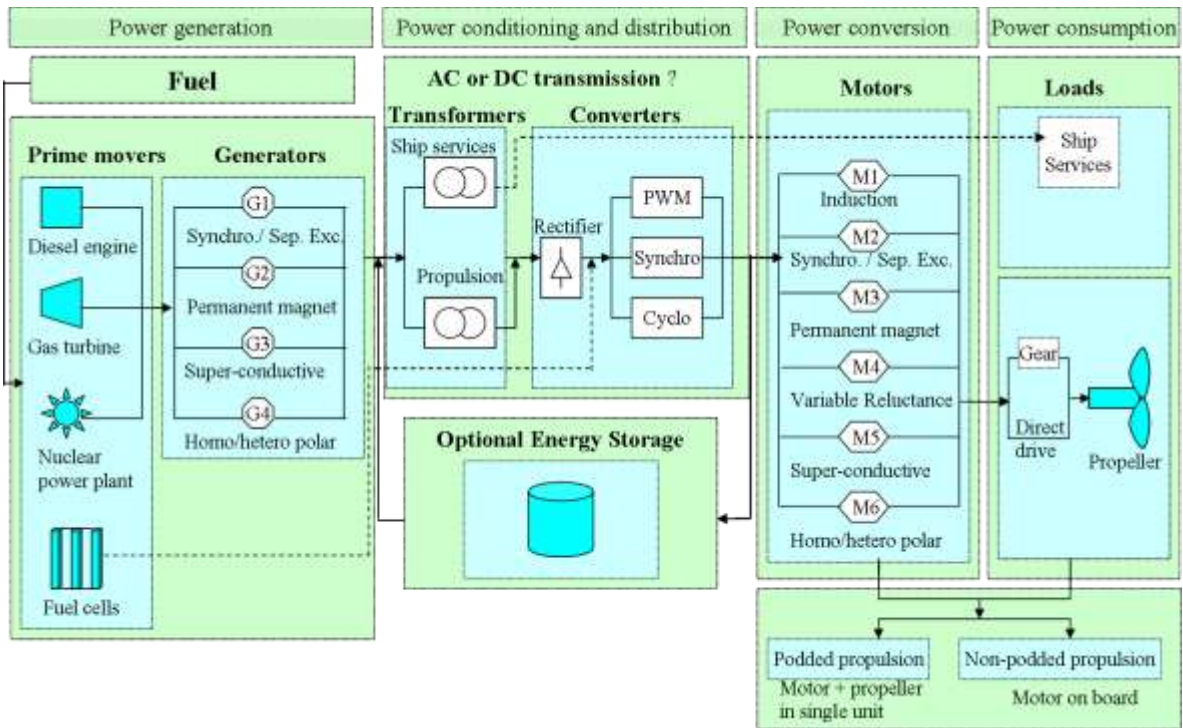


Figure 2-1: Power train options.

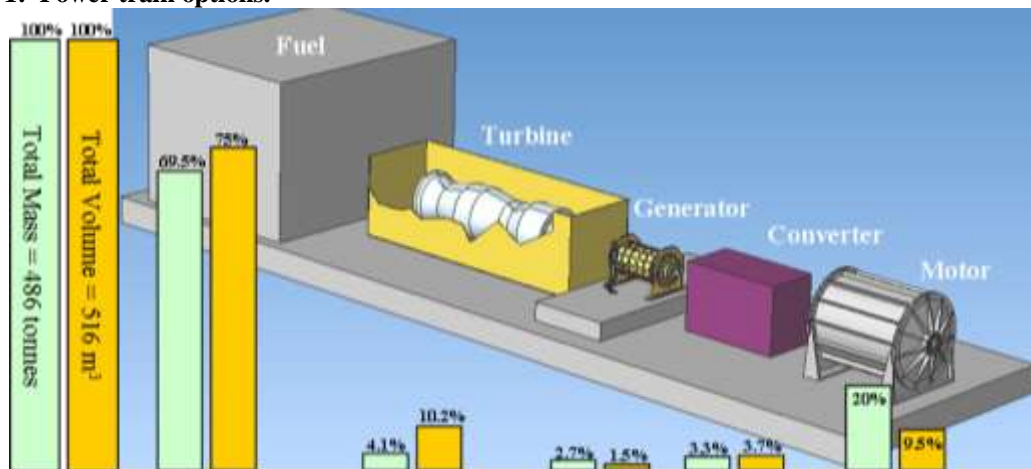


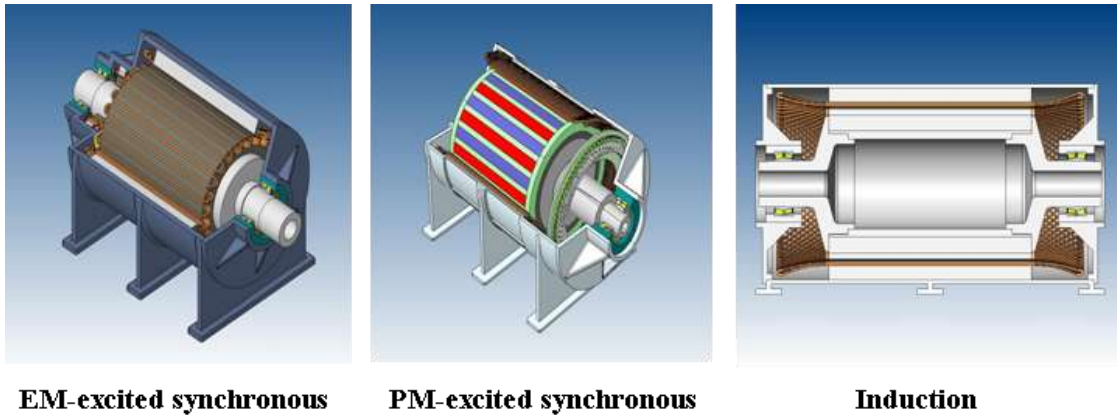
Figure 2-2: Baseline power train.

After completing the study, a five-member external panel from industry and government participated in a review of our power train technology development program. Valuable comments, suggestions, and recommendations were made. The panel recommended that we focus on the ship power system as a whole, so development of a model of such a system became the main topic of our future efforts. In addition, the panel recommended that we look at optimized high-speed gen-sets, mainly gas turbine and generator sets, to replace the presently used equipment which is large and inefficient. The panel also recommended that we look at the integration of power electronics with the motor and the generator since these machines are large and tend to have a considerable, and unused, inner space that can be used to accommodate additional parts.

5.2.2. Study of 40 MW Propulsion Motors

We looked at 40 MW propulsion motors to assess their size and the feasibility of installing them in pods. We considered three different topologies. An EM-excited synchronous motor, a PM-excited synchronous motor, and an induction motor. Models of the three motors are shown in Figure 2-3. Among the three

topologies considered, the PM motor was the smallest in weight and volume. We then considered the feasibility of housing the 40 MW PM motor in a pod sized for a destroyer. The pod sizing was based on information gathered from various sources, including communications with experts in the field. The preliminary analysis indicates that a 40 MW PM motor cannot fit in a destroyer pod using available technology. Figure 2-4 shows the maximum podded-motor output power as a function of temperature and size of the pod considered. An upper limit of 30 MW at 60° C was found. Special design compromises, such as allowing for a small power factor, may result in an increase of podded-motor power. Figure 2-5 shows inboard and outboard 40 MW propulsion motors for size and location comparison.



EM-excited synchronous PM-excited synchronous
Figure 2-3: 40 MW propulsion motors.

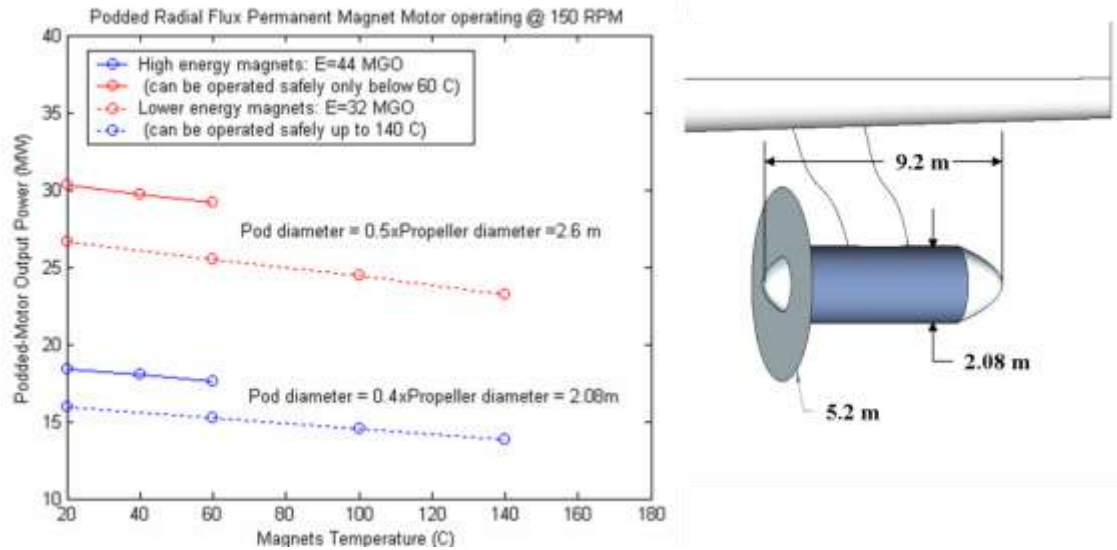


Figure 2-4: Podded-motor power.



Figure 2-5: Inboard and outboard 40 MW propulsion motors.

5.2.3. Integration of Power Electronics with a Propulsion Motor

We studied the potential for volume and mass reduction through the integration of power electronics into a propulsion motor, as recommended by panel members who reviewed our 20 MW power train work. Using the existing 20 MW PM motor design and the 20 MW PWM inverter, we considered two integration schemes. The two approaches are depicted in Figure 2-6. The first design places the power electronics external to the rotor but within the stator housing, while the second design places the power electronics inside the unused space in the hollow rotor. The first option adds about 7750 kg to the stand-alone motor, but eliminates the need for inverter housing and cooling auxiliaries. The different approaches result in tradeoffs on shaft and bearing designs. In both schemes, the power electronics cooling system is integrated with that of the stator windings. The design used for the second approach uses existing available space and does not increase motor volume significantly as compared to the previous approach. However, due to the large shaft diameter, new types of bearings are needed. Hydrostatic bearings are found to be a good alternative.

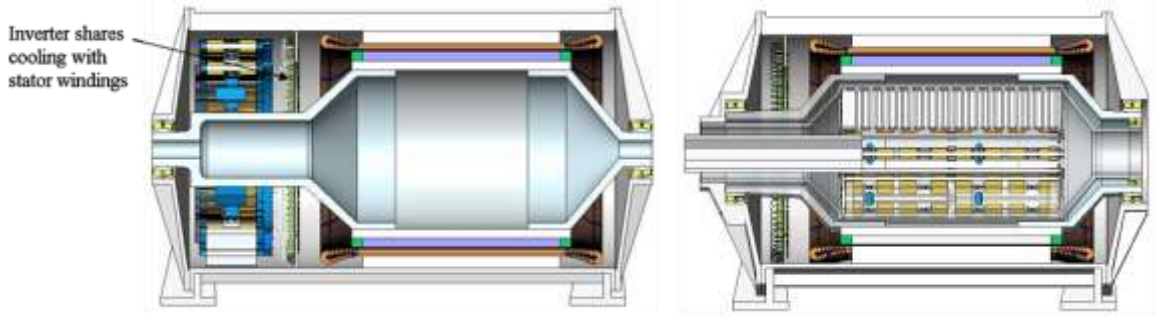


Figure 2-6: Inverter components inside stator housing (left) and inside hollow rotor (right).

5.2.4. Modeling and Analysis of ONR/AMSC 5 MW Superconducting Motor

Modeling efforts by the Center for Electromechanics supported tests of the 5 MW superconducting motor conducted at the Center for Advanced Power Systems at Florida State University. The University of Texas' role in this testing process was to provide physics-based machine models to assist in interpretation of test data, to provide information needed to evaluate motor control performance, and to help validate design and analysis methods that will be used for future generations of motors using this new technology. The geometric data were obtained either directly from the manufacturers or from related publications and conference presentations. The set of data collected was incomplete however, and prudent assumptions were made whenever necessary. The model of the 5 MW high temperature superconducting motor was later refined using initial test data. The finite element method was used to calculate various machine parameters using two- and three-dimensional models. A three-dimensional finite element model was built using OPERA-3d software from Vector Fields Inc. The model and the magnetic flux density distribution in all parts of the machine are shown in Figure 2-7.

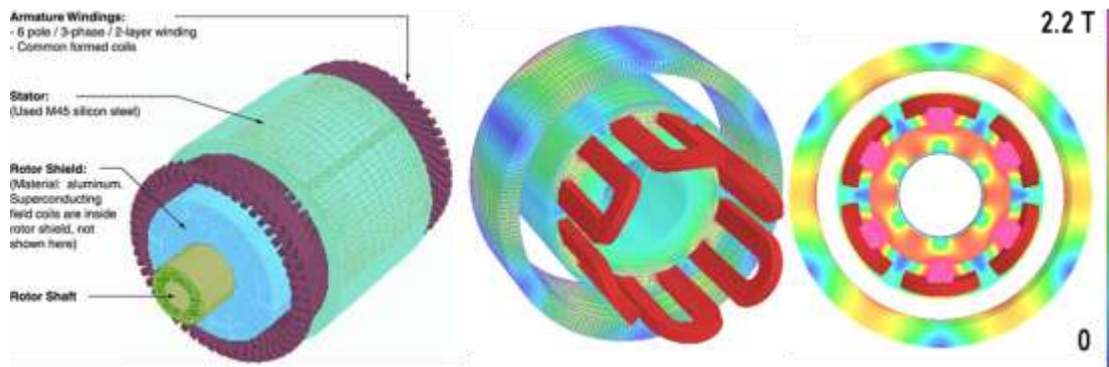


Figure 2-7: Three-dimensional FEA model and magnetic flux distribution.

An important result that came out of this testing and analysis process is the realization that the presumed superconducting air-core rotor cannot generate the measured level of flux density without magnetic material in the rotor core. With this additional magnetic material, the machine parameters, geometry, and excitation levels provided by AMSC are correct. The measured and predicted flux density in the air-gap, with and without magnetic material, are shown in Figure 2-8. The modeling results of the 5 MW high temperature superconducting motor were presented at a workshop organized by FSU. A comparison of our predictions with the available test data was presented and discussed. In addition to the important results of the “non-air-core” nature of the rotor of the HTSC motor, the behavior of the rotor shield during the frequency-response test was impressively close to the prediction of our model. Figure 2-8 shows the measured and predicted values of machine impedance as a function of frequency. These results are very important and the agreement gives good confidence in the design of the motor drive controller. It is important to note that the magnetic nature of the rotor core doesn’t influence the outcome of these frequency response tests since the rotor is not energized and not moving during testing.

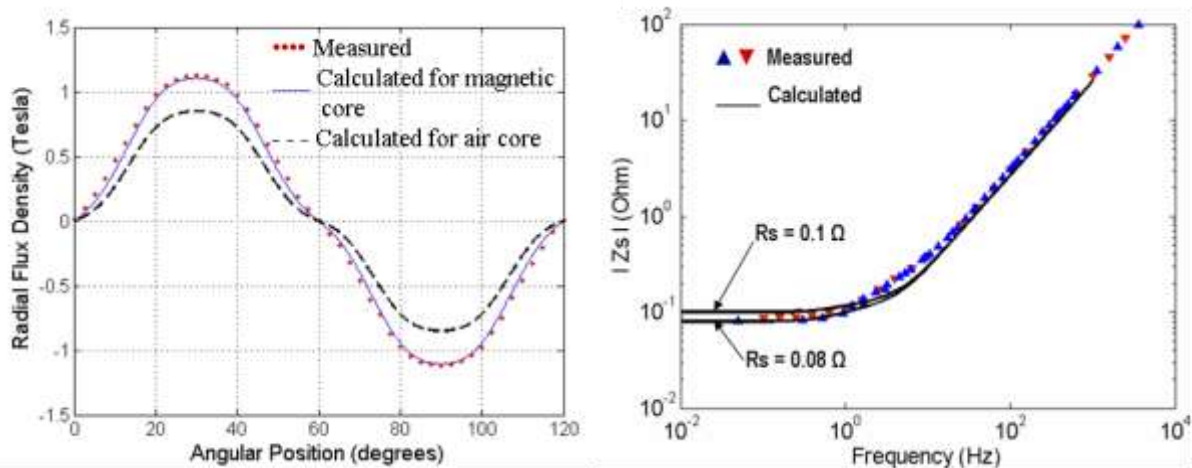


Figure 2-8: Comparison between measured and predicted values of air-gap radial flux density and machine impedance as a function of frequency in the 5 MW HTS motor.

5.2.5. Modeling and Simulation of the Electric Ship Power System

We developed several MATLAB/Simulink[®] models of the electric ship power system that reflect the notional DD architecture. In the initial modeling effort, pre-programmed component models from the SimPowerSystems commercial toolbox were used. The initial model consisted of two 36.5 MW power trains and power equipment for ship services for one zone, which includes eight different loads. The model includes four synchronous generators, four switchboards, two propulsion transformers, two propulsion rectifiers, two PWM motor drives, and two permanent-magnet propulsion motors. The ship service section of the model has two load-center transformers, two rectifiers, a ship service transformer, an inverter, a dc-dc converter, several switches and breakers, and eight different loads. The top level Simulink[®] model is shown in Figure 2-9. The model was first exercised by simulating a ground fault at the terminals of one of the propulsion motors. The ground fault occurs after the ship was accelerated from rest to a sustained speed of 30 knots, then slowed-down to a cruising speed of 20 knots. The response of motor currents to the fault is shown in Figure 2-10.

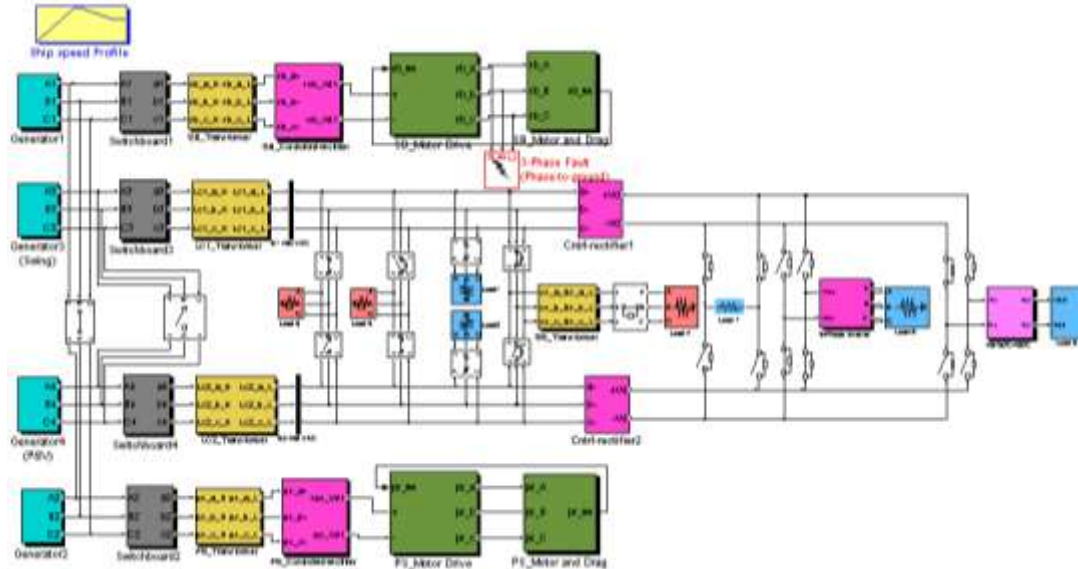


Figure 2-9: Initial electric ship power system model.

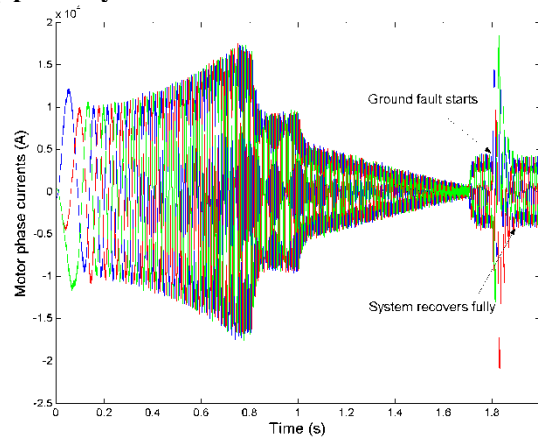


Figure 2-10: Motor phase current during and after the ground fault (fault is initiated at $t=1.8$ s and removed 20 ms later).

5.2.6. Modeling and Simulation of a Naval EM Railgun System

A Simulink[®] model of a naval electromagnetic railgun system was initially developed using the commercial pre-programmed blocks. The power supply was sized for projectiles with 64 MJ muzzle energy, 12 round/min shot rate, and five stored shots. It consists of eight high-speed pulsed alternator sets. Each set includes two rectifiers, a PWM drive, a 5 MW charging motor, a 2.8 GVA alternator, and breakers and switches. A top level schematic is shown in Figure 2-11. Figure 2-12 shows an example, including pulse current and voltage traces, in which an EM gun shot is taken while the ship is cruising at 20 knots. Figure 2-13 shows the response of the bus voltage to the high power pulse.

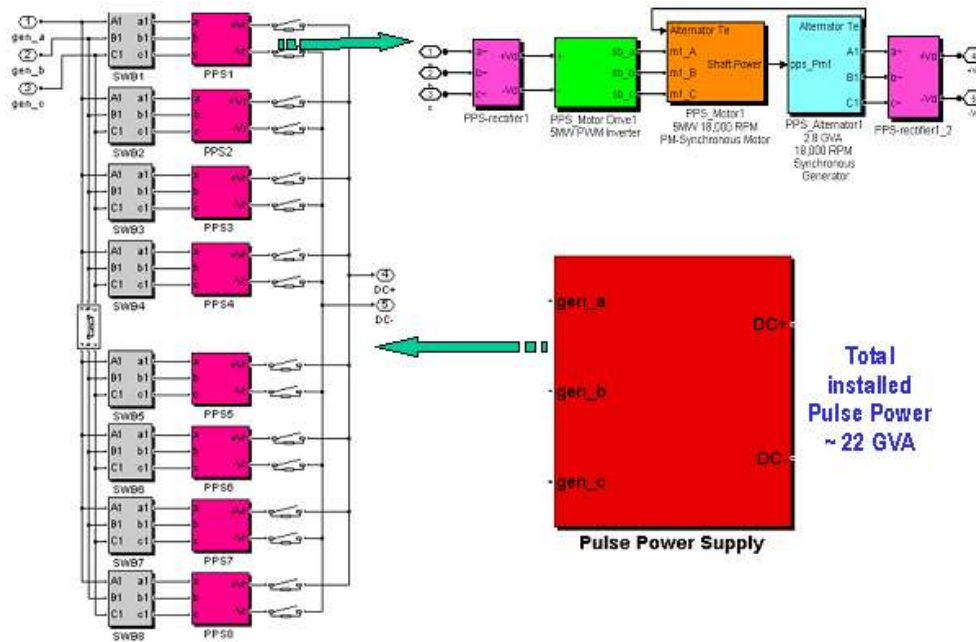


Figure 2-11: Pulse power supply model.

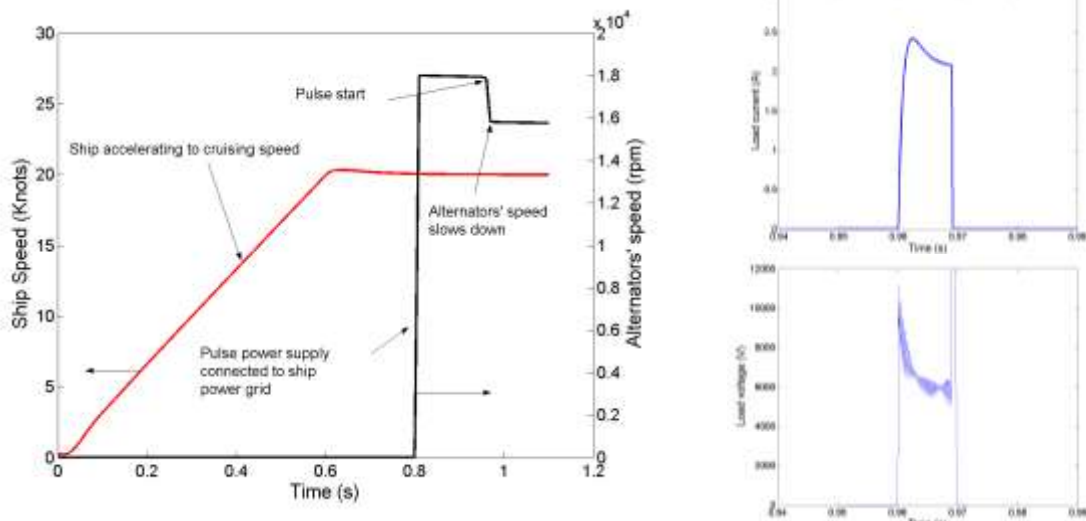


Figure 2-12: EM gun pulse example.

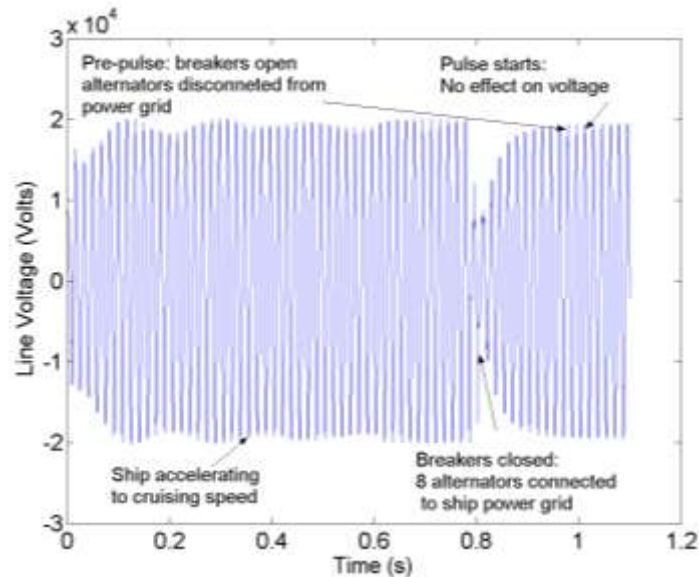


Figure 2-13: Bus voltage response during a high-power pulse.

5.2.7. Active Filtering of the Electric Ship Power System using Stored Energy and Power Electronics Equipment of a Naval EM Railgun

The intermittent nature of high power pulse loads onboard future naval vessels make the pulse power supply a highly inefficient subsystem, in terms of power density, if it is used solely for the purpose for which it was primarily intended. In order to enhance its functionality, we investigated the potential use of the energy stored in the rotors of high-speed alternators of a naval EM gun power supply, and its power electronics components, as an active filter to reduce harmonic pollution generated by various power conditioning equipment. To demonstrate the feasibility of this dual-function, a Simulink[®] model of a propulsion power train with an integrated pulse power supply and active filter was developed. Figure 2-14 shows the top level model where only a single propulsion power train and a single 36 MW generator were used for simplicity. The energy storage block and an inverter are explicitly extracted out of the pulse power supply to clearly show their dual use with the help of the various switches shown.

The active filter works by injecting currents into the distribution lines to eliminate harmonic currents, or reduce their detrimental effects on sensitive loads. The energy storage components are the rotors of the eight alternators of the naval EM railgun power supply, as mentioned earlier, and the dc link capacitors to which they are connected. The control block consists of a calculation block, a hysteresis control block, and an LC filter to reduce inverter switching harmonics.

When separate energy storage elements and inverters are used in the model, i.e., filter and pulse power supply components are independent, the simulation runs relatively well given the complexity of the model. In this example, the propulsion power train is consuming ~11 MW to keep the ship moving at its cruising speed of 20 knots. Active filtering results are shown in Figure 2-15 where voltage and current THDs are reduced from 6.7% to 4.2% and from 28.5% to 8.2%, respectively. While the voltage and current signals are improved, the filtering is not perfect because, in part, the filter parameters are not optimized. Also, the presence of high frequencies in the resulting signals is due to the fact that a single inverter was used, thereby requiring very high switching frequencies (>30 kHz). Using additional inverters, from the eight available, should reduce the required switching frequency considerably and improve signal quality.

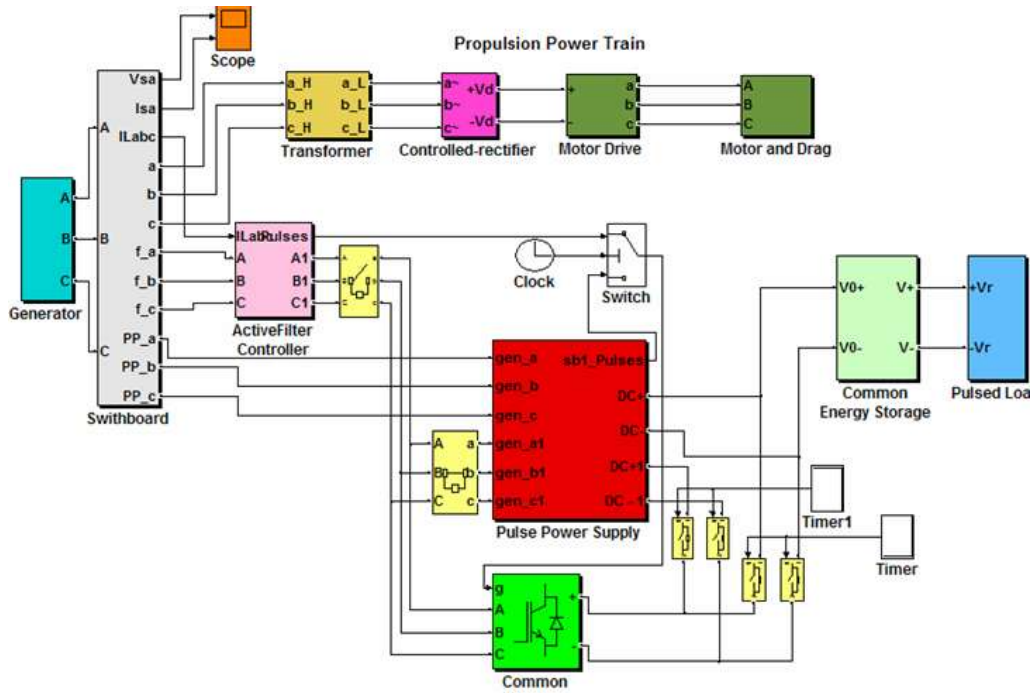


Figure 2-14: Integration of pulse power supply and the active filter with the propulsion power train model.

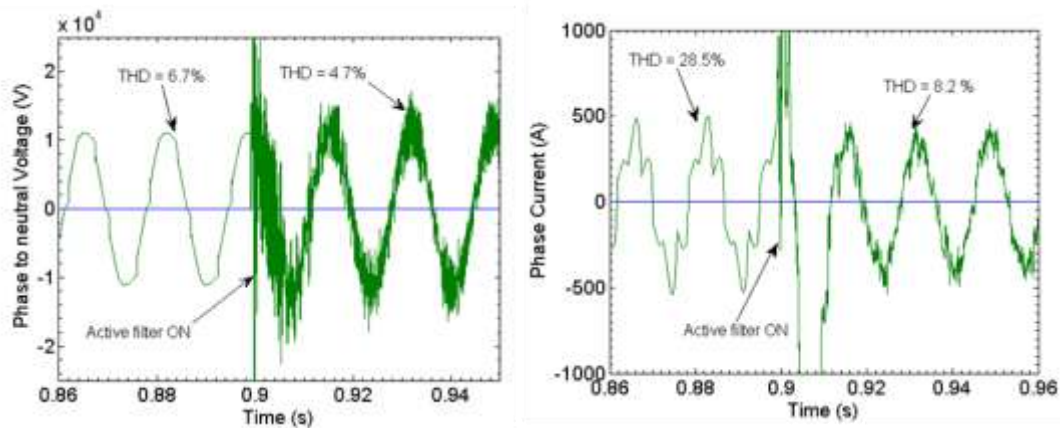


Figure 2-15: Phase voltage and current with and without active filtering.

5.2.8. Improvement of Simulink® Power System Model and Investigation of a New Modeling Environment

During the modeling process, we found that running simulations of realistic scenarios takes a very long time and errors occur often without the ability to determine the cause or correct them when using pre-programmed commercial blocks. Consequently, it was necessary to look at other options or approaches for modeling the electric ship power system. One approach was to use a different modeling environment and a second approach was to re-build the models using Simulink® native blocks only, i.e., without the use of commercial toolboxes. We tested both options. A power system model was developed in MATLAB/Simulink® without the use of pre-programmed commercial blocks. The new model, using blocks from the native Simulink® library only, is shown in Figure 2-16. Service loads for only one of eight identical zones were modeled, and gas turbine models were not included.

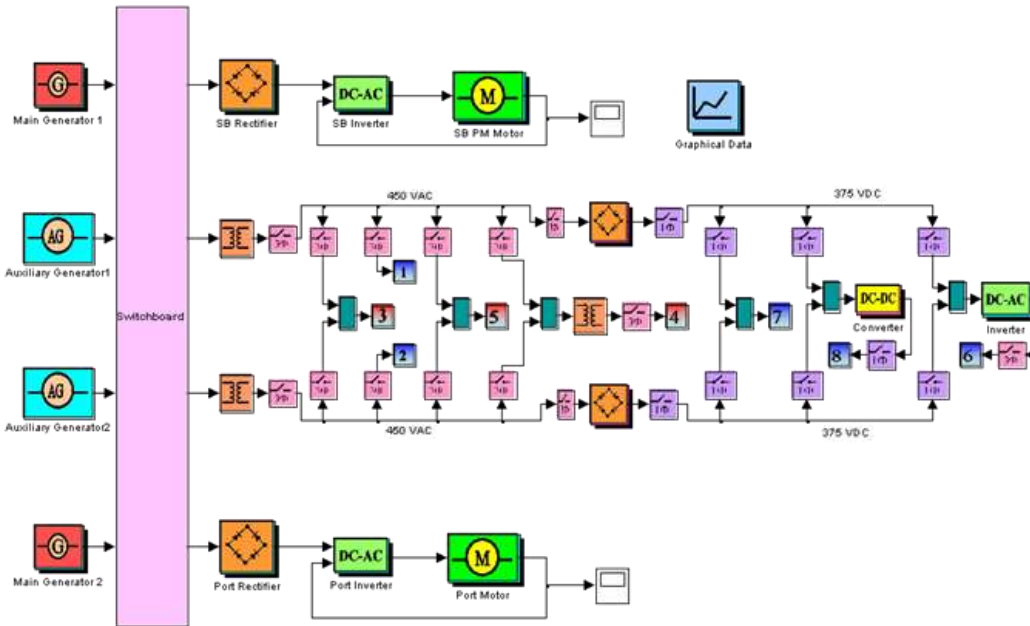


Figure 2-16: Top level Simulink® power system model with propulsion and service loads.

In addition, the same power system model was developed in the ACSL computing environment. Figure 2-17 shows the ACSL model, which was built using blocks with similar functionality as those in Simulink® whenever possible.

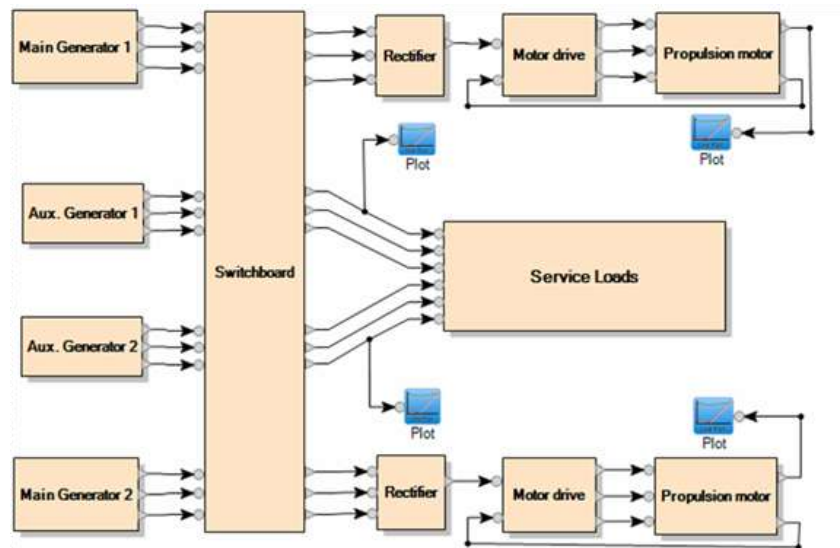


Figure 2-17: Top level ACSL model of the power system with propulsion and service loads.

The ACSL block library has only a small set of basic blocks which forces the users to build their own blocks when needed, using the ACSL CSL programming language that allows the inclusion of C and FORTRAN code if desired. This direct programming in the ACSL environment seems to be the reason the ACSL model of the overall power system runs somewhat faster than its Simulink® counter part, but without a major improvement. While the Simulink® model was made solely of inherent library blocks, the ACSL model had several user-programmed blocks. However, it is possible to directly program Simulink® blocks by writing S-functions using MATLAB, C, or FORTRAN languages. In terms of ease of modeling, Simulink® is more flexible than ACSL. Figure 2-18 depicts results of a sample run

completed in the two environments, showing the ramp-up of the propulsion motors from rest to full speed. During this run all service loads were concurrently supplied with their respective powers.

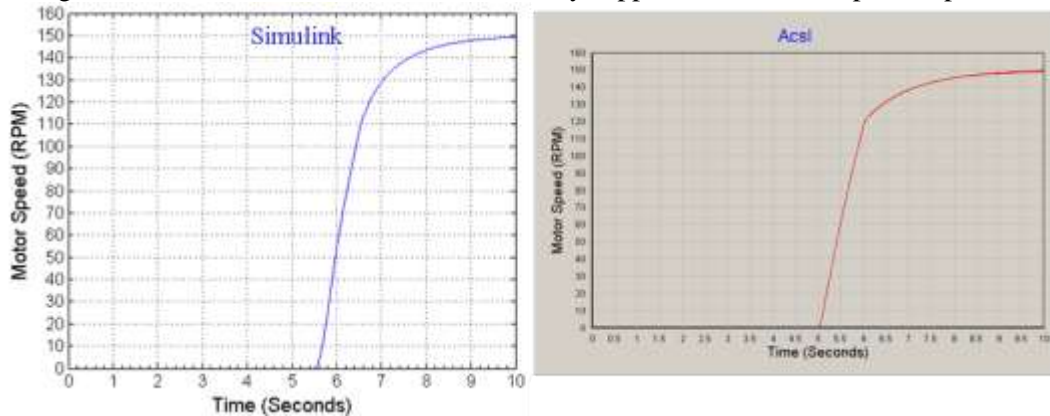


Figure 2-18: Sample run result showing motor speed from Simulink® and ACSL models.

The modeling of various electric machines, mainly the generators and propulsion motors, have been given particular attention since the parameters used in the model for these components are obtained through design work performed at the Center for Electromechanics. This effort allows a realistic representation of machines that are presently under development or projected for the future. However, the breakers, the propulsion transformers and rectifiers, and inverter switches in these test models were ideal and simulations with a discrete solver and a fixed time step of 1 μ s were completed in reasonable times.

The Simulink® model of the electric ship power system was subsequently improved by including more realistic models of the breakers and by adding models of the propulsion transformers and rectifiers for better fidelity and broader flexibility. Considerable efforts were made to make the model user-friendly for a third party. The model was given to a graduate student at the Naval Postgraduate School for use in his research project. In this model, Simulink® native blocks were used to solve the differential equations describing all the components in the system except for the inverter switches which were modeled as ideal switches. As will be discussed later, modeling all switching events as they occur naturally and adding large pulse loads create considerable numerical challenges to the Simulink® discrete solver.

An example illustrating the analyses the model can perform is a transfer of power during a major fault. In this scenario, one of the main generators, initially supplying one of the propulsion power trains, is damaged while the ship is moving at full speed. The model allows the simulation of transfer of power from the working generator to the affected propulsion line. Appropriate breakers are set to close and open and motor controllers are set to request a speed that is compatible with the available power. Figure 2-19 shows the top level Simulink® model, the propulsion motor speed response during fault and after power transfer, and the motor current response.

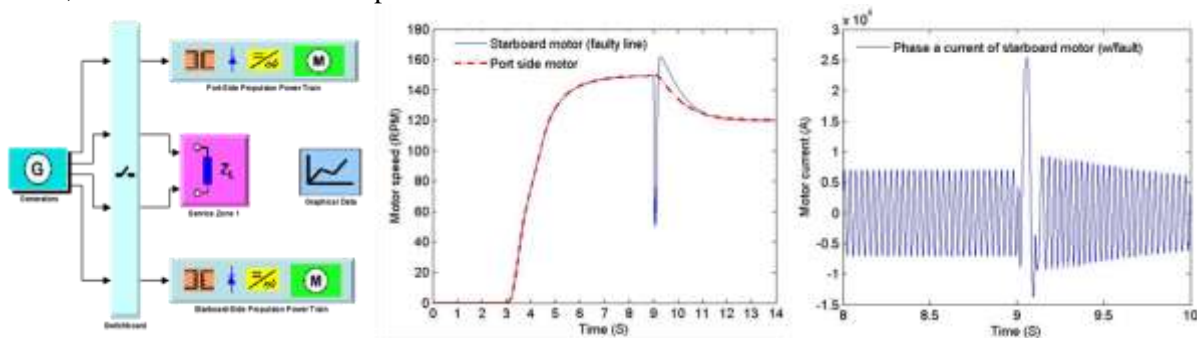


Figure 2-19: Simulink® model, motor speed, and current during fault and after power transfer.

The Simulink® model was further improved by including commutation effects in the rectifier models and adding a realistic representation of the inverter switches. This addition was in response to comments made by several attendees at various conferences concerning the importance of these details for studies of switching events and especially during fault condition. The added details and the resulting complexity of

this effort was to study the coordination of large pulse loads for optimum use of installed power and stored energy onboard electric ships, and to show that power can be shared among various ship components. Specifically, it was shown that the energy stored in the rotors of the electromagnetic rail launcher can be used as a power source for a free electron laser system. A top-level representation of the integrated power system model that includes an EM rail launcher which operates in conjunction with an FEL system is shown in Figure 2-23. The FEL system model was simplified to appropriately represent the power level and width of each pulse, as well as take into account the power needed by the auxiliary equipment necessary for FEL operation. The FEL output power consists of 20 MW, 5 s long pulses spaced by 2 s intervals. The EM launcher stores 800 MJ in the rotors of 8 alternators which is adequate for 5 EM shots. The power system model was exercised to simulate a scenario that demonstrates the sharing of power among high power loads. The exercise consisted of accelerating the ship from rest to full speed, reducing the ship speed to free-up power for charging the EML energy storage system, charging the EML, firing an EML shot and, without recharging, firing 4 FEL shots using the remaining stored energy in the EML power supply. The ship was also set to accelerate to full speed during the FEL pulse firing sequence to simulate evasive action that requires full installed power onboard, while defensive measures are taken by the FEL system which is powered by the energy stored in the EML power supply. Figure 2-24 shows power consumption during the scenario just described. This result shows that power can be shared effectively between the FEL and EML systems. A factor that is important for optimum design and operation of future electric ships. Details of this analysis were compiled in a paper and presented at an EML conference in Berlin.

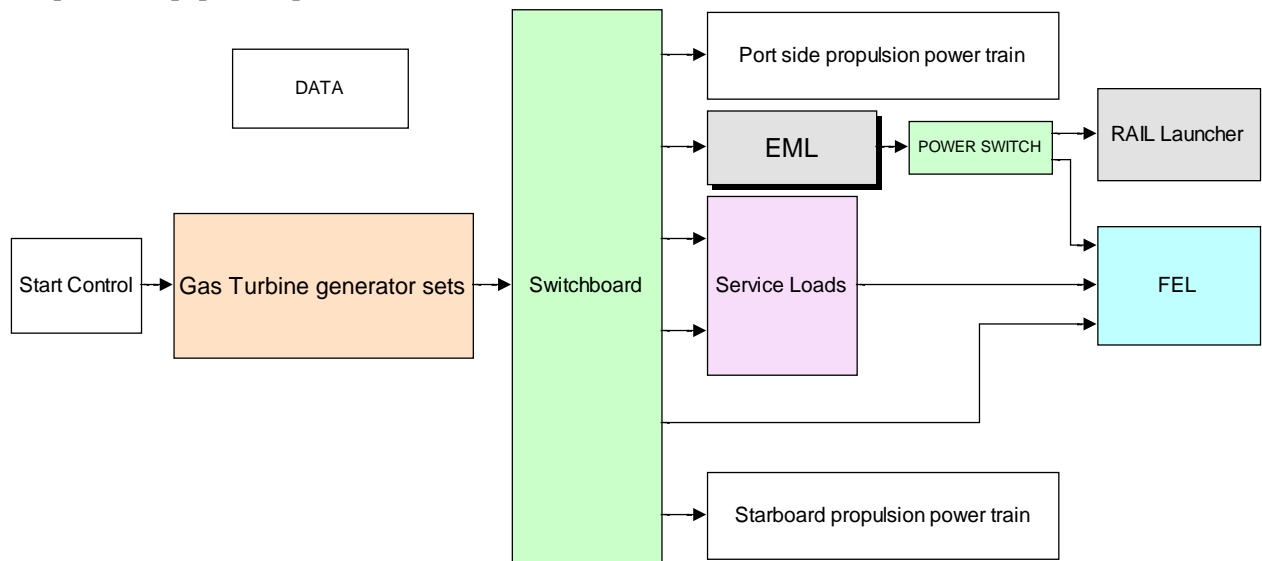


Figure 2-23: Top level model of the electric ship power system with integrated FEL and EML systems.

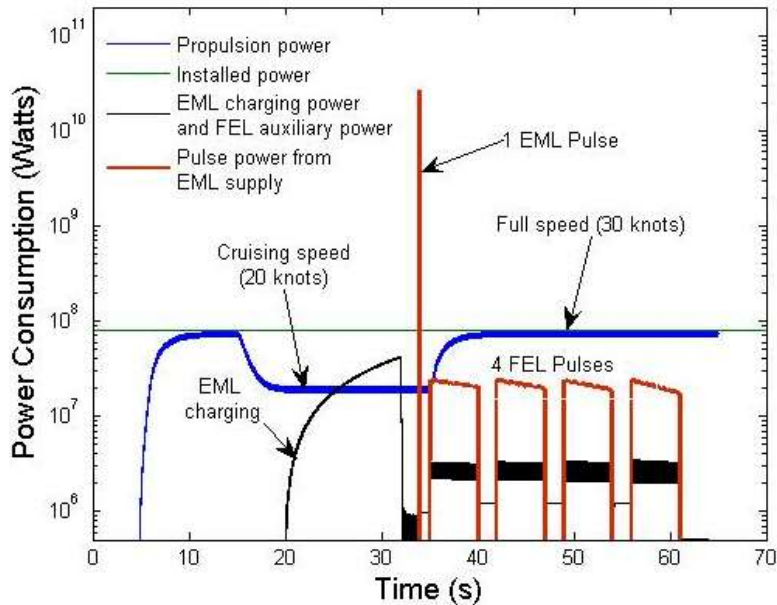


Figure 2-24: Power balance during EML/FEL operation while ship is in motion.

5.2.10. Generator-set Optimization Studies

Present-day electric power generation on ships often uses high-speed gas turbines coupled to lower-speed generators via gear boxes and installed on lower decks, thereby requiring large volumes to accommodate the intake and exhaust ducts. This architecture is inefficient. As an alternative, a high-speed gen-set system, with no gear box, has a potential to improve power density and efficiency considerably. In addition, reviewers of our initial study of the 20 MW propulsion power train suggested that a 50% reduction in the gas turbine-generator size would allow their installation on upper decks, freeing a considerable volume otherwise occupied by the air ducts. The goal of our research on this topic was to ascertain quantitatively whether that is the case. We used two different approaches in addressing this problem. In the first approach, gas turbine and generator scaling laws were used to show that increasing operating speed and directly coupling the turbine to the generator would indeed improve power density, as long as the prime power generator-set assembly is installed on upper decks since the air ducts dominate the overall volume.

In the second approach we examined engine parameter relationships from a fundamental point of view. A practical expression relating gas turbine speed to its output power, shown in Figure 2-25, was derived [1]. The derivation was based on fundamental thermodynamics and supersonic flow constraints in turbine blades. Results of a survey of existing gas turbines used for power generation world-wide are also included in Figure 2-25 for comparison. As can be seen, the turbine speed decreases as power increases. This result indicates that high-power gas turbines, such as the 36 MW MT30 gas turbine that is being considered for use on future Navy ships, cannot run at high speeds. In fact, the MT30 turbine runs at 3600 rpm, which is within the calculated range. This seemingly simple result is in contrast with the initial assumption that a major gain in power density can be achieved by increasing the operating speed. This may be true, however, only at low power levels which are much less than the 80 MW total installed-power planned for future Navy destroyers. The gas turbines currently used on DDG-51 for electric power generation (Allison 501 engine), with power level around 4.5 MW, run at much higher speed (14,340 rpm) as predicted by our calculations; a fact that further re-enforces this result. Consequently, the issue of granularity, i.e., the number of engines and corresponding power levels in a multiple gas turbine system, becomes important.

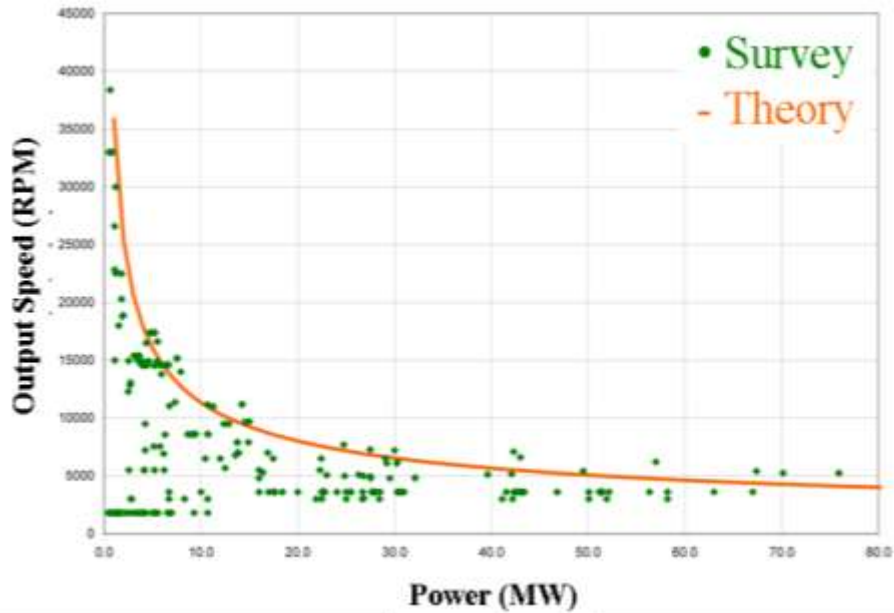


Figure 2-25: Gas turbine speed vs. output power.

A combinatory method has been developed that eventually can be used to select an optimum configuration. Simplified gas turbine engine design methods were adapted to provide the engine's volume as a function of power. The combinatory analysis of the optimum configuration involves determining the combinations of engines that would provide the desired 80 MW of power with the minimum total volume, while still maintaining a reasonable number of engines. Preliminary results were based on a minimum engine size of 10 MW. The analysis began with a single (80 MW) engine and a trend became apparent when eight engines were used. An analysis with sixteen engines was then conducted. The results are shown in Figure 2-26. It was found that the smallest volume results from using the smallest engines with equal power. This is due to the fact that the volume is, approximately, a monotonically increasing function of power.

The generator volume was calculated using the well established relation for synchronous generators relating power, speed, current density, flux density, air-gap diameter, and active length. The generator and engine volumes, as well as the total gen-set volume, as a function of power are also shown in Figure 2-26. This result gives a general insight on the relative variation of volume for different components, but a more realistic comparison would require the inclusion of the enclosures, frames, and other necessary auxiliary equipment such as cooling and control systems. The important result is that the gas turbine engine and generator have comparable sizes and both increase monotonically with power.

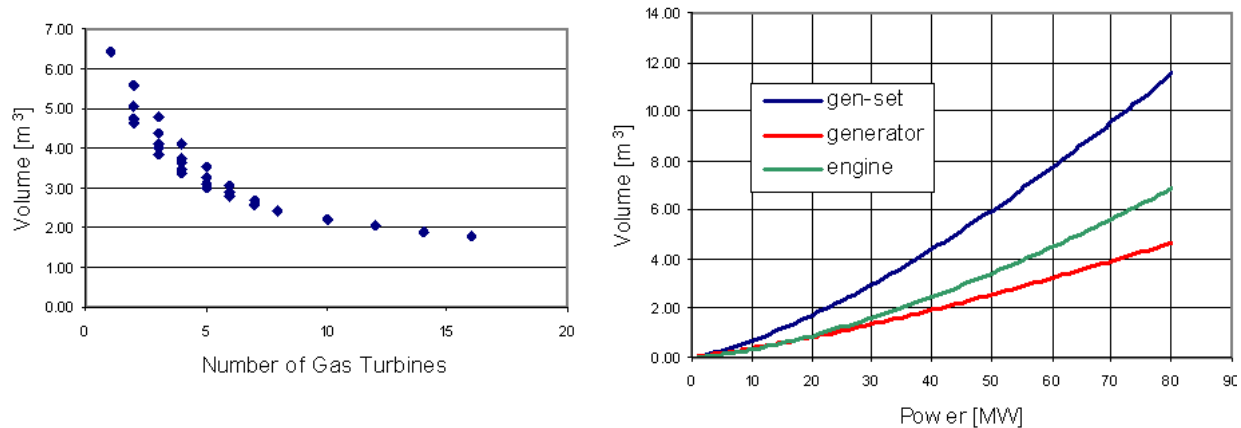


Figure 2-26: System volume for varying number of gas turbine engines (left) and engine, generator, and gen-set volumes vs. power (right).

In our engine analysis, certain input parameters required adjustment to agree with production engines. The new gas turbine data available comes from the Rolls-Royce AE 1107C-Liberty engine, rated at 5 MW. The analysis predicts a radius similar to the Liberty engine, but with a much smaller length. Further investigation of the compressor stage length-to-height ratio showed that the value changed considerably from inlet to exit, but in the analysis it was held constant. The other two parameters of interest are the turbine inlet temperature and the flow velocity. In the analysis, both parameters were held constant, but it is possible that they vary with power. Furthermore, the analysis and actual turbine data show that the turbine inlet temperature is a major parameter which affects the actual size of the engine. This parameter is not usually released by the manufacturers, a fact that makes the comparison of our analysis results with existing gas turbines difficult.

5.2.11. Design and Analysis Study of High-speed Gas Turbine-generator Systems

In cooperation with two industrial partners, we completed a design and analysis study of high-speed gas turbine-generator sets. In this study, the anticipated benefits of a 5 MW, 15,000 rpm, 3-phase, 60 Hz, 4160 V system were examined. The main benefit stems from the fact that a directly-coupled gas turbine-generator set eliminates the need for a reduction box and has a much lighter generator as compared to conventional low-speed generators, thereby, considerably improving power density. Four generator types were considered: permanent-magnet synchronous, wound-field synchronous, switched-reluctance, and induction generators. The permanent-magnet and wound-field synchronous topologies were studied in detail, while the switched-reluctance and induction generators were found inadequate for applications where stand-alone power systems are required. It was found that the permanent-magnet topology presents the best solution and offers a weight savings of ~20,000 kg over commercially available 5 MW gas turbine-generator-based power systems. This weight savings accounts for the additional 2,500 kg of power electronics needed to reduce the high-speed generator frequency down to 60 Hz. The overall system is shown Figure 2-27.

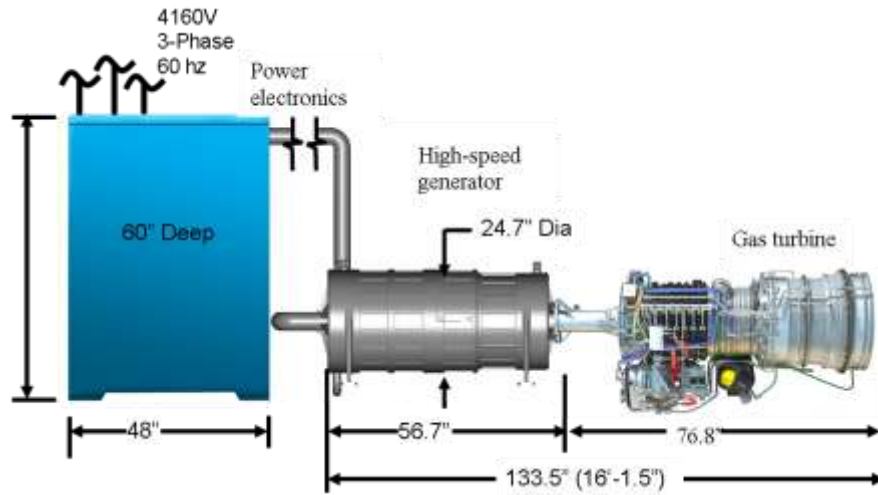


Figure 2-27: 5 MW, 15,000 rpm high-speed gas turbine-generator set.

Generator design and analysis were conducted with a detail level commensurate with the goals of the study. Figure 2-28 shows general views of the permanent-magnet generator and magnetic bearings. The results of the study were presented at an international conference [11] and can be summarized as follows:

- The permanent-magnet generator topology provides the most compact, power dense, and efficient 5 MW/15,000 rpm system.
- The wound-field generator is limited at 15,000 rpm by stresses and rotor dynamics issues and is less efficient than the permanent-magnet topology.
- The induction and switched-reluctance topologies have lower torque density and require external excitation with complex control systems and advanced switching power electronics.

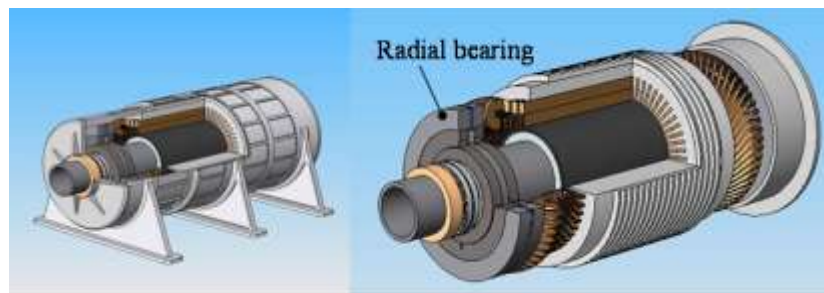


Figure 2-28: Permanent-magnet generator with radial magnetic bearings.

5.2.12. Study of Prime Power Generation Onboard Electric Ships Using Directly-coupled Gas Turbine Permanent-magnet Generator Sets

As a continuation of the work we did on the 5 MW gen-set, we conducted a study to assess the advantages of prime power generation onboard future naval all-electric ships based on directly-coupled gas turbine and permanent-magnet generator sets. In order to ascertain the effectiveness and practical benefits of this approach, we conducted a design study of four additional gen-set units that include 11, 15, 20, and 40 MW permanent-magnet generators, their direct coupling with existing marine gas turbines, and their corresponding power rectifiers that convert the generators' ac power to dc power for distribution. Mass and volume of the generators and rectifiers were determined and sizes of the complete gen-sets were estimated.

It was found that this topology reduces system mass and volume significantly, as compared to electric power systems installed on present-day navy ships, and improves efficiency through removal of the

reduction gears, rotor windings, and exciter found in conventional turbo-generator machinery. Furthermore, it was found that a significant benefit this topology brings is a reduction in gas turbine air duct volume if the compact gen-sets are relocated on or near the ship's upper decks. In addition, a combinatory analysis revealed that the choice of the number of generating units and their respective power levels has a significant influence on overall efficiency. However, the addition of power electronics that control the output electric power from the generators adds to system weight at levels which are reasonable for basic topologies, but contributes additional losses. Additional power conditioning may be necessary, however, to reduce the detrimental effects of harmonic distortions which are inherent to power electronics. A summary of the main results describing the topology, the gas turbines, the permanent magnet generators, and the power rectifiers are presented. A discussion on gen-set installation location onboard ships and an analysis of fuel consumption will also be presented.

5.2.12.1. Topology

As mentioned earlier, conventional wound-field generators found on present-day navy ships are coupled to gas turbines through reduction gears and output power at 60 Hz. Since most loads onboard all-electric ships require conversion of power, including propulsion loads which can consume up to 90% of installed power, the 60 Hz prime power generation frequency is not necessary. Removing the reduction gears and allowing the generator to operate at the turbine speed results in a generation frequency that is higher than 60 Hz for gas turbines with power ratings less than 20 MW [1]. This high-speed operation enables a reduction in the generator size and the use of permanent magnets for excitation allows further reduction in size and an improvement in efficiency. The high-frequency output power can be converted to dc power by readily available power diodes and other power switches. The resulting topology, shown in Figure 2-29, enables considerable savings in weight and footprint [1], and improves efficiency.

While they are compact and reliable, gas turbines are inefficient and require expensive fuel. There are two types of configurations, single-shaft and twin-shaft, and both can be used to drive electric generators. An inherent characteristic of gas turbines is their speed-power relationship where speed decreases with power, while the size increases. Figure 2-30 shows the variation of speed and size (blades' outer radii) with respect to power [1]. This trend also applies to the gas generator part of twin-shaft turbines.

The primary parameter that affects efficiency and size of the gas turbine is the turbine inlet temperature. The development of new materials and cooling techniques of turbine blades present major challenges for improving power density and efficiency. Figure 2-30 also shows the variation of efficiency with specific work for two different turbine temperatures [1].

The important result to note from the gas turbine analysis is that high-power gas turbines need to run at slower speeds and have large sizes. This is due to limitations on blade stresses and air-flow velocity which needs to be kept sub-sonic in order to avoid losses associated with shock waves [1].

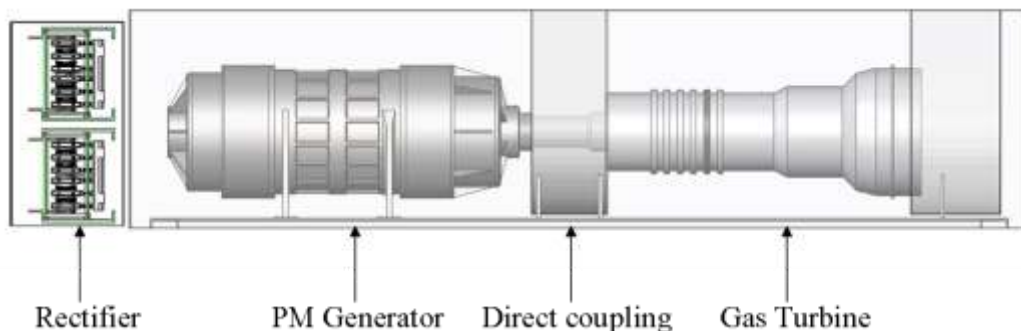


Figure 2-29: Directly coupled gas turbine PM generator topology.

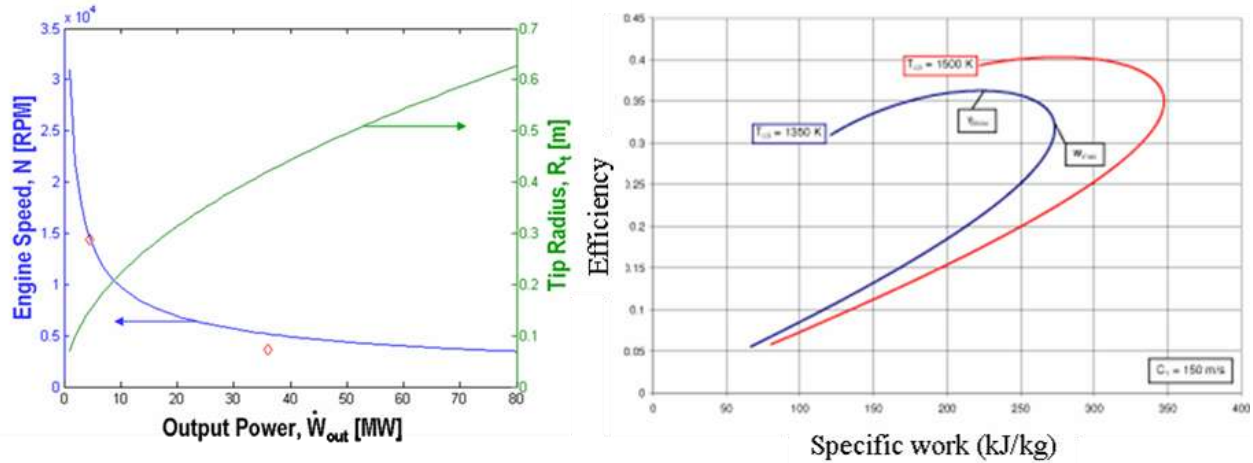


Figure 2-30: Gas turbine speed and size as a function of power (left) and efficiency vs. specific work.

5.2.12.2. Permanent Magnet Synchronous Generators

In the permanent-magnet topology used in this study, magnets are mounted on the rotating member of the machine, thereby eliminating the need of an excitation winding, which results in a reduction of the overall losses and size of the rotor. The magnets are held in place by a composite banding and a harmonic shield. A cross section describing the surface-mounted radial flux topology is shown in Figure 2-31. An expanded view of a typical rotor configuration that includes magnetic bearing laminations is included in Figure 2-32.

Unlike gas turbines where shaft speed decreases with increasing power, the output power of a synchronous generator is directly proportional to its shaft speed. Increasing generator speed is therefore advantageous in reducing size. For low to intermediate gas turbine power (1 to 15 MW) where shaft speed is higher than the conventional 3,600 rpm, the high speed advantage is very effective in reducing the generator size when direct coupling is considered. This is particularly true for low power engines (1 to 5 MW) where speed is $\sim 15,000$ rpm or higher.

While magnetic loading is limited by stresses and magnet material, a high electric loading can be achieved by actively cooling the armature winding. A section of the cooling manifold and a 3d FEA model of a multi-pole multi-phase armature winding used to calculate the synchronous reactance and verify the torque capability of the machine are shown in Figure 2-32.

In order to determine component ratings and size of potential power generating units for an 80 MW electric ship, we studied 5 gas turbine gen-set systems:

- 5 MW 15,000 rpm PM generator coupled with an MT5 gas turbine
- 11 MW 11,000 rpm PM generator coupled with a Solar 100 gas turbine
- 15 MW 7,900 rpm PM generator coupled with an LM1600 gas turbine
- 20 MW 3,600 rpm PM generator coupled with an LM2500 gas turbine
- 40 MW 3,600 rpm PM generator coupled with an MT30 gas turbine

Figure 2-33 is a general view of the 5 gen-sets that allows a relative comparison among the various gen-sets. Table 2-1 gives corresponding parameters, weights, and volumes.

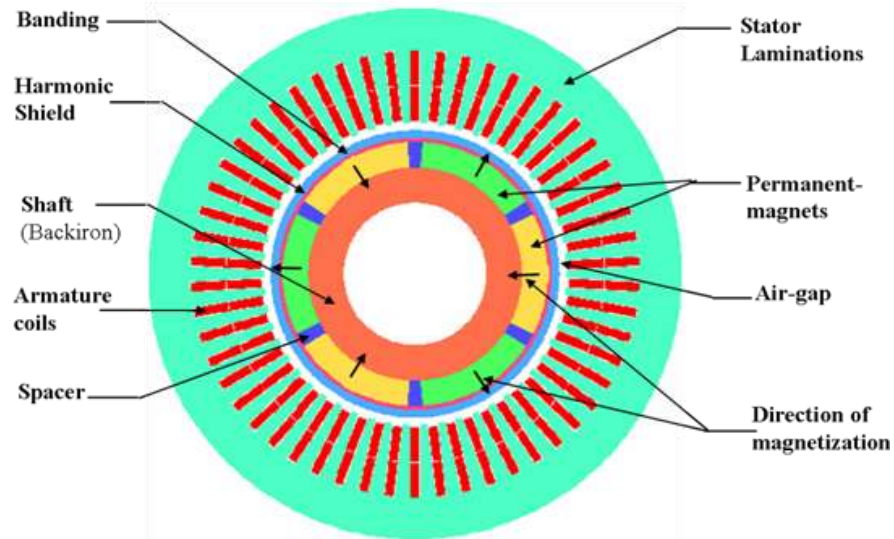


Figure 2-31: Cross section of a surface-mounted radial flux permanent magnet generator.

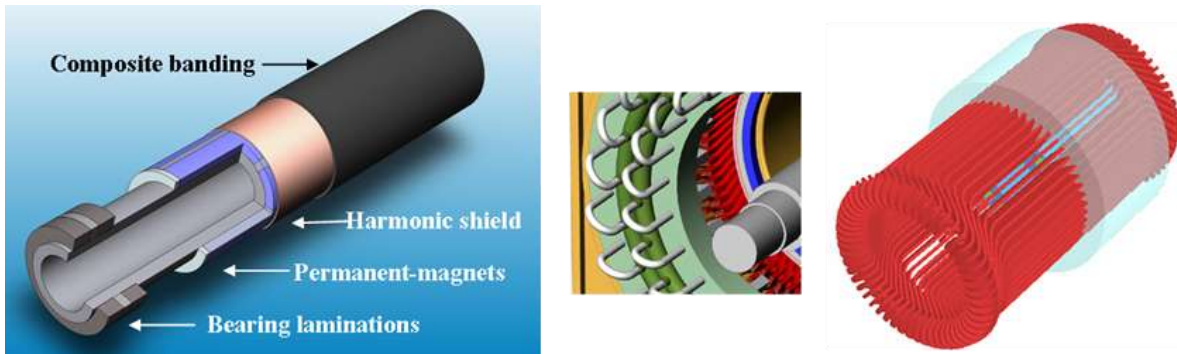


Figure 2-32: Permanent-magnet rotor assembly, cooling manifold, and armature winding model.

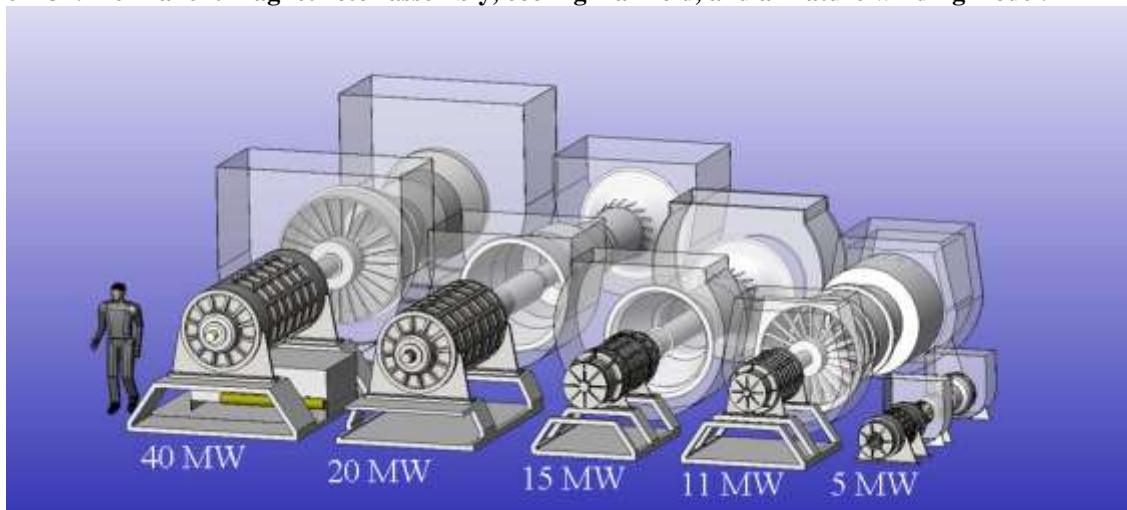


Figure 2-33: Permanent-magnet generator sets.

Table 2-1: Permanent-magnet generator parameters.

Generator Parameters							
Power (MW)	Speed (rpm)	Electric Frequency (Hz)	Voltage (kV)	Power factor	Magnetic Bearings	Weight (kg)	Volume (m ³)
5	15,000	750	6.6	0.84	Yes	1700	2.34
11	11,000	733	6.6	0.84	Yes	2700	7.25
15	7,900	395	6.6	0.88	Yes	5000	13.23
20	3,600	480	6.6	0.86	No	9000	33.37
40	3,600	600	6.6	0.82	No	13030	38.4

5.2.12.3. Power Conversion

The last components of the gen-set systems are the power rectifiers. In order to determine the size and performance of power rectifiers in the 5 to 40 MW range, we conducted a design study of 6-, 12-, and 18-pulse diode rectifiers. All power rectifiers were designed for 6.6 kV generator output voltage. The power diodes were selected from a set of diodes obtained through a general survey of existing commercial power diodes worldwide. Figure 2-34 shows the ratings of the most performing power diodes. A rectifier for the 5 MW gen-set unit is shown on Figure 2-35 along with the corresponding heat sink and thermal analysis results. A summary describing weight, volume, cooling flow rates and topology for 6-pulse rectifiers is given in Table 2-2.

Results of all rectifiers' performance analyses are summarized in Table 2-3. Figure 2-36 shows variation of THDs with power for the 6-, 12-, and 18-pulse rectifier topologies.

The important result to note from the rectifiers' analysis is that higher pulse rectifiers improve the performance significantly by reducing the harmonic distortions, but add to weight and volume. For comparison, the 5 MW gen-set is shown in Figure 2-37 with the 6- and 12-pulse rectifier units along with the corresponding weight, volume, and performance measures.

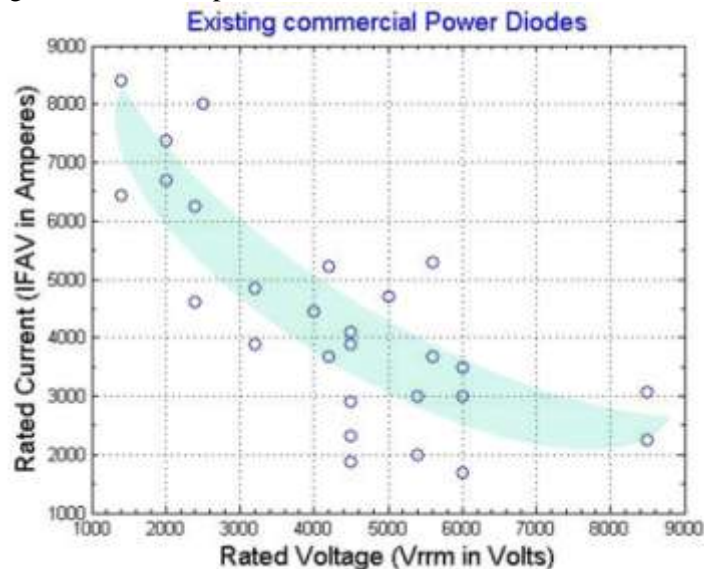


Figure 2-34: Commercial high-power diodes.



Figure 2-35: 1-phase leg, assembly, heat sink, and temperature distribution in 5 MW rectifier.

Table 2-2: 6-pulse rectifier parameters.

		6-pulse Rectifier Parameters					
Power (MW)	Topology	Diodes	Weight (kg)	Volume (m3)	Flow rate (gpm)	THD (%) Current	THD (%) Voltage
5	3 series	18	159	0.237	0.77	20	25
11	3 series	18	165	0.237	1.31	11	30
15	3 series	18	165	0.237	1.03	13	30
20	3 series	18	165	0.237	1.03	19	25
40	3 series 2 parallel	36	300	0.4	1.14	19	25

Table 2-3: Rectifiers' performance.

Power (MW)	6-Pulse			12-Pulse			18-Pulse		
	Diode count	THD _i (%)	THD _v (%)	Diode count	THD _i (%)	THD _v (%)	Diode count	THD _i (%)	THD _v (%)
5	18	18.4	25	24	5.36	14.5	18	2.5	9.8
11	18	19.5	25	24	3.5	14.6	18	1.6	9.7
15	18	22.7	22	24	6.1	13.4	18	2.8	9.6
20	18	22.4	22	24	5.6	13.5	18	2.5	9.1
40	36	8.3	30.7	48	1.1	13.8	36	0.5	11

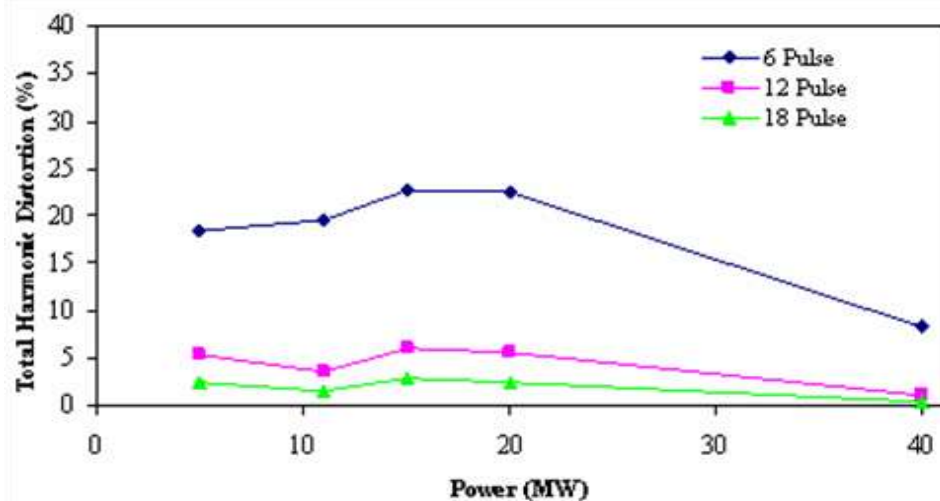


Figure 2-36: Current THD vs. power for 6-, 12-, and 18-pulse rectifiers.

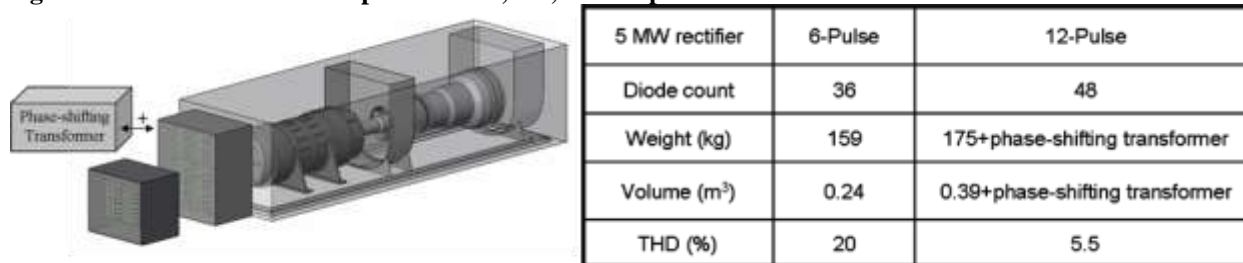


Figure 2-37: 5 MW gen-set with 6- and 12-pulse rectifiers.

5.2.12.4. Complete Gas Turbine Permanent Magnet Generator Sets

Finally, for size comparison, the 5 and 40 MW gen-set systems are shown in Figure 2-38 and the complete 5 gen-sets with 12-pulse rectifiers units are shown in Figure 2-39. Table 2-4 gives the sizes of the gen-set systems and their components, including the 12-pulse rectifiers.

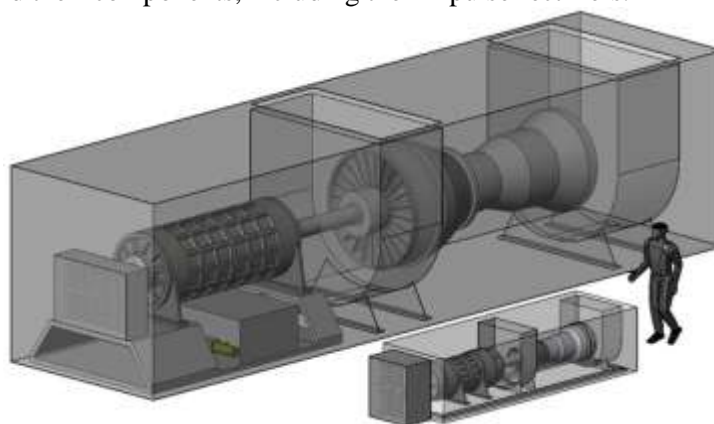


Figure 2-38: 5 MW and 40 MW gen-sets with 12-pulse rectifiers.

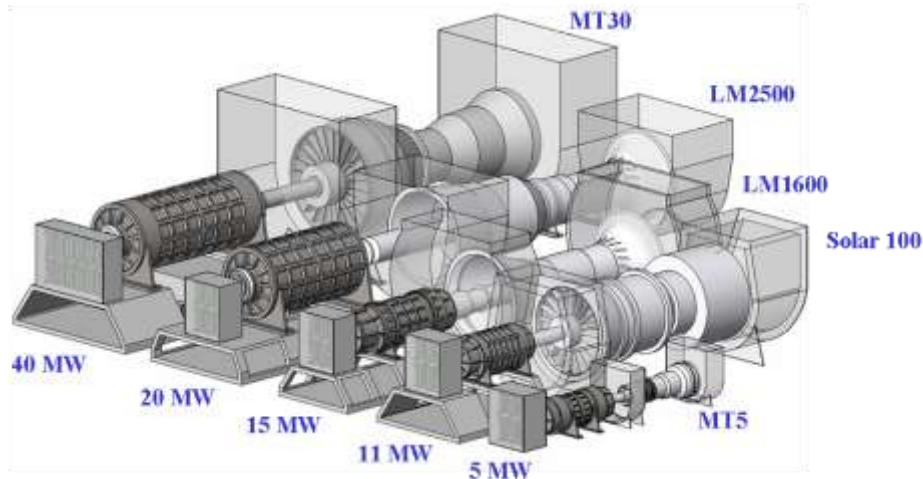


Figure 2-39: All gen-set units with 12-pulse rectifiers.

Table 2-4: Parameters of all gen-set systems.

Power (MW)	Turbines	Generators		Rectifiers		Gen-sets
	Volume (m ³)	Weight (kg)	Volume (m ³)	Weight (kg)	Volume (m ³)	Volume (m ³)
5	2.99	1700	2.34	175	0.39	5.72
11	26.33	2700	7.25	175	0.39	33.97
15	19.25	5000	13.23	175	0.39	32.87
20	35	9000	33.37	175	0.39	68.76
40	51.06	13030	38.4	443	0.66	90.12

5.2.12.5. Gen-set Installation Location

Four gen-sets, totaling 80 MW, were chosen for the next analysis. These were 5 MW, 15 MW, 20 MW, and 40 MW gen-sets. In order to determine their relative size with respect to the ship, these gen-sets were installed on a DD-type destroyer. The ship model was constructed using public information obtained from various sources. Figure 2-40, which is to scale, clearly shows the relative sizes between the electric ship and the 80 MW prime power generation system. As can be seen in Figure 2-41, when the two large gen-sets are installed on the lower deck, they require long air ducts that span all ship deck levels with a length of about 12 m (40 ft) each. By installing these gen-sets on a higher deck level, the air ducts' length is reduced to 5.5 m (18 ft), resulting in a total volume savings of about 156 m³, which is very significant. The corresponding installation is also shown in Figure 2-41.

The 5 MW gen-set was installed on the highest deck level possible to indicate the possibility of eliminating most of the ducts and saving maximum space. This may be possible since the low power gen-set is small enough in weight and volume not to cause any instability problems. The 15 MW mid-size gen-set can also be installed at a position where the air ducts are also short. The actual installation of the prime power generation system on board future electric ships is probably different from the one shown in this analysis, but this example illustrates the importance of gas turbine air ducts on power density and the possibility to reduce their volume by locating the prime power gen-sets on the highest deck levels possible.

The stability concerns raised by this topology can be addressed in several ways, including the option of installing the large and heavy propulsion motors and their drives on the lowest deck since they don't require air ducts.

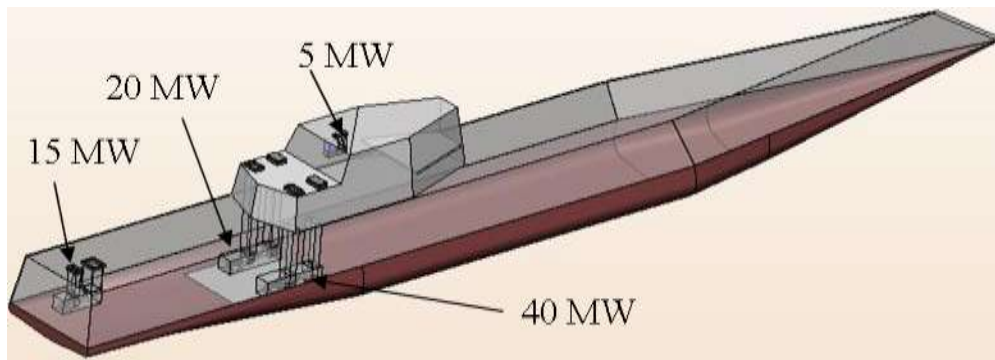


Figure 2-41: Installed 80 MW directly-coupled gas turbine PM generator sets.

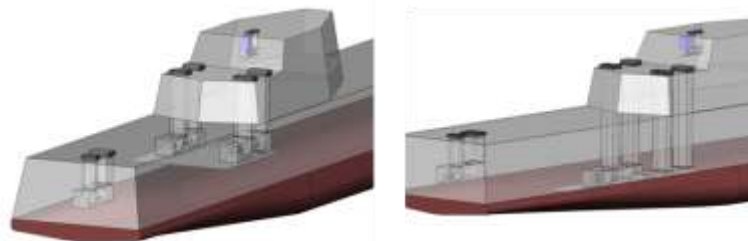


Figure 2-42: Installation options on upper decks (left) and lower decks (right).

The next analysis we performed involved determining the most efficient 80 MW gen-set system that powers an electric ship with a known, or pre-determined, mission profile. The combinatorial analysis method we developed determines the power level at which each gas turbine needs to run for a given segment of the mission profile so that the fuel consumed over the whole mission is minimal. In the initial calculation, the program was set up to accept a given number of gas turbines, each with a known power capacity and known specific fuel consumption characteristics. The calculation uses an actual mission profile for present-day destroyers (DDG-51) which was limited to a 24-hour period. The DDG-51 mission profile and the corresponding 24-hour power demand profile are shown in Figure 2-42. The propulsion power demand used in the calculation is that of the notional DD electric ship and is included in Figure 2-42. The ship service power was fixed during the duration of the mission to 8 MW. Table 2-5 contains results of an analysis of three groups of gen-sets each totaling 80 MW. The calculation shows that fuel consumed by the system considered earlier in the air duct analysis, i.e., 5, 15, 20, and 40 MW, is less than that consumed by a system made of four 20 MW gen-sets, as well as the system used in the notional DD electric ship, i.e., 4, 4, 36, and 36 MW. In addition, the calculation also determines which gen-sets are used and at what power level during each segment of the mission. Details of the analysis can be found in [1]. The calculation can be extended to accept any number of prime power units, with any power level, as long as fuel consumption characteristics for each unit are known. This analysis can also be useful to the electric ship power system designers if they want to determine fuel consumption performance when deciding among several options for prime power generation in terms of number of units and the power level of each unit. In addition, once the number of units and their respective powers have been decided, the mode of operation can also be determined by indicating which and how each gen-set is to be used to provide power for a given load.

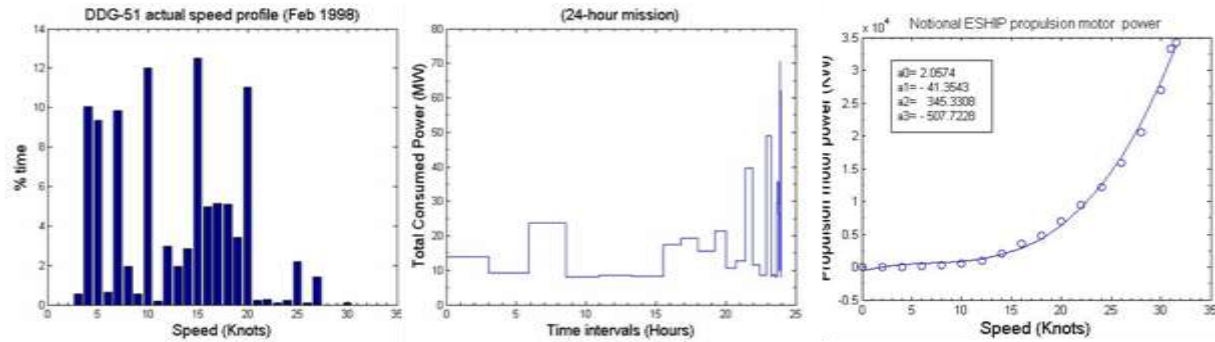


Figure 2-42: Actual mission profile, 24-hour power consumption profile, and propulsion load.

Table 2-5: Fuel consumption for three 80 MW gen-set systems.

Combination (MW)				Fuel Volume (m3)
5	15	20	40	101
20	20	20	20	112
4	4	36	36	117

5.2.13. Summary

The results summarized in the preceding figures and tables show that a prime power generation system based on directly-coupled gas turbine permanent-magnet generators offers considerable advantages in terms of space savings and efficiency improvement for an all-electric navy ship. Apparent shortcomings often associated with permanent-magnet machines, such as potential high voltage hazards due to the permanent excitation and potential permanent demagnetization under fault condition, have not been addressed in detail in this study. However, we believe that these potential problems can be solved in a satisfactory manner through rigorous power conditioning schemes and innovative concepts that allow a fast slowing down of the rotor during fault conditions.

The quantitative results obtained in this study, however, should give designers of power system architectures for all-electric navy ships a valuable insight in terms of size, efficiency, and performance when considering this particular prime power generation system: the directly-coupled gas turbine permanent-magnet generator topology.

5.2.14. Study of Propulsion Cross Connection Concept

In present-day Navy ships with mechanical propulsion, such as in DDG-51 ships, the gas turbines drive the propellers independently, i.e., each propeller is connected to a set of gas turbines through reduction gears with no connection between the two propulsion power lines. Consequently, when the ship is sailing at low speeds all propulsion turbines are required to operate well below their rated power with high fuel consumption rates. This mode of operation is very inefficient and a potential solution to this problem has been proposed by D. Clayton and T. Doyle [iii]. Figure 2-43, adapted from their presentation at an ASNE meeting in 2006, describes the concept of cross connecting the propulsion power lines by adding disconnect clutches, power take-off gears, 6 MW motor/generators, and control units that allow a transfer of power between the two propulsion power lines. When the ship is sailing at very low speed, the main propulsion turbines are turned off and ship service power is transferred to propel the ship through the motor/generator units. R&D options indicated by the authors include, among many, electric machines. In our first analysis of the concept, we considered the motor/generator unit and determined, through a design study, the size and weight of a 6 MW/3600 rpm PM motor/generator. The initial choice of the type and topology of the machine, as well as the speed, were arbitrary and other options are possible. A

perspective view of the PM machine, which weighs 2700 kg and has a volume of 1.35 m³, is included in Figure 2-43.

Power converters and power take-off gearboxes were then considered in order to have an estimate of the size of the additional equipment required by this concept and determine whether it is feasible. The power take-off gearbox is not standard and needs to be custom-made for the application. In order to estimate its volume and weight, a very simple approach allowed a first order estimate as shown in Figure 2-44. The assembly drawing in this figure with the generator installed on top of the main gearbox, as initially shown on the concept sketches, is to scale and gives a size comparison between the existing and added equipment. A more realistic installation of the generator would be on the deck floor as shown in Figure 2-44.

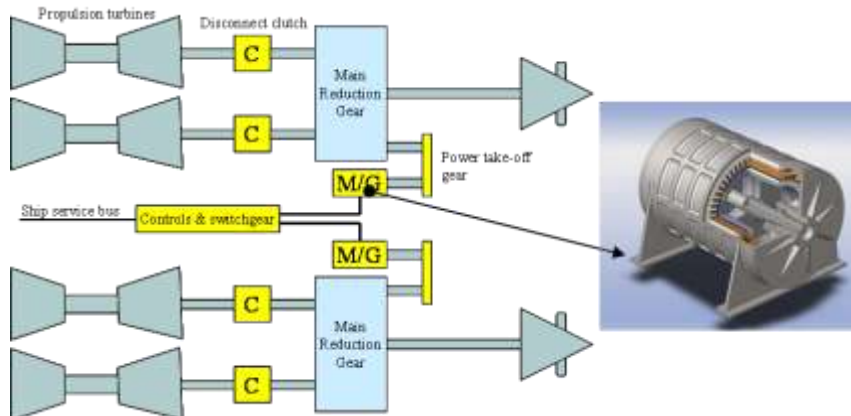


Figure 2-43: Propulsion cross-connect concept and 6 MW PM motor/generator.

Power converters at the 6 MW power level are readily available. Since our goal is to estimate weights and volumes, we looked at only one manufacturer and selected two options. The two converters are water-cooled, but only one has a filter. The option with filter was considered here since improving efficiency is the main goal of this concept. Figure 2-45 shows, to scale, the two converters with the other components for comparison. Adding the filter does indeed increase the size of the converter significantly. A detailed trade study between the added size of the filter and the gain in efficiency would be needed to justify the need for the filter. The very large size of the added power converters is highly noticeable as compared to the 6 MW PM generator. It may be necessary to custom design the power converters using advanced components in order to reduce their size as compared to commercial converters.

If the filters are not used then the size is reduced but is still significant. The two propulsion power lines, the added motors/generators, and the converters without the filters are included in Figure 2-45. Additional components are still needed. These are the disconnect clutches and other control electronics. However, their size should be very small as compared to that of the converters.

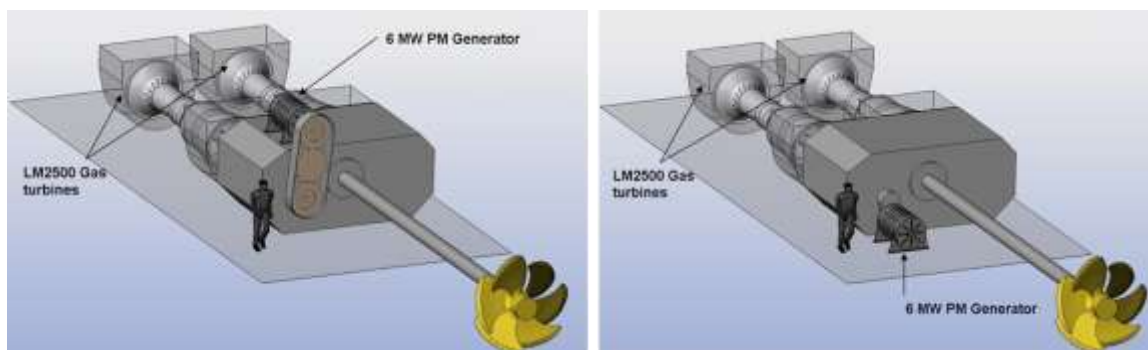


Figure 2-44: Generator and power take-off gearbox as proposed in initial concept (left) and a more practical installation (right).

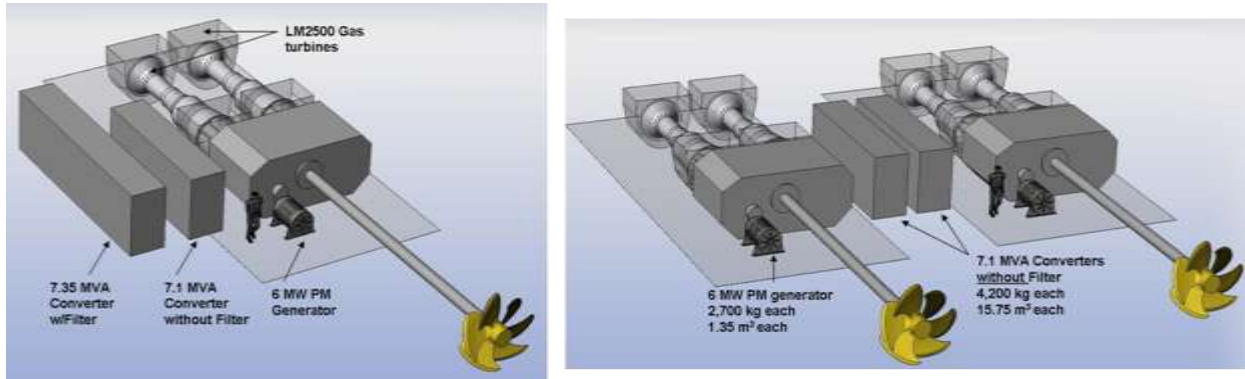


Figure 2-45: Power converters with and without filters (left) and propulsion power trains with cross-connect equipment (right).

5.2.15. Study of the Effect of Electric Frequency on Generator Size

Unlike the terrestrial power consumers that use the 60 Hz frequency imposed by the utility power grid, the electric ship is an independent entity that produces and consumes its own power and, therefore, is not restricted to such frequency. Consequently, any other frequencies that present advantages in terms of size, efficiency, and operational effectiveness need to be considered. The selection of such power generation frequency in future all-electric Navy ships has recently been a subject of intense discussions within the Navy community because it has major implications concerning the power system architecture. It affects the overall power system efficiency, the size of the power generating machinery, the distribution equipment, the power conversion equipment, and ultimately the overall ship design.

In order to determine the effect of the generation frequency on one of the factors mentioned above, mainly size, we conducted a design study to estimate the mass and volume of electric generators that produce the same power level but operate at different frequencies. We selected permanent-magnet synchronous generators for this study but other types of generators, such as wound-field synchronous generators, exhibit the same trends. Four generators rated at 20 MW 3600 rpm each with generating frequencies of 60, 120, 240, and 480 Hz were considered. The design and analysis level was such that the results were within an acceptable error range. Table 2-6 gives volumes and masses of the four generators. Figure 2-46 shows plots of mass and volume as a function of frequency. It can be seen from these plots that the variations are significant when compared to the conventional 60 Hz case. However, increasing the frequency from 240 to 480 Hz does not result in a considerable reduction in mass and volume as increasing the frequency from 60 to 120 Hz or 240 Hz does. Therefore, the 120 or 240 Hz cases are the best candidates since increasing the generating frequency has other disadvantages. These are mainly an increase in losses and an increase in machine reactance which translates into an increase of the power factor. Figure 2-47 shows models of the four generators for relative size comparison.

Table 2-6: Generator mass and volume for various frequencies.

Frequency (Hz)	60	120	240	480
Volume (m ³)	17.2	12.9	10.1	9.9
Mass (kg)	27727	15766	10450	9930

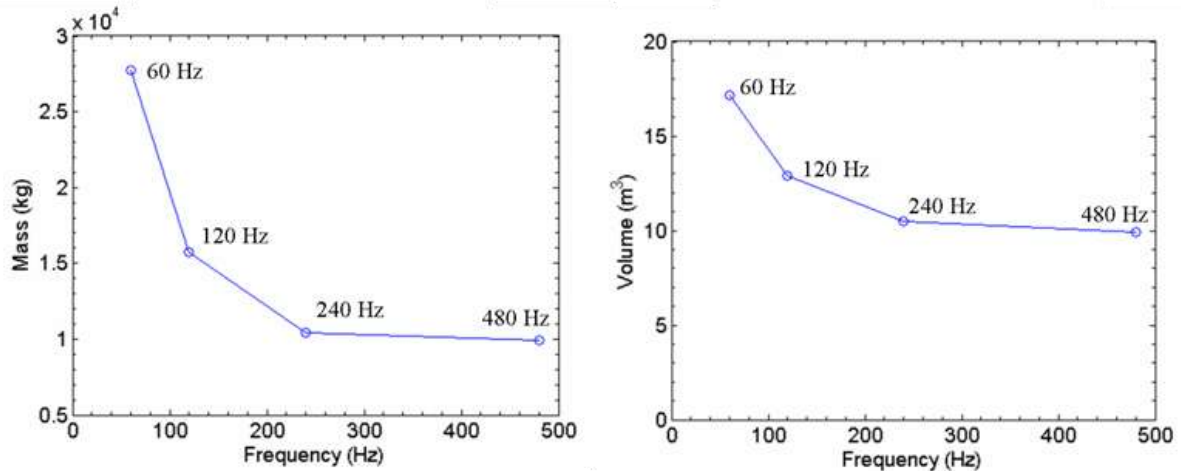


Figure 2-46: Generator mass and volume vs. electric frequency.



Figure 2-47: Generator sizes for various frequencies.

5.2.16. Study of Energy Storage Challenge Problems

We completed an initial study of the energy storage challenge problems proposed by NAVSEA. These problems include four events that involve the use of energy storage onboard Navy ships and required modeling and simulation. We analyzed two of them. The physics models that describe various components of the energy storage module and the electric ship power system have been thoroughly presented in this study. Model equations have been explicitly stated whenever needed for completeness and further reference. A detailed report of the analyses is available for consultation and our main results are summarized here.

As part of that work, we developed a MATLAB/Simulink[®] model of a 100 MJ flywheel energy storage system (FESS). The FESS model consists of a rectifier model, a charging synchronous motor model, a flywheel model describing the dynamics of the rotating rotor mass, a synchronous generator model, a second rectifier model, and a PWM inverter model. Figure 2-48 is a top level representation of the model.

In the latest modeling and simulation efforts, we added details to various components that are necessary for a dynamic analysis of the effects of energy storage on the electric ship power system. As an example, the circuit and model equations of a 3-phase rectifier that include the commutating reactance is shown in Figure 2-49.

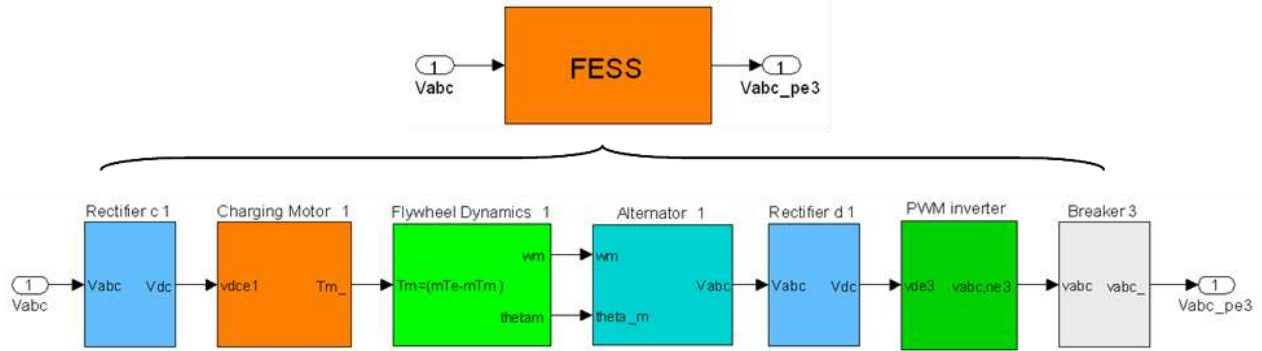


Figure 2-48: Top level model of a flywheel energy storage system.

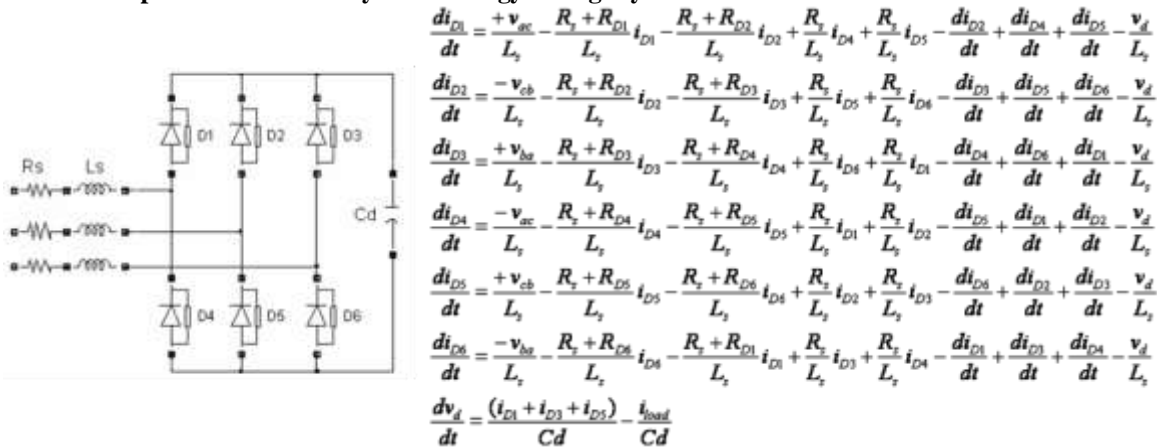


Figure 2-49: Electric circuit and model equations for a 3-phase diode rectifier.

In the first simulation event requested by NAVSEA in their energy challenge problem, the UPS function after the loss of a generator was demonstrated using a simplified model of the power system that includes three generators, breakers, two load center transformers, a ship service transformer, and five AC loads. The top level model is shown in Figure 2-50, along with the model of the loads and other related components. The PMM1 and PMM2 modules represent the two propulsion power trains which were not included in the simulation.

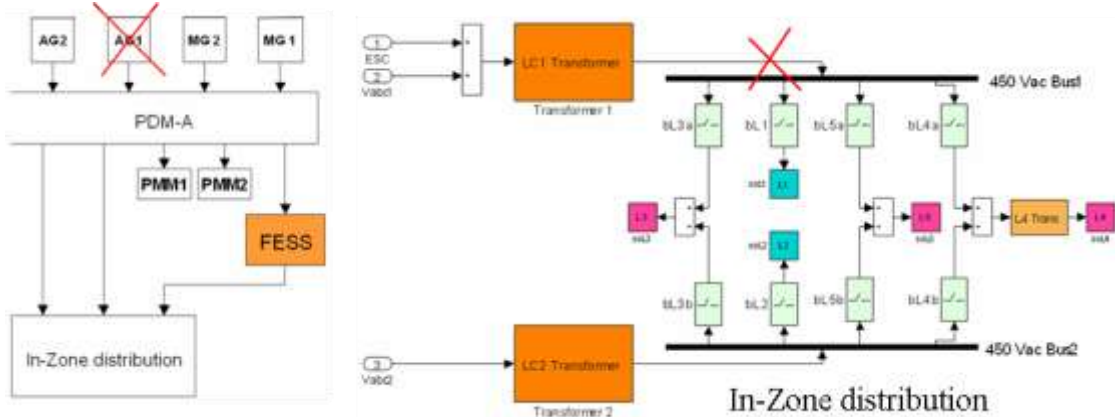


Figure 2-50: Model used for the demonstration of UPS function of energy storage after loss of a generator.

Results of the simulation showing charging generator and flywheel speeds, bus voltage, and bus current during the energy transfer are shown, respectively, in Figures 2-51 and 2-52. The insert in Figure 2-51 shows the drop in generator speed during the charging cycle. As mentioned earlier, the main result of interest in this study is to understand the impact of energy storage on the over-all power system in terms of disturbances and possible instabilities and other detrimental effects. The large spikes in bus voltage and current during the transition, as shown in Figure 2-52, are two results that need to be determined with

good confidence. To do so, the various component parameters that are used in the model need to have a high degree of fidelity in addition to a correct mathematical description of the system.

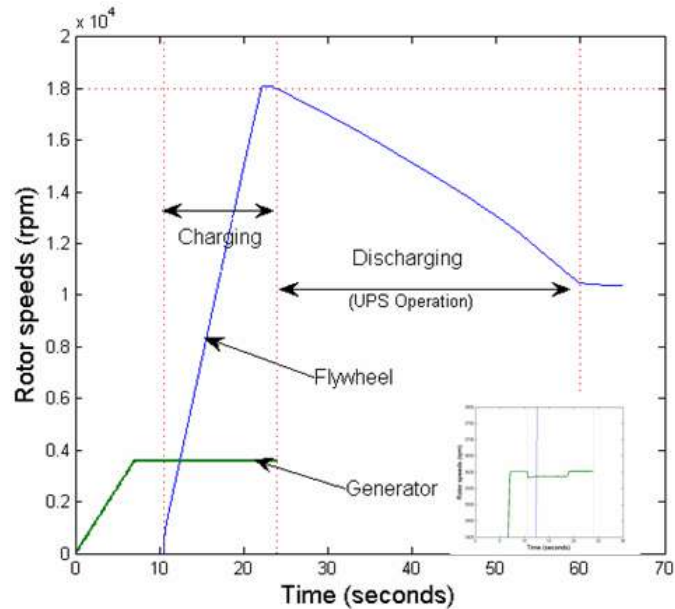


Figure 2-51: Generator and flywheel speeds during charging/discharging cycle.

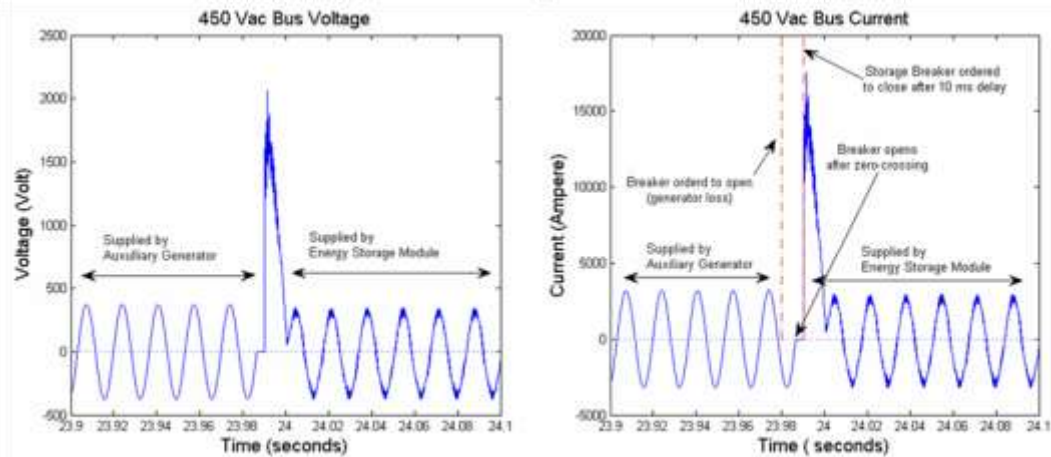


Figure 2-52: Bus voltage and current during energy transfer.

The MATLAB/Simulink[®] modeling environment used in this study has several advantages that include a user-friendly interface which allows graphical programming of complex problems with relative ease. However, there are serious problems with the solver that we need to use in this application. For small systems with few discrete events, such as those encountered in intermittent high-power pulse loads, a continuous solver using a variable time-step can successfully resolve any discontinuities within reasonable precision and solution time. However, for large systems with numerous discrete events, such as the all-electric ship power system and its power electronics modules, a continuous solver using a variable time step is not appropriate because the solution time would be exorbitant. Consequently, for the large electric ship power system model, a discrete solver with a fixed time step is the method that allows a reasonable execution time and acceptable precision level. A fixed time step of 1 μ s seems to be adequate for resolving the dynamics of transient events of interest. However, the discrete solver fails to step through large discontinuities when used to solve discrete MATLAB/Simulink[®] models. This is a major drawback since the environment does not provide means for controlling the discrete solver and changing its parameters, if any.

Our experience working on modeling and simulation of the electric ship power system, with its inherent discontinuities due to high power switching events, indicates that developing a solver specifically tailored to handle the conditions found in a shipboard power system is the most cost effective and efficient approach for a successful use of modeling and simulation as an integral part in the design and analysis of future electric ship power systems.

While the electric ship power system contains several components, the differential equations and other control algorithms that define it are not too large to manage. Most of the differential equations involved have been included in the energy storage report and a numerical code to solve them using any of the widely used languages, e.g., C or FORTRAN, can be developed within a reasonable time. In addition, the development of the numerical code would be such that it can be used to run on desktop PCs as well as on high-end cluster machines when fast results are needed. The availability and affordability of such high performance computing power add greatly to the benefits of this approach. We recommend that this approach be considered.

5.3.Improved Gas Turbine Performance (PI: David Bogard)

5.3.1. 1. Overview and Motivation

The efficiency of operation of any gas turbine engine is closely coupled to the maximum permissible temperature for the turbine section of the engine. A critical technology for allowing higher operating temperatures in the turbine section is the film cooling of the turbine airfoils. A major part of the design of these turbine airfoils involves the design of coolant flows through the airfoil and exiting holes in the airfoil to form a “film” of coolant protecting the surface from the hot combustion gases. Engine manufacturers rely on databases for film cooling performance for these designs. However, these databases are essentially based on the performance of new airfoils. Recently it has become quite evident that turbine sections for in-service engines are modified significantly by accumulation of contaminants. This affects the surface roughness and clogs coolant holes in the airfoils of the turbine, significantly altering cooling performance. Contaminant effects are particularly important for gas turbines used on Navy ships because of the corrosive contaminants that exist in the marine environment. Consequently, it is important to evaluate how seriously these contaminants can compromise the turbine operation. A further objective of this research program was to develop new cooling techniques for the turbine components that would be immune to the contaminant effects occurring in the marine environment. In this research program, the effects of contaminants on turbine cooling were simulated using experimental models of gas turbine vanes in a specially modified wind tunnel facility. This experimental program provided details of how the film cooling performance is altered for realistic in-service turbine engines, with particular emphasis on the effects of the marine environment. Furthermore, new film cooling configurations were designed to mitigate the effects of contaminants and tested in the wind tunnel facility. These designs were shown to significantly improve the film cooling performance for turbine components subjected to high levels of contaminants. These experimental studies were complemented by a computational study to examine the interaction of the solid wall conduction with the convective heat transfer from the overflowing gases. Results from these experimental and computational research programs are presented here.

5.3.2. Studies of Turbine Film Cooling Performance for Flows with Contaminants Simulating the Marine Environment

An experimental program was conducted to determine how the cooling of turbine airfoils are degraded when extended operation of the turbine engine in harsh environments, e.g., the marine environment, causes a degradation of the airfoil surface conditions. The current state-of-the-art gas turbines employ film cooling schemes in the turbine section to allow the turbine to withstand combustor exit temperatures that without film cooling would literally melt the turbine section. During the life of a turbine section, it experiences wear, such as pitting, deposits, or spallation, which increases the surface roughness of the turbine components. This wear degrades the film cooling performance of the turbine blades and vanes.

During the five-year research program, several aspects of degraded film cooling performance due to contaminants were investigated. Specific research programs that were completed were:

- Determination of the degradation of film cooling adiabatic effectiveness due to increased surface roughness that would occur during operation in marine environments. These results were published in Rutledge et al. [liii, liv] and Somawardhana and Bogard [lv, lvi].
- Determination of the effects of surface roughness on the heat transfer coefficients and net heat flux reduction for film cooled turbine vanes. These results were published in Rutledge et al. [liv, liv].
- Evaluation of the effects of near hole obstructions, due to depositions of contaminants, on film cooling performance. These results were published in Demling and Bogard [lvii] and Somawardhana and Bogard [lv, lvi].
- Development of improved film cooling performance using shallow transverse trenches, and evaluation of performance enhancement with surface roughness and near hole obstructions. These results were published in Wayne and Bogard [lviii] and Somawardhana and Bogard [lvi].

A synopsis of these experimental programs, including facilities, experimental procedures, results, and conclusions are presented.

5.3.2.1. Experimental Facilities and Procedures

The facility used in this study consisted of a closed loop wind tunnel powered by a 50 hp variable speed blower. The nine times scale, three-vane linear cascade was placed in the test section of the wind tunnel as shown in Figure 2-53. The center vane, shown in Figure 2-54, was used for test measurements, while the outer wall of the test section was adjusted to achieve a non-dimensional pressure distribution around the vane that matched an inviscid CFD simulation of the actual engine geometry and conditions. The inlet velocity to the cascade was set at 5.8 m/s and the exit velocity was accelerated to 28 m/s, producing an exit Reynolds number of 1.06×10^6 (based on a true chord length of $C = 594$ mm) to match realistic engine conditions. A removable passive turbulence generator consisting of 38 mm diameter rods spaced 85 mm apart was located 0.5 m upstream of the cascade. Hot-wire measurements showed an approach high turbulence level of $Tu_{app} = 21\%$ with turbulence integral length scale $\Lambda_f/d = 10$, measured 107 mm (0.18C) upstream of the vane leading edge. For the low turbulence case, an array of 19 mm rods was placed at nominally 1 m upstream of the vane. Low turbulence levels were $Tu_{app} = 5.2\%$ with turbulence integral length scale of $\Lambda_f/d = 10.7$. Due to the flow acceleration at the test location, $s/C = 0.37$ to 0.54, the high and low turbulence levels were $Tu_{\infty} = 3.9\%$ and $Tu_{\infty} = 1.0\%$, respectively. Local turbulence integral length scales were similar to the length scales in the approach flow.

The test airfoil was machined in sections out of a low conductivity polyurethane foam, $k = 0.048$ W/(m·K), which provided a nominally adiabatic wall for adiabatic effectiveness measurements. The current study was conducted on the second row of cooling holes on the suction side of the vane located at $s/C = 0.367$. The baseline case had $d = 4.11$ mm cylindrical holes with a 30° injection angle spaced $p/d = 2.775$ apart.

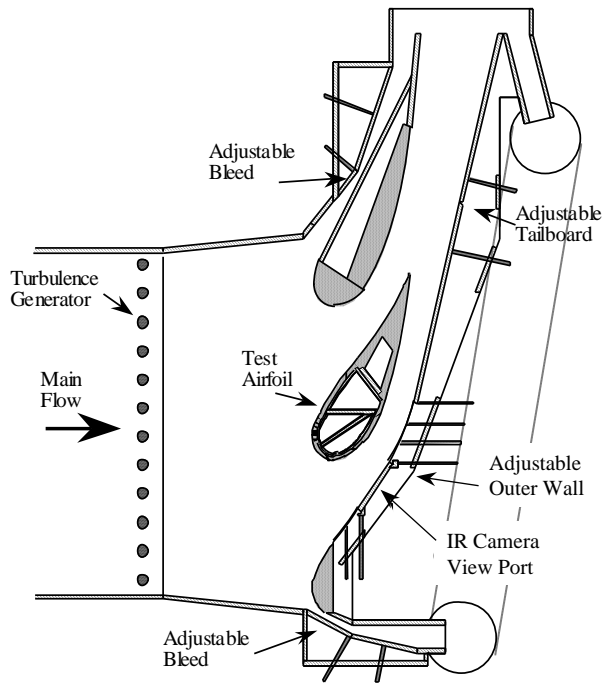


Figure 2-53: Schematic of the simulated turbine vane cascade test section.

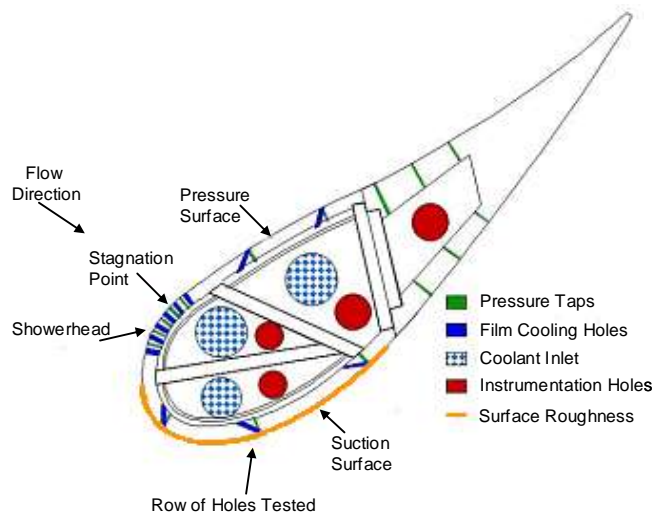


Figure 2-54: Schematic of test vane in detail.

Quantification of film cooling performance requires two separate experiments to determine the heat transfer coefficient and the adiabatic effectiveness. The heat transfer coefficient is a parameter that indicates the rate of heat transfer into the wall for a given temperature difference between wall and external fluid. The adiabatic effectiveness is a parameter that indicates how the coolant injection into the external flow has reduced the temperature of the external fluid flowing around the airfoil. Results of these two experiments are then analytically combined to determine the net heat flux reduction to the vane surface.

Adiabatic effectiveness measurements were obtained from surface temperature measurements using infrared thermography via a FLIR ThermaCAM P20 camera. The camera was calibrated using Type E ribbon thermocouples that were embedded between the sand grains and the foam surface (the paper portion of the sandpaper was removed due to its insulating effects). Camera resolution was 1.5 pixels/mm and the usable field of view when setup and viewing through a circular NaCl IR window was 260 x 240

pixels. Beaded wire Type E thermocouples were used to obtain the coolant and mainstream temperatures. The coolant temperature was obtained using two thermocouples with the thermocouple junctions at the center of different coolant holes, just outside the field of view. The two mainstream thermocouples were placed upstream of the vane. Two thermocouples for each temperature measurement were used to identify any instrumentation errors and the measurements were averaged between the two thermocouples. All thermocouple data was collected using a National Instruments Data Acquisition system (NI DAQ). Adiabatic effectiveness, η , was calculated using the following definition:

$$\eta = \frac{T_{\infty} - T_{av}}{T_{\infty} - T_C} \quad (2.1)$$

Liquid nitrogen was used to cool the secondary loop air that was used for the coolant. A density ratio of $DR = 1.3$ was used for all tests. Though density ratios closer to two are more common in actual engines, Cutbirth and Bogard [11] found that low density ratio coolant jets can give a good approximation of adiabatic effectiveness results and are on the order of only 10% lower than the high density ratio case when using high mainstream turbulence.

A range of blowing ratios were used, from $M = 0.4$ to 1.6, but the majority of the data presented is for $M = 0.4, 0.6,$ and 1.2. These blowing ratios were chosen based on $M = 0.6$ being the peak value for the rough walled baseline case and $M = 0.4$ and 1.2 representing a lower and upper bound, respectively. With the low temperatures used, although the foam vane has a low conductivity, there is still a slight conduction through the foam, making the surface temperatures slightly cooler than they should be. Radiation was determined to be negligible and a conduction correction was calculated using steady state values with no blowing. A constant conduction correction of $\eta_o = 0.04$ was used for both high and low Tu on smooth wall tests and $\eta_o = 0.02$ or $\eta_o = 0.03$ was used for high and low Tu on rough walled tests, respectively. The conduction correction values were calculated using a 1-D conduction model described by Ethridge et al. [12]:

$$\eta = \frac{\eta_{meas} - \eta_o}{1 - \eta_o} \quad (2.2)$$

Uncertainty used was based on test-to-test repeatability. A statistical analysis produced an uncertainty of $\delta\bar{\eta} = \pm 0.015$ and $\delta\bar{\eta} = \pm 0.012$ over 11 repeated experiments of the baseline case with a rough wall over the full range of blowing ratios. For the tests with obstructions, it was the standard to also run a case without obstructions within the same test. This practice provided a good basis to calculate test-to-test repeatability as well as serve as a check between tests to ensure that testing conditions were the same between tests. Systematic errors from individual thermocouples, the IR camera temperature calibration, and the conduction correction used in the data reduction produced an additional $\delta\bar{\eta} = \pm 0.006$ using a propagation of uncertainty. If the data in this study were to be compared to other studies, the total uncertainty of the data would be $\delta\bar{\eta} = \pm 0.021$.

Spatial heat transfer coefficient data were obtained by application of a uniform heat flux and measuring the temperature distribution via infrared thermography (a FLIR ThermaCAM P20 infrared camera calibrated *in situ* using type E thermocouples). The thermocouple data were acquired using a National Instruments Data Acquisition system (NI DAQ). LabVIEW software was written to compute parameters in real time and write the data to disk.

The uniform heat flux was applied using electrical heating of a stainless steel foil attached to the surface of the vane. The electrical heat flux was determined by measuring the voltage drop across the heat flux plate and the current through the heat flux plate. A rough heat flux plate had the roughness array stamped in it and was 0.002 inches thick. The smooth heat flux plate was necessarily 0.004 inches thick in order to provide the structural rigidity required to maintain a smooth surface. Lateral heat conduction was determined to be negligible. A one-dimensional heat conduction model (utilizing the known surface and interior boundary conditions and thermal conductivity of the vane material) was used to correct the surface heat flux for conduction into the substrate. At most, 5% of the electrical heat flux was lost due to

conduction. A numerical model demonstrated that two-dimensional conduction issues were only significant at the edges of the heat flux plate. Heat transfer due to radiation was also subtracted from the total heat flux in order to determine the convective heat flux. The maximum heat loss due to radiation was typically 9% of the electrical heat flux. The convective heat transfer coefficient was determined through the following equation:

$$h = \frac{q_{\text{electrical}} - q_{\text{radiation}} - q_{\text{conduction}}}{T_s - T_{aw}} \quad (2.3)$$

Although roughness was at times placed upstream of the first row of suction side coolant holes, the heat flux was only applied in the region downstream of the coolant holes. If the heat flux was applied upstream as well, the jets would displace the existing thermal boundary layer, thus initiating a new thermal boundary layer. Since the purpose of this study was to isolate the hydrodynamic effects of film cooling on heat transfer, a heated starting length was not used upstream of the injection.

Uncertainty in the measurement of the heat transfer coefficients was caused by uncertainty in the heat flux and uncertainty in the temperature measurements. Because the heat transfer coefficient is inversely proportional to the temperature difference between the freestream and the surface temperature, uncertainty in h was extremely high at the leading edge of the heat flux plate due to the small ΔT . However, data is accurate for $x/D > 3$ where the uncertainty is typically approximately 5%, but always less than 7%.

A concept known as “net heat flux reduction” has been used as a way of predicting the percentage reduction in local heat flux on an actual vane. The net heat flux reduction is given by

$$\Delta q_r \equiv 1 - \frac{q_f}{q_0} = 1 - \frac{h_f(T_{aw} - T_w)}{h_0(T_\infty - T_w)} = 1 - \frac{h_f}{h_0} \left(1 - \frac{\eta}{\phi}\right), \quad (2.4)$$

where ϕ is defined as:

$$\phi = \frac{T_\infty - T_s}{T_\infty - T_c}, \quad (2.5)$$

where T_s is the surface “metal” temperature for the actual airfoil. Based on expected values for ϕ given in the literature, a value of $\phi = 0.6$ was presumed for this analysis (Sen et al. [ixi]).

A negative net heat flux reduction indicates a net heat flux increase. For the purposes of this study, we have modified (2.4) to provide a technique for predicting the net change in heat load due to roughness. In order to emphasize the fact that roughness increases the heat load, the effect is presented simply as the quantity, $q_{f,rough}/q_{f,smooth}$, given by

$$\frac{q_{f,rough}}{q_{f,smooth}} = \frac{h_{f,rough}(T_{aw,rough} - T_w)}{h_{f,smooth}(T_{aw,smooth} - T_w)} = \frac{h_{f,rough}(\eta_{rough} - \phi)}{h_{f,smooth}(\eta_{smooth} - \phi)} \quad (2.6)$$

Combining low density ratio heat transfer data with high density ratio adiabatic effectiveness data requires selection of a blowing parameter that aligns the measurements. In the absence of definitive data that suggests which of blowing ratio, momentum flux ratio, or velocity ratio is best suited for the task,

blowing ratio was selected for this study. Furthermore, it will be shown that \bar{h} is relatively insensitive to the 26% or 60% change in M required to match the momentum flux ratio or velocity ratio, respectively.

In addition to the heat transfer and adiabatic effectiveness measurements, a hot wire anemometer was used to make velocity measurements. An A.A. Lab Systems Ltd. AN-1003 Hot Wire/Hot Film Anemometry System was employed, and the same NI DAQ hardware was used for the data acquisition. For the rough wall condition, sandpaper was used to simulate roughness. Bogard et al. [xii] characterized typical surface roughness and created a plate with uniform cones having a precise geometry to obtain a hydrodynamic representation for the nine times scale facility used in their study. The representative surface roughness created in [xii] had an equivalent sand grain roughness of $k_s = 0.5$ mm. The sandpaper used in this study had a CAMI grit designation of 36, which corresponds to an average grit diameter of 0.53 mm, close to [xii]’s k_s . In addition, an extensive study conducted by Dees [xiii] showed that the 36-

grit sandpaper had similar hydrodynamic effects to the conical roughness. A summary of all test conditions is presented in Table 2-7.

The sandpaper, along with all other surfaces, was painted flat black to ensure a uniform emissivity for the IR camera and the sandpaper was attached $29d$ upstream of the row of cooling holes and $34d$ downstream of the holes using double-sided tape, with the edge of the sandpaper aligned with the leading or trailing edge of the holes. A microscopic inspection was used to confirm that the added paint did not alter the roughness profile. An example of the setup is given in Figure 2-55. No roughness was between the holes, but contour plots showed that the $0.15d$ step change did not affect the film cooling performance as far as the coolant impinging and spreading between the holes before going downstream, as evidenced by the distinct jets with no lateral spreading due to the sandpaper edge.

In Demling's study [lvii], the Shape #2 obstruction, shown in Figure 2-56, was found to have the most significant effects, so this same shape was used for this study. The obstructions were created out of quarter round styrene strips and the obstruction size used was $1/2d \times 1d \times 1/2d$, (*height x spanwise width x streamwise length*). The width was chosen to replicate the obstructions used by Demling and Bogard [lvii] and the $1/2d$ height and respectively scaled length was chosen based on a study by Wammack et al. [lxiv]. Wammack found peak deposition levels of $310 \mu\text{m}$; when scaled to this study, deposition heights did not exceed $1d$, but $1/2d$ was easily justified. These obstructions were placed on top of the sandpaper with the sand grains removed beneath the obstructions and were painted flat black for uniform emissivity.

Table 2-7: Test Conditions for adiabatic effectiveness and heat transfer coefficient experiments.

True Chord Length	594 mm	
Vane Span	549 mm	
Vane Pitch	457 mm	
Inlet Velocity	5.8 m/s	
Exit Reynolds Number	1.06×10^6	
Test Location	$s/C = 0.367$ to 0.540	
High Mainstream Turbulence at Inlet/Test Location	$Tu_{app} = 21\%$	$Tu_{\infty} = 3.9\%$
	$A_f = 41$ mm	
Low Mainstream Turbulence at Inlet/Test Location	$Tu_{app} = 5.2\%$	$Tu_{\infty} = 1.0\%$
	$A_f = 44$ mm	
Film Cooling Hole Diameter	4.11 mm	
Hole Length (baseline)	27.5 mm ($L/d = 6.7$)	
Hole Length (trench)	23.4 mm ($L/d = 5.7$)	
Trench Height / Width	2.1 mm ($h/d = 0.5$)	
Trench Width	4.2 mm ($w/d = 2.0$)	
Injection Angle	30°	
Hole Pitch	11.4 mm ($p/d = 2.78$)	
Surface Roughness	CAMI 36-grit	
Obstructions	#2 – $1/2d \times 1d \times 1/2d$	
Density Ratio	1.3 to 1.6 (for η)	
	1.0 (for h)	

All tests with obstructions were conducted with three consecutive holes, in the center of the row with 18 holes, containing the obstructions. There were two reasons for this. The first was to ensure the consistency between the three obstructed holes to verify the uniformity of the obstruction placement during each experiment. The second was to improve the accuracy of the laterally averaged values, by having three holes available over which to average. To ensure the results produced by obstructing three consecutive holes were not affecting the results in any way compared to blocking just one hole, a test was run obstructing only one hole. Results from this test confirmed the obstructions on three holes had the same effects as a single hole.

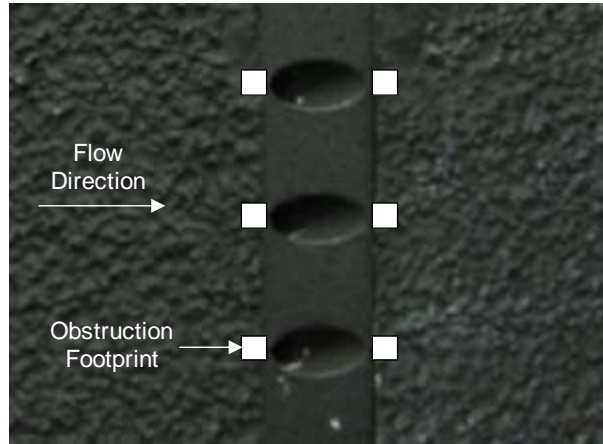


Figure 2-55: Photograph of coolant holes showing sandpaper placement.

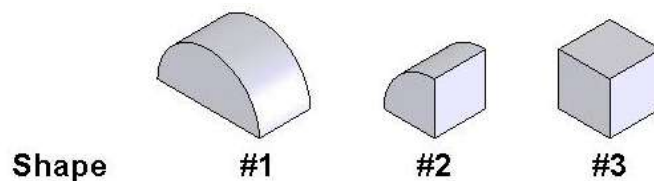


Figure 2-56: Isometric projections of obstruction shapes tested.

5.3.2.2. Synopsis of Results for Study of Roughness Effects on Adiabatic Effectiveness Heat Transfer Coefficients, and Net Heat Flux Reduction

The spatial h distribution for a rough wall with a typical operating condition of a blowing ratio of $M = 0.7$ is presented in Figure 2-57. These results were with the showerhead off and high mainstream turbulence. Aside from the individual roughness elements being quite evident, the interesting observation with the rough surface downstream of injection is that the heat transfer coefficient is lower downstream of the holes than between the holes, which is the opposite of what was observed on the smooth surface. In fact, by comparing rough surface h distributions with and without film cooling, it is evident that the regions downstream of the holes experience a decrease in h due to blowing, but an increase in h between the holes. The lower h downstream of the holes may be attributed to the decrease in velocity downstream of a jet that is evident by boundary layer measurements. The increase in turbulence intensity due to the jet on a rough surface is negligible compared to the reduced interaction with roughness elements due to a lower velocity coolant jet.

Roughness had a substantial effect on h , as shown in Figure 2-58, for a test with low mainstream turbulence. There was as much as a doubling of \bar{h} , which is consistent with the results of [lxv] who used a flat surface test plate. With roughness, there was no difference in \bar{h} with coolant injection relative to no coolant injection. Although not shown here, results with high mainstream turbulence levels showed no change in \bar{h} relative to low mainstream turbulence results.

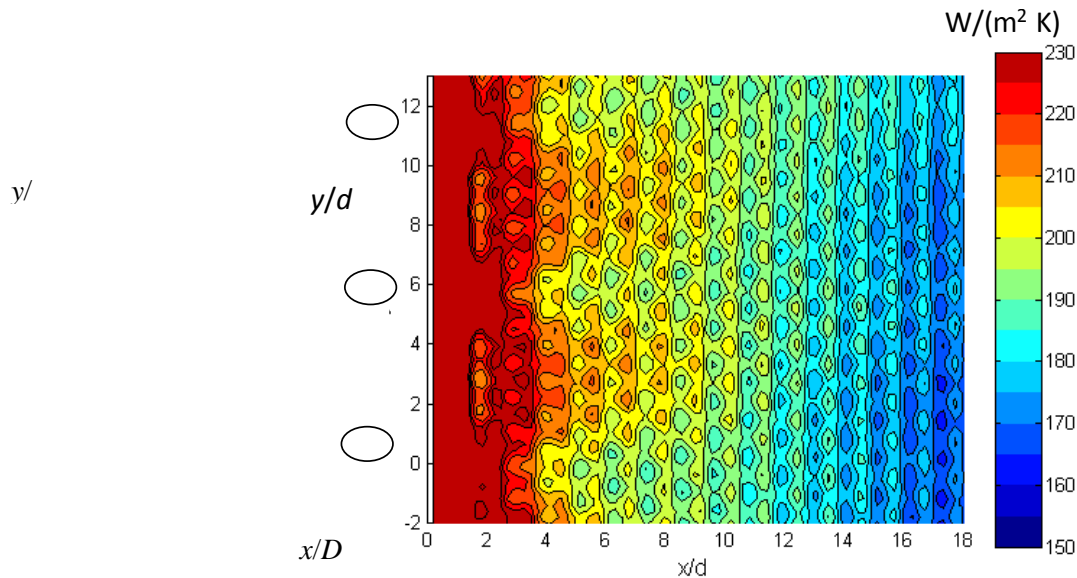


Figure 2-57: Heat transfer coefficient distribution, $M = 0.7$. Downstream rough, showerhead off, high turbulence.

Adding roughness upstream of the film cooling holes caused as much as a 10% decrease in h compared to the case with roughness only downstream of the holes. Otherwise the general trends were similar. The lower h values observed with full roughness rather than downstream roughness may be attributed to a thickening of the boundary layer upstream of the coolant holes.

Increases in the heat load due to the transition from a completely smooth to a rough surface are shown in Figure 2-59 for several different blowing rates with showerhead cooling. As the surface finish changes from smooth to rough over this region of the vane, the uncooled vane was found to have a 50-130% increase in heat load depending on position. Coolant injection from the showerhead alone does little to reduce the effect of surface roughness. However, combined showerhead and suction side coolant injection significantly reduces the increase in heat load with surface roughness with the maximum increase in heat load being reduced to 70%.

Results from testing the adiabatic effectiveness for the two rough surfaces and the smooth surface are presented in terms of the spatially averaged adiabatic effectiveness in Figure 2-60. The 36-grit and 60-grit rough wall surfaces caused a 30% reduction in the maximum adiabatic effectiveness. This is a significant loss in performance due to roughness effects. Interestingly there was no significant difference in adiabatic effectiveness for the two rough surfaces, even though the roughness levels differed by almost a factor of two.

The two rough surfaces caused the boundary layer thickness to more than double compared to the smooth wall case, which was attributed to the rough surfaces inducing transition to a turbulent flow. The large decrease in performance caused by the rough surface was due to the thicker boundary layer not turning the coolant jet towards the wall as effectively, and the higher turbulence levels dispersing the coolant more.

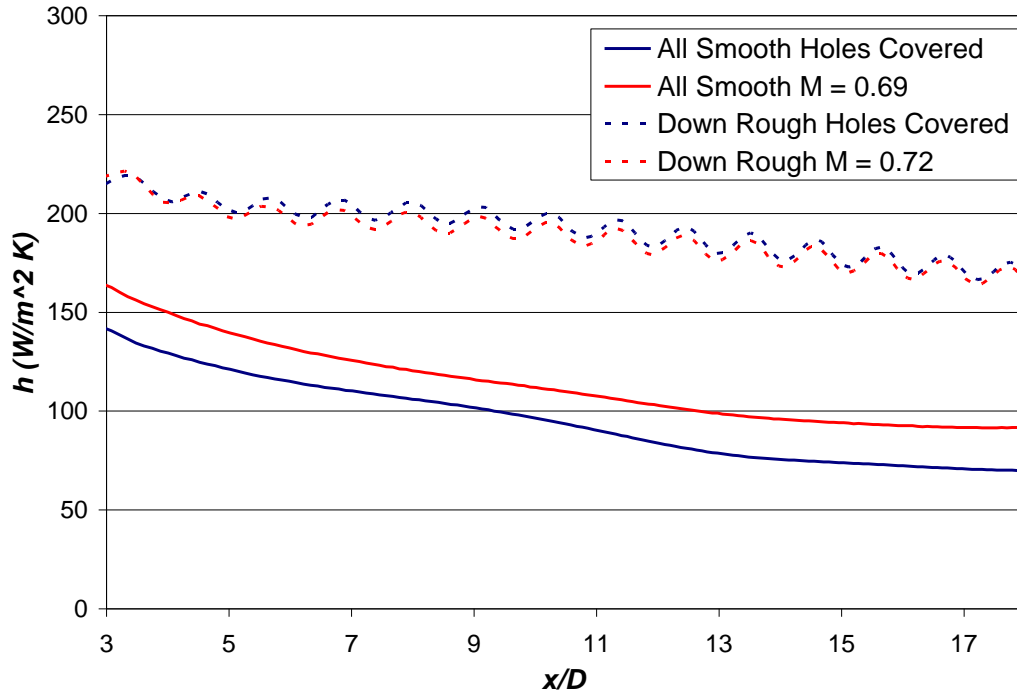


Figure 2-58: Influence of downstream roughness on spanwise averaged heat transfer coefficients. Upstream smooth, showerhead off, low turbulence.

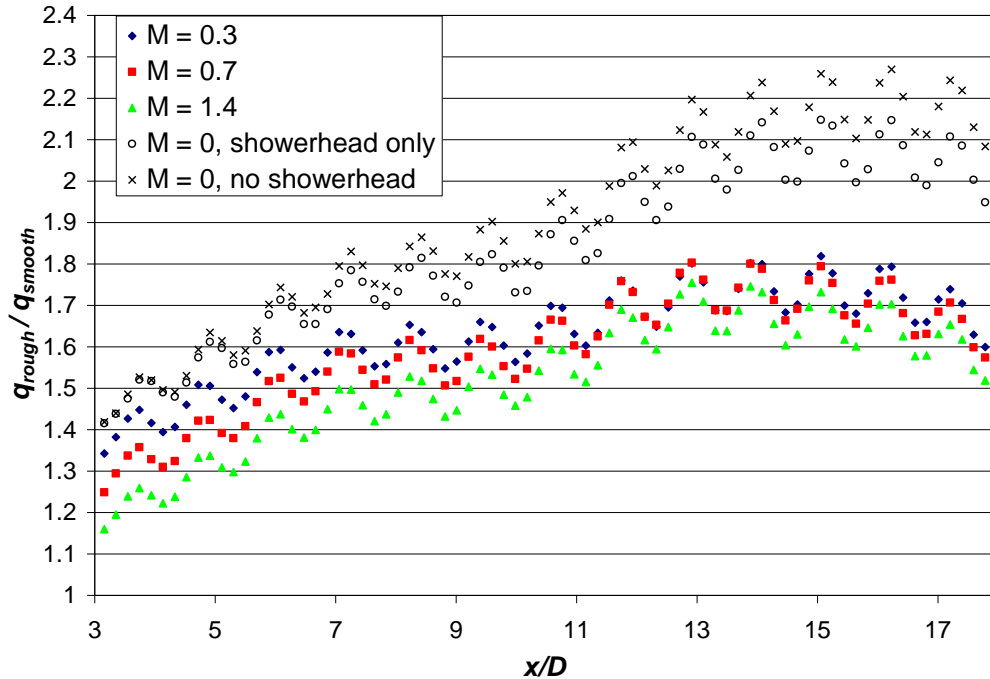


Figure 2-59: Heat flux increase due to adding upstream and downstream roughness. High turbulence, showerhead on for cases with suction side cooling.

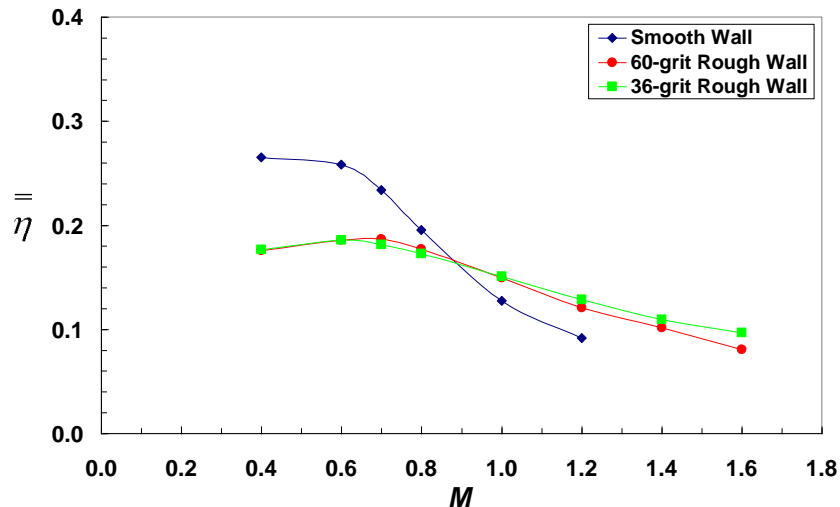


Figure 2-60: Spatially averaged effectiveness of varying surface roughness.

5.3.2.3. Synopsis of Results for Study of Near Hole Obstruction Effects on Adiabatic Effectiveness

Though it is intuitive that near-hole obstructions could degrade film cooling effectiveness, an intensive examination was conducted to quantify these effects. All of the obstruction characteristics were varied individually in order to determine each characteristic's contribution to any resultant effects.

Naturally occurring obstructions are random events, so there is not one defining shape. Three different shapes were tested in this study: a fully rounded shape, a combination round and square shape in the form of a quarter round, and a fully square shape, designated #1, #2, and #3, respectively, and pictured in Figure 2-56. The #2 shape had the flat edge facing the hole in both the upstream and downstream position. Because the #2 shape is not symmetric and could be flipped, tests were also conducted with the #2 shape, but with the rounded edge facing the coolant hole in both the upstream and downstream position and this was designated #2 (bkwd). Demling and Bogard's [lvii] study was similar to this study, but conducted in an area of high curvature and found that the #2 shape had the largest impact on adiabatic effectiveness.

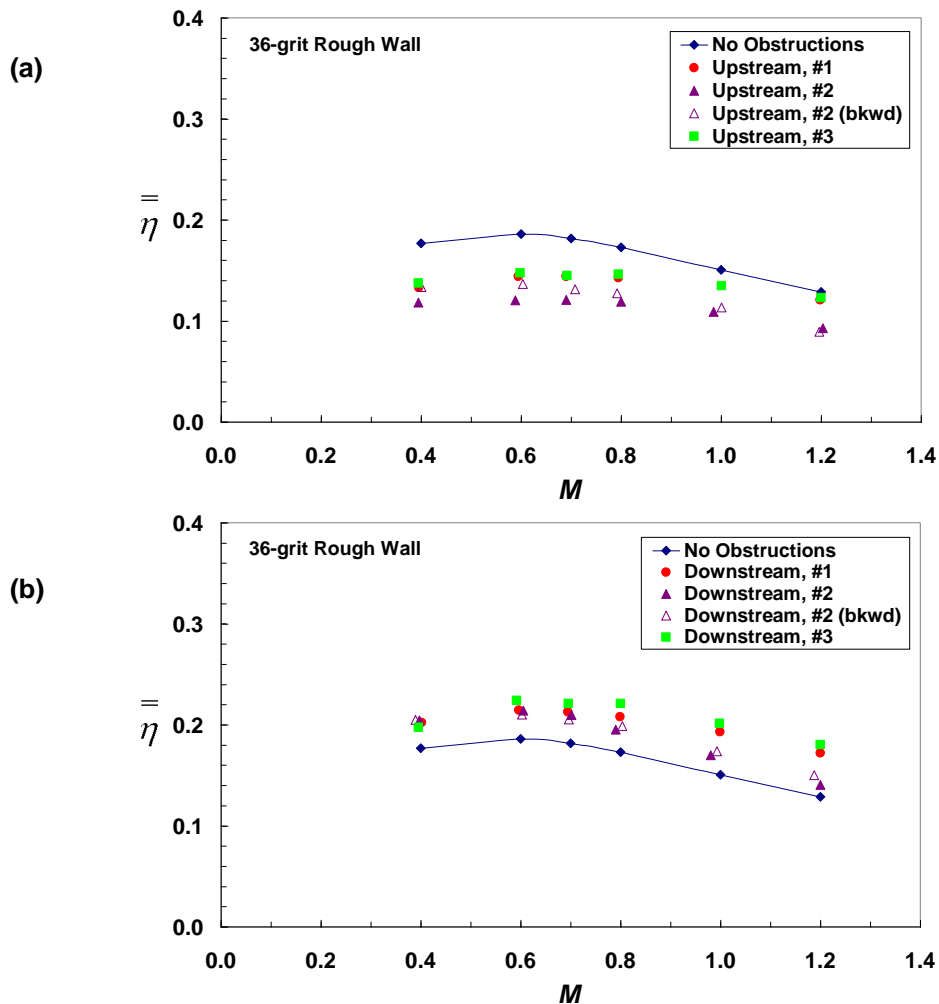
A comparison of shape was repeated in this study, shown in Figure 2-60. All of the differences outside of uncertainty between the various shapes were observed at high blowing ratios. In the upstream position, the #2 and #2 (bkwd) caused about a 25% degradation from the level of performance seen in the upstream position with the #1 and #3 shapes. In the downstream position, the #2 and #2 (bkwd) performed about 20% less than the #1 and #3 shapes in the same configuration. When considering obstructions on a whole across all blowing ratios in relation to the no obstruction baseline, overall, shape was found to have a minor effect and the obstruction placement seemed to dominate. The finding of shape not being a dominating factor is important because it allows for the results of this study to be generally applicable to obstructions as a whole, considering that naturally occurring obstructions will always have a randomized shape.

Studies of the sensitivity to the width and length of the obstructions showed that they had marginal effects. Height was the final dimension to be examined. In order to minimize the number of overall tests, the entire obstruction was scaled with the height. In addition, overall scaling was done because randomly occurring obstructions due to deposition of foreign particles traveling with the combustion products will most likely adhere in a geometrically proportional fashion. The geometrically proportional sizes tested were $1/8d$, $1/4d$, $1/2d$, and $1d$; this set of tests was performed only in the upstream position due to the primary focus being on degradation effects caused by obstructions. Figure 2-61 gives an isometric view of the various size proportions in relation to a film cooling hole footprint.

Overall, obstruction size was found to play a significant role in effects on adiabatic effectiveness. From Figure 2-62, it is clear that as the obstruction gets closer to the dimensions of the sand grain size of the

overall surface roughness, the degradation caused by an upstream obstruction becomes less. Because the size $1/8d \times 1/8d \times 1/8d$ obstruction was essentially the same size as the grit size for the baseline 36-grit rough wall, these small obstructions were tested on the less rough 60-grit surface which had sand grains on the order of $d/16$, with the results shown in Figure 2-63. The $1/8d \times 1/8d \times 1/8d$ obstruction had little effect on adiabatic effectiveness with the 60 grit surface, and it can be inferred that it would also have no effect on the 36-grit surface. Finally, the $1/4d \times 1/4d \times 1/4d$ obstruction performed similarly for both roughness levels, again presented in Figure 2-63. This is as expected since the two surfaces have similar hydrodynamic effects, as was previously mentioned.

To improve film cooling performance and to mitigate effects of surface roughness and near-hole obstructions, coolant holes were embedded in a transverse, shallow trench. The dimensions of this shallow trench are presented in Table 2-7 and schematic and photograph are shown in Figure 2-64. The shallow trench provides uniform film cooling coverage and therefore better adiabatic effectiveness levels than cylindrical holes. The major advantage of the narrow trench is that it inhibits separation, causing the coolant to fill the trench first, and then exit the trench as a sheet rather than individual jets. The increased performance due to the trench over standard cylindrical holes was also observed when roughness and obstructions were present.



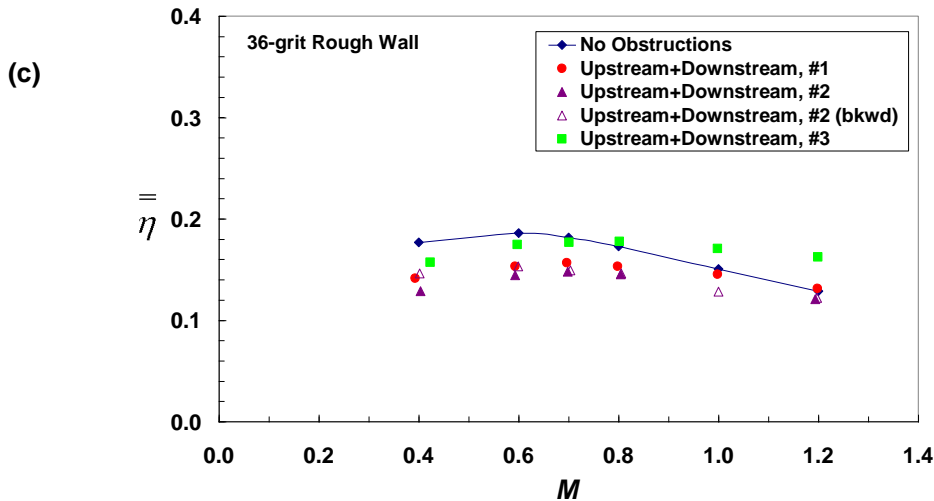


Figure 2-60: Spatially averaged effectiveness with a 36-grit rough wall comparing the various shapes in the (a) Upstream, (b) Downstream, and (c) Upstream+Downstream configurations. Note that all shapes are of size $1/2d \times 1/2d \times 1/2d$ except for shape #1, which is of size $1/2d \times 1/2d \times 1d$ due to its geometrical constraints.

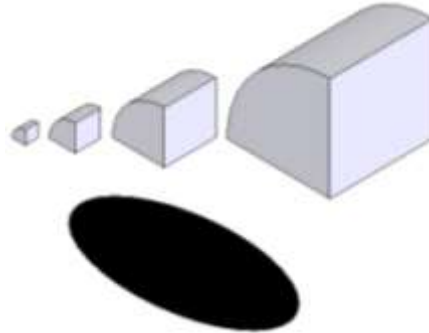


Figure 2-61: Isometric view of the various uniformly scaled sizes of shape #2 tested in comparison to the film cooling hole footprint (from left to right: $1/8d \times 1/8d \times 1/8d$, $1/4d \times 1/4d \times 1/4d$, $1/2d \times 1/2d \times 1/2d$, and $1d \times 1d \times 1d$).

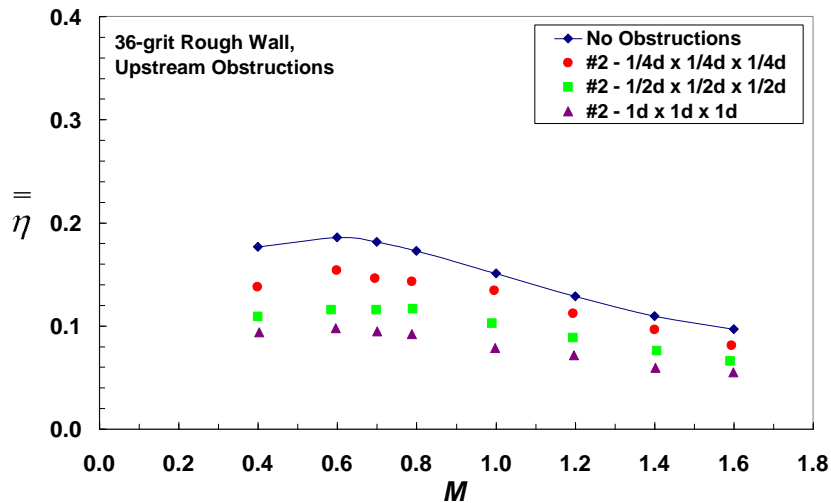


Figure 2-62: Spatially averaged effectiveness with a 36-grit rough wall and upstream obstructions comparing overall size effects with shape #2.

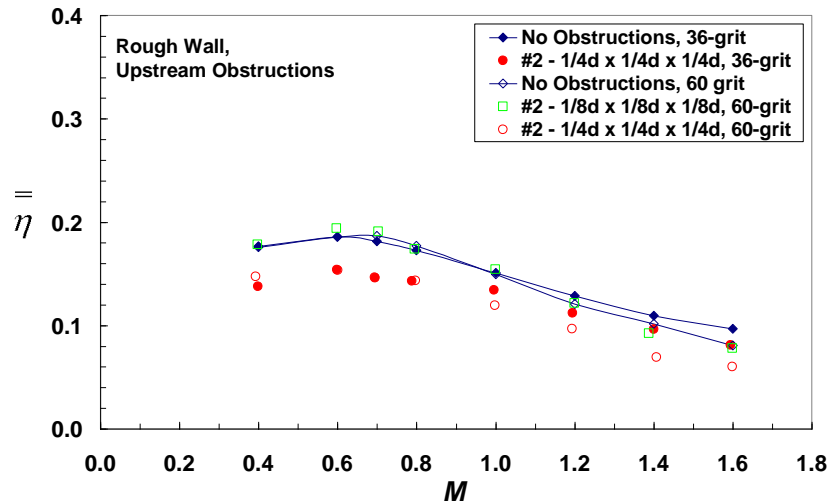


Figure 2-63: Spatially averaged effectiveness with varying surface roughness and upstream obstructions comparing overall size effects with shape #2.

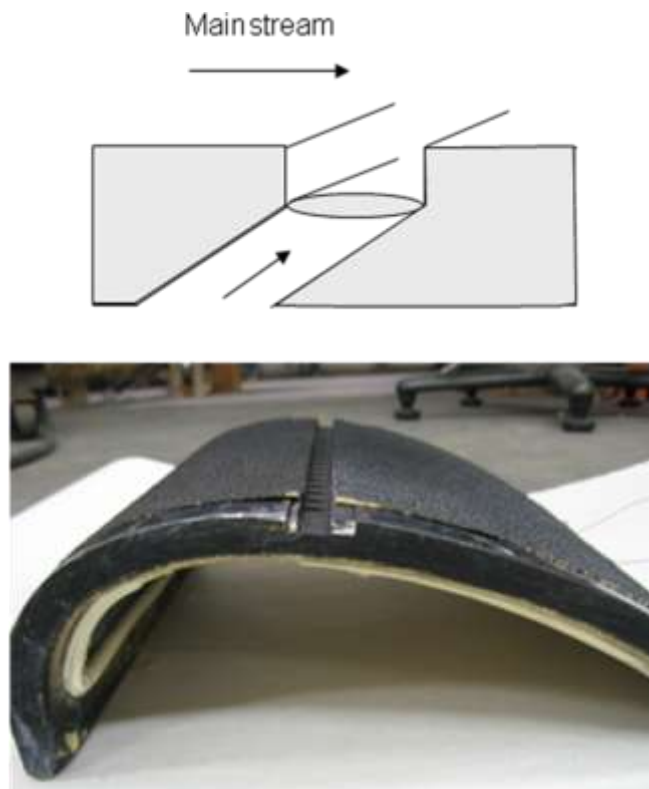


Figure 2-64: Schematic and photograph of trench configuration.

Unlike the baseline case, adiabatic effectiveness with the narrow trench is relatively constant across the range of blowing ratios, as shown in Figure 2-65. Furthermore, this constant level occurs for smooth and rough surfaces. The largest difference between smooth and rough surfaces when using a narrow trench is at low blowing ratios, with a degradation of only 15% which is quickly eliminated with increasing blowing ratio. This leads to the conclusion that film cooling performance with a trench is insensitive to the effects of surface roughness, especially at the mid to high blowing ratios.

Knowing that the trench mitigates rough surface effects, the next determination was how obstructions affect trench performance. These results are presented in Figure 2-66, which shows the spatially averaged adiabatic effectiveness for obstructions normalized by the no obstruction case. Figure 2-66 shows that upstream obstructions cause degradation across all blowing ratios, downstream obstructions cause a slight

increase at high blowing ratios, and obstructions upstream and downstream simultaneously fall between Upstream and Downstream configurations for most blowing ratios. Overall, the variation from unity due to obstructions is relatively small, with a maximum degradation of 15% compared to a maximum degradation of almost 40% for the baseline case. Compared to the baseline, the trench significantly minimizes most of the effects due to obstructions.

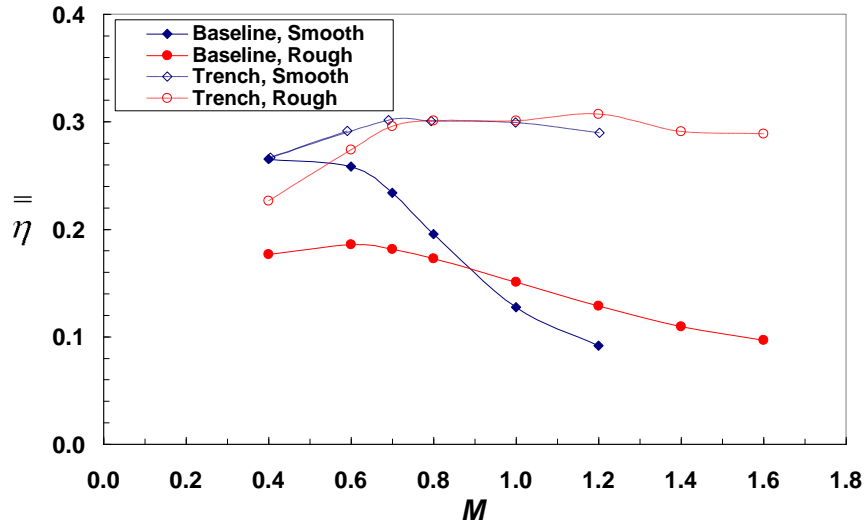


Figure 2-65: Spatially averaged adiabatic effectiveness of both the baseline and trench cases with both smooth and rough surfaces.

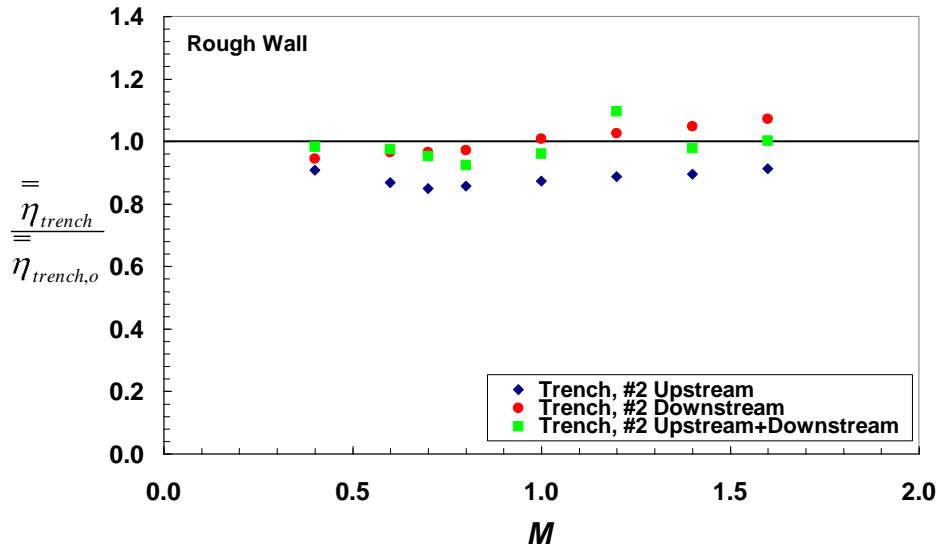


Figure 2-66: Spatially averaged adiabatic effectiveness of trench case with a rough wall and various obstruction configurations normalized by the rough wall trench case with no obstructions.

5.3.3. Conclusions

This research program has shown that surface roughness and near-hole obstructions caused by contaminants attaching to turbine airfoil surfaces can seriously degrade the film cooling performance. However, this degradation can be countered by embedding coolant holes in shallow trenches. The performance of shallow trench configurations were investigated for simulated deteriorated surface conditions, i.e. increased surface roughness and near hole obstructions. The study involved determining the effects on cylindrical holes and then seeing how cylindrical holes embedded in a trench performed in comparison. It was found that regardless of the surface conditions, embedding cylindrical holes in a trench will always outperform standard cylindrical holes.

From the cylindrical hole study, it was determined that when $0.5d$ high obstructions are present, degrading effects from surface roughness are overshadowed by the dominating effects of near hole obstructions. With no trench, obstructions upstream of the coolant holes produced as much as a 50% degradation, while downstream obstructions actually enhanced adiabatic effectiveness. When both upstream and downstream obstructions were present simultaneously, the upstream obstruction effects dominated.

The trench showed the most promising results. Not only did the narrow trench significantly improve adiabatic effectiveness relative to the baseline, it eliminated the degrading effects from surface roughness. For rough wall conditions, the trench more than doubled the adiabatic effectiveness. Furthermore, when a narrow trench was used, the degrading effects due to near hole obstructions were negligible. As the blowing ratio increased, the benefits of the trench over cylindrical holes also increased, similar to the performance of shaped holes.

Power Train Design of Permanent Magnet Synchronous Machines At Purdue University

For permanent magnet synchronous machines a new position observer was developed that uses sensed vibration in tandem with a single hall-effect sensor to predict rotor position with accuracy approaching that of a high precision position encoder. Specifically, a coupled piezoelectric/single-Hall-effect (CPSH) sensor-based position observer was derived. The CPSH observer uses a zero order Taylor Series approximation of the integral of rotor velocity to estimate rotor position between Hall-effect sensor transitions. During startup and at low rotor speeds the piezoelectric washer is used to determine the rotor position (in addition to its primary mission of providing feedback for torque ripple mitigation).

The observer extends the applicability of the torque mitigation strategies used for permanent magnet machines by reducing the cost of position sensing. Advantages using the observer are 1) near-maximum start-up torque is guaranteed 2) no reverse rotation of the rotor occurs during startup, 3) the observer does not require knowledge of back-emf or cogging torque harmonics, 5) it is applicable to machines with arbitrary back-emf waveform and stator slot configuration, and 6) it is relatively low-cost. The CPSH-based observer has been validated in hardware using a 3-phase, 8-pole, 1 slot/pole/phase machine. Through experiment, it is shown that start-up performance nearly matches that of start-up obtained using an in-line position encoder. In addition, when the torque ripple mitigation algorithm is applied, the 6th and 12th order harmonics of torque are eliminated. Thus, in navy applications, a vibration sensor that is used to monitor drive system health or for torque ripple mitigation control, could be readily used in a dual role to improve drive fault tolerance. The details of this research were published in

P. Beccue, S. Pekarek, "A Coupled Piezoelectric/Single-Hall-Sensor Position Observer for Permanent Magnet Synchronous Machines," IEEE Transactions on Industry Electronics: Special Issue on Latest Advances in Machines/Drives, Vol. 54, No. 5, Oct. 2007, pp. 2389-2397.

A patent was also filed on the technique.

Related, a new sensor was derived that uses torque-ripple-induced vibration to establish the speed/position of induction machines. The sensor is relatively easy to implement, and can serve a dual use role as part of a vibration-based health monitoring system. Although requiring a higher cost than "sensorless" techniques, they are much less expensive than tachometers and encoders. The proposed sensor does not require knowledge of machine parameters and is relatively straightforward to implement. The effort of machine analysis and modeling is minimized. Moreover, the vibration sensors can serve a dual-use role as a means for fault-detection/health monitoring. We envision the sensor could be readily placed on the IPS propulsion drive for fault detection and for a primary or secondary speed observer.

D. Wu, S. Pekarek, "Using Mechanical Vibration to Estimate Rotor Speed in Induction Motor Drives," Proceedings of the 2007 Power Electronics Specialists Conference, June 2007, pp. 2412-2417.

A button cell steady state model of an SOFC was extended to capture electrical and thermal transients in addition to flow dynamics through a SOFC stack. Time averaged dc-dc boost converter, dc-ac converter for extended system analysis were developed. The SOFC model serves as the primary power source for powertrain system model simulations and hybrid fuel cell based systems for energy recovery. The fuel cell model is composed of four submodels: the electrochemical model, the transient electrical model, the thermal model, and the dynamic flow model. The submodel codes are coupled to produce a SOFC stack model for use in power system simulations.

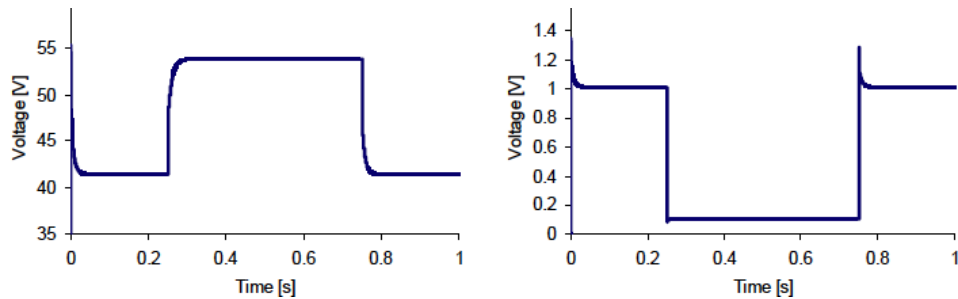


Figure 22 SOFC “charge double layer” response to a loading transient: a) current response; b) voltage response

Related publication:

T.E. Brinson, W. Ren, J.C. Ordonez, C.A. Luongo, and T. Baldwin, "Fuel Cell-Based Powertrain System Modeling and Simulation for Small Aircraft Propulsion Applications," *Journal of Fuel Cell Science and Technology* ASME , 2008.

1.2.2.Optimized PEM and Solid Oxide fuel cell unit geometry

We have developed a model and performed an optimization of the internal structure of PEM fuel cells and a unit solid oxide fuel cell (SOFC). The internal structure, which accounts for the thickness of the two electrodes and the electrolyte, and the flow channels geometry, is optimized. The model is developed using a control volume approach, in which, all relevant thermal and electrochemical interactions between adjacent elements are accounted for. The optimized internal structure results from optimal balances between the thickness of anode and cathode, channel shoulder aspect ratio, and the number of fuel and oxidant channels. The optima found are sharp and therefore, important to be identified in actual SOFC and PEM design.

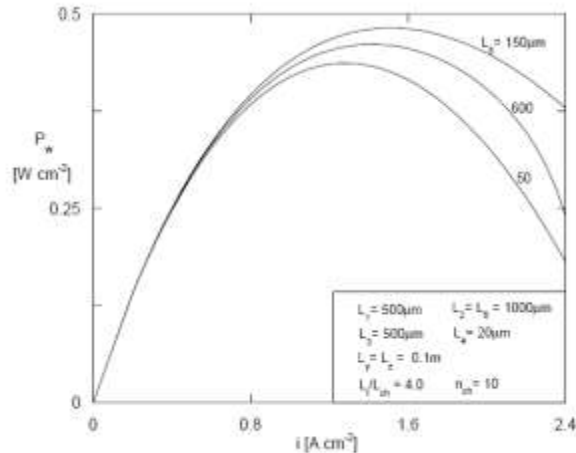


Figure 3. Anode supported SOFC power density curves for different cathode thickness

The effect of cathode thickness (L_5) in an anode supported SOFC is illustrated in Fig. 3. The separation of power density curves at the high working current density region illustrates that the cathode thickness affects considerably the fuel cell performance. Fig. 3 also shows that very large or very small cathode thickness does not benefit SOFC power density. Such behavior is explained physically by analyzing two extremes: i) for large cathode thickness, L_5 , the activation overpotentials decrease due to large wetted areas, but both ohmic (due to the large thickness) and concentration (due to large oxidant path to the reaction site) overpotentials increase and decrease the power density, P_w ; and ii) for small cathode thickness, both ohmic resistance (due to small thickness) and concentration (due to shorter oxidant path to reach the reaction site) overpotentials decrease, but the activation potential will be large due to lack of reaction area (poor electrocatalysis), so power density, P_w , decreases at this extreme too. Therefore, there must be an intermediate optimal thickness between the two extremes that maximizes power density.

In Fig. 3, for three values of L_5 , in the range [50, 600] μm , a maximum power density was found with respect to current density. The largest value of the maximum power density was observed for the intermediate value of the cathode thickness, i.e., $L_5=150 \mu\text{m}$, demonstrating the existence of an optimal design for the studied single SOFC.

Related publications:

1. S. Chen, J.C. Ordonez, and J.V.C. Vargas, "Transient Operation and Shape Optimization of a Single PEM Fuel Cell", *Journal of Power Sources*, 162(1), (2006) 356-368.
2. A.M. Morega, J.C. Ordonez, J.V.C. Vargas and S. Kosaraju. "A Finite Element Method (FEM) Analysis and Optimization of a PEM-Fuel Cell with Interdigitated Flow Field Design", *International Journal of Energy Technologies and Policy*, 2007.
3. J.C. Ordonez, S. Chen, J.V.C. Vargas, "Constructal Flow Structure for a Single SOFC", submitted to *International Journal of Energy Research*, 2006.
4. J.V.C. Vargas, J.C. Ordonez, and A. Bejan, "Constructal PEM Fuel Cell Stack Design", *International Journal of Heat and Mass Transfer*, 48 (2005) 4410- 4427.

1.2.3 Instrumented the CAPS Advanced Prototype Test Bed for thermal management experiments.

Figure 1 depicts bed extensively ESRDC for superconducting hardware in-the-Various sea maneuvers can time digital test bed is principal bed are two 2.5 drives, a process deionized water main heat

water/deionized water and process-water/sea side). Additional hardware is in the process of being installed, including a 1 MW DC load with 2.5 MW pulse capability, adding to the flexibility of the test bed. The new pulse load capability will add interesting system dynamics to the test bed. During the first phase of the ESRDC we have added the thermal instrumentation which enhances the already existing electrical instrumentation. This effort adds to our capabilities for model development and validation.

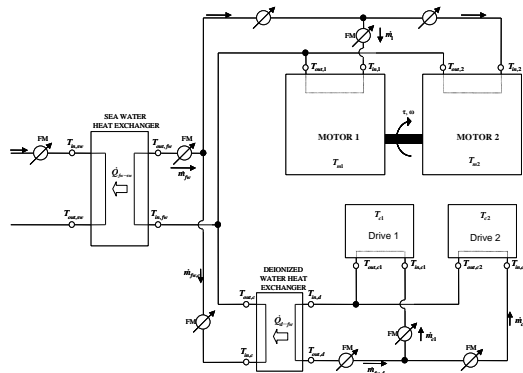


Figure 4. Schematic of CAPS test bed principal

a section of the test-used within the testing of the 5 MW motor and for loop experiments. conditions and ship be studied with the real simulator to which the connected. The components in the test MW motors, their water cooling loop, a cooling loop, and two exchangers (process

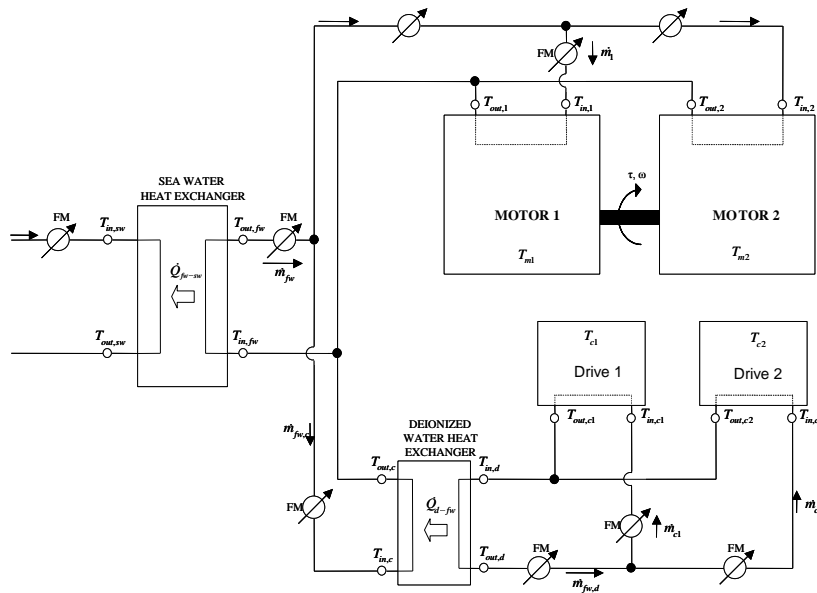


Figure 4. Schematic of CAPS test bed principal

Related publications

R. Hovsopian, J.C. Ordonez, J.V.C. Vargas, P.G. McLaren, “Thermodynamic Analysis of a 5MW Dynamometer Set to Simulate Ship Propulsion and Propulsion Load of an All-electric Ship”, Proceedings of the Brazilian Congress of Thermal Engineering and Sciences - ENCIT, Curitiba, Brazil, 2006

1.2.4. HTS Motor Thermal Modeling.

The results of our lumped thermal model for the armature of and HTS motor have been presented in two conference papers [1,2]. They describe our study on a cooling concept for a synchronous motor that has a High Temperature Superconductor (HTS) field winding. The thermal analysis reported is based on equivalent, lumped thermal circuits of two types: (a) a simplified circuit, aimed at delivering fast, design class results, that may be solved analytically; (b) more complex schemes aimed at assessing variable regimes, which are solved numerically by a circuit simulator. Both approaches are valuable, and complement each other in the quest for a meaningful preliminary design.

Related publications

[1] A. Morega, J.C. Ordonez and J.V.C. Vargas. Thermal model for the AC armature winding of a High Temperature Superconductor airborne motor. ASME-IMECE. Orlando, November, 2005.

[2] Morega, J.C. Ordonez, P.A. Negoias. Higher Resolution Thermal Design of an HTS AC Armature Winding. "Caius Iacob" National Conference of Fluid Mechanics and Tehnical Applications. Institute of Statistical Mathematics and Applied Mathematics, Romanian Academy. Bucharest, Nov. 25-26, 2005.

1.2.5. Developed a volume element based methodology for the thermal and psychrometric modeling of ships, ship compartments, and ship thermal signature.

A general computational model for all electric ships and internal compartments (open and closed domains) that contain heat sources and sinks has been developed. In it, a simplified physical model, which combines principles of classical thermodynamics and heat transfer, is developed and the resulting three-dimensional differential equations are discretized in space using a three-dimensional cell centered finite volume scheme. Two case were studied: a simulation of a whole ship at sea, and one of the ship's internal compartments (or cabinet). The proposed model was utilized to simulate numerically the steady state responses of the systems in both cases. Of particular interest in the first case is the possibility of predicting the ship's thermal signature at sea. Mesh refinements were conducted to ensure the convergence of the numerical results. The converged mesh in both cases was relatively coarse (175 and 320 cells), therefore the solutions were obtained with low computational time. Since accuracy and low computational time are combined, the model is shown to be efficient and could be used as a tool for simulation, design, and optimization of thermal management of all electric ships, internal compartments and cabinets.

Related publications:

1. J.C. Ordonez, J.V. C. Vargas and R. Hovsapiian, "Modeling and Simulation of the Thermal and Psychrometric Transient Response of All Electric Ships, Internal Compartments and Cabinets," Transactions of the Society for Modeling and Simulation International, 2008

6.1.Key Accomplishments

Thermal management research under the auspices of the consortium has been focused throughout on the following key issues:

- Development of physics-based models for system-level simulations
- Definition and investigation of the architectural characteristics of future electric ship thermal-electrical systems, subsystems, and components
- Modeling, simulation, and evaluation of advanced system components and controls that may be appropriate to the electric ship environment

Key accomplishments, in approximate chronological order, include:

- Developed convective heat transfer model for the Virtual Test Bed (VTB)
- Developed fuel cell stack model targeted for the VTB
- Developed approach for handling thermo-physical properties in the VTB
- Implemented Cycle-Tempo modeling software for steady-state simulations
- Developed steady-state, baseline representation of thermal management systems for the Arleigh-Burke class destroyer
 - based on data and drawings obtained from NSWC-Philadelphia and Joint Computer Aided and Logistic Support database (JCALS)
 - included major subsystems (turbines, A/C plants, dedicated seawater cooling, refrigeration plant, prairie/masker air, etc.), centralized seawater cooling systems, and chilled water cooling system
- Modeled thermal system for “Pilot Ship” installation of integrated electric propulsion system in Cycle-Tempo
 - superimposed an integrated electric power system on the DDG-51 by adding a section to the ship’s architecture
 - added a new seawater-to-freshwater cooling loop
- Implemented the *ProTRAX* modeling environment for dynamic system simulations
- Introduced 1,1,1,2-tetrafluoroethane (R-134a) refrigerant into *ProTRAX* modeling environment using NIST formulation
- Developed dynamic thermal load representation of pulsed electric weapon system
- Developed dynamic chiller model based on existing York 200-ton chillers on Arleigh-Burke class destroyer
- Created transient, thermodynamic model of the Rolls-Royce MT30 gas turbine engine for use in an integrated propulsion system thermal model
- Validated modular, capacitive-based, pulse-forming network model of a railgun system against experimental data from Maxwell Lab’s Green Farm system
- Completed 3-D, transient, finite difference simulation of the thermal management provided by multiple cooling channels through the rails of a railgun
- Completed model for energy storage technologies to optimize system designs and highlight the advantages and disadvantages of hybridizing energy storage
- Modeled active, phased-array, radar to demonstrate the thermal load scaling pertinent to future all-electric ship radars
- Worked with a student officer team from the Naval Post Graduate School to investigate cooling options for electric weaponry as a part of a total ship system
- Implemented mathematical model of the Alstom 19 MW, Advanced Induction Motor in *ProTRAX* and performed first integration of this model with appropriate propeller characteristics
- Developed review paper addressing System-Level Thermal Calculations for a Notional All-Electric Ship patterned after the DDG-1000

- Completed simulations in *ProTRAX* of an integrated propulsion system (IPS) modeled after the DDG-1000
- Investigated advanced chilling systems focused on utilization of waste heat for regenerative cooling or electricity generation purposes (on-going work)
- Developed a generic, in-house, modeling and simulation environment for thermal management (on-going work)

6.2. Technical Detail

Key technical results from our five-year research effort in ship system thermal management are presented in terms of the applicable student theses, as listed below. These are presented in chronological order such that the progress and direction of the program over time can be followed.

- *Improved Thermal Management of an All-Electric Ship Through Modeling and Simulation*, August 2004.
- *Steady-State and Dynamic Simulations of Large, Ship-Based Thermal Systems*, December 2005.
- *Thermal Management of Pulsed Loads on an All-Electric Ship*, August 2006.
- *Dynamic Thermal-Mechanical-Electrical Modeling of the Integrated Power System of a Notional All-Electric Naval Surface Vessel*, May 2007.
- *Creation of a Modeling and Simulation Environment for Thermal Management of an All-Electric Ship*, December 2007.

The technical details that follow summarize the work contained in these theses. Full technical detail is best obtained from the base document and associated publications.

6.2.1. *Improved Thermal Management of an All-Electric Ship Through Modeling and Simulation*

The major technical topic headings in the body of this thesis are:

- *Chap 2: Convective Heat Transfer Model*
- *Chap 3: Fuel Cell Model Development*
- *Chap 4: Fuel Reforming*
- *Chap 5: Simulation of a DIR Molten Carbonate Fuel Cell*

In this thesis, two models were developed that provide new simulation tools capable of addressing key thermal management issues. Attention was focused on the Virtual Test Bed (VTB) simulation software. Initially, work was focused on the existing convection model in VGB. This model required the user to specify a constant convection coefficient, thermal capacitance, and effective heat transfer area. All of these parameters are easily quantified with the exception of the heat transfer coefficient, which is dependent on geometry, flow characteristics, environment, and working fluid. To mitigate these shortcomings, a convective heat transfer model was developed that incorporated a graphical user interface, a database of convective heat transfer correlations, and thermo-physical property data for common fluids. This work identified both the utility and the limitations of the VTB and set the stage for developing a comprehensive fuel cell model.

Within the scientific literature, no fuel cell model previously provided a system-level, fundamental perspective of transient fuel cell operation with recognition of electrical irreversibilities and kinetics of fuel reforming. The comprehensive fuel cell model developed as an element of this work includes all relevant thermodynamics, chemistry, and electrical characteristics of the major fuel cell types. The main objective was to provide a system-level model capable of predicting the transient behavior of a fuel cell stack to external conditions such as reactant flow properties, operating conditions such as pressure and temperature, and event-driven circumstances such as changes in load flows. The simulation model tracks the transient temperature response of a fuel cell stack, chemical specie concentrations of exhaust gases, and electrical characteristics. The results provide a concise parametric evaluation of how operating conditions and user-controlled parameters influence fuel cell performance. A first principle, control

volume approach was employed such that the system is governed by an array of molar concentration balances, for each chemical species appearing in the fuel cell, and a global energy balance. The resulting nonlinear, first order differential equations are supported by thermodynamic and chemical kinetic relationships with recognition of all major electrical irreversibilities. Inputs to the model are the type of fuel cell under consideration (Proton Exchange Membrane, Solid-Oxide, Molten Carbonate, Alkaline, etc.), physical characteristics (number of cells, cell area, footprint), performance characteristics (limiting current, fuel crossover current, activation current, effective cell resistance, etc.), and fuel and oxidant flow properties (flow rate, feed pressure and temperature). Unlike most transient fuel cell studies, this model does not assume chemical equilibrium for the fuel reforming or electrochemical reactions but instead employs temperature, pressure, and reactant/product concentration dependent chemical rate equations. For the fuel reformation case, the rate equations are based on the Langmuir-Hinshelwood-Hougen-Watson (LHHW) approach to catalytic chemical reactions.

Principal results from this work are available in the open literature in two papers:

- B. Carroll, T. Kiehne, K. Ball, "Development of a Comprehensive Fuel Cell Model for Marine Applications," Proc. American Society of Naval Engineers Naval Electric Power Symposium, Philadelphia, Pennsylvania, January 2004.
- B. Carroll, T. Kiehne, M. Lukas, "Thermo-Kinetic Representation and Transient Simulation of a Molten Carbonate Fuel Cell," Proc. ASME Third International Conference on Fuel Cell Science, Engineering and Technology, Ypsilanti, Michigan, May 23-25, 2005.

6.2.2. Steady-State and Dynamic Simulations of Large, Ship-Based Thermal Systems

The major technical topic headings in the body of this thesis are:

- *Chap 2: Modeling of Fuel Cell-Gas Turbine Hybrid System*
- *Chap 3: Simulation of DDG-51 Thermal Management Systems*
- *Chap 4: Analysis of Through-Hull Heat Exchange*
- *Chap 5: ProTRAX Simulation System User Overview*
- *Chap 6: Implementation of 1,1,1,2-Tetrafluoroethane (R134a) Thermodynamic Properties into the ProTRAX Simulation System*
- *Chap 7: Dynamic Model of a Vapor Compression Refrigeration Cycle*
- *Chap 8: Dynamic Chiller Simulation Results*

The overarching theme of this thesis is thermal management modeling and simulation for large naval ship systems. One goal of the work was to provide current and future researchers working on similar projects with the foundation necessary to understand the operation of the thermal systems onboard current naval vessels and the modeling tools employed to analyze these systems. The *Arleigh-Burke* (DDG-51) class destroyer was chosen as a baseline for modeling and simulation work because these ships are similar in size and are expected to conduct missions comparable to the first class of all-electric ship. The following paragraphs outline the content of this thesis and briefly describe the work performed.

The initial work focused on learning to use the steady-state software package, Cycle-Tempo, which is used for thermodynamic analysis and optimization of energy systems. The Cycle-Tempo solution strategy is discussed, a simple example problem is introduced and modeled to gain an understanding of the software's operation and performance, and a hybrid gas turbine, fuel cell system is modeled and validated to prove capability. Using Cycle-Tempo, a number of the DDG-51 thermal management subsystems are described and modeled. These subsystems include an air conditioning plant (chiller), the dedicated seawater cooling system, the centralized seawater cooling system, and the chilled water system. Models of the seawater and chilled water systems are validated against operational data.

A novel cooling scheme was investigated for future all-electric ships. This cooling system uses a chilled water loop. Part of the chilled water is in direct contact with the ship's hull, and transfers heat through the hull directly into the sea. The purpose of this approach to cooling is to reduce the size of the centralized seawater and chilled water systems, or to be able to utilize these systems for other tasks. Another reason is to provide supplementary cooling for additional thermal loads that will be present on the all-electric

ship. A preliminary analysis was conducted, a parametric investigation was performed, and an estimate was made whereby a portion of the chilled water system was removed, and replaced by rejecting the waste heat using hull-based heat exchangers.

The purpose of the foregoing steady-state analysis was to serve as a departure point and provide initial conditions for subsequent dynamic modeling. The *ProTRAX* simulation environment was employed for dynamic simulations. This software allows one to conduct dynamic analysis of thermodynamic systems. As a precursor to modeling, this relatively complex simulation tool is described in the thesis. The description includes an overview of the modeling environment, construction of models, model parameterization, generation of an executable model, model execution, and a discussion of custom coding. Chillers onboard the newest flight of the DDG-51 use the refrigerant R134a. The properties of this refrigerant were implemented in the *ProTRAX* modeling environment. The National Institute of Standards and Technologies Reference Fluid Thermodynamic and Transport Properties database was used for this purpose. Source code contained within this database was modified for use with *ProTRAX*. The modified code was then tested and validated.

The foundation of the cooling system on the DDG-51 is its air conditioning plants. To determine the impact of future thermal loads on the ship (some of which may be dynamic in nature), a dynamic chiller model was created. Components modeled in a dynamic sense include the condenser, evaporator, compressor, and a control system. The chiller model was subsequently executed while simulating various loading conditions. Steady-state results of the dynamic model were compared to the chiller model results from Cycle-Tempo. The response of the chiller to various changes in load was also simulated.

Principal results from this work are available in the open literature in two papers:

- S. Haag, T. Kiehne, "Simulation of DDG-51 Thermal Management Systems," 2004, Proc. American Society of Naval Engineers High Powered Systems for Electric Ships Symposium, Annapolis, Maryland, December 7-9, 2004.
- "Steady State Representation of a Gas Turbine-Solid Oxide Fuel Cell Hybrid System," (with S. Haag), Office of Naval Research Contract Report, 2004.

Publication of the dynamic chiller model remains to be done and is the subject of on-going work.

6.2.3. Thermal Management of Pulsed Loads on an All-electric Ship

The major technical topic headings in the body of this thesis are:

- *Chap 2: Electromagnetic Railgun Background Information*
- *Chap 3: Energy Storage*
- *Chap 4: Capacitor-based Railgun System Simulation*
- *Chap 5: Rotating Machine-based Railgun System Simulation*
- *Chap 6: Railgun Barrel Cooling Techniques and Analysis*
- *Chap 7: ProTRAX Simulation*

The use of an Integrated Electric Propulsion System (IPS) on future all-electric ships will free up electrical power that was previously dedicated to the propulsion of the ship, ultimately allowing for the addition of pulsed electric weaponry. The addition of advanced electric weaponry will increase the ship-level thermal loads by more than an order of magnitude over the current warships. The work reported in this thesis addresses the design and optimization of an energy storage module for low load conditions on the ship, quantification of the expected thermal loads for a large scale electromagnetic railgun, analysis of both conventional and non-conventional rail cooling techniques, and analysis of a system-level model mating representations of thermal management systems with pulsed thermal loads representing the launch of an electromagnetic railgun.

The two commonly accepted pulsed power options for a ship-based railgun are a capacitor-based system and a rotating machine-based system. However, with the addition of these weapon systems, the magnitude of the thermal loads that require active cooling are likely to increase by more than an order of magnitude over the current class of warships. After providing background information on railgun systems, the initial work for this thesis focused on designing and optimizing an energy storage module.

The energy storage module provides emergency power for the all-electric ship and is necessary for a fully functioning IPS. Multiple energy storage devices were both qualitatively and quantitatively considered in order to select devices for an optimization study. The lithium ion and flywheel batteries were selected because of their high energy and power densities compared to the selected datum, lead-acid/nickel-based batteries. An optimization process was then invoked with the key parameters being the minimization of system mass, system volume, and the power deficiency across multiple power distribution scenarios. It was concluded that a hybrid energy storage system would be the best solution, as the high power output capability of the flywheel battery could provide the output power for large pulsed peaks, while the lithium ion batteries could provide the bulk energy storage.

Next the candidate pulsed power options were modeled in MATLAB to quantify pulsed thermal loads generated in the railgun system. A numerical model of a capacitor-based railgun system was developed by modeling the circuit representing the system. The numerical model outputs the rail current profile in addition to addressing a full energy balance and plots of projectile position, velocity, and acceleration with time. The numerical simulation was validated against both a previous numerical study and experimental data from a launch at the Green Farm facility. The MATLAB code accurately models the output current through the rails and the pulsed thermal loads within the circuit elements, indicating which elements may need to be actively cooled. The greatest thermal burden was revealed to be the resistive heating in the rails from which heat will need to be removed between successive shots to prevent structural degradation of the conductor material. The second candidate system, the pulsed rotating machine-based railgun system, was also modeled in MATLAB. Each numerical simulation provides the necessary inputs to the system-level dynamic chiller model developed within *ProTRAX*.

Since the greatest pulsed thermal load for the railgun system originates in the rails, two potential methods of cooling the barrel were explored. A finite-difference method was employed to study the effects of multiple through-hole heat exchangers to cool the rails. The three-dimensional analysis outputs multiple temperature contour plots at the breech of the railgun, the average and maximum rail temperatures with time, and the average exit coolant temperature with time. The copper rails are cooled from approximately 343 K to an average temperature of less than 320 K in six seconds. Consequently, the results show that an extremely large convective heat transfer coefficient likely will be necessary to reach the high rate of fire that the Navy proposes. More importantly, the results act as validation for less computationally and less time consuming numerical models to be input into the *ProTRAX* simulation environment.

A finite difference method was also employed to explore the use of a phase-change insert to aid in cooling of the rails. Lithium was selected as the phase-change material due to its favorable thermal characteristics. Realistic initial conditions were used to study the effects of the lithium insert on the average temperature in the breech of the railgun as a function of time. The simulation utilized the greatest volume of phase-change material possible with the assumed rail dimensions. It was concluded that the energy stored by the phase transition of the lithium from a solid to a liquid is not great enough to justify the complexity associated with introducing a phase-change material into the rail system.

Finally, a simple lumped capacitance representation of the rails was developed and compared to the full three-dimensional finite-difference analysis for accuracy. The model was then coded in FORTRAN as a custom module in the dynamic thermal software package, *ProTRAX*. The custom railgun module was then coupled to a dynamic chiller model, such that *ProTRAX* output the average coolant fluid temperature and evaporator level with time. The simple lumped capacitance model accurately models the convective heat transfer from the rails to the coolant fluid.

Principal results from this work are available in the open literature in two papers:

- C. Holsonback, T. Webb, C. Conner-Seepersaad, T. Kiehne, “*System-Level Modeling and Optimal Design of an All-Electric Ship Energy Storage Module*”, Electric Machines Technology Symposium, Philadelphia, PA, May 23-25, 2006.
- T. Webb, T. Kiehne, “*System-Level Thermal Management of Pulsed Loads on an All-Electric Ship*”, IEEE Transactions on Magnetics, January 2007, Volume 43 Number 1, pp 469-473.

6.2.4. Dynamic Thermal-Mechanical-Electrical Modeling of the Integrated Power System of a Notional All-Electric Naval Surface Vessel

The major technical topic headings in the body of this thesis are:

- *Chap 2: Estimation of IPS Thermal Loads on DDG 1000*
- *Chap 3: Rolls-Royce MT30 Gas Turbine Engine Modeling*
- *Chap 4: Rolls-Royce RR4500 Gas Turbine Modeling*
- *Chap 5: Propulsion Motor Modeling*
- *Chap 6: Propeller and Ship Hydrodynamic Modeling*
- *Chap 7: Generator and Distribution System Modeling*
- *Chap 8: Integrated Power System Modeling*

The goal of this research was to develop a dynamic, physics-based thermal-mechanical-electrical model of a naval integrated power system (IPS), nominally based on the DDG-1000. This model would then serve as the baseline for future testing of advanced shipboard thermal management technologies and architectures. The model reported in this thesis was implemented in *ProTRAX*, a dynamic thermodynamic modeling software product designed for land-based power plants. Custom coding within *ProTRAX* and other modeling environments was used as needed to develop models of the IPS components, which were then individually validated against data from the open literature. The model is now being moved to our in-house software architecture, described in Section 4.2.5.

Chapter 2 contains a detailed analysis of the expected heat loads aboard a DDG-1000 class ship. If the gas turbine exhaust is not considered a load, the ship service loads and propulsion motors and converters will be the largest source of waste heat production. It is clear that the ship cannot be outfitted with enough refrigeration capability to actively cool all of the equipment waste heat loads; seawater cooling must be used extensively. Unfortunately, this may limit the operational environments of the ship or increase the design, acquisition, and life-cycle costs of the ship. Electric propulsion does allow for generator scheduling, resulting in reasonable overall system efficiency and specific fuel consumption (SFC) across the range of ship speeds. At the highest speeds, the overall system efficiency and SFC approach that of the main gas turbine engines. Therefore, increasing the efficiency and/or decreasing the SFC of the main gas turbines should be a major focus of investment in the future. A significant amount of energy will be simply dumped to the atmosphere in the gas turbine exhaust. At full speed, the exhaust contains more than ten times the energy that is dissipated as waste heat by other components in the ship. This represents a clear opportunity for energy recovery and/or combined cycle technologies that draw upon the high-temperature energy in the turbine exhaust streams. This energy may be used either to increase the power and chilling available for current ship systems or allow for a reduction in mass and/or volume of the current system.

Components of the notional all-electric ship modeled in this work are two Rolls-Royce (RR) MT30 gas turbine engines, two RR4500 auxiliary gas turbine engines, associated wound-field synchronous generators, an ac electrical distribution system, ship service loads, four Alstom (now Converteam) VDM 25000 motor drives, two sets of tandem Alstom Advanced Induction Motors (AIMs), and two conventional fixed-pitch propellers. Short summaries of these models are provided below. Specific detail may be accessed in the thesis in Chapters 3 through 7.

The US Navy recently selected the Rolls-Royce Marine Trent (MT) 30 to power the IPS engineering demonstrator for the DDG-1000 and the Littoral Combat Ship. The UK MOD also chose the MT30 to power the Royal Navy's future all-electric aircraft carrier. The MT30 is an advanced aero-derivative engine that shares 80% commonality with its Trent 800 forbearer. At ISO conditions (15° C, 1.013 bar, 60% relative humidity, no inlet or exhaust losses) the MT30 is rated at 36 MW output power, 0.21 kg/kW-hr SFC, better than 40% thermal efficiency, 113 kg/s exhaust mass flow, and 466° C exhaust temperature. Like the Trent 800, the MT30 is a multi-spool engine, having intermediate and high-pressure spools that are aerodynamically coupled to each other and a free power turbine. The MT30 gas turbine engine model in this thesis was evolved from a simple, steady state air-standard analysis to a dynamic model in *ProTRAX*. In each iteration of the model, simplifying assumptions were removed and

additional complications were addressed, resulting in an increasingly realistic and robust representation of the MT30 engine. The unrefined results of the dynamic model were compared to the available fuel consumption data from the literature, and good agreement was found above about 50% load. To achieve complete agreement with experimental data, a bleed air schedule was adopted, which generally increased the model's SFC. Example dynamic responses to step-changes in load presented in the thesis show that the model is relatively robust and the control system well-tuned.

The RR4500 auxiliary gas turbine is derived from the Rolls-Royce Allison 501-K family of gas turbines; it has been selected as the auxiliary genset for the IPS engineering demonstrator. The RR4500 is a single shaft, high pressure ratio gas turbine engine. It is composed of a 14-stage axial compressor, a "boost" compressor module, and a four-stage turbine. It is rated at 3.9 MWe up to 37.8° C, but can produce 4.5 MWe up to 15° C. The exhaust mass flow rate is 18.3 kg/s at 547° C. Again, the RR4500 model was evolved from a simple steady state analysis. The initial model was based on a spreadsheet model of the 501-KB7 using a dry, air-standard analysis at ISO conditions with no losses. Steady state operation, quasi 1-D flow, ideal gas behavior, adiabatic components, and no compressor air bleeds were assumed. These characteristics were then progressively added back in and the model migrated into the *ProTRAX* dynamic environment. Native *ProTRAX* modules were used, and the steady state SFC characteristics were compared to a model from the literature. Example dynamic responses to step-changes in load illustrated that the model is well controlled, especially for step increases in load.

Alstom (now Converteam) was commissioned in 1995 to design and deliver a large electromagnetic motor capable of providing ship propulsion for a destroyer-class ship to the U.S. Navy's IPS. Alstom called their product the Advanced Induction Motor (AIM) because of its advanced characteristics such as high power factor and efficiency, large airgap for shock standards, and variable-speed capability. A tandem version of the AIM was integrated into the Flight I design of the DDG-1000. Alstom designed the IPS AIM for 19 MW at 150 rpm. At rated conditions, it has an efficiency of 95.7% and a slip of 1.23%. Fifteen phases, arranged to create twelve poles, power the stator. The stator phases are arranged in three symmetrical groups of five, which allows the motor to run on five, ten, or fifteen phases as desired. The IPS AIM has a power factor of between 0.85-0.9 over a large portion of its operating range. The pulse-width modulation (PWM) VDM 25000 motor converter, and the use of a low source frequency, contributes to such high performance. The "practical" per-phase equivalent circuit is used in our analysis. A discussion of alternative topologies for induction motor per-phase equivalent circuits can be found in the thesis. In this work, the collection of element values for a motor model is denoted an equivalent circuit parameter (ECP) set. Several pertinent ECP sets from the literature were investigated. It is left as future work to incorporate thermal characteristics into the model of the IPS AIM, including temperature-dependent resistances. For this analysis, the IPS AIM model is assumed to be at thermal equilibrium, with temperature-independent resistances at the nominal ECP values. A steady state model of the AIM was developed and validated against the limited information available in the literature. The first iteration of a dynamic IPS AIM model was implemented in MATLAB. In this construct, the operator creates a dynamic speed demand, as a percentage of rated speed, through a vector that contains the demand and the timeframe over which the demand is valid. The model responds well to the demand, transitioning smoothly between motoring and generating operation in either rotational direction. AIM model results from MATLAB exhibit the expected responses to changes in the demanded speed. The model was then transitioned into the *ProTRAX* dynamic modeling environment. Several refinements were incorporated into this version of the model to increase the torque output of the motor, limit regeneration to a reasonable level, and control speed transitions. Once initial testing of the AIM model was completed, the four pairs of motors and controllers were implemented in the *ProTRAX* IPS model, along with two shafts and two propellers.

Quantifying the interaction of the propellers and ship is critical to predicting the operating condition of the motors and gensets during ship transients. Since *ProTRAX* was designed for land-based, commercial power plants, it clearly does not have native models for a propeller or ship hydrodynamics.

Consequently, these elements had to be developed from first principles and custom coded in *ProTRAX*. The custom-coded shaft, propeller, and ship models were implemented via SOURCE and MACRO

blocks. Two propulsion motors were assigned to power each shaft, and two shafts and propellers accelerate the ship. A full discussion of the characteristics of the propeller and ship systems is provided Chapter 8 of the thesis.

The generators and distribution system of the DDG-1000 are the lynchpins that connect the prime movers, which use conventional technology from land-based power plants, and the propulsion and ship service loads, which are unique to naval applications. The loads are highly dynamic and large relative to the total amount of generation. However, from a thermal management perspective, the generators and distribution system are well understood and are not anticipated to be primary thermal loads for the DDG-1000 propulsion system. Therefore, considerably less effort was expended to model these components and very simplified models were incorporated into the IPS model in *ProTRAX*.

After the development and validation of the turbines, generators, distribution system, propulsion motors and controllers, propeller shafts, propellers, and ship hull, these models were integrated in a single *ProTRAX* workspace to form a model of the global IPS of the DDG-1000. During simulation runtime, variables flowed through the model as illustrated in Figure 4-1.

ing simulation runtime, variables flowed through the model as illustrated in Figure 4-1.

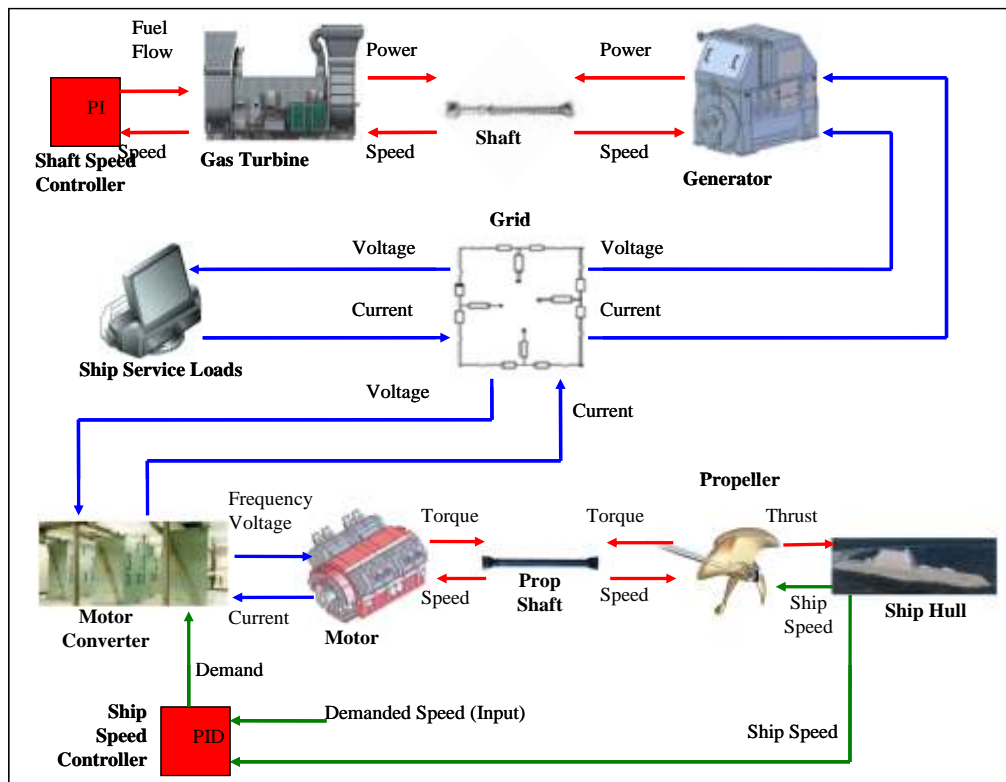


Figure 4-1: Variable flow throughout IPS model at runtime.

Simulations were performed for crashback and acceleration-to-cruise maneuvers. Simulation results at full speed were compared with the initial estimates from Chapter 2 and excellent agreement was found. Results indicate that the turbine models should be refined to include a friction load that will allow for idle without any mechanical load. Also, it was noted that loading one auxiliary gas turbine with an “idle load” while forcing the other to supply a small amount of power to the ship service loads during regeneration caused significant differences in the spool speeds of the two turbines. Results for the acceleration maneuver reveal that waste heat production can be significantly reduced at low ship speeds by using only two motors to power the shafts. Finally, the crashback results were compared to the literature, and qualitative agreement was found.

Principal results from this work are recorded in the open literature in one paper:

- C. Holsonback, T. Kiehne, “Estimation of System-Level Thermal Loads on the DDG1000,” Workshop on Transportable Megawatt Power Systems, March 2007, Austin, Texas.

A second paper, titled “Thermal Aspects of the DDG 1000” is currently in preparation for presentation at ASNE Day 2008.

6.2.5. Creation of a Modeling and Simulation Environment for Thermal Management of an All-Electric Ship

The major technical topic headings in the body of this thesis are:

- *Chap 2: Simulation Software Overview*
- *Chap 3: Basic Component Models*
- *Chap 4: Solving Resistive Networks*
- *Chap 5: Thermal/Fluid Models*
- *Chap 6: Heat Exchanger Modeling*
- *Chap 7: Automatic Controls*
- *Chap 8: Model of Starboard Fresh Water System*

The all-electric ship is complex and composed of many coupled subsystems that are considered large in their own right, e.g., two main power plants, two auxiliary power plants, and several chilled water plants, all serviced by seawater, fresh water, and chilled water cooling systems. Developing an efficient means by which future loads can be cooled will require new technologies and methods. New cooling architectures are best validated in a system sense via modeling and simulation. Because of the nature of the future all-electric ship, this modeling must include a dynamic component. This approach will not only allow for examination of new technologies or system topologies, but will also allow for the investigation of dynamic situations such as system reconfiguration. This thesis documents the development of a simulation environment designed to accommodate physics-based, dynamic models pertinent to future all-electric ships.

The central issue addressed in the second chapter is how to model large systems in various energy domains, i.e., the electrical, thermal, and mechanical domains. In our approach, a component model is built from the bottom up and largely simulated from the bottom up. In other words, each component model in the system is driven by its own simulation. This gives the developer complete flexibility in creating models. With this flexibility, the developer at the component-level is free to model and simulate component level internal dynamics in a manner best suited to the component in question. The physical system around which the research is demonstrated consists of a simplified model of the starboard section of the freshwater cooling loop aboard a DDG-51 class destroyer. Thus loads range from simple HVAC cooling coils to heat exchangers for vital equipment such as the high-energy sonar sensor system. The loads are handled by dynamic models of the existing 200-ton centrifugal chiller. While the DDG-51 is an established vessel, the longer range intent of this research is to investigate notional future systems and technologies to evaluate options in the design process.

The third chapter describes the construction of generic component models. The two types of models that are allowed are referred to as flow and potential models. These values are akin to what are traditionally called “through” and “across” variables. However, the term “through” and “across” are often used to describe an impedance network which is solved using nodal analysis. Because the methodologies developed here do *not* necessarily employ such an analysis, the terminology has been established in this way, i.e., flow and potential, to avoid confusion. This chapter discusses the classes used as the basic building blocks for all physical models that are subsequently developed. Because these are base models, the terminology used in this chapter is very general. All concepts are equally applicable across each energy domain (e.g., fluid, mechanical, and electrical).

The fourth chapter discusses the solution algorithms developed for resistive networks. There are three such solvers: a linear system solver, a simple nonlinear system solver, and a global nonlinear system solver. This set presents a robust capability to a system model developer and may be easily improved

upon as required. As a system becomes larger, it is desirable to have the number of calculations required to simulate the system increase in proportion with the number components. In this case, the order of calculations is said to grow at a rate on the order n where n is the number of components in the system. The primary simulation approach accomplishes this feat by having the requirement that each component simulate itself. There are times when it is desirable to have a system where it is not possible for the components to handle their own calculations. These systems are referred to as resistive networks because the components are resistive elements connected to one another. Matrix algebra is required to resolve these systems. Because the matrix algebra requires matrix inversion, the number of calculations may not be in proportion to the number of components.

Specific models for thermal/fluids components are developed in chapter five, six, and seven. These models introduce the differential equations used to model heat transfer and represent the basis upon which the example system presented herein can be modeled. The next chapter presents more complex thermal/fluid models, i.e., a concentric tube heat exchanger and a single phase shell-and-tube heat exchanger. The phase change heat exchanger was developed in a separate effort and has now been integrated into this architectural environment. The last chapter of model development is dedicated to controls. The basic architecture of these models is centered on the idea of a block diagram. A block diagram offers a natural approach for development of control algorithms as they are often the means for a control engineer to design and model automatic controls. Though primarily used to create control algorithms, these models can be used to represent any model that can be presented as a linear ordinary differential equation. In general, the objective of the control models is to provide the greatest flexibility to the user. To this end, the objects created to simulate controllers are based on objects that are capable of simulating an arbitrary block diagram.

The final chapter uses the DDG-51 starboard side, chilled water loop as an example simulation to exercise the simulation environment. The simulation is a startup scenario where all the loads are activated at once and valve controls are used to govern flows.

The model uses all primary elements which this thesis presents: a resistive network to solve for flows, a heat transfer calculation to solve for enthalpies, and automatic controls to govern flow rates.

This thesis was completed in December of 2007 and is the subject of on-going work within the research group. Publications will be forthcoming.

7. CONTROLS

The behaviors of power systems, especially power electronic systems, are defined by the controls applied to those systems. In contrast to the often rudimentary controls that can be applied to slowly-reacting mechanical systems, increasingly sophisticated controls must be developed and applied to power electronic systems. Several breakthroughs were developed in this area. The application of synergetic control theory, initially developed by our Russian colleagues, to control of power electronic and energy systems has been highly developed under this program. These applications are now supported by software tools, based on symbolic processing, that were developed to assist in synthesis of synergetic control laws. The application of polynomial chaos theory to design of robust controllers provides a new way of admitting and compensating for tolerances in the controlled systems. Methods and procedures for rapid prototyping of controls, based on incremental virtual prototyping, have been defined and proven out. Finally, the application of multiagent systems to diagnostics, monitoring, and control of electric systems has been developed.

In the last 5 years the researchers in Controls group at CAPS-FSU performed research on four different topics. The topics are as below:

- Multi-agent based reconfiguration of shipboard power systems
- Dynamic load shedding scheme for shipboard power systems
- PMSM condition based maintenance
- Active current harmonic detection

In the area of agent based reconfiguration, the research had significant impact on the way distributed control is seen as solution to problems like reconfiguration and energy management. One major outcome of the reconfiguration approach was to successfully push for load based reconfiguration approach (bottom to top approach) as compared to traditional generation based approach (top to bottom). The outcomes of this research has helped convincing ONR that load based reconfiguration approach is better in meeting the electrical needs on an shipboard power system (SPS). The research outcomes of dynamic load shedding scheme showed the importance of considering the factors, other than pre-defined priorities, while making load-shedding decisions. Through the method developed in this research both quantitative and subjective factors can be accounted in the decision making process at the runtime even if they are dynamic in nature. The research on PMSM condition based maintenance resulted in development of a fault detection and diagnosis algorithm that can estimate not only constant parameters but also slowly time varying and abruptly changing parameters in a fast manner. Besides the detection of PMSM internal faults, this algorithm can also provide accurate parameters for the sensor fault detection algorithm. Additionally a Particle Swarm Optimization based fault diagnosis approach was also developed to find the fault location and severity information of a stator winding turn-to-turn fault. The research on active filter harmonic detection resulted in a reconfigurable power conversion system to solve power quality problems in SPS without increasing system cost and space requirements. The research approaches associated with reconfigurable control include two modes. In the lower level mode the active front end converters of existing motor drives were reconfigured to function like harmonic cancellation and reactive power compensation filters. In the higher level mode multiple drives were reconfigured in a coordinate way by functioning them

as harmonic or reactive power compensators to achieve high power rating power quality improvement requirements.

In each research topic significant progress were made and the key accomplishments were presented in conferences and published in several journals and conference proceedings. The results were critically very well received by the peers.

7.1. Technical Details by Task or Project

7.2. Multi Agent Based Reconfiguration of Shipboard Power Systems

In the past 5 year of research work a prototype MAS has been developed that reconfigures a simulated shipboard power system (SPS) that acts without human intervention and without centralized scheduling. Distributed software agents are used to perform high-level control on each critical system component. In [1], the case is made that a decentralized MAS that is load centric, has a decentralized control, employs service discovery and uses power source cost modeling, avoids reliability and scalability problems associated with a centralized control architecture. Initially algorithms for an radial system reconfiguration was developed [1,3]. After a thorough testing the algorithm was extended for a ring structured SPS. While developing the reconfiguration algorithm using a decentralized approach, redundant information accumulation (RIA) problem was encountered. The agent based solution of RIA problem demanded a different approach than what has been used for radial system [4, 19-21]. Comprehensive test were conducted to prove the algorithm and then it was extended for mesh structured systems [17, 22-26]. The developed agents and reconfiguration approach were tested with a shipboard power system simulated in real time environment (RTDS – Real Time Digital Simulator) as well as in non real time environment (VTB – Virtual Test Bed). LEAP library combined with JADE was used as the agent development framework. The developed agents have been implemented on handheld devices (HP iPAQ pda) [25].

7.2.1. MAS Architecture

Fig.1 shows the MAS based approach which consists of two layers. There is an upper communication and computation layer, consisting of agents and connective peer to peer communications. The SPS is the lower layer with its controlled electric components. Each agent in the MAS represents a major electric component in the SPS, such as a generator, motor, breaker, or bus. The agents can send control signals and receive status information from the electric component that it represents. Agents exchange information via peer-to-peer connections in the upper layer MAS; while power flows through the connection between electric components in SPS.

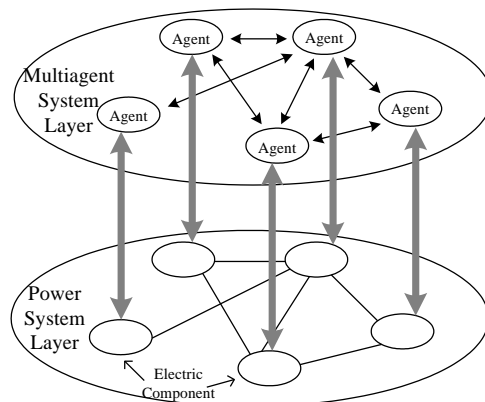


Fig. 1. Two layered structure for the reconfiguration of a shipboard power system

The agents sense the environment and then react accordingly by reconfiguring the SPS to fulfil the current ship mission and at the same time they try to optimize generation and distribution cost of electrical energy. The agents make sure that vital loads, which are essential for ship's survivability, are operational in the event of a contingency aboard the ship. In the event of emergency situations such as generation shortage, these agents also dynamically determine the loads that should be shed and the corresponding control actions such that SPS is alleviated of the constraining situation. The agents in the MAS are restricted to communicate only with their neighboring agents. This constraint makes MAS work in a completely decentralized manner. No central agent is setup in the MAS and no agent in the MAS can get information from beyond its neighboring agents. Each agent makes control decision autonomously based on the information it receives from its neighboring agents and the corresponding electric component. Further details of MAS architecture can be found in [17, 22-26].

7.2.2. Redundant Information Accumulation (RIA)

The net power, c_i , of an agent i is computed using (1).

$$c_i = \text{Power}_{\text{generated}} - \text{Power}_{\text{consumed}} \quad (1)$$

In a four-agent ring structured MAS, shown in Fig. 2(a), agents exchange accumulated c_i in order to route power in the power system. Accumulated net power in the system ($ANPS$) is the sum of net power of all the agents in the MAS. The arrows inside the ring structure show the first round of information flow in the MAS. Assume that the Agent1 starts the information flow. Agent1 sends its net power c_1 to Agent2, informing that Agent2 can get c_1 from Agent1. When Agent2 receives c_1 from Agent1, it adds c_1 to its own power capacity c_2 , resulting in accumulated net power c_1+c_2 . Then Agent2 sends c_1+c_2 to Agent3 and so on. Following the same logic, at the end of first round of information flow, Agent1 receives $ANPS$ after round 1, from Agent4. In round 2 of information flow, shown by arrows outside the ring, Agent1 sends $ANPS+c_1$ to Agent2. As compared with the information flow in the first round, $ANPS$ gets added to the information flow in second round. Furthermore, $ANPS$ will keep on accumulating to the information flow in each later round leading to RIA. An obvious solution for RIA problem is those agents pass not only the net power but also their identification. This solution although effective for small mesh systems is highly inefficient for large complex system and will not only lead to increase in communication bandwidth requirement but could also complicate and slow down the inter agent communication.

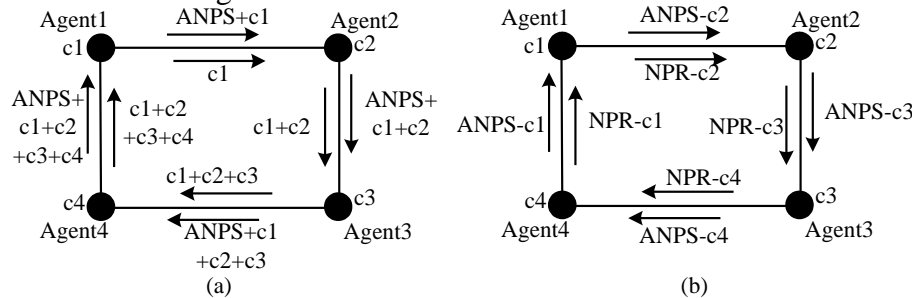


Fig. 2. Information flow in a ring structured MAS

However, if $ANPS$ for the agent system is known and each agent knows its neighbors' c values before information flow starts, RIA problem can be avoided using two rules. *Rule 1*: The agent that starts the information flow sends its neighbor j the information as $ANPS-c_j$; *Rule 2*: An agent

i sends its neighbor j the power information as $ANPS-c_j+c_i$. A spanning tree based solution has been developed. Details of this solution are discussed in [5,28].

7.2.3. Reconfiguration in a Mesh Structured System

7.2.3.1. Agent Modeling Approach

According to the electric component with which an agent interacts, the agents in the MAS are classified into four categories as generator agent, load agent, breaker agent, and bus agent. A generator agent can receive current information of the corresponding generator in the power system. This information consists of generation capacity, real/reactive power output, generation cost, fault alarm, etc. A generator agent can also exchange information with its neighboring agents. A load agent is an agent that is associated with a load in the SPS. The goal of a load agent is to make sure that the corresponding load is supplied in the SPS. A bus agent is an agent that is associated with a bus in the SPS. A bus agent monitors the current information of the corresponding bus in the power system, the information includes voltage, current injection, etc. Each of these agents uses a set of rules, discussed in [22] for making reconfiguration decision. A breaker agent is an agent that is associated with a circuit breaker in the SPS. The breaker agent receives the status of the corresponding breaker, and it can also send control signals to the corresponding breaker. Based on the information received from neighboring agents, the breaker agent can reconfigure the power system by controlling the corresponding circuit breaker.

7.2.3.2. Agent Behaviors

The agents in the MAS use behaviours to achieve the reconfiguration of the SPS. Each behaviour consists of functions for reasoning and communicating of the agents. These behaviours are – initialization, spanning tree, upstream, downstream, and update. Details of these behaviours and there order of execution are discussed in [22].

7.2.3.3. Implementation Platform and Test Results

In order to validate the reconfiguration algorithm and test MAS performance these approaches need to be tested and validated in a framework that captures their impact on the total integrated system. The developed agents and reconfiguration approach were tested with a shipboard power system simulated in real time environment provided by RTDS as well as in non real time environment of VTB. Details of VTB based test results can be found in [29]. The real time simulation platform for validating the proposed reconfiguration method is shown in Fig. 3a.

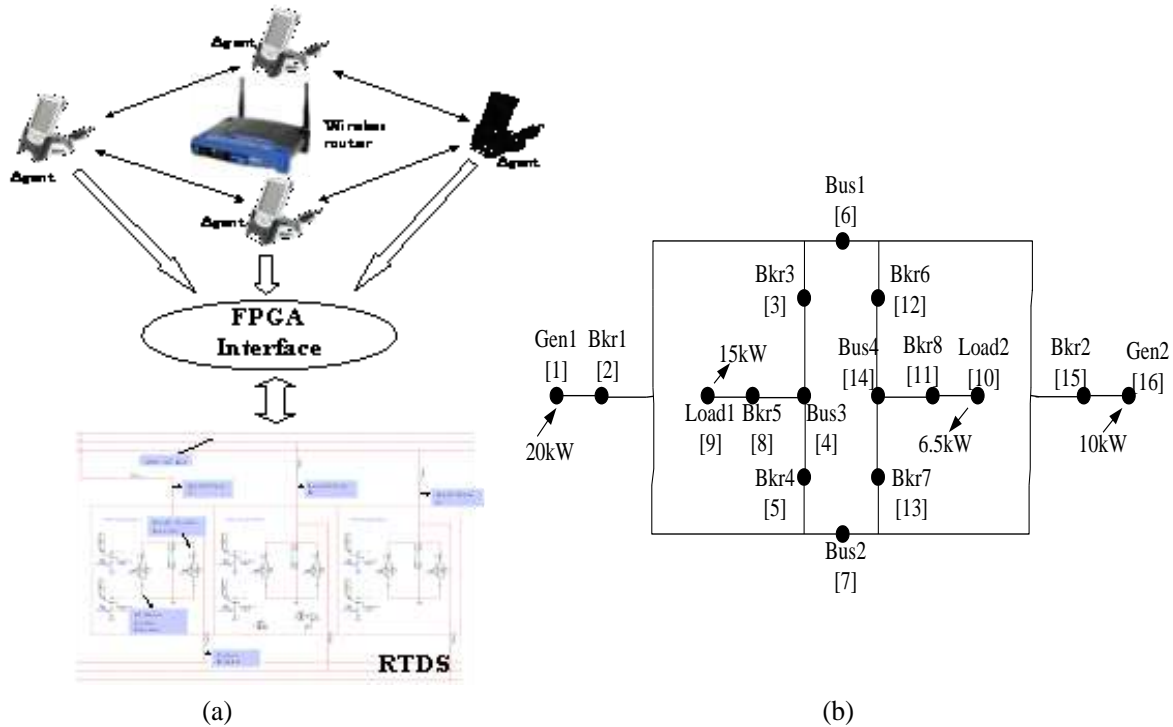


Fig. 3 Simulation platform and test simulation

In this simulation platform, the test SPS is simulated in RTDS and agents are implemented on HP-iPAQs. An FPGA interface between RTDS and the iPAQs was developed to facilitate interactions between agents on iPAQ and corresponding electrical components in RTDS [22]. In Fig. 3b mesh structured test SPS is shown. There are two generators and two loads in the power system. Gen1 and Gen2 are two generators with power capacity of 20kw and 10kw respectively. Load1 and Load2 have power demand of 15kw and 6.5kw respectively. Assume that Load1 is a vital load and Load2 is a nonvital load. The numbers in the brackets are the id numbers of the corresponding agents. In Fig 4 simulation results for test cases are shown. In the first case it is assumed that a fault happens at the Gen2. When Gen2 is disconnected, Gen1 cannot supply both loads in the SPS. Because Load1 is a vital load and Load2 is a nonvital load, Agent11 opens Bkr8 to disconnect Load2 from the system. Fig. 4(a) & (b) show the change of current that flows into Load2 and power of Load2 respectively due to the reconfiguration. In the second case it is assumed that the fault on Gen 2 is cleared and hence the agents take reconfiguration steps resulting in reconnection of Gen 2 and Load 2. Figure 4 (a) & (b) show the change of the current that flows into Load2 and the power of Load2 respectively. Further details can be found in [22].

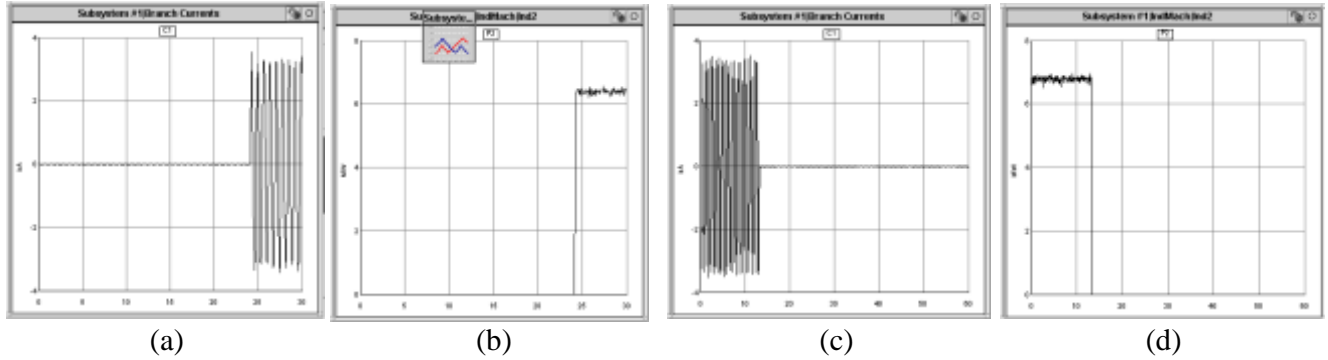


Fig. 4 Simulation results

7.2.4. Conclusions

In the 5 years of research work the agent based reconfiguration approach has advanced from radial to ring to a fully mesh structured system. Capability of agents to perform fast reconfiguration in an efficient manner has been validated and demonstrated. In future further research need to be done to look into the effects of network latency, communication bandwidth on agents' behaviour and decision making process.

7.3. Dynamic Load Shedding Scheme for Shipboard Power Systems

Current SPS load shedding is normally provided in several stages or levels, which only shed loads based on fixed priority categories [30]. Three disadvantages exist with this approach: (1) in most cases, more loads are disconnected than necessary to meet the reduced generator capacity; (2) the original load shedding system assumes that loads' priorities are fixed regardless of changing situations; and (3) only the static priority of the load is considered while other factors, that may be critical depending on the natures of loads and may also play a valuable role in deciding which loads to shed, are not considered. Moreover, generally the loads are shed manually. The realtime dynamic load shedding scheme (LSS) for Navy SPS developed at CAPS-FSU, in which analytic hierarchy process (AHP) is adopted for dynamically prioritizing loads based on changing priorities (vital, non-vital, semi-vital, etc.) of loads and system critical natures of loads, takes care of these disadvantages. In the work done at CAPS-FSU, system critical natures of loads that were considered included inrush current, harmonic content, restoration process, power factor and full load power rating. The load shedding scheme maximizes various system benefits and minimizes load curtailment. Expert system is used to facilitate the load shedding decision-making process. The developed scheme was then implemented on a test system simulated in RTDS. This test system was a part of a validated notional SPS simulation in RTDS. The realtime implementation and simulation of the LSS on a test SPS and the results obtained from various experiments proved the effectiveness of the LSS in a dynamically changing environment.

7.3.1. Methodology

The block diagram of the proposed load shedding scheme is shown in Fig. 5. The LSS consists of a dynamic database, a set of system critical natures of loads, an AHP load prioritization module (ALPM), and an expert system control actions module (ECAM). The proposed LSS assumes that the amount of load to be shed will be provided by some external application. The ALPM takes as input the various system critical natures of loads, electrical parameters and status of loads from a dynamic database. The dynamic database is constantly updated with present state of the SPS. ALPM also takes as inputs the present mission(s) from a dynamic database. A ship at any given time may be executing one mission or a combination of several missions. Taking these inputs, the ALPM uses AHP [30] to order the loads of the SPS in an increasing order of priority and passes this list to the ECAM. ECAM searches the dynamic database to obtain the system

state information, consisting of various static, connectivity and realtime data, such as status of circuit breakers (CBs), bus transfers (BTs), and relays. It also takes as input the amount of load to be shed. Using these inputs and based on a pre-existing set of rules, the ECAM identifies loads to shed and determines the least number of control actions required to shed these loads. Finally ECAM outputs the list of control actions to be executed and loads to be shed. Each module is described in more detail in the following subsections.

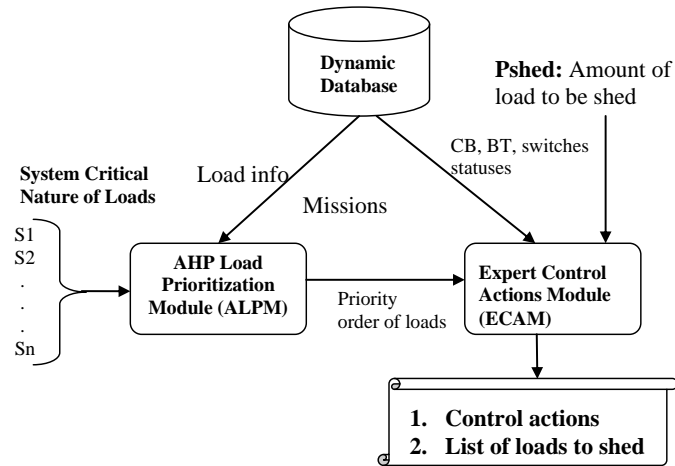


Fig. 5. Block diagram of LSS

7.3.2. Implementation

ALPM requires formation of two judgment matrices to calculate weight factors for load prioritization. Judgment matrices of different significance levels and system critical natures of loads can be formulated by analyzing the survey results from experienced system operators. A software program is written to implement the ALPM. An expert system shell [20] was used to develop the ECAM, which identifies the loads with lowest priorities that should be shed and also tries to determine the optimal control actions to shed the identified loads. In order to test the dynamic performance of the developed LSS, the scheme was implemented in a realtime environment in RTDS. To apply the LSS on a test system in RTDS, a load shedding a user defined component (UDC) was developed. Fig. 6 shows the control block diagram of the overall implementation of LSS in RTDS. The UDC inputs and the available generator capacity are used to compute the overload amount or the required shedding amount. The UDC outputs the switching actions required to shed loads. These switching actions are then implemented on the simulated test system. The realtime effect of these actions is reflected in the outputs of the simulation in RTDS at runtime. For loads that are selected to be shed, their CBs are opened and the realtime effect of these actions can be immediately seen in RTDS at runtime.

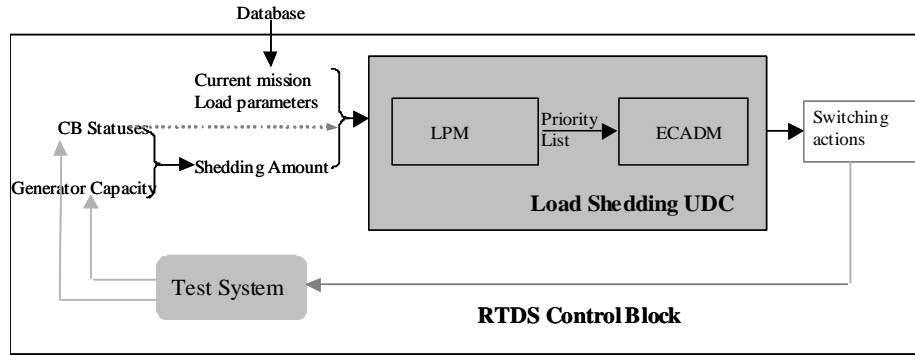


Fig. 6. Control block diagram in RTDS

7.3.3. Test Results

A test system representing a 10-load DC zone of a notional destroyer class SPS simulation model was selected for the study [30]. This DC zone consists of a DC bus of 800 V and an AC bus of 450 V. Eight DC loads are fed from the DC bus, and two AC loads are fed from an AC bus. A DC- AC inverter supplies the 450 VAC bus from the 800 VDC distribution bus. Current injections were added to simulate the load harmonic current and inrush current. Based on the given input parameters, ALPM prioritizes loads for different mission or combinations of missions, as shown in Table 1 [30]. Various scenarios were tested using this setup.

Table 1: Cost and Ranking of Loads in Different Scenartios

	Cost M1	Rank M1	Cost M2	Rank M2	Cost M3	Rank M3	Cost M1, 2	Rank M1, 2	Cost M3, 2	Rank M3, 2	Cost M1, 2, 3	Rank M1, 2, 3
L9	1.9728	1	0.5734	3	1.9728	1	1.0648	2	1.0648	3	1.9729	1
L10	1.1841	2	1.1841	2	1.1841	3	1.1842	1	1.2015	2	1.2015	3
L3	0.4533	3	1.5595	1	1.5595	2	0.8418	3	1.5283	1	1.5283	2
L4	0.2877	5	0.2877	5	0.0799	10	0.2878	4	0.1679	7	0.2878	6
L5	0.4277	4	0.1188	8	0.1188	8	0.2496	5	0.1188	8	0.2496	5
L6	0.1164	8	0.4191	4	0.4191	5	0.2445	6	0.4135	4	0.4191	4
L7	0.1037	9	0.1037	9	0.3735	6	0.1038	9	0.2179	6	0.2179	8
L8	0.1199	7	0.1199	7	0.4318	4	0.1199	8	0.2519	5	0.2519	7
L1	0.1004	10	0.1005	10	0.1004	9	0.1005	10	0.097	10	0.097	10
L2	0.1378	6	0.1379	6	0.1378	7	0.1379	7	0.1335	9	0.1335	9

L1, L2, ..., L10 are the names of loads; Cost M1: cost of load in mission 1 ; Rank M1 : priority rank of load in Mission 1 ; Cost M3, 2 : cost of load in concurrent missions of 1 and 2 ; Rank M1,2,3 : priority of rank in concurrent missions of 1,2, and 3.

In one scenario, it is assumed that the ship is cruising (mission1) and all loads are working in normal condition. Suddenly, one generator is taken offline due to a generator fault, leading to an overload condition. An overload of 109.1 kW was detected while the ship is operating under the above conditions in mission1. For this scenario the simulation results showed that Load 1, 6 and 7 are shed. This result can be verified from Table 1. In total 111 kW was shed.

Continuing with the previous scenario, after the load shedding has been performed, the ship is assumed to be in battle conditions. This leads to the assumed damage of an operating generator, causing a further decrease in the electrical energy available to this zone. Meanwhile, mission2 (combating) is invoked immediately to engage in battle scenario. Also, the LSS is invoked again to alleviate the overload situation by performing load shedding while the ship operates in concurrent missions of 1 and 2. In this case, generator capacity decreases by 45 kW, from 401

kW to 356 kW in. Load 8 is shed by LSS in this scenario to get rid of the overload condition. The developed LSS was tested with several cases similar to as presented above. The illustrations indicate the possibility of implementing the proposed scheme in real time applications by taking into account the dynamically changing environment of SPS in the decision making process. The detailed description of these scenarios and overall LSS methodology can be found in [30-33].

7.3.4. Conclusions

The present load shedding practices for Navy shipboard power systems tend to shed more load than necessary. In this research work an alternative load shedding scheme for shipboard power systems is developed that minimizes load curtailment by considering system critical natures of loads such that system benefits are improved. Dynamic prioritization of the loads with respect to changing scenarios makes the proposed load shedding scheme more flexible and practical. Realtime implementation and simulation of the load shedding scheme on a test shipboard power system demonstrates the effectiveness of the novel load shedding scheme in a dynamically changing environment.

7.4. PMSM Condition Based Maintenance

Faults in engineering systems are difficult to avoid and may result in serious consequences. Effective fault detection and diagnosis (FDD) can improve system reliability and avoid expensive maintenance. FDD is especially important for some special applications, such as Navy ships operating in hostile environment. So far, the FDD for nonlinear systems have not been fully explored. There is still a big gap between the FDD theories and applications. During the past years, we tried to fill the gap by developing an integrated FDD system structure and a series of algorithms for FDD of Permanent Magnet Synchronous Motors (PMSM).

A fault model is proposed for the stator winding turn-to-turn fault of PMSM. The model provides a good compromise between computational complexity and model accuracy and is versatile for both the healthy and the fault condition. Simulation studies demonstrate a good coincidence with both the theoretical analysis and the experimental observations in existing literature. The model is especially important for the designs of model based FDD algorithms. Based on the fault model, a series of algorithms are proposed for the fault detection and diagnosis of PMSM. Since the reliability of sensors is the basis of FDD and control systems, a nonlinear parity relation based algorithm is proposed for sensor fault detection. The algorithm can successfully detect single faults in the currents and speed sensors. To track the parameter variations, which are symptoms of system internal changes and faults, an adaptive synchronization based parameter estimation algorithm is proposed. Simulation and experimental studies demonstrate that the algorithm can estimate not only constant parameters but also slowly time varying and abruptly changing parameters in a fast manner. Besides the detection of PMSM internal faults, the algorithm can also provide accurate parameters for the sensor fault detection algorithm. Based on the fault data, a Particle Swarm Optimization based fault diagnosis approach is proposed to find the fault location and severity information of a stator winding turn-to-turn fault. To improve accuracy and efficiency, the real time implementation of the PSO based identification algorithm is also studied. Finally, the proposed algorithms are integrated into a general FDD system structure as shown in Fig. 7.

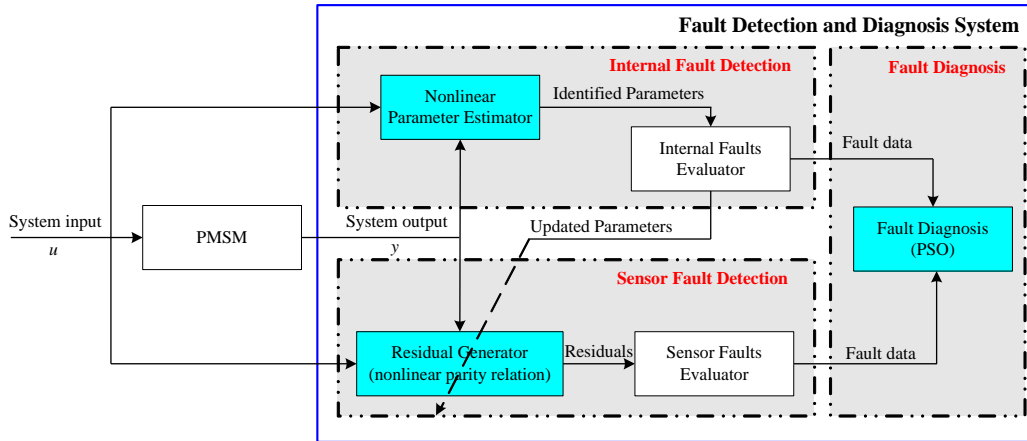
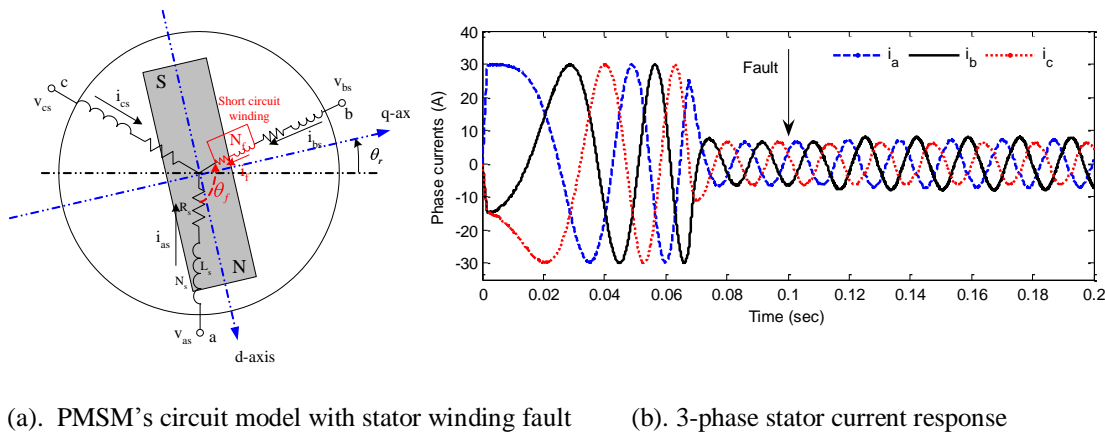


Fig. 7. Structure of the integrated FDD system

7.4.1. PMSM modeling under normal and stator fault condition

For model-based approaches, effective fault detection and diagnosis relies on successful distinction of system behaviors under various operating modes. Fault detection is used to judge whether a fault happens or not, and fault diagnosis is used to obtain detailed information of the fault based on further analysis of the fault symptoms. Both of the two tasks rely on analytical models of the monitored system. Acquisition of an appropriate PMSM model is the first step of model based FDD. We proposed a new model for PMSM operating with stator winding short fault. The fault is the most common electrical fault in PMSM. The model is used in following FDD research. Fig. 8(a) illustrates the stator winding short fault occurring in phase b. In the fault model, two new variables introduced to represent fault location and fault severity.



(a). PMSM's circuit model with stator winding fault (b). 3-phase stator current response
 Fig. 8: Modeling and simulation of PMSM stator winding fault
 Fig 8(b) displays PMSM response to a stator winding fault. Simulation studies demonstrated consistencies with practical observations and existing literatures. The proposed PMSM model is applicable to both healthy and stator winding turn-to-turn fault conditions. The model consists of fault location and fault severity information, which can be used for fault diagnosis.

7.4.2. Nonlinear fault detection for PMSM

Successful operation of a model based FDD system depends on the quality of the measured data. If the sensor is not working correctly, the data provided to FDD system may lead to wrong decisions. Thus, sensor faults, which are typically additive faults, must be identified beforehand. Based on the data provided by these fault free sensors, a synchronization based adaptive parameter estimation algorithm is also proposed for the detection of PMSM internal anomalies.

7.4.2.1. PMSM Sensor Fault Detection

Modern sensors can provide better measurement of signals with increasing robustness. However, faults still may occur to sensors under severe conditions, especially after long operation. The occurrence of sensor faults is at the same level as the system internal faults. Considering the importance of sensors to monitoring and control systems, the detection of sensor faults should be the first priority in a FDD system.

Parity relation based sensor fault detection algorithm is simple in implementation and suitable for the detection of additive faults. Thus, we proposed a nonlinear parity equation based approach for the detection of PMSM sensor faults. Some simulation results are provided in Fig. 9

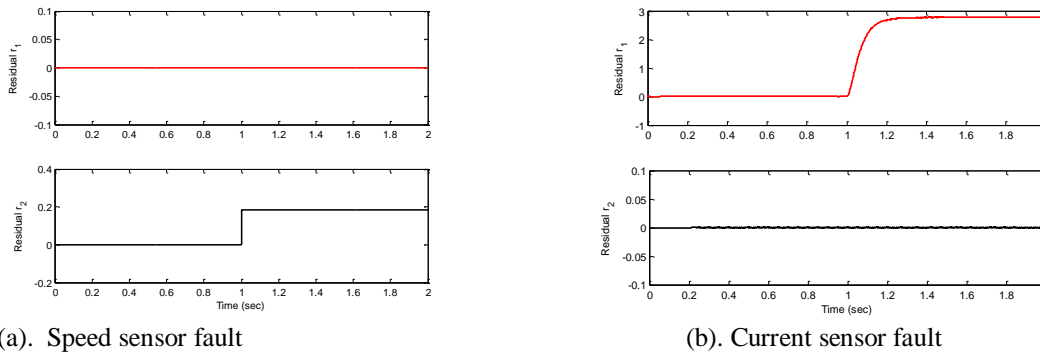


Fig. 9 Simulation results for Parity Relation Based Sensor Fault Detection

From the simulation results, it can be seen that the algorithm identifies the speed sensor fault and current sensor fault successfully, provided the threshold and dwell time are properly set.

7.4.2.2. PMSM Internal Faults Detection

Since system internal fault is usually reflected as changes in model parameters, parameter estimation is an effective way to identify system internal changes or faults. From the structure of the dq model, we can see that it is difficult to identify the internal parameters. There is also no general applicable nonlinear estimation algorithm that can be directly applied to this problem. Parameter estimation algorithm has to be designed specifically for this application. Here, a synchronization based adaptive estimation algorithm is designed for the identification of stator resistance and inductance. Some simulation results are show in Fig. 10.

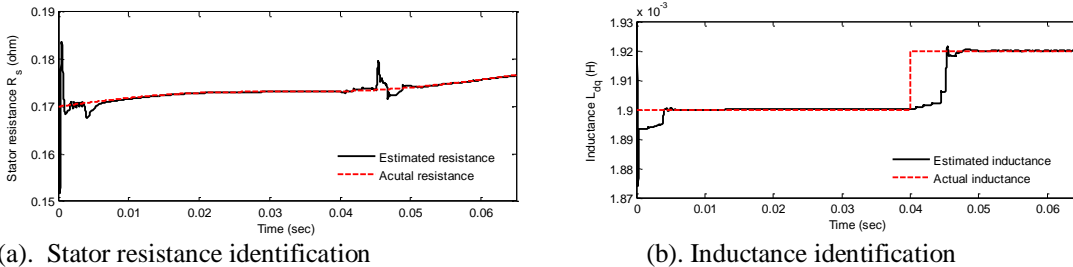


Fig. 10: Simulation results for Parameter Estimation Based Internal Change Detection

These two figures show the performance of the proposed algorithm for the estimation of time-varying parameters. In the test, the stator resistance was set to be slowly time varying, furthermore, a step change is added to the inductance. Good estimation results are obtained for both parameters. The estimated parameters can be used to determine the occurrences of internal faults in PMSM. Further diagnosis can be used to obtain specific knowledge of the detected internal faults.

7.4.3. Particle Swarm Optimization Based Diagnosis for PMSM Stator Winding Fault

Particle Swarm Optimization (PSO) is a new population based stochastic search algorithm. PSO algorithm is simple in concept, computationally efficient, and easy to implement. It gains popularity in a short time and has been widely applied in recent years. The method we proposed can be applied to a broader class of identification and optimization problems.

According to the equations of PMSM stator winding fault model, it can be seen that the distribution of the parameters to be identified is very complex, which makes the design of nonlinear identification algorithm very difficult. To overcome this problem, the identification problem is transformed into an optimization problem. And then PSO is applied to solve the optimization problem. The block diagram is shown in Fig. 11 and some simulation results are provided in Fig. 12.

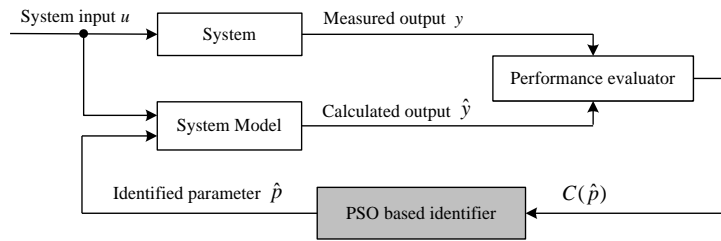
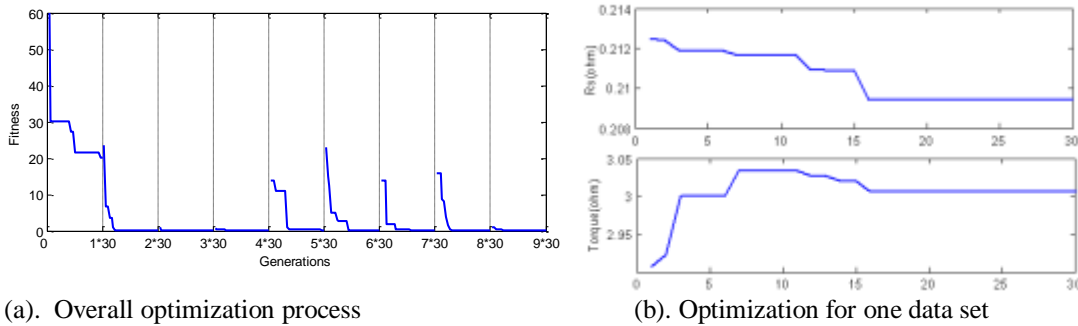


Fig. 11: Block diagram of the PSO based fault diagnosis algorithm



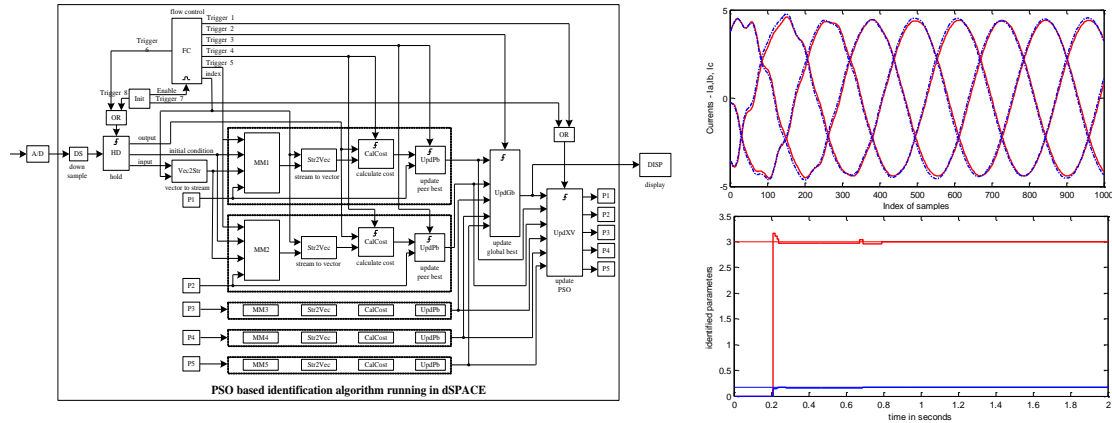
(a). Overall optimization process

(b). Optimization for one data set

Fig. 12: Simulation results for Parameter Estimation Based Internal Change Detection

7.4.4. Real-Time Implementation of PSO Based Parameter Identification

So far nearly all PSO based optimization and identification applications can only be realized offline. The reason is because of the unavoidable time needed for simulations, which are used to evaluate the candidate solutions. The objective of our “real time” implementation is to finish the predefined number of iterations within the same amount of time used for measurement. Besides using advanced hardware to achieve faster simulation, we can also modify the time constant of system model to obtain faster than real time simulation. The block diagram of the PSO algorithm running in hardware controller is shown in Fig. 13(a). Some simulation results are provided in Fig. 13(b).



(a). Block diagram of realtime implementation of PSO (b). Real time simulation results
 Fig. 13: Implementation and simulation results of realtime PSO based PMSM parameter identification

From the above simulation results we can see that the parameters in PMSM model has been successfully identified. Since the algorithm is purely implemented using basic Simulink modules and Matlab Embedded functions, the program can run in most popular hardware controllers. The approach can be extended to other online identification and optimization problems.

7.5. Active Current Harmonic Detection

During the past five years, a reconfigurable power conversion system is proposed to solve power quality problems in shipboard power systems (SPS) without increasing system cost and space requirements. The research approaches associated with reconfigurable control include two modes. The lower level mode is single drive reconfiguration, in which active front end converters of existing motor drives will be reconfigured to function like harmonic cancellation and reactive power compensation filters. The higher level mode is multiple drive coordination control, in which multiple drives will be reconfigured in a coordinate way by functioning them as harmonic or reactive power compensators to achieve high power rating power quality improvement requirements. With proposed reconfigurable power conversion systems, the power quality problem can be solved locally and the global SPS power quality will be improved.

To achieve reconfigurable power conversion, a novel harmonic selective detection method, a new stationary current controller and an optimized coordination control will be developed. The harmonic detection method takes advantage of adaptive detection methods and PSO method. Therefore, the new harmonic detection method has fast identification speed, harmonic selective ability, phase independency, frequency tracking ability, simplicity and flexibility. PSO method is expected to have both offline and online tuning ability to the detection method's gains, which makes the adaptive detection method optimized for different nonlinear load characteristics. The control of the inverter is expected to solve the problem associated with existing P+Resonant controller for harmonic injection. PSO based optimization applies to the controller's gains selection, which makes old trial and error method out of date. The new controller is able to control the harmonic or fundamental current flow precisely and quickly to the power network for power quality improvement. Optimized coordination control is also applied to achieve the whole system's power quality improvement by operating different drives in an organized way. At last, analysis, design and control of the reconfigurable power conversion system are discussed and experimental results verify the whole system's proper operations. The proposed reconfigurable power conversion system is not limited to SPS, and it is also applicable to commercial power distribution systems.

7.5.1. Harmonic Detection Algorithms

Different harmonic detection algorithms have been implemented and tested both in simulation and experiments for reconfigurable power conversion systems. Those harmonic detection algorithms include the d-q method, active noise cancellation method, adaptive neuron method (also called multiple adaptive feed forward cancellation method, MAFC), improved adaptive gradient method and Prony method. Above five developed algorithms are divided into three groups as traditional d-q method, adaptive methods and Prony method. Their characteristics are summarized in Table 2. It clearly demonstrates that the best candidates for our applications are in the adaptive detection group. However, in our applications, multiple methods may be used. With simulated and experimental results, more analysis and scientific work related to these adaptive algorithms should continue.

Table 2: Comparisons of Three Group Detection Methods

	d-q method	Adaptive methods	Prony method
Start Transient	Fast	Fast	Medium~ Fast
Load change transient	Fast	Fast	Medium~ Fast
Single phase system	Complicated	Easy application	Easy application
Three phase system	Easy Application	Easy application	Easy application
Frequency estimation	PLLs	Included	Included
Flexibility	Limited	High	Medium
Computational burden	Small	Small	Very high
Three phase unbalanced systems	Complicated	Phase independent	Phase independent
Real time implementation	Easy	Easy	Difficult

7.5.2. Current Control

Current control is an important issue for power electronic converters. In general, stationary frame controllers are regarded as being unsatisfactory for ac current regulation because conventional PI controller cannot reach good steady state and dynamic performance. The control is usually implemented in so called d-q rotating reference frame. The basic principle of rotating reference frame control is that three phase currents or voltages are first transformed to dq0 frame, where the ac component can be transformed to dc values. Therefore, traditional linear controller such as PI controller can reach zero steady state error and good dynamic performance. After inverse d-q transformation, the system then can be excited by controller ac currents or voltages. Different current control algorithms have also been simulated for reconfigurable power conversion systems. Those current control algorithms include rotating frame PI and LQR controller, Hysterisis Controller and PIS controller.

Table 3 shows the comparisons of tested algorithm and investigated advanced current controller. The best candidate for our application is based on PIS controller, which is simple, good for sinusoidal reference tracking and with fixed switching frequency.

Table 3: Comparisons of tested current control methods

	Linear PI	Linear LQR	Hysterisis	PIS
Start Transient	Fast	Fast	Fast	Fast
Load change transient	Fast	Fast	Fast	Fast
Single phase system	Complicated	Complicated	Easy application	Easy application
Three phase system	Easy Application	Easy application	Easy application but phase dependent	Easy application
Flexibility	High	High	High	High
Computational burden	Small	Small	Small	Small
Three phase unbalanced systems	Medium	Medium	Complicated	Simple
Real time implementation	Easy	Easy	Easy	Easy
Reference signals	dc	dc	Any form	Dc and sinusoidal
Switching frequency	Fixed	Fixed	Varying Fixed (complicated modification)	Fixed

7.5.3. Motor Control

The modeling and control of induction motors (IM) has been intensively investigated. In other previous work, the common vector control is used to separate the torque and flux channels in the induction machine. Indirect vector control using proportional-integral (PI) controllers in d (torque) and q (flux) axis is applied to IM control. The speed error between the reference speed and the measured speed is controlled with an outer loop PI controller to generate the corresponding current reference. The d and q axis currents in the synchronous speed reference frame are controlled separately with inner loop PI controllers to generate the corresponding voltage references. After the inverse d-q transformation, the three-phase voltage reference is obtained. Feed forward control is also used to improve the controller dynamic performance. A simplified speed control block diagram of an IM is shown in Figure 14.

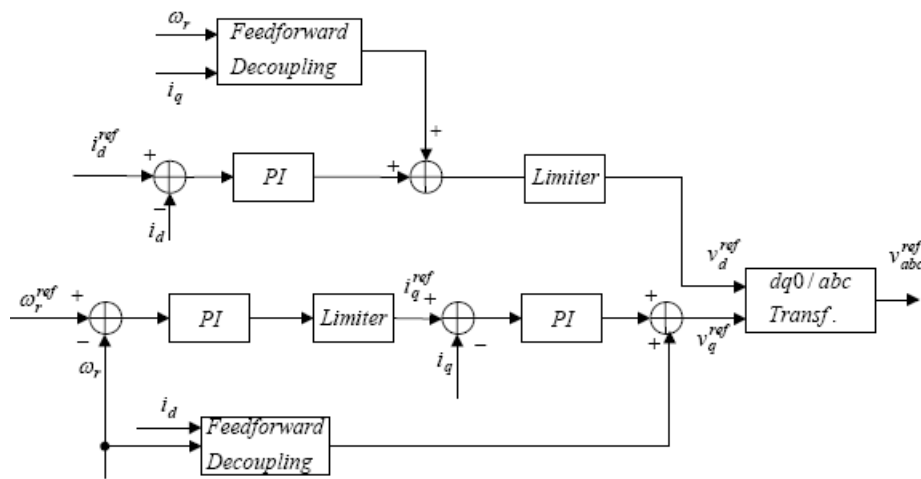


Fig. 14: Simplified speed control block diagram of an IM drive

7.5.4. Experimental Setup and Tests

To support the proposed reconfigurable power conversion system, an experimental setup of a prototyping reconfigurable power conversion drives is under going. Figure 15(a) shows a simplified reconfigurable power conversion system under experimental setup. A back-to-back converter connecting to supply bus is used to generate an experimental bus for reconfigurable power conversion system tests. An adjustable nonlinear load is used to generate current harmonics in the test bus. An induction motor drive with back-to-back converter setup is the reconfigurable system under study and it is controlled to have the harmonic or reactive power compensation ability at its active front-end converter while controlling the motor with normal operation. A PMSM motor drive system can be controlled for coordination operation with induction motor drive for advanced reconfigurable control of canceling current harmonics.

After about one year's work, most of the equipment is positioned and well wired and tested. Harmonic detection algorithms are all tested experimentally and verified the simulation results. Separate current experimental setup is shown in Figure 15(b). dSPACE controller and replacement control interface card are also installed and tested. A dSPACE controller collecting measured current and voltage signals is running in realtime for control purpose. With this completed experimental setup, harmonic detection algorithms were fully tested by using two different nonlinear loads

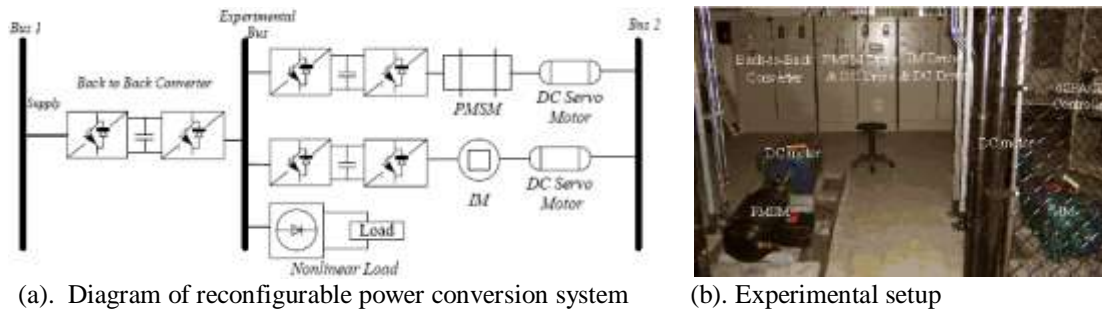


Fig. 15: Diagram and experimental setup of the reconfigurable power conversion system

Another completed setup is the connection of dSPACE controller with RTDS (Real Time Digital Simulator) to form a RT-HIL (Real Time-Hardware In the Loop) test bed as shown in Figure 16. With this completed experimental setup, target electrical systems can be simulated in real time way and control algorithms can be fully tested in the controller before they are applied to proposed real electrical systems. Therefore, controller’s performance and potential errors inside can be identified before it deteriorate or even damage a real electrical system.

7.6.Key Accomplishments

- Developed MATLAB/Simulink[®] model of a notional, all-electric, mesh shipboard power system (SPS)
- Developed a reconfiguration strategy for the SPS model and implemented it in MATLAB/Simulink[®]
- Added Energy Storage capability to the SPS model
- Used the MATLAB/Simulink[®] model to study:
 - Optimum techniques for calculating the optimization functions
 - Dynamic behavior of the SPS model when switching between different model states
 - Effects of energy storage module on simulations.

7.7.Technical Detail

7.7.1. Power System Architecture

7.7.1.1. System Reconfiguration

The work under this task focused on the topic of reconfiguration for electric powered ships. Power grid reconfiguration has two functions. First of all, reconfiguration refers to the ability of the system to redirect power flow to the remaining loads in the event of a component failure, generator loss, or grid infraction. Secondly, it is the ability to direct power delivery in non-emergency conditions to maximize power efficiency and utilization of available transmission and generation. Fault control, on the other hand, is focused on recognizing and isolating short circuits. It is a much simpler process that is typically handled with differential relays and circuit breakers. The purpose of fault control is to clear or isolate the short circuit as quickly as possible, and this effort is only directed at the short circuit. However, if the grid is represented with equivalent impedances, as will be discussed later, both fault control and reconfiguration can be accomplished.

The electric power system allows for reconfigurability. Faults can be detected quickly, and the system can be configured in order to isolate the fault. Instantaneous response to system damage prevents it from propagating, allowing as many loads as possible to function. Reconfiguration also allows power to be quickly diverted to high power applications for very small time frames, which is vital for next generation, high-power weapons. Furthermore, the system can be reconfigured in non-emergency situations in order to optimize power consumption. The optimization can be directed toward overall efficiency, power to the

loads, or power loss, and a combination of the same. Reconfiguration can also be performed in order to satisfy system constraints or criteria, such as desired load consumption or current ratings.

7.7.1.2. Modeling of the Power System

Research began by developing a method of using current and voltage measurements to create dynamic series and parallel impedance phasors for detecting faults and determining optimum system configuration in a meshed power system. This allows the state of the power system to be monitored even through transients, and allows the system to continuously optimize its configuration. The use of phasor measurements has been demonstrated as a successful method in the development of a wide area measurement/monitoring system (WAMS) in Chinese power systems. In these large-scale power systems that span wide geographic distances, communication delay is one of the key issues, but on a ship where all measurements are taken in close proximity, this is less of a problem.

The mesh architecture of the naval electric ship can be modeled as an $n \times n$ grid, as seen in Figure 5-1. With this layout, loads share power produced by the generators. The multiple loads and trunk lines can be represented as T branches, with the load represented by an impedance connected to ground, and resistive line losses as two impedances in series [lxvi, lxvii].

The impedances of the branch lines and loads can be determined through the measurement of voltage and current by sensors throughout the grid. For the T branch shown in Figure 5-2, at any point in time, Z_s

and Z_p can be calculated with the formulas $Z_{smn} = \frac{2(V_m - V_n)}{(I_m - I_n)}$, $Z_{pmn} = \frac{(V_n I_m - V_m I_n)}{(I_m^2 - I_n^2)}$, in which m and

n represent the two nodes surrounding the “T” branch, and V and I indicate voltages and currents, respectively [lxvi]. These parameters are dynamic, as load demands can vary at any time. Thus, measurements must be taken frequently to accurately model the current state of the power system.

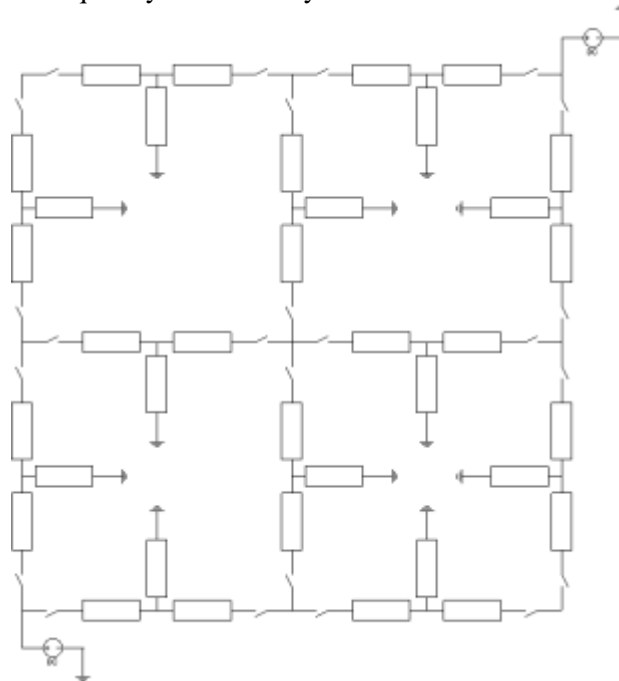


Figure 5-1: Circuit model of naval ship power system.

Switches are placed at every T branch, next to the branch resistors. These switches represent breakers that are used to respond to a fault or to optimize the power consumption of the circuit. In the event of a ground fault occurring at one of the loads, the switches open to isolate the fault. The switches can also be used to control the power characteristics of the system, such as the power delivered to the loads.

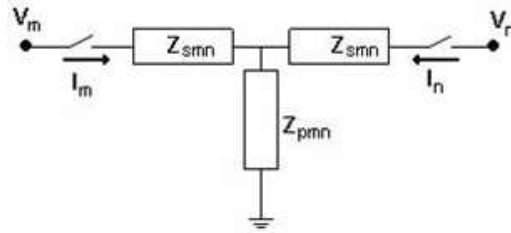


Figure 5-2: T branch modeling line losses and loads.

Because generators are assumed to be ideal voltages, and nominal line and load impedances are considered model parameters, the only dynamic inputs to the physical system are the desired switch vector, $\bar{x}(t)$, and the dynamic multiplication factor that varies the nature of the loads, $\bar{l}f(t)$. In this thesis, $\bar{l}f(t)$ will be considered a disturbance and $\bar{x}(t)$ the means of controlling the system. Outputs from the system are the actual switch vector, $\bar{x}_{act}(t)$, the vector of measured voltages, $\bar{V}(t)$, and the vector of measured currents, $\bar{I}(t)$. The goal of automatic reconfiguration will be to use these system outputs to determine the best desired input switch position signal, $\bar{x}(t)$, so that the SPS operates in a safe and efficient manner. The term “safe” refers to keeping the system within defined operating constraints and “efficient” refers to operating so that a predefined performance index is maximized. Figure 5-3 shows a graphical illustration of how this is accomplished and how the three reconfiguration stages interact with the SPS physical model.

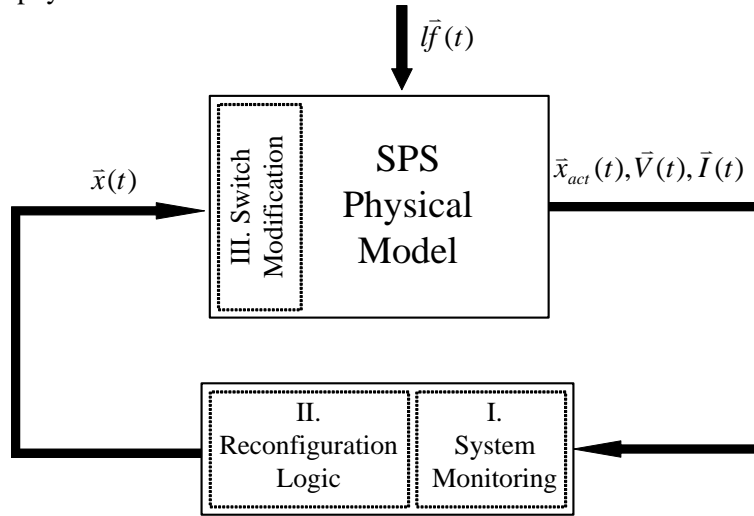


Figure 5-3: Simplified block diagram of power system reconfiguration model.

7.7.2. Mathematical Formulation of the Reconfiguration Problem

In order to proceed, we must decide what defines an “optimal state.” The problem statement could include objectives, such as minimization of power loss, maximum power delivery to the loads, maximum power delivery to a single load, etc. The optimization index used is the power lost minus the power delivered to the loads, as expressed in (5.1), subject to the constraints in (5.2). Minimize

$$f = \sum i_s^2 Z_s - \sum i_p^2 Z_p \quad (5.1)$$

subject to

$$I \leq I_{\max}, P_{gen} \leq P_{\max}, P_{load} \geq P_{\min}. \quad (5.2)$$

The function f is a scalar. The first summation term, $\sum i_s^2 Z_s$, represents the power loss in the transmission lines, in which i_s is the current through the series impedance, represented by Z_s . The

second summation, $\sum i_p^2 Z_p$, is the power delivered to the parallel loads, in which i_p is the current delivered to the load, represented by Z_p . The constraints are formulated as vector inequalities. The variable I is composed of the branch currents, and I_{\max} specifies the current limits on each branch. P_{gen} and P_{load} specify the power produced by each generator and the power consumed by each load, respectively, and they are restricted by P_{\max} and P_{\min} . The dimension of each inequality depends on the number of branches, loads, and generators that are under restriction. The independent variable of the reconfiguration problem is the switch state, which is represented by x , a vector of binary integer elements. For each switch x_i , the i^{th} element of x , is given a value of 0 or 1, which indicates a closed or open switch, respectively, as seen in Figure 5-4. Although x does not appear explicitly in the problem statement, the impedances of the system depend on x , and therefore, it determines the current and voltage variables throughout the system. Instead of changing the topology of the circuit for each configuration, a high impedance is used to model an open switch, and zero impedance is used to represent a closed switch. The impedance of a switch i is modeled by the function $Z(x_i) = 10^6 x_i$. The branch impedances can be expressed as $Z_{si}(x_i) = Z_{s0i} + Z(x_i)$.



Figure 5-4: Binary representation of switch state.

Inequality constraints are typically more difficult to implement than equality constraints in an optimization procedure. However, these inequalities can be transformed to an equality constraint using the max function, which simply returns the largest input argument. The inequality $I_s \leq I_{\max}$ can be transformed into an equality constraint $g(x) = 0$, in which $g(x) = \max(0, I_s - I_{\max})$, which returns a 0 whenever the inequality is satisfied. The inequalities define the constraints for the problem. For many systems, the current cannot exceed a certain rating placed on the lines. We also want to ensure that the system is not demanding more power than the generators can provide, so we may need to implement the second inequality. The third inequality ensures that each load receives a sufficient amount of power. The early work for the ESRDC focused on the steady-state power for a given configuration. Consequently, we are only concerned about the best configuration, not the manner in which it is achieved. When transient behavior is taken into account, the optimal set of switching actions to obtain the desired configuration, i.e., the order in which the switches should be toggled, is another optimization problem within itself, and this particular problem is being addressed by other researchers [lxviii]. Also, solely looking at the steady-state power, each circuit impedance can be treated as truly resistive. This can be done without loss of generality, because each value placed on the resistors can represent whatever is desired, such as apparent power, real power, or reactive power. The direct search procedure is very straightforward and follows the solution procedure illustrated below. For step 1, in which a switch state is assumed, the procedure simply cycles through each switch combination. Checks are performed to ensure that certain switch combinations do not take place. For instance, if switch 1 and switch 2 surround a certain load, any configuration in which both switches are open should be skipped, so the program would immediately move to the next configuration if the product $x_1 x_2 = 1$.

7.7.3. Solution Procedure

- 1) Assume a switch state x and check state against undesirable combinations. If switch state is invalid, move to new switch state. Otherwise, move to step 2.

- 2) Solve for necessary system variables.
- 3) Calculate optimization index f . If f is best solution, update solution and move to step 3. Otherwise, return to step 1.
- 4) Check for constraint violations.

Return to step 1, unless all states have been searched.

Step 1. The procedure cycles through each switch combination. The direct search can be sped up substantially by avoiding certain switch combinations that are known to isolate loads. It is not desirable to program for every bad switch combination, so only those combinations occurring most often and least damaging to the performance index are chosen. If an invalid switch combination is encountered, the direct search immediately moves to the next combination.

Step 2. Once a switch state is selected, the impedances and currents of each branch are calculated.

Step 3. The performance index $f = \sum i_s^2 Z_s - \sum i_p^2 Z_p$ is calculated. If the solution for the current iterate is the best so far, the solution is updated. If the solution is not, the procedure immediately moves to the next switch state.

Step 4. A check is performed to ensure that all constraints are satisfied, including load isolation. Since Step 1 does not avoid every infeasible switch combination, a check can be performed to ensure that every load receives some power.

Since every feasible switch combination is evaluated, the direct search procedure is completely accurate. However, the exhaustiveness of the search also serves as a disadvantage. For a problem of N switches, there are 2^N combinations to evaluate, without considering bad switch combinations. The x domain quadruples for each switch pair added to the problem, so the computational time will grow rapidly with problem size. The overhead on computation motivates the search for a faster method. The advantage of the three other methods is that, although they are not completely accurate, they can possibly obtain a good solution without searching every switch combination.

7.7.4. Investigation of Optimization Methods

Using the above model, we explored four different optimization methods and how well they work for the network reconfiguration problem. The goal was to find a method that is fast and provides an accurate solution; that is, one that finds the global optima or another solution close in value. Also, it is desirable to have a method that is simple and is not subject to multiple parameters.

The most basic method is the direct search, or brute force method; this procedure simply searches through every feasible switch combination and reports the best solution. The second method studied was the genetic algorithm, which is a stochastic method that simulates the processes of genetics and natural selection in order to find the “fittest” solution. The procedure maintains a population of x values, termed “chromosomes” in this procedure. These chromosomes mate in pairs to send their genetic information to a new generation, and those that are most fit are the most likely to reproduce. Another stochastic method known as constrained simulated annealing was studied, which derives inspiration from the cooling of a molten solid. The search along the x domain is done in the same manner that a molecule moves around a cooling solid. At the beginning the procedure “bounces around”, searching a wide range of x values and changing position rapidly; but as the method progresses, the search “settles down” to a smaller region of x . The last method studied was the binary integer programming with branch and bound. This procedure optimizes a linearized form of the optimization index and returns the global optima while only evaluating a subset of the switch configurations, rejecting subsets of configurations that are known to produce a non-optimal value.

7.7.5. Dynamic Modeling

In the next body of work, the steady state model of a SPS was modified and control elements were incorporated into the dynamic model to simulate an automatic reconfigurable power system that responds to changing load conditions. The use of equivalent impedances and centralized reconfiguration logic was

implemented on a dynamic system whereas past studies have relied on steady state models. One advantage of this scheme is that the reconfiguration algorithm is characterized by real time current and voltage data throughout the system that infers the state of the system in recommending the next optimal state. This dynamic simulation demonstrates operating a ship in the most efficient manner possible (defined by an objective function) while protecting the system from generator and line overloads. In order to take the more cautious approach to reconfiguration, an additional Simulink® block is needed between the steady state reconfiguration block and the SPS physical model. Whenever an optimal steady state switch solution differs from the previous solution, the active switches are flagged and an algorithm determines each of the possible sequences involving these switches that will bring the system to the new target. In order for a switch sequence to be acceptable, node voltage equations are solved for each of the intermediate configurations and each solution must satisfy user specified constraints. Since these constraints deal with configurations of the system that are very short in duration, the transient constraints may be different from the constraints used in the steady-state optimization search. This algorithm is included in the Simulink® model as an S-Function with inputs \bar{x}_{act} , \bar{x}_{best} and the modified current and power constraints (i_{srate} , i_{pmin} , and p_{max}). The output of the S-Function is a vector of switch numbers that indicates the order that each switch change should be activated.

Once an acceptable switching sequence is determined, switches are activated one at a time until the optimal target switch vector is reached. If the optimal switch vector changes during the transition, a new sequence is calculated based on the existing switch position. Stateflow is used to simulate this process, and the corresponding chart is shown in Figure 5-6. This chart illustrates the interaction between the transition-based reconfiguration logic and the Simulink® environment. Table 5-1 defines the connected input and output signals.

There are 11 events defined within the Stateflow chart. The first 10 correspond to any rising or falling change in the individual components of the instantaneous switch position vector and the 11th corresponds to any rising or falling of the input clock pulse. The clock pulse is defined such that each pulse corresponds to a new calculation of the input, \bar{x}_{best} . In the case that a delay is introduced to \bar{x}_{best} , the clock signal is delayed as well.

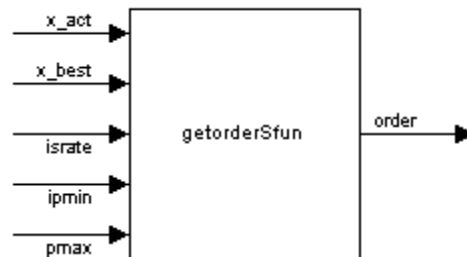


Figure 5-5: Switching order S-function.

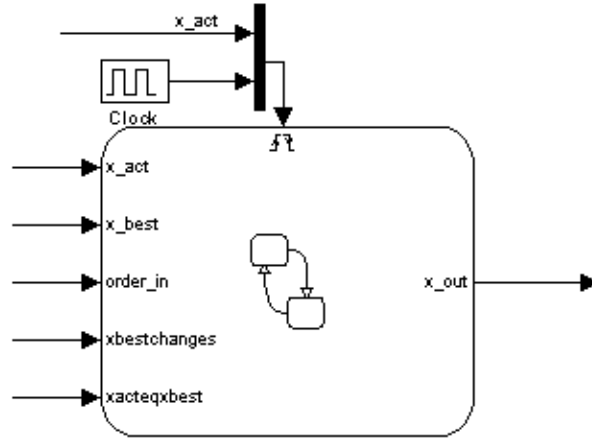


Figure 5-6: Stateflow chart for switch transition logic.

Table 5-1: Input and output signals for switch transition logic.

Name	Input / Output	Description
x_act	Input	Actual instantaneous switch vector
x_best	Input	Optimal steady-state switch vector
order_in	Input	Switching sequence vector
xbestchanges	Input	True if current optimal switch vector is different from the previous
xacteqxbest	Input	True if instantaneous switch vector is equal to the optimal
x_out	Output	Output switch vector sent to SPS Model

7.7.6. Energy Storage

Electric ships using gas turbines for primary power experience considerable fuel inefficiency when the turbines operate away from their optimum design points. Fluctuating power demand inherently leads to changes in the gas turbine operating point. Running turbines at inefficient operating points can be mitigated to some extent by proper power scheduling of turbines of dissimilar size. However, secondary constraints often prohibit this type of scheduling. A prime example occurs when the ship is idling at low power. Because the Navy places a high priority on outage avoidance, typically two turbines will operate in parallel. For fuel economy, it is highly desirable to operate one turbine near maximum capacity, and employ energy storage to ride through an outage of that turbine long enough to bring up another turbine. A more challenging problem is to employ energy storage to perform continuous load leveling. A turbine is made to operate at its optimum power level; perturbations in demand either take power from the energy storage or put it into the energy storage. The first problem is called the redundant turbine problem and the second, the load leveling problem.

A reconfigurable, dynamic, SPS model was created and simulated in the MATLAB/Simulink[®] environment. In addition, a basic model of the flywheel subsystem was developed to be compatible with the modeled grid. The design was based in part on flywheels previously tested at CEM for the Advanced Locomotive Propulsion System (ALPS). Because improved energy efficiency is the ultimate objective, the flywheel subsystem model was simplified, as shown in Figure 5-7. Figure 5-8 shows the Simulink[®] representation of this model.

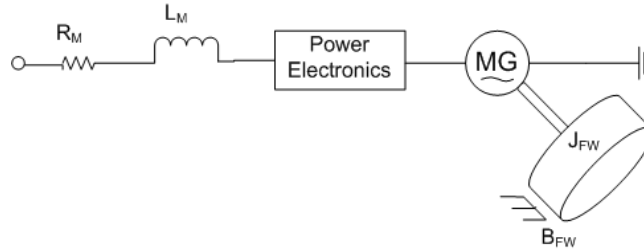


Figure 5-7: Simplified view of flywheel energy storage module.

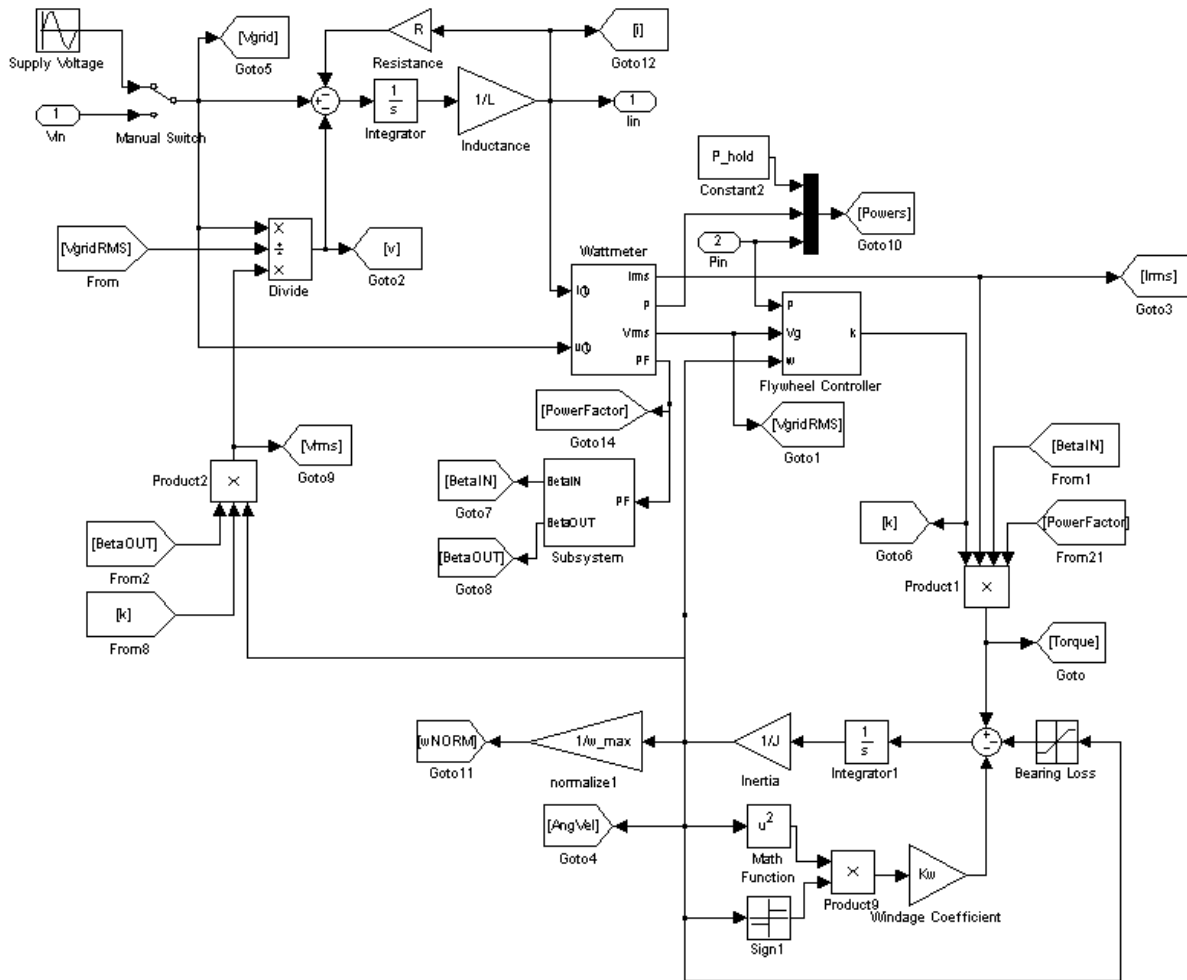


Figure 5-8: Simulink[®] model of flywheel energy storage module.

As modeled, the system can be described using two states – the flux linkage of the series inductance and the angular momentum of the flywheel, λ and h , respectively. These states are determined by equations

$$\dot{\lambda} = V_G - \frac{R}{L} \lambda - V_f = L \frac{di}{dt}, \text{ and} \quad (5.3)$$

$$\dot{h} = T_f - T_B - \frac{k_W}{J^2} h^2 = J \frac{d\omega}{dt}. \quad (5.4)$$

Equation (5.3) corresponds with the upper-left electrical portion of the block diagram, while (5.4) represents the bottom right mechanical portion. Because the flywheel is driven by a balanced, three-phase motor, only real (electrical) power is converted to mechanical torque. A subsystem representing a

watt meter uses four evenly-spaced readings over a quarter-cycle of 60 Hz voltage and current to estimate the current I_{rms} , grid voltage $V_{g,rms}$, and real power P :

$$V = A \cos(\omega t) + B \sin(\omega t), \quad (5.5)$$

$$V = \begin{bmatrix} V(t_1) \\ V(t_2) \\ V(t_3) \\ V(t_4) \end{bmatrix} = \begin{bmatrix} \cos(\omega t_1) & \sin(\omega t_1) \\ \cos(\omega t_2) & \sin(\omega t_2) \\ \cos(\omega t_3) & \sin(\omega t_3) \\ \cos(\omega t_4) & \sin(\omega t_4) \end{bmatrix} \begin{bmatrix} A \\ B \end{bmatrix} = D \begin{bmatrix} A \\ B \end{bmatrix}, \quad (5.6)$$

$$V = C \cos \omega t - \phi_V, \quad C = \sqrt{A^2 + B^2}, \quad \phi_V = \arctan\left(\frac{B}{A}\right), \quad (5.7)$$

$$P_{avg} = \frac{1}{2} C_V I_V \cos(\phi_V - \phi_I). \quad (5.8)$$

Note that the dc-dc link between the motor/generator and the grid allows the back EMF, V_f , to be treated as a voltage-controlled voltage source, such that its phase matches that of the grid voltage. This means the flywheel power factor, current, and back EMF magnitude are determined as

$$PF = \frac{R}{|Z|}, \quad (5.9)$$

$$I_{rms} = \frac{P_{desired}}{V_{g,RMS} * PF}, \quad (5.10)$$

$$V_{f,rms} = V_{g,RMS} - |Z| * I_{rms}. \quad (5.11)$$

The resultant torque acting on the flywheel T_f is calculated using conservation of energy with a fixed input/output efficiency of β . The formula depends on the flywheel angular velocity and the direction of power flow.

$$T = \frac{\beta * I_{rms} * PF * (R * V_{g,RMS}^2 - P * Z^2) P_{desired}}{\omega V_{g,RMS} R}, \quad \text{Charging (P>0)}, \quad (5.12)$$

$$T = \frac{I_{rms} * PF * (R * V_{g,RMS}^2 - P * Z^2) P_{desired}}{\beta * \omega V_{g,RMS} R}, \quad \text{Discharging (P<0)}, \quad (5.13)$$

$$T_{hold} Z^2 = \beta * R * k * (V_{g,RMS} - k\omega), \quad \text{Holding (P>0, } \omega > 0.99 * \omega_{Max}), \quad (5.14)$$

$$T = k * I_{RMS}. \quad (5.15)$$

Where T_{hold} is the torque required to offset windage and bearing losses at the rated speed. A simple test was designed to ensure the control algorithm operates properly in all three modes, and the results are shown in Figure 5-9.

During the first portion of the test, the flywheel needs to receive excess power from the grid. Despite starting at 0 W, the actual power quickly reaches the desired level. (Note that initial values were not properly selected, increasing the overshoot.) Because its initial angular velocity was near the rated value, the flywheel now gradually reduces the power to avoid exceeding that level. Finally, when current is extracted from the flywheel, the actual power quickly settles on the desired value with little visible overshoot.

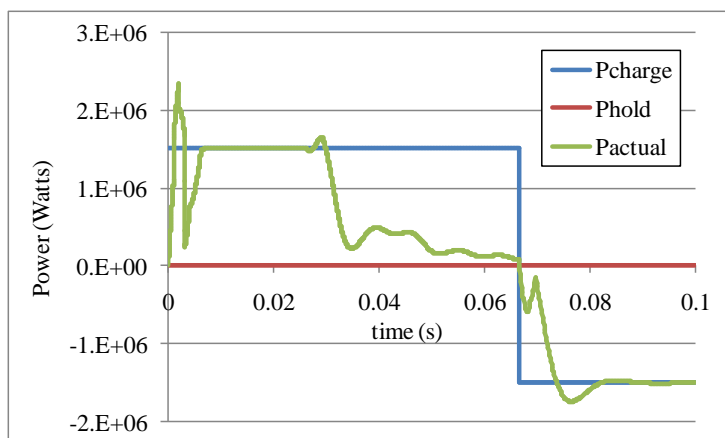


Figure 5-9: Flywheel power: actual vs. desired.

In addition to operation of the flywheel, certain design criteria must be addressed when considering its interaction with the grid reconfiguration and optimization. The simplified grid used for our modeling purposes, as shown in Figure 5-10, contains two turbine-generators and five generic loads, each of which could represent large individual devices or additional branches of smaller ones.

Several factors must be considered in deciding where to connect available energy storage modules. How can we ensure critical loads will receive necessary power if a generator trips? Will the current ratings of certain transmission lines restrict operation of these modules? Should the modules be treated just like other loads when running reconfiguration algorithms? Should the flywheel be treated differently based on its operation mode? Is it wise to distribute the modules throughout the grid or to concentrate them at one grid-tie location? Tradeoffs like these must be properly explored when evaluating the advantages and disadvantages of bulk energy storage on the AES.

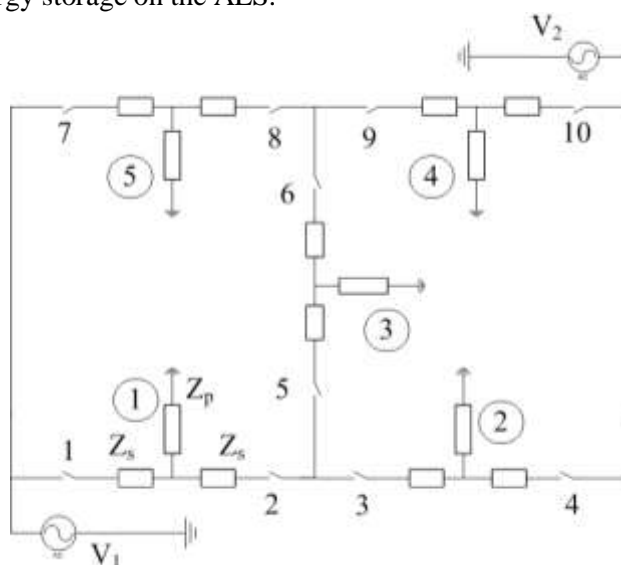


Figure 5-10: SPS grid layout.

7.7.7. Conclusions

7.7.7.1. Speed of Calculation

The problem of reconfiguration for the electric ship was investigated. When considering reconfiguration, it is important to find a numerical method that can find an effective switch state in a short amount of time, so that a naval electric ship can respond quickly to changing demands. In Chapter Two, four methods were investigated, in which the theoretical basis and general procedures were discussed. How the optimization routines could be applied to the reconfigurable network was also examined. In Chapter 3,

each method was applied to the reconfiguration problem for three case studies and the results were summarized.

Choosing the best optimization method is not an easy task, as it depends on the problems and the criteria that must be met. For a lightly constrained problem as seen in Case 1, the binary integer procedure is the best method for lower accuracy requirements due to its speed, but its performance is surpassed by CSA and the genetic algorithm for higher accuracy standards. For a tightly constrained problem, CSA performs the best overall, although the genetic algorithm is the fastest for a percentage error less than 1%. For a medium constrained problem, CSA or the BI procedure perform the best across every accuracy standard.

Concerning the overall performance, the genetic algorithm is a fast and accurate method that works well across each of the cases, but it is difficult to design. The binary integer procedure works very quickly and is the simplest procedure to implement, but it is limited in terms of accuracy for both lightly and heavily constrained problems. The constrained simulated annealing method worked well for each of the case studies in terms of both speed and accuracy, although it is surpassed by the genetic algorithm for the most stringent accuracy requirements. For CSA, the parameter interaction with the procedure is easier to understand and is more consistent through each case study.

It is difficult to make a recommendation for a procedure that works across every scenario encountered in the reconfiguration problem. It appears that the same trends occur for each case study, however. For problems in which the percentage error must be 2% or less, the genetic algorithm is recommended due to its speed. For less severe requirements, however, the constrained simulated annealing procedure is recommended, due to its small computational demands and setup time. If a recommendation must be made on a single method, the constrained simulated annealing method performs well across each of the cases. For most standards of accuracy, it performs fairly quickly, and it can also be easily designed to be as fast or as accurate as the needs of the problem.

7.7.7.2. Dynamic Modeling

Several conclusions are now given about its operation. First, the method of monitoring the SPS using equivalent impedances is a useful method for monitoring loads, but it does have some limitations. Mainly, this method is limited to monitoring the system during equilibrium or quasi-equilibrium conditions, due to the inherent assumption behind the equivalent impedance estimation that frequency is constant. Any dynamics occurring at faster frequencies, such as those induced by switching cause erroneous readings.

Secondly, filtering equivalent impedances requires ignoring values that are deemed erroneous, and this can limit the speed at which the system can be monitored. After each transient event, such as a switching action or an abrupt load change, a minimum of two sampling periods are needed to obtain valid readings again. In the case that switching occurs frequently in short time periods and fast transients dominate the system, it can be difficult for an accurate picture of the system status to be formulated using the equivalent impedance approach.

By introducing noise into voltage and current measurements, the responsiveness to changing optimal switch configurations can be limited greatly. Noise has undesirable effects on the calculation of Z_s , which is vital to the calculation of line currents and generator power in the optimization routine; large fluctuations caused by noise can indicate false line or generator overloads. Since Z_s is not as dynamic as Z_p , allowable Z_s fluctuation should typically be set much smaller than Z_p . This requires a good estimate of the initial condition of Z_s because a small f_z may not allow Z_s values to update very often.

The test cases studied demonstrated that care must be taken in developing transition-based reconfiguration logic. Basing switching decisions only on the steady-state optimal switch solution and allowing current and voltage zeros alone to determine switching order is not acceptable because this can cause loads or generators to be temporarily disconnected from the rest of the system. By using an

algorithm that finds valid switch sequences, this can be prevented, but increased safety comes at the cost of speed.

After considering all the factors that limit the speed and accuracy of reconfiguration, it is important to realize that there will be a limit to the type of SPS dynamics that a centralized control system such as this can effectively respond to. Step changes in loads are easily detectable, but gradual changes are more difficult to detect. Allowable fluctuations in impedance must be chosen in order to distinguish between transients, noise, and actual load changes. Load change dynamics with time constants on the order of six to seven cycles are easily detectable in the case of a generator overload scenario that involves many changes in switch configurations; faster load changes will be detectable when fewer switch transitions are involved.

Since the SPS has been modified to include energy storage, it may now be used to investigate factors affecting distribution of energy storage modules in the reconfigurable grid. In order to do this, the reconfigurable optimization approach will be modified to account for (and take advantage of) energy storage.

The work outlined in this report can be studied in detail in the theses published by the students who conducted this research:

- Chance D. Meek, "Investigation of optimization methods used for reconfiguration of the naval electric ship power system," Master's Thesis, The University of Texas at Austin, December 2004.
- J.A. Park, "Dynamic Modeling and analysis of an automatic reconfigurable shipboard power system," Master's Thesis, The University of Texas at Austin, May 2006.

Agent Based Control of DC Distribution Systems

The use of agents in association with measurement systems has been theorized and reported in literature in recent years. Many other pieces of work present insight and the details of specific applications, for example, where the agents are applied to the monitoring of distributed and complex environments, one of the most beneficial fields of the application of agents in measurement. For the purpose of monitoring, another application of agents can be found in state estimation. Agents in power applications, though, have been utilized for various functions, not limited to the measurements. For what concerns the application of agents to diagnostics, a very detailed description of a multi agent system for the condition monitoring of transformers, the more general problem of condition monitoring for power systems is addressed exploiting the agent technology. A direct consequence of the use of agents for power system monitoring is its use for protection and automation of substations. On the other hand, multi-agent systems have been used for control purpose. In particular the application to micro-grid operation and the problem of power system restoration is addressed using an agent system.

In this work the problem of monitoring and control of the power electronic power system on board ships is addressed as a whole. The agent structure proposed here is capable of interfacing with other environments to support data acquisition (LabVIEW), load control (Simulink DSpace) and simulation-aided decision making (Virtual Test Bed). In previous works the development of agent interfaces oriented to simulation environment. The integrated operation of the multi-agent system for monitoring and control has been developed, where the agent capabilities are not fully exploited, though; in that application in fact, the monitoring, control and diagnostic agents do not actively exchange information and commands but rather statically perform the same operation all the time. A measurement application is presented, that builds ActiveX technology on the top of socket programming to enable users to easily configure the

agents of a distributed system is introduced. As a result, users in different network locations may request services to external applications to accomplish complex tasks such as diagnosis or transient simulation for the analysis of “what-if” scenarios.

In this work the agents have been all developed in Java Agent Development framework (JADE) and interfaces to monitoring, control and simulation environments have been implemented. These agents are active and pro-active.

Three main factors, in our view, can lead to a significant progress in the monitoring and control of complex power systems with limited power generation capability. The first factor is flexible power distribution. Competing loads fed by power electronics systems can be regulated, based on the state of the system and power availability. As a consequence though, reconfiguration becomes an even more complex problem than what we can refer to as hard reconfiguration, consisting of breakers status management or load shedding. Instead, the virtually infinite degrees of freedom of the power demand of controlled loads and energy routing converters, allow for a soft approach to reconfiguration, under either normal or faulty operating conditions. With this approach, hard reconfiguration can be seen as a particular case of soft reconfiguration. The second factor is the dynamic knowledge of “what-if” scenarios. This is made possible by simulation, based on a reliable model of the system. The third and major factor is the flexibility of the data acquisition system. On one hand it must be possible to feed the acquired data to the simulation system so that the simulation as consistent as possible with the current state of the system. On the other hand the data acquisition system should be ready to change its own configuration and operating parameters, based on external requirements. These requirements may originate, for example, from the need of diagnostic tests during normal operation, or can originate from the need for a reliability check of the system model.

In this work the experimental testbed is a reduced complexity power electronic system. In particular the structure has been chosen to exemplify one section of a DC zonal system in a hybrid AC-DC power distribution system. The US Navy is considering a DC zonal structure the power distribution of the future all-electric ships. The DC zones are areas of the electric distribution system, fed through a DC bus by a large converter. An AC system supplies the DC zones through large AC/DC converters and feeds directly only the propulsion drives.. All the other loads are connected to the DC bus of their zone. Since most loads are controlled and are fed through a converter anyway, the DC zonal system is a suitable supply..

In this work we assume that the DC zone can provide a limited power, furthermore we assume that the DC bus voltage is maintained at rated level, therefore, the power limit is set in terms of maximum current limit. The three loads fed by the DC bus are: one induction motor drive and two regulated RL networks. A scheme of the system is shown in Figure 23. A summary of the main hardware components is reported in

Table 3: main hardware components.

The loads are controlled with a dSpace board dS1103. The data acquisition system is a NI PXI. The load current sensors are LEM built in the inverter boards.

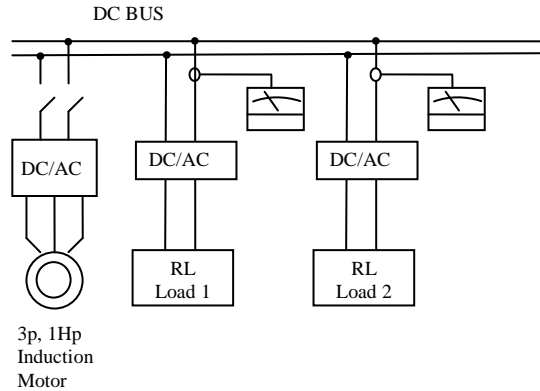


Figure 23: scheme of the power electronic power system

Table 3: main hardware components

Load 1 and International	Switching frequency	20 kHz
Load 2 DC/AC Rectifier	IRAMS10UP60A	
Motor	Baldor ZDM3581T	750W, 4 poles, 230/460V
DC bus power supply	Xantrex XRF	60V, 20A

The multi-agent system structure

A multi-agent system architecture has been designed to realize the integration between the data acquisition, the control and the simulation sections. In particular the following categories of agents have been implemented:

data-acquisition agents: an agent in this category provides measurement capability to the multi-agent-system. It provides all the features of a smart sensor and a high capability of reconfiguration. In the experimental activity proposed here, upon request, it acquires load current, broadcasts a buffer of current values to the peer agent that requested the service, reconfigures the data acquisition based on the request of a peer agent. A PXI-LabVIEW platform is chosen for data acquisition.

simulation agent: it provides the interface to a simulation engine to be used for dynamic analysis of “what-if” scenarios. In the experimental activity proposed here, it provides the evolution in time of the bus current during the transient of a load insertion.. Parameters of the simulation can be changed in run-time upon request of another agent. The Virtual Test Bed (VTB) is chosen as simulation environment.

load agent: this agent is the interface between the monitoring structure and the local control. It is capable of controlling power delivery to a local load, subject to availability and conditions determined by the monitoring system. In the experimental activity proposed here a dSpace platform is chosen to implement the control action.

Diagnostic agent: this agent determines whether or not a desired load change can be implemented; this decision is based on the system limitations, the current operating state and the dynamic forecast of the simulated reconfigured system.

Each agent interacts with the environment that supports its capabilities in order to fulfill the needs of the system. For example, the simulation agent controls the VTB simulation platform and is capable of understanding when simulated data are needed.

The agents have been implemented in JADE and are designed to interface the other software environments through Component Object Model (COM) technology. The creation of an interface between JADE and COM components has been one of the significant challenges of this work. Furthermore, it is desirable that the agents developed in JADE, communicate in Foundation of Intelligent Physical Agents (FIPA). Various options were considered while selecting an appropriate multi-agent system (MAS) development platform for the case study presented here, so a comparison between MAS development platforms is introduced, before describing the implementation details.

The selection of a MAS development platform depends on the architecture of the system and poses significant challenges in the case of the integrated system assumed here as a case study. The choice depends on the provision of capabilities for the agents to interact with different software besides the easiness of building the agents. The developed MAS, monitors and controls an electrical power system through multiple interfaces between the agents and other software, in particular VTB, Matlab/Simulink and LabVIEW. The development of these interfaces has a huge impact on the choice of the multi-agent development platform.

The following options were considered for the multi-agent development platform:

- Agent development using LabVIEW
- Web Services as Agents
- JADE-Leap over .NET (J#)
- JADE (Java)

We have developed and described a multi-agent system, using LabVIEW as a development platform. Various areas such as the medium of communication, language of communication and the format of the data exchanged between the agents in this platform had to be elaborated. Since LabVIEW is not a conventional agent development platform, a custom language that could be parsed and understood by the agents had to be developed. This language did not adhere to the FIPA defined standards for agent communication language (ACL). This deviation from the ACL standards is as a limiting factor when it comes to compliance between heterogeneous agencies. This limitation is not a factor in this work, in fact these results refer to one single agency that, although comprises agents different in nature, does not interact with other agencies. In particular, these agents look for and understand the FIPA ACL message format that contains a set of one or more message parameters. The selection of the parameters needed for effective communication varies with situation and task. Any message that is not compliant with ACL format might be rejected, generating a “not-understood” message. The compliance with the standards is an enabling factor of inter-agency operation, but still requires the development of a shared ontology. It may also be noted that FIPA allows the inclusion of user defined parameters for ACL. Thus, although it is possible in principle to make LabVIEW agents comply with FIPA ACL standards, this effort would shift the focus from the development of agent based applications to the development of agent development platforms.

One of the primary goals in the development of the agency presented here, is the introduction of the simulation Agent to answer “what-if” scenario questions. To implement this functionality, the interface to the simulation environment has evolved through stages. The initial interfaces were based on a web service front and a COM server wrapper. In both the cases, the VTB simulation platform merely acts as a service provider. This behavior does not support autonomous operations, such as the execution of model validation tasks in case the simulation agent suspects a mismatch between model and actual system. We have thus designed a simulation agent that not only can project VTB as a service provider but also can act as an intelligent entity. This proactive nature characterizes an agent against a web service, Agents developed in JADE, in particular, are equipped with proactive capabilities.

Other desired capabilities of the system, such as data acquisition and instrument control could easily be implemented using the same approach mentioned above, using COM wrappers around legacy systems, for example COM servers for LabVIEW and Matlab. Such approach, though, would miss out altogether the potentiality of proactive behavior. While the option of using Web Services together with agents for some functionalities is in principle still feasible it also requires, for each Web Service, a translator from Agent Communication language (ACL) to a language that Web Services can interpret. Standards for XML format of ACL communication have been specified in.

Finally, the ACL standard allows for auxiliary parts in addition to the content of a message, for example the intended recipients, the sender and the message type. JADE also allows users to develop Ontologies that define the concepts and the language that the agents would use for communication. These ontologies can be derived from higher level ontologies like LISP (LIST Processing) and CYC (enCYClopedia) that are currently being developed as world standards for ontologies.

JADE is a very robust and efficient platform for developing distributed multi-agent systems. It adheres to the FIPA standards and supports the development of large scale multi-agent systems. While JADE does not support the (Belief-Desire-Intention) BDI model, agents could be developed in JadeX to make them more proactive. It may be worthwhile pointing out that the authors refer to the categorization of agents as “intelligent” if they act as intentional systems [40]. The agents defined in agency presented in this research work have information attitudes but do not have pro-attitudes [40]. In [40] the authors define desire and intention as pro-attitudes which may be required to drive the action of the agent and thereby giving it its proactive nature.

With reference to the agent development environment that we have chosen, the need to develop agents that can interact with the different software mentioned above, requires the import of COM components into the Java/JADE environment. The built-in GUI support for JADE enables faster development of agents and their debugging. It provides a visual representation of the message exchange between the generated agents.

JADE-Leap allows users to port the JADE environment to the .NET platform. Using JADELeap allows users to run JADE agents in the .Net platform making it easier to instantiate ActiveX components. However, inadequate documentation of JADE over .Net is a major obstacle in the development of the multi-agent system. Additionally, the properties file for the multi-agent system has to be changed to accommodate new agents and the .Net version of JADE-

Leap does not support a GUI. This analysis was effective and useful to converge on a decision to use JADE to develop the MAS.

SOFTWARE INTERFACES FOR AGENTS

Every agent in the network has been allotted a specific task that helps in the governing of the physical system. These tasks include data acquisition, data storage and parsing, running simulations, controlling loads and performing diagnostics. The common ground for each of these different tasks is that they require functionalities that are beyond the scope of the agent development platform. The solution is to perform co-simulation and link software together to build the applications using COM programming.

We have described a prototype of a multi-agent network that has been developed in LabVIEW considering the convenience to develop COM interfaces for the agents with different external software that assist them to complete their specific tasks. However, in the quest of doing so, the developed agency does not show compliance with the FIPA defined IEEE industrial standards for agent development, communication and negotiation. This shortcoming has been overcome in this evolution of our work. However, there is a significant challenge in importing COM components on the JADE platform. The use of JACOB dlls allows the agents to call COM Automation components from Java. It makes use of JNI (Java Native Interface) to make native calls into COM. These libraries were used to interface JADE with LabVIEW and VTB. In particular, notice that this interfacing technique is more flexible and easier than those provided by National Instruments.

In the multi-agent system defined here, every agent, with the exception of the diagnostic agent, relies on a COM interface with some application server to complete its tasks. Any action taken by the user, either to add or to drop a load is performed through agents that are associated with the loads. The loads are controlled through a complex interface where LabVIEW is used to execute commands on Matlab/Simulink/DSPACE through a COM interface. LabVIEW in turn is also controlled by the agents through another COM interface with JADE. A direct interface between JADE and DSPACE has subsequently been implemented [41]. This direct interface reduces the overheads required to invoke DSPACE through LabVIEW while providing the same results as the previous interface. Similarly, the measurement agents for each load use LabVIEW Real Time to get the instantaneous value of the current drawn by the loads. The agents load and run VIs on the Real-Time target machine and report the values of the current to the simulation agent. The simulation agent is a special case where the COM server, providing the data from the system simulation from VTB, has been developed in-house at the University of South Carolina. This has given the users complete control over the format of execution of the simulation as well as the format of the extraction of data at any times. For example, functionalities like changing the simulation time step and also varying the duration of the simulation dynamically before each data extraction are under development.

Thus the multi-agent system under consideration here is a combination of multiple software like VTB, Matlab/Simulink/DSPACE, LabVIEW and most important the agent development platform JADE.

COMMUNICATION AND NEGOTIATION BETWEEN AGENTS

For purpose of test and validation of the proposed approach a case study has been considered. The operational steps of this scenario are summarized in Figure 24. The operation details are herein described.

The multi-agent system supports a variety of agents working in conjunction to monitor and control the electrical system. The agent performing the simulation of the system in VTB gets initiated when the measurement agents report the instantaneous current being absorbed by each load from the power supply. The measurement agents kick in when the user tries to add a new load to the bus. The whole process is started by an agent that monitors the system for a user defined change in the load settings. As soon as a user adds an extra load, the agent associated with that load simultaneously reports the change to the simulation agent and also requests the measurement agents associated with each load to send the reading of the actual current being absorbed by the corresponding loads to the simulation agent. The simulation agent makes use of this data, status, user's command and measurements, to start a simulation representing the exact physical system under consideration here in VTB.

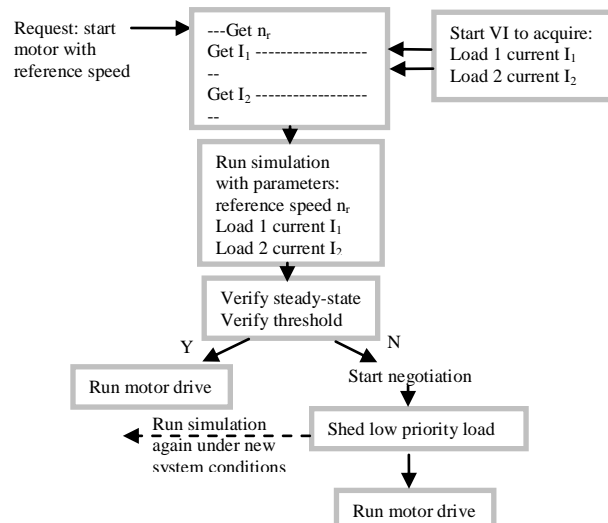


Figure 24: block scheme of the sequence operations

The simulation agent provides the diagnostic agent with the data from the simulation. There are two ways of data extraction from the VTB simulation. A random extraction of data while the simulation runs in continuous mode and a systematic extraction of data at each time step while the simulation is run in stepping mode. The variable of interest here is the total current that is being drawn by the combination of all the loads that were already connected to the power supply together with the load the user intends as new. The current supply limit of the power supply is a predetermined value and is used as a mark to compare the simulated total current being drawn by the loads. The diagnostic agent is capable of stepping the simulation after receiving data at each time step and analyses the data to determine if steady state has been reached in case the current limit is not exceeded. In such a case, the agent controlling the loads is given an approval to add the new load.

In the event that the current readings from the simulation exceed the current limit of the power supply, the diagnostic agent initiates a negotiation between the load agents. All the load agents (three in this case) receive an initiate command from the diagnostic agent. The load agents

exchange information about their current priority levels and the one with the least priority drops the load associated with it.

Experimental results

The experimental results that are presented in this paragraph demonstrate the capability of the agent system to manage load reconfiguration and reconfigure data acquisition.

Assuming the system is operating in normal steady state conditions, suppose the activation of only one load is entered at the control agent level. In the experimental setup presented here, the load to be activated is an induction motor drive, with set reference speed equal to 1500 rpm. The start command is not immediately implemented, since, the system has limited power capabilities and, due to current loading condition, the increased power demand may not be accommodated without exceeding limit power.

The load activation request is dispatched to the Load Agents and before it can be accepted and actuated, a “what-if” scenario corresponding to the load change is analyzed in simulation, with the purpose of verifying if power limit will or will not be exceeded with the new load insertion.

The simulation agent needs collaboration from the peer agents to provide the necessary outcome, in fact it needs data of the current loading state and the entity of the load change request, in the form of motor drive speed reference. For this purpose the data acquisition and control agents are activated. The data acquisition agent manages the data acquisition system to provide the current values of the active loads. For this purpose, the data acquisition agent interacts with LabVIEW Real Time, through a custom developed interface: the agent runs the data acquisition VIs to acquire the current and it has the data sent out to the simulation agent. The control agent provides the speed reference as was initially entered by the user.

The simulation agent is designed to interface with the Virtual Test Bed (VTB), the simulation environment chosen for this experiment. The simulation agent receives the input from the data acquisition agents and control agents and it is capable of opening the simulation file containing the scheme of the system under observation, changing the system parameters according to the current state and run it.

The simulation of a specific schematic file and the parameter changes are set to get the actual scenario, as it would appear after the activation of the motor drive load. It is important to underline that the simulation agent can work with different simulation schematics in order to provide the same service to different load control units within the same system.

In fact it is important to use schematics that focus on the local detailed representation of the system to obtain a reasonable compromise between accuracy and computational burden. In Figure 25, it is possible to observe the following parts (enclosed in numbered ellipses):

1. model of the control of the drive
2. model of the rest of the system simplified by a simple ideal current source. This assumption makes the simulation more focused on the details of the specific load under analysis taking for the rest of the system a realistic simplified assumption
3. averaged model of the power converter allowing for longer time-step with respect to a switching model and a model of the motor. We are not interested in the details of the waveform while at the main elements of the power flow.

The consistency of the VTB model of the system with the physical system under analysis has been previously validated, as presented. The simulation represents the system scenario in case the load change requested is granted and the motor is started. The most significant variable, for the purpose of this application, is the total current drained from the DC bus. In this experiment, the total load current must not exceed the limit of 1.2A as this is the value that has been set for the power supply that is feeding the dc bus.

More sophisticated criteria can be adopted to define the limits of a given application. While these criteria are being considered, the focus on maximum current chosen in this case study is a meaningful exemplification of limited power capability. The check on the maximum current value is performed by the Diagnostic Agent. This agent receives simulated data from the Simulation Agent, verifies that steady state has been reached during the simulation and verifies whether the maximum allowable current has been exceeded.

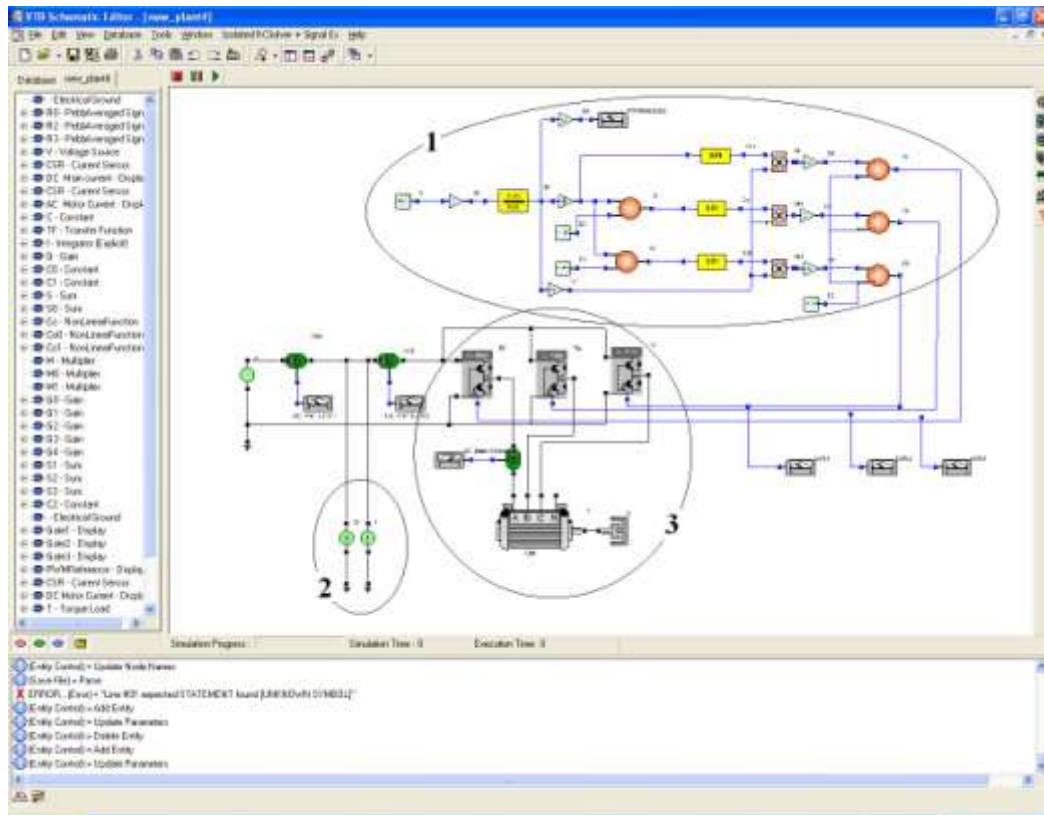


Figure 25: the VTB schematic used for “what if” scenario analysis

In the first scenario that has been considered, there is virtually no load fed by the DC bus, so we expect to be able to run the motor drive without any other load to be shut off.

The simulation is fed with the current values of the loads other than the motor. These currents are virtually zero. The simulation is set to run with zero current from the two loads and 1500 rpm reference speed for the motor. Simulated DC bus current obtained in these conditions is shown in Figure 26. In this case the maximum current is not exceeded in the forecast, thus the maximum value and limit comparison provides a negative answer and the diagnostic agent broadcasts an approval flag to load change. The control agent at this point implements the load activation with 1500 rpm reference speed. The actuation is performed through the dSpace controller board, that controls all the loads by creating the PWM switching signals. In this

experiment the interface between Matlab/Simulink and JADE was not yet available, therefore the interaction between the Control Agent and the actuator is not direct. This case is particularly interesting to show the survivability of the agent-based de-centralized monitoring and control system. This feature of agent-based system is of great interest in particular for military applications or for any application that must be capable of surviving damage. In fact, if the system is hit and parts of it are destroyed, it is possible that part of the intelligence that controls the system is destroyed with it. In such situation, the ability for a neighboring agent to step-in for the one that is out of service is critical. As in the case described here, the control agent may not have the capability to communicate directly with its actuator. It can anyway do so though another agent that has that capability. In particular, the control agent (in JADE) can not communicate directly with Matlab/Simulink (dSpace), but it can communicate with the monitoring agent (JADE) that can interface LabVIEW, that in turn can interface Matlab/Simulink. (note that a direct interface between JADE and DSpace has been later developed but was not available at the time of these tests [41])

In the second scenario that has been considered, the two RL loads are up and running and each absorbing a current equal to 0.3A. The monitoring agent runs the Vis to acquire these two load currents and sends the value to the simulation. The simulation runs the system schematic with load current 1 and 2 equal to 0.3A and reference motor speed equal to 50Hz.

The resulting simulated DC bus current is shown in Figure 27. In this case the maximum current is exceeded in the forecast, thus the comparison provides a positive answer and the diagnostic agent broadcasts a stop to load change and a start of negotiation aiming to load reconfiguration to accommodate the new power demand.

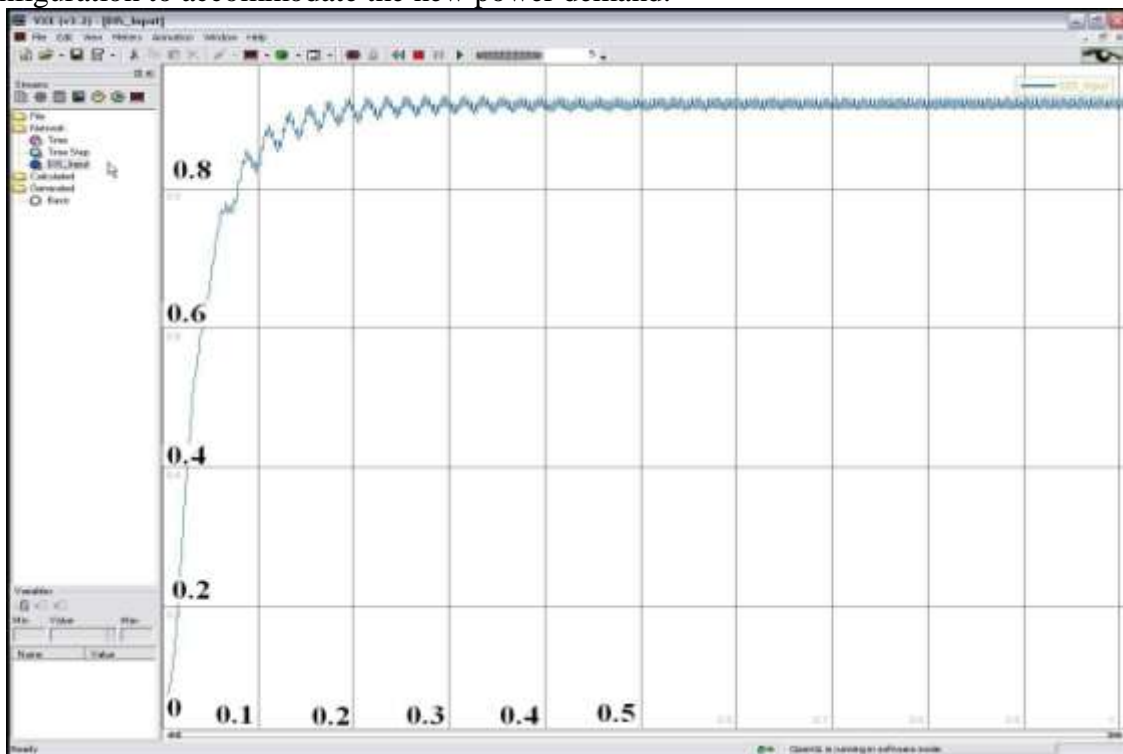


Figure 26: dc bus transient current [A] vs time [s] at motor start-up in simulation; no other load is active at this time

The new configuration is negotiated by the load agents. In this application this negotiation is based on priority levels, under the assumption that each load agent knows its own priority but it is not aware of the presence of other load agents and their own priority levels. Notice that the priority levels are dynamic, they can be reassigned by the user or they may be state-dependent and thus change on the run, though not during the negotiation. Notice also that in general load agents can be added or eliminated from the agency without notice to the other peers. As a consequence, for example, a load agent whose priority is 2, does not know in general if a priority 1 load is present or not in the system.

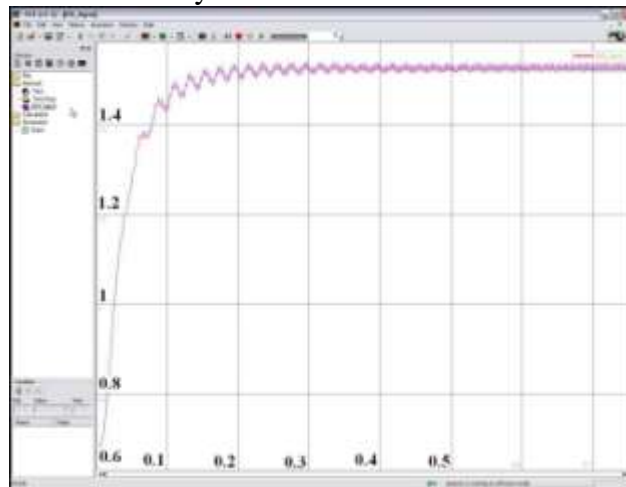


Figure 27: dc bus transient current [A] vs time [s] at motor start-up in simulation; the other loads are active at this time

The negotiation identifies the load to be sacrificed. In this application a simple load shedding is performed at this point, for sake of simplicity so the load agent with least priority forces the control to shut down its corresponding load. In this experiment load 1 had lowest priority therefore it is shed. The RL load currents are shown in Figure 28, where the signals are captured at the time in which the negotiation has been completed and the load 1 agent has implemented the outcome of the negotiation shutting off load 1.

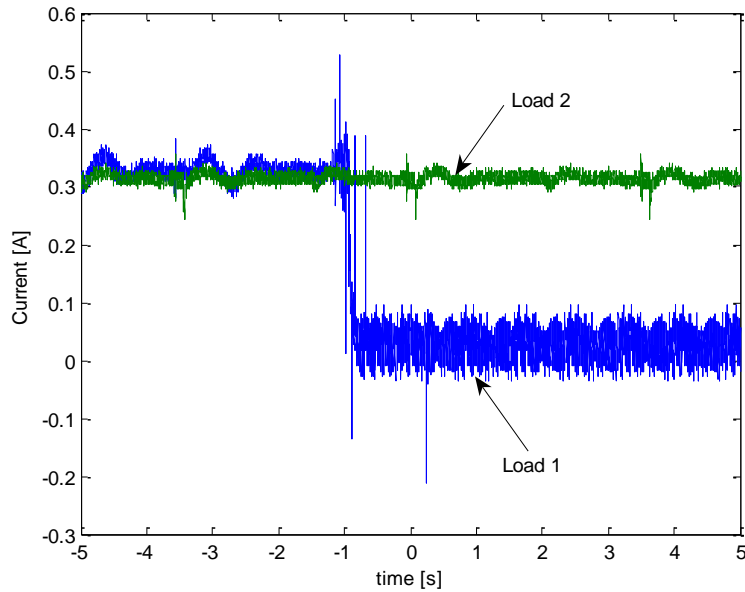


Figure 28: currents of the two RL loads at the time when the lowest priority load is shed to allow for the motor to start

We are still working on the implementation of gentle performance deterioration criteria that would allow keeping all the loads active while accommodating the new power demand. This could be easily done in a situation where there is always a power converter as interface between the DC bus and the load: a modulation of the duty cycle control can achieve virtually any value of power absorption.

At this point the motor drive is started. This simplified procedure, based on knowledge of the system does not perform any further verification of the state of the system, while in fact the simulation/negotiation procedure could be reiterated to validate the load management decision. The system though is set to perform an a posteriori validation. For this purpose the monitoring agent, whenever a decision based on negotiation is implemented, modifies the virtual instrumentation set-up, running a specific Virtual Instrument (VI). This VI is capable of measuring the currents that are being drawn by the two resistive loads and also has the capacity to drop the measurement of a certain load that has been shed for the next round of negotiation i.e. when the user decides to make another change in the system, the VI measures the current only from the active loads on the system.

The agents are equipped with a certain degree of autonomy at different levels of abstraction within the agency. This autonomy consists of the selection of the kind of communication protocol that the agent want to use, the method and settings for the measurement of data and also the determination if a need for negotiation between agents exists.

The multi-agents system presented rely on the assumption that the negotiation between the agents will always converge. The difference of this architecture lies in the fact that the negotiation does not exist between the service/utility provider agents and the user/load agents but lies amongst the load agents themselves.

In the scenario presented here, the agents use a very basic negotiation scheme. In the event of a limit breach in the simulated total current measurement, the agents negotiate to

discover the load with the least priority and a command is issued to shed that load. The advantage of this negotiation scheme is that the negotiating agents can take into account the dynamic nature of the priority levels. The agents are not aware of the state of the other loads and their priorities before the negotiation starts and can autonomously decide which load has to be dropped. In the event that the load decides that it has to be shut off or has to accept gentle degradation in its performance in order to reduce the current demand, it can proceed to do so without the intervention of any other agent. A time-out is set for the response of the simulation agent. With the current setting, if this agent is not responsive the loads are shut down for safety.

The disadvantage of this scheme is that the loads have no direct say in the decision made to add/drop loads. The result of the negotiation cannot be challenged by the load which is scheduled to be dropped.

8. ESRDC DESCRIPTION OF FACILITIES

The Electric Ship Research and Development Consortium (ESRDC) is powered by some of the most sophisticated and state-of-the-art research facilities in the world. Together, team members Florida State University, Mississippi State University, the University of South Carolina, the University of Texas at Austin, the Massachusetts Institute of Technology, Purdue University and the U.S. Naval Academy, offer research and laboratory settings that maximize each other's strengths and provide a truly unique setting to achieve great success.

The following are brief summaries of the research capabilities of each institution.

The Florida State University Center for Advanced Power Systems (CAPS) Research Facilities

The FSU Center for Advanced Power Systems (CAPS) occupies 33,000 square feet of research laboratory, test facility and office space in Tallahassee's Innovation Park, adjacent to the National High Magnetic Field Laboratory (NHMFL) and the FAMU-FSU College of Engineering. Power systems research facility capabilities developed in whole or in part under the ONR ESRDC program consist of an advanced prototype test facility for testing and analysis of power systems and electric machinery and components up to 5 MW, real-time digital modeling and simulation capability for power systems research and hardware in the loop experimentation, and a variety of specialized power and controls-related laboratory areas supporting graduate and undergraduate education in power systems through the FAMU-FSU College of Engineering.

The Advanced Prototype Test Facilities are being developed in multiple phases toward a flexible environment for testing electric machines, components and systems at up to 5 MW.

The CAPS test facility offers various possibilities for equipment and system-oriented testing under dynamic, real-life conditions by using the Real Time Digital Simulator.

The test facility provides for multiple experiments to be conducted simultaneously, and currently offers or will soon include the following capabilities:

- 5 MW dynamometer, 0 – 450 RPM with 10 MW overload capability for 60 seconds. The dynamometer can be used for other speed ratings if a gear box is used.
- 5 MW variable voltage and frequency converter to simulate weak power grids.
- Experimental DC bus, 500 – 1150 V dc, rated for 2.8 MW at 1150 V dc. This converter can deliver or absorb the rated power
- 450 V ac, 2 MW experimental bus.

The test facility is fully staffed and supports all testing activities starting with equipment installation, commissioning, testing, data collection, as well as disassembly, decommissioning and shipment of the equipment. The test activities are supported and coordinated by three engineers and four technicians who are assigned full-time to the test facility.

Real-Time Hardware-in-the-Loop Modeling and Simulation. In addition to a variety of PC-based modeling and simulation tools such as MATLAB/Simulink and PSCAD/EMTDC, the CAPS facility features a specialized high-performance Real Time Digital Simulator (RTDS) designed particularly for real-time solution of complex power systems models. This system has been gradually expanded under the ONR-funded program to include nine "racks" consisting of a large number of parallel processors (typically 26-30 each). The entire system is capable of simulating in real-time approximately 500 electrical nodes and 5,000 control components.

Entire simulations can be run in real-time at time-steps of 50 μ s, and, with a recently implemented Gigahertz Processing Card (GPC), critical portions of a simulation, such as power electronics devices, can be simulated in real-time at time steps down to 1 μ s.

To support sophisticated tests with real electric machines and components, the RTDS has extensive I/O, including more than 1,000 binary I/O channels and more than 300 16-bit analog (A/D, D/A) I/O channels. Fiber-optics transceivers provide I/O connections directly into the RTDS from points throughout the advanced prototype test facility areas, including high-power and low-power dynamometer test stands.

The nine-rack RTDS system is fully commissioned and in routine use in a variety of research thrusts within the ONR ESRDC program. It played a vital role in the testing of the 5 MW AMSC HTS motor, including the ability to simulate dynamic at-sea conditions up to sea-state five. The DC-zonal IFTP system is fully modeled in the RTDS and is being continuously validated and improved. Variations developed for different purposes are being used in a number of independent ESRDC research thrusts at CAPS.

Purdue University Laboratory Facilities and Research Centers

Purdue University maintains extensive laboratory facilities for the study of electric machinery, power electronics, and power electronics-based distribution and propulsion systems.

Purdue's Energy Conversion Research Laboratory (ECRL)



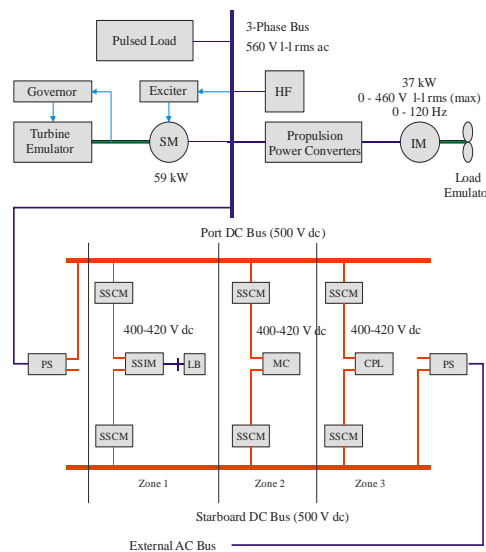
was established in August 1999 and represents an approximate \$2 million investment by Purdue, the National Science Foundation, the Office of Naval Research, and the Naval Sea Systems Command. This laboratory consists of nine research stations at a variety of power capabilities up to 110 kW. Equipment includes several low-power hysteresis brake dynamometers (Two 28 Nm, 20,000 rpm units; one 6.2 Nm, 20,000 rpm), a 15 kW, 5900 rpm four-quadrant dynamometer, a 37 kW, 3900 rpm four-quadrant dynamometer with sound room, and a 112 kW, 3600 rpm four quadrant dynamometer. Supporting equipment includes numerous Tektronix TDS420A, TDS 754D, and TDS7054 series oscilloscopes with high voltage differential voltage probes and Hall-effect based current probes, Voltech PM3000A series power analyzers, Sorenson DC power supplies, an HP4284A precision LCR meter for stand-still frequency response testing, and an Agilent 16 channel data acquisition system. Lab control and data acquisition are based on National Instruments LabView. All stations can be interconnected through multiple 3-phase distribution systems running throughout the lab.

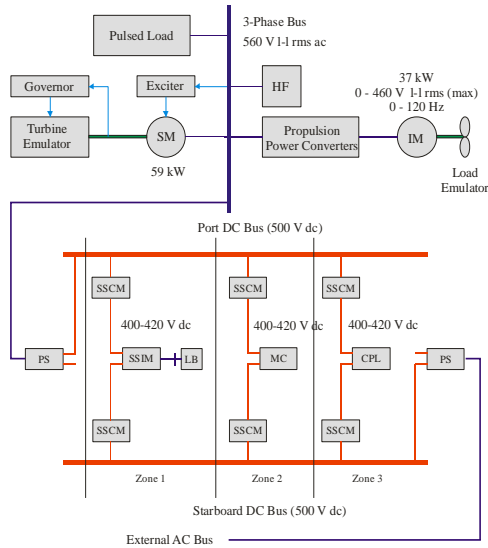
The Genetic Optimization System Engineering Tool (GOSET) is a MATLAB® based code for solving optimization problems. In the course of its development, it was used extensively to solve a variety of engineering problems – particularly those related to magnetics, electric machinery, power electronics and power and

propulsion systems. It has been used to automatically design inductors, brushless DC motors, power supplies, and inverters. It has also been used for the parameter identification of synchronous machines, induction machines, gas turbines, etc. It is meant primarily as an engineering tool, although it is quite generic in its ability to solve both single-objective and multi-objective optimization problems. Because it solves these problems using evolutionary algorithms, it is very robust in its ability to seek global rather than local optimum, as well as in its ability to contend with functions that are not “friendly” in that they are, for example, discontinuous. GOSET provides the means for the user to either be blissfully unaware of the algorithms and parameters used, or to become intimately involved in the exact algorithms as well as the parameters used in these algorithms. It also allows the user to either work from a text-based environment or to utilize a graphical user interface. In short, it provides the user with a powerful tool for the automation of the engineering design process.

The Genetic Optimization Processing Array (GOPA) consists of 216 high-end processors operated in parallel and used to obtain solutions of genetic optimization problems. In particular, it is suited for solving problems related to parameter identification and component/system design. Design parameters are represented as genes on artificial chromosomes, and the population of design evolves by natural selection. Genetic optimization tasks are remotely submitted to this computer array, which uses parallel processing to evolve the design population. The facility is currently being used for the design of energy conversion components such as electric machinery and power electronics converters.

The Naval Combat Survivability Testbed (NCST) was developed through the support of Naval Sea Systems Command and ONR for the purpose of validating new approaches to design, control, modeling and simulation of the next generation of naval power distribution and propulsion systems. The NCST is a scaled version of a future naval power distribution and propulsion concept. A one-line diagram of the NCST facility appears below. Therein, blue interconnections/busses represent AC portions of the system; red interconnections/busses represent DC portions of the system, green interconnection are mechanical linkages, and cyan interconnections are signal paths. In the upper (AC) portion of the system, the SM is a synchronous machine that produces the bulk of the power. The IM denotes the induction machine used as a propulsion motor, and HF is a harmonic filter. The system includes a pulsed load of the type appropriate for rail gun applications. At the bottom of the diagram, the external AC bus represents a second high-power AC bus. In an actual Navy system, this would be another high-power AC bus. The central part of the diagram represents the DC distribution system. The two PS (power supply) units each supply a DC bus; ship service converter modules (SSCM’s) reduce the voltage level and provide fault protection. The SSCMs supply the ship service inverter modules (SSIMs) that in turn feed low-voltage AC load banks (LBs). The SSCMs also supply a motor controller (MC), and a constant power load (CPL).





University of Texas Laboratory Facilities

The University of Texas, in its Center for Electromechanics, has extensive in-house fabrication, assembly and testing facilities housed in a 140,000-square-foot, air-conditioned, high-bay laboratory. The 70-foot-tall high bay features two 25-ton cranes with an additional 25-ton crane servicing a machine shop area. In addition to main high-bay laboratory, an additional 10,000 square feet of air-conditioned space is available in eight satellite labs, along with a 1,200-square-foot welding/fabrication shop. The photo below shows the layout of the main high bay. Visible in the right foreground is a granite surface plate for dimensional inspections. A 200-ton hydraulic assembly press is visible in the left foreground and the main high bay doors and the six coaxial inductors of the Balcones Homopolar Generator Power Supply (BHPG) are visible in the background.



The university's approach to fabrication is a distributed manufacturing approach. Novel machines are designed by the research staff, and component testing is done to provide the engineering data needed to fabricate these first-of-a-kind machines. Components that can be fabricated using conventional industrial practices are fabricated by experienced suppliers. When materials or other factors beyond current industrial practice are required, the university staff develops new fabrication processes in-house. If those new processes are needed routinely, they are also transferred to competent industrial suppliers. In this way, the university researchers remain focused on

novel systems, but the results of the earlier work are available to others through a competent base of industrial suppliers.

Final fabrication and testing is typically done in the university facilities. When there is a high likelihood that subsequent similar machines will be needed, the university teams with a manufacturer that participates in the assembly and test activities. This is an effective way to transfer the technology to an industrial supplier.

The facility also houses a high-energy spin test bunker designed to safely contain a 20 psig internal overpressure. The 600-square-foot spin test bunker features 30-inch-thick fiberglass-reinforced concrete walls with 6-inch-thick aluminum door, window and roof closures. A stainless steel tie-down structure is rated for 5 million-pound vertical load and torque loads of up to 20 million pounds per foot. A metal building located immediately adjacent to the spin test bunker was designed for installation and testing of gas turbines, with openings for intake air and integral exhaust ducting in the roof. This structure can also be used for local instrumentation and data acquisition for experiments being conducted in the spin test bunker.

A 75-foot-deep vertical gun range is located between the north end of the main high bay and the spin test bunker. The seven-story vertical range is serviced by a three-person elevator and currently houses a 90 mm bore by 10-meter long railgun and bore honing system.

Fabrication and Machine Shop

The Center's machining capabilities were updated in 2003 with the installation of new machine tools, including lathes, manual mills, and a horizontal band saw. An important addition to the machine shop is a HAAS Model VF7 CNC machining center (pictured at left). The machining center provides fully programmable four-axis machining with automatic tool changing.



The machine shop is also supported by a fully stocked tool crib, including measuring and inspection tools under NIST traceable calibrations. In addition to the extensive machining capabilities, the Center also maintains a welding and fabrication shop.

Composites Processing Facility

There is significant in-house expertise in the design, analysis and manufacture of composite structures used in high-performance rotating machines. To help in rapidly prototyping complex composite structures with known mechanical properties, we have developed a set of linked computer codes called CEMWIND. The code generates detailed material property data that can be exported to finite element analysis codes, along with programs that control fiber placement and orientation in the filament winding machine.

Electronics and Instrumentation

In-house testing and experiments are supported by a wide array of electronic test equipment and instrumentation. The facility contains two dedicated EMI/RFI shielded control rooms to isolate instrumentation and controls during high energy testing.

Balcones Homopolar Generator Power Supply

The Center's laboratory facility was built in 1985 as an energy-storage and pulsed-power prototype test facility. To support this effort, The University of Texas funded the manufacture and installation of the Balcones Homopolar Generator Power Supply (BHPG). The 60 MJ BHPG power supply includes six 10-MJ homopolar generators and six 2-turn coaxial inductors along with a high current, high voltage bus turret to enable flexible series/parallel interconnection. The generators are installed in a hexagonal pit in the high bay with the central bus and inductors mounted at floor level.

University of South Carolina Facilities and Laboratories

The Power and Energy Systems research group at the University of South Carolina occupies about 6,000 square feet of space in the Swearingen Engineering Building, comprising the Real-time Electromechanics Laboratory, the Power Electronics Laboratory, the Power Sources Laboratory, and several rooms of office space for graduate students and computing facilities.

Realtime Electromechanics Laboratory

This laboratory focuses on real-time interactions (hardware in the simulation loop and control of power converters) between power electronics and electromechanical systems. It includes small rotating machines and test stands up to 2 kW, four dSpace systems for rapid control prototyping, a variety of microcontroller and dsp prototyping kits including for Infineon C167, Texas DSP TMS320C240F, Xilinx FPGA, and National Instruments PXI and VXI data acquisition/control/computing platforms.

Power Electronics Laboratory

This laboratory focuses on characterization of power electronic devices and fabrication of power converters. It contains cryogenic test stands for power electronics, high-speed test and measurement instrumentation including wideband (GHz) arbitrary waveform generators, and facilities for fabrication of printed circuit boards.

Power Sources Laboratory

Work in this laboratory addresses issues related to power sources, especially fuel cell power sources and hybrid configurations of those sources that include integral energy storage systems and power management systems. The laboratory contains a PEM fuel cell, advanced batteries and supercapacitors, and power supplies operating at up to kW levels. The laboratory also houses a modular linear permanent magnet motor of 3m length.

Simulation facilities

Computing facilities include a wide variety of desktop systems, a quad-processor Itanium computer, and access to the College of Engineering's new cluster computer.

Mississippi State University Research Capabilities

Mississippi State University equipment resources contributing to the ESRDC projects have a combination of software and hardware capabilities to allow continuing research activities as well as branching into new areas. The following hardware is available at MSU:

- 2 PM-1000 American Superconductor PEBB Modules
- 1 10kW Siemens 6RA70 thyristor control rectifier
- Tektronix Oscilloscope 1GHZ, 4CH w/ acc & probes DSK B052756
- 1 National Instruments PXI-1002 with data acquisition cards
- 1 National Instruments PXI-1002 with RT controller and ADC/DAC cards
- Dranetz BMI Power Platform
- S&C's Intelliteam II

- S&C's IntelliCap
- Virginia Tech/TVA Frequency Disturbance Recorder
- 2 SEL Adaptive Multichannel Systems
- 2 SEL 351S Distribution Relays
- SEL 421 Transmission Relay
- 2 SEL 487B Differential Relays

MSU also has a variety of software tools for simulation capabilities. Over 20 computers are dedicated to the ESRDC activities. Besides traditional programming environments such as C++, researchers at MSU have access to the following software:

- Simulink/Matlab
- LINGO
- XML Spy
- VTB
- PSS/E
- PowerWorld
- PSCAD
- CAPE
- RDAP
- Metrowerks Codewarrior
- Protel DXP
- National Instruments LABVIEW Real-Time

The MSU team capabilities are enhanced for 2006 activities through the involvement of researchers involved with the MSU High Voltage Laboratory (<http://www.ece.msstate.edu/research/hvl>). The High Voltage Laboratory has the following hardware equipment:

- 3000 kV, 56 kJ Impulse Generator
- 1000 kV, 60 Hz, 1000 kVA Conventional Test Transformer with Regulator and Measurement System
- 40 kV, 60 Hz, 10 kVA Conventional Test Transformer with Regulator and Measurement System
- Dielectric Test System, Pulse Frequency from 200 Hz to 40 kHz, +/-1600 V
- Digital Storage Oscilloscope with Waveform Analysis
- Digital Partial Discharge Measurement System
- Computing System for Analysis and Database Storage
- Conventional Voltage Impulse Dividers

Software tools complement the hardware capabilities of the laboratory. MSU has special software allowing for three-dimensional analysis and characterization of partial discharge in cables and insulation of motors. Additionally, commercial software to analyze the statistics of breakdown and the aging phenomena in dielectric materials is available.

Massachusetts Institute of Technology Research and Facilities Capabilities

The Principal investigators have access to a numerous facilities and laboratories at MIT such as the Propeller Tunnel and the Design Laboratory. The following are of particular relevance to the ESRDC-sponsored research.

The Laboratory for Electromagnetic and Electronic Systems (LEES) includes a 1,000-square-foot, well-equipped, modern electronics laboratory and a complete machine shop suitable for assembling and packaging prototypes. LEES has oscilloscopes, network analyzers, spectrum analyzers,

power supplies, LCR/impedance meters and other modern test equipment. The lab also contains a dozen Pentium II to IV class computers with microcontroller development systems, and a complete suite of tools for the assembly and testing of prototype discrete component electronic circuits. The machine shop is equipped to mill, drill and cut metal, wood and plastics for fabrication. LEES has recently installed an HVAC/compressor test facility capable of running with test compressors in the 0.5 to 5 horsepower range. There are two clean-rooms for testing sensors and MEMS devices and optical microscopy facilities. We have access to high-voltage test areas for projects such as insulation/dielectric testing.

The Design Laboratory of the MIT Center for Ocean Engineering was founded in 1972 by Professor Chrysostomidis to research ship design and marine topics using CAD (Computer Aided Design) methods. The lab's research is in ship design, offshore structure design, marine robotics, geometric modeling, solid modeling, advanced manufacturing (solid free-form fabrication), distributed systems, computational geometry, ship building, producibility, and life-cycle issues.

The Marine Hydrodynamics Laboratory is home to a recirculating, variable pressure water tunnel. Originally developed for the testing of ship propellers, the water tunnel employs a moving stream of water rather than a moving object as in a towing tank. It has a test section 1.2 meters long by 50 cm square through which an extremely uniform stream of water can be moved at speeds up to 10 m/s. State-of-the-art flow visualization and measurement devices are used at this facility, including Particle Image Velocimetry and Laser Doppler Velocimetry. Upcoming additions include a fiber probe for the LDV system and stereo PIV capabilities. Recent work includes drag reduction tests with electro-magneto-hydrodynamics, turbulence reduction through fish-like swimming motions, snake-swimming and flapping foil experiments.

The Center for Advanced Scientific Computing and Visualization at the Brown University Laboratory gives the team access to an IBM SP4 and two 64-processor Linux clusters. These will become useful when we deal with modeling the big system and introducing multi-dimensional uncertainties.

MIT also houses the Naval Construction and Engineering Program which trains active-duty U.S. Navy and U.S. Coast Guard officers. Participants earn graduate degrees in naval engineering and ship design through a curriculum sponsored by Naval Sea Systems Command. Besides providing the officers with a comprehensive education in naval engineering, it emphasizes their future roles as advocates for innovation in ship design and acquisition. We believe that, through our close connection with this program, the MIT ESRDC team will be able to place the technology we develop directly into the hands of the people who will be using it.

The MIT ESRDC consortium will establish an organizational structure similar to a virtual laboratory. As specific issues or problems arise, researchers with a particular expertise, either from MIT or nearby universities, can be brought onto the team. Researchers' involvement can lessen when their role in the research is fulfilled. In this way, we expect to maintain both flexibility and a wide array of skills and expertise throughout the life of the project.

9. PUBLICATIONS (OCT 2002 – MARCH 2008)

Journals

1. “Modeling the Growth of Streamers during Liquid Breakdown,” R.E. Hebner, M. Kim, and G.A. Hallock, submitted to *IEEE Transactions on Dielectrics and Electrical Insulation*, Vol. 15, No. 2, April 2008, pp. 547-553.
2. “Modeling and simulation of electric ships’ power system components and their interaction,” A. Ouroua, J. Jackson, J. Beno, R. Thompson, and E. Schroeder, 2007 Summer Computer Simulation Conference (SCSC’07), sponsored by the Society for Modeling and Simulation International, San Diego, California, U.S.A., July 15-18, 2007.
3. “Effects of obstructions and surface roughness on film cooling effectiveness with cylindrical holes and holes embedded in a transverse trench,” R.P. Somawardhana and D.G. Bogard, accepted for publication in *ASME Journal of Turbomachinery*, October 2007.
4. “Some results on nonlinear observer design for discrete-time systems,” H.-G. Lee, A. Arapostathis, and S.I. Marcus, *IEEE transactions on Automatic Control*, submitted July 2007, not published.
5. “Capacity of a class of cognitive radio channels: interference channels with degraded message sets,” W. Wu, Sriram Vishwanath, and A. Arapostathis, *IEEE Transactions on Information Theory*, accepted for publication June 2007, not yet published.
6. “Development and analysis of trapped field magnets in electromechanical devices,” K.R. Davey, R. Weinstein, and Ravi Sawh, *IEEE Transactions on Magnetics*, under review June 2007, not yet published.
7. “Initiation from a point anode in a dielectric liquid,” W.F. Schmidt, M. Kim, and R.E. Hebner, *IEEE Transactions on Dielectrics and Electrical Insulation*, Vol. 14, No. 3, June 2007, pp. 762-763.
8. “Latin hypercube sampling and pattern search in magnetic field optimization problems,” K.R. Davey, *IEEE Transactions on Magnetics*, under review June 2007, accepted to *IEEE Transactions on Magnetics*.
9. “A novel QPC detector for the health monitoring of rotating machines,” T. Kim, E.J. Powers, W.M. Grady and A. Arapostathis, *IEEE Transactions on Instrumentation and Measurement*, submitted May 2007, not yet published.
10. “Broadcasting in sensor networks: the role of local information,” Sundar Subramanian, Sanjay Shakkottai, and A. Arapostathis, *Proc. 25th IEEE International Conference on Computer Communications (INFOCOM 2006)*, Barcelona, Spain, 23-29 April 2006, pp. 1-12, to appear in *IEEE/ACM Transactions on Networking*, submitted May
11. “Detection of flicker caused by interharmonics,” T. Kim, E.J. Powers, W.M. Grady, and A. Arapostathis, *IEEE Transactions on Instrumentation and Measurement*, submitted May 2007, not yet published.
12. “High resolution film cooling effectiveness measurements of axial holes embedded in a transverse trench with various trench configurations,” S.K. Wayne and D.G. Bogard, *ASME J. of Turbomachinery*, Vol. 129, No. 2, pp. 294-302, 2007.
13. “The equivalent T circuit of the induction motor: its nonuniqueness and use to the magnetic field analyst,” K.R. Davey, K.R. Davey, 12th Biennial IEEE Conference on Electromagnetic Field Computation (CEFC 2006), Miami, Florida, USA, 30 April-3 May 2006, p. 175, *IEEE Transactions on Magnetics*, Vol. 43, No. 4, April 2007, pp. 1745-1748.

14. "Stability and controllability of planar, conewise linear systems," A. Arapostathis and M.E. Broucke, *Systems & Control Letters*, Vol. 56, February 2007, pp. 150-158.
15. "System-level thermal management of pulsed loads on an all-electric ship," T.W. Webb, T.M. Kiehne, and S.T. Haag, *IEEE Transactions on Magnetics*, Vol. 43, No. 1, part 2, January 2007, pp. 469-473.
16. "Initiation from a point anode in a dielectric liquid," M. Kim and R.E. Hebner, *Transactions on Dielectrics and Electrical Insulation*, Vol. 13, No. 6, December 2006, pp. 1254-1260.
17. "On the capacity of multiple access channels with state information and feedback," W. Wu, S. Vishwanath, and A. Arapostathis, to *IEEE Transactions on Information Theory*, submitted 2006, not yet published.
18. "A new strategy for management and reconfiguration of self-contained power systems," K.R. Davey and R.E. Hebner, *IEEE Transactions on Power Delivery*, Vol. 21, No. 3, July 2006, pp. 1565-1570.
19. "A new strategy for representation and control of self-contained power systems," K.R. Davey and R.E. Hebner, *IEEE Transactions on Power Delivery*, Vol. 21, No. 3, July 2006, pp. 1558-1564.
20. "Degradation of film cooling performance on a turbine vane suction side due to surface roughness," J.L. Rutledge, David Robertson, and D.G. Bogard, *ASME Journal of Turbomachinery*, Vol. 128, July 2006, pp. 547-554.
21. "Optimization of gas turbine generator-sets for improved power density," Mark A. Pichot, Joseph J. Zierer, A. Ouroua, and J.H. Beno, *ASNE Naval Engineers Journal*, Vol. 118, No. 4, 2006, pp. 49-56.
22. "Power frequency magnetic properties and aging of 4130 steel," A.T. Wilder, 49th Annual Conference on Magnetism and Magnetic Materials, 7-11 November 2004, Jacksonville, Florida, USA, *Journal of Magnetism and Magnetic Materials*, Vol. 300, No. 2, May 2006, pp. L257-L261.
23. "Optimal power allocation for a time-varying wireless channel under heavy-traffic approximation," W. Wu, A. Arapostathis, and Sanjay Shakkotai, *IEEE Transactions on Automatic Control*, Vol. 51, No. 4, April 2006, pp. 580-594.
24. "On the existence of stationary optimal policies for partially observed MDPs under the long-run average cost criterion," S.-P. Hsu, Dong-Ming Chuang, and A. Arapostathis, *Systems and Control Letters*, Vol. 55, 2006, pp. 165-173.
25. "Power quality indices for transient disturbances," Y.-J. Shin, E.J. Powers, W.M. Grady, and A. Arapostathis, *IEEE Transactions on Power Delivery*, Vol. 21, No.1, January 2006, pp. 253-261.
26. "Application of time-frequency domain reflectometry for detection and localization of a fault on a coaxial cable," Y.-J. Shin, E.J. Powers, Tok-Son Choe, Chan-Young Hong, Eun-Seok Song, Jong-Gwan Yook, and Jin Bae Park, *IEEE Transactions on Instrumentation and Measurement*, Vol. 54, No. 6, December 2005, pp. 2493-2500.
27. "Control of Markov chains with safety bounds," A. Arapostathis, Ratnesh Kumar, and S.-P. Hsu, *IEEE Transactions on Automation Science and Engineering*, Vol. 2, No. 4, October 2005, pp. 333-343.
28. "Designing pulse power generators," K.R. Davey and John Uglum, *Plasma Science*, Vol. 33, No. 4, August 2005, pp. 1170-1176.
29. "Numerical design of synchronous generators," K.R. Davey and Bruce B. Gamble, *IEEE Transactions on Magnetics*, Vol. 41, No. 8, August 2005, pp. 2391-2397.
30. "Differential games with ergodic payoff," Mrinal K. Ghosh and K. S. Mallikarjuna Rao, *Society for Industrial and Applied Mathematics (SIAM) Journal on Control and Optimization*, Vol. 43, No. 6, June 2005, pp. 2020-2035.

31. "Minimum outage probability transmission with imperfect feedback for MISO fading channels," Yongzhe Xie, Costas N. Georghiades, and A. Arapostathis, *IEEE Transactions on Wireless Communications*, Vol. 4, No. 3, May 2005, pp. 1084-1091.
32. "Ship component in hull optimization," K.R. Davey, *Marine Technology Society Journal*, Vol. 39, No. 2, 2005, pp. 35-42.
33. "A nonzero-sum stochastic differential game in the orthant," Mrinal K. Ghosh, K. Suresh Kumar, *Journal of Mathematical Analysis and Applications*, Vol. 305, January 2005, pp. 158-174.
34. "Existence of value and saddle point in infinite-dimensional differential games," Mrinal K. Ghosh and A. J. Shaiju, Communicated by L. D. Berkovitz, *Journal of Optimization Theory and Applications*, Vol. 121, No. 2, May 2004, pp. 301-325.
35. "A hybrid systems approach for dynamic reconfiguration," A. Arapostathis, W.M. Grady, and E.J. Powers, 1st WSEAS International Conference on Electrosience and Technology for Naval Engineering and All-Electric Ship, special session "Power System Controls for the Future Electric Ship," Vouliagmeni, Athe
36. "Fault analysis on a naval power grid using equivalent impedances," K.R. Davey, 1st WSEAS International Conference on Electrosience and Technology for Naval Engineering and All-Electric Ship, Vouliagmeni, Athens, Greece, 12-13 July 2004, *IASME Transactions*, Vol. 1, No. 2, April 2004, pp. 247-252.
37. "Reconfiguration of shipboard power systems," K.R. Davey and R.E. Hebner, 1st WSEAS International Conference on Electrosience and Technology for Naval Engineering and All-Electric Ship, Vouliagmeni, Athens, Greece, 12-13 July 2004, *IASME Transactions*, Vol. 1, No. 2, April 2004, pp. 241-246.
38. "Research progress at University of Texas," system reconfiguration and harmonic studies," J. Billo, J. Carroll, Y.-J. Shin, A. Arapostathis, W.M. Grady, and E.J. Powers, 1st WSEAS International Conference on Electrosience and Technology for Naval Engineering and All-Electric Ship, special session "Power System Controls
39. "Zero-sum stochastic games with partial information," M.K. Ghosh, D. McDonald, and S. Sinha, Communicated by L. D. Berkovitz, *Journal of Optimization Theory and Applications*, Vol. 121, No. 1, April 2004, pp. 99-118.
40. "Linearization of discrete-time systems via restricted dynamic feedback," Hong-Gi Lee, A. Arapostathis, and Steven I. Marcus, *IEEE Transactions on Automatic Control*, Vol. 48, No. 9, September 2003, pp. 1646-1650.
41. "Controlled Markov chains with safety upper bound," Aristotle Arapostathis, Ratnesh Kumar, and Sekhar Tangirala, *IEEE Transactions on Automatic Control*, Vol. 48, No. 7, July 2003, pp. 1230-1234.

42. Hardware-in-the-Loop Testing Platform for Distributed Generation Systems, A. Monti, F. Ponci, Z. Jiang, R. Dougal, *International Journal of Energy Technology and Policy*, pp. 241-257, Volume 5, No. 2, 2007.
43. A Virtual Instrument for Time-Frequency Analysis of Park Power Components, A. Monti, F. Ponci, S. Pelizzari, L. Cristaldi, *Electric Power Quality and Utilization Journal*, Vol. XIII, No. 1, pp. 121-128, 2007.
44. Power Quality Indexes in an Agent-based Reconfiguration Strategy for Ship Power Systems , F. Ponci, A. Monti, L. Cristaldi, *Electrical Power Quality and Utilization Journal*, Vol. XIII, No. 1, pp. 105-112, 2007.
45. Diagnostic of a Faulty Induction Motor Drive via Wavelet Decomposition, F. Ponci, L. Cristaldi, M. Lazzaroni, A. Monti, , *IEEE Transactions on Instrumentation and Measurement*, Volume 56, Issue 6, pp. 2606-2615, December 2007.

46. Proximity Coupled Interdigitated Sensors to Detect Insulation Damage in Power System Cables, R. H. Bhuiyan, R. A. Dougal, M. Ali, IEEE Sensors Journal, Vol. 7, Issue 12, pp. 1589-1596, December 2007.
47. Multi-Agent Systems for Power Engineering Applications - Part I: Concepts, Approaches and Technical Challenges, F. Ponci, S. D. J. McArthur, E. M. Davidson , V. M. Catterson, A. Dimeas, N. Hatziargyriou, T. Fanab, IEEE Transactions on Power Systems, Vol. 22, Issue 4, pp. 1743-1752, November 2007.
48. Multi-Agent Systems for Power Engineering Applications - Part II: Technologies, Standards, and Tools for Building Multi-agent Systems, F. Ponci, S. D. J. McArthur, E. M. Davidson , V. M. Catterson, A. Dimeas, N. Hatziargyriou, , IEEE Transactions on Power Systems, pp. 1753-1759, Vol. 22, Issue 4, November 2007.
49. Adaptive Control Strategy for Active Power Sharing in Hybrid Fuel Cell/Battery Power Sources, Z. Jiang, L. Gao, R. Dougal, IEEE Transactions on Energy Conversion, Vol. 22, No. 2, pp. 507-515, June 2007.
50. Indirect Measurements Via Polynomial Chaos Observer, A. Monti, A. Smith, F. Ponci , IEEE Transaction on Instrumentation and Measurements, Vol. 56, Issue 3, pp. 743-752, May 2007.
51. Maximum Entropy Analytical Solution for Stochastic Differential Equations based on the Wiener-Askey Polynomial Chaos, A. Monti, G. D'Antona, F. Ponci, L. Rocca, IEEE Transaction on Instrumentation and Measurement, pp. 689-695, Vol. 56, Issue 3, May 2007.
52. A Low Cost Real-Time Hardware-In-the-Loop Testing Approach of Power Electronics Controls, B. Lu, X. Wu, H. Figueroa, A. Monti, IEEE Transaction on Industrial Electronics, Vol. 54, No. 2, pp. 919-931, April 2007.
- 53.
54. Destruction-free Parameter Extraction for a Physics-based Circuit Simulator IGCT Model, X. Wang, J.L. Hudgins, E. Santi, P.R. Palmer, IEEE Trans. Industry Applications, Volume 42, No. 6, pp. 1395-1402, November/December 2006.
55. Parameter Setting and Analysis of a Dynamic Tubular SOFC Model, W. Jiang, R. Fang, R. A. Dougal, J. Khan, Journal of Power Sources, Vol. 162, Issue 1, pp. 316-326, November 2006.
56. Dynamic Centrifugal Compressor Model for System Simulation, W. Jiang, J. Khan, R.A. Dougal, Journal of Power Sources, Vol. 158, Issue 2, pp. 1333-1343, August 2006.
57. A Compact Digitally-Controlled Hybrid Fuel Cell/Battery Power Source, Z. Jiang, R. Dougal, IEEE Transactions on Industrial Electronics, Vol. 53, No. 4, pp. 1094-1104, August 2006.
58. An Advanced Direct Time Domain BEM for 3-D Wave Propagation in Acoustic Media, D. C. Rizos, S.Zhou, Journal of Sound and Vibration, Vol. 293 (1-2), pp. 196-212, May 2006.
59. Power Anomaly Effects and Costs in Low-voltage Mobile Power Systems, S. Liu, C. Singer, R. Dougal , IEEE Transactions on Aerospace and Electronic Systems, Vol. 42, No. 2, pp. 612-624, April 2006.
60. Two-Step Parameter Extraction Procedure with Formal Optimization for Physics-Based Circuit Simulator IGBT and pin Diode Models, A. T. Bryant, X. Kang, E. Santi, P. R. Palmer, J. L. Hudgins, IEEE Transactions on Power Electronics, Volume 21, Issue 2, pp.295-309, March 2006.
61. Miniature Circularly Polarized Rectenna with Reduced out of Band Harmonics, M. Ali, G. Yang, R. Dougal, IEEE Antennas and Wireless Propagation Letters, Vol. 5, pp. 107-110, March 2006.
62. An Analytical Solution to Li/Li+ Insertion into a Porous Electrode, Liu S., Solid State Ionics, Vol. 177, No. 1-2, pp. 53-58, January 2006.

63. Power Quality Indices for Transient Disturbances, Y. J. Shin, E. J. Powers, W. Mack Grady and A. Arapostathis, IEEE Transactions on Power Delivery, Vol. 21, No. 1, pp. 253-261, January 2006.
64. Journals 2005 (15)
65. Application of Time-Frequency Domain Reflectometry for Detection and Localization of a Fault on a Coaxial Cable, Y. J. Shin, T. Choe, E. Song, J. Park, J. Yook, and E. J. Powers, IEEE Transactions on Instrumentation and Measurement, Vol. 54, No. 6, pp. 2493-2500, December 2005.
66. Automatically Building Customized Circuit-based Simulation Models using Symbolic Computing, J. Bastos, A. Monti, Mathematics and Computers in Simulation, Vol. 70, No. 4, pp. 203-220, 2005.
67. Design of an Autonomous Photovoltaic Power Plant for Telecommunication Relay Station, S. Liu, R. Dougal and E. Solodovnik, IEE Proceedings of Generation, Transmission, and Distribution, Vol. 152, No. 6, pp. 745-754, November 2005.
- 68.
69. Wideband Circularly Polarized Microstrip Patch Antenna for Wireless LAN Applications, G. Yang, M. Ali, R. Dougal, Microwave and Optical Technology Letters, Vol. 45, Issue 4, pp. 279 - 285, April, 2005.
70. A New Circularly Polarized Rectenna for Wireless Power Transmission and Data Communication, M. Ali, G. Yang, R. Dougal, IEEE Antennas and Wireless Propagation Letters, Vol. 4, pp. 205-208, April 2005.
71. Design and Simulation of a Permanent-Magnet Electromagnetic Aircraft Launcher, D. Patterson, A. Monti, C. Brice, R. A. Dougal, R. Pettus, S. Dhulipala, D. Kovuri, T. Bertonecelli, IEEE Transactions on Industry Applications, Vol. 41, pp. 566-575, March/April 2005.
72. Simulation of Thermally Coupled Metal Hydride Hydrogen Storage and Fuel Cell Systems, Z. Jiang, R. Dougal, S. Liu, S. Gadre, A. Ebner, J. Ritter, Journal of Power Sources, Volume 142, Issues 1-2, pp. 92-102, March 2005.
73. A Simplified Physics-based Model for Nickel Hydrogen Battery, S. Liu, R. A. Dougal, J. Weidner, L. Gao, Journal of Power Sources, Vol. 141, No. 2, pp. 326-339, Mar. 2005.
74. A Virtual Environment Simulation of Dynamically Coupled Metal Hydride Hydrogen Storage and Fuel Cell Systems, Z. Jiang R. Dougal, S. Liu, S. Gadre, A. Ebner, J. Ritter, Journal of Power Sources, Vol. 142, Issues 1-2, pp. 92-102, March 2005.
75. A Virtual Environment for Remote Testing of Complex Systems, L. Cristaldi, A. Ferrero, A. Monti, F. Ponci, W. McKay, R. Dougal, IEEE Transactions on Instrumentation and Measurement, Vol. 54, No. 1, pp. 123-133, Feb. 2005.
76. Analysis of an Automatic Energy Recovery System for Partially Spent Batteries, R. A. Dougal, Z. Jiang, L. Gao, Journal of Power Sources, Vol. 140, Issue 2, pp. 400-408, Feb. 2005.
77. Effectiveness Analysis of Energy Reclamation from Partially Depleted Batteries, R. A. Dougal, L. Gao, Z. Jiang, Journal of Power Sources, Vol. 140, No. 2, pp. 409-415, Feb. 2005.
78. Evaluation of Active Hybrid Fuel Cell/Battery Power Sources, L. Gao, Z. Jiang, R. A. Dougal, IEEE Transaction on Aerospace and Electronic Systems, Vol. 41, No. 1, pp. 346-355, Jan. 2005.
79. Flexible Multiobjective Control of Power Converter in Active Hybrid Fuel Cell/Batter Power Sources, Z. Jiang, L. Gao, R. A. Dougal, IEEE Transactions on Power Electronics, Vol. 20, No. 1, pp. 244-253, Jan. 2005.
80. Power Enhancement of an Actively Controlled Battery/Ultracapacitor Hybrid, L. Gao, R. A. Dougal, S. Liu, IEEE Transaction on Power Electronics, Vol. 20, No. 1, pp. 236-243, Jan. 2005.

81. Simulation of A Thermally Coupled Metal-Hydride Hydrogen Storage and Fuel Cell System, Z. Jiang, R. A. Dougal, S. Liu, S. A. Gadre, A. Ebner, J. Ritter, *Journal of Power Sources*, 142 (2005), 92-102, December 2004 (online).
82. Resistive Companion Modeling of Batteries in a Virtual Test Bed, Q. Zhang, Q. Guo, S. Liu, R. Dougal, R. White, *Journal of Power Sources*, 141 (2005), pp. 359-368, December 2004 (online).
83. Real-time Strategy for Active Power Sharing in A Fuel Cell Powered Battery Charger, Z. Jiang, R. A. Dougal, *Journal of Power Sources*, 142 (2005), pp. 253-263, December 2004 (online).
84. VTB-Based Design of a Standalone Photovoltaic Power System, S. Liu, R. A. Dougal, E. E. Solodovnik, *International Journal of Green Energy*, Vol. 1, No. 3, pp 279-300, 2004.
85. Mathematical Model of a Direct Methanol Fuel Cell, Brenda L. Garcia, Vijay A. Sethuraman, John W. Weidner, Ralph E. White, and Roger Dougal, *Journal of Fuel Cell Science and Technology*, Vol. 1, pp 43-48, Nov. 2004.
86. Maximum Power Tracking and Pulse-Width-Modulated Shunt for Satellite Power Systems, S. Liu, R. A. Dougal, E. V. Solodovnik, *Journal of Propulsion and Power*, Vol. 20, No. 5, pp 911-918, Sept – Oct. 2004.
87. Power Controller Design for Maximum Power Tracking in Solar Installations, E. V. Solodovnik, S. Liu, R. A. Dougal, *IEEE Transactions on Power Electronics*, Vol. 19, No. 5, pp. 1295-1304, Sept. 2004.
88. A Neuro-Fuzzy Application for AC Motor Drives Monitoring System, Monti A., L. Cristaldi, M. Lazzaroni, F. Ponci, *IEEE Trans. on Instrumentation and Measurement*, vol.53, No.4, pp. 1020-1027, Aug. 2004.
89. Synergetic Control for Power Electronics Applications: A Comparison with the Sliding Mode Approach, E. Santi, A. Monti, D. Li, K. Proddatur, R.A. Dougal, *WSP Journal of Circuits, Systems and Computers*, Vol. 13, No. 4, pp. 737-760, August 2004.
90. Synergetic Control of Power Converters for Pulse Current Charging of Advanced Batteries from a Fuel Cell Power Source, Z. Jiang, R.A. Dougal, *IEEE Trans on Power Electronics*, Vol. 19, No 4, pp 1140-1150, July 2004.
91. Power Coordination in a Fuel-cell-battery Hybrid Power Source using Commercial Power Controller Circuits, *Journal of Power Sources*, Vol. 134, No.1, pp 139-147, July 2004.
92. Control Strategies for Active Power Sharing in a Fuel-cell-powered Battery Charging Station, Z. Jiang, R.A. Dougal, *IEEE Trans on Industry Applications*, Vol. 40, No. 3, pp 917-924, May-June 2004.
93. A Thin Wideband Microstrip Patch Antenna with Two Adjacent Slots, Y. Guangli, M. Ali, R. Dougal, *Microwave and Optical Technology Letters*, Vol. 41, No. 4, pp 261-266, May 2004.
94. Design and Experimental Tests of Control Strategies for Active Hybrid Fuel Cell/battery Power Sources, Z. Jiang, L. Gao, M.J. Blackwelder, R.A. Dougal, *Journal of Power Sources*, Vol. 130, pp 163-171, May 2004.
95. An Actively Controlled Fuel Cell/battery Hybrid to meet Pulsed Power Demands, L. Gao, Z. Jiang, and R.A. Dougal, *Journal of Power Sources*, Vol. 130, pp 202-207, May, 2004.
96. Temperature Effects on Trench-gate Punch-through IGBTs, E. Santi, X. Kang, A. Caiafa, J.L. Hudgins, P.R. Palmer, D. Goodwine and A. Monti, *IEEE Trans. Industry Applications*, Vol. 40, No. 2, pp. 472-482, March/April 2004.
97. Symbolically-aided Model Development for an Induction Machine in Virtual Test Bed, W. Gao, E. V. Solodovnik, R. A. Dougal, *IEEE Trans on Energy Conversion*, 19, No. 1, pp 125-135, Mar 2004.
98. Ultracapacitor Model with Automatic Order Selection and Capacity Scaling for Dynamic System Simulation, R. A. Dougal, L. Gao, S. Liu, *Journal of Power Sources*, Vol. 126, No. 1-2, pp. 250-257, February 2004.

99. Synergetic control for DC-DC Boost Converter: Implementation Options, E. Santi, A. Monti, D. Li, K. Proddatur, R. A. Dougal, IEEE Transactions on Industry Applications, Vol. 39, No. 6, pp. 1803-1813, November/December 2003.
100. A Virtual Environment for Remote Testing of Complex Systems, Monti A., L. Cristaldi, A. Ferrero, F. Ponci, W. McKay, R. Dougal, IEEE Trans. on Instrumentation and Measurement, vol.53, No. 5, Oct. 2003.
101. Un Sistema Di Diagnostica Basato Su Tecniche Neuro-Fuzzy, Ponci F., Cristaldi L., Lazzaroni M., Monti A., invited paper on Italian Annual Record of the Research on Instrumentation and Measurements, pp. 336-345, Sep. 2003.
102. Circuit Simulator Models for the Diode and IGBT with Full Temperature Dependent Features, P.R. Palmer, E. Santi, J.L. Hudgins, X. Kang, J.C. Joyce, P.Y. Eng, IEEE Trans. Power Electronics, Vol. 18, No. 5, pp. 1220-1229, Sept. 2003.
103. Characterization and Modeling of High-voltage Field-stop IGBTs, X. Kang, A. Caiafa, E. Santi, J.L. Hudgins, P.R. Palmer, IEEE Trans. Industry Applications, Vol. 39, No. 4, pp. 922-928, July 2003.
104. Application of VTB in Design and Testing of Satellite Electrical Power Systems, Z. Jiang, R. Dougal, S. Liu, Journal of Power Sources, Vol. 122, No. 1, pp. 95-108, July 2003.
105. Design and Testing of Spacecraft Power Systems using VTB, Z. Jiang, S. Liu, R.A. Dougal, IEEE Trans on Aerospace and Electronics Systems, Vol. 39, No 3, July 2003.
106. An Assessment of Wide Bandgap Semiconductors for Power Devices, J.L. Hudgins, G. Simin, E. Santi and M.A. Khan, IEEE Trans. Power Electronics, Vol. 18, No. 3, pp. 907-914, May 2003.
107. Rapid Prototyping of Digital Controls for Power Electronics, A. Monti, E. Santi, R.A. Dougal, M. Riva, IEEE Trans on Power Electronics, Vol. 18, No 3, pp 915-923, May 2003.
108. Design and Testing of a Fuel-Cell-Powered Battery-Charging Station, Z. Jiang and R. Dougal, Journal of Power Sources, Vol. 115, No. 2, pp 279 - 287, April 2003.
109. Dynamic Lithium Ion Battery Model for System Simulation, IEEE Transactions. on Components and Packaging Technology, Gao, L., S. Liu, R. A. Dougal, Vol. 25, No. 3, September 2002.
110. Virtual Test Bed for Advanced Power Sources, R.A. Dougal, M. Blackwelder, S. Liu, L. Gao, Journal of Power Sources, Vol. 110, No 2, pp 285-294, Aug 2002.
111. Mathematical Modeling of Lithium and Nickel Battery Systems, Parthasarathy M. Gomadam, John W. Weidner, Roger A. Dougal, Ralph E. White, Journal of Power Sources Vol. 110, No 2, pp 267-284, Aug 2002.
112. Dynamic Multi-Physics Model for Solar Array, Liu, S., R. Dougal, IEEE Transactions on Energy Conversion, Vol. 17, No. 2, pp. 285-294, June 2002.
113. Jian Wu, Noel N. Schulz and Wenzhong Gao, "Distributed Simulation For Electric Power System Analysis," Electric Power Systems Research, Vol. 77, Issue 8, June 2007, pp. 1124-1131.
114. Sarika Khushalani, Jignesh M. Solanki and Noel N. Schulz, "Optimized Restoration of Unbalanced Distribution Systems," IEEE Transactions on Power Systems, Vol. 22, No. 2, May 2007. pp. 624-630.
115. Sarika Khushalani, Jignesh Solanki and Noel Schulz, "Development of Three Phase Unbalanced Power Flow with Multiple Distributed Generators and Study of their Impact on Distribution Systems," IEEE Transactions on Power Systems, Vol. 22, Issue 3, Aug. 2007, pp. 1019-1025.
116. Jignesh Solanki, Sarika Khushalani and Noel N. Schulz, "A Multi-Agent Solution to Distribution Systems Restoration," IEEE Transactions on Power Systems, Vol. 22, Issue 3, Aug. 2007, pp. 1026-1034.

117. Yanfeng Gong, Yan Huang and Noel N Schulz, "Integrated Protection System Design for Shipboard Power Systems," IEEE Transactions on Industrial Applications, accepted and in press.
118. Jian Wu, Yong Cheng, Noel N. Schulz and Herbert L. Ginn, "Impact of Standardized Models, Programming, Interfaces and Protocols on Shipboard Power Systems, IEEE Transactions on Industrial Applications, Vol. 44, No. 2, March-April 2008, pp. 455-462.
119. Sarika Khushalani, Jignesh Solanki and Noel N. Schulz, "Optimized Restoration of Combined AC/DC Shipboard Power Systems Including Distributed Generation and Islanding Techniques," Electric Power Systems Research, vol. 78, no. 9, September 2008, p. 1528-1536.
120. Sujatha Kotamarty, Sarika Khushalani and Noel N. Schulz, "Impact of Distributed Generation on Distribution Contingency Analysis," Electric Power System Research, Elsevier, vol. 78, no. 9, September 2008, p. 1537-1545.
121. Tang, Yanfeng Gong, Noel Schulz, Mischa Steurer and Peter G. McLaren, "Hardware Implementation of Ship-Wide Area Differential Protection Scheme," IEEE Transactions on Industrial Applications, accepted and in press.
122. Konstantin Borisov, Herbert L. Ginn III, and Andrzej M. Trzynadlowski: "Attenuation of Electromagnetic Interference in a Shunt Active Power Filter," IEEE Transactions on Power Electronics, Vol. 22, Sept. 2007, No. 5, pp. 1912-1918.
123. Herbert L. Ginn III, "A Hybrid Reference Signal Generator for Active Compensators," Electrical Power Quality and Utilisation Journal, Volume XIII, Number 1, July 2007, pp. 51-57.
124. Herbert L. Ginn III, "A Flexible Reference Signal Generation Algorithm for Active Filters", submitted to IEEE Transactions on Power Delivery.
125. Konstantin Borisov, Herbert Ginn, and Guangda Chen, "A computationally efficient RDFT based Reference Signal Generator for Active Compensators," submitted to IEEE Transactions on Power Delivery.
126. Herbert L. Ginn III and Guangda Chen, "Flexible Active Compensator Control for Variable Compensation Objectives", submitted to IEEE Transactions on Power Electronics.
127. J.L. Cale, S.D. Sudhoff, "Accurately Modeling EI Core Inductors Using a High Fidelity Magnetic Equivalent Circuit Approach," IEEE Transactions on Magnetics, Vol. 42, Issue 1, Jan 2006, pp. 40-46.
128. J.L. Cale, S.D. Sudhoff, "An Improved Magnetic Characterization Method for Highly Permeable Materials," IEEE Transactions on Magnetics. Vol. 42, Issue 8, August 2006
129. J. Lian, Y. Lee, S.D. Sudhoff, S.H. Žak, "Self-Organizing Radial Basis Function Network for Real-Time Approximation of Continuous-Time Dynamical Systems," IEEE Transactions on Neural Networks, Vol. 19, No. 3, March 2008, pp. 460-474.
130. R.R. Chan, Y. Lee, S.D. Sudhoff, E.L. Zivi, "Evolutionary Optimization of Power Electronics Based Systems," accepted for IEEE Transactions on Power Electronics (Accepted February 2008)
131. J.L. Cale, S.D. Sudhoff, R.R. Chan, "A Field-Extrema Hysteresis Loss Model for High-Frequency Ferrimagnetic Materials" accepted for IEEE Transactions on Magnetics (Accepted March 2008)
132. Y. Lee, S. Hui, E. Zivi and S. H. Žak, "Variable neural adaptive robust controllers for uncertain systems," International Journal of Adaptive Control and Signal processing, Vol. 22, 2008, in print.
133. W. Zhu, B. Fahimi, and S. Pekarek, "A Field Reconstruction Method for Optimal Excitation of Surface Mounted Permanent Magnet Synchronous Machines," IEEE Transactions on Energy Conversion, Vol. 21, No. 2, June 2006, pp. 303-313.

134. W. Zhu, S. Pekarek, B. Fahimi, B. Deken, "Investigation of Force Generation in a Permanent Magnet Synchronous Machine," *IEEE Transactions on Energy Conversion*, Vol. 22, No. 3, September 2007, pp. 557-565.
135. D. Wu, S. Pekarek, B. Fahimi, "A Field Reconstruction Technique for Efficient Modeling of the Fields and Forces within Induction Machines," accepted for publication in *IEEE Transactions on Energy Conversion* – to appear in 2008.
136. P. Beccue, S. Pekarek, "A Coupled Piezoelectric/Single-Hall-Sensor Position Observer for Permanent Magnet Synchronous Machines," *IEEE Transactions on Industry Electronics: Special Issue on Latest Advances in Machines/Drives*, Vol. 54, No. 5, Oct. 2007, pp. 2389-2397.
137. D. Wu, S. Pekarek, B. Fahimi, "A Voltage-Input-Based Field Reconstruction Technique for Efficient Modeling of the Fields and Forces within Induction Machines," invited for publication in the *IEEE Transactions on Industrial Electronics*, 2008.
138. Hover, F.S., "Dynamic Optimization with Legendre Chaos," *Automatica*, in press, 2007.
139. Prempraneerach P., F.S. Hover, M.S. Triantafyllou, T.J. McCoy, C. Chryssostomidis, and G.E. Karniadakis, "Sensitivity Analysis of the Shipboard Integrated Power System," *Naval Engineering Journal* 119, No. 2, 2007.
140. Taylor, J.A., and F.S. Hover, "Cubature Using Sparse Grids with Shifted Indexing," *Mathematics of Computation*, submitted, September 2007.
141. Prempraneerach P., Hover F., Triantafyllou M.S., Chryssostomidis C. and Karniadakis G.E., "Uncertainty Quantification in Simulations of Power Systems: Multi-Element Polynomial Chaos methods", submitted, *International Journal of Electrical Power and Energy Systems* (Ms. Ref. No.: IJEPES-D-07-00302).
142. Prempraneerach P., Hover F., Triantafyllou M.S., Chryssostomidis C. and Karniadakis G.E., "Stochastic Sensitivity Methods and Application to the Shipboard Power System", submitted, *IEEE Transactions on Power Systems*.
143. J.C. Ordonez, J.V. C. Vargas and R. Hovsapian, "Modeling and Simulation of the Thermal and Psychrometric Transient Response of All Electric Ships, Internal Compartments and Cabinets," *Transactions of the Society for Modeling and Simulation International*, 2008
144. T.E. Brinson, W. Ren, J.C. Ordonez, C.A. Luongo, and T. Baldwin, "Fuel Cell-Based Powertrain System Modeling and Simulation for Small Aircraft Propulsion Applications," *Journal of Fuel Cell Science and Technology*, 2008
145. W. Wechsato, S. Lorente, A. Bejan and J.C. Ordonez, Elemental Shapes (T- and Y-Shapes) of Tree Networks Constructed of Ducts with Various Cross-Sectional Shapes, *Journal of Hydraulics*, 2008
146. R. Hovsapian, J.V. C. Vargas, J.C. Ordonez, A. Krothapalli, J.A. R. Parise, J.C. Berndsen. Thermodynamic Optimization of a Solar System for Cogeneration of Water Heating and Absorption Cooling, *International Journal of Energy Research*, 2008
147. R. L. S. Mainardes, R. S. Matos, J. V. C. Vargas, and J.C. Ordonez, "Optimally staggered finned circular and elliptic tubes in turbulent forced convection," *Journal of Heat Transfer*, vol. 129, pp. 674-678, 2007
148. S. Chen, J.C. Ordonez, and J.V.C. Vargas, "Transient Operation and Shape Optimization of a Single PEM Fuel Cell", *Journal of Power Sources*, 162(1), (2006) 356-368.
149. A.M. Morega, J.C. Ordonez, J.V.C. Vargas and S. Kosaraju. "A Finite Element Method (FEM) Analysis and Optimization of a PEM-Fuel Cell with Interdigitated Flow Field Design", *International Journal of Energy Technologies and Policy*, 2007. (In press)
150. J.C. Ordonez, S. Chen, J.V.C. Vargas, "Constructal Flow Structure for a Single SOFC", submitted to *International Journal of Energy Research*, 2006. (In press)

151. J.V.C. Vargas, J.C. Ordonez, and A. Bejan, "Constructal PEM Fuel Cell Stack Design", *International Journal of Heat and Mass Transfer*, 48 (2005) 4410- 4427.
152. L.S. Mainardes, R.S. Matos, J.V.C. Vargas, and J.C. Ordonez, "Optimally Staggered Finned Circular and Elliptic Tubes in Turbulent Forced Convection", *Journal of Heat Transfer*, 2007.
153. P.J. Masson, P.Tixador, J.C. Ordonez, A.M. Morega, and C.A. Luongo, "Electro-Thermal Model for HTS Motor Design", *IEEE Transactions on Applied Superconductivity*, 2007.
154. W. Wechsato, J.C. Ordonez, and S. Kosaraju, "Constructal Dendritic Geometry and the Existence of Asymmetric Trees", *Journal of Applied Physics*, 100 (2006) 113514, 1-11.
155. J. V. C. Vargas, J. C. Ordonez, C. Zamfirescu, M.C. Campos and A. Bejan, "Optimal Ground Tube Length for Cooling of Electronics Shelters", *Heat Transfer Engineering*, 26 (10):8-20, 2005.
156. 1. Da Zhang, Hui Li, Emmanuel Collins, "Digital anti-windup PI controllers for variable-speed motor drives using FPGA and stochastic theory", *IEEE Transaction on Power Electronics*, Vol. 21, Issue 5, 2006, Page(s):1496-1501.
157. 2. Hui Li, Da Zhang, Simon Foo, "A Stochastic Digital Implementation of a Neural Network Controller for Small Wind Turbine Systems", *IEEE Transaction on Power Electronics*, Vol.21, Issue 5, 2006, Page(s):1502-1507
158. 3. Da Zhang and Hui Li, "A Stochastic-based controller for an induction motor drive with integrated Neural Network algorithms," *IEEE Transactions on Industrial Electronics*, Vol. 55, Issue 2, 2008, Page(s): 551-561
159. 4. Danwei Liu, Hui Li, "A ZVS bi-directional dc-dc converter for multiple energy storage elements", *IEEE Transaction on Power Electronics*, Vol. 21, Issue 5, 2006, pp.1513-1517.
160. 5. Keli Shi, Hui Li, "Optimized PWM Strategy Based on Genetic Algorithms", *IEEE Transaction on Industrial Electronics*, Volume 52, Issue 5, Oct. 2005 Page(s): 1458 – 1461
161. Li, H.; Liu, D.; Luongo, C.A.;"Investigation of Potential Benefits of MOSFETs Hard-Switching and Soft-Switching Converters at Cryogenic Temperature", *IEEE Transactions on Applied Superconductivity*, Volume 15, Issue 2, June 2005 Page(s): 2376-2380
162. Li, H.; Baldwin, T.L.; Luongo, C.A.; Zhang, D.;"A Multilevel Power Conditioning System for Superconductive Magnetic Energy Storage", *IEEE Transactions on Applied Superconductivity*, Volume 15, Issue 2, June 2005 Page(s):1943-1946
163. Hui Li; Cartes, D.; Steurer, M.; Haibin Tang, "Control design of STATCOM with superconductive magnetic energy storage", *IEEE Transactions on Applied Superconductivity*, Volume 15, Issue 2, June 2005 Page(s):1883 – 1886
164. Li-Hsiang Sun, David Cartes, "A Multi-Agent System for Reconfiguration of Shipboard Power Systems," *IASME Transactions*, Vol. 1, No. 2, April 2004, pp. 312-317.
165. L.-H. Sun, G. Morejon, D. Cartes, "Interfacing Software Agents with Power System Simulations," *IASME Transactions*, Vol. 1, No. 2, April 2004, pp. 312-317.
166. K. Huang, S. K. Srivastava, D. A. Cartes, and L. Sun, "Market based Multi-agent System for Reconfiguration of Shipboard Power Systems," submitted to *Electric Power Systems Research*.
167. K. Huang, D. A. Cartes, and S. K. Srivastava, "A Multi-agent Based Algorithm for Ring-structured Shipboard Power System Reconfiguration," *IEEE Transactions on Systems, Man, and Cybernetics Part C*, Vol. 37, Issue 5, September 2007, pp. 1016-1021.
168. K. Huang, S. K. Srivastava, and D. A. Cartes, "Solving Information Accumulation Problem in Mesh Structured Agent System," *IEEE Transactions on Power Systems*, Vol. 20, Issue 1, February 2007, pp. 493-495.
169. Z. Ding, S. K. Srivastava, D. Cartes, and S. Suryanarayanan, "Dynamic Simulation Based Analysis of a New Load Shedding Scheme for a Notional Destroyer Class Shipboard Power System," submitted to *IEEE Transactions of Industry Applications*.

170. Li Liu, and D.A. Cartes, "Synchronization Based Adaptive Parameter Identification for Permanent Magnetic Synchronous Motors," IET Proc. Control Theory & Applications, Vol. 1, Issue 4, pp. 1015-1022, July 2007.
171. Li Liu, K.P. Logan, D.A. Cartes, and S.K. Srivastava, "Fault Detection, Diagnostics, and Prognostics: Software Agent Solutions," IEEE Trans. on Vehicular Technology, Vol. 56, Issue. 4, Part 1, pp. 1613-1622, July 2007.
172. Lewei Qian, David Cartes, and Hui Li, "An Improved Adaptive Detection Method for Power Quality Improvement," IEEE Transactions on Industry Applications, accepted and in press.
173. Li Qi, Lewei Qian, David Cartes and S. Woodruff, "Prony Analysis for Power System Transient Harmonics," EURASIP Journal of Applied Signal Processing, accepted and in press.
174. Lewei Qian, Li Liu and David Cartes, "A Flexible Experimental Footprint for Power Electronics and Power Systems Research," IEEE Transactions on Power Systems, first review completed and under second revision.
175. Wei Ren, Lewei Qian, David Cartes and M. Steurer, "A Multivariable Control Method in STATCOM Application for Performance Improvement," IEEE Transactions on Industry Applications, under review.
176. Qiang Zhang, Lewei Qian, Chongwei Zhang and David Cartes, " Study On Grid Connected Inverter Used in High Power Wind Generation System," IEEE Transactions on Industry Applications, under review.
177. Lewei Qian, Wenxin Liu, David Cartes and Hui Li, " A Particle Swarm Optimization Tuned Adaptive Harmonic Detection Method," IEEE Transactions on Power Delivery, under review.
178. Lewei Qian, David Cartes and Hui Li, "Experimental Verification and Comparison of Adaptive and D-Q Selective Harmonic Detection Methods," IEEE Transactions on Industrial Electronics, under review.

Theses/Dissertations

1. "Creation of a Modeling and Simulation Environment for Thermal Management of an All-Electric Ship," Patrick Paullus, Master's Thesis, The University of Texas at Austin, December 2007.
2. "Dynamic thermal-mechanical-electrical modeling of the integrated power system of a notional all-electric naval surface vessel," C.R. Holsonback, Master's Thesis, The University of Texas at Austin, Engineering, May 2007.
3. "Computational and experimental study of film cooling performance including shallow trench configurations," K.L. Harrison, Master's Thesis, The University of Texas at Austin, December 2006.
4. M. Shelton, BS, ECE, December 2006.
5. A. Wang, BS, ECE, December 2006.
6. "Rough wall and near-hole obstruction effects on film cooling with and without a transverse trench," R.P. Somawardhana, Master's Thesis, The University of Texas at Austin, December 2006.
7. "Thermal management of pulsed loads on an all-electric ship," T.W. Webb, Master's Thesis, The University of Texas at Austin, Department of Mechanical Engineering, August 2006.

8. "Dynamic modeling and analysis of an automatic reconfigurable shipboard power system," J.A. Park, Master's Thesis, The University of Texas at Austin, Department of Mechanical Engineering, May 2006.
9. "Effects of Regular and Random Roughness on the Heat Transfer and Skin Friction Coefficient on the Suction Side of a Gas Turbine Vane," J.E. Dees, Master's Thesis, The University of Texas at Austin, 2006.
10. "Optimizing a system of gas turbine engines and generators for marine power generation," S. Vijlee, Master's Thesis, The University of Texas at Austin, Department of Mechanical Engineering, May 2006.
11. "Steady-state and dynamic simulation of large, ship-based thermal systems," S.T. Haag, Master's Thesis, The University of Texas at Austin, December 2005.
12. "Dynamic reconfiguration of shipboard power systems preserving stability," K.C. Nagaraj, Master's Thesis, The University of Texas at Austin, Department of Electrical Engineering, August 2005.
13. "Numerical simulations for a discrete-time stochastic LQG problem with observation cost," G.S. Rajadhyaksha, Master's Thesis, The University of Texas at Austin, Department of Electrical Engineering, May 2005.
14. "Investigation of optimization methods used for reconfiguration of the naval electric ship power system," C.D. Meek, Master's Thesis, The University of Texas at Austin, December 2004.
15. "Improved thermal management of an all-electric ship through modeling and simulation," B.C. Carroll, Master's Thesis, The University of Texas at Austin, Department of Mechanical Engineering, August 2004.
16. "Theory and application of time-frequency analysis to transient phenomena in electric power and other physical systems," Y.-J. Shin, PhD Dissertation, The University of Texas at Austin, August 2004.
17. "Roughness impact on turbine vane suction side film cooling effectiveness," D. Robertson, Master's Thesis, The University of Texas at Austin, May 2004.
18. "Suction side roughness effects on film cooling heat transfer on a turbine vane," J. Rutledge, Master's Thesis, The University of Texas at Austin, May 2004.
19. "Models and methods for shipboard power system reconfiguration," J. Billo, Master's Thesis, The University of Texas at Austin, Department of Electrical Engineering, December 2003.
20. "Higher-order spectral analysis for machine condition monitoring," B. Jang, Master's Thesis, The University of Texas at Austin, May 2003.
21. Nicholas Amann, Masters of Science Thesis, "ADAPTIVE OVERCURRENT PROTECTION SCHEME FOR SHIPBOARD POWER SYSTEMS," 2004.
22. Jian Wu, Masters of Science Thesis, "Data modeling for shipboard power system", 2004.
23. Yan Huang, Masters of Science Thesis, "FAST RECONFIGURATION ALGORITHM DEVELOPMENT FOR SHIPBOARD POWER SYSTEMS", 2005.
24. Yanfeng Gong, PhD Dissertation, "DEVELOPMENT OF AN IMPROVED ON-LINE VOLTAGE STABILITY INDEX USING SYNCHRONIZED PHASOR MEASUREMENT", 2005.
25. Anil Kondabathini, Masters of Science Thesis, "An Accurate Method to Measure Harmonics and Interharmonics in Shipboard Power Quality Analysis, May 2006.
26. Yong Cheng, Masters of Science Thesis, "Power Electronics Controller Prototyping Tool for Power System Applications, May 2006.
27. Jian Wu, PhD Dissertation, "Generalized Three Phase Distributed Simulation of Power System Applications, May 2006.
28. Sarika Khushalani, "PhD Dissertation, "DEVELOPMENT OF POWER FLOW WITH DISTRIBUTED GENERATORS AND RECONFIGURATION FOR RESTORATION OF UNBALANCED DISTRIBUTION SYSTEMS," August 2006.

29. Sujatha Kotamarthy, Masters of Science Thesis, "Impact of Distributed Generation on Distribution Contingency Analysis, May 2006.
30. Daxa Patel, Masters of Science Thesis, "Modeling and Testing of An Instantaneous Overcurrent Relay Using VTB and VTB-RT, June 2006.
31. Qinghua Huang, Masters of Science Thesis, " Digital Phase-locked Loop Design for Naval Applications, December 2006.
32. Jignesh Solanki, PhD Dissertation, "MULTI-AGENT BASED CONTROL AND RECONFIGURATION FOR RESTORATION OF DISTRIBUTION SYSTEMS WITH DISTRIBUTED GENERATORS, December 2006.
33. Hymiar Hamilton, Master of Science Thesis, "AN IMPACT STUDY OF DC PROTECTION TECHNIQUES FOR SHIPBOARD POWER SYSTEMS", Mississippi State University, August 2007.
34. Oluwaseun Adeyemi Amoda, Masters of Science Thesis, "DEVELOPMENT OF AN ADAPTIVE PROTECTION SCHEME FOR SHIPBOARD POWER SYSTEMS", Mississippi State University, August 2007.
35. Konstantin A. Borisov, PhD Dissertation, "MULTIFUNCTIONAL VOLTAGE SOURCE CONVERTER FOR SHIPBOARD POWER SYSTEMS", Mississippi State University, August 2007.
36. Sandhya Sankar, Masters of Science Thesis, "INTELLIGENT PLACEMENT OF METERS/SENSORS FOR SHIPBOARD POWER SYSTEM ANALYSIS", Mississippi State University, December 2007.
37. Koteswar Reddy Padamati, Masters of Science Thesis, "RECONFIGURATION OF SHIPBOARD POWER SYSTEMS USING A GENETIC ALGORITHM", Mississippi State University, December 2007.
38. Prashanth Duvor, Masters of Science Thesis, "Energy Storage System Requirements for Shipboard Power Systems Supplying Pulsed Power Loads, December 2007.
39. Prempraneerach P., "Uncertainty Analysis in a Shipboard Integrated Power System using Multi-Element Polynomial Chaos", Ph.D. thesis defense, Feb. 2007.
40. Mitchell, G., "Shipboard Fluid System Diagnostics using Non-Intrusive Load Monitoring," June 2007
41. Bennett, P., "Using the Non-Intrusive Load Monitor for Ship-Board Supervisory Control," June 2007
42. Piber, M., "Improving Shipboard Maintenance Practices Using Non-Intrusive Load Monitoring," June 2007
43. Cox, R., "Minimally Intrusive Strategies for Fault Detection and Energy Monitoring," September 2006 (Professor at University of North Carolina, Charlotte).
44. McKay, T.D., "Diagnostic Indicators for Shipboard Mechanical Systems Using Non-Intrusive Load Monitoring," June 2006
45. Mosman, J., "Evaluation of Non-Intrusive Load Monitoring for Shipboard Cycling System Diagnostics," (Naval Engineer), June 2006
46. Denucci, T., "Diagnostic Indicators for Shipboard Systems using Non-Intrusive Load Monitoring," (Mechanical and Navel Engineering), June 2005.
47. Greene, W. "Evaluation of Non-Intrusive Monitoring for Condition Based Maintenance Applications on US Navy Propulsion Plants," June 2005.
48. Ramsey, J., "Shipboard Applications of Non-Intrusive Load Monitoring," June 2004.
49. Guanglei Wang, Real Time Simulation on Multiple DSP Platform, May 2008.
50. Anton Smith, Robust and Optimal Control Using Polynomial Chaos Theory, May 2007.
51. Zimin Wu Vilar, Effect of Large Load Disturbances on a Limited-size AC Power System including a High Speed Turbo-generator, May 2007.
52. Aalhad Deshmukh, Agent Based Control and Monitoring System for Dynamic Reallocation of Loads in a Limited Power Supply Scenario, December 2006.

53. Liqing Lu, Physical Modeling Of Variable-Lifetime P-I-N Diodes And Of Two-Dimensional Effects In Insulated Gate Bipolar Transistors (IGBTs), December 2006.
54. Kinjal Patel, A Prototype of a Modular Linear Motor, August 2006.
55. Wei Jiang, Models Development and System Simulation of Solid Oxide Fuel Cell / Gas Turbine Hybrid Cycle, August 2006.
56. Guangli Yang, Conformal Multi-functional Antennas and Rectifying Circuits for Wireless Communication and Microwave Power Beaming, December 2005.
57. Santiago Lentijo, Processor-in-the-Loop and Power-Hardware-in-the Loop Procedures for Virtual Prototyping, December 2005.
58. Nivert Rathle, Design Procedure for Active Filters for Improving Power Quality, December 2005.
59. Saiying Zhou, An Advanced Boundary Element Method for Ship/Water Dynamic Interaction Analysis, August 2005.
60. Donghong Li, *Application of Synergetic Control to Switching Converter: Synthesis, Stability Analysis and Implementation*, August 2005.
61. Yujie Song, Wavelet Neural Networks in Nonlinear System Modeling and Motor Drives, August 2005.
62. Davide Franzoni, An Active Filter for Fuel Cell Applications, August 2005.
63. Jimena Bastos, Nonlinear Control Design via Symbolic Computation: Applying Synergetics to the Control of Power Electronics Systems, August 2005.
64. Hernan Figueroa, Novel Interface based on the Firing Signal Averaging Method for Accurate Hardware-in-the-Loop Testing of Digital Controllers for Power Electronics Applications, May 2005.
65. Xin Wu, Methods for Partitioning the System and Performance Evaluation in Power Hardware in the Loop Simulations, May 2005.
66. Igor Kondratiev, A Synergetic Control for Parallel-connected DC-DC Buck Converters, May 2005.
67. Mark Blackwelder, System-Level Model of a Polymer Electrolyte Membrane Fuel Cell Stack, May 2005.
68. Teems Lovett, A Polynomial Chaos Approach to Network Simulation Under Uncertainty, December 2004.
69. Xiaobin Wang, Characteristics and Simulation of Integrated Gate Commutated Thyristor (IGCT), May 2004.
70. Antonio Caiafa, Cryogenic Behavior of Insulated Gate Bipolar Transistors (IGBTs) May 2004.
71. Zhenhua Jiang, A Fuel Cell Powered Battery-Charging Station, August 2003
72. Lijun Gao, Design and Optimization of Fuel Cell/Battery Supercapacitor Hybrid Power Sources for Electric Vehicles, August 2003.
73. Xiaosong Kang, Characterization and Modeling of Trench Gate Punch through IGBTs, December 2002.

Proceedings / Technical Reports

1. "Dynamic Thermal-Mechanical-Electrical Modeling of the Integrated Power System of a Notional All-Electric Naval Surface Ship," C.R. Holsonback and T.M. Kiehne, submitted for publication and presentation at ASNE Day, June 2008.
2. "Condition monitoring based on estimating the complex coupling coefficients," H. Park, E.J. Powers, W.M. Grady, and A. Arapostathis, submitted to the IEEE International Instrumentation & Measurement Technology Conference (I2MTC'08), Victoria, BC, Canada, May 12-15, 2008.
3. "Led lamp flicker caused by interharmonics," T. Kim, M.Rylander, E.J. Powers, W.M. Grady and A. Arapostathis, submitted to the IEEE International Instrumentation & Measurement Technology Conference (I2MTC'08), Victoria, BC, Canada, May 12-15, 2008.
4. "Stability and controllability of planar, conewise linear systems," A. Arapostathis and M.E. Broucke, IEEE Conference on Decision and Control, December 2007.
5. "Stability and controllability of planar, conewise linear systems," A. Arapostathis and M.E. Broucke, IEEE Conference on Decision and Control, December 2007.
6. "Electrical insulation challenges for rotating machines used on future electric ships," R.E. Hebner, Proc. 28th Electrical Insulation Conference, held in conjunction with 2007 EIC/Electrical Manufacturing Expo (2007 EIC/EMExpo), Nashville, Tennessee, U.S.A., October 22-24, 2007, pp. 1-4.
7. "Reconfiguration in shipboard power systems," K.R. Davey, R. Longoria, W.L. Shutt, J. Carroll, K.C. Nagaraj, J.A. Park, T. Rosenwinkel, W. Wu, and A. Arapostathis, 2007 American Control Conference (ACC '07), New York, NY, USA, 11-13 July 2007.
8. "Markov decision processes with controlled observations and the sensor querying problem," W. Wu and A. Arapostathis, European Control Conference (ECC 2007), Kos Island, Greece, 2-5 July 2007, pp. 611-618.
9. "Development and analysis of trapped field magnets in electromechanical devices," K.R. Davey, R. Weinstein, and R. Sawh, 16th International Conference on the Computation of Electromagnetic Fields (COMPUMAG 2007), Aachen, Germany, 24-28 June 2007.
10. "Latin hypercube sampling and pattern search in magnetic field optimization problems," K.R. Davey, 16th International Conference on the Computation of Electromagnetic Fields (COMPUMAG 2007), Aachen, Germany, 24-28 June 2007.
11. "Machine condition monitoring utilizing a novel bispectral change detection," H. Park, B. Jang, E.J. Powers, W.M. Grady, and A. Arapostathis, Proc. IEEE Power Engineering Society General Meeting, Tampa, Florida, USA, 24-28 June 2007.
12. "ASD system condition monitoring using cross bicoherence," T. Kim, W. Cho, E.J. Powers, W.M. Grady and A. Arapostathis, Proc. IEEE Electric Ship Technologies Symposium (ESTS 2007), Arlington, Virginia, USA, 21-23 May 2007, pp. 378-383.
13. "Directly-coupled gas turbine permanent magnet generator sets for prime power generation on board electric ships," S. Vijlee, A. Ouroua, L.N. Domaschk, J.H. Beno, Proc. IEEE Electric Ship Technologies Symposium (ESTS 2007), Arlington, Virginia, USA, 21-23 May 2007, pp. 340-347.
14. "Enhancement and application of a voltage sag station to test transient load response," M.R. Rylander, W.M. Grady, A. Arapostathis, E.J. Powers, Proc. IEEE Electric Ship Technologies Symposium (ESTS 2007), Arlington, Virginia, USA, 21-23 May 2007, pp. 428-433.
15. "Optimal power generation scheduling of a shipboard power system," W. Wu, D. Wang, A. Arapostathis, and K.R. Davey, Proc. IEEE Electric Ship Technologies Symposium (ESTS 2007), Arlington, Virginia, USA, 21-23 May 2007, pp. 519-522.
16. "Perspectives on power system reconfiguration for shipboard applications," K.C. Nagaraj, J. Carroll, T. Rosenwinkel, A. Arapostathis, W.M. Grady, and E.J. Powers, Proc. IEEE Electric Ship Technologies Symposium (ESTS 2007), Arlington, Virginia, USA, 21-23 May 2007, pp. 188-195.

17. "Practical considerations in implementing shipboard power system reconfiguration control schemes," M. Shasteen, K.R. Davey, R. Longoria, W.L. Shutt, Proc. IEEE Electric Ship Technologies Symposium (ESTS 2007), Arlington, Virginia, USA, 21-23 May 2007, pp. 196-200.
18. "System-level thermal management for all-electric ships," T.M. Kiehne, S.T. Haag, T.W. Webb, C.R. Holsonback, and P.E. Paullus, Proc. IEEE Electric Ship Technologies Symposium (ESTS 2007), Arlington, Virginia, USA, 21-23 May 2007, presentation only.
19. "Thermal characterization of an integrated electric propulsion system on a notional DDG 1000," T.M. Kiehne, S. Haag, T. Webb, C. Holsonback, and P. Paullus, IEEE Electric Ship Technologies Symposium, Arlington, Virginia, USA, May 21-23, 2007
20. "CFD predictions of film cooling adiabatic effectiveness for cylindrical holes embedded in narrow and wide transverse trenches," K.L. Harrison and D.G. Bogard, ASME Turbo Expo 2007 – Gas Turbine Technical Congress & Exposition, paper GT2006-28005, Montreal, Canada, 14-17 May 2007.
21. "Effects of obstructions and surface roughness on film cooling effectiveness with and without a transverse trench," R.P. Somawardhana and D.G. Bogard, ASME Turbo Expo 2007 – Gas Turbine Technical Congress & Exposition, paper GT2007-28003, Montreal, Canada, 14-17 May 2007.
22. "Effects of surface roughness and near hole obstructions on film cooling effectiveness," R.P. Somawardhana and D.G. Bogard, ASME Turbo Expo 2007 – Gas Turbine Technical Congress & Exposition, paper GT2007-28004, Montreal, Canada, 14-17 May 2007.
23. "Turbine airfoil net heat flux reduction with cylindrical holes embedded in a transverse trench," K.L. Harrison, J.R. Dorrington, J.E. Dees, D.G. Bogard, and R.S. Bunker, ASME Turbo Expo 2007 – Gas Turbine Technical Congress & Exposition, paper GT2007-27996, Montreal, Canada, 14-17 May 2007.
24. "A novel QPC detector for the health monitoring of rotating machines," T. Kim, E.J. Powers, W.M. Grady and A. Arapostathis, Proc. IEEE Instrumentation and Measurement Technology Conference (IMTC 2007), Warsaw, Poland, 1-3 May 2007.
25. "Detection of light flicker caused by high-frequency interharmonics," T. Kim, A. Wang, E.J. Powers, W.M. Grady, and A. Arapostathis, Proc. IEEE Instrumentation and Measurement Technology Conference (IMTC 2007), Warsaw, Poland, 1-3 May 2007.
26. "Composite banding for DRS HSG rotor using a novel assembly approach," R. Thompson, Workshop on Transportable Megawatt Power Systems, Austin, Texas, USA, 6-7 March 2007, presentation only - no paper.
27. "Design challenges in wound-rotor high speed motors and generators," J.D. Herbst, Workshop on Transportable Megawatt Power Systems, Austin, Texas, USA, 6-7 March 2007, presentation only - no paper.
28. "Estimation of system-level thermal loads on DDG 1000," C.R. Holsonback and T.M. Kiehne, Workshop on Transportable Megawatt Power Systems, Austin, Texas, USA, March 6-7, 2007, paper under review.
29. "Generator life and power electronics," K.R. Davey, R. Rodriguez, H. Jordan, R. Limpaecher, and R.E. Hebner, Workshop on Transportable Megawatt Power Systems, Austin, Texas, USA, 6-7 March 2007, presentation with paper under review.
30. "Magnetic materials for high rotational velocity machines: a fresh look at an old problem," A.T. Wilder, Workshop on Transportable Megawatt Power Systems, Austin, Texas, USA, 6-7 March 2007, presentation with paper under review.
31. "Multi-megawatt gas turbine permanent magnet generator sets for electric ships," A. Ouroua, L.N. Domaschk, S. Vijlee, J.R. Jackson, and J.H. Beno, Workshop on Transportable Megawatt Power Systems, Austin, Texas, USA, 6-7 March 2007, presentation only - no paper.

32. "Optimal power generation scheduling of a shipboard power system with energy storage," W. Wu, D. Wang, A. Arapostathis, and K.R. Davey, Workshop on Transportable Megawatt Power Systems, Austin, Texas, USA, 6-7 March 2007, presentation only - no paper.
33. "Power grid for a naval electric ship - ac versus dc," K.R. Davey, Workshop on Transportable Megawatt Power Systems, Austin, Texas, USA, March 6-7, 2007, presentation with paper under review.
34. "Propulsion system simulation of a DDG 1000-like ship," C.R. Holsonback, Workshop on Transportable Megawatt Power Systems, Austin, Texas, USA, 6-7 March 2007, presentation only - no paper.
35. "Soft switching drive for a megawatt class, variable speed, motor/generator," A.L. Gattozzi, R.F. Thelen, A.S. Williams, Workshop on Transportable Megawatt Power Systems, Austin, Texas, USA, 6-7 March 2007, presentation with paper under review.
36. "System-level thermal management on an all-electric ship," T.M. Kiehne, Workshop on Transportable Megawatt Power Systems, Austin, Texas, USA, 6-7 March 2007, presentation only - no paper.
37. "Technical challenges in high speed gen-set systems – an overview," R.E. Hebner, Workshop on Transportable Megawatt Power Systems, Austin, Texas, USA, 6-7 March 2007, presentation only - no paper.
38. "The electric ship – ac versus dc?," K.R. Davey and R.E. Hebner, Workshop on Transportable Megawatt Power Systems, Austin, Texas, USA, 6-7 March 2007, presentation with paper under review.
39. "Use of CFD to improve film cooling performance for gas turbine airfoils incorporating shallow trenches," K.L. Harrison, and D.G. Bogard, Workshop on Transportable Megawatt Power Systems, Austin, Texas, USA, 6-7 March 2007, presentation only - no paper.
40. "Some benefits of pulsed alternators as electromagnetic gun power supplies on power systems for future electric ships," R.E. Hebner, J.A. Pappas, J.R. Kitzmiller, K.R. Davey, J.D. Herbst, A. Ouroua, J.H. Beno, Engine as a Weapon II, London, UK, 5-6 December 2006.
41. "Analytical modeling of SRAM dynamic stability," B. Zhang, M. Orshansky, and A. Arapostathis, IEEE/ACM 2006 International Conference on Computer-Aided Design (ICCAD 2006), San Jose, California, 5-9 November 2006, pp. 314-322.
42. "Continuum models for broadcasting over sensor networks," S. Subramanian, S. Shakkotai and A. Arapostathis, INFORMS Annual Meeting, Pittsburgh, Pennsylvania, USA, 5-8 November 2006, presentation only.
43. "Examination of the influence of streamer growth criteria on morphology," M. Kim, R.E. Hebner, and G.A. Hallock, 2006 Annual Report IEEE Conference on Electrical Insulation and Dielectric Phenomena (CEIDP), Kansas City, Missouri, USA, 15-18 October 2006, pp. 772-775.
44. "Higher frequency performance of stress-grading systems for HV large rotating machines," R.E. Hebner, H. El-Kishky, M. Abdel-Salam, and F. Brown, 2006 Annual Report IEEE Conference on Electrical Insulation and Dielectric Phenomena, Kansas City, MO, pp. 218-221, 15-18 October 2006.
45. "Minimization of local field enhancement along stress-grading systems of HV large rotating machines," H. El-Kishky, R. Hebner, M. Abdel-Salam, and F. Brown, 2006 Annual Report IEEE Conference on Electrical Insulation and Dielectric Phenomena, Kansas City, MO, pp. 214-217, 15-18 October 2006.
46. "Robust interharmonic detection in adjustable speed drives using cross bicoherence," T. Kim, E.J. Powers, W.M. Grady, and A. Arapostathis, 12th IEEE International Conference on Harmonics and Quality of Power (ICHQP'2006), Cascais, Portugal, 1-5 October 2006.
47. "Capacity results for multiple access channels with transmitter state and feedback," W. Wu, S. Vishwanath, and A. Arapostathis, Proc. 2006 International Symposium on Information Theory (ISIT 2006), Seattle, Washington, USA, July 2006, pp. 962-966.

48. "On optimal control of Markov chains with safety constraint," S.-P. Hsu, A. Arapostathis and Ratnesh Kumar, Proc. 2006 American Control Conference (2006 ACC), paper FrA10.1, Minneapolis, Minnesota, USA, 14-16 June 2006.
49. "Coordination of large pulsed loads on future electric ships," L.N. Domaschk, A. Ouroua, R.E. Hebner, O.E. Bowlin, and W.B. Colson, 13th Electromagnetic Launch Technology Symposium, Potsdam, Brandenburg, Germany, 22-25 May 2006.
50. "High speed generator trade study," K.R. Davey, J.D. Herbst, J. Bravo, R. Ricket, and B. Gamble, ASNE Electric Machines Technology Symposium 2006 (EMTS 2006), Integrated System Approach of the All Electric Force, Philadelphia, PA, USA, 22-24 May 2006.
51. "HTS trapped field magnet-based motors for naval applications," K.R. Davey and R. Weinstein, ASNE Electric Machines Technology Symposium 2006 (EMTS 2006), Integrated System Approach of the All Electric Force, Philadelphia, Pennsylvania, USA, 22-24 May 2006.
52. "System-level modeling and optimal design of an all-electric ship energy storage module," C.R. Holsonback, T.W. Webb, T.M. Kiehne, and C. Conner-Seepersaad, ASNE Electric Machines Technology Symposium 2006 (EMTS 2006), Integrated System Approach of the All Electric Force, Philadelphia, Pennsylvania, USA, 22-24 May 2006.
53. "System-level thermal management of pulsed loads on an all-electric ship," T.W. Webb, T.M. Kiehne, and S.T. Haag, 13th Electromagnetic Launch Technology Symposium, Potsdam, Brandenburg, Germany, 22-25 May 2006.
54. "Observations of stimulated acoustic events concurrent with partial discharge events," A.T. Wilder and J.N. Murdock, IEEE International Power Modulator Conference 2006, Arlington, Virginia, USA, 14-18 May 2006, pp. 61-65, presented at the High Voltage workshop.
55. "High resolution film cooling effectiveness comparison of axial and compound angle holes on the suction side of a turbine vane," S.K. Waye and D.G. Bogard, Proc. ASME Turbo Expo 2006: Power for Land, Sea, and Air (GT 2006), paper GT2006-90225, Barcelona, Spain, 8-11 May 2006.
56. "High resolution film cooling effectiveness measurements of axial holes embedded in a transverse trench with various trench configurations," S.K. Waye and D.G. Bogard, Proc. ASME Turbo Expo 2006: Power for Land, Sea, and Air (GT2006), paper GT2006-90226, Barcelona, Spain, 8-11 May 2006.
57. "The effects of obstructions on film cooling effectiveness on the suction side of a gas turbine vane," P. Demling and D.G. Bogard, Proc. ASME Turbo Expo: Power for Land, Sea, and Air (GT2006), paper GT2006-90577, Barcelona, Spain, 8-11 May 2006.
58. "Useful Techniques for field analysts in the design and optimization of induction motors," K.R. Davey and R.C. Zowarka, 12th Biennial IEEE Conference on Electromagnetic Field Computation (CEFC 2006), Miami, Florida, USA, 30 April-3 May 2006, p. 505.
59. "Challenges and solutions for the use of flywheel energy storage in high power applications," J.D. Herbst, M.T. Caprio, A.L. Gattozzi, and C. Graf, Electrical Energy Storage Applications and Technologies Conference (EESAT 2005), San Francisco, California, USA, 16-19 October, 2005.
60. "A voltage-only method for estimating the location of transmission faults," M. Vatani, W.M. Grady, and A. Arapostathis, Proc. 8th International Conference on Electrical Power Quality and Utilisation (EPQU' 05), Cracow, Poland, 21-23 September 2005, pp. 515-521.
61. "Analyzing voltage sags to determine daily and seasonal variations in transient stability load models," M.R. Rylander, W.M. Grady, A. Arapostathis, and E.J. Powers, Proc. 8th International Conference on Electrical Power Quality and Utilisation (EPQU' 05), Cracow, Poland, 21-23 September 2005, pp. 359-363.
62. "Laminate induction efficiency under biaxial tensile stress at power frequencies," A.T. Wilder, 17th Soft Magnetic Materials Conference (SMM17), Bratislava, Slovakia, 7-9 September 2005.

63. "A voltage sag-based procedure for determining transient stability models of conventional loads," M.R. Rylander, W.M. Grady, A. Arapostathis, and Edward Powers, Proc. IEEE Electric Ship Technologies Symposium (ESTS 2005), Philadelphia, Pennsylvania, USA, 25-27 July 2005, pp. 321-324.
64. "Characterization of power losses in soft magnetic materials," A.T. Wilder, Proc. IEEE Electric Ship Technologies Symposium (ESTS 2005), Philadelphia, Pennsylvania, USA, 25-27 July 2005.
65. "Dynamic reconfiguration preserving stability," J. Carroll, K.C. Nagaraj, A. Arapostathis, W.M. Grady, and E.J. Powers, Proc. IEEE Electric Ship Technologies Symposium (ESTS 2005), Philadelphia, Pennsylvania, USA, 25-27 July 2005, pp. 105-107.
66. "Electric ship power system - research at the University of Texas at Austin," R.E. Hebner, Proc. IEEE Electric Ship Technologies Symposium (ESTS 2005), Philadelphia, Pennsylvania, USA, 25-27 July 2005.
67. "Electric ship power system integration analyses through modeling and simulation," A. Ouroua, L.N. Domaschk, and J.H. Beno, Proc. IEEE Electric Ship Technologies Symposium (ESTS 2005), Philadelphia, Pennsylvania, USA, 25-27 July 2005.
68. "Electro-mechanical actuators for the navy's ships," D. Tesar, Proc. IEEE Electric Ship Technologies Symposium (ESTS 2005), Philadelphia, Pennsylvania, USA, 25-27 July 2005.
69. "Introduction of the concept of friendliness power to characterize the harmonic emission of nonlinear loads," G. Tilte, W.M. Grady, E.J. Powers, A. Arapostathis, and J. Lobry, Proc. IEEE Electric Ship Technologies Symposium (ESTS 2005), Philadelphia, Pennsylvania, USA, 25-27 July 2005, pp. 306-312.
70. "Materials for advanced electric machines: an overview," A.T. Wilder, Proc. IEEE Electric Ship Technologies Symposium (ESTS 2005), Philadelphia, Pennsylvania, USA, 25-27 July 2005, pp. 478-480.
71. "Real and reactive power analysis for interharmonics," T. Kim, E.J. Powers, W.M. Grady, and A. Arapostathis, Proc. IEEE Electric Ship Technologies Symposium (ESTS 2005), Philadelphia, Pennsylvania, USA, 25-27 July 2005, pp. 244-247.
72. "Reconfiguration: a tool for designing new ships," K.R. Davey and R.E. Hebner, Proc. IEEE Electric Ship Technologies Symposium (ESTS 2005), Philadelphia, Pennsylvania, USA, 25-27 July 2005, pp. 81-85.
73. "The incipient mode of streamers in a dielectric liquid as a function of electric field," M. Kim, S.D. Reedy, and R.E. Hebner, 15th IEEE International Conference on Dielectric Liquids (ICDL 2005), Coimbra, Portugal, 26 June-1 July 2005.
74. "Solid dielectric material influence on fast impulse partial discharge behavior," A.T. Wilder, W.K. Eickelberg, and J.W. Wilder, 15th IEEE International Pulsed Power Conference (PPC2005), Monterey, California, USA, 13-17 June 2005, pp. 1155-1158.
75. "Optimal control of stochastic systems with costly observations - the general Markovian model and the LQG problem," W. Wu and A. Arapostathis, Proc. 2005 American Control Conference (ACC 2005), Portland, Oregon, USA, 8-10 June 2005, Vol. 1, pp. 294-299.
76. "Degradation of film cooling performance on a turbine vane suction side due to surface roughness," J.L. Rutledge, D. Robertson, and D.G. Bogard, Proc. ASME Turbo Expo 2005: Power for Land, Sea, and Air, paper GT2005-69045, Reno-Tahoe, Nevada, USA, 6-9 June 2005.
77. "Thermo-kinetic representation and transient simulation of a molten carbonate fuel cell," B.C. Carroll, T.M. Kiehne, and M.D. Lukas, Proc. ASME Third International Conference on Fuel Cell Science, Engineering and Technology, paper FuelCell 2005-74121, Ypsilanti, Michigan, USA, 23-25 May 2005.
78. "Approaches to shipboard power management," K.R. Davey, C.D. Meek, D.W. Tucker, W.L. Shutt, and R.E. Hebner, ASNE Reconfiguration and Survivability Symposium 2005, paper session III-1, Atlantic Beach, Florida, USA, 16-18 February 2005.

79. "Ergodic control of jump diffusions in R^d under a near-monotone cost assumption," A. Arapostathis and M.K. Ghosh, Proc. 43rd IEEE Conference on Decision and Control (CDC 2004), Atlantis, Paradise Island, Bahamas, 14-17 December 2004, Vol. 4, pp. 4140-4145.
80. "On non-stationary policies and maximal invariant safe sets of controlled Markov chains," W. Wu, A. Arapostathis, and R. Kumar, Proc. 43rd IEEE Conference on Decision and Control (CDC 2004), Atlantis, Paradise Island, Bahamas, 14-17 December 2004, Vol. 4, pp. 3696-3701.
81. "An electromagnetic gun power supply as a component of an electric ship power system," R.E. Hebner, J. Pappas, J.R. Kitzmiller, K.R. Davey, J.D. Herbst, A. Ouroua, and J.H. Beno, Proc. American Society of Naval Engineers High Powered Weapons Systems for Electric Ships 2004, Annapolis, Maryland, USA, 7-9 December
82. "Simulation of DDG-51 thermal management systems," S.T. Haag and T.M. Kiehne, Proc. American Society of Naval Engineers High Powered Weapon Systems for Electric Ships Symposium 2004, Annapolis, Maryland, USA, 7-9 December 2004.
83. "Competitive Markov decision processes with partial observation," S.-P. Hsu and A. Arapostathis, Proc. 2004 IEEE International Conference on Systems, Man and Cybernetics (SMC 2004), The Hague, The Netherlands, 10-13 October 2004, Vol. 1, pp. 236-241.
84. "Safety control of partially observed MDPs with applications to machine maintenance problems," S.-P. Hsu and A. Arapostathis, Proc. 2004 IEEE International Conference on Systems, Man and Cybernetics (SMC 2004), The Hague, The Netherlands, 10-13 October 2004, pp. 261-265.
85. "Strict-sense constrained Markov decision processes," S.-P. Hsu and A. Arapostathis, Proc. 2004 IEEE International Conference on Systems, Man and Cybernetics (SMC 2004), The Hague, The Netherlands, 10-13 October 2004, Vol. 1, pp. 194-199.
86. "Development of a test bed system for robot actuators," J.G. Yoo, P. Hvass, C. Kapoor, D. Tesar, Proc. ASME 2004 International Design Engineering Technical Conference and Computers and Information in Engineering Conference (DETC'04), Salt Lake City, Utah, USA, 28 September-2 October 2004.
87. "Determination of transient disturbance energy flow in electric power systems via cross time-frequency distribution," Y.-J. Shin, E.J. Powers, W.M. Grady, and A. Arapostathis, SPIE-Advanced Signal Processing Algorithms, Architectures, and Implementations X, Denver, Colorado, USA, August 2004.
88. "Stability of 2D switched linear systems with conic switching," H. Lens, M.E. Broucke, and A. Arapostathis, Proc. 16th International Symposium on Mathematical Theory of Networks and Systems (MTNS 2004), Katholieke Universiteit Leuven, Belgium, 5-8 July 2004.
89. "A note on some new results on the ergodic control of partially observed Markov chains," S.-P. Hsu and A. Arapostathis, Proc. 2004 American Control Conference, Boston, Massachusetts, USA, 30 June-2 July 2004, vol 1, pp. 708-709.
90. "Effect of EM weapons requirements on the electric ship power system," J.H. Beno, A. Ouroua, and M.M. Flynn, IMAREST Engine as a Weapon Symposium 2004, Bristol, UK, 9-10 June 2004.
91. "Managing multiple and varying energy demands by means of energy storage in combatants with integrated electric propulsion," E.A. Lewis and J.H. Beno, IMAREST Engine as a Weapon 2004, Bristol, UK, 9-10 June 2004.
92. "Pulsed power electromechanics - permanent magnets versus copper coils," K.R. Davey and R.E. Hebner, 2004 Power Modulator Conference, San Francisco, California, USA, 23-26 May 2004.
93. "Machine fault detection using bicoherence spectra," B. Jang, C. Shin, E.J. Powers, and W.M. Grady, 2004 IEEE Instrumentation and Measurement Technology Conference (IMTC 2004), Como, Italy, 18-20 May 2004, pp. 1661-1666.

94. "Virtual power quality analysis for ship power system design," Y.-J. Shin, A. Monti, F. Ponci, A. Arapostathis, W.M. Grady, E.J. Powers, and R.A. Dougal, IEEE Instrumentation and Measurement Technology Conference (IMTC 2004), special session "Electric Power Quality Measurements and Relevant Uncertainty Estimation," Como, Italy, 18-20 May 2004, Vol. 3.
95. "Optimal power allocation for a wireless channel under heavy traffic approximation," W. Wu, A. Arapostathis, and S. Shakkotai, 38th Annual Conference on Information Sciences and Systems, Princeton University, USA, 17-19 March 2004.
96. "Design and analysis of a 20 MW propulsion power train," J.H. Beno, M.M. Flynn, R.J. Hayes, R.E. Hebner, J.R. Jackson, A. Ouroua, M.A. Pichot, E. Schroeder, J.J. Zierer, and D.A. Weeks, 7th International Naval Engineering Conference and Exhibition (INEC), Amsterdam, The Netherlands, 16-18 March 2004.
97. "Development of a comprehensive fuel cell model for marine applications," B.C. Carroll and T.M. Kiehne, Electric Machine Technology Symposium (EMTS) 2004, The Technical and Economic Challenges of the All Electric Force, Philadelphia, Pennsylvania, USA, 27-29 January 2004.
98. "Development of electric propulsion motors with integrated power electronics," E. Schroeder, M.A. Pichot, A. Ouroua, M.M. Flynn, and J.H. Beno, Electric Machine Technology Symposium (EMTS) 2004, The Technical and Economic Challenges of the All Electric Force, Philadelphia, Pennsylvania, USA, 27-29 January 2004.
99. "An algorithm for linearization of discrete-time systems via restricted dynamic feedback," H.-G. Lee, A. Arapostathis, and S.I. Marcus, Proc. 42nd IEEE Conference on Decision and Control, Maui, Hawaii, USA, 9-12 December 2003, Vol. 2, pp. 1362-1367.
100. "State-feedback control of Markov chains with safety bounds," A. Arapostathis, R. Kumar, S.-P. Hsu, Proc. 42nd IEEE Conference on Decision and Control, Maui, Hawaii, USA, 9-12 December 2003, Vol. 6, pp. 6283-6288.
101. "A fundamental look at energy storage focusing primarily on flywheels and superconducting energy storage," K.R. Davey and R.E. Hebner, Electric Energy Storage Applications and Technologies EESAT 2003 Conference Abstracts, San Francisco, California, USA, 27-29 October 2003.
102. "Evaluation of the fault impedance in coaxial cable via time-frequency domain reflectometry," Y.-J. Shin, E.J. Powers, T.-S. Choe, S.-H. Sung, J.-G. Yook, and J.-B. Park, Proc. of the SPIE-Advanced Signal Processing Algorithms, Architectures, and Implementations XIII, Vol. 5205, San Diego, California, August 3-8, 2003, pp. 38-46.
103. "Detection and estimation of a fault on coaxial cable via time-frequency domain reflectometry," T. Choe, C. Young Hong, E. Song, J.-G. Yook, J. Park, Y.-J. Shin, and E.J. Powers, IEEE Instrumentation and Measurement Technology Conference, Vail, Colorado, USA, 20-22 May 2003.
104. "Effects of coolant density ratio on film cooling performance on a vane," J.M. Cutbirth, and D.G. Bogard, ASME Paper No. GT2003-38582, 2003.
105. Integrated Circuit Implementation for a GaN HFETs Driver Circuit, B. Wang, M. Riva, J. Bakos, A. Monti, IEEE Applied Power Electronics Conference and Exposition (APEC), pp. 901-906, Austin, TX, February 2008.
106. Uncertainty and Worst Case Analysis fo a low pass filter using Polynomial Chaos Theory, Smith A.H.C.,Monti A, Ponci F, 2007 IEEE International Workshop on Advance Methods for Uncertainty Estimation in Measurement, pp. 1-5, Sardagna, Trento, Italy, July 2007.
107. Robust Stability and Performance Analysis using Polynomial Chaos Theory, A. H. C. Smith, A. Monti, F. Ponci , 2007 Summer Computer Simulation Conference, Society of Modeling and Simulation International, pp. 45-52, San Diego, CA, July 2007.

108. Decoupling of Natural Systems in Multi-rate Parallel Simulations, R. Leonard, R. A. Dougal, Summer Simulation Multiconference, Society for Modeling and Simulation International, pp. 181-189, San Diego, CA, July 2007.
109. Virtual Prototyping as a Mechanism for Simulation-based Design, R. A. Dougal, B. Langland, A. Monti, Summer Simulation Multiconference, Society for Modeling Simulation International, CD only, San Diego, CA, July 2007.
110. A Co-Simulation Approach for Real-Time Transient Analysis of Electro-Thermal System Interactions on Board of Future All-Electric Ships, T. Chiochio, R. Leonard, Y. Work, R. Fang, M. Steurer, A. Monti, J. Khan, J. Ordonex, M. Sloderbeck, Summer Simulation Multiconference, Society for Modeling and Simulation International, CD only, San Diego, CA, July 2007.
111. Distributed Simulation using the Virtual Test Bed and its Real-time Extension, J. L. Bastos, J. Wu, N. Schulz, R. Liu, A. Monti, Summer Simulation Multiconference, Society for Modeling and Simulation International, pp. 757-765, San Diego, July 2007.
112. From Simulation to Hardware Testing: A Low Cost Platform for Power Hardware in the Loop Experiments, A. Monti, S. D'Arco, A. Deshmukh, Y. Work and A. Lentini, 2007 Summer Computer Simulation Conference, Society for Modeling and Simulation International, pp. 134-140, San Diego, CA, July 2007.
113. Synergetic Control Strategies for Shipboard DC Power Distribution Systems, I. Kondratiev, R. Dougal, American Control Conference, pp. 4744-4749, New York, NY, July 2007
114. Control Strategies for Start-up and Part-Load Operation of Solid Oxide Fuel Cell / Gas Turbine Hybrid System , W.Jiang, R. Fang, R. A. Dougal, J. A. Khan, ASME, 5th International Conference on Fuel Cell Science, Engineering and Technology, New York, NY, June 2007.
115. A Virtual Testing Facility for Elevator and Escalator Systems, A. Monti, S. D, Power Electronics Specialists Conference (PESC) 2007, pp. 820-825, Orlando, FL, June 2007
116. Current Distribution Control Design for Parallel DC/DC Converters Using Synergetic Control Theory, Kondratiev I. Dougal R., 38th Annual Power Electronic Specialist Conference, pp. 851-857, Orlando, FL, June 2007.
117. Implementing a Processor-in-the-loop with a Universal Controller in the Virtual Test Bed, R. Liu and A. Monti, G. Francis, R. Burgos, F. Wang and D. Boroyevich, Power Electronics Specialists Conference (PESC 2007), pp. 945-950, Orlando, FL, June 2007.
118. Power Quality Assessment and Management in an Electric Ship Power System, P. Crapse, J. Wang, J. Abrams, Y.J. Shin, R. Dougal, IEEE Electric Ship Technologies Symposium (ESTS), pp. 328-334, Arlington, VA, May 2007.
119. Performance Prediction and Dynamic Simulation of Electric Ship Hybrid Power System, W.Jiang, R. Fang, J. Khan, R. A. Dougal , IEEE Electric Ship Technologies Symposium (ESTS) 2007, pp. 490-497, Arlington, VA, May 2007.
120. System-Level Dynamic Thermal Modeling and Simulation for an All-Electric Ship Cooling System in VTB, R. Fang, W. Jiang, A. Monti, M. Zerby, G. Anderson, P. Bernotas, J. Khan, IEEE Electric Ship Technologies Symposium (ESTS) 2007, pp. 462-469, Arlington, VA, May 2007.
121. A Decentralized Information Filter for the State Estimation in Electrical Power Systems, A. Monti, F. Ponci, G. D, IEEE Instrumentation and Measurement Technology Conference, pp. 7-11, Warsaw, Poland, May 2007.
122. Power-quality Index Negotiation Criterion for Power System Soft Reconfiguration, A.Deshmukh, F. Ponci, L.Cristaldi, M. Faifer, IEEE Instrumentation and Measurement Technology Conference, pp. 38-42, Warsaw, Poland, May 2007.

123. Velocity and Pressure Measurements for Microturbine Control in NMR Application, S. D'Arco, F. Ponci, F. D. Doty, J. Staab, IEEE Instrumentation and Measurement Technology Conference, pp. 95-99, Warsaw, Poland, May 2007.
124. Diagnostics and Prognostics of Wiring Integrity via Joint Time-Frequency Domain Reflectometry, J. Wang, P. Crapse, J. Abrams, Y.J. Shin, R. Dougal, Aging Aircraft 2007, conference CD, Palm Springs, CA, April 2007.
125. A Decentralized State Estimator for Non-linear Electric Power Systems, A. Monti, F. Ponci, G. D, 1st Annual IEEE Systems Conference, pp 247-252, Waikiki Beach, Honolulu, Hawaii, April 2007
126. The Virtual Test Bed as a Tool for Rapid System Engineering, A. Monti, R. Dougal, 2007 1st Annual IEEE Systems Conference, pp. 1-6, Waikiki Beach, Hawaii, April 2007.
127. Virtual Prototyping of Universal Control Architecture Systems by Means of Processor in the Loop Technology, R. Liu, R. Burgos, J. Francis, A. Monti, D. Boroyevich, 2007 Applied Power Electronics Conference, pp. 21-27, Dallas, TX, February 2007.
- 128.
- 129.
130. Dynamic Electro-thermal Simulation of a Tubular Solid Oxide Fuel (SOFC), W. Jiang, R. Fang, R. A. Dougal, J. A. Khan, 2006 ASME International Mechanical Engineering Congress & Exposition (IMECE) on conference CD (IMECE2006-16279), Chicago, IL, November 2006.
131. Multidisciplinary Simulation Tools for Design of Advanced Naval Propulsion Systems, R. Dougal, A. Monti, ASNE Advanced Naval Propulsion Symposium (presentation only), Arlington, VA, October 2006.
132. Robust Controller Using Polynomial Chaos Theory, F. Ponci, A. Smith, A. Monti, IEEE Industry Application Society Annual Meeting conference CD, Tampa, FL, October 2006.
133. Physical Modeling and Parameter Extraction Procedure for p-i-n Diodes with Lifetime Control, E. Santi, L. Lu, A. Bryant, J.L. Hudgins, P.R. Palmer, IEEE 41st Industry Applications Society Annual Meeting (IAS) conference CD, Tampa, FL, October 2006.
134. Physics-Based Model of IGBT Including MOS Side Two-Dimensional Effects, E. Santi, L. Lu, A. Bryant, J.L. Hudgins, P.R. Palmer, IEEE 41st Industry Applications Society Annual Meeting (IAS) conference CD, Tampa, FL, October 2006.
135. Analysis of Transient Signatures of Arc Faults in Power Distribution Systems via Time-Frequency Analysis, Y. J. Shin, P. Crapse, J. J. Wang, Y. J. Shin, R. Dougal, Proceedings of SPIE-Advanced Signal Processing Algorithms, Architectures, and Implementations X, SPIE, Vol. 6313, pp 63130 U-1~12, San Diego, CA, August 19, 2006.
136. Multidisciplinary Simulation of Power Electronics Systems, R. A. Dougal, A. Monti, SCS Intern Conf on Modeling and Simulation - Methodology, Tools, Software Applications, pp. 177-182, Calgary, Canada, July 2006.
137. Power Quality Indexes in an Agent-based Reconfiguration Strategy for Ship Power Systems, F. Ponci, L. Cristaldi, A. Monti, IEEE Seventh International Workshop on Power Definitions and Measurements under Non-Sinusoidal Conditions, pp. 73-77, Cagliari, Italy, July 10-12, 2006
138. A Virtual Instrument for Time-Frequency Analysis of Park Power Components, L. Cristaldi, A. Monti, S. Pellizzari, F. Ponci, Seventh International Workshop on Power Definitions and Measurements under Non-Sinusoidal Conditions, pp. 130-135, Cagliari, Italy, July 2006
139. A Modular Real-Time Simulation Platform Based on the Virtual Test Bed, A. Monti, R. A. Dougal, H. P. Figueroa, J. L. Bastos, Invited to IEEE International Symposium on Industrial Electronics (ISIE 06), pp. 1537-1541, Montreal, Canada, July 2006.
140. General Synergetic Control Strategies for Arbitrary Number of Paralleled Buck Converters Feeding Constant Power Load: Implementation of Dynamic Current Sharing, I.

- Kondratiev, R. Dougal, IEEE International Symposium on Industrial Electronics (ISIE 06), pp. 257-261, Montreal, Canada, July 2006.
141. The Incremental Design Process for Power Electronic Building Blocks, A. Monti, R. Dougal, F. Ponci, Invited to IEEE Power Engineering Society Annual Meeting, June 2006.
 142. Integrated Power System Onboard Platform for the IFTP-DD(X) Warship, L. Nastac, P. Wang, S. Kuloor, O. Nayak, R. A. Dougal, S. Leeb, ASNE Day presentation only, Philadelphia, PA, June 2006.
 143. Nonlinear Synergetic Control for m Parallel-Connected DC-DC Buck Converters: Droop Current Sharing, I. Kondratiev, E. Santi, R. Dougal, Proc. IEEE Power Electronics Specialists Conference, pp. 220-226, Jeju, Korea, June 2006.
 144. Incipient Fault Diagnosis in Electrical Drives by Tuned Neural Networks, F. Ponci, A. Azzini, L. Cristaldi, M. Lazzaroni, A. Monti, A.G.B. Tettamanzi, IEEE Instrumentation and Measurement Technical Conference, pp. 1284-1289, Sorrento, Italy, April 2006.
 145. A Distributed State Estimator for Electric Power Systems in Avionic and Naval Applications, A. Monti, G. D'Antona, F. Ponci, L. Rocca, Instrumentation and Measurement Technology Conference, pp. 2312-2316, Sorrento, Italy, April 2006.
 146. Multi Agent Systems: An Example of Dynamic Reconfiguration, A. Deshmukh, F. Ponci, A. Monti, L. Cristaldi, R. Ottoboni, M. Riva, M. Lazzaroni, Instrumentation and Measurement Technology Conference, pp. 1172-1177, Sorrento, Italy, April 2006.
 147. Incipient Fault Diagnosis in Electrical Drives by Tuned Neural Networks, A. Azzini, L. Cristaldi, M. Lazzaroni, A. Monti, F. Ponci, A.G.B. Tettamanzi, IEEE Instrumentation and Measurement Technology Conference, pp. 1284-1289, Sorrento, Italy, April 2006
 148. Indirect Measurements Via Polynomial Chaos Observer, A. Smith, A. Monti, F. Ponci, IEEE International Workshop on Advanced Methods for Uncertainty Estimation in Measurements 2006, pp. 27-32, Sardinia, Italy, April 2006.
 - 149.
 150. Maximum Entropy Analytical Solution for Stochastic Differential Equations Based on the Wiener-Askey Polynomial Chaos, A. Monti, G. D'Antona, F. Ponci, L. Rocca, IEEE International Workshop on Advanced Methods for Uncertainty Estimation in Measurements 2006, pp. 62-67, Sardinia, Italy, April 2006.
 151. FPGA Implementation of Neural Network-Based Controllers for Power Electronics Applications, J. Bastos, H. Figueroa, A. Monti, IEEE Applied Power Electronic Conference (APEC 2006), pp. 1443 - 1448, Dallas, TX, March 2006.
 152. A Miniature Packaged Rectenna for Wireless Power Transmission and Data Telemetry, M. Ali, G. Yang, and R. Dougal, 2006 IEEE International Workshop on Antenna Technology: Small Antennas and Novel Meta-Materials, pp. 225-228, White Plains, NY, March 2006.
 - 153.
 154. Modeling of Uncertainty and Applications in Monitoring and Control of Power Electronics, A. Monti, F. Ponci, T. Lovett, A. Smith, and R. Dougal, invited paper for IEEE ACC 2005, Portland, OR.
 155. A Nonlinear Model for Studying Synchronous Machine Dynamic Behavior in Phase Coordinates, W. Gao, S. Meliopoulos, E. Solodovnik, R. Dougal, IEEE International Conference on Industrial Technology (ICIT2005), pp. 1092-1097, Hong Kong, China, December 2005.
 156. Multi-Agent system for Diagnostics, Monitoring and Control of Electric Systems, F. Ponci, A. Deshmukh, A. Monti, M. Riva, L. Cristaldi, Invited to IEEE Intelligent Systems Application to Power Systems, pp. 201-206, Washington, DC, November 2005.
 157. A Polynomial Chaos Theory Approach to Uncertainty in Electrical Engineering, A. Monti, F. Ponci, T. Lovett, Invited to IEEE Intelligent Systems Application to Power Systems, pp. 534-539, Arlington, VA, November 2005.

158. An Incremental Modeling Approach with a Hierarchical Structure and Progressive Accuracy using Dyadic Wavelet-Based Neural Networks, F. Ponci, Y. Song, Invited to IEEE Intelligent Systems Application to Power Systems, pp. 194-200, Washington, DC, November 2005.
159. Thermal Analysis of a Single Sided Axial Flux Permanent Magnet Motor, Z. Vilar, D. Patterson, R. Dougal, IEEE Industrial Electronics Society, pp. 2570-2574, Raleigh, NC, November 2005.
160. Methods for Partitioning the System and Performance Evaluation in Power-Hardware-in-the-Loop Simulations--Part II, X. Wu, A. Monti, IEEE Industrial Electronics Society (IECON 05), pp. 257-262, Raleigh, NC, Nov. 2005.
161. Implementation of a Low-Cost Real-Time Virtual Test Bed for Hardware-in-the-Loop Simulations, B. Lu, X. Xu, A. Monti, IEEE Industrial Electronics Society (IECON 05), pp. 239- 244, Raleigh, NC, November 2005.
162. Modeling Power Diode by Combining the Behavioral and the Physical Models, H. Wu, R. Dougal, C. Jin, IEEE Industrial Electronics Society, pp. 685-690, Raleigh, NC, November 2005.
163. Dynamic Multi-Resolution Modeling of Power Super Capacitor, H. Wu, R. Dougal , 37th North American Power Symposium, pp. 241-246, Ames, Iowa, October 2005.
164. Physical Modeling of Forward Conduction in IGBTs and Diodes, L. Lu, S.G. Pytel, E. Santi, A. Bryant, J.L. Hudgins, P.R. Palmer, Proc. IEEE 40th Industry Applications Society Annual Meeting, pp. 2635-2642, Hong Kong, China, October 2005.
165. Modeling of IGBT Resistive and Inductive turn on Behavior, L. Lu, S.G. Pytel, E. Santi, A. Bryant, J.L. Hudgins, P.R. Palmer, Proc. IEEE 40th Industry Applications Society Annual Meeting, pp. 2643-2650, Hong Kong, China, October 2005.
166. Deploying Modelica Models into Multiple Simulation Environments, Y. Chernukhin, M. Polenov, C. Vemulapally, E. Solodovnik, A. Mantooth, R. Dougal , IEEE International Behavioral Modeling and Simulation Conference (BMAS 2005), pp. 134-139, San Jose, CA, September 2005.
167. Development of Transient Power Quality Indices based on Time-frequency Distribution, Y. J. Shin, P. Crapse, International Society of Optical Engineering, Vol. 5910, San Diego, CA, August 2005.
168. An Active Filter for Fuel Cell applications , D. Franzoni, E. Santi, A. Monti, F. Ponci, D. Patterson, N. Barry, Proc. IEEE Power Electronics Specialists Conference (PESC'05), June 2005.
169. A Geometric Approach to Large-signal Stability of Switching Converters under Sliding Mode Control and Synergetic Control, E. Santi, D. Li, A. Monti, A. M. Stankovic, Proc. IEEE Power Electronics Specialists Conference (PESC'05), June 2005.
170. A FPGA-Based Approach To The Digital Control Of A Class-D Amplifier For Sound Applications , F.M. Ested, S. Lentijo, A. Monti, Proc. IEEE Power Electronics Specialists Conference (PESC'05), June 2005.
171. New Developments in Gallium Nitride and the Impact on Power Electronics, M.A. Khan, G. Simin, S.G. Pytel, A. Monti, E. Santi and J.L. Hudgins, Proc. IEEE Power Electronics Specialists Conference (PESC'05), June 2005.
172. A Compact Diode Model for the Simulation of Fast Power Diodes Including the Effects of Avalanche and Carrier Lifetime Zoning, A.T. Bryant, P.R. Palmer, E. Santi, J.L. Hudgins, Proc. IEEE Power Electronics Specialists Conference (PESC'05), June 2005.
173. Symbolic Modeling of Non-linear Devices for the Virtual Test Bed, R. Dougal, E. Solodovnik, Proceedings of IEEE PES General Meeting, Sun Francisco, CA, conference CD, June 2005.

174. Interface for Multi-Agent Platform Systems , F. Ponci, A. Deshmukh, L. Cristaldi, R. Ottoboni, IEEE-Instrumentation and Measurement Technical Conference, vol.3 pg. 2226-2230, Ottawa, Canada, May 2005.
175. Genetic Algorithm Optimization of Neural Networks for Fault Identification in Electrical Drives , L. Cristaldi, M. Lazzaroni, A. Monti, F. Ponci, F.E. Zocchi, IEEE-Instrumentation and Measurement Technical Conference, Ottawa, Canada, 17-19 May 2005.
176. A Polynomial Chaos Approach to Measurement Uncertainty, A. Monti, T. Lovett, F. Ponci, IEEE Advanced Methods for Uncertainty Management on Electrical Measurements, pp. 33-38, Ottawa, Canada, May 2005.
177. Virtual System Fault Models For Training Fuzzy-Wavelet Identifiers In Electrical Drive Diagnostic: An Experimental Validation , L. Farronato, A. Monti, F. Ponci, L. Cristaldi, M. Lazzaroni, IEEE-Instrumentation and Measurement Technical Conference, vol .3 pg. 2310-2315, Ottawa, Canada, 17-19 May 2005.
178. Uncertainty propagation in diagnostic systems based on wavelet decomposition and neuro-fuzzy techniques , L. Cristaldi, F. Ponci, IEEE-Instrumentation and Measurement Technical Conference, Ottawa, Canada, 17-19 May 2005.
179. The Load Impedance Measurement in the Time-Frequency Domain Reflectometry System, Y. Shin, T. Choe, J. Park, Proceedings of IEEE Instrumentation and Measurement Technology Conference, Ottawa, Ontario, Canada, pp.497-500, May 2005..
180. Evaluation of Non-failure Operation Time of Power System Elements in Virtual Test Bed Environment via Time-Frequency Analysis, Y. Shin, R. Dougal, G. Balim, V. Lyashev, V. Popov, Proceedings of IEEE Instrumentation and Measurement Technology Conference, pp. 737-741, Ottawa, Canada, May 2005..
181. Design and Implementation of a Power-Hardware in the Loop Interface: a Non-Linear Load Case Study , X. Wu, S. Lentijo, A. Deshmukh, A. Monti, F. Ponci, proceedings of the IEEE Applied Power Electronics Conference, Austin, TX, Mar. 2005.
182. An Advanced BEM FOR 3D Scalar Wave Propagation and Fluid-Structure Interaction Analysis, S Zhou, D. C. Rizos, The 27th World Conference on Boundary Elements and Other Mesh Reduction Methods, Eds. A. Kassab, C.A. Brebbia, D. Poljak, Orlando Florida, pp 395-404, March 2005.
183. Wavelet Neural Network based Battery State-of-Charge Estimation for Portable Electronics Applications, L. Gao, Y. Song, R. A. Dougal, proceedings of the IEEE Applied Power Electronics Conference, Austin, TX, pp.998-1002, Mar. 2005.
184. A Novel Brushless DC Motor Speed Estimator Based on Space-Frequency Localized Wavelet Neural Networks (WNNs), Y. Song, F. Ponci, A. Monti, L. Gao, R. A. Dougal, proceedings of the IEEE Applied Power Electronics Conference, Austin, TX, pp.927-932, Mar. 2005.
185. A Novel Digital Power Controller for Fuel Cell/Battery Hybrid Power Sources, Z. Jiang, R. A. Dougal, R. Leonard, proceedings of the IEEE Applied Power Electronics Conference, Austin, TX, pp.467-473, Mar. 2005.
186. A Novel, Digitally-controlled, Portable Photovoltaic Source, Z. Jiang, R. A. Dougal, proceedings of the IEEE Applied Power Electronics Conference, Austin, TX, pp. 1797-1802, Mar. 2005.
187. Design and Testing of a Modular Permanent Magnets Brushless Linear Drive, K. Patel, S. D'Arco, A. Monti, D. Patterson, R. A. Dougal, proceedings of the IEEE Applied Power Electronics Conference, Austin, TX, pp.1883-1888, Mar. 2005.
188. Simulation Environment for Performance Assessment of Reconfiguration Controls in Zonal Systems, E. Solodovnik, R. Dougal, A. Monti, ASNE Reconfiguration and Survivability Symposium 2005, Atlantic Beach, FL, February 2005.

189. Joint Time-Frequency Domain Reflectometry for Diagnostics of Coaxial Cables,' Y. Shin, R. Dougal, E.J. Powers, 8th Joint NASA/FAA/DoD Conference on Aging Aircraft, February 2005.
190. Modeling and Simulation of a Ship's Power Distribution System, E. Solodovnik, R. Dougal, Z. Wu, Advanced Naval Propulsion Symposium 2004, Herndon, VA, November 16-17, 2004.
191. Synergetic Control Approach for Induction Motor Speed Control, Y. Son, T. Heo, E. Santi, and A. Monti, Proc. of the 30th Annual Conference of the Industrial Electronics Society (IECON'04), Nov. 2004.
192. Analysis of the Interleaved Type Power Factor Correction (pfc) Converter in Discontinuous Current Mode, Tae-Won Heo, Young-Dae Son, and E. Santi, Proc. of the 30th Annual Conference of the Industrial Electronics Society (IECON'04), Nov. 2004.
193. Destruction-free Parameter Extraction for a Physics-based Circuit Simulator IGCT Model, X. Wang, J.L. Hudgins, E. Santi, P.R. Palmer, Proc. IEEE 39th Industry Applications Society Annual Meeting (IAS'04), pp. 2542-2549, Oct. 2004.
194. Multi-level device models developed for the Virtual Test Bed (VTB), X. Wang, L. Lu, S. Pytel, D. Franzoni, E. Santi, J.L. Hudgins, and P.R. Palmer, Proc. IEEE 39th Industry Applications Society Annual Meeting (IAS'04), pp. 2528-2531, Oct. 2004.
195. Turn-off operation of non-punch-through and punch-through IGBTs at cryogenic temperatures, A. Caiafa, A. Snezhko, J. L. Hudgins, E. Santi, P. R. Palmer, R. Prozorov, Proc. IEEE 39th Industry Applications Society Annual Meeting (IAS'04), pp. 2532-2541, Oct. 2004.
196. Design and Analysis of a Current-Mode Controlled Battery/Ultracapacitor Hybrid, S. Liu, R. A. Dougal, proceedings of IEEE Industry Applications Society Annual Meeting, Seattle, WA, CD# 04CH37569C IAS30p5, Oct. 2004.
197. Multiobjective MPPT/Charging Controller for Standalone PV Power System under different Insolation and Load Conditions, Z. Jiang, R. A. Dougal, proceedings of IEEE Industry Applications Society Annual Meeting, Seattle, WA, pp. 1154-1160, Oct. 2004.
198. The Virtual Test Bed Concept for Virtual Prototyping of Complex Systems R. A Dougal and A. Monti, Advanced Engineering Design Conf, Glasgow, UK, Sept 2004.
199. Rapid Prototyping of Digital Control Systems: The Virtual Test Bed Approach A. Monti, R. A. Dougal, H. Figueroa, S. Lentijo, X. Wu, Advanced Engineering Design Conf, Glasgow, UK, Sept 2004.
200. A Novel Interface for Power-Hardware-In-the-Loop Simulation , X. Wu, S. Lentijo, A. Monti, Ninth IEEE Workshop on Computers in Power Electronics (COMPEL'04), August 2004.
201. A Multi-Functional Stacked Patch Antenna for Wireless Power Beaming and Data Telemetry, G. Yang, M. Ali, R. A. Dougal, proceedings of the IASTED International Conference on Antennas, Radar, and Wave Propagation, Banff, Canada, July 2004.
202. A Polynomial Chaos Theory Approach to the Control Design of a Power Converter , T.Lovett, A.Monti, F.Ponci, proceedings of IEEE Power Electronics Specialists Conference, Aachen, Germany, pp. 4809-4813, June 2004.
203. Testing of Digital Controllers Using Real-Time Hardware in the Loop Simulation ,Wu X. , Figueroa H. , A. Monti , proceedings of IEEE Power Electronics Specialists Conference, Aachen, Germany, pp. 3622-3627, June 2004.
204. A Real-Time Processor-in-the-Loop Simulation and Hardware Validation of Embedded Control Implementation for a Fuel Cell-Powered Battery-Charging Station , Jiang Z., Leonard R., Dougal R., Figueroa H., Monti, proceedings of IEEE Power Electronics Specialists Conference, Aachen, Germany, pp. 2251-2257, June 2004.

205. Multi-Objective Control of Power Converter in Active Hybrid Fuel Cell/Battery Power Sources, Z. Jiang, L. Gao, R. A. Dougal, proceedings of IEEE Power Electronics Specialists Conference, Aachen, Germany, pp. 3804-3811, June 2004.
206. Synergetic Control of DC-DC Buck Converters with Constant Power Load , I. Kondratiev, R. Dougal, E. Santi, G. Veselov, proceedings of IEEE Power Electronics Specialists Conference, Aachen, Germany, pp. 3758-3764, June 2004.
207. Synergetic Control for m Parallel-Connected DC-DC Buck Converters, I. Kondratiev, R. Dougal, E. santi, G. Veslov, proceedings of IEEE Power Electronics Specialists Conference, Aachen, Germany, pp. 3758-3764, June 2004.
208. Performance of Power Converters in Hybrid Fuel Cell/ Battery Power Sources , L. Gao, Z. Jiang, and R. Dougal, proceedings of IEEE Power Electronics Specialists Conference, Aachen, Germany, pp. 2018-2022, June 2004.
209. AlGaN/GaN MOSHFET integrated circuit power converter, S.G. Pytel, S. Lentijo, A. Koudymov, S. Rai, H. Fatima, V. Adivarahan, A. Chitnis, J. Yang, J.L. Hudgins, E. Santi, A. Monti, G. Simin, and M. Asif Khan, Proc. IEEE Power Electronics Specialists Conference (PESC'04), pp. 579-584, June 2004.
210. Cryogenic Germanium power diode circuit simulator model including temperature dependent effects, S.G. Pytel, A.S. Hoenshel, L. Lu, E. Santi, J.L. Hudgins, P.R. Palmer, Proc. IEEE Power Electronics Specialists Conference (PESC'04), pp. 2943-2949, June 2004.
211. FPGA based sliding mode control for high frequency power converters, S. Lentijo, S. Pytel, A. Monti, J.L. Hudgins, E. Santi, G. Simin, Proc. IEEE Power Electronics Specialists Conference (PESC'04), pp. 3588-3592, June 2004.
212. Implementation and validation of a physics-based circuit model for IGCT with full temperature dependencies, X. Wang, A. Caiafa, J.L. Hudgins, E. Santi, P.R. Palmer, Proc. IEEE Power Electronics Specialists Conference (PESC'04), pp. 597-603, June 2004
213. IGBT Operation at Cryogenic Temperatures: Non-punch-through and Punch-through Comparison, A. Caiafa, A. Snezhko, J. Hudgins, E. Santi, R. Prozorov, Proc. IEEE Power Electronics Specialists Conference (PESC'04), pp. 2960-2966, June 2004
214. The Failure of Punch-through IGBTs to Reach Forward Conduction Mode at Low Temperatures, A. Caiafa, A. Snezhko, J. Hudgins, E. Santi, R. Prozorov, Proc. IEEE Power Electronics Specialists Conference (PESC'04), pp. 2967-2970, June 2004
215. Design and Implementation of a Nonlinear Speed Control for a PM Synchronous Motor using the Synergetic Control Technique, J. Bastos, A. Monti, E. Santi, Proc. IEEE Power Electronics Specialists Conference (PESC'04), pp. 3397-3402, June 2004
216. A Monitoring System Based on a Multi-Agent Platform , L. Cristaldi, A. Deshmukh, M. Lazzaroni, A. Monti, F. Ponci, R. Ottoboni, Proc. Instrumentation and Measurements Technology Conference 2004, Vol. 1, pp. 907-911, May 2004.
217. Diagnostic and Model validation of a Faulty Induction Motor Drive via Wavelet Decomposition , L. Cristaldi, M. Lazzaroni, A. Monti, F. Ponci, Proc. Instrumentation and Measurements Technology Conference 2004, Vol. 1, pp. 1460-1464, Como, Italy, May 2004.
218. "Overview of system-level thermal management research in the Electric Ship Research and Development Consortium," T.M. Kiehne, ONR Thermal Management Program PI Meeting, Hilton Head Island, South Carolina, 25-28 September 2007.
219. "Thermal characterization of an integrated electric propulsion system on a notional DDG 1000," T.M. Kiehne, ONR Thermal Management Program PI Meeting, Hilton Head Island, South Carolina, 25-28 September 2007.
220. "Overview of ESRDC consortium," R.E. Hebner, Naval Construction and Engineering Ship Design and Technology Symposium, 9 May 2007.
221. "Prime power generation studies, film cooling of gas turbines airfoils, and material characterization work at the University of Texas," A. Ouroua, J.R. Jackson, J.H. Beno, A.T.

- Wilder, David Bogard, and K.L. Harrison, ESRDC Workshop, Massachusetts Institute of Technology, 7-8 May 2007.
222. "System-level thermal management on an all-electric ship," T.M. Kiehne, C.R. Holsonback, P.E. Paullus, P. Hewlett, T.W. Webb, and S.T. Haag, ESRDC Workshop, Massachusetts Institute of Technology, 7-8 May 2007.
 223. "Latin Hypercube Sampling and Optimization in an Electric Ship," K.R. Davey, August 2, 2006. This is just a paper Kent put together - I do not think it was even sent to ONR.
 224. "Detection of flicker caused by high-frequency interharmonics," T. Kim and Teri Houle, Electric Ship Research and Development Consortium May meeting, Columbia, South Carolina, 31 May-1 June 2006.
 225. "Dynamic modeling and analysis of an automatic reconfigurable shipboard power system," J.A. Park, K.R. Davey, and W.L. Shutt, Electric Ship Research and Development Consortium meeting, Columbia, South Carolina, 31 May-1 June 2006.
 226. "Dynamic optimal generation scheduling of shipboard power systems," W. Wu and K.R. Davey, Electric Ship Research and Development Consortium May meeting, Columbia, South Carolina, 31 May-1 June 2006.
 227. "Energy-based grid reconfiguration," J. Carroll and T. Rosenwinkel, Electric Ship Research and Development Consortium May meeting, Columbia, South Carolina, 31 May-1 June 2006.
 228. "The Cost of Operating Electric Ships with Torque or Speed Control," K.R. Davey, intended for this to be included with the June 2006 quarterly report, but we don't send attachments, but Bob said this could be included on the web site
 229. "Higher-order spectral analysis software tool with applications to machine condition monitoring," H. Park, Electric Ship Research and Development Consortium May meeting, Columbia, South Carolina, 31 May-1 June 2006.
 230. "HOS-based ASD condition monitoring," T. Kim, Electric Ship Research and Development Consortium May meeting, Columbia, South Carolina, 31 May-1 June 2006.
 231. "Optimal control and stabilization of power systems via switching," W. Wu, K.R. Davey, and A. Arapostathis, Electric Ship Research and Development Consortium May meeting, Columbia, South Carolina, 31 May-1 June 2006.
 232. "Power train work at UT CEM: Overview of recent results," A. Ouroua, Electric Ship Research and Development Consortium meeting, Columbia, South Carolina, 31 May-1 June 2006.
 233. "Voltage sag based station to determine transient stability load models," M.R. Rylander, Electric Ship Research and Development Consortium May meeting, Columbia, South Carolina, 31 May-1 June 2006.
 234. "Steady state representation of a gas turbine-solid oxide fuel cell hybrid system," S.T. Haag and T.M. Kiehne, Office of Naval Research Contract Report, 2004.
 235. "Electromagnetic materials for machinery, part 1: laminates & composite magnetic materials," A.T. Wilder, Appendix I of the quarterly report from The University of Texas at Austin to the Advanced Electric Ship Consortium, December 2002.
 236. Y. Baez-Rivera and N. N. Schulz, "Robust Control of Multigenerators for the All-Electric Ship", GSA Research Symposium presentation, Mississippi State University, March 30, 2007.
 237. H. Hamilton, N. N. Schulz and H. L. Ginn, "DC Protection for Naval Shipboard Power Systems", 2007 Mississippi Academy of Science (MAS), February 21 – 23, 2007, Hunter Henry Center and Bost Extension Center, Mississippi State University, MS.
 238. H. Hamilton, N. N. Schulz and H. L. Ginn, "DC Protection and Considerations," January 25 – 27, 2007, 2007 AGEM Winter Scholar Symposium, Oxford Conference Center, Oxford, MS.

239. S. Palla, A. K. Srivastava and N. N. Schulz, "Modeling and Simulation of Power System Components", GSA Research Symposium presentation, Mississippi State University, March 30, 2007.
240. D. Khaniya, A. K. Srivastava and N. N. Schulz, "Continuation Power Flow," GSA Research Symposium presentation, Mississippi State University, March 30, 2007.
241. S. Grzybowski, C. Taylor, and J.C. Fulper, "Electrical Degradation of Ship Machine Winding Insulation," IEEE Workshop on Transportable Megawatt Power Systems, Austin, Texas, March 6-7, 2007.
242. J. L. Bastos, Y. Zhang, A. K. Srivastava, and N. N. Schulz, "A Design Paradigm for Integrated Protection of Shipboard Power Systems", 2007 Summer Computer Simulation Conference (SCSC'07), San Diego, CA, July 16-18, 2007.
243. J. L. Bastos, J. Wu, N. N. Schulz, R. Liu, and A. Monti, "Distributed simulation using the Virtual Test Bed and its Real-Time Extension", 2007 Summer Computer Simulation Conference (SCSC'07), San Diego, CA, July 16-18, 2007.
244. J. L. Bastos, "MSU ESRDC Group's Research Activities Overview", Collaboration-seeking visit to Florida State University Center for Advanced Power Systems (FSU-CAPS), Tallahassee, FL, June 11-13, 2007.
245. Y. Zhang, "Design of Adaptive Protection Devices for SPS", Collaboration-seeking visit to Florida State University Center for Advanced Power Systems (FSU-CAPS), Tallahassee, FL, June 11-13, 2007.
246. V. Vijapurapu, "Differential Relay as agent in Power System Protection", Collaboration-seeking visit to Florida State University Center for Advanced Power Systems (FSU-CAPS), Tallahassee, FL, June 11-13, 2007.
247. Q. Huang, "Distributed Simulation Applied to SPS", Collaboration-seeking visit to Florida State University Center for Advanced Power Systems (FSU-CAPS), Tallahassee, FL, June 11-13, 2007.
248. Y. Zhang, J. L. Bastos, N. N. Schulz and D. Patel, "Modeling and Testing of Protection Devices for SPS using MATLAB/Simulink and VTB", IEEE Electric Ship Technologies Symposium 2007 (ESTS 07), Arlington, VA, May 21-23, 2007.
249. Q. Huang, J. Wu, J. L. Bastos and N. N. Schulz, "Distributed Simulation Applied to Shipboard Power Systems", IEEE Electric Ship Technologies Symposium 2007 (ESTS 07), Arlington, VA, May 21-23, 2007.
250. N. N. Schulz, J. L. Bastos, A. K. Srivastava, D. Patel, Y. Zhang, S. Palla, C. Zhang and V. Vijapurapu, "Modeling and Simulation of Protection Devices Using Real-Time Hardware-in-the-Loop Experiments", Electric Ship Research and Development Consortium (ESRDC) Workshop, Massachusetts Institute of Technology, Boston, MA, May 7-8, 2007.
251. J. L. Bastos and A. Monti, "Rapid prototyping using VTB: Computer-Aided Design of Nonlinear Synergetic Controllers", 2006 VTB Users and Developers Conference, Columbia, SC, October 19-20, 2006.
252. J. L. Bastos, "MSU ECE Power and High Voltage Research Group: Modeling and Simulation (M&S) Capabilities", Northrop Grumman Ship Systems visit to MSU, Center for Advanced Vehicular Systems (CAVS), September 29, 2006.
253. N. N. Schulz, A. K. Srivastava, J. L. Bastos, S. Khushalani, J. Solanki, S. Kotamarthy, Q. Yu, Y. Baez-Rivera, H. Hamilton, O. Amoda, S. Sankar, M. Lin, D. Khaniya, and B. Gautum, "Adaptive Protection and Stable Reconfiguration to Increase the Survivability of the All-Electric Ship System", Electric Ship Research and Development Consortium (ESRDC) Workshop, May 7-8, 2007, Massachusetts Institute of Technology, Boston, MA, USA.
254. S. Grzybowski, P. Trnka, and J.C. Fulper, "Aging of High Voltage Cables by Switching Impulse," CD-ROM, 2007 IEEE Electric Ship Technologies Symposium, Arlington, VA.
255. S. Grzybowski, "Experimental Evaluation of Lightning Protection Zone Used on

- Ship,” CD-ROM, 2007 IEEE Electric Ship Technologies Symposium, Arlington, VA, May 21-23, 2007.
256. W. Gao, “Modeling and Analysis of a Wind/PV/Fuel Cell Hybrid Power System in HOMER” in IEEE Conference on Industrial Electronics and Applications, May 23-25, Harbin, China .
 257. Q. Yu and N.N. Schulz, “MAS-Based Reconfiguration of An Integrated Power System,” presented in ESRDC conference at Boston, Massachusetts, May 21-23, 2007.
 258. K. Borisov, “ Multifunctional voltage source converter for shipboard power systems” Dissertation defense, Mississippi State, MS, April 2007.
 259. K. Borisov and H. L. Ginn, “Multifunctional voltage source converters for shipboard power systems” Massachusetts Institute of Technology, Cambridge, MA, May 2007.
 260. K. Borisov and H. L. Ginn, “Modeling and simulations of multifunctional voltage source converters in Virtual Test Bed”, Electric ship Technology Symposium, ESTS 2007, May 2007, Arlington VA.
 261. K. Borisov, H. L. Ginn, and G. Chen, ”Computationally efficient RDFT based reference signal generator for active compensators” Power Electronic Specialist Conference, Orlando, FL.
 262. M. Lin, A. K. Srivastava, and N. N. Schulz, “A Generic Digital Model of Multiphase Synchronous Generator for Shipboard Power System”, IEEE Electric Ship Technologies Symposium (ESTS), May 21-23, 2007, Arlington, VA.
 263. M. Lin, A. K. Srivastava, and N. N. Schulz, “Modeling Consideration in Static and Dynamic Voltage Stability Studies of Shipboard Power System”, SummerSim, 2007, July 15-18, 2007, San Diego, CA.
 264. D.C. Zhang, A. K. Srivastava, J. L. Bastos and N. N. Schulz, “Hardware in the Loop Simulation of Protective Relay Using RTDS”, Electric Ship Research and Development Consortium (ESRDC) Workshop, May 7-8, 2007, Massachusetts Institute of Technology, Boston, MA, USA.
 265. C. Zhang, V. K. Vijapurapu, A. K. Srivastava, N. N. Schulz, J. L. Bastos and R. Wierckx, “Hardware-in-the-Loop Simulation of Distance Relay Using RTDS”, 2007 Summer Simulation Multiconference (SummerSim'07), Jul 14, 2007 - Jul 19, 2007, San Diego, CA United States.
 266. A. K. Srivastava, J. L. Bastos, N. N. Schulz and H. L. Ginn, “AC/DC Power System Modeling and Analysis for Shipboard Applications”, IEE PES GM 2007, June 24 -28, Tampa, Florida, USA.
 267. S. Mohammed, W. Gao and N. N. Schulz, “Analysis & Development of a Proto-type Hybrid Fuel Cell Distributed Generation Power System for Stand-alone Applications,” in IEEE Power Electronics Drives and Energy. PEDES 2006 conference in New Delhi, India.
 268. J. L. Bastos, “Rapid Systems Prototyping using VTB: Computer-Aided Design of Nonlinear Synergetic Controllers”, 2006 VTB Users and Developers Conference, Columbia, SC, October 19-20, 2006.
 269. O. Amoda and N. N. Schulz, “Development of Adaptive Protection for Shipboard Power Systems,” Poster, 2007 Electric Ship Research and Development Consortium Annual Meeting, MIT, Boston, MA, May 2007.
 270. S. Palla, A. K. Srivastava and N. N. Schulz, “Hardware-in-the-loop Simulation for Protective Relay using National Instrument Systems, Poster, 2007 Electric Ship Research and Development Consortium Annual Meeting, MIT, Boston, MA, May 2007.
 271. D. Khaniya, A. K. Srivastava and N. N. Schulz, “Voltage Stability Analysis of Shipboard Power Systems Using Continuation Power Flow,” Poster, 2007 Electric Ship Research and Development Consortium Annual Meeting, MIT, Boston, MA, May 2007.
 272. H. Hamilton and N. N. Schulz, “DC Protection,” Poster, 2007 Electric Ship Research and Development Consortium Annual Meeting, MIT, Boston, MA, May 2007.

273. M. Lin, A. K. Srivastava and N. N. Schulz, "Static and Dynamic Voltage Stability Assessment of Shipboard Power Systems," Poster, 2007 Electric Ship Research and Development Consortium Annual Meeting, MIT, Boston, MA, May 2007.
274. Y. Zhang, J. L. Bastos, N. N. Schulz and D. Patel, "Modeling and Simulation of Protection Devices for SPS Using MATLAB/Simulink and VTB," Poster, 2007 Electric Ship Research and Development Consortium Annual Meeting, MIT, Boston, MA, May 2007.
275. K. R. Padamati, Y. Huang and N. N. Schulz, "Optimal Reconfiguration of Shipboard Power Systems Using a Genetic Algorithm," Poster, 2007 Electric Ship Research and Development Consortium Annual Meeting, MIT, Boston, MA, May 2007.
276. Q. Yu and N. N. Schulz, "MAS-Based Reconfiguration of An Integrated Power System," Poster, 2007 Electric Ship Research and Development Consortium Annual Meeting, MIT, Boston, MA, May 2007.
277. Q. Huang, J. L. Bastos and N. N. Schulz, "Time Delay Effect Model Embedded in the Interface of the Distributed Simulation," Poster, 2007 Electric Ship Research and Development Consortium Annual Meeting, MIT, Boston, MA, May 2007.
278. B. R. Gautam, N. N. Schulz and A. K. Srivastava, "Contingency Analysis of a Shipboard Power System to Increase Survivability," Poster, 2007 Electric Ship Research and Development Consortium Annual Meeting, MIT, Boston, MA, May 2007.
279. O. Amoda and N. N. Schulz, "An Adaptive Protection Scheme for Shipboard Power Systems," Proceedings of the IEEE Electric Ship Technologies Symposium 2007 (ESTS 07), Arlington, Virginia, May 2007.
280. Yamilka Báez-Rivera, Noel N. Schulz and Wenzhong Gao, "Advanced Modeling of Micro-Turbine for System Analysis," Proceedings of the Power Systems Conference: Advanced Metering, Protection, Control Communication and Distributed Resources, March 2006, Clemson.
281. Y. Baez-Rivera, L. Brown III and N. N. Schulz, "Using Graduate Internships to Enhance Graduate Student Education and Research," Proceedings of the ASEE Annual Meeting, June 2007, Honolulu, Hawaii.
282. J. L. Bastos, Y. Zhang, A. K. Srivastava, and N. N. Schulz, "A Design Paradigm for Integrated Protection of Shipboard Power Systems", Proceedings of the 2007 Summer Computer Simulation Conference (SCSC'07), San Diego, July 2007.
283. J. L. Bastos, J. Wu, N. N. Schulz, R. Liu, and A. Monti, "Distributed simulation using VTB and VTB-RT," Proceedings of the 2007 Summer Computer Simulation Conference (SCSC'07), San Diego, July 2007.
284. K. Borisov, H. L. Ginn, and G. Chen, "A computationally efficient RDFT based harmonic detection method for active compensators," IEEE Power Electronics Specialist Conference – PESC 2007, 17-21 Jun 2007, Orlando, FL.
285. K. Borisov and H. L. Ginn, "A novel reference signal generator for active compensators based on recursive DFT", 2007 European Conference on Power Electronics and Applications (EPE), 02-05 Sept, Aalborg, Denmark..
286. K. Borisov and H. L. Ginn, "Modeling of multifunctional shunt connected current controllers for shipboard power system in virtual test bed," Proceedings of the IEEE Electric Ship Technologies Symposium, ESTS 2007, 21-23 May, Arlington, VA.
287. K. Borisov and H. L. Ginn, "Fortescue based reference signal generator for the multifunctional Voltage Source Converter", IEEE Industrial electronics conference, IECON07.
288. K. Borisov, A. Trzynadlowski and H. L. Ginn, "Attenuation of electromagnetic interference in a shunt active power filter", The 33rd Annual Conference of the IEEE Industrial Electronics Society (IECON) Nov. 5-8, 2007, Taipei, Taiwan, pp.1886-1891.
289. Konstantin Borisov, Herbert L. Ginn III, and Andrzej M. Trzynadlowski: "Mitigation of Electromagnetic Noise in a Shunt Active Power Filter using Random PWM," The 33rd

- Annual Conference of the IEEE Industrial Electronics Society (IECON) Nov. 5-8, 2007, Taipei, Taiwan, pp.1886-1891.
290. Konstantin Borisov, and Herbert L. Ginn III: "A Novel Fortescue Based Reference Signal Generator for Multifunctional VSC," The 33rd Annual Conference of the IEEE Industrial Electronics Society (IECON) Nov. 5-8, 2007, Taipei, Taiwan, pp.1691-1696.
 291. Yong Cheng, Jian Wu, and Herbert L. Ginn III, "Active Compensator Prototyping Tools for Electric Ship Applications," Proceedings of the IEEE Electric Ship Technologies Symposium (ESTS '05), Philadelphia, July 2005.
 292. Y.Cheng, J. Wu, A. K. Srivastava, N. N. Schulz and H. L. Ginn, "Hardware in the Loop Test for Power System Modeling and Simulation," Proceedings of the IEEE PES Power Systems Conference and Exhibition, Atlanta, Georgia, October 2006.
 293. Yong Cheng, Jian Wu, Anurag Srivastava, Noel Schulz and Herbert Ginn, "Hardware in the Loop Test for Power System Modeling and Simulation," Proceedings of the IEEE PES Power Systems Conference and Exhibition, Atlanta, Georgia, October 2006.
 294. Herbert L. Ginn III, and Guangda Chen: "PEBB Based Multifunctional Shunt Voltage Sourced Converters," The 33rd Annual Conference of the IEEE Industrial Electronics Society (IECON) Nov. 5-8, 2007, Taipei, Taiwan, pp.1937-1942.
 295. Yanfeng Gong, Yan Huang, and Noel Schulz, Mississippi State University, Integrated Protection System Design for Shipboard Power System, Proceedings of the 2005 IEEE Electric Ship Technologies Symposium, Philadelphia, PA, July, 2005.
 296. Yanfeng Gong and Noel N. Schulz, "Integrated Protection and Reconfiguration Design for the All- Electric Ship," Proceedings of the American Society of Naval Engineers Reconfiguration and Survivability Symposium 2005, Atlantic Beach, Florida, February 2005.
 297. Yanfeng Gong and Noel N. Schulz, and Armando Guzman, "Synchrophasor-Based Real-Time Voltage Stability Index," Proceedings of the Western Protective Relaying Conference, Spokane, WA, October, 2005.
 298. S. Grzybowski, P. Trnka, J.C. Fulper, "Aging of High Voltage Cables by Switching Impulse," 2007 IEEE Electric Ship Technologies Symposium, Arlington, VA, May 21-23, 2007.
 299. S.Grzybowski, "Experimental Evaluation of Lightning Protection Zone Used on Ship," 2007 IEEE Electric Ship Technologies Symposium, Arlington, VA, May 21-23, 2007.
 300. H. Hamilton and N. N. Schulz, "DC Protection on the Electric Ship," Proceedings of the IEEE Electric Ship Technologies Symposium 2007, (ESTS 07), Arlington, Virginia, May 2007.
 301. Q. Huang, J. Wu, J. L. Bastos and N. N. Schulz, "Distributed Simulation Applied to Shipboard Power Systems," "Distributed Simulation Applied to Shipboard Power Systems," Proceedings of the IEEE Electric Ship Technologies Symposium 2007 (ESTS 07), Arlington, Virginia, May 2007.
 302. Qinghua Huang, Konstantin Borisov, Herbert L. Ginn III, PEBB-Based Shunt Active Power Filter for Shipboard Power Systems," Proceedings of the IEEE Electric Ship Technologies Symposium (ESTS '05), Philadelphia, July 2005.
 303. Sarika Khushalani and Noel N. Schulz, "Analysis of the DC Zonal Electric Shipboard Power System," Proceedings of the 35th North American Power Symposium, Rolla, Missouri, October 2003.
 304. Sarika Khushalini And Noel N. Schulz, "Optimized Reconfiguration Of Distribution Systems With Distributed Generation," Proceedings of the 2003 Power Systems Conference on Distributed Generation And Advanced Metering, Clemson, SC, March 2003.
 305. Sarika Khushalani and Noel N. Schulz, "Unbalanced Distribution Power Flow with Distributed Generation," Proceedings of the IEEE PES Transmission and Distribution Conference, May, 2006, Dallas, Texas.

306. Sarika Khushalani and Noel N. Schulz, "Restoration Optimization With Distributed Generation Considering Islanding," Proceedings of the IEEE Power Engineering Society 2005 General Meeting, San Francisco, CA, June 2005.
307. Sarika Khushalani and Noel N. Schulz, "Optimized Restoration of Shipboard Power Systems with IPS Architecture and Distributed Generation," Proceedings of the American Society of Naval Engineers Reconfiguration and Survivability Symposium 2005, Atlantic Beach, Florida, February 2005.
308. K. Kondabathini, H. L. Ginn III, and G. M. Molen, "Accurate Method to Measure Harmonics and Interharmonics in Shipboard Power Quality Analysis," Proceedings of the IEEE Electric Ship Technologies Symposium (ESTS '05), Philadelphia, July 2005.
309. M. Lin, A. K. Srivastava and N. N. Schulz, "Modeling Considerations in Static and Dynamic Voltage Stability Studies of Shipboard Power Systems," Proceedings of the 2007 Summer Computer Simulation Conference (SCSC'07), San Diego, July 2007.
310. M. Lin, A. K. Srivastava and N. N. Schulz, "A Generic Digital Model of Multiphase Synchronous Generator for Shipboard Power Systems," Proceedings of the IEEE Electric Ship Technologies Symposium 2007 (ESTS 07), Arlington, Virginia, May 2007.
311. Antonello Monti, F. Ponci, E. Santi, and R. Dougal, G. Monnat, W. Shutt, and R. Hebner, D. Cartes, Florida State University, N. Schulz, H. Ginn, F. Wang and D. Boroyevich, S. Pekarek and S. Sudhoff, "Ship Power System Control: A Technology Assessment," Proceedings of the 2005 IEEE Electric Ship Technologies Symposium, Philadelphia, PA, July, 2005.
312. S. Sankar and N. N. Schulz, "Intelligent Placement of Meters/Sensors for Shipboard Power System Analysis," Proceedings of the IEEE Electric Ship Technologies Symposium 2007 (ESTS 07), Arlington, Virginia, May 2007.
313. N.N. Schulz, H.L. Ginn and S.M Halpin, "Electric Ship Research Activities and Capabilities at Mississippi State University and Its Partners," Proceedings of the IEEE Electric Ship Technologies Symposium (ESTS '05), Philadelphia, July 2005.
314. N. N. Schulz, H. L. Ginn, S. Grzybowski, A. K. Srivastava and J. L. Bastos, "Modeling and Simulation Activities for Advanced Shipboard Power System Analysis at Mississippi State University," Proceedings of the IEEE Electric Ship Technologies Symposium 2007. Arlington, Virginia, May 2007.
315. N. N. Schulz, H. L. Ginn, S. Grzybowski, A. K. Srivastava and J. L. Bastos, "Ship-to-Shore Collaborations: Integrating Research of Shipboard Power Systems into Today's Power Engineering Research Activities," Proceedings of the ASEE Annual Meeting, June 2007, Honolulu, Hawaii.
316. N. N. Schulz, H. L. Ginn, S. Grzybowski, A. K. Srivastava and J. L. Bastos, "Integrating Shipboard Power System Topic into the Curriculum," Proceedings of the ASEE Annual Meeting, June 2007, Honolulu, Hawaii.
317. S. Palla, A. K. Srivastava and N. N. Schulz, "Hardware in the Loop Test for Relay Model Validation, Proceedings of the ESCAPE Conference, Mississippi State University, Mississippi, March 2-3, 2007.
318. T. Qian, B. Lehman, A. Bhattacharya, H.L. Ginn and G. M. Molen, "Parallel Operation of Shunt Active Power Filters for Damping of Harmonic Propagation in Electric Ship Power Systems," Proceedings of the IEEE Electric Ship Technologies Symposium (ESTS '05), Philadelphia, July 2005.
319. Ting Qian, B. Lehman, G. Escobar, H. Ginn, M. Molen, "Adaptive Saturation Scheme to Limit the Capacity of a Shunt Active Power Filter," Proceedings of the IEEE Conference on Control Applications (CCA 2005), 28-31 Aug. 2005, pp. 1674-1679.
320. Jignesh M. Solanki, Noel N. Schulz, and Wenzhong Gao, "Reconfiguration for Restoration of Power Systems Using a Multi-Agent System," Proceedings of the 37th Annual

- North American Power Symposium, Iowa State University, Ames, Iowa, October 23-25, 2005
321. Jignesh Solanki and Noel N. Schulz, "Multi-Agent System for Islanded Operation of Distribution Systems," Proceedings of the IEEE PES Power Systems Conference and Exhibition, Atlanta, Georgia, October 2006.
 322. Jignesh M. Solanki and Noel N. Schulz, "Autonomous Control of Dispersed Generation in Unbalanced Three Phase Distribution Systems," Proceedings of the American Society of Naval Engineers Reconfiguration and Survivability Symposium 2005, Atlantic Beach, Florida, February 2005.
 323. Jignesh M. Solanki and Noel N. Schulz, "Using Intelligent Multi-Agent Systems for Shipboard Power System Reconfiguration," Proceedings of the 13th International Conference on Intelligent Systems Application to Power Systems, Doubletree Crystal City Hotel, Arlington, Virginia, USA, November 6-10, 2005
 324. J. Solanki and N. N. Schulz, "Multi-Agent System for Islanded Operation of Distribution Systems," Proceedings of the IEEE PES Power Systems Conference and Exhibition, Atlanta, Georgia, October 2006.
 325. A. K. Srivastava, N. N. Schulz, H. L. Ginn and J. L. Bastos, "AC/DC Power System Modeling and Analysis for Shipboard Applications," Proceedings of the 2007 IEEE PES General Meeting, Tampa, Florida, June 2007.
 326. Haibin Wang, Noel N. Schulz, David Cartes, Li-Hsiang Sun and Sanjeev Srivastava, "System Reconfiguration Strategy for Shipboard Power Systems Using Multi-Agent Systems," Proceedings of the American Society of Naval Engineers Reconfiguration and Survivability Symposium 2005, Atlantic Beach, Florida, February 2005.
 327. Jian Wu, Noel N. Schulz and Wenzhong Gao, "Generalized Three Phase Coupling Method for Distributed Simulation," Proceedings of the IEEE Power Engineering Society General Meeting June 2006, Montreal.
 328. Jian Wu, Yan Huang, Wenzhong Gao and Noel N. Schulz, "Power System Load Modeling in Virtual Test Bed," Proceedings of the IEEE Power Engineering Society General Meeting, June 2006, Montreal.
 329. Jian Wu and Noel N. Schulz, Overview of CIM-Oriented Database Design and Data Exchanging in Power System Applications, Proceedings of the 37th Annual North American Power Symposium, Iowa State University, Ames, Iowa, October 23-25, 2005
 330. Jian Wu and Noel N. Schulz, "Generalized Three Phase Coupling Method for Distributed Simulation," Proceedings of the 37th Annual North American Power Symposium, Iowa State University, Ames, Iowa, October 23-25, 2005
 331. Simulation," Proceedings of the 37th Annual North American Power Symposium, Iowa State University, Ames, Iowa, October 23-25, 2005
 332. Jian Wu, Noel N. Schulz and Herb Ginn, "Extending the Common Information Model for Electric Ship Power Systems," Proceedings of the 35th North American Power Symposium, Rolla, Missouri, October 2003.
 333. J. Wu, N. N. Schulz and W. Gao, "Power System Load Modeling in Virtual Test Bed," Proceedings of the 2007 Summer Computer Simulation Conference (SCSC'07), in press, San Diego, July 2007.
 334. Jian Wu and Noel N. Schulz, "Experimental Design for Remote Hardware-In-the-Loop Testing," Proceedings of the American Society of Naval Engineers Reconfiguration and Survivability Symposium 2005, Atlantic Beach, Florida, February 2005.
 335. Jian Wu, Yong Cheng, Noel N. Schulz, and Herbert L. Ginn, The Impact of Standardized Models, Programming Interfaces, and Protocols on Shipboard Power System, Proceedings of the 2005 IEEE Electric Ship Technologies Symposium, Philadelphia, PA, July, 2005
 336. Jian Wu, Yong Cheng, Shrivastava A. K., Schulz N. N., Ginn H. L., "Hardware in the Loop Test for Power System Modeling and Simulation", Power Systems Conference and Exposition, 2006. PSCE '06 IEEE PES Oct. 29-Nov. 1 2006 Page(s):1892-1897.

337. Q. Yu, S. Khushalani, J. Solanki, N. N. Schulz, H. L. Ginn, S. Grzybowski, A. K. Srivastava and J. L. Bastos, "Shipboard Power Systems Research Activities at Mississippi State University," Proceedings of the IEEE Electric Ship Technologies Symposium 2007 (ESTS 07), Arlington, Virginia, May 2007.
338. Y. Zhang, J. L. Bastos, N. N. Schulz and D. Patel, "Modeling and Testing of Protection Devices for SPS using MATLAB/Simulink and VTB," Proceedings of the IEEE Electric Ship Technologies Symposium 2007 (ESTS 07), Arlington, Virginia, May 2007.
339. Y. Zhang, V. Vijapurapu, A. K. Srivastava, J. L. Bastos, N. N. Schulz and R. Wierckx, "Hardware in the Loop Simulation of Distance Relay Using RTDS," Proceedings of the 2007 Summer Computer Simulation Conference (SCSC'07), San Diego, July 2007.
340. A.M. Cramer, R.R. Chan, S.D. Sudhoff, Y. Lee, M.R. Surprenant, N.S. Tyler, E.L., Zivi, R.A. Youngs, "Modeling and Simulation of an Electric Warship Integrated Engineering Plant," 2006 SAE Power Systems Conference, New Orleans, Louisiana, November 7-8, 2006.
341. J. Cale, S.D. Sudhoff, "EI Core Inductor Designs using Population-Based Design Algorithms," 2007 Applied Power Electronics Conference, Anaheim, CA, February 25-March 1, 2007.
342. R.R. Chan, S.D. Sudhoff, S.H. Žak, Y. Lee, E.L. Zivi, "Evolutionary Optimization of Power Electronics Based Power Systems" 2007 Applied Power Electronics Conference, Anaheim, CA, February 25-March 1, 2007
343. A. Cramer, S. Sudhoff, E. Zivi, "Performance Metrics for Electric Warship Integrated Engineering Plant Battle Damage Response," IEEE Electric Ship Technologies Symposium, Arlington, VA, May 21-23, 2007
344. B. Cassimere, R. Chan, J. Cale, A. Cramer, S. Sudhoff, "Evolutionary Design of Electromagnetic and Electromechanical Devices," IEEE Electric Ship Technologies Symposium, Arlington, VA, May 21-23, 2007
345. C. Sullivan, S. Sudhoff, E. Zivi, S. Žak, "Methods of Optimal Lyapunov Function Generation With Application to Power Electronic Converters and Systems," IEEE Electric Ship Technologies Symposium, Arlington, VA, May 21-23, 2007
346. S. Sudhoff, B. Loop, J. Byoun, A. Cramer, "A New Procedure for Calculating Immittance Characteristics Using Detailed Computer Simulation," Power Electronic Specialist Conference, Orlando, FL, June 17-21, 2007
347. C. Kwon, S. Hui, S. C. Sudhoff, and S. H. Žak, "Rotor flux and speed observers for induction motors," Proc. International Conference on Power Electronics and Intelligent Control for Energy Conversion, Warsaw, Poland, Paper ID: 141, October 16--19, 2005.
348. S. Hui, S. D. Sudhoff, and S. H. Žak, "On estimating regions of stability of the estimation error of sliding mode observers for uncertain systems," Proc. 2006 American Control Conference, Minneapolis, Minnesota, Session ThB15.6, pp. 3328--3333, June 14--16, 2006.
349. Jianming Lian, Yonggon Lee, Scott D. Sudhoff, and Stanislaw H. Žak, "Variable Structure Neural Network Based Direct Adaptive Robust Control of Uncertain Systems," to appear in Proceedings of 2008 American Control Conference, Seattle, WA, June 11--13, 2008.
350. Jianming Lian, Scott D. Sudhoff, and Stanislaw H. Žak, "Control of Uncertain Systems with Guaranteed Performance," to appear in Proceedings of 2008 American Control Conference, Seattle, WA, June 11--13, 2008.
351. B. Deken, S. Pekarek, B. Fahimi, "An Enhanced Field Reconstruction Technique for Design of PM Synchronous Machines," Proceedings of the 2007 Vehicular Power and Propulsion Conference (VPPC 2007), September 2007, TS6-3 (CD-ROM Proceeding).
352. D. Wu, S. Pekarek, B. Fahimi, "A Field Reconstruction Technique for Efficient Modeling of the Fields and Forces within Induction Machines," Proceedings of the 2007 Industrial Electronics Society Conference (IECON 2007), November 2007, pp. 1274-1279.

353. D. Wu, S. Pekarek, "Using Mechanical Vibration to Estimate Rotor Speed in Induction Motor Drives," Proceedings of the 2007 Power Electronics Specialists Conference, June 2007, pp. 2412-2417.
354. Presentation at the University of Illinois, Urbana-Champaign, "Design Metrics for Electric Warship Design," February 6, 2006
355. Presentation at the Electric Ship Research and Development Consortium Modeling and Simulation Workshop, "Population Based Design of Electric Warship Components and Systems," February 15, 2006.
356. Presentation at the ESRDC MIT/Purdue/USNA Review, "Activities in Evolutionary Design," Boston, MA, May 9, 2006.
357. Short Course: "Genetic Algorithms Short Course," for Rockwell, January 17-18, 2006
358. Short Course for Engineering Professional Education (Available on DVD, Streaming Video, and I-Pod) "Engineering Analysis and Design Using Genetic Algorithms" (taught twice in 2006)
359. Short course prepared and in accepted in 2006, but taught in 2007 "Power Electronics Analysis and Design Using Evolutionary Algorithms," February 25, 2007, APEC Conference in Anaheim, CA
360. Short course, S.D. Sudhoff, S.D. Pekarek, "Design Strategies for Mobile Electric Generators," given at Tactical Power Sources Summit 2008, January 28-30, 2008, Georgetown University Conference Center, Washington DC (one-half day course)
361. S.D. Pekarek, S.D. Sudhoff, "Alternate Electric Machine Designs for Man-Portable Power Systems," Tactical Electronics & Rotating Machinery Workshop, Ft. Belvoir, Virginia, January 23, 2008
362. J. Cale, "Computationally Efficient Magnetic Modeling and Material Characterization Methods for Automated Ferrimagnetic Inductor Design", PhD Dissertation, Purdue University, July 2007
363. A. Cramer, "Metric Based Design of Integrated Engineering Plants for Robust Performance During Hostile Disruptions" PhD Dissertation, Purdue University, July 2007
364. Brandon Cassimere, "Modeling and Evolutionary Design of Permanent Magnet Synchronous Machines," PhD Dissertation, Purdue University, May 2008
365. Brant Cassimere, "Computationally Efficient Modeling and Characterization of Power Semiconductor Losses," PhD Dissertation, Purdue University, May 2008
366. C. Sullivan, "Optimization of Estimated Restricted Regions of Attraction with Application to Power Electronic Converters and Systems," PhD Dissertation, Purdue University, May 2008
367. Wan X. and Karniadakis G.E., "Recent Advances in Polynomial Chaos Methods", NATO Workshop, Dec 3-7, Athens, Greece. Proceeding of the RTO AVT-147 Symposium on Computational Uncertainty.
368. Taylor, J.A., and F.S. Hover, "High Dimensional Stochastic Simulation and Electric Ship Models," IEEE Electric Ship Technologies Symposium, Arlington, Virginia, June 2007, 402-407.
369. Greytak, M., and F. Hover, "Exponentially Stable Underactuated Dynamic Positioning of Marine Vehicles." Dynamic Positioning Conference 2007, Houston, TX, October 2007.
370. Prempraneerach P., F.S. Hover, M.S. Triantafyllou, T.J. McCoy, C. Chrysostomidis, and G.E. Karniadakis, "Sensitivity Analysis of the Shipboard Integrated Power System," ASNE Proceedings on Fuel Tank to Target: Building the Electric Fighting Ship, June 2007.
371. Ramsey, J.S., S.B. Leeb, T. Denucci, J. Paris, M. Obar, R. Cox, C. Laughman, T. McCoy, "Shipboard Applications of Non-Intrusive Load Monitoring," American Society for Naval Engineers Reconfiguration and Survivability Symposium, Orlando, FL, February 2005.
372. Greene, W.C., J.S. Ramsey, S.B. Leeb, T. Denucci, J. Paris, M. Obar, R. Cox, C. Laughman, T. McCoy, "Non-Intrusive Monitoring for Condition-Based Maintenance,"

- American Society for Naval Engineers Reconfiguration and Survivability Symposium, Orlando, FL, February 2005.
373. DeNucci, T, R. Cox, S.B. Leeb, J. Paris, T.J. McCoy, C.R. Laughman, W.C. Greene, "Diagnostic Indicators for Shipboard Systems using Non-Intrusive Load Monitoring," IEEE Electric Ship Technologies Symposium, Philadelphia, PA, July 2005.
 374. Cox, R.W., S.B. Leeb, S.R. Shaw, L.K. Norford, "Transient Event Detection for Nonintrusive Load Monitoring and Demand Side Management using Voltage Distortion," Applied Power Electronics Conference, Dallas, TX, March 2006.
 375. Cox, R.W., J.P. Mosman, D. McKay, S.B. Leeb, T. McCoy, "Diagnostic Indicators for Shipboard Cycling Systems Using Non-Intrusive Load Monitoring," American Society for Naval Engineers Day 2006, Arlington, VA, June 2006.
 376. Cox, R., P. Bennett, D. McKay, J. Paris, S.B. Leeb, "Using the Non-Intrusive Load Monitor for Shipboard Supervisory Control," IEEE Electric Ship Technologies Symposium, Arlington, VA, May 2007.
 377. Cox, R.W., M. Piber, G. Mitchell, P. Bennett, J. Paris, W. Wichakool, S.B. Leeb, "Improving Shipboard Maintenance Practices Using Non-Intrusive Load Monitoring," ASNE Intelligent Ships Symposium VII, Philadelphia, PA, May 2007.
 378. Wichakool, W., A. Avestruz, R.W. Cox, S.B. Leeb, "Resolving Power Consumption of Variable Power Electronic Loads Using Nonintrusive Monitoring," IEEE Power Electronics Specialists Conference, Orlando, FL, June 2007.
 379. G. Mitchell, R.W. Cox, M. Piber, , P. Bennett, J. Paris, W. Wichakool, S.B. Leeb, "Shipboard Fluid System Diagnostic Indicators Using Nonintrusive Load Monitoring," ASNE Day 2007, Arlington, VA June, 2007.
 380. Da Zhang, Hui Li, "Hybrid Stochastic and Neural Network Approach for Efficient FPGA Implementation of a Field-oriented Induction Motor Drive Controller ", Conf. Rec. IEEE IAS Annual Meeting 2006, Tampa, FL.
 381. Da Zhang, Hui Li, Simon Y. Foo," A Simplified FPGA Implementation of Neural Network Algorithms Integrated with Stochastic Theory for Power Electronics Applications", Conf. Rec. IECON 2005, pp. 1018-1023
 382. Da Zhang, Hui Li, "Hybrid Stochastic and FPGA Implementation of Machine Parameters Estimator for Motor Drive Control Application", Conf. Rec. 2nd International Conference on Cybernetics and Information Technologies, Systems and Applications (CITSA) 2005, Orlando, FL.
 383. Hui Li, Danwei Liu,"Power Distribution Strategy of Fuel Cell Vehicle System with Hybrid Energy Storage Elements Using Triple Half Bridge (THB) Bidirectional DC-DC Converter", IEEE IAS 2007, Sept. 2007, Page(s): 636-642
 384. Danwei Liu, Hui Li, "Design Of A 6 kW Multiple-Input Bidirectional DC-DC Converter With Decoupled Current Sharing Control For Hybrid Energy Storage Elements", IEEE APEC, Feb 2007, Page(s): 509-513
 385. Danwei Liu, Hui Li, "A Three-Port Three-Phase DC-DC Converter for Hybrid Low Voltage Fuel Cell and Ultracapacitor", IEEE IECON, Nov. 2006, Page(s): 2558-2563
 386. Da Zhang, Hui Li, "Hybrid Stochastic and Neural Network Approach for Efficient FPGA Implementation of a Field-oriented Induction Motor Drive Controller ",IAS 06 Proceedings, Vol. 4, Oct. 2006 Page(s): 1752 – 1759
 387. Da Zhang, Zhong Du, Hui Li, "Hybrid Modulation Control for Cascaded H-Bridges Multilevel Motor Drive System," presented at ASNE EMTS, Philadelphia, May, 2006
 388. Danwei Liu, Hui Li , "Design and Implementation of A DSP Based Digital Control System for A Dual Bridge Isolated Bi-directional DC-DC Converter," Proceeding of IEEE APEC 2006, Dallas, TX, Page(s): 5pp

389. Da Zhang, Hui Li, Simon Y. Foo, "A Simplified FPGA Implementation of Neural Network Algorithms Integrated with Stochastic Theory for Power Electronics Applications", IECON proceeding IECON 2005, Page(s): 1018-1023
390. Danwei Liu, Hui Li, "A Novel Multiple-Input ZVS Bidirectional DC-DC Converter", IECON proceeding IECON 2005, Page(s): 579-584
391. Danwei Liu, Hui Li, "Dynamic Modeling and Control Design for Bi-directional DC-DC Converter for Fuel Cell Vehicles with Battery as Energy Storage Element", proceeding of IEEE IAS Annual Meeting, 2005, Vol. 3, Page(s): 1632-1635
392. Da Zhang, Hui Li, "Hybrid Stochastic and FPGA Implementation of Machine Parameters Estimator for Motor Drive Control Application", presented at 2nd International Conference on Cybernetics and Information Technologies, Systems and Applications (CITSA) 2005, Orlando, July 14 - 17, 2005
393. Hui Li, Danwei Liu, "Small Signal Analysis of A Dual Half Bridge Isolated ZVS Bi-directional dc-dc converter for Electrical Vehicle Applications", proceeding of IEEE Power Electronics Specialist Conference 2005, Recife, Brazil, Page(s): 2777-2782
394. Hui Li, M. Steurer, D. Cartes, "Investigations on a 5-Level VSI-Chopper for a Superconductive Magnetic Energy Storage (SMES) Power Conditioning System," Conf. Rec. IECON, 2003, pp.531-537
395. Keli Shi, Hui Li, "An Optimized PWM Method using Genetic Algorithms," Conf. Rec. IECON, 2003, pp.7-11
- D. A. Cartes, and S. K. Srivastava, "Agent Applications and their Future in Power Industry," invited for IEEE Power Engineering Society General Meeting, 24-28 Jun 2006, Tampa.
396. K. Huang, D. Cartes, and S. K. Srivastava, "A Multi-agent Based Algorithm for Mesh-structured Shipboard Power System Reconfiguration," 13th International Conference on Intelligent Systems Application to Power Systems (ISAP), 2005.
397. S. K. Srivastava and D. A. Cartes, "Agent Technology Applied to Monitoring, Security and Diagnosis of Energy Systems", Proceedings of American Nuclear Society 10th International Conference on Robotics and Remote Systems for Hazardous Environments, 28 - 31 March 2004.
398. Kai Huang, David A. Cartes, Sanjeev K. Srivastava, "A Novel Algorithm for Reconfiguration of Shipboard Ring-structured Power System using Multi-Agent System" Reconfiguration & Survivability Symposium 2005, 16-18 February 2005, Jacksonville, FL.
399. K. Huang, D. A. Cartes, S. K. Srivastava, "A novel algorithm for agent based reconfiguration of ring-structured shipboard power system," Proceedings of IEEE Industry Application Society (IAS) 2005, Oct 2-6, 2005, Hong Kong, China, vol. 2, pp. 1311-1316.
400. K. Huang, D. Cartes, and S. K. Srivastava, "A multiagent based algorithm for ring-structured shipboard power system reconfiguration," Proceedings of IEEE International conference on System, Man and Cybernetic (SMC) 2005, Oct. 10-12, 2005, Big Island, HI, vol. 1, pp. 530-535.
401. K. Huang, S. K. Srivastava, and D. A. Cartes, "Agent Based Reconfiguration for Shipboard Power Systems," ASNE Automation and Control Symposium 2007, Biloxi, Mississippi, December 11-12, 2007.
402. K. Huang, S. Srivastava, D. A. Cartes, and L. Liu, "Agent Solutions for Navy Shipboard Power Systems," 2007 IEEE/SMC International Conference on System of Systems Engineering (SoSE), San Antonio, TX, April 16-18, 2007.
403. **K. Huang, S. K. Srivastava, and D. A. Cartes**, "Decentralized Reconfiguration for Power Systems using Multi Agent System," 1st Annual IEEE Systems Conference, April 9-12, 2007, Honolulu, Hawaii.
404. K. Huang, S. Srivastava, and D. A. Cartes, "Validation of Agent Based Reconfiguration Scheme Using Modeling and Simulation Approach," Summer Computer Simulation Conference 2007 (SCSC 2007), San Diego, California, July 15-18, 2007.

405. K. Huang, S. Srivastava, and D. A. Cartes, "A Multi-agent Based Algorithm for Mesh-structured Shipboard Power System Reconfiguration," 14th International Conference on Intelligent Systems Application to Power Systems (ISAP), Kaohsiung, Taiwan, November 4-8, 2007.
406. H. Wang, N. N. Schulz, D. Cartes, L.-H. Sun, and S. Srivastava, "System Reconfiguration Strategy for Shipboard Power Systems Using Multi-Agent Systems", Reconfiguration & Survivability Symposium 2005, 16-18 February 2005, Jacksonville, FL.
407. K. Huang, D. Cartes, and S. K. Srivastava, "A Solution for Information Accumulation in Multi-agent System for Reconfiguration of Shipboard Power System," Electric Machine Technology Symposium (EMTS) 2006, Philadelphia, PA, May 22-24, 2006.
408. G. Morejon, S. K. Srivastava, and D. A. Cartes, "Integrating Virtual Test Bed and JADE Agent platform Using CORBA for Reconfiguration of Shipboard Power Systems," IEEE Power Engineering Society General Meeting, 18-22 Jun 2006, Montreal, QC, Canada.
409. Z. Ding, S. K. Srivastava, D. A. Cartes, and S. Suryanarayanan, "Dynamic Simulation Based Analysis of a New Load Shedding Scheme for a Notional Destroyer Class Shipboard Power System," IEEE Electric Ship Technologies Symposium, ESTS 2007, May 21-23, Philadelphia.
410. Z. Ding, S. Srivastava, and D. Cartes, "Expert System based Dynamic Load Shedding Scheme for Shipboard Power Systems," IEEE Industry Applications Society 41st Annual Meeting 2006, Oct. 8-12, 2006, Tampa, FL, pp. 1338-1344.
411. Z. Ding, David A. Cartes, and S. Srivastava, "Expert System based Load Shedding of Shipboard Power Systems," Electric Machine Technology Symposium (EMTS) 2006, Philadelphia, PA, May 22-24, 2006.
412. Z. Ding, D. A. Cartes, and S. Srivastava, "New load shedding scheme for islanded power systems," Proceedings of 2006 IEEE/SMC International Conference on System of Systems Engineering (SoSE), Los Angeles, CA, April 24-26, 2006, pp. 167 – 172.
413. Li Liu, David A. Cartes, and Wenxin Liu, "Application of Particle Swarm Optimization to PMSM Stator Fault Diagnosis," accepted for presentation at IEEE World Congress on Computational Congress (WCCI 2006), Jul. 16-21, 2006, Vancouver, BC, Canada.
414. Li Liu, and David A. Cartes, "A Particle Swarm Optimization Approach for Automatic Diagnosis of PMSM Stator Fault," accepted for presentation at IEEE American Control Conference, Jun. 4-16, 2006, Minneapolis, MN, USA.
415. Li Liu, and David A. Cartes, "New Permanent Magnet Synchronous Motor Modeling Approach for Fault Diagnosis Purposes," accepted for presentation at ASNE Electric Machine Technology Symposium (EMTS 2006), May 22-23, 2006, Philadelphia, PA, USA.
416. Li Liu, Kevin P. Logan, and David A. Cartes, "Fault Detection, Diagnostics, and Prognostics: Software Agent Solutions," proceedings of 1st IEEE Symposium on Electric Ship Technologies (ESTS), pp. 425 – 431, 26-27 Jul. 25-27, 2005, Philadelphia, PA, USA.
417. Li Liu, and David A. Cartes, "On-line Identification and Robust Fault Diagnosis for Nonlinear PMSM Drives," proceedings of IEEE American Control Conference, pp. 2023 – 2027, Jun. 8-10, 2005, Portland, Oregon, USA.
418. Li Liu, and David A. Cartes, "Robust Fault Diagnosis for Electric Ship Propulsion Motors," CD-room proceedings of ASNE Intelligent Ship Symposium VI, June 1-2, 2005, Philadelphia, PA, USA.
419. Li Liu, and David A. Cartes, "Robust Fault Diagnosis with Parameter Adaptation Applied to Propulsion PMSM Motor Drives," CD-room proceedings of ASNE Advanced Naval Propulsion Symposium, Nov. 16-17, 2004, Herndon, Virginia, USA.
420. Lewei Qian, Li Liu, and David Cartes, "A Reconfigurable and Flexible Experimental Footprint for Control Validation in Power Electronics and Power Systems Research," accepted and presented at 2007 Power Electronics Specialist Conference (PESC'07), Orlando, FL, USA

421. Lewei Qian, David Cartes, Hui Li and Li Qi, "An Extended Adaptive Detection Method and Its Application in Power Quality Improvement," accepted and presented at 2007 IEEE Power Engineering Society General Meeting, Tampa, FL, USA.
422. Lewei Qian, D. Cartes, and Hui Li, "Experimental Verification and Comparison of MAFC Method and DQ Method for Selective Harmonic Detection Load," Proc. IEEE International Conference on Industrial Electronics (IECON'06), Paris, France, Nov. 2006.
423. Lewei Qian, David Cartes, Hui Li, "An Improved Adaptive Detection Method for Power Quality Improvement", conference record of 2006 IEEE 41st Industry Application Society Annual Meeting, Volume 2, Page(s): 1067 – 1072, 8-12 Oct. 2006.
424. Qiang Zhang, Lewei Qian, Chongwei Zhang and David Cartes, "Study On Grid Connected Inverter Used in High Power Wind Generation System", conference record of 2006 IEEE 41st Industry Application Society Annual Meeting, Volume 2, Page(s): 1053 – 1058, 8-12 Oct. 2006.
425. Li Qi, Lewei Qian, David Cartes, S. Woodruff, "Initial Results in Prony Analysis for Harmonic Selective Active Filters," IEEE Power Engineering Society 2006 General Meeting, Montreal, Canada, paper no. 1216.82
426. Wei Ren, Lewei Qian, David Cartes, M. Steurer, "A Multivariable Control Method in STATCOM Application for Performance Improvement," conference record of 2005 IEEE 40th Industry application Society Annual Meeting, Volume 3, Page(s):2246 – 2250, 2-6 Oct. 2005.
427. W. Ren, Lewei Qian, Yazhou Liu, M. Steurer, D. Cartes, "Real Time Digital Simulations Augmenting the Development of Functional Reconfiguration of PEBB and Universal Controller," Proceeding of American Control Conference, Portland, Oregon, June, 2005.
428. Lewei Qian, David Cartes and Qiang Zhang, "Three-Phase Harmonic Selective Active Filter Using Multiple Adaptive Feed Forward Cancellation Method", 2006 International Power Electronics and Motion Control Conference, Volume 2, Page(s):1 – 5, 14-16 Aug. 2006
429. Lewei Qian, David Cartes, Hui Li, and S. K. Srivastava, "A reconfigurable induction motor drive with harmonic cancellation feature," Proceedings of IEEE Electric Ship Technologies Symposium (ESTS) 2005, 25-27 July 2005, Philadelphia, PA, pp. 93 - 98.
430. Lewei Qian, David Cartes and Huui Li, "A Harmonic Selective Shunt Active Filter Using an Adaptive Control Method," American Society of Naval Engineers (ASNE), Reconfiguration & Survivability Symposium 2005.
431. Lewei Qian, D.Cartes and Hui Li, "A reconfigurable induction motor drive with selective harmonic cancellation," 2006 World Marine Technology Conference, London, UK.
432. Lewei Qian, David Cartes, Siyu Leng, "A Standardized Simulation and Real Time Hardware in the Loop Simulation Procedure for Power Electronics and Power Systems Research," 2007 Summer Computer Simulation Conference, San Diego, CA, USA.
433. J.V. C. Vargas, J.C. Ordonez, R. Hovsopian and F.G. Dias, "Modeling, Simulation and Optimization of a Solar System for Water Heating and Absorption Cooling," Proceedings of ES2008, ASME Energy Sustainability 2008, Jacksonville, FL, August 10-14, 2008
434. J.V. C. Vargas, J.C. Ordonez, R. Hovsopian and F.G. Dias, "All electric ships, internal compartments and cabinets thermal and psychrometric simulation," Grand Challenges in Modeling and Simulation, University of Edinburgh, Edinburgh, Scotland, June 16-19, 2008
435. J.V.C. Vargas, J.C. Ordonez and R. Hovsopian, Modeling and Simulation of the Thermal and Psychrometric Transient Response of All Electric Ships, Internal Compartments and Cabinets, 2007 Summer Computer Simulation Conference (SCSC'07), San Diego, CA, July 2007

436. N. Brooks, T. Baldwin, T. Brinson, J.C. Ordonez and C. Luongo , “Analysis of Fuel Cell Based Power Systems Using EMTDC Electrical Power Simulator”, Proceedings of the IEEE Thirty-Sixth Southeastern Symposium on System Theory, March 2004, 270-274.
437. R. Hovsopian, J.C. Ordonez, J.V.C. Vargas, P.G. McLaren, “Thermodynamic Analysis of a 5MW Dynamometer Set to Simulate Ship Propulsion and Propulsion Load of an All-electric Ship”, Proceedings of the Brazilian Congress of Thermal Engineering and Sciences - ENCIT, Curitiba, Brazil, 2006.
438. J. V. C. Vargas, J.C. Ordonez and A. Bejan, “Fuel Cells: Constructal Optimization and Research Perspectives”, ASME. Second International Conference on Fuel Cell Science, Engineering and Technology. Rochester, NY, 2004.
439. M. Mathur, A.P.Negoias, J.C. Ordonez, and A.M. Morega, “Thermal Stability of an HTS Armature Winding,” Proceedings of the Fluent Users Group Meeting, Sinaia, Romania, March 30-31, 2006.
440. A.M. Morega, J.C. Ordonez. “A higher resolution, local thermal analysis of an ac armature winding of a high temperature superconductor motor”, Paper IMECE2006-13825, 2006 ASME International Mechanical Engineering Congress and Exposition, IEMEC-2006, Nov. 5-10, Chicago, Illinois, USA
441. A. Morega, J.C. Ordonez and J.V.C. Vargas. “Thermal model for the AC armature winding of a High Temperature Superconductor Airborne Motor”, ASME-IMECE. Orlando, November, 2005.
442. A. Morega, J.C. Ordonez., “Thermal Stability of an HTS AC Armature Winding”, FEMLAB Conference. Boston, MA, Oct. 23-25, 2005.
443. A.M. Morega and J.C. Ordonez, “Constructal Design of Concurrent Power Distribution Networks”, Proceedings of the COMSOL Users Conference, Boston, 2006.
444. A. Morega, J.C. Ordonez, A.P. Negoias and R. Hovsopian, “Spherical Photovoltaic Cells: A Constructal Approach to their Optimization”, Proceedings of the 10th International Conference on Optimization of Electrical and Electronic Equipment, OPTIM’06, Brasov, Romania, May 18-19, 2006.
445. J.C. Ordonez, J.V.C. Vargas and S. Chen, “Optimal Heat Exchanger Area Allocation for Power and Refrigeration”, 18th International Conference on Efficiency, Cost, Optimization, Simulation and Environmental Impact of Energy Systems. ECOS, Trondheim, Norway, 2005.
446. J.C. Ordonez and S. Chen, “ Maximum Power Extraction from a Hot Stream in the Presence of Phase Change Under Limiting Collecting Temperatures”, Proceedings of HT-FED 2004. ASME Heat transfer/ Fluids Engineering Summer Conference, Charlotte, NC, 2004.
447. J. C. Ordonez and J.V.C. Vargas, “Constructal Optimization of the Coupling Between a Hot and a Cold Stream for Power and Refrigeration”, IMECE2004-62102. ASME International Mechanical Engineering Congress and Exposition, November 13-20, 2004, Anaheim, California USA.
448. W. Wechsato, S. Lorente, A. Bejan, J.C. Ordonez and S.C. Kosaraju, “Optimization of Elemental Flow Passages of Fluid Flow Networks”, Proceedings of the 13th International Heat Transfer Conference, Sydney, Australia, 13-18 August, 2006

9.1.Inventions

1. S.D. Sudhoff, J.L. Cale, US Patent Application 11/807,196, “Methods and Apparatus for Characterizing Magnetic Properties of Materials”

2. S. Pekarek, P. Beccue, "Rotor Position Sensing Apparatus and Method Using Piezoelectric Sensor and Single Hall Effect Sensor," Patent Application Submitted December 2007.
3. TechID # 08-115: J.V.C. Vargas, J. Gardolinski, J.C. Ordonez and Z. Hovsapiian, "Alkaline Membrane Fuel Cell (AMFC)", Florida State University, Feb., 2008.

9.2.Honors

1. IEEE Instrumentation and Measurement Technology Conference (IMTC'07) Student Travel Award – Taekhyun Kim, Edward J. Powers, W. Mack Grady and Ari Arapostathis, "A Novel QPC Detector for the Health Monitoring of Rotating Machines."
2. Barbara Matta – (support staff) 2007 Bagley College of Engineering Outstanding Research Support Award, Mississippi State University.
3. Noel Schulz – 2007 Outstanding Engineering Educators Award, Mississippi State University
4. Stanislaw Grzybowski – Recognition of the Fellow of the EMC Society, Mississippi State University
5. Yamilka Baez-Rivera (PhD student) - 2007 Outstanding Graduate Woman Award, Mississippi State University
6. Konstantin Borisov (PhD student) – 2007 Bagley College of Engineering Outstanding Graduate Student, Mississippi State University
7. Stanislaw Grzybowski – 2007 Career Achievement Award, Bagley College of Engineering, Mississippi State University
8. Noel Schulz elected as Secretary of the IEEE Power Engineering Society, 2004-2007; elected Treasurer of the IEEE Power Engineering Society, November 2007
9. Sarika Khushalani, PhD student won 1st place in the student paper contest at the IEEE PES Transmission and Distribution Conference and Exposition in May of 2006.
10. Sudhoff, 2008 Fellow, IEEE
11. Sudhoff, 2006 IEEE Power Engineering Society Cyril Veinott Electromechanical Energy Conversion Award for outstanding contributions to the field of electromechanical energy conversion.
12. Dr. Roger Dougal received the Gregory Professorship in the spring of 2007.
13. Dr. Roger Dougal received the College of Engineering Research Achievement Award in April 2007.
14. Dr. Antonello Monti received the Mungo Undergraduate Teaching Award in April 2007.
15. Dr. Antonello Monti received the College on Engineering Research Progress Award in April 2007.
16. Dr. Dougal was the keynote speaker at the SCS Summer Simulation Multiconference.
17. Modeling of IGBT Resistive and Inductive Turn on Behavior, Proceedings of the IEEE 40th Industry Applications Society Annual Meeting (IAS'05), L. Lu, S.G. Pytel, E. Santi, A. Bryant, J.L. Hudgins, P.R. Palmer, pp. 2643-2650, Hong Kong, Oct. 2005. (IAS Portnoy award winner given by the Power Electronics Devices and Components Committee of IAS)
18. Dr. Dougal, Dr. Monti and Dr. Ponci have been invited to present a paper on VTB for ship design at next IEEE PES Annual Meeting
19. Dr. Monti and Dr. Dougal have been invited to present a paper at next IEEE ISIE conference for a special session on Real Time simulation.
20. Elected as member of the Editorial Advisory Board of the Journal Thermal Engineering Institution to: Dr. Juan C. Ordonez of Florida State University

- from: Brazilian Society of Mechanical Sciences and Engineering.
21. First Place Oral Presentation Award (Engineering Category), Graduate Student Day
to: Ms. Kinjal Patel of University of South Carolina
from: The Graduate School, University of South Carolina Graduate Student Day provides graduate students an opportunity to present their scholarly and creative work. Graduate students are expected to describe their work and its potential value to society as well as answer brief questions from the judges.
 22. Recognition of his dedication and invaluable contributions to the Society
to: Dr. Edward Powers of The University of Texas at Austin
from: ISOPE (The International Society of Offshore and Polar Engineers)
In June 2005, Dr. Edward Powers was the recipient of an ISOPE (The International Society of Offshore and Polar Engineers) Award “in recognition of his dedication and invaluable contributions to the Society as a member of the Board of Directors, 2003-2005.
 23. IEEE Fellow to: Dr. Kent Davey of The University of Texas at Austin from: Institute of Electrical and Electronics Engineers
 24. TVA Endowed Professorship in Power Systems Engr. to: Dr. Noel N. Schulz of Mississippi State University from: TVA (Tennessee Valley Authority) Endowed Professor with discretionary funding
 25. G.E. Karniadakis received the 2007 CFD award by the US Association in Computational Mechanics (USACM).

9.3. Book or Chapters

1. “Time-frequency analysis of electric power disturbances,” E.J. Powers, Y.-J. Shin, and W.M. Grady, Time-Frequency Signal Analysis and Processing: a Comprehensive Reference, B. Boashash, Editor, chapter 15.1, pp. 628-634, Elsevier, Oxford, UK, 2003 (ISBN: 0-08-044335-4).
2. A.M. Morega and J.C. Ordonez, “Multiphysics Modeling and Simulation in Engineering,” In: Recent Advances in Modeling and Simulation, I-Tech Education and Publishing KG, Vienna, Austria, EU. pp. 337-360, 2008

10. PERSONNEL STATISTICS (OCT 2002 – MARCH 2008)

Total Number of Co-PI (45)

FSU-	11
USC -	7
UT- Austin	8
MSU	10
MIT	4
PU/USNA	5

- No of Woman Co-PI (5)
- No of Minority Co-PI (1)

Total Number of Students working on the grant

- Total Graduate (228)
 - Woman Graduate Students (52)
 - Minority Graduate Students (18)
- Total Undergraduate (69)
 - Woman Undergraduate Students (15)
 - Minority Undergraduate Students (8)
- Total Post Docs (44)
 - Woman Post Docs (12)
 - Minority Post Docs (02)
- Number of degrees granted during this report period (127)
 - MS: 79
 - PhD: 48

- [ⁱ] Y.-J. Shin, A. Monti, F. Ponci, A. Arapostathis, W.M. Grady, E.J. Powers, and R.A. Dougal, "Virtual power quality analysis for ship power system design," *Proc. of IEEE Instrumentation and Measurement Technology Conference*, Como, Italy, Vol. 3, pp. 1758-1763, May 18-20, 2004.
- [ⁱⁱ] Y.-J. Shin, E.J. Powers, W.M. Grady, A. Arapostathis, "Power quality indices for transient disturbances," *IEEE Trans. on Power Delivery*, Vol. 21, No. 1, Jan. 2006, pp. 253-261.
- [ⁱⁱⁱ] Y.-J. Shin, E.J. Powers, W.M. Grady, and A. Arapostathis, "Determination of transient disturbance energy flow in electric power systems via cross time-frequency distribution," *Proc. of SPIE-Advanced Signal Processing Algorithms, Architectures, and Implementations X*, Denver, Colorado, USA, August 2004.
- [^{iv}] Y.-J. Shin, E.J. Powers, T.-S. Choe, C.-Y. Hong, E.-S. Song, J.-G. Yook, and J.B. Park, "Application of time-frequency domain reflectometry for detection and localization of a fault on a coaxial cable," *IEEE Trans. on Instrumentation and Measurement*, Vol. 54, No. 6, December 2005, pp. 2493-2500.
- [^v] T.-S. Choe, C.-Y. Hong, E.S. Song, J.-G. Yook, J.-B. Park, Y.-J. Shin, and E.J. Powers, "Detection and estimation of a fault on coaxial cable via time-frequency domain reflectometry," *IEEE Instrumentation and Measurement Technology Conference*, Vail, Colorado, USA, May 20-22, 2003, pp. 190-195.
- [^{vi}] Y.-J. Shin, E.J. Powers, T.-S. Choe, S.-H. Sung, J.-G. Yook, and J.-B. Park, "Evaluation of the fault impedance in coaxial cable via time-frequency domain reflectometry," *Proc. of the SPIE-Advanced Signal Processing Algorithms, Architectures, and Implementations XIII*, Vol. 5205, San Diego, California, August 3-8, 2003, pp. 38-46.
- [^{vii}] T. Kim, E.J. Powers, W.M. Grady, and A. Arapostathis, "Real and reactive power analysis for interharmonics," *Proc. of IEEE Electric Ship Technology Symposium*, Philadelphia, USA, July 25-27, 2005, pp. 244-247.
- [^{viii}] T. Kim, E.J. Powers, W.M. Grady, and A. Arapostathis, "Robust interharmonic detection in adjustable speed drives using cross bicoherence," *Proc. of 12th IEEE International Conference on Harmonics and Quality of Power*, Cascais, Portugal, October 1-5, 2006, pp. 378-383.
- [^{ix}] T. Kim, A. Wang, E.J. Powers, W.M. Grady, and A. Arapostathis, "Detection of light flicker caused by high-frequency interharmonics" *Proc. of IEEE Instrumentation and Measurement Technology Conference*, Warsaw, Poland, May 1-3, 2007, pp.1-5.
- [^x] T. Kim, E.J. Powers, W.M. Grady, and A. Arapostathis, "Detection of flicker caused by interharmonics," submitted to *IEEE Trans. on Instrumentation and Measurement*, 2007.
- [^{xi}] T. Kim, M.R. Rylander, E.J. Powers, W.M. Grady, and A. Arapostathis, "LED lamp flicker caused by interharmonics," accepted to the *IEEE International Instrumentation and Measurement Technology Conference*, Victoria, British Columbia, Canada, May 12-15, 2008.
- [^{xii}] B. Jang, C. Shin, E.J. Powers, and W.M. Grady, "Machine fault detection using bicoherence spectra," *Proc. of IEEE Instrumentation and Measurement Technology Conference*, Como, Italy, Vol. 3, pp. 1661-1666, May 18-20, 2004.
- [^{xiii}] H. Park, B. Jang, E.J. Powers, W.M. Grady, and A. Arapostathis, "Machine condition monitoring utilizing bispectral change detection," *Proc. IEEE Power Engineering Society General Meeting (PES'07)*, Tampa, FL, Jun. 2007, pp.1-6.
- [^{xiv}] H. Park, E.J. Powers, W.M. Grady, and A. Arapostathis, "Condition monitoring based on estimating the complex coupling coefficients," accepted to the *IEEE International Instrumentation & Measurement Technology Conference*, Victoria, BC, Canada, May 12-15, 2008.
- [^{xv}] T. Kim, W. Cho, E.J. Powers, W.M. Grady, and Ari Arapostathis, "ASD system condition monitoring using cross bicoherence," *Proc. of IEEE Electric Ship Technology Symposium*, Arlington, VA, USA, May 21-23, 2007, pp. 378-383.
- [^{xvi}] T. Kim, E.J. Powers, W.M. Grady, and A. Arapostathis, "A novel QPC detector for the health monitoring of rotating machines," *Proc. of IEEE Instrumentation and Measurement Technology Conference*, Warsaw, Poland, May 1-3, 2007, pp.1-6.
- [^{xvii}] T. Kim, E.J. Powers, W.M. Grady, and A. Arapostathis, "A novel QPC detector for the health monitoring of rotating machines," submitted to *IEEE Trans. on Instrumentation and Measurement*, 2007.
- [^{xviii}] Cohn, Anthony G. "Qualitative Reasoning." *Advanced Topics in Artificial Intelligence (Lecture Notes in Computer Science*, volume 345.) New York, NY: Springer, 1988, 60-95.
- [^{xix}] Kuipers, Benjamin. "Qualitative Simulation." In: R. A. Meyers (Ed.), *Encyclopedia of Physical Science and Technology*, Third Edition, New York, NY: Academic Press, 2001.
- [^{xx}] Struss, Peter, "Problems of Interval-Based Qualitative Reasoning D.S.Weld and de Kleer (Eds.), *Readings in Qualitative Reasoning About Physical Systems*, pp.288-305. San Mateo, CA: Morgan Kaufmann, 1990.
- [^{xxi}] P. J. Hayes, "The Second Naive Physics Manifesto." In: J. Hobbs and B. Moore (Eds.), *Formal Theories of the Commonsense World*, pp.1--36. Norwood, NJ: Ablex, 1985. Also in: Weld and de Kleer (Eds.), *Readings in Qualitative Reasoning About Physical Systems*, pp.46-63. San Mateo, CA: Morgan Kaufmann, 1990.
- [^{xxii}] B. Kuipers, "Qualitative reasoning", MIT Press
- [^{xxiii}] D.G. Bobrow, "Qualitative Reasoning about Physics systems", MIT Press
- [^{xxiv}] R.E.Moore, *Interval Analysis*, Prentice Hall, Englewood Cliffs, NJ, 1996.
- [^{xxv}] N.Femia,G.Spagnuolo, M.Vitelli: "Tolerance design of dc-dc switching regulators", IEEE-ISCAS 2002.

-
- [^{xxvi}] P. Balaban, J. J. Golembki, "Statistical Analysis for Practical Circuit Design". *IEEE Trans. Circuits & Systems*. Vol cas-22, no.2, pp100-108, February 1975.
- [^{xxvii}] N. Femia, & G. Spagnuolo, True Worst-Case Circuit Tolerance Analysis Using Genetic Algorithms and Affine Arithmetic. *IEEE Transactions on Circuits and Systems*, Vol 47,NO 9. September 2000, 1285-1296.
- [^{xxviii}] R.G. Ghanem, 1999. Ingredients for a general purpose stochastic finite element formulation. *Comp. Meth. Appl. Mech. Eng.* Vol. 168: 19-34.
- [^{xxix}] R.G Ghanem., & P. Spanos, 1991. *Stochastic finite elements: a spectral approach*, Springer-Verlag.
- [^{xxx}] N. Wiener, "The homogeneous chaos", *Amer J. Math*, 1938, Vol. 60, pp. 897-936
- [^{xxxi}] R.H. Cameron, W.T. Martin, "The orthogonal development of non-linear functionals in series of Fourier-Hermite functionals", *Ann. Math.*, 1948, vol. 48, page 385.
- [^{xxxii}] M. Loeve , *Probability theory*, Fourth edition. Springer-Verlag, 1977
- [^{xxxiii}] D. Xiu, & G.E. Karniadakis, The Wiener-Askey polynomial chaos for stochastic differential equations. *SIAM J. Sci. Comput.*, vol. 24, pp. 619-644, 2002
- [^{xxxiv}] R. Askey, & J. Wilson, 1985. Some basic hypergeometric polynomials that generalize Jacobi polynomials. *Memoirs Amer. Math. Soc.*, AMS, Providence RI, 319
- [^{xxxv}] D. Xiu, & G.E. Karniadakis, 2002b. Modeling uncertainty in flow simulations via generalized polynomial chaos. *J. Comput. Phys.* , vol 187, pp. 137-167, 2003.
- [^{xxxvi}] D. Xiu, D. Lucor, Su, C.-H. & Karniadakis, G.E. 2002. Stochastic modeling of flow-structure interactions using generalized polynomial chaos, *J. Fluid Eng.* Vol. 124: 51-59
- [^{xxxvii}] T.E. Lovett, F. Ponci and A. Monti, "A Polynomial Chaos Approach to Measurement Uncertainty", *IEEE Transactions on Instrumentation and Measurement*, vol. 55, no. 3, June 2006, 729-736
- [^{xxxviii}] A. Smith, A. Monti, F. Ponci, "Uncertainty And Worst Case Analysis For A Low-Pass Filter Using Polynomial Chaos Theory", *IEEE AMUEM 2007*, Trento, Italy, July 2007
- [^{xxxix}] G. D'Antona, A. Monti, F. Ponci and L. Rocca, "Maximum Entropy Multivariate Analysis of Uncertain Dynamical Systems Based on the Wiener-Askey Polynomial Chaos", *IEEE Transactions on Instrumentation and Measurement*, vol. 56, no. 3, June 2007, 689-695.
- [^{xl}] T.Lovett, A.Monti, F.Ponci: "A Polynomial Chaos Theory Approach to the Control Design of a Power Converter", in *Proc. IEEE PESC 04*, 2004, pp. 4809-4813
- [^{xli}] Smith A., Monti A., Ponci F, "Robust Controller Using Polynomial Chaos Theory", on *Proceeding of IEEE IAS 2006*, Tampa, FL (USA), October 2006.
- [^{xlii}] A.H.C. Smith, A. Monti, F. Ponci, "Robust Stability and Performance Analysis using Polynomial Chaos Theory", *Society of Computer Simulation Summer Conference*, July 2007, Pages 45-52
- [^{xliiii}] P. Voglewede, A. Monti, "Variation Analysis of a Two-Planar Manipulator Using Polynomial Chaos Theory", *Mechanisms and Robotics Conference*, Philadelphia, Sep. 2006.

-
- [^{xdiv}] A.H.C. Smith, A. Monti and F. Ponci, "Indirect Measurements via a Polynomial Chaos Observer", IEEE Transactions on Instrumentation and Measurement, vol 56, no. 3, June 2007, 743-752.
- [^{xv}] A.Monti, F.Ponci, T.Lovett: "A Polynomial Chaos Theory Approach to Uncertainty in Electrical Engineering", invited to IEEE Intelligent Systems Application to Power Systems (ISAP) 2005, Nov. 7-10, Washington DC, USA, pgg. 534-539
- [^{xvii}] L. O. Chua, P.-M. Lin, *Computer-aided Analysis of Electric Circuits : Algorithms and Computational Techniques*. Englewood Cliffs, New Jersey : PRENTICE-HALL, INC, 1975.
- [^{xviii}] Sandu, A., Sandu, C., and Ahmadian, M., "Modeling multibody dynamic systems with uncertainties. Part I: Theoretical and computational aspects," *Multibody System Dynamics*, vol. 15, no. 4, pp. 369–391, May 2006a.
- [^{xix}] Sandu, A., Sandu, C., and Ahmadian, M., "Modeling multibody dynamic systems with uncertainties. Part II: Numerical applications," *Multibody System Dynamics*, vol. 15, no. 3, pp. 241–262, April 2006b.
- [^{xx}] Prempraneerach, Pradya, "Uncertainty analysis in a shipboard integrated power system using multi-element polynomial chaos", PhD Thesis, MIT, 2007 available at <http://dspace.mit.edu/handle/1721.1/40364>
- [I] S. Vijlee, "Optimizing a system of gas turbine engines and generators for marine power generation," Master's thesis, The University of Texas at Austin, May 2006.
- [ⁱ] K. Pesyna, R. Hebner, A. Ouroua, R. Thompson, and E. Bowles, "High-speed generator options for direct coupled gas turbine flight and ground based power system," presentation at the 8th Annual Directed Energy Symposium, Hawaii, USA, 14-18 November 2005.
- [ⁱⁱ] D. Clayton and T. Doyle, "Propulsion cross-connect on DDG 51," ASNE Advanced Naval Symposium 2006, Arlington, Virginia, USA 30-31 October 2006.
- [ⁱⁱⁱ] J.L. Rutledge, D.R. Robertson, and D.G. Bogard, "Degradation of film cooling performance on a turbine vane suction side due to surface roughness," ASME Gas Turbine Expo, GT2005-69045, Reno, Nevada, June, 2005.
- [^{iv}] J.L. Rutledge, D. Robertson, and D.G. Bogard, "Degradation of film cooling performance on a turbine vane suction side due to surface roughness," *ASME J. of Turbomachinery*, Vol. 128, 2006, pp. 547-554.
- [^v] R.P. Somawardhana and D.G. Bogard, "Effects of surface roughness and near hole obstructions on film cooling effectiveness," ASME Gas Turbine Expo, paper GT2007-28004, Montreal, Canada, May, 2007.
- [^{vi}] R.P. Somawardhana and D.G. Bogard, "Effects of obstructions and surface roughness on film cooling effectiveness with cylindrical holes and holes embedded in a transverse trench," *ASME J. of Turbomachinery*, 2007.
- [^{vii}] P. Demling, and D.G. Bogard, "The effects of obstructions on film cooling effectiveness on the suction side of a gas turbine vane," ASME Gas Turbine Expo, paper GT2006-90577, Barcelona, Spain, May, 2006.
- [^{viii}] S.K. Wayne and D.G. Bogard, "High resolution film cooling effectiveness measurements of axial holes embedded in a transverse trench with various trench configurations," *ASME J. of Turbomachinery*, Vol. 129, No. 2, pp. 294-302, 2007.
- [^{ix}] J.M. Cutbirth, and D.G. Bogard, "Effects of coolant density ratio on film cooling performance on a vane," ASME Paper No. GT2003-38582, 2003.
- [^x] M.I. Ethridge, J.M. Cutbirth, and D.G. Bogard, "Scaling of performance for varying density ratio coolants on an airfoil with strong curvature and pressure gradient effects," *J. of Turbomachinery*, Vol. 123, pp. 231-237, 2001.
- [^{xi}] B. Sen, D.L. Schmidt, and D.G. Bogard, "Film cooling with compound angle holes: heat transfer," *ASME J. of Turbomachinery*, Vol. 118, No. 4, pp. 800-806, 1996.
- [^{xii}] D.G. Bogard, D. Snook, and A. Kohli, "Rough surface effects on film cooling of the suction side surface of a turbine vane," ASME Paper No. IMECE2003-42061, 2003.
- [^{xiii}] J.E. Dees, "Effects of regular and random roughness on the heat transfer and skin friction coefficient on the suction side of a gas turbine vane," Master's Thesis, The University of Texas at Austin, 2006.
- [^{xiv}] J.E. Wammack, J. Crosby, D. Fletcher, J.P. Bons, and T.H. Fletcher, "Evolution of surface deposits on a high pressure turbine blade, Part I: Physical characteristics," ASME Paper No. GT2006-91246, 2006.
- [^{xv}] D.G. Bogard, D.L. Schmidt, M. Tabbita, "Characterization and laboratory simulation of turbine airfoil surface roughness and associated heat transfer," *J. of Turbomachinery*, Vol. 120, pp. 337-342, 1998.
- [^{xvi}] Kent Davey, "Fault analysis on a naval power grid using equivalent impedances," IASME Transactions, Vol. 1, No. 2, pp. 247-252, April 2004.
- [^{xvii}] Kent R. Davey and Robert E. Hebner, "A new strategy for representation and control of self-contained power systems," IEEE Transactions on Power Delivery, Vol. 21, No. 3, pp. 1558-1564, July 2006.
- [^{xviii}] A. Arapostathis, "Safe and stable dynamic reconfiguration for preventive and restorative regulation of power systems – a hybrid control approach," Control Methodologies for Reconfigurable Power Systems in Future Electric Ships Section I, Center for Electromechanics, Austin, TX, 2004.